Electronic Matrix Elements and Their Derivatives for Radiative and Non-Radiative Rate Constants: Development and Applications

---

Inaugural-Dissertation

zur

Erlangung des Doktorgrades der

Mathematisch-Naturwissenschaftlichen Fakultät

der Heinrich-Heine-Universität Düsseldorf

vorgelegt von

Fabian Meitza, geb. Dinkelbach

aus Krefeld

Düsseldorf, April, 2023

aus dem Institut für Theoretische Chemie und Computerchemie
der Heinrich-Heine-Universität Düsseldorf

Gedruckt mit der Genehmigung der
Mathematisch-Naturwissenschaftlichen Fakultät der
Heinrich-Heine-Universität Düsseldorf

Berichterstatter:

1. Univ.-Prof. Dr. Christel M. Marian
2. PD Dr. Oliver Weingart

Tag der mündlichen Prüfung: 19.06.2023

Eidesstattliche Erklärung

Ich versichere an Eides Statt, dass die Dissertation von mir selbständig und ohne unzulässige fremde Hilfe unter Beachtung der „Grundsätze zur Sicherung guter wissenschaftlicher Praxis an der Heinrich-Heine-Universität Düsseldorf“ erstellt worden ist. Die aus fremden Quellen direkt oder indirekt übernommenen Gedanken sind als solche gekennzeichnet. Die Dissertation wurde in der vorliegenden oder in ähnlicher Form noch bei keiner anderen Prüfungsbehörde eingereicht. Es wurden keine früheren erfolglosen Promotionsversuche unternommen.

Meerbusch, den

There is no way that you can ever really repeat something. I have this great belief that the magic of the moment can never be recaptured.

Brian May

Summary

The design of efficient organic light-emitting diodes (OLEDs) requires a thorough understanding of the emitter's excited state processes. To obtain high internal quantum efficiencies (IQE), harvesting of all excitons is necessary which typically is achieved by employing thermally activated delayed fluorescence (TADF) and phosphorescence emitters. One major downside of these emitters is their slow emissive channel enabling exciton loss by non-radiative deactivation processes. To bypass the slow emission, hyperfluorescent and hyperphosphorescent emitter systems utilize TADF and phosphorescent molecules in combination with excitation energy transfer (EET) to populate the singlet moiety of a fluorophore.

In this thesis, new tools and methods are developed to supply electronic matrix elements as well as their gradients for the evaluation of radiative and non-radiative rate constants. Herein the newly developed DensityEngine plays a central role supplying spin-conserving as well as spin-flip reduced one-electron transition density matrices for configuration interaction singles (CIS) and density functional theory / multi-reference configuration interaction (DFT/MRCI) wave functions. In general, these density matrices can be utilized to obtain electric transition dipole moments, spin–orbit coupling matrix elements (SOCMEs) and excitonic coupling matrix elements (ECMEs) required to describe emission, intersystem crossing (ISC) and EET processes.

To treat vibronic effects, first-order derivatives of these properties are available through the newly developed Gradienator tool. The Gradienator is utilized throughout this thesis to determine emissive and ISC rate constants employing the Herzberg–Teller (HT) approximation for systems like pyrazine, 2CzPN and heptazines. Pyrazine and the investigated heptazines are particularly interesting as their molecular symmetry imposes strong constraints on the emission and ISC processes.

Spoiler, a program to obtain SOCMEs from linear-response time-dependent density functional theory (TDDFT) was extended to allow the evaluation of phosphorescence rate constants. In good agreement with the benchmark of 2017, Spoiler shows that SOCMEs and ISC rate constants can be obtained in the framework of TDDFT as long as no charge-transfer (CT) states, Rydberg states or states with important double excitations are involved. The performance for phosphorescence applications remains to be tested.

To calculate triplet excitation energy transfer (TEET) rate constants, the monomer transition density (MTD) method was extended with the new singlet-triplet density matrices. Additionally, well established diabatization schemes like Boys and Edmiston–Ruedenberg (ER) diabatization were implemented. Applying the methods to a set of bridged donor-acceptor systems revealed that the MTD implementation was missing important short-range electron transfer contributions. Utilizing the ethylene dimer as a much simpler system, the missing contributions were identified and implemented. Since the current implementation is limited to a HOMO-LUMO picture, further studies are necessary to generalize the approach.

In addition to the developed methods and their applications, a set of triarylboranes showing room temperature phosphorescence (RTP) was investigated. Typically, RTP is observed in purely organic compounds only if atoms with lone pairs are present, which following El-Sayed's rule speed up ISC by introducing low-lying $n \rightarrow \pi^*$ excitations. ISC in the triarylboranes is enabled by the boron center's empty p-orbital and competes with fluorescence, while environmental constraints are required to efficiently suppress non-radiative deactivation channels.

Zusammenfassung

Die Entwicklung effizienter organischer Licht-emittierender Dioden (OLEDs) erfordert ein tiefgreifendes Verständnis der Prozesse angeregter Zustände. Effiziente Emitter zeichnen sich durch eine hohe interne Quantenausbeute (IQE) aus, welche die Konversion von möglichst vielen Exzitonen in Photonen voraussetzen. Thermisch aktivierte verzögerte Fluoreszenz (TADF) und phosphoreszente Emitter erlauben eine IQE von 100 %, verlieren jedoch viele Exzitonen durch strahlungslose Desaktivierungsprozesse, welche mit den langsamen Emissionskanälen konkurrieren können. Um die langsame Emission zu umgehen, werden TADF und phosphoreszente Emitter mit einem fluoreszenten Emitter zu einem hyperfluoreszentem bzw. hyperphosphoreszenten Emittersystem kombiniert. Diese Systeme erlauben es, mithilfe von Energietransferprozessen den schnellen Emissionskanal des Fluorophors zu verwenden.

In dieser Arbeit wurden neue Werkzeuge und Methoden zur Ermittlung von elektronischen Matrixelementen sowie deren Gradienten für die Berechnung von strahlenden und strahlungslosen Ratenkonstanten entwickelt. Hierbei spielt die neu entwickelte Programmbibliothek DensityEngine eine zentrale Rolle in der Verfügbarmachung von Spin-erhaltenden und Spin-verändernden reduzierten Einelektronenübergangsdichtematrizen zur Ermittlung von elektronischen Übergangsdipolmomenten, Spin–Bahn- (SOCMEs) sowie exzitonischen Kopplungsmatrixelementen (ECMEs). Diese Matrixelemente finden im weiteren Verlauf Verwendung, um Ratenkonstanten strahlender und strahlungsloser Prozesse zu erhalten.

Vibronische Effekte können dabei mithilfe der Herzberg–Teller Näherung berücksichtigt werden, welche die Kenntnis der Ableitungen der genannten Matrixelemente voraussetzt. Zur Ermittlung dieser Ableitungen kann der neu entwickelte Gradienator eingesetzt werden, ein Werkzeug, welches im Rahmen mehrerer Publikationen zur Behandlung vibronischer Effekte in Systemen wie Pyrazin, 2CzPN sowie Heptazin genutzt wurde. Pyrazin und Heptazin sind besonders interessant, da in diesen Systemen starke Symmetriebeschränkungen die Emission und Interkombination (ISC) beeinflussen.

In einem weiteren Projekt wurde Spoiler, ein Programm zur Ermittlung von SOCMEs für Amplituden der zeitabhängigen Dichtefunktionaltheorie (TDDFT) erweitert, um Phosphoreszenzratenkonstanten berechnen zu können. Spoiler zeigt mit guter Übereinstimmung zum Benchmark von 2017, dass SOCMEs und ISC Ratenkonstanten im Rahmen von TDDFT ermittelt werden können, solange keine Charge-Transfer (CT)- oder Rydberg Zustände und Zustände mit nicht vernachlässigbaren Doppelanregungscharakter involviert sind. Die Anwendung auf Phosphoreszenz steht noch aus.

Im Energietransfer-Projekt wurde der MTD Ansatz zur Berechnung von Triplett-Triplett Energietransfer (TEET) Ratenkonstanten unter Benutzung der neu verfügbaren Singulett-Triplett Dichtematrizen erweitert. Zusätzlich wurden bereits etablierte Diabatisierungsmethoden wie die Boys und Edminston–Ruedenberg (ER) Diabatisierung implementiert. Ein Benchmark mit verbrückten Donor-Akzeptor Systemen zeigt, dass Beiträge wichtiger kurzreichweitiger Elektronentransferprozesse innerhalb der MTD Methode nicht berücksichtigt werden. Anhand des Ethylen Dimers, einem deutlich weniger komplizierten System, wurden die fehlenden Beiträge identifiziert und implementiert. Die möglichen Anwendungen sind derzeit stark limitiert, da ein HOMO-LUMO Ansatz in der Implementierung verwendet wird und daher eine Generalisierung des Ansatzes erforderlich ist.

Zusätzlich zu der Methodenentwicklung und deren Anwendung wurde eine Gruppe von Triarylboranen untersucht, welche Raumtemperaturphosphoreszenz (RTP) zeigen. RTP kann

in rein organischen Verbindungen auftreten, wenn Heteroatome mit freien Elektronenpaaren enthalten sind. Diese Atome sorgen für tief liegende $n \rightarrow \pi^*$ Anregungen welche nach El-Sayed's Regel zu einem schnelleren ISC führen. Die untersuchten Triarylborane enthalten keine Atome mit freien Elektronenpaaren, jedoch wird ISC mit konkurrenzfähiger Geschwindigkeit zur Fluoreszenz durch das leere p-Orbital am Bor-Zentrum ermöglicht. Zusätzlich sind Umgebungseffekte notwendig, um strahlungslose Desaktivierungsprozesse effektiv zu unterdrücken.

Danksagung

An dieser Stelle möchte ich mich bei allen Personen bedanken, die mich während der Promotion begleitet und unterstützt haben.

Zuerst möchte ich mich besonders bei meiner Doktormutter Prof. Dr. Christel M. Marian für die Möglichkeit und Betreuung meiner Promotion bedanken. Ihre herausragende Expertise und professioneller Rat hat mir stets weitergeholfen.

Mein Dank gilt auch PD Dr. Oliver Weingart für die Übernahme des Zweitgutachtens sowie die Unterstützung in vielen Fragen rund um Gaussian.

Prof. Michael Schmidt möchte ich dafür danken, dass er sich als Mentor zur Verfügung gestellt hat.

Auch möchte ich mich beim gesamten Arbeitskreis der TC für die gute und produktive Atmosphäre bedanken. Besonders Dr. Martin Kleinschmidt gilt hier mein Dank dafür, dass er sich immer Zeit genommen hat um fachliche und technische Fragen zu beantworten. Ebenfalls Danke an meine Bürokolleginnen und Bürokollegen für die gute Zeit und die spannenden Teepausengespräche.

Der Deutschen Forschungsgesellschaft (DFG) möchte ich für die finanzielle Unterstützung dieser Promotion durch das Graduiertenkolleg ModISC (Projektnummer 396890929/GRK 2482) danken.

Vielen Dank auch an die Korrekturleser, meine Familie und besonders an meine Frau Carina für die viele Unterstützung.

Contents

1 Introduction **1**
- 1.1 Organic Light-Emitting Diodes . . . 1
- 1.2 Transitions Between Electronic States . . . 2
- 1.3 Structure of the Thesis . . . 5

2 Theory **9**
- 2.1 Density Functional Theory . . . 9
- 2.2 Configuration Interaction Singles . . . 11
- 2.3 Time-Dependent Density Functional Theory . . . 12
- 2.4 Second Quantization . . . 15
- 2.5 Configuration State Functions . . . 16
- 2.6 Auxiliary Many-Electron Wave Functions . . . 17
- 2.7 DFT/MRCI . . . 18
- 2.8 Reduced Density Matrices . . . 21
- 2.9 Relativistic Effects . . . 22
  - 2.9.1 Spin–Orbit Mean-Field Operator . . . 22
  - 2.9.2 Spin–Orbit Coupling Quasi-Degenerate Perturbation Theory . . . 24
  - 2.9.3 DFT/MRSOCI . . . 24
- 2.10 Radiative and Non-Radadiative Rate Constants . . . 25
  - 2.10.1 Non-Radiative Rate Constants . . . 26
  - 2.10.2 Radiative Rate Constants . . . 27
- 2.11 Excitation Energy Transfer . . . 28
  - 2.11.1 Förster Resonance Energy Transfer . . . 28
  - 2.11.2 Excitonic Coupling In The Two-Level System . . . 29
  - 2.11.3 Diabatization Approaches . . . 30
  - 2.11.4 Monomer Transition Density Approach . . . 31
  - 2.11.5 Electron Transfer Contributions . . . 33

3 Room Temperature Phosphorescence **35**
- 3.1 Persistent RTP from Triarylboranes . . . 37
- 3.2 Aggregation-induced dual phosphorescence from o-BrTAB . . . 39

4 Reduced One-Electron Density Matrices **43**
- 4.1 The DensityEngine . . . 45
- 4.2 The CsfEngine . . . 48
  - 4.2.1 Genealogical CSF Construction . . . 49
  - 4.2.2 CSF Construction from Subsystems . . . 50

4.3 The Densomat : DFT/MRCI Density Matrices . . . 51
4.4 TheoDORE Extension – Analysis of Triplet States . . . 53

5 Vibronic Coupling **55**
5.1 Numerical Gradients . . . 55
5.2 Phase Corrections . . . 56
5.2.1 Phase Correction Utilizing Reference Matrix Elements . . . 56
5.2.2 Phase Correction of Pure-Spin Wave Functions . . . 58
5.2.3 Phase Corrections for Mixed-Spin Wave Functions . . . 60
5.3 Implementations . . . 62
5.3.1 Extension of the SNF Program for SPOILER . . . 62
5.3.2 Python Scripts for Vibronic Coupling . . . 62
5.3.3 The GRADIENATOR . . . 63
5.4 Vibronic and Spin–Orbit Coupling Effects in Pyrazine . . . 66
5.5 Intersystem Crossing in the 2CzPN Emitter . . . 69
5.6 Intersystem Crossing in Heptazine Derivatives . . . 71

6 Spin–Orbit Coupling from Linear Response TDDFT (SPOILER) **75**
6.1 Implementation . . . 76
6.2 Usage . . . 80
6.3 2017 Benchmark . . . 82
6.4 2022 Benchmark . . . 84
6.4.1 Extended SOCME Benchmark . . . 84
6.4.2 Applications for ISC Rate Constants . . . 89

7 Excitation Energy Transfer **95**
7.1 Redesign and Extension of the Programs . . . 97
7.1.1 IDA Mode . . . 98
7.1.2 MTD Modes . . . 98
7.1.3 Diabatization Modes . . . 103
7.1.4 SpectralOverlap Mode . . . 105
7.2 TEET Donor–Bridge–Acceptor Systems . . . 106
7.3 The Ethylene Dimer . . . 110
7.4 Generalization of the MTD-TI Approach . . . 112

8 Conclusions **117**

A Appendix **131**
A.1 Spoiler 2022 Benchmark: Computational Data . . . 131
A.2 Derivation Of Matrix Elements For Excitonic Couplings . . . 139
A.3 TEET Donor-Bridge-Acceptor Systems: Computational Data . . . 144
A.4 The Ethylene Dimer: Computational Data . . . 154

B Included Papers **157**

List Of Publications

Included in this thesis

1. **Persistent Room Temperature Phosphorescence from Triarylboranes: A Combined Experimental and Theoretical Study**
   Angew. Chem. Int. Ed., **2020**, 59, 17137-17144
   Zhu Wu, Jörn Nitsch, Julia Schuster, Alexandra Friedrich, Katharina Edkins, Marcel Loebnitz, Fabian Dinkelbach, Vladimir Stepanenko, Frank Würthner, Christel M. Marian, Lei Ji and Todd B. Marder

   Contributions: Calculation of one triarylborane compound, supervision assistance of the master thesis of Marcel Loebnitz, creation of figures, supporting information for one triarylborane compound, proofreading of the manuscript.

2. **Aggregation-induced dual phosphorescence from (o-bromophenyl)-bis(2,6-dimethylphenyl)borane at room temperature**
   Chem. Eur. J., **2022**, 28, e202200525
   Zhu Wu, Fabian Dinkelbach, Florian Kerner, Alexandra Friedrich, Lei Ji, Vladimir Stepanenko, Frank Würthner, Christel M. Marian and Todd B. Marder

   Contributions: All calculations, all theoretical figures, theoretical part of the supporting information, draft of the theoretical results, proofreading of the manuscript.

3. **Vibronic and spin–orbit coupling effects in the absorption spectra of pyrazine: A quantum chemical approach**
   J. Serb. Chem. Soc., **2019**, 84, 819-836
   Fabian Dinkelbach and Christel M. Marian

   Contributions: Implementation of numerical gradients for vibronic coupling (Python Scripts/SOMEGRAD), all calculations, all figures, first draft

4. **Intersystem crossing processes in the 2CzPN emitter: a DFT/MRCI study including vibrational spin–orbit interactions**
   Phys. Chem. Chem. Phys., **2021**, 23, 3668-3678
   Angela Rodriguez-Serrano, Fabian Dinkelbach and Christel M. Marian

   Contributions: Implementation of numerical gradients for vibronic ISC (Gradienator), calculation of the numerical gradients, implementation of DFT/MRCI singlet-triplet density matrices, extension of TheoDORE for the analysis of triplet

states using the correct DFT/MRCI singlet-triplet density matrices, proofreading of the manuscript.

5. **Large Inverted Singlet–Triplet Energy Gaps Are Not Always Favorable for Triplet Harvesting: Vibronic Coupling Drives the (Reverse) Intersystem Crossing in Heptazine Derivatives**
   J. Phys. Chem. A, **2021**, 125, 10044-10051
   Fabian Dinkelbach, Mario Bracker, Martin Kleinschmidt and Christel M. Marian

   Contributions: Implementation of numerical gradients for vibronic fluorescence/phosphorescence (GRADIENATOR), implementation of the GRADIENATOR interface to Mario Brackers DELTA program, all calculations, all figures, first draft

Not included in this thesis

6. **Impact of fluorination on the photophysics of the flavin chromophore: a quantum chemical perspective**
   Phys. Chem. Chem. Phys., **2019**, 21, 9912-9923
   Mario Bracker, Fabian Dinkelbach, Oliver Weingart and Martin Kleinschmidt

   Contributions: Guidance in using the computational tools and check of the obtained results (Python Scripts/SOMEGRAD), development of the normal mode fitting procedure together with Mario Bracker, proofreading of the manuscript.

7. **Vibronic effects accelerate the intersystem crossing processes of the through-space charge transfer states in the triptycene bridged acridine–triazine donor–acceptor molecule TpAT-tFFO**
   Chem. Sci., **2022**, 13, 7057
   Jeremy Kaminski, Angela Rodriguez Serrano, Fabian Dinkelbach, Hector Miranda-Salinas, Andrew P. Monkman and Christel M. Marian

   Contributions: Guidance in using the computational tools (GRADIENATOR) and check of the obtained results, proofreading of the manuscript.

8. **Conformational, host and vibrational effects giving rise to dynamic TADF behavior in the through-space charge transfer, triptycene bridged acridine-triazine donor acceptor TADF molecule TpAT-tFFO**
   J. Phys. Chem. C., **2022**, submitted Hector Miranda-Salinas, Angela Rodriguez-Serrano, Jeremy Kaminski, Fabian Dinkelbach, Nakagawa Hiromichi, Yu Kusakabe, Hironori Kaji, Christel M. Marian and Andrew Monkman

   Contributions: Guidance in using the computational tools (GRADIENATOR) and check of the obtained results, proofreading of the manuscript.

List of Abbreviations

2CzPN 4,5-di(9H-carbazol-9-yl)-phthalonitrile.

ADC2 algebraic diagrammatic construction scheme.

ALDA adiabatic local density approximation.

AMEW auxiliary many-electron wave function.

B3-LYP Becke-3 Lee–Yang–Parr hybrid density functional.

BH-LYP Becke Half and Half Lee–Yang–Parr hybrid density functional.

BrTAB (bromophenyl)-bis(2,6-dimethylphenyl)borane.

CASPT2 complete active space perturbation theory.

CASSCF complete active space self-consistent field.

cc-pVTZ-PP correlation-consistent triple-zeta basis set for pseudo potentials.

CDCB carbazolyl dicyanobenzene.

CI configuration interaction.

CIS configuration interaction singles.

CISD configuration interaction singles and doubles.

CPU central processing unit.

CSF configuration state function.

CT charge-transfer.

Cz carbazole.

DCB dicyanobenzene.

def-SV(P) Karlsruhe split-valence basis set with polarization functions on all atoms except hydrogen.

def2-SVP Karlsruhe split-valence basis set with polarization functions on all atoms.

defpp-ecp relativistic pseudopotential.

DFT density functional theory.

DFT/MRCI density functional theory / multi-reference configuration interaction.

DFT/MRSOCI density functional theory / multi-reference spin–orbit coupling interaction.

DRTP dual room temperature phosphorescence.

DSCF direct self-consistent field.

ECME excitonic coupling matrix element.

EET excitation energy transfer.

EQE external quantum efficiency.

ER Edmiston–Ruedenberg.

ET electron transfer.

FC Franck–Condon.

FCD fragment charge difference.

FED fragment excitation difference.

FRET Förster resonance energy transfer.

HAP-3MF 2,5,8-tris(4-fluoro-3-methylphenyl)-1,3,4,6,7,9,9b-heptaazaphenalene.

HF Hartree–Fock.

HOMO highest occupied molecular orbital.

HT Herzberg–Teller.

Hz heptazine.

IC internal conversion.

ICT intermolecular charge-transfer.

IDA ideal dipole approximation.

IQE internal quantum efficiency.

ISC intersystem crossing.

IST inverted singlet-triplet.

ITO indium-tin-oxide.

LE local excitation.

LED light-emitting diode.

LUMO lowest unoccupied molecular orbital.

LYP Lee–Yang–Paar.

m-BrTAB (meta-bromophenyl)-bis(2,6-dimethylphenyl)borane.

MCSCF multi-configuration self-consistent field.

MRCI multi-reference configuration interaction.

MRCI/CIS configuration interaction singles calculation utilizing the DFT/MRCI program.

MRMP2 multi-reference Møller–Plesset second-order perturbation theory.

MTD monomer transition density.

MTD-TI monomer transition density combined with transfer integral.

MTD-ORTHO monomer transition density with orthogonalization corrections.

NACME nonadiabatic coupling matrix element.

NRMSD normalized root-mean-square deviation.

o-BrTAB (ortho-bromophenyl)-bis(2,6-dimethylphenyl)borane.

OLED organic light-emitting diode.

OpenMP open multi-processing library for loop- and function-level parallelization.

p-BrTAB (para-bromophenyl)-bis(2,6-dimethylphenyl)borane.

PBE0 Perdew–Burke–Ernzerhof hybrid density functional.

PCM polarizable continuum model.

PMMA polymethylmethacrylate.

PN phthalonitrile.

RI resolution-of-the-identity.

RI-SOMF spin–orbit mean field operator utilizing the resolution of the identity approach for two-electron integrals.

RI-CC2 coupled-cluster model CC2 using the resolution-of-the-identity approximation.

RISC reverse intersystem crossing.

RMSD root-mean-square deviation.

RT room temperature.

RTP room temperature phosphorescence.

SCF self-consistent field.

SEET singlet excitation energy transfer.

SOC spin–orbit coupling.

SOCME spin–orbit coupling matrix element.

SOCQDPT spin–orbit coupling quasi-degenerate perturbation theory.

SOMF spin–orbit mean-field.

SVP split-valence basis set with polarization functions on all atoms.

TAB triarylborane.

TADF thermally activated delayed fluorescence.

TDA Tamm–Dancoff approximation.

TDC transition density cube.

TDDFT time-dependent density functional theory.

TDFI transition-density-fragment interaction.

TDFI-TI transition-density-fragment interaction combined with transfer integral.

TDHF time-dependent Hartree–Fock.

TEET triplet excitation energy transfer.

TI transfer integral.

TSEET triplet–singlet excitation energy transfer.

TXB tris(2,6-dimethylphenyl)borane.

TZVP valence triple-zeta basis set with one set of polarization functions on all atoms.

TZVPP valence triple-zeta basis set with two sets of polarization functions on all atoms.

VWN Vosko–Wilk–Nusair.

1 Introduction

1.1 Organic Light-Emitting Diodes

Illumination plays a crucial role in our 24/7 society with key applications in area lights, displays and safety signs. To drive these technologies, efficient and affordable luminescent devices are required. Improvement of these devices is a 'hot' topic where organic light-emitting diodes (OLEDs) are especially central to current research. OLEDs are optoelectronic devices utilizing organic emitter systems to convert electric charge into photons. Their unique selling points are true black states in display applications and the manufacturing of flexible devices. They do however struggle to achieve comparable brightness to inorganic light-emitting diodes (LEDs) and their high operational stability.[1] The basic structure of OLED devices utilized today (Fig. 1.1) was proposed by Tang and Van Slyke in 1987 requiring at least four layers.[2] The bottom layer is a transparent anode composed of indium-tin-oxide (ITO) glass providing holes and allowing light to exit the device while the top layer is the cathode supplying electrons. On top of the ITO glass, a layer of aromatic diamine forms the hole transportation layer followed by the emission layer of a flurophore (Alq_3) where the electrons and holes recombine to excitons driving the emission of light.[1,2]

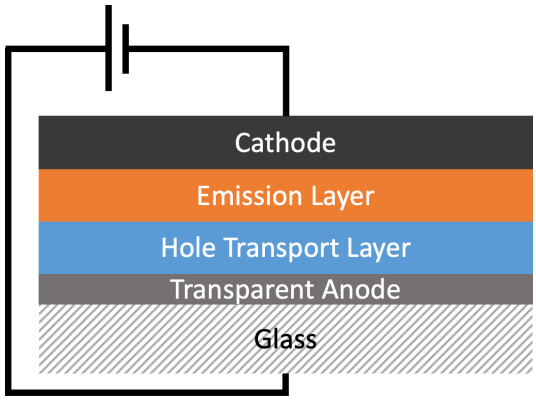

Figure 1.1: Diagram of the OLED structure proposed by Tang and Van Slyke.[2]

The devices' ability to produce light is measured as internal quantum efficiency (IQE) and external quantum efficiency (EQE). The IQE is used to describe the emitters' ability to convert electric excitations into light.[1] To reach a high IQE, the emitter has to harvest both singlet and triplet excitons, which are generated during electrical excitation due to spin-statistics as 25 % singlets and 75 % triplets.[1,3,4] Additionally, a fast emission pathway is required to reduce exciton loss due to non-radiative deactivation processes. The EQE measures the whole devices' ability to produce light considering effects like reflections and

self-absorption causing a lowered amount of extractable light. To improve OLEDs, one has to raise both efficiencies by either finding more suited emitter systems boosting the IQE or advancing the devices' design enhancing light extraction.[1]

1.2 Transitions Between Electronic States

The search for well suited emitter systems requires knowledge of the emitter's excited state kinetics offering an understanding of the emission's origin as well as guidance for chemical alterations improving the system's exciton to photon conversion. Central to the study of excited state kinetics is the Jablonski diagram (Fig. 1.2) classifying the processes between ground and excited states.

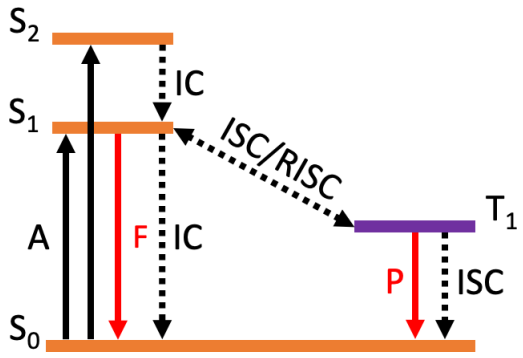

Figure 1.2: Simplified Jablonski diagram – dashed lines depict non-radiative transitions, red lines depict emission processes. The depicted radiative and non-radiative processes are Absorption (A), Fluorescence (F), Phosphorescence (P), Internal Conversion (IC) and (Reverse) Intersystem Crossing ((R)ISC).

- **Fluorescence (F)**: The fluorescence process drives chemical and biological sensors as well as day-to-day applications like fluorescent lamps and white LED lighting. Mechanistically, fluorescence is the radiative relaxation of an excited singlet state (S_n) to the ground state (S_0) which following Kasha's rule[5] originates in most systems from the first excited singlet state (S_1). As a typically fast process, fluorescence outperforms phosphorescence and internal conversion (IC) (Tab. 1.1) offering a reliable and efficient emission channel.

- **Phosphorescence (P)**: Phosphorescence plays an important role in applications such as biological imaging, anti-counterfeiting, illumination of watch dials and safety signs. Compared to fluorescence, phosphorescence is the spin-forbidden radiative relaxation of an excited triplet state (T_n) to the ground state (S_0). The conversion between singlet and triplet states is driven by spin–orbit coupling (SOC) typically requiring heavy elements to lift the spin restrictions. Due to its spin-forbidden nature, phosphorescence in organic systems is orders of magnitudes slower than fluorescence (Tab. 1.1) and therefore often only observed at low temperatures. Room temperature phosphorescence (RTP) is visible at room temperature (RT) and is a 'hot' topic these days especially with purely organic emitters systems.

- **Intersystem crossing (ISC)**: Intersystem crossing (ISC) drives the interconversion between states of differing multiplicity and is a key component in achieving high IQE

(> 25%) for OLED- and RTP systems. The radiationless and spin-forbidden process is similar to phosphorescence driven by SOC allowing to interconvert singlet to triplet states and vice versa. If the two states taking part in the interconversion are separated by a small energy barrier, ISC can occur in both directions. In this case, ISC is the favored process leading to the state lower in energy while the process leading to the energetically higher state is referred to as reverse intersystem crossing (RISC).

- **Internal conversion (IC)**: As opposed to ISC, internal conversion (IC) drives the de-excitation between states of equal multiplicity. Applications like OLEDs require emitter molecules with fast fluorescence or phosphorescence channels outperforming or at least competing with IC.

- **Excitation energy transfer (EET)**: Excitation energy transfer (EET) is a non-radiative process playing an important role in OLED devices,[6,7] bio-imaging[8] and structure determination of biomolecules.[9] Mechanistically, EET transfers the excitation energy of an excited system (donor) to an unexcited system (acceptor) where donor and acceptor can be two separate systems or two fragments of the same system. The excitation energy can be transferred following a resonance energy transfer mechanism de-exciting the donor, while simultaneously exciting the acceptor as described by Theodore Förster in 1948[10,11] or by short-range electron transfer processes proposed by David L. Dexter in 1953.[12]

Table 1.1: Radiative and non-radiative processes in excited fluorophores[13]

Process	Transition	Rate constant $[s^{-1}]$
Absorption	$S_1 \rightarrow S_n$, $T_1 \rightarrow T_n$	10^{15}
Fluorescence	$S_1 \rightarrow S_0$	$10^7 - 10^9$
Phosphorescence	$T_1 \rightarrow S_0$	$10^{-2} - 10^3$
Internal conversion	$S_n \rightarrow S_1$, $T_n \rightarrow T_1$	$10^{10} - 10^{14}$
Internal conversion	$S_1 \rightarrow S_0$	$10^6 - 10^7$
Intersystem crossing	$S_n \rightarrow T_n$, $T_n \rightarrow S_n$	$10^5 - 10^8$

The interplay of these processes can render an emitter suited for the application in OLEDs. Herein favorable decay pathways are classified as fluorescent, phosphorescent and thermally activated delayed fluorescence (TADF) emitters.

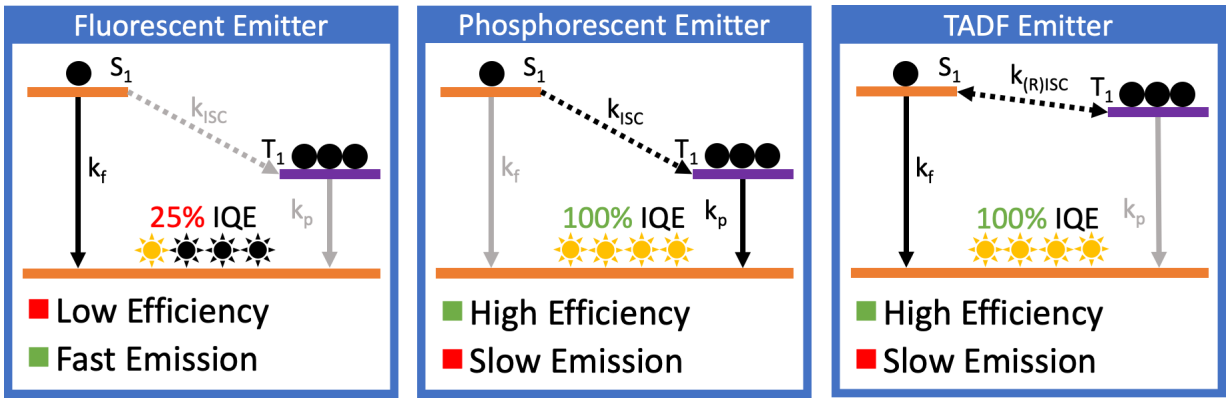

Figure 1.3: OLED emitter categories.

- **Fluorescence Emitter**: A fluorescence emitter utilizes the singlet state's radiative relaxation to the ground state for emission capping its theoretical IQE to 25 %. Due to the lack of SOC, the interconversion of singlet excitons to triplet excitons and vice versa is inhibited and phosphorescence is only visible at low temperatures. The lifetime of the excited singlet state is of the order of nanoseconds rendering the emission process fast and therefore allows to outperform non-radiative deactivation processes.[14,15] In contrast to their lacking IQE, fluorescent emitters are well researched and widely available offering high operational stability even for blue light applications.[16]

- **Phosphorescence Emitter**: In contrast to fluorophores, phosphorescent emitters can generate light from singlet and triplet excitons allowing a theoretical IQE of about 100 %. Herein heavy elements are used to lift the spin restrictions on ISC by SOC to convert singlets into triplets. Triplet lifetimes of phosphors are in the microsecond range enabling non-radiative deactivation processes to compete with the emission channel.[14,15,17] At low temperatures, these non-radiative deactivation processes can be inhibited, while at room-temperature aggregation effects can have a similar influence.[18,19] Phosphorescence emitters applied in OLEDs are known to suffer from low operational stability especially for blue OLEDs, where the lifetime of the cell is limited to about 1000 hours.[20]

- **Thermally Activated Delayed Fluorescence Emitter**: While phosphors use ISC to convert singlet excitons to triplet excitons, TADF emitters utilize the reverse process converting triplets to singlets. This RISC process is possible if the energy gap between the respective states is lower than $0.1-0.2\,\mathrm{eV}$ which can be achieved by minimizing the exchange interaction. Emitters utilizing RISC can overcome this small energy barrier at room temperature harvesting singlet and triplet excitons via a fluorescent emission channel with a theoretical IQE of about 100 %.[14,15]

TADF and phosphorescent emitters theoretically allow harvesting of all generated singlet and triplet excitons. The typical downside of these emitters is a slow emissive channel with lifetimes of the order of microseconds forcing emission to compete with non-radiative deactivation processes. To circumvent these processes and reduce the exciton loss, these emitters are paired with fluorophores such that the excitons can be transferred via EET to utilize the fluorophore's fast emission channel (Fig. 1.4).

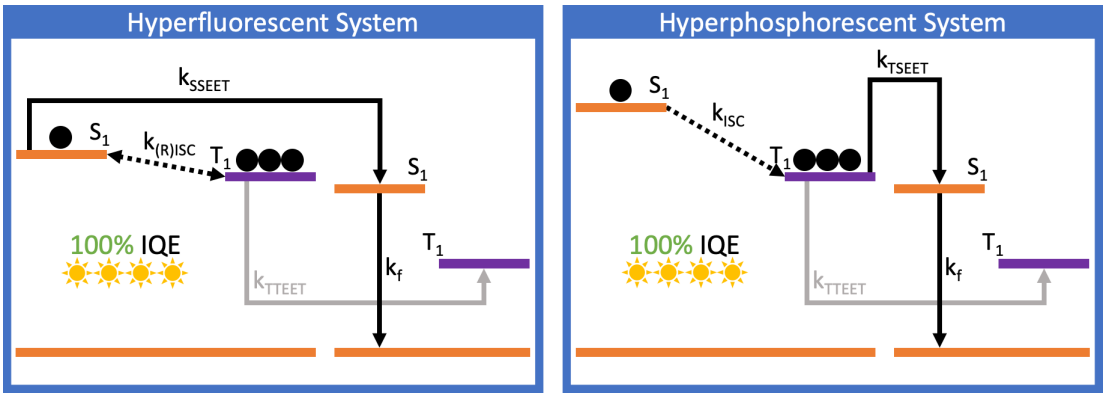

Figure 1.4: Hyperfluorescent (left) and hyperphosphorescent (right) system.

The combination of a TADF emitter and a fluorophore is known as hyperfluorescent emitter system and has proven to increase the OLED's quantum yield significantly by transferring the harvested excitons via singlet excitation energy transfer (SEET).[6,15] In the case of a phosphorescent emitter, the excitons are transferred by triplet–singlet excitation energy transfer (TSEET) from the phosphor's triplet state to the fluorophore, an emitter system known as hyperphosphorescence.[7] In both of these systems, triplet excitation energy transfer (TEET) should be avoided by design to prohibit exciton loss on the fluorophore.

To study the discussed emitter systems in a theoretical context, computational methods are required to describe the rate constants of the involved processes. Within this thesis, established methodologies are used and extended to describe the systems above.

1.3 Structure of the Thesis

Due to the widespread topics ranging from applications on RTP over method development and applications for emission and ISC processes including contributions by vibrational coupling as well as the extension of EET methodologies this thesis is split into six parts:

1. In the second chapter the theoretical foundations of the work presented in this thesis are established. Herein the computational methods central to the optimization of ground and excited state geometries as well as the determination of their respective properties are introduced. These methods are density functional theory (DFT) and its time-dependent variant (TDDFT) along with the density functional theory / multi-reference configuration interaction (DFT/MRCI) computational scheme. Furthermore, the evaluation of excited state properties utilizing reduced one-electron (transition) density matrices is laid out which is used throughout this thesis to obtain spin–orbit coupling matrix elements (SOCMEs) in addition to electric transition dipole moments. These properties play an important role in the determination of the rate constants given in Table 1.1 which can be obtained in a static picture employing the Franck–Condon (FC) approximation or in a dynamic picture utilizing the Herzberg–Teller (HT) formalism incorporating the property's first-order derivatives. The chapter is closed by the introduction of methodologies concerned with the evaluation of EET. Herein established diabatization schemes as well as the monomer transition density (MTD) approach are explained.

2. In the third chapter the work and publications on RTP are presented. RTP, especially from pure organic compounds, is a 'hot' topic as it has many applications in daily life. Herein the conditions for RTP to occur as well as two cooperative studies with experimental groups from Würzburg, Manchester and Xi'an are presented. In the first study a group of triarylboranes is investigated with respect to their emission mechanism where two of the compounds show RTP. The second study enhances RTP in one of these triarylboranes by introducing bromine into the system speeding up the ISC and phosphorescence processes.

3. The fourth chapter presents the evaluation of reduced one-electron (transition) density matrices and their usage in quantum chemistry and applications throughout this work. Density matrices pose a useful tool to obtain expectation values of quantum

mechanical operators or for the purpose of wave function analysis. In this thesis, these density matrices are utilized heavily in the evaluation of SOCMEs within the Spoiler program (Chapter 6), the description of excitation energy transfer within diabatization schemes as well as within the MTD approach (Chapter 7). The DensityEngine and the Densomat will be presented, a library and a program that implements an efficient parallel computational scheme for the evaluation of density matrices employing methods like configuration interaction singles (CIS) and DFT/MRCI. The reduced one-electron (transition) density matrices, between singlet and triplet states play next to their application in the MTD method an important role for the analysis of DFT/MRCI wave functions in the TheoDORE program package.

4. Chapter five is dedicated to the investigation of vibrational effects on the system's radiative and non-radiative properties. These vibronic effects can be incorporated in quantum chemical calculations utilizing the HT formalism which employs the first-order derivatives of the quantum chemical operator's matrix elements with respect to a reference geometry. The Gradienator, a program developed to supply these derivatives in a numerical fashion, is presented and applied in multiple studies. The first publication discusses vibronic effects in pyrazine, where the singlet-singlet absorption spectra show clear evidence of vibronic coupling, while these effects are absent in the singlet-triplet absorption spectrum. Herein some light is shed on the interpretation of the absorption spectra as well as the location of the T_2 state where the literature reports contradicting insights. The second publication investigates the 4,5-di(9H-carbazol-9-yl)-phthalonitrile (2CzPN) molecule, a member of the carbazolyl dicyanobenzene (CDCB) family, which is heavily studied for applications as TADF emitter in OLEDs. The study clarifies the system's emission and (R)ISC processes showing a speed-up of the latter by a factor of 2 by vibronic coupling. The last publication on this topic presents heptazines which are known as systems exhibiting an inverted singlet-triplet (IST) gap, where the first excited singlet state resides energetically slightly below the first excited triplet state. Such systems are expected to efficiently populate the singlet moiety as the triplet to singlet ISC is a downhill process. The presented study finds, that a IST system is not always favorable for efficient (R)ISC and that vibronic coupling drives the emission and (R)ISC processes in heptazine (Hz) and its derivative 2,5,8-tris(4-fluoro-3-methylphenyl)-1,3,4,6,7,9,9b-heptaazaphenalene (HAP-3MF).

5. The sixth chapter introduces Spoiler, a program initially developed during my master's thesis which allows evaluating SOCMEs for time-dependent density functional theory (TDDFT) calculations. Spoiler has proven in a benchmark of 14 organic molecules to be almost on par with SOCMEs obtained at multi-reference Møller–Plesset second-order perturbation theory (MRMP2) and DFT/MRCI level. The chapter presents the 2017 Spoiler version and newly added extensions. The extensions include an interface to Gaussian[21] allowing users outside the Turbomole[22] community to utilize the program as well as extending the capabilities of Spoiler for the investigation of phosphorescence. Additionally, Spoiler can be used in combination with the Gradienator to supply inexpensive numerical SOCME gradients. A second benchmark extends the benchmark of 2017 to additional systems and actual applications, where ISC rate constants are compared to experimental results.

6. The last chapter discusses EET processes and methodologies to obtain energy transfer

rate constants. First the different processes are introduced and established methodologies utilized to evaluate rate constants for these processes are presented. The implementation of the MTD approach in the ExETracKt program package is shown in detail and a reimplementation as well as extensions to the program package are discussed. One of these extensions renders TEET accessible within the MTD method and is utilized together with implementations of diabatization schemes like BoysOV and Edmiston–Ruedenberg (ER) diabatization for a set of donor-acceptor systems to obtain their respective transfer rate constants. The comparison shows that short-range electron transfer processes play an important role for TEET and have to be incorporated to predict accurate transfer rates. The origin of the short-range electron transfer processes is discussed and a similar scheme to Fujimoto's transition-density-fragment interaction combined with transfer integral (TDFI-TI) approach[23] is implemented to show that these short-range contributions can be recovered for the ethylene dimer.

2 Theory

2.1 Density Functional Theory

Density functional theory (DFT) is rooted in the Thomas-Fermi method, a semiclassical quantum mechanic model for many-body problems developed in the 1920s.[24] The Thomas-Fermi method describes the system by its electron density $n(x)$ instead of each electron's coordinate, as embodied in the Hartree–Fock (HF) equations. The total energy in this method is given by:

$$E = \frac{3h^2}{10m_e}\left(\frac{3}{8\pi}\right)^{\frac{2}{3}} \int n(x)^{5/3}dx - e\int n(x)V_N dx - e\frac{1}{2}n(x)V_e dx + U_N \tag{2.1}$$

The terms are from left to right the kinetic energy of the electrons, the electron-nuclear attraction, the electron-electron repulsion and the nucleus-nucleus interaction.[24] The Thomas-Fermi method proved useful for the description of atoms even if harsh approximations were applied in the derivation of the kinetic energy term and the electron exchange was completely missing. The latter was introduced by Dirac leading to the Thomas-Fermi-Dirac method.[25]

In 1964, Hohenberg and Kohn paved the way for DFT with the two Hohenberg–Kohn theorems showing that the electron density can be used instead of the $3N$ electron coordinates to describe a system's ground state Ψ.[26]

1. To use the electron density instead of the electron coordinates one has to proof first that the electron density describes the ground state Ψ unambiguously. Assuming that a second ground state $\Psi^{'}$ exists with the same density $n(x)$ as Ψ, the energy of both states is evaluated by the following Hamiltonian,

$$\hat{\mathcal{H}} = \hat{\mathcal{T}} + \hat{\mathcal{V}} + \hat{\mathcal{U}} \tag{2.2}$$

$$\hat{\mathcal{T}} = -\frac{1}{2}\sum_i^N \nabla_i^2 \qquad \hat{\mathcal{V}} = \sum_i^N V(x_i) \qquad \hat{\mathcal{U}} = \sum_{i<j}^N U(x_i, x_j) \tag{2.3}$$

where $\hat{\mathcal{T}}$ is the kinetic energy of the electrons, $\hat{\mathcal{V}}$ is the influence of an external potential and $\hat{\mathcal{U}}$ is the electron-electron interaction. The energies E and $E^{'}$ of Ψ and $\Psi^{'}$ are then given by:

$$\begin{aligned} E &= \langle\Psi|\mathcal{H}|\Psi\rangle \\ E^{'} &= \langle\Psi^{'}|\mathcal{H}^{'}|\Psi^{'}\rangle \end{aligned} \tag{2.4}$$

Following the Rayleigh-Ritz principle, the ground state exhibits the lowest energy while all other state's energies are larger.

$$\begin{aligned} E &= \langle\Psi|\mathcal{H}|\Psi\rangle < \langle\Psi^{'}|H|\Psi^{'}\rangle \\ E^{'} &= \langle\Psi^{'}|\mathcal{H}^{'}|\Psi^{'}\rangle < \langle\Psi|H^{'}|\Psi\rangle \end{aligned} \tag{2.5}$$

Both expressions can be reformulated to contain the energies of both ground states.

$$\begin{aligned} E &< \langle\Psi^{'}|H^{'}|\Psi^{'}\rangle + \langle\Psi^{'}|H - H^{'}|\Psi^{'}\rangle = E^{'} + \langle\Psi^{'}|V - V^{'}|\Psi^{'}\rangle \\ E^{'} &< \langle\Psi|H|\Psi\rangle + \langle\Psi|H^{'} - H|\Psi\rangle = E + \langle\Psi|V^{'} - V|\Psi\rangle \end{aligned} \tag{2.6}$$

Adding the inequalities gives rise to a contradiction showing that no second ground state can exist for the same density $n(x)$ without degeneracies.

$$E + E^{'} < E + E^{'} \tag{2.7}$$

2. Secondly, it has to be proven that the energy functional $E_0[n(x)]$ has a minimum for the electron density $n(x)$ at the ground state's energy E and therefore a variation principle exists for the functional $E_0[n(x)]$. Following from the first theorem, the ground state's energy can be written as the functional $E_0[n(x)]$.

$$E_0[n(x)] = \int V(x)n(x)dx + F[n(x)] = \int V(x)n(x)dx + T[n(x)] + U[n(x)] \tag{2.8}$$

Where $T[n(x)]$ and $U[n(x)]$ are the functionals of the kinetic energy and electron-electron interaction respectively. Hohenberg and Kohn showed that the variation principle exists and for the correct electron density $n(x)$, $E_0[n(x)]$ is equal to the ground state energy E.

Kohn and Sham used the Hohenberg–Kohn theorems and introduced one-electron functions ϕ into the DFT theory to find expressions for the functional $F[n(x)]$.[27]

$$\begin{aligned} F[n(x)] &= T[n(x)] + U[n(x)] = T_s[n(x)] + J[n(x)] + E_{xc}[n(x)] \\ T_s[n(x)] &= \sum_i^N \left\langle \phi_i \middle| \left(-\frac{\hbar^2}{2m_e}\nabla_i^2 \right) \middle| \phi_i \right\rangle, \qquad J[n(x)] = \int\int \frac{n(x)n(x')}{|x-x'|}dxdx' \end{aligned} \tag{2.9}$$

The system of interacting electrons is herein approximated by a system of non-interacting electrons given by the one-electron functions ϕ. This allows for the division of $T[n(x)]$ into the kinetic energy of non-interacting electrons $T_s[n(x)]$ and a remainder $(T[n(x)] - T_s[n(x)])$. The known expression for the Coulomb interaction $J[n(x)]$ and the unknown remainders $(T[n(x)] - T_s[n(x)])$ as well as $(U[n(x)] - J[n(x)])$ are collected in the exchange-correlation functional $V_{xc}[n(x)]$. The energy functional is then given by:

$$E[n(x)] = \int V(x)n(x)dx + T_s[n(x)] + J[n(x)] + V_{ex}[n(x)] \tag{2.10}$$

Utilizing this formulation of the energy functional, Kohn and Sham derived the Kohn-Sham equations which, similar to the HF equations, have to be solved in a self-consistent manner.

$$\left(\frac{1}{2}\nabla_i^2 + V(x) + \int \frac{n(x')}{|x-x'|} + \frac{\delta E_{xc}[n(x)]}{\delta n(x)} \right)\psi_i = \epsilon_i\psi_i \tag{2.11}$$

It is important to note, that up to this point DFT is an exact theory. Applications however, require an evaluable expression for the exchange-correlation functional $V_{xc}[n(x)]$. Typical expressions are obtained semi-empirically by fitting to experimental data rendering the method an approximation.

Throughout this thesis the following hybrid density functionals were utilized:

- **B3-LYP**:[28]
  The B3-LYP functional combines the three-parameter Becke exchange functional with the Lee–Yang–Paar (LYP)[29] and Vosko–Wilk–Nusair (VWN)[30] correlation functionals with 20 % exact HF exchange.

$$E_{xc}^{B3LYP} = 0.8E_x^{Slater} + 0.2E_x^{HF} + 0.72E_x^{Becke} + 0.81E_c^{LYP} + 0.19E_c^{VWN} \tag{2.12}$$

- **PBE0**:[31,32]
  The PBE0 functional combines the original Perdew–Burke–Ernzerhof density functional with 25 % exact HF exchange.

$$E_{xc}^{PBE0} = 0.75(E_x^{Slater} + E_x^{PBE(x)}) + 0.25E_x^{HF} + E_c^{PW} + E_c^{PBE(c)} \tag{2.13}$$

- **BH-LYP**:[33]
  The BH-LYP functional combines the Becke exchange functional with the LYP correlation functional and 50 % exact HF exchange.

$$E_{xc}^{BHLYP} = 0.5(E_x^{Slater} + E_x^{Becke}) + 0.5E_x^{HF} + E_c^{LYP} \tag{2.14}$$

The B3-LYP and PBE0 functionals are mainly utilized in this thesis for the optimization of ground and excited state geometries, frequency analyses as well as obtaining excited state amplitudes for the use in auxiliary many-electron wave functions (AMEWs) within Spoiler. The BH-LYP functional is employed in all DFT/MRCI calculations conducted in the thesis and associated papers since the DFT/MRCI method is parametrized for this functional.

2.2 Configuration Interaction Singles

Configuration interaction singles (CIS) is an ab initio method extending the HF approach to excited states. Following Dreuw and Head-Gordon[34] the CIS equations can be derived as follows: Within configuration interaction (CI) the excited state's wave function is constructed as a linear combination of excited Slater determinants relative to a reference which is typically the ground state's determinant. Instead of including all possible excited determinants, CIS only allows single excitations relative to the reference into the wave function's linear combination.

$$\Psi_{CIS} = \sum_{ia} c_i^a |\Phi_i^a\rangle \tag{2.15}$$

Here Φ_i^a represents a single excited Slater determinant where an electron is moved from an occupied orbital ϕ_i to a virtual orbital ϕ_a. To obtain excited state wave functions, the CIS expansion Ψ_{CIS} is employed in the time-independent Schrödinger equation.

$$\begin{aligned} \hat{\mathcal{H}}\Psi_{CIS} &= E_{CIS}\Psi_{CIS} \\ \hat{\mathcal{H}}\sum_{ia} c_i^a|\Phi_i^a\rangle &= E_{CIS}\sum_{ia} c_i^a|\Phi_i^a\rangle \end{aligned} \tag{2.16}$$

Multiplication with $\langle\Phi_j^b|$ yields the projection onto the space of singly excited determinants.

$$\begin{aligned}\sum_{ia}\langle\Phi_j^b|\hat{\mathcal{H}}|\Phi_i^a\rangle c_i^a &= E_{CIS}\sum_{ia} c_i^a\langle\Phi_j^b|\Phi_i^a\rangle \\ \sum_{ia}[(E_0+\epsilon_a-\epsilon_i)\delta_{ij}\delta_{ab}+(ia||jb)]c_i^a &= E_{CIS}\sum_{ia} c_i^a\delta_{ij}\delta_{ab} \\ \sum_{ia}[(\epsilon_a-\epsilon_i)\delta_{ij}\delta_{ab}+(ia||jb)]c_i^a &= \omega_{CIS}\sum_{ia} c_i^a\delta_{ij}\delta_{ab}\end{aligned} \tag{2.17}$$

Where $\omega_{CIS} = E_{CIS} - E_0$ is the excitation energy, ϵ_i and ϵ_a are the orbital energies of the two orbitals involved in the single excitation and $(ia||jb)$ is the anti-symmetrized two-electron integral. Equation 2.17 can be rewritten in matrix representation to yield the CIS equation,

$$\mathbf{AX} = \omega\mathbf{X} \tag{2.18}$$

where ω is the diagonal matrix of the excitation energies, $\mathbf{X}$ is the matrix containing the expansion coefficients c_i^a and the matrix elements of $\mathbf{A}$ are given by:

$$A_{ia,jb} = (\epsilon_a-\epsilon_i)\delta_{ij}\delta_{ab}+(ia||jb) \tag{2.19}$$

Due to its limitation to singly excited Slater determinants, CIS is a very cost-efficient method allowing to investigate huge molecular systems, while the simplicity of the approach imposes some draw backs. CIS is known to overestimate excitation energies by about $0.5-2$ eV in comparison with experimental results. This overestimation is rooted in the HF mean-field approach calculating the orbital energies ϵ_a in the field of $N+1$ electrons.[34] Additionally, CIS does only yield qualitative transition dipole moments as it does not obey the Thomas–Reiche–Kuhn dipole sum rule.[34] CIS is used in this thesis mainly for proof of concept calculations and to visualize important couplings within an easy-to-understand scope.

2.3 Time-Dependent Density Functional Theory

Time-dependent density functional theory (TDDFT) is the extension of DFT for the description of excited states and their properties. To formulate a time-dependent theory based on DFT, the Hohenberg–Kohn theorems, which are only valid for the stationary ground state, have to be extended to the time–dependent regime.

$$i\frac{\partial}{\partial t}\Psi(x,t) = \hat{\mathcal{H}}(x,t)\Psi(x,t) \tag{2.20}$$

The Runge–Gross theorems represent this extension and use the time-dependent Schrödinger equation (Eq. 2.20) to prove that:[35]

1. The time-dependent wave function $\Psi(x,t)$ is a function of the electron density and is determined up to a constant as well as a time-dependent phase factor. Therefore, similar to the ground state, a one-to-one mapping exists between the potentials and functionals.

$$\Psi(x,t) = \Psi[n(x,t)](t)e^{-i\alpha(t)} \tag{2.21}$$

2. Analog to the second Hohenberg–Kohn theorem, a variational principle exists which is given by the action integral corresponding to a stationary point of the time-dependent Schrödinger equation.

$$A = \int_{t_0}^{t_1} dt \left\langle \Psi(x,t) \middle| i\frac{\partial}{\partial t} - \hat{\mathcal{H}}(x,t) \middle| \Psi(x,t) \right\rangle \tag{2.22}$$

Utilizing the first Runge–Gross theorem (Eq. 2.21) the action integral can be reformulated by means of density functionals:

$$A[n(x,t)] = \int_{t_0}^{t_1} dt \left\langle \Psi[n(x,t)](x,t) \middle| i\frac{\partial}{\partial t} - \hat{\mathcal{H}}(x,t) \middle| \Psi[n(x,t)](x,t) \right\rangle \tag{2.23}$$

The exact density of the stationary point can then be obtained using the Euler equation:

$$\frac{\partial A[n(x,t)]}{\partial n(x,t)} = 0 \tag{2.24}$$

As for the Hohenberg–Kohn theorems, the Kohn–Sham equations have a time–dependent variant too. The Kohn–Sham equations approximate the system of interacting electrons by a system of non-interacting electrons exhibiting in TDDFT the now time-dependent density $n_S(x,t)$ which is assumed to be equal to the exact electron density $n(x,t)$. The non-interacting system of electrons is given as a single Slater determinant constructed from the one-electron orbitals $\phi_i(x,t)$.

$$n(x,t) = n_S(x,t) = \sum_i |\phi_i(x,t)|^2 \tag{2.25}$$

The time-dependent Kohn–Sham equations are then given by

$$i\frac{\partial}{\partial t}\phi_i(x,t) = \left(-\frac{1}{2}\nabla_i^2 + V(x,t) + \int d^3x' \frac{n(x,t)}{|x-x'|} + \frac{\delta A_{XC}[n(x,t)]}{\delta n(x,t)} \right) \phi_i(x,t) \tag{2.26}$$

where $A_{XC}[n(x,t)]$ is the exchange-correlation part of the action integral. Similar to DFT, TDDFT is up to this point an exact theory. However, the correct expression for $A_{XC}[n(x,t)]$ is unknown and needs to be approximated. One of the approximations, the adiabatic local density approximation (ALDA), is the assumption that the density only changes slowly with respect to time allowing the substitution of $A_{XC}[n(x,t)]$ by a time-independent exchange-correlation functional $A_{XC}[n(x)]$.[34] Therefore, ALDA allows to employ the many known and established DFT functionals for TDDFT.

The time–dependent Kohn–Sham equations can be solved by means of linear response theory leading to a non-Hermitian eigenvalue problem and the central equation of linear response TDDFT:

$$\begin{pmatrix} \mathbf{A} & \mathbf{B} \\ \mathbf{B} & \mathbf{A} \end{pmatrix} \begin{pmatrix} \mathbf{X} \\ \mathbf{Y} \end{pmatrix} = \omega \begin{pmatrix} 1 & 0 \\ 0 & -1 \end{pmatrix} \begin{pmatrix} \mathbf{X} \\ \mathbf{Y} \end{pmatrix} \tag{2.27}$$

Here ω is a diagonal matrix containing the excitation energies and the amplitudes $\mathbf{X}$ and $\mathbf{Y}$ describe the excitation and de-excitation relative to the ground state reference. The definitions of the matrices $\mathbf{A}$ and $\mathbf{B}$ differ if pure- or hybrid density functionals are employed.

- **Pure density functional**:

$$\begin{aligned} A_{ia,jb} &= \delta_{ij}\delta_{ab}(\epsilon_a - \epsilon_i) + (ia|jb) + (ia|f_{xc}|jb) \\ B_{ia,jb} &= (ia|bj) + (ia|f_{xc}|bj) \end{aligned} \tag{2.28}$$

- **Hybrid density functional**:

$$\begin{aligned} A_{ia,jb} &= \delta_{ij}\delta_{ab}(\epsilon_a - \epsilon_i) + (ia|jb) - c_{HF}(ij|ab) + (1 - c_{HF})(ia|f_{xc}|jb) \\ B_{ia,jb} &= (ia|bj) - c_{HF} + (1 - c_{HF})(ia|f_{xc}|bj) \end{aligned} \tag{2.29}$$

The indices (i, j) correspond to occupied and (a, b) to unoccupied orbitals while f_{xc} is the exchange–correlation kernel. For hybrid functionals, the coefficient c_{HF} is determined by the amount of exact HF exchange in f_{xc}.
Eq. 2.27 is typically transformed into two eigenvalue equations due to its non-Hermiticity:

$$\begin{aligned} (\mathbf{A} - \mathbf{B})(\mathbf{A} + \mathbf{B})|(\mathbf{X} + \mathbf{Y})\rangle &= \omega^2|(\mathbf{X} + \mathbf{Y})\rangle \\ (\mathbf{A} + \mathbf{B})(\mathbf{A} - \mathbf{B})|(\mathbf{X} - \mathbf{Y})\rangle &= \omega^2|(\mathbf{X} - \mathbf{Y})\rangle \end{aligned} \tag{2.30}$$

Where $|(\mathbf{X} - \mathbf{Y})\rangle$ and $|(\mathbf{X} + \mathbf{Y})\rangle$ represent the left and right eigenvectors respectively and are normalized in biorthogonal sets by:

$$\begin{aligned} \langle(\mathbf{X} - \mathbf{Y})_M|(\mathbf{X} + \mathbf{Y})_N\rangle &= \delta_{MN} \\ \sum_{ia}\left(X_{ia}^2 - Y_{ia}^2\right) &= 1 \end{aligned} \tag{2.31}$$

Employing the Tamm–Dancoff approximation (TDA), the non-Hermitian eigenvalue problem of Eq. 2.27 is reduced to a Hermitian one, similar to CIS (Eq. 2.18), by setting the matrix $\mathbf{B} = 0$.[34,36]

$$\mathbf{AX} = \omega\mathbf{X} \tag{2.32}$$

Here the difference between TDDFT/TDA and CIS is rooted in the definition of the matrix $\mathbf{A}$'s elements. Within TDDFT/TDA the amplitudes $\mathbf{X}$ do not belong to a biorthogonal set anymore yielding a norm similar to wave function methods.

$$\sum_{ia} X_{ia}^2 = 1 \tag{2.33}$$

TDDFT is widely used for the calculation of excited state geometries and their associated properties yielding excitation energies with errors between 0.1 to 0.5 eV depending on the density functional.[34] As a rather inexpensive method, TDDFT is prone to problems regarding Rydberg- and charge-transfer (CT) states as well as excited states with double excitations.[37–40] Within this thesis TDDFT is used for excited state geometry optimizations and frequency analysis in combination with the B3-LYP and PBE0 density functionals as well as for the construction of AMEWs by means of Spoiler.

2.4 Second Quantization

Second quantization utilizes an occupation vector to represent the electronic state of a system by occupation numbers of the respective spin orbitals ϕ.[41]

$$|\Psi\rangle = |\phi_1, \bar{\phi_1}, \ldots, \phi_n, \bar{\phi_n}\rangle \tag{2.34}$$

Here ϕ_i is used to represent orbitals with α and $\bar{\phi_i}$ for orbitals with β spin. A special occupation vector is the vacuum state $|0\rangle$ representing an electronic state where all spin orbitals are unoccupied. Every electronic state $|\Psi\rangle$ can be constructed from the vacuum state $|0\rangle$ by occupying the respective spin orbitals ϕ.

$$|\Psi\rangle = \prod_i (\hat{a}^\dagger_{i\sigma_i})^{n_i}|0\rangle \tag{2.35}$$

Here $\hat{a}^\dagger_{i\sigma_i}$ is a creation operator occupying the spin orbital ϕ_i or $\bar{\phi}_i$ depending on the spin $\sigma_i \in \alpha, \beta$ and the occupation number $n_i \in 0, 1$. Corresponding to the creation operator, an annihilation operator $\hat{a}_i$ exists, which removes occupation from the spin orbital ϕ_i. The creation and annihilation operators act on the first element of the occupation vector. To create an electron in the spin orbital, the operator $\hat{a}^\dagger_{i\sigma_i}$ creates the orbital at the start of the occupation vector requiring permutations with the other spin orbitals to reach its position. Each permutation with an occupied spin orbital introduces a sign flip. The annihilation operator on the other hand requires the orbital to be annihilated at the start of the occupation vector requiring similar permutations.

$$\begin{aligned} \hat{a}^\dagger_{2\alpha}|\phi_1\rangle &= |\phi_2, \phi_1\rangle = -|\phi_1, \phi_2\rangle \\ \hat{a}_{2\alpha}|\phi_1, \phi_2\rangle &= -\hat{a}_{2\alpha}|\phi_2, \phi_1\rangle = -|\phi_1\rangle \end{aligned} \tag{2.36}$$

Creation of an electron in already occupied spin orbitals or annihilation in an unoccupied spin orbital yields an invalid state:

$$\begin{aligned} \hat{a}^\dagger_{i\alpha}|\phi_i\rangle &= 0 \\ \hat{a}_{j\alpha}|0\rangle &= 0 \end{aligned} \tag{2.37}$$

The creation and annihilation operators can be combined to define excitations, where first an electron is annihilated in the spin orbital ϕ_j and created consecutively in the spin orbital ϕ_i. The spin-conserving single excitation operator $\hat{E}^j_i$ and double excitation $\hat{e}_{ikjl}$ operators are defined as follows:

$$\begin{aligned} \hat{E}^j_i &= \left(\hat{a}^\dagger_{i\alpha}\hat{a}_{j\alpha} + \hat{a}^\dagger_{i\beta}\hat{a}_{j\beta}\right) \\ \hat{e}_{ikjl} &= \left(\hat{E}^j_i\hat{E}^l_k - \delta_{jk}\hat{E}^l_i\right) \end{aligned} \tag{2.38}$$

Using the expressions of Eq. 2.38, one- and two-electron operators can be expressed in second quantization by:[42]

$$\begin{aligned} \hat{\mathcal{O}}_{ij} &= O_{ij}\hat{E}^j_i \\ \hat{\mathcal{O}}_{ikjl} &= O_{ikjl}\left(\hat{E}^j_i\hat{E}^l_k - \delta_{jk}\hat{E}^l_i\right) \end{aligned} \tag{2.39}$$

Here O_{ij} and O_{ikjl} represent the one- $\langle\phi_i|\hat{\mathcal{O}}(1)|\phi_j\rangle$ and two- $\langle\phi_i\phi_k|\hat{\mathcal{O}}(1,2)|\phi_j\phi_l\rangle$ electron integrals, respectively.

The second quantization formalism is used within this thesis as easy and straight forward approach to evaluate matrix elements between configuration state functions (CSFs). The density operators employed for reduced one-electron (transition) density matrices between spin-conserving ($\hat{\mathcal{S}}_i^a$) and spin-flip ($\hat{\mathcal{T}}_{i,\gamma}^a$) excitations are utilized to obtain electric transition dipole moments, SOCMEs or excitonic coupling matrix elements (ECMEs) and can be expressed using the excitation operators (Eq. 2.38) by:

$$\begin{aligned}
\hat{\mathcal{S}}_i^j &= \left(\hat{a}_{i\alpha}^\dagger \hat{a}_{j\alpha} + \hat{a}_{i\beta}^\dagger \hat{a}_{j\beta}\right) \\
\hat{\mathcal{T}}_{i,+1}^j &= \hat{a}_{i\alpha}^\dagger \hat{a}_{j\beta} \\
\hat{\mathcal{T}}_{i,0}^j &= \left(\hat{a}_{i\alpha}^\dagger \hat{a}_{j\alpha} - \hat{a}_{i\beta}^\dagger \hat{a}_{j\beta}\right) \\
\hat{\mathcal{T}}_{i,-1}^j &= \hat{a}_{i\beta}^\dagger \hat{a}_{j\alpha}
\end{aligned} \tag{2.40}$$

Or in their tensorial form:

$$\begin{aligned}
\hat{S}_i^j &= \frac{1}{\sqrt{2}}\left(\hat{a}_{i\alpha}^\dagger \hat{a}_{j\alpha} + \hat{a}_{i\beta}^\dagger \hat{a}_{j\beta}\right) \\
\hat{T}_{i,+1}^j &= -\hat{a}_{i\alpha}^\dagger \hat{a}_{j\beta} \\
\hat{T}_{i,0}^j &= \frac{1}{\sqrt{2}}\left(\hat{a}_{i\alpha}^\dagger \hat{a}_{j\alpha} - \hat{a}_{i\beta}^\dagger \hat{a}_{j\beta}\right) \\
\hat{T}_{i,-1}^j &= \hat{a}_{i\beta}^\dagger \hat{a}_{j\alpha}
\end{aligned} \tag{2.41}$$

2.5 Configuration State Functions

Configuration state functions (CSFs) are linear combinations of Slater determinants δ_i and are eigenfunctions of the $\hat{\mathcal{S}}^2$ and $\hat{\mathcal{S}}_z$ operators instead of solely the $\hat{\mathcal{S}}_z$ operator.[43]

$$|S, M_s, \omega, w\rangle = \sum_i c_i(S, M_s, \omega)\delta_i(M_s, \omega) \tag{2.42}$$

Here w is the occupation vector, ω the index indicating the different eigenfunctions of the $\hat{\mathcal{S}}^2$ and $\hat{\mathcal{S}}_z$ operators. S is the spin quantum number and M_s the magnetic spin quantum number respectively. Applying an operator to the CSFs $|S, M_s, \omega, w\rangle$ and $|S', M_s, \omega', w'\rangle$ yields the spin-couplings η.[44]

$$\begin{aligned}
&\langle S', M_s', \omega', w'| \sum_{ij} O_{ij} \hat{E}_i^j |S, M_s, \omega, w\rangle \\
&= \sum_{ij} O_{ij} \langle S', M_s', \omega', w'| \hat{E}_i^j |S, M_s, \omega, w\rangle \\
&= \sum_{ij} O_{ij} \cdot \eta(S, S', M_s, M_s', \omega, \omega', w, w')
\end{aligned} \tag{2.43}$$

Utilizing CSFs the Hamiltonian can be transformed into a block structure with respect to spin-symmetry. This process eases the computational effort to solve the eigenvalue problem. However, the CSF basis has to be constructed up front requiring some effort before the actual

problem can be solved while the reduced computational cost typically outweigh the effort to construct the CSF basis.[45] For the construction of CSFs multiple procedures exist[46] of which two, the genealogical construction as well as the construction employing CSFs of subsystems are discussed in more detail in section 4.2.

2.6 Auxiliary Many-Electron Wave Functions

Auxiliary many-electron wave functions (AMEWs) bridge the gap between TDDFT and wave function methodology by employing the amplitudes of linear response TDDFT calculations as CSF weights in a many-electron wave function. As linear response TDDFT does only consider singly excited configurations relative to the ground state the AMEWs contain only CSFs corresponding to the employed configurations. Originally, AMEWs were utilized to offer easy access to nonadiabatic coupling matrix elements (NACMEs)[47,48] and were later extended to obtain SOCMEs.[49–52]
The AMEWs for excited singlet and triplet states relative to the singlet ground state $|\Psi_0\rangle$ are given by Eq. 2.44 as long as magnetic interactions do not split up the triplet components energetically.[53]

$$\begin{aligned}
|\Psi_S\rangle &= \sum_{i}^{n_{occ}} \sum_{a}^{n_{virt}} c_i^a(S) \hat{\mathcal{S}}^i_a |\Psi_0\rangle \\
|\Psi_{T,+1}\rangle &= \sum_{i}^{n_{occ}} \sum_{a}^{n_{virt}} c_i^a(T) \hat{\mathcal{T}}^i_{a,+1} |\Psi_0\rangle \\
|\Psi_{T,0}\rangle &= \sum_{i}^{n_{occ}} \sum_{a}^{n_{virt}} c_i^a(T) \hat{\mathcal{T}}^i_{a,0} |\Psi_0\rangle \\
|\Psi_{T,-1}\rangle &= \sum_{i}^{n_{occ}} \sum_{a}^{n_{virt}} c_i^a(T) \hat{\mathcal{T}}^i_{a,-1} |\Psi_0\rangle
\end{aligned} \tag{2.44}$$

Employing real valued left ($\mathbf{X}-\mathbf{Y}$) and right ($\mathbf{X}+\mathbf{Y}$) linear response TDDFT amplitudes of the non-Hermitian eigenvalue problem (Eq. 2.27) an AMEW with multiplicity M and CSFs $|\psi_i^a\rangle$ can be constructed in two ways.

$$\begin{aligned}
|\Psi_M^R\rangle &= \sum_{i}^{n_{occ}} \sum_{a}^{n_{virt}} (\mathbf{X}-\mathbf{Y})_i^a(M) |\psi_i^a\rangle \\
\langle\Psi_M^L| &= \sum_{i}^{n_{occ}} \sum_{a}^{n_{virt}} (\mathbf{X}+\mathbf{Y})_i^a(M) \langle\psi_i^a|
\end{aligned} \tag{2.45}$$

Both L- and R-AMEWs can be utilized to evaluate matrix elements for operators like the electric transition dipole operator $\hat{\mu}_{el}$ or SOC operators $\hat{\mathcal{H}}_{SO}$ yielding multiple possible matrix elements depending on the choice of amplitudes.

$$\begin{aligned}
A_{MN}^{LL} &= \langle\Psi_M^L|\hat{\mathcal{O}}|\Psi_N^L\rangle \\
A_{MN}^{LR} &= \langle\Psi_M^L|\hat{\mathcal{O}}|\Psi_N^R\rangle \\
A_{MN}^{RL} &= \langle\Psi_M^R|\hat{\mathcal{O}}|\Psi_N^L\rangle \\
A_{MN}^{RR} &= \langle\Psi_M^R|\hat{\mathcal{O}}|\Psi_N^R\rangle \\
A_{MN}^{aver} &= \mathrm{sign}(A_{MN}^{LR}) \cdot \sqrt{|A_{MN}^{LR} A_{MN}^{RL}|}
\end{aligned} \tag{2.46}$$

The nontrivial A_{MN}^{aver} matrix element is constructed similar to non-Hermitian eigenvalue problems in equation-of-motion and response coupled-cluster calculations.[54,55] The employed TDDFT amplitudes are normalized in biorthogonal sets (Eq. 2.31) and therefore the AMEWs are not properly normalized from a pure wave function point of view. Restoring a typical wave function norm using the normalization coefficients $N = (\sum_{ia} c_i^a)^{-1/2}$ yields the normalized AMEWs $A_{MN}^{CD_{norm}}$.[53]

$$A_{MN}^{CD_{norm}} = \frac{1}{\sqrt{N_M^C N_N^D}} A_{MN}^{CD} \tag{2.47}$$

AMEWs represent the foundation for the evaluation of SOCMEs from linear response TDDFT amplitudes utilizing Spoiler.[53] Spoiler was extended in this thesis for the evaluation of electronic transition dipole moments employing AMEWs for the computation of reduced one-electron (transition) density matrices to access phosphorescence rate constants through the spin–orbit coupling quasi-degenerate perturbation theory (SOCQDPT) method.

2.7 DFT/MRCI

Ab initio methods like the multi-reference configuration interaction (MRCI) are known to offer chemically accurate descriptions by including static and dynamic correlation effects. The configuration interaction method extends the wave function in the basis of n-fold excitations relative to a reference configuration, which is typically the ground state.

$$|\Psi_{CI}\rangle = c_0|\Phi_0\rangle + \sum_{ia} c_i^a|\Phi_i^a\rangle + \sum_{\substack{i<j \\ a<b}} c_{ij}^{ab}|\Phi_{ij}^{ab}\rangle + \sum_{\substack{i<j<k \\ a<b<c}} c_{ijk}^{abc}|\Phi_{ijk}^{abc}\rangle + \dots \tag{2.48}$$

Here the indices i, j, k indicate occupied and a, b, c unoccupied orbitals of the reference configuration Φ_0 where electrons are moved from occupied to unoccupied orbitals to construct excited configurations. Due to the sheer amount of configurations, the expansion is truncated typically after the second or third term leading to the CIS and configuration interaction singles and doubles (CISD) methods. The truncation ignores higher excited configurations, which might play important roles in the wave function description. Therefore, the CI method can be improved by applying a selection criterion to include configurations into the wave function instead of utilizing a maximum allowed excitation order relative to a reference. The selection process is typically applied to select a set of reference configurations next to the ground state reference forming the reference space and allowing configurations into the wave function, which exhibit an n-fold excitation relative to one of these references.

$$\Psi_{MRCI} = \sum_R c_R \Phi_R + \sum_S \sum_a c_S^a \Phi_S^a + \sum_D \sum_{ab} c_D^{ab} \Phi_D^{ab} + \dots \tag{2.49}$$

The reference space consists of the configurations Φ_R weighted by the coefficients c_R and the singly (Φ_S^a) and doubly (Φ_D^{ab}) excited configurations relative to the reference space.[56] The indices S and D indicate the single and double hole states created from the reference configurations while a and b represent the unoccupied orbitals of the reference configurations. Similar to CIS the following eigenvalue problem has to be solved employing the wave function

expansion Ψ_{MRCI}:

$$\begin{aligned} \hat{\mathcal{H}}\Psi_{MRCI} &= E\Psi_{MRCI} \\ \text{Where} \qquad \hat{\mathcal{H}} &= \sum_{ij} h_{ij}\hat{E}_i^j + \frac{1}{2}\sum_{ijkl} V_{ikjl}\left(\hat{E}_i^j\hat{E}_k^l - \delta_{jk}\hat{E}_i^l\right) \end{aligned} \tag{2.50}$$

The Hamiltonian $\hat{\mathcal{H}}$ is here expressed in second quantization[57] and can be reformulated following Wetmore and Segal[43] as:

$$\begin{aligned} \hat{\mathcal{H}} = E^{SCF} &- \sum_i F_{ii}\bar{w}_i + \frac{1}{2}\sum_{ij}\left(V_{ijij} - \frac{1}{2}V_{ijji}\right)\bar{w}_i\bar{w}_j \\ &+ \sum_{ij} F_{ij}\hat{E}_i^j - \sum_{ijk}\left(V_{ikjk} - \frac{1}{2}V_{ikkj}\right)\bar{w}_k\hat{E}_i^j \\ &+ \frac{1}{2}\sum_{ijkl} V_{ikjl}\left(\hat{E}_i^j\hat{E}_k^l - \delta_{jk}\hat{E}_i^l\right) \end{aligned} \tag{2.51}$$

Here E_{SCF} is the self-consistent field (SCF) energy and F_{ii} are the diagonal elements of the Fock matrix with occupation numbers $\bar{w}_i$:

$$F_{ij} = h_{ij} + \sum_k \bar{w}_k\left(V_{ikjk} - \frac{1}{2}V_{ikkj}\right) \tag{2.52}$$

Moving from small to large molecular systems MRCI calculations become less advantageous due to the strong scaling of the computational costs.[37] One of the factors driving up the costs, is the appropriate description of dynamic correlation within the MRCI approach requiring long expansions of doubly excited and higher excited configurations. The idea behind DFT/MRCI is to combine DFT and MRCI, where DFT is used to account for dynamic correlation while MRCI describes the static correlation reducing the required expansion space and therefore the associated computational costs. Static correlation is not contained within DFT, as it is caused by near-degeneracies, and fully covered by the MRCI method, while dynamic correlation is present in both methods and requires adjustment to prevent double counting.[58] The original DFT/MRCI approach was developed by Grimme and Waletzke[37] utilizing Eq. 2.51 as a starting point to divide the Hamiltonian matrix elements into diagonal and off-diagonal contributions of one- and two-electron differences. The Kohn–Sham orbital energies and scaled two-electron integrals are then utilized to correct the matrix elements.[37,43] The DFT/MRCI Hamiltonian was subject to change over the last years exhibiting two major redesigns that will be presented in the following discussion of the diagonal and off-diagonal matrix elements.

- **Diagonal Matrix Elements**:
  The diagonal matrix elements of the DFT/MRCI Hamiltonian are given by:

$$\begin{aligned} \langle\omega w|\hat{\mathcal{H}}^{DFT} - E^{DFT}|\omega w\rangle = \langle\omega w|\hat{\mathcal{H}} - E^{HF}|\omega w\rangle &- \sum_{i\in c}^{n_{ex}}(F_{ii}^{HF} - F_{ii}^{KS}) \\ &+ \sum_{i\in a}^{n_{ex}}(F_{ii}^{HF} - F_{ii}^{KS}) + \Delta E_{coul} - \Delta E_{exch} \end{aligned} \tag{2.53}$$

Here the HF orbital energies are replaced by the corresponding Kohn–Sham orbital energies while a refers to annihilators, c to creators and n_{ex} is the excitation order relative to the reference configuration. It is important to note that F^{HF} and E^{HF} do not resemble the HF orbital energies and the total HF energy but are effective one-electron matrix elements of the Kohn–Sham orbitals constructed in a HF like manner. The terms ΔE_{coul} and ΔE_{exch} arise due to typically smaller energy gaps using the Kohn–Sham orbitals instead of HF orbitals and are used to scale the two-electron contributions.

Grimme and Waletzke[37] used different scaling parameters to correct for the exchange integrals of singlet and triplet states given by ${}^m p[N_0]$ where N_0 is the number of open shells. The Coulomb interaction is scaled by p_J exhibiting values close to 0.5 for the parametrization with the BH-LYP functional (Eq. 2.14).

$$\Delta E_{coul}^{orig} - \Delta E_{exch}^{orig} = \frac{1}{N_{ex}} \sum_{i \in c}^{n_{ex}} \sum_{j \in a}^{n_{ex}} (p_J V_{ijij} - {}^m p[N_0] V_{ijji}) \tag{2.54}$$

$$\begin{aligned} {}^1 p[N_0] &= {}^1 p[0] + N_0 {}^1 \alpha \\ {}^3 p[N_0] &= N_0 {}^3 \alpha \end{aligned} \tag{2.55}$$

Lyskov *et al.*[59] suggested a new expression during the first redesign in 2016 (R2016 Hamiltonian) introducing a multiplicity independent scaling factor (p_X) for the exchange correction unifying the multiplicity dependent treatment by Grimme and Waletzke.

$$\begin{aligned} \Delta E_{coul}^{red-even} - \Delta E_{exch}^{red-even} &= p_J \left(- \sum_{\substack{i,j \in c \\ i>j}}^{n_{ex}} V_{ijij} - \sum_{\substack{i,j \in a \\ i>j}}^{n_{ex}} V_{ijij} + \sum_{i \in c}^{n_{ex}} \sum_{j \in a}^{n_{ex}} V_{ijij} \right) \\ &= p_X \left(\frac{1}{2} \sum_{i \in c}^{n_{ex}} \sum_{j \in a}^{n_{ex}} V_{ijji} + \sum_{\substack{i,j \in o \\ i>j}}^{N_0} V_{ijji} \eta_{ij}^{ji} \right) \end{aligned} \tag{2.56}$$

The operator can be utilized for systems with even numbers of electrons where additional to the annihilators (a) and the creators (c) a term for open shell (o) contributions arises weighting the exchange integral with a corresponding spin–coupling coefficient η_{ij}^{ji}. A more recent extension of the Hamiltonian by Heil *et al.* extended the Hamiltonian for systems with even and odd numbers of electrons.[60]

- **Off-Diagonal Matrix Elements**:
  Off-diagonal matrix elements involving different CSFs belonging to the same configuration or configurations of unequal spacial occupations are treated differently. For CSFs of equal configurations originally the unscaled CI Hamiltonian matrix element were used while the R2016 and newer Hamiltonians employ a scaling of $(1 - p_X)$ to maintain a consistent energy splitting.

$$\begin{aligned} &\text{Original :} \\ &\quad \langle \omega w | \hat{\mathcal{H}}^{DFT} | \omega' w \rangle = \langle \omega w | \hat{\mathcal{H}} | \omega' w \rangle \\ &\text{R2016/R2017 :} \\ &\quad \langle \omega w | \hat{\mathcal{H}}^{DFT} | \omega' w \rangle = \langle \omega w | (1 - p_X) \hat{\mathcal{H}} | \omega' w \rangle \end{aligned} \tag{2.57}$$

The dynamic correlation introduced by utilizing the Kohn–Sham orbitals in the diagonal elements has to be treated to prohibit double counting. This feat is achieved by excluding all molecular orbitals exhibiting energies larger than 2 Hartree from the CI space, while utilizing a damping function to scale down contributions to the off-diagonal matrix element. The original approach and the redesigns employ different damping functions.

$$\begin{aligned}
&\text{Original :}\\
&\quad \langle \omega w|\hat{\mathcal{H}}^{DFT}|\omega' w\rangle = \langle \omega w|\hat{\mathcal{H}}|\omega' w\rangle p_1 e^{-p_2 \Delta E^4_{ww'}}\\
&\text{R2016/R2017 :}\\
&\quad \langle \omega w|\hat{\mathcal{H}}^{DFT}|\omega' w\rangle = \langle \omega w|\hat{\mathcal{H}}|\omega' w\rangle \frac{p_1}{1+(p_2\Delta E_{ww'})arctan(p_2\Delta E_{ww'})^5}
\end{aligned} \tag{2.58}$$

Throughout this thesis the DFT/MRCI method is used for various calculations employing either the original or in most cases the redesigned R2016 Hamiltonian.

2.8 Reduced Density Matrices

Reduced density matrices offer easy access to matrix elements and expectation values of quantum mechanical operators easing the evaluation of molecular properties like electronic transition dipole moments, SOCMEs and ECMEs.

$$\begin{aligned}
\langle \Psi_F|\hat{\mathcal{O}}(1)|\Psi_I\rangle &= \sum_{ij} D^{F\leftarrow I}_{ij} O_{ji} = tr\Big(D^{F\leftarrow I} O\Big)\\
\langle \Psi_F|\hat{\mathcal{O}}(1,2)|\Psi_I\rangle &= \sum_{ijkl} D^{F\leftarrow I}_{ijkl} O_{kilj}
\end{aligned} \tag{2.59}$$

Here $D^{F\leftarrow I}$ is the density matrix between the final- and initial state and O are the integrals of the one- or two-electron operator $\hat{\mathcal{O}}$, respectively.
Density matrices can be derived following McWeeny[61] starting with the probability density (Eq. 2.60) of the wave function, which multiplied by the volume element $dx_1 dx_2 \dots dx_n$ gives the probability to find each electron at its respective coordinate, e.g., electron e_1 at x_1, electron e_2 at x_2 and so forth.

$$\rho(x_1, x_2, \dots, x_n) = \Psi(x_1, x_2, \dots, x_n)\Psi^*(x_1, x_2, \dots, x_n) \tag{2.60}$$

If the location of one or two electrons is of interest, the positions of all other electrons can be integrated out to construct the reduced one- (ρ) and two-electron (π) density functions.

$$\begin{aligned}
\rho(x_1) &= N \int \Psi(x_1, x_2, \dots, x_n)\Psi^*(x_1, x_2, \dots, x_n) dx_2 \dots dx_n\\
\pi(x_1, x_2) &= N(N-1) \int \Psi(x_1, x_2, \dots, x_n)\Psi^*(x_1, x_2, \dots, x_n) dx_3 \dots dx_n
\end{aligned} \tag{2.61}$$

Integration over the spin (s) of the observed one or two electrons yields the spin-free reduced one- (P) and two-electron (Π) density functions.

$$\begin{aligned}
P(x_1) &= N \int_s \int \Psi(x_1, x_2, \dots, x_n)\Psi^*(x_1, x_2, \dots, x_n) dx_2 \dots dx_n ds_1\\
\Pi(x_1, x_2) &= N(N-1) \int_s \int \Psi(x_1, x_2, \dots, x_n)\Psi^*(x_1, x_2, \dots, x_n) dx_3 \dots dx_n ds_1 ds_2
\end{aligned} \tag{2.62}$$

To determine the expectation values of operators, an auxiliary coordinate x' is introduced in the density function specifying the position of the electron before action of the operator.

$$\begin{aligned} P(x_1; x_1') &= N \int_s \int \Psi(x_1, x_2, \ldots, x_n)\Psi^*(x_1', x_2, \ldots, x_n) dx_2 \ldots dx_n ds_1 \\ \Pi(x_1, x_2; x_1', x_2') &= N(N-1) \int_s \int \Psi(x_1, x_2, \ldots, x_n)\Psi^*(x_1', x_2', \ldots, x_n) dx_3 \ldots dx_n ds_1 ds_2 \end{aligned} \tag{2.63}$$

Utilizing the reduced one- and two-electron density functions, the wave function expressions within the expectation values can be substituted:

$$\begin{aligned} \langle\Psi| \sum_i \hat{\mathcal{O}}(i) |\Psi\rangle &= \int_{x_1=x_1'} \left[\hat{\mathcal{O}}(1) p(x_1; x_1')\right] dx_1 \\ \langle\Psi| \sum_{i,j} \hat{\mathcal{O}}(i,j) |\Psi\rangle &= \int_{\substack{x_1=x_1' \\ x_2=x_2'}} \left[\hat{\mathcal{O}}(1,2) \pi(x_1, x_2; x_1', x_2')\right] dx_1 dx_2 \end{aligned} \tag{2.64}$$

Expanding the density functions in the basis of orbitals yields the reduced one- (ρ_{ij}) and two-electron (π_{ijkl}) density matrices:

$$\begin{aligned} \rho(x_1; x_1') &= \sum_{ij} \rho_{ij} \cdot \phi_i(x_1)\phi_j(x_1') \\ \pi(x_1, x_2; x_1', x_2') &= \sum_{ijkl} \pi_{ijkl} \cdot \phi_i(x_1)\phi_k^*(x_1)\phi_j(x_2)\phi_l^*(x_2) \end{aligned} \tag{2.65}$$

In second quantization the density matrices can be expressed in their spin-free form utilizing the operators from Eq. 2.40 to formulate, e.g., singlet-singlet and triplet-triplet reduced one-electron density matrices.

$$P_{ij} = \langle\Psi|\hat{\mathcal{S}}|\Psi\rangle \tag{2.66}$$

Utilizing the same expression for different electronic states $\Psi_F \neq \Psi_I$ reduced one-electron transition density matrices can be expressed for e.g. singlet-singlet, triplet-triplet and singlet-triplet transitions.

$$\begin{aligned} D_{ij}^{S_F \leftarrow S_I} &= \langle {}^1\Psi_F|\hat{\mathcal{S}}|{}^1\Psi_I\rangle \\ D_{ij}^{T_F \leftarrow T_I} &= \langle {}^3\Psi_F|\hat{\mathcal{S}}|{}^3\Psi_I\rangle \\ D_{ij}^{S_F \leftarrow T_{I,\gamma}} &= \langle {}^1\Psi_F|\hat{\mathcal{T}}_{-\gamma}|{}^3\Psi_{I,\gamma}\rangle \\ D_{ij}^{T_{F,\gamma} \leftarrow S_I} &= \langle {}^3\Psi_{F,\gamma}|\hat{\mathcal{T}}_{\gamma}|{}^1\Psi_I\rangle \end{aligned} \tag{2.67}$$

2.9 Relativistic Effects

2.9.1 Spin–Orbit Mean-Field Operator

SOC operators like the Breit–Pauli operator (Eq. 2.68) contain one- and two-electron terms, where especially the two-electron terms are computationally demanding. Even today approximations are required to apply such operators to larger systems.

$$\hat{\mathcal{H}}_{SO}^{BP} = \frac{e^2}{2m_e^2c^2}\left(\hat{h}_{SO}^{BP}(1) + \hat{H}_{SO}^{BP}(1,2)\right) \tag{2.68}$$

The one-electron part of the Breit–Pauli operator describes the interaction of the electron spin's magnetic moment in the field of magnetic moments spanned by the nuclei. The two-electron part consists of three terms which describe the interaction of the orbital's magnetic moment and the electron's spin in the field of all electrons. The first term is denoted as the same-spin-orbit term as the spin's and orbital's magnetic moments stem from the same electron while in the remaining two spin-other-orbit terms the momenta belong to different electrons.

$$\begin{aligned}
\hat{h}_{SO}^{BP}(1) &= \sum_i \left(-\nabla_i \left(\sum_I \frac{Z_I}{\hat{r}_{iI}} \right) \times \hat{p}_i \right) \cdot \hat{s}_i \\
\hat{H}_{SO}^{BP}(1,2) &= \sum_i \sum_{j \neq i} \left(\nabla_i \left(\frac{1}{\hat{r}_{ij}} \right) \times \hat{p}_i \right) \cdot \hat{s}_i \\
&+ \sum_i \sum_{j \neq i} \left(\nabla_j \left(\frac{1}{\hat{r}_{ij}} \right) \times \hat{p}_j \right) \cdot \hat{s}_i \\
&+ \sum_j \sum_{i \neq j} \left(\nabla_i \left(\frac{1}{\hat{r}_{ji}} \right) \times \hat{p}_i \right) \cdot \hat{s}_j
\end{aligned} \tag{2.69}$$

To reduce the computational cost of the two-electron terms a HF like mean-field approach is employed yielding the spin–orbit mean-field (SOMF) operator.

$$\hat{\mathcal{H}}_{SO}^{eff}(1) = \hat{H}_{SO}(1) + \hat{H}_{SO}^{mf}(1) \tag{2.70}$$

$\hat{H}_{SO}(1)$ remains the pure one-electron term while $\hat{H}_{SO}^{mf}(1)$ replaces the two-electron terms by a mean-field, where a SOCME between the valence orbitals i and j evaluates to summation over the occupied orbitals a with the occupation number γ_a:[62]

$$\langle i|\hat{H}_{SO}^{mf}(1)|j\rangle = \sum_a \gamma_a \left\{ \langle ia|\hat{H}_{SO}(2)|ja\rangle - \frac{3}{2}\langle ia|\hat{H}_{SO}(2)|aj\rangle - \frac{3}{2}\langle ai|\hat{H}_{SO}(2)|ja\rangle \right\} \tag{2.71}$$

The SOMF operator reduces the number of required integrals drastically such that these integrals can easily be kept in memory throughout the calculation. Additionally, the operator yields SOCME contributions only between CSFs that differ by a single excitation. Utilizing the second quantization formalism the SOMF operator can be expressed as:[62]

$$\hat{H}_{SO}^{eff}(1) = \sum_{i,j} h_{ij} \hat{a}_i^\dagger \hat{a}_j = \sum_{i,j} l_{ij} \left(\sum_{\mu,\nu} s_{\mu\nu} \hat{a}_{i\mu}^\dagger \hat{a}_{j\nu} \right) \tag{2.72}$$

The evaluation of SOCMEs between two wave functions can be expressed by means of the trace of the product between the transition's density matrix $D^{F \leftarrow I}$ with the SOMF integrals H_{SO}^{mf} yielding the central equations for SOCME evaluation in the SPOCK and Spoiler programs.

$$\langle \Psi_F|\hat{\mathcal{H}}_{SO}|\Psi_I\rangle = tr\left(D^{F \leftarrow I} H_{SO}^{mf} \right) \tag{2.73}$$

The costs for the SOMF integrals can be reduced further by replacing the molecular mean-field by a sum of atomic mean-fields (one-center approximation), which utilizes the spin-orbit Hamiltonian's steep falloff ($1/r^3$). Herein the largest two-electron contributions are associated to molecular core orbitals which do not differ much from their atomic counterparts. The approximation yields errors of 5 % or less in organic systems.[63–65]

2.9.2 Spin–Orbit Coupling Quasi-Degenerate Perturbation Theory

Spin–orbit coupling quasi-degenerate perturbation theory (SOCQDPT) is a method to obtain mixed-spin wave functions and their properties by utilizing the spin-free Hamiltonian $\hat{\mathcal{H}}_{SF}$ and treating the SOC operator $\hat{\mathcal{H}}_{SO}$ in a perturbative manner. For this purpose the perturbation matrix (Eq. 2.74) is constructed and diagonalized yielding first-order energies $E^{(1)}_{k;a}$ of the coupled states.[66]

$$\begin{pmatrix} \langle\Psi^{(0)}_{k;1}|\hat{\mathcal{H}}_{SO}|\Psi^{(0)}_{k;1}\rangle & \langle\Psi^{(0)}_{k;2}|\hat{\mathcal{H}}_{SO}|\Psi^{(0)}_{k;1}\rangle & \dots & \langle\Psi^{(0)}_{k;d}|\hat{\mathcal{H}}_{SO}|\Psi^{(0)}_{k;1}\rangle \\ \langle\Psi^{(0)}_{k;1}|\hat{\mathcal{H}}_{SO}|\Psi^{(0)}_{k;2}\rangle & \langle\Psi^{(0)}_{k;2}|\hat{\mathcal{H}}_{SO}|\Psi^{(0)}_{k;2}\rangle & \dots & \langle\Psi^{(0)}_{k;d}|\hat{\mathcal{H}}_{SO}|\Psi^{(0)}_{k;2}\rangle \\ \vdots & \vdots & \ddots & \vdots \\ \langle\Psi^{(0)}_{k;1}|\hat{\mathcal{H}}_{SO}|\Psi^{(0)}_{k;d}\rangle & \langle\Psi^{(0)}_{k;2}|\hat{\mathcal{H}}_{SO}|\Psi^{(0)}_{k;d}\rangle & \dots & \langle\Psi^{(0)}_{k;d}|\hat{\mathcal{H}}_{SO}|\Psi^{(0)}_{k;d}\rangle \end{pmatrix} \tag{2.74}$$

The eigenvectors $|\Psi^{(0)}_{k;a}\rangle$ are expanded in the spin–free wave functions including wave functions of different multiplicities typically restricted to singlet and triplet states.

$$|\Psi^{(0)}_{k;a}\rangle = \sum_{b=1} c^{(0)}_{k;a,b}|\Psi^{(0)}_{k;b}\rangle \tag{2.75}$$

In Rayleigh-Schrödinger type perturbation theory, the mixed-spin wave functions corresponding to $E^{(1)}_{k;a}$ are given by:

$$|\Psi^{(1)}_{k;a}\rangle = \sum_{i\neq k}^{\infty}\sum_{b} \frac{\langle\Psi^{(0)}_{i;b}|\hat{\mathcal{H}}_{SO}|\Psi^{(0)}_{k;a}\rangle}{E^{(0)}_{i} - E^{(0)}_{k}}|\Psi^{(0)}_{i;b}\rangle \tag{2.76}$$

Following Eq. 2.76, Matrix elements of the mixed-spin wave functions like electric transition dipole moments can be obtained as the sum of the weighted pure-spin properties. Here the expansion is restricted to singlet and triplet contributions only.[66]

$$\begin{aligned} \langle\Psi^{(1)}_{0}|\hat{\mu}|\Psi^{(1)}_{1,\gamma}\rangle = &\sum_{i}^{n_{singlets}} \frac{\langle{}^1\Psi^{(0)}_{i}|\hat{\mathcal{H}}_{SO}|{}^3\Psi^{(0)}_{1,\gamma}\rangle}{{}^1E^{(0)}_{i} - {}^3E^{(0)}_{1}}\langle{}^1\Psi^{(0)}_{0}|\hat{\mu}|{}^1\Psi^{(0)}_{i}\rangle \\ + &\sum_{i}^{n_{triplets}} \frac{\langle{}^1\Psi^{(0)}_{0}|\hat{\mathcal{H}}_{SO}|{}^3\Psi^{(0)}_{i,\gamma}\rangle}{{}^3E^{(0)}_{i} - {}^1E^{(0)}_{0}}\langle{}^3\Psi^{(0)}_{i,\gamma}|\hat{\mu}|{}^3\Psi^{(0)}_{1,\gamma}\rangle \end{aligned} \tag{2.77}$$

While SOCQDPT is a computational inexpensive approach, it is heavily dependent on the number of states employed in the perturbation expansion as it converges slowly.[66] Typically, 41 singlets and 40 triplets are utilized in calculations throughout this thesis ensuring convergence. The SOCQDPT method is employed in SPOCK and Spoiler methods to obtain mixed-spin wave functions or AMEWs and their electric transition dipole moments for the evaluation of phosphorescence rate constants.

2.9.3 DFT/MRSOCI

Treatment of SOC as a perturbation is problematic in cases where the zero-field splitting is of the same order as the correlation energy requiring a more sophisticated approach. The

density functional theory / multi-reference spin–orbit coupling interaction (DFT/MRSOCI) method treats SOC variationally at the same time as electron correlation by utilizing the DFT/MRCI pure-spin wave functions and SOCMEs obtained with the SOMF operator. The pure-spin wave functions and their SOCMEs are used to construct start vectors utilizing the SOCQDPT approach. Davidson diagonalization of the complex valued Hamiltonian matrix and updating of the CI coefficients at each iteration leads to mixed-spin wave functions that can be used to obtain reduced one-electron (transition) density matrices and therefore properties like electric transition dipole moments.[44]

2.10 Radiative and Non-Radadiative Rate Constants

Radiative and non-radadiative rate constants are important properties to investigate and explain experimentally observed behavior of molecular systems after excitation. Rate constants can be evaluated following the FC and HT approximations:

- **Franck–Condon Approximation**
  Within the FC approximation the molecule is assumed to retain its geometry throughout the excitation enabling the separation of the wave function into electronic and vibrational part.[67]

$$\langle \Psi_F | \hat{\mathcal{O}} | \Psi_I \rangle = \langle \psi_F | \hat{\mathcal{O}} | \psi_I \rangle \langle \chi_F | \chi_I \rangle \tag{2.78}$$

  The FC overlap of the vibrational functions $\langle \chi_F | \chi_I \rangle$ can be expanded into overlaps of vibrational states $\langle \nu_b | \nu_a \rangle$ also known as FC integrals. Assuming only population of the initial states vibrational level ν_{Ia} the expansion yields:

$$\langle \chi_F | \chi_I \rangle = \sum_b \langle \nu_{Fb} | \nu_{Ia} \rangle \tag{2.79}$$

- **Herzberg–Teller Approximation**
  In the case of small electronic couplings, the effect of vibrational motions on the coupling can not be neglected anymore and the FC approximation has to be extended. Herzberg and Teller supplied these extensions by incorporating vibrational effects through a Taylor expansion:[68]

$$\begin{aligned} \sum_b \langle \Psi_{Fb} | \hat{\mathcal{O}} | \Psi_{Ia} \rangle = \langle \Psi_F | \hat{\mathcal{O}} | \Psi_I \rangle |_{Q_0} \sum_b \langle \nu_{Fb} | \nu_{Ia} \rangle \\ + \sum_k \left. \frac{\partial \langle \Psi_F | \hat{\mathcal{O}} | \Psi_I \rangle}{\partial Q_k} \right|_{Q_0} \sum_b \langle \nu_{Fb} | Q_k | \nu_{Ia} \rangle + \dots \end{aligned} \tag{2.80}$$

  Initially the HT approximation was utilized to treat vibronic contributions to absorption spectra employing the first two terms of the Taylor expansion for the electric transition dipole moment operator ($\hat{\mathcal{O}} = \hat{\mu}_{el}$). The HT terms were implemented in the VIBES program by Mihaljo Etinski[69–71] for the use with the electric transition dipole operator as well as SOC operators to evaluate radiative rate constants and ISC rate constants, respectively.

2.10.1 Non-Radiative Rate Constants

Non-radiative rate constants can be evaluated following Fermi's Golden Rule which is obtainable from first-order time-dependent perturbation theory:[70,72]

$$k_{nr} = \frac{2\pi}{\hbar} \sum_b |\langle \Psi_{Fb}|\hat{\mathcal{O}}|\Psi_{Ia}\rangle|^2 \delta(E_F - E_I) \tag{2.81}$$

The use of perturbation theory requires the perturbation to be small. Utilizing the FC approximation, Fermi's Golden Rule can be simplified by separating the electronic and vibrational parts.

$$\begin{aligned} k_{nr} &= \frac{2\pi}{\hbar} \sum_b \left| \langle \Psi_F|\hat{\mathcal{O}}|\Psi_I\rangle|_{Q_0} \langle \nu_{Fb}|\nu_{Ia}\rangle \right|^2 \delta(E_F - E_I) \\ k_{nr}^{FC} &= \frac{2\pi}{\hbar} \left| \langle \Psi_F|\hat{\mathcal{O}}|\Psi_I\rangle \right|_{Q_0}^2 \sum_b |\langle \nu_{Fb}|\nu_{Ia}\rangle|^2 \delta(E_F - E_I) \\ &= \frac{2\pi}{\hbar} \left| \langle \Psi_F|\hat{\mathcal{O}}|\Psi_I\rangle \right|_{Q_0}^2 \rho^{FC}(E) \end{aligned} \tag{2.82}$$

Here $\rho^{FC}(E)$ is the FC weighted density of states describing the probability to find the initial- and final vibrational states at the same energy.[73] Temperature dependency of the rate constant can be included in the expression employing a Boltzmann distribution for the population of the initial state's vibrational levels.

$$k_{nr}^{FC} = \frac{2\pi}{\hbar Z} \sum_b \left| \langle \Psi_F|\hat{\mathcal{O}}|\Psi_I\rangle|_{Q_0} \right|^2 \sum_{wu} e^{\frac{-E_{Iau}}{k_B T}} |\langle \nu_{Fbw}|\nu_{Iau}\rangle|^2 \delta(E_{Iau} - E_{Fw}) \tag{2.83}$$

The partition function Z is given by the Boltzmann distribution:

$$Z = \sum_u e^{\frac{-E_{Iau}}{k_B T}} \tag{2.84}$$

Moving from the FC approximation to the HT approximation the electronic and vibrational parts of the wave function can not be separated anymore as done in Eq. 2.82 yielding two expressions in addition to Eq. 2.83. The first additional term mixes FC and HT like contributions

$$\begin{aligned} k_{nr}^{FC/HT} =& \frac{4\pi}{\hbar Z} \sum_\gamma R \Bigg(\langle \Psi_{Fb,\gamma}|\hat{\mathcal{O}}|\Psi_{Ia}\rangle \Big|_{Q_0} \\ & \times \sum_{wu} e^{\frac{-E_{Iau}}{k_B T}} \langle \nu_{Fbw}|\nu_{Iau}\rangle \langle \nu_{Fbw}|b^\dagger \mathcal{Q}_I|\nu_{Iau}\rangle \delta(E_{Iau} - E_{Fw}) \Bigg) \end{aligned} \tag{2.85}$$

while the second additional term arises solely from vibrational contributions.

$$k_{nr}^{HT} = \frac{2\pi}{\hbar Z} \left(\sum_{wu} e^{\frac{-E_{Iau}}{k_B T}} |\langle \nu_{Fbw}|b^\dagger \mathcal{Q}_I|\nu_{Iau}\rangle|^2 \delta(E_{Iau} - E_{Fw}) \right) \tag{2.86}$$

The expression contains the first-order derivatives of the electronic coupling:

$$b_k = \frac{\partial \langle \Psi_{Fb}|\hat{\mathcal{O}}|\Psi_{Ia}\rangle}{\partial \mathcal{Q}_k} \Big|_{\mathcal{Q}_0} \tag{2.87}$$

These gradients are typically evaluated numerically by displacements along the normal modes $\mathcal{Q}_k$ utilizing finite-difference techniques as done in this thesis for the electric transition dipole moment and SOC operators.
The direct evaluation of the FC integrals $\langle \nu_{Fb} | \nu_{Ia} \rangle$ is computationally very expensive due to the sheer amount of integrals.[69] A more favorable approach is to use a time-dependent scheme based on the reformulation of Eq. 2.82 in the Heisenberg picture. In this approach, a correlation function is converged in the time domain and integration of the correlation function yields the FC weighted density of states $\rho^{FC}(E)$.[69,70]

$$k_{nr,corr}^{FC} = |\langle \Psi_F | \hat{\mathcal{O}} | \Psi_I \rangle|^2 \int_{\infty}^{\infty} F_{corr}(t) dt \tag{2.88}$$

The normal modes of the final- and initial state $\mathcal{Q}_F$ and $\mathcal{Q}_I$ are related by the Duschinsky transformation allowing to express the vibrational wave functions of both states in either one.[74]

$$\mathcal{Q}_F = \mathbf{J}\mathcal{Q}_I + \mathbf{D} \tag{2.89}$$

Here matrix $\mathbf{J}$ is the Duschinsky rotation matrix and $\mathbf{D}$ the displacement vector. Both approaches are implemented in the VIBES program while only the latter is utilized in this thesis to evaluate rate constants due to its lower computational costs.

In the case of EET processes, the FC weighted density of states is often approximated with the spectral overlap integral:

$$k_{EET} = \frac{2\pi}{\hbar} |V_{DA}|^2 \int_0^{\infty} A_A(\omega) E_D(\omega) d\omega \tag{2.90}$$

The spectral overlap integral is the integral of the product function of the acceptor's absorption and the donor's emission spectrum. The approximation assumes that the spectral broadening is homogeneous and that the coupling proceeds between two independent vibrational levels of the donor and acceptor molecules. The spectral overlap is highly sensitive with respect to the difference of donor and acceptor energies requiring very accurate excitation energy estimates.[73] Evaluating this equation, especially for TEET rate constants, proves to be difficult because experimental triplet spectra are not always accessible from the literature.[75]

2.10.2 Radiative Rate Constants

Radiative rate constants can be obtained in FC approximation following equation (Eq. 2.91) by employing the electric transition dipole moment $\langle \Psi_0 | \hat{\mu}_{el} | \Psi_I \rangle$ and the energetic distance $E_I - E_0$ between the emissive state Ψ_I and the ground state Ψ_0.

$$k_{rad} = \frac{4e^2}{3c^3\hbar^4} |\langle \Psi_0 | \hat{\mu}_{el} | \Psi_I \rangle|^2 \cdot (E_I - E_0)^3 \tag{2.91}$$

Following the time-integration approach discussed for non-radiative rate constants, absorption and emission spectra can be calculated by performing a Fourier transformation of the correlation function with the VIBES program. Integration of the emission spectrum yields the radiative rate constant:[76]

$$k_{rad} = \int I(\omega) d\omega \tag{2.92}$$

Due to improper normalization in the VIBES program, the spectrum has to be scaled appropriately. For a FC spectrum, the area of the spectrum has to be $\int S^{FC}(\omega)d\omega = 1$, where $S(\omega)$ is the spectral density. For HT spectra a renormalization has to be applied which scales $S^{HT}(\omega)$ by the spectral density of the FC spectrum $S^{FC}(\omega)$.[76,77]

$$k_{rad}^{HT} = \int I^{HT}(\omega)d\omega = \frac{4}{3c^3\hbar}\frac{\int \omega^3 S^{HT}(\omega)d\omega}{\int S^{FC}(\omega)d\omega} \tag{2.93}$$

2.11 Excitation Energy Transfer

2.11.1 Förster Resonance Energy Transfer

Within Förster resonance energy transfer (FRET) the EET rate constant is approximated for a weakly coupled donor-acceptor system utilizing Fermi's Golden Rule approach (Eq. 2.82):

$$k_{EET} = \frac{2\pi}{\hbar}|V_{DA}|^2\rho(E) \tag{2.94}$$

The coupling matrix element V_{DA} is assumed to be the Coulomb coupling between both fragments and is expanded in the donor ($\vec{\mu}_{D,el}$) and acceptor ($\vec{\mu}_{A,el}$) electric dipole moments separated by the distance $\vec{X}$ employing the ideal dipole approximation (IDA):

$$V_{DA} \approx J_{DA} \approx \frac{\vec{\mu}_{D,el}\vec{\mu}^*_{A,el}}{|\vec{X}|^3} - 3\frac{\vec{X}\vec{\mu}_{D,el}\vec{X}\vec{\mu}^*_{A,el}}{|\vec{X}|^5} \tag{2.95}$$

The coupling matrix element can be simplified further introducing an orientation factor κ:

$$\kappa = \vec{n}_D\vec{n}_A - 3(\vec{e}_{DA}\vec{n}_D)(\vec{e}_{DA}\vec{n}_A) \tag{2.96}$$

where $\vec{n}_D, \vec{n}_A$ is the unit vector of the respective donor or acceptor transition dipole moments and $\vec{e}_{DA}$ is the unit vector along $\vec{X}$. Employing the orientation factor, the coupling can be expressed as:

$$V_{DA} = \kappa\frac{|\vec{\mu}_{D,el}||\vec{\mu}^*_{A,el}|}{|\vec{X}_{DA}|^3} \tag{2.97}$$

The representation in terms of transition dipole moments allows to employ the donor emission spectrum and acceptor absorption coefficient, where $E_D(\omega)$ and $A_A(\omega)$ are the respective FC emission and absorption spectra.

$$I_D(\omega) = \frac{4\omega^3}{3c^3}|\vec{\mu}_{D,el}|^2 E_D(\omega) \tag{2.98}$$

$$\alpha_A(\omega) = \frac{4\pi^2\omega n_{mol}}{3\hbar c}|\vec{\mu}^*_{A,el}|^2 A_A(\omega) \tag{2.99}$$

Inserting Eq. 2.97 - 2.99 into Eq. 2.94 yields the Förster equation.

$$k_{FRET} = \frac{9c^4}{8\pi n_{agg}}\frac{\kappa^2}{|\vec{X}|^6}\int I_D(\omega)\alpha_A(\omega)\frac{d\omega}{\omega^4} \tag{2.100}$$

Here the variables n_{mol} and n_{agg} are the respective volume densities of the acceptor and the aggregate molecules. A property of the Förster equation, the Förster radius R_F, is used to express the energy transfer's efficiency. The Förster radius is the donor-acceptor distance at which the energy transfer rate constant is equal to the radiative rate constant of the donor:

$$k_{FRET}(R_F) = k_{rad}^D = \frac{1}{\tau_D} \tag{2.101}$$

An important factor in EET is the relative orientation of the donor and acceptor fragments. The orientation factor κ^2 can take values between 0 and 4, where the lowest factor is obtained for an orthogonal arrangement of the transition dipole moments with respect to the distance vector, while the largest factor is obtained for transition dipole moments oriented exactly along the distance vector. In experiments where donor and acceptor can move freely, an isotropic distribution of the transition dipole moments is assumed leading to $\kappa^2 = \frac{2}{3}$.

2.11.2 Excitonic Coupling In The Two-Level System

In many situations an explicit solvable two-level system can be used to model the donor–acceptor interaction effectively. To obtain the adiabatic eigenvalues and eigenstates for a molecular system the Schrödinger equation has to be solved:

$$\hat{\mathcal{H}}|\Psi\rangle = E|\Psi\rangle \tag{2.102}$$

The adiabatic states $|\Psi\rangle$ are expanded in the basis of diabatic eigenstates.

$$|\Psi\rangle = c_1|\psi_1\rangle + c_2|\psi_2\rangle \tag{2.103}$$

The Hamiltonian is given by

$$H = \begin{pmatrix} \epsilon_1 & V \\ V^* & \epsilon_2 \end{pmatrix} \tag{2.104}$$

where ϵ_1 and ϵ_2 are the diabatic eigenvalues while V is the Hamiltonian coupling matrix element between both diabatic states. Solving the linear equations yields the respective adiabatic eigenvalues and eigenstates.

$$\begin{pmatrix} \epsilon_1 & V \\ V^* & \epsilon_2 \end{pmatrix} \begin{pmatrix} c_1 \\ c_2 \end{pmatrix} = E \begin{pmatrix} c_1 \\ c_2 \end{pmatrix} \tag{2.105}$$

Solutions of the linear equations can be obtained by evaluating the secular determinant:

$$\begin{aligned} \begin{vmatrix} E-\epsilon_1 & V \\ V & E-\epsilon_2 \end{vmatrix} &= 0 \\ E_\pm = \frac{1}{2}\left(\epsilon_1+\epsilon_2 \pm \sqrt{(\epsilon_1-\epsilon_2)^2+4|V|^2}\right) & \end{aligned} \tag{2.106}$$

If both diabatic states have the same energy, like corresponding states in a homo dimer (e.g. $\epsilon_1 = \epsilon_2$), the solution can be simplified to:

$$E_\pm = \epsilon \pm |V| \tag{2.107}$$

Following Eq. 2.107 the energetic splitting of the dimer states is symmetrical in the homo dimer and equal to $|V|$. This symmetrical splitting is known as Davydov splitting and named

after Alexander Sergeevich Davydov who investigated the excitonic splitting in molecular crystals. The Davydov splitting allows easy access to the excitonic coupling if the dimer energy levels are known. Reversing the process discussed above and returning to the adiabatic picture yields V from the energy difference between the dimer states.

$$V = \frac{\Delta E}{2} = \frac{E_- - E_+}{2} \tag{2.108}$$

2.11.3 Diabatization Approaches

Typical EET applications do seldom involve homo dimers or require a non-symmetrical splitting. Therefore, diabatization approaches were developed for hetero dimers. The target of these approaches is similar to the Davydov procedure obtaining the excitonic coupling from calculations of the full dimer system. To move from the adiabatic dimer Hamiltonian H_a to a diabatic representation H_d, a rotation of the Hamiltonian is required which can be expressed by a unitary transformation:

$$U^\dagger H_a U = U^\dagger \begin{pmatrix} E_+ & 0 \\ 0 & E_- \end{pmatrix} U = \begin{pmatrix} \epsilon_1 & V \\ V^* & \epsilon_2 \end{pmatrix} = H_d \tag{2.109}$$

where the transformation matrix U is given by:

$$U = \begin{pmatrix} cos(\theta) & sin(\theta) \\ -sin(\theta) & cos(\theta) \end{pmatrix} \tag{2.110}$$

Inserting into Eq. 2.109 yields:

$$V = \frac{1}{2} sin(2\theta)(\epsilon_2 - \epsilon_1) \tag{2.111}$$

Therefore the adiabatic-to-diabatic transformation requires finding the correct mixing angle θ. If more than two states are employed in the diabatization approaches, the rotation of the Hamiltonian can be performed pairwise for each combination of two states.[78,79] The correct mixing angle is determined by maximizing physical properties utilized in the diabatization scheme:

- **Boys:**[79,80]
  The Boys diabatization maximizes the electric transition dipole moment to obtain proper diabatic states separating the charge of the employed adiabatic states.

$$f_{Boys}(U) = \sum_{i,j=1} |\langle \Psi_i | \vec{\mu} | \Psi_i \rangle - \langle \Psi_j | \vec{\mu} | \Psi_j \rangle|^2 \tag{2.112}$$

  Charge separation does only occur in intermediate states of the EET process and therefore the Boys diabatization can only obtain diabatic states for electron transfer (ET). Subotnik *et al.*[79] extended the Boys diabatization for the use with EET by assuming different electrostatic fields for the electrons and holes.

$$\begin{aligned} f_{BoysOV}(U) = \sum_{i,j=1} & |\langle \Psi_i | \vec{\mu}_{occ} | \Psi_i \rangle - \langle \Psi_j | \vec{\mu}_{occ} | \Psi_j \rangle|^2 \\ & + |\langle \Psi_i | \vec{\mu}_{virt} | \Psi_i \rangle - \langle \Psi_j | \vec{\mu}_{virt} | \Psi_j \rangle|^2 \end{aligned} \tag{2.113}$$

The operators $\vec{\mu}_{occ}$ and $\vec{\mu}_{virt}$ consider contributions to the transition dipole moments from occupied-occupied and virtual-virtual orbital blocks of the density matrices, respectively. The choice of different electrostatic potentials for holes and electrons for EET is not correct, but aids to obtain localized electronic states on the fragments participating in the EET process. This treatment is only valid for CIS or TDDFT excited states, where the off-diagonal blocks of the reduced one-electron (transition) density matrices between excited states are always zero. For methods incorporating higher excitation orders than single excitations, this procedure can only be used approximately for mostly singly excited states ignoring off-diagonal contributions to the density matrices.

- **Edmiston–Ruedenberg (ER):**[79–81]
  The ER diabatization maximizes the self interaction to obtain diabatic states applicable to ET and EET.

$$f_{ER}(U) = \sum_{i=1} \int dr_1 dr_2 \frac{\langle \Psi_i | \hat{\rho}(r_2) | \Psi_i \rangle \langle \Psi_i | \hat{\rho}(r_1) | \Psi_i \rangle}{|r_1 - r_2|} \tag{2.114}$$

  Evaluation of the self-interaction requires the costly calculation of two-electron integrals followed by the contraction with the employed adiabatic state's transition densities rendering this approach computational very demanding.

Within this thesis the Boys, BoysOV and ER diabatization were implemented in the EET program to supply reference ECMEs for the extension of the MTD approach to TEET.

2.11.4 Monomer Transition Density Approach

While the diabatization approaches introduced above resemble easy and straight forward procedures to obtain the excitonic coupling, performing such calculations prove to be computationally very demanding. These approaches require the quantum chemical calculation of the full system, limiting the choice of quantum chemical methods as well as their associated accuracy. Instead of evaluating the ECME starting from the full system, it can be derived by fragmentation approaches considering the system fragments directly involved in the energy transfer. Fragmentation lowers the computational effort and allows the application of more sophisticated quantum chemical methods to derive the fragment's properties at higher accuracy.

One of these fragmentation schemes is the MTD approach, which employs an aggregate Hamiltonian, where $\hat{\mathcal{H}}_m$ contains all contributions within fragment m and $\hat{\mathcal{V}}_{mn}$ denotes the intramolecular interactions between the fragments:[82]

$$\hat{\mathcal{H}}_{agg} = \sum_m \hat{\mathcal{H}}_m + \frac{1}{2} \sum_{mn} \hat{\mathcal{V}}_{mn} \tag{2.115}$$

The MTD approach utilizes a Hartree-Product to construct the wave function of the full system.[82–84]

$$\begin{aligned} \Psi^{HP}_{D^*A} &= \psi_{D^*} \psi_A \\ \Psi^{HP}_{DA^*} &= \psi_D \psi_{A^*} \end{aligned} \tag{2.116}$$

Here ψ_{D^*} and ψ_{A^*} denote the excited fragments' states while ψ_D and ψ_A denote their respective ground states. Due to the product ansatz, the de-excitation and excitation processes remain localized on the donor and acceptor fragments. To describe the transfer process, the two-level system is utilized employing a superposition of the Hartree products to solve the eigenvalue equation:

$$\hat{\mathcal{H}}\Psi^{HP} = E\Psi^{HP} \tag{2.117}$$

where Ψ^{HP} is constructed as linear combination $\Psi^{HP} = c_1\Psi^{HP}_{DA^*} + c_2\Psi^{HP}_{D^*A}$. The corresponding Hamiltonian is given by:

$$\mathbf{H} = \begin{pmatrix} \langle\Psi^{HP}_{D^*A}|\hat{\mathcal{H}}_{agg}|\Psi^{HP}_{D^*A}\rangle & \langle\Psi^{HP}_{D^*A}|\hat{\mathcal{H}}_{agg}|\Psi^{HP}_{DA^*}\rangle \\ \langle\Psi^{HP}_{DA^*}|\hat{\mathcal{H}}_{agg}|\Psi^{HP}_{D^*A}\rangle & \langle\Psi^{HP}_{DA^*}|\hat{\mathcal{H}}_{agg}|\Psi^{HP}_{DA^*}\rangle \end{pmatrix} \tag{2.118}$$

The energies of the dimer states are obtained solving the secular equation, where the excitonic coupling is given by $\langle\Psi^{HP}_{DA^*}|\hat{\mathcal{H}}_{agg}|\Psi^{HP}_{D^*A}\rangle$:

$$\begin{vmatrix} \langle\Psi^{HP}_{D^*A}|\hat{\mathcal{H}}_{agg}|\Psi^{HP}_{D^*A}\rangle - E & \langle\Psi^{HP}_{D^*A}|\hat{\mathcal{H}}_{agg}|\Psi^{HP}_{DA^*}\rangle \\ \langle\Psi^{HP}_{DA^*}|\hat{\mathcal{H}}_{agg}|\Psi^{HP}_{D^*A}\rangle & \langle\Psi^{HP}_{DA^*}|\hat{\mathcal{H}}_{agg}|\Psi^{HP}_{DA^*}\rangle - E \end{vmatrix} = 0 \tag{2.119}$$

$$\begin{aligned} E_\pm = \frac{1}{2}\Bigg(&\langle\Psi^{HP}_{D^*A}|\hat{\mathcal{H}}_{agg}|\Psi^{HP}_{D^*A}\rangle + \langle\Psi^{HP}_{DA^*}|\hat{\mathcal{H}}_{agg}|\Psi^{HP}_{DA^*}\rangle \\ &\pm \sqrt{(\langle\Psi^{HP}_{D^*A}|\hat{\mathcal{H}}_{agg}|\Psi^{HP}_{D^*A}\rangle - \langle\Psi^{HP}_{DA^*}|\hat{\mathcal{H}}_{agg}|\Psi^{HP}_{DA^*}\rangle)^2 + 4\langle\Psi^{HP}_{DA^*}|\hat{\mathcal{H}}_{agg}|\Psi^{HP}_{D^*A}\rangle}\Bigg) \end{aligned} \tag{2.120}$$

Evaluating the involved matrix elements of the Hamiltonian, the following expressions are obtained:

$$\begin{aligned} \langle\Psi^{HP}_{D^*A}|\hat{\mathcal{H}}_{agg}|\Psi^{HP}_{D^*A}\rangle &= \langle\Psi^{HP}_{D^*A}|\hat{\mathcal{H}}_D + \hat{\mathcal{H}}_A + \hat{\mathcal{V}}_{DA}|\Psi^{HP}_{D^*A}\rangle \\ &= \langle\psi_{D^*}\psi_A|\hat{\mathcal{H}}_D + \hat{\mathcal{H}}_A + \hat{\mathcal{V}}_{DA}|\psi_{D^*}\psi_A\rangle \\ &= \langle\psi_{D^*}|\hat{\mathcal{H}}_D|\psi_{D^*}\rangle\langle\psi_A|\psi_A\rangle + \langle\psi_A|\hat{\mathcal{H}}_A|\psi_A\rangle\langle\psi_{D^*}|\psi_{D^*}\rangle + \langle\Psi^{HP}_{D^*A}|\hat{\mathcal{V}}_{DA}|\Psi^{HP}_{D^*A}\rangle \\ &= \epsilon_{D^*} + \epsilon_A + \langle\Psi^{HP}_{D^*A}|\hat{\mathcal{V}}_{DA}|\Psi^{HP}_{D^*A}\rangle \end{aligned} \tag{2.121}$$

$$\begin{aligned} \langle\Psi^{HP}_{DA^*}|\hat{\mathcal{H}}_{agg}|\Psi^{HP}_{DA^*}\rangle &= \langle\Psi^{HP}_{DA^*}|\hat{\mathcal{H}}_D + \hat{\mathcal{H}}_A + \hat{\mathcal{V}}_{DA}|\Psi^{HP}_{DA^*}\rangle \\ &= \langle\psi_D\psi_{A^*}|\hat{\mathcal{H}}_D + \hat{\mathcal{H}}_A + \hat{\mathcal{V}}_{DA}|\psi_D\psi_{A^*}\rangle \\ &= \langle\psi_D|\hat{\mathcal{H}}_D|\psi_D\rangle\langle\psi_{A^*}|\psi_{A^*}\rangle + \langle\psi_{A^*}|\hat{\mathcal{H}}_A|\psi_{A^*}\rangle\langle\psi_D|\psi_D\rangle + \langle\Psi^{HP}_{DA^*}|\hat{\mathcal{V}}_{DA}|\Psi^{HP}_{DA^*}\rangle \\ &= \epsilon_D + \epsilon_{A^*} + \langle\Psi^{HP}_{DA^*}|\hat{\mathcal{V}}_{DA}|\Psi^{HP}_{DA^*}\rangle \end{aligned} \tag{2.122}$$

The diagonal matrix elements evaluate to sums of the fragment energies ϵ and involve the van der Waals like expressions $\langle\Psi^{HP}_{D^*A}|\hat{\mathcal{V}}_{DA}|\Psi^{HP}_{D^*A}\rangle$ and $\langle\Psi^{HP}_{DA^*}|\hat{\mathcal{V}}_{DA}|\Psi^{HP}_{DA^*}\rangle$. The off-diagonal matrix elements represent the ECME $\langle\Psi^{HP}_{DA^*}|\hat{\mathcal{V}}_{DA}|\Psi^{HP}_{D^*A}\rangle$:

$$\begin{aligned} \langle\Psi^{HP}_{DA^*}|\hat{\mathcal{H}}_{agg}|\Psi^{HP}_{D^*A}\rangle &= \langle\Psi^{HP}_{DA^*}|\hat{\mathcal{H}}_D + \hat{\mathcal{H}}_A + \hat{\mathcal{V}}_{DA}|\Psi^{HP}_{D^*A}\rangle \\ &= \langle\psi_D\psi_{A^*}|\hat{\mathcal{H}}_D + \hat{\mathcal{H}}_A + \hat{\mathcal{V}}_{DA}|\psi_D\psi_{A^*}\rangle \\ &= \langle\psi_D|\hat{\mathcal{H}}_D|\psi_{D^*}\rangle\langle\psi_{A^*}|\psi_A\rangle + \langle\psi_{A^*}|\hat{\mathcal{H}}_A|\psi_A\rangle\langle\psi_D|\psi_{D^*}\rangle + \langle\Psi^{HP}_{DA^*}|\hat{\mathcal{V}}_{DA}|\Psi^{HP}_{D^*A}\rangle \\ &= \langle\Psi^{HP}_{DA^*}|\hat{\mathcal{V}}_{DA}|\Psi^{HP}_{D^*A}\rangle \end{aligned} \tag{2.123}$$

Due to the missing anti-symmetrization present in the Hartree product, the exchange contributions to the two-electron interaction vanishes leaving solely the Coulomb part.

$$\langle \Psi^{HP}_{DA^*} | \hat{\mathcal{V}}_{DA} | \Psi^{HP}_{D^*A} \rangle = \int\int \frac{\rho_D(x_1)\rho_A(x_2)}{r_{12}} dx_1 dx_2 \tag{2.124}$$

Expressed in terms of reduced one-electron transition densities, the ECME for SEET reads:

$$\langle {}^1\Psi^{HP}_{DA^*} | \hat{\mathcal{V}}_{DA} | {}^1\Psi^{HP}_{D^*A} \rangle = \sum_{ijkl} D_{ij}^{S_{D^*} \to S_D} D_{kl}^{S_A \to S_{A^*}} V_{ikjl} \tag{2.125}$$

Expressing TEET within the same formalism is not possible, because its ECME involves the exchange interaction. The exchange interaction can be reintroduced.[82]

$$\langle {}^1\Psi^{HP}_{DA^*} | \hat{\mathcal{V}}_{AD} | {}^1\Psi^{HP}_{D^*A} \rangle = \sum_{ijkl} D_{ij}^{S_{D^*} \to S_D} D_{kl}^{S_A \to S_{A^*}} (V_{ikjl} - \frac{1}{2} V_{iklj}) \tag{2.126}$$

For TEET the excitonic coupling is given by:[85]

$$\begin{aligned} \langle {}^1\Psi^{HP}_{DA^*} | \hat{\mathcal{V}}_{DA} | {}^1\Psi^{HP}_{D^*A} \rangle = -\sum_{ijkl} V_{iklj} \Bigg(& D_{ij}^{T_{D^*,+1} \to S_D} D_{kl}^{S_A \to T_{A^*,+1}} \\ & + D_{ij}^{T_{D^*,-1} \to S_D} D_{kl}^{S_A \to T_{A^*,-1}} + \frac{1}{2} D_{ij}^{T_{D^*,0} \to S_D} D_{kl}^{S_A \to T_{A^*,0}} \Bigg) \end{aligned} \tag{2.127}$$

Here only the transfer between triplet components belonging to the same magnetic spin quantum number is considered, as the Coulomb operator does not allow for spin-flips. In contrast to the Coulomb interaction, the exchange interaction falls off exponentially instead of r^{-1} rendering TEET a purely short-range process.

2.11.5 Electron Transfer Contributions

The discussion of the ECME did, so far, only consider simultaneous processes where de-excitation and excitation of the donor and acceptor (SEET) or ET reactions exchanging two electrons between the systems (SEET, TEET) contribute to EET. Besides these processes additional ET contributions to EET arise involving intermediate CT states.[23,86–88]

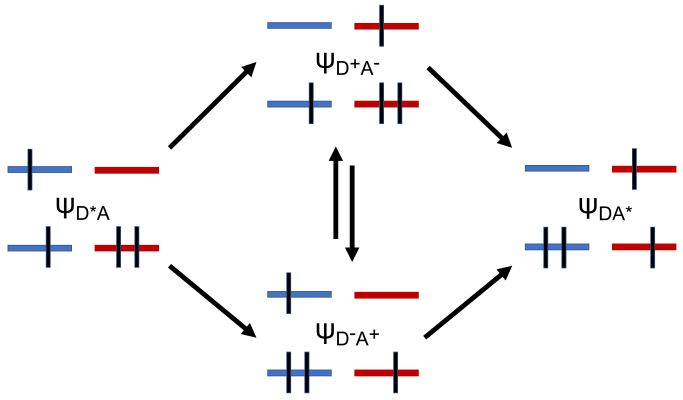

Figure 2.1: Short-range ET processes contributing to EET.[23,89]

Harcourt *et al.*[86] used a perturbative approach to account for ionic configurations in the evaluation of the ECME allowing the system's wave function to admix CT character. The initial- Ψ_I and final Ψ_F transfer states, where the excitation is centered on the donor or acceptor, respectively, are constructed as linear combinations between neutral and CT configurations.

$$\begin{aligned} \Psi_I &\approx N(\Psi_{D^*A} + \lambda\Psi_{D^+A^-} + \mu\Psi_{D^-A^+}) \\ \Psi_F &\approx N(\Psi_{DA^*} + \mu\Psi_{D^+A^-} + \lambda\Psi_{D^-A^+}) \end{aligned} \tag{2.128}$$

Evaluation of the coefficients λ and μ in first-order perturbation theory yields additional ET contributions via charged configurations, which are scaled by the energy difference with respect to the donor's excited state:

$$\begin{aligned} V_{DA} = &\langle\Psi_{DA^*}|V_{DA}|\Psi_{D^*A}\rangle \\ &- \frac{\langle\Psi_{DA^*}|ET_{DA}|\Psi_{D^+A^-}\rangle\langle\Psi_{D^+A^-}|ET_{DA}|\Psi_{D^*A}\rangle}{E_{D^+A^-} - E_{D^*A}} \\ &- \frac{\langle\Psi_{DA^*}|ET_{DA}|\Psi_{D^-A^+}\rangle\langle\Psi_{D^-A^+}|ET_{DA}|\Psi_{D^*A}\rangle}{E_{D^-A^+} - E_{D^*A}} \end{aligned} \tag{2.129}$$

Fujimoto extended the transition-density-fragment interaction (TDFI)[90,91] approach, a variation of the MTD method for usage with CIS and TDDFT calculations, with the ET integrals found by Harcourt et al. to create the TDFI-TI[23] approach. The transfer integrals are treated within a HOMO-LUMO approach utilizing Koopman's theorem[92] to obtain the energies required for the correct scaling of the interactions. The use of Koopman's theorem and the restriction to a HOMO-LUMO approach renders the method less usable as a general approach, while the application to the ethylene dimer showed that ET is responsible for the majority of short-range contributions to the ECME. As shown in this work, estimation of TEET requires an accurate treatment of these terms, as the ET contributions outweigh the direct contributions to EET at short distances.

3 Room Temperature Phosphorescence

The design of room temperature phosphorescence (RTP) emitters is presently a 'hot' topic with many applications in biological imaging, anti-counterfeiting, illumination of watch dials and safety signs as well as optoelectronic devices.[18] For RTP to occur two conditions have to be met:

- A phosphorescence channel has to exist, which is faster than its respective non-radiative deactivation channels. As phosphorescence is by definition a slow process, this requirement poses a difficult molecular design challenge especially at RT where the speed of the deactivation channels is hard to overcome.

- An ISC channel has to exist, which either directly or indirectly by utilizing internal conversion from higher triplet states, populates the emissive triplet state. This channel has to be faster than fluorescence and/or non-radiative deactivation processes originating in the singlet state such that an efficient singlet to triplet exciton conversion can take place.

To fulfill both conditions strong SOC is needed to mediate these spin–forbidden processes. Typically, phosphorescence emitters use heavy atoms like iridium (**Ir**) and platinum (**Pt**) to increase SOC and speed up the ISC and phosphorescence processes tremendously. Designing purely organic phosphorescence emitters still poses a challenge today as on the one hand ISC is slow in organics due to small SOC and on the other hand phosphorescence is efficiently quenched by non-radiative deactivation processes.
The design of organic RTP emitters involves typically inclusion of atoms with lone pairs like oxygen (**O**) and/or nitrogen (**N**) to increase the number of low-lying $n\pi^*$ states. Following El-Sayed's rule,[93] these $n\pi^*$ states can open up fast ISC channels as electronic transitions are strong if the excitation character of the two connected states differs. Therefore, ${}^1\pi\pi^* \rightsquigarrow {}^3n\pi^*$ and ${}^1n\pi \rightsquigarrow {}^3\pi\pi^*$ transitions can pose as efficient ISC channels.
Similar to ISC, the phosphorescence process is spin-forbidden and depends on SOC to circumvent the spin restrictions. In addition to strong SOC, the emissive state has to be bright and therefore its electric transition dipole moment is required to be strong. The size of the transition dipole moment (Eq. 2.77) is mostly determined by intensity borrowing through the SOC driven admixture of bright singlet states into the emissive triplet state. The strength of the mixing is stronger the closer the singlet states and triplet states are located energetically. In organics, bright singlet states are typically of $\pi\pi^*$ character requiring the phosphorescent state to be of $n\pi^*$ character to ensure strong coupling and allow phosphorescence speeds to surpass the non-radiative deactivation channels. Additionally, the non-radiative processes can be inhibited to allow phosphorescence to compete by embedding the emitter into rigid environments such as crystals or films.

In cooperation with researchers from Würzburg, Manchester and Xi'an, a group of triaryboranes was investigated of which two compounds showed RTP of up to four seconds. These triarylboranes were particularly interesting to investigate as their molecular structure does not include atoms with lone pairs and therefore ISC and phosphorescence was expected to be slow. The RTP project covers two publications on triarylboranes:

1. In the first publication[18] four triarylboranes were investigated and the origin of the RTP shown by two components as well as its mechanism was analyzed. The aim was to understand the effects driving the ISC and RTP processes in these compounds.

2. The second publication[19] addressed one RTP component from the previous study aimed at enhancing the ISC process by bromine substitution in ortho-, meta- and para-position of the unsubstituted aryl ring. Interestingly, the ortho-component showed dual room temperature phosphorescence (DRTP) in rigid environments indicating that environmental effects have a major influence on the mechanism.

Computationally, similar protocols were applied in both projects. Ground state equilibrium geometries were optimized with DFT utilizing the B3-LYP functional in the first study and PBE0 in the second one. Excited state geometries were obtained within the framework of linear response TDDFT, where for triplet states the TDA was employed additionally. The SVP[94,95] and def2-SVP[94,95] basis sets from the Turbomole[22] basis set library were used to describe the atomic orbitals on all atoms except bromine. For bromine the cc-pVTZ-PP[96] basis set was utilized in combination with the defpp-ecp[96] pseudopotential to incorporate scalar relativistic effects. The obtained equilibrium geometries were established as minima by frequency analysis performed in the first project purely numerically with the SNF[97] program while in the second publication analytical second derivatives available through the Gaussian[21] program package were used speeding up the computations tremendously.
Energies and MRCI wave functions were obtained with the DFT/MRCI method applying the redesigned R2016 Hamiltonian. Orbitals as basis for the DFT/MRCI computations were constructed utilizing DFT employing the BH-LYP functional. Absorption spectra were obtained from the corresponding DFT/MRCI line spectra by broadening through Gaussian functions. SOCMEs and phosphorescence rate constants were computed by means of the SPOCK program package. For the latter the DFT/MRSOCI procedure was utilized to obtain mixed-spin wave functions and their respective transition dipole moments. The VIBES[69,71] program supplied the FC emission spectra and intersystem crossing rate constants including temperature effects by a Boltzmann distributed population of the vibrational modes in the initial electronic state.

3.1 Persistent RTP from Triarylboranes

[Paper 1] Persistent Room Temperature Phosphorescence from Triarylboranes: A Combined Experimental and Theoretical Study[18]

In this publication, four triaryboranes were investigated of which two show RTP of up to four seconds in the crystalline state and in highly doped polymethylmethacrylate (PMMA) films. Since the triarylboranes (Fig. 3.1) do not contain atoms with lone pairs like oxygen (**O**) and nitrogen (**N**), it was unexpected to find RTP in these systems. This lead to interest in the mechanism as well as the circumstances enabling RTP. The molecular structures of these triarylboranes (Fig. 3.1) consist of a boron (**B**) center which is connected to three aryl substituents differing in the number of methyl substituents. The steric interactions of the aryl groups enforce a propeller-like structure, where the pitch of the aryl groups depends strongly on the methyl substitutions. Component **3** is particularly interesting, as it is $\mathcal{C}_3$ symmetric in the ground state causing Jahn–Teller distortions in its excited states due to doubly degenerate E-symmetric states. Even though the other components are not $\mathcal{C}_3$ symmetric, the degeneracy effects can still be seen.

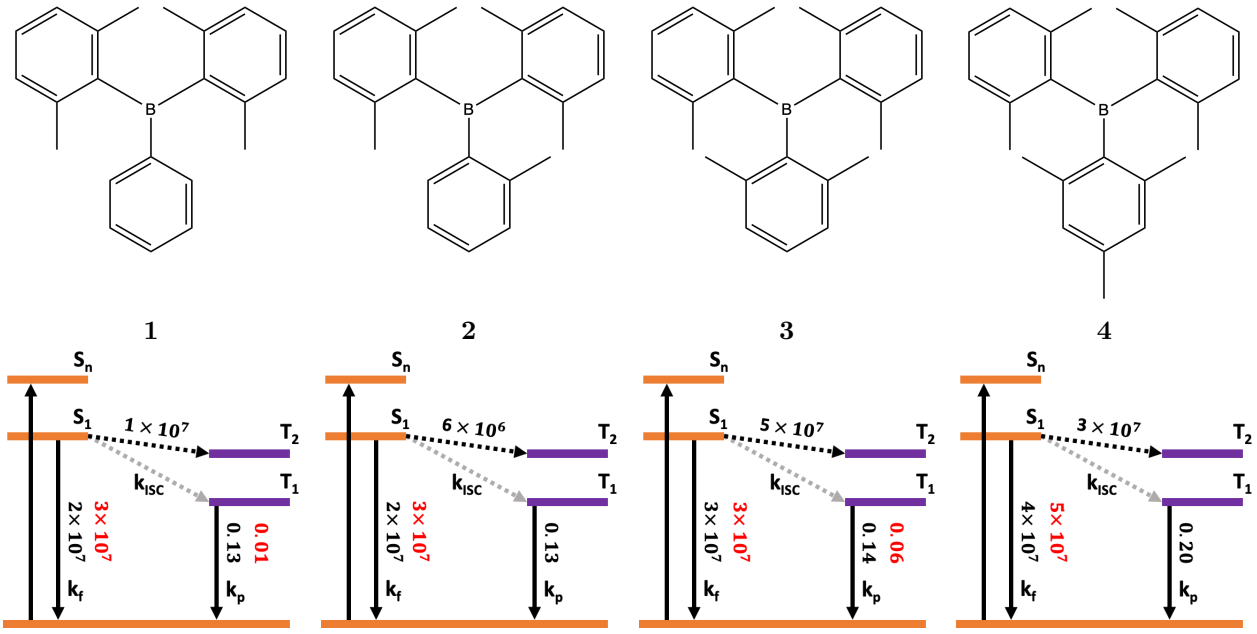

Figure 3.1: Structures and rate constants [s^{-1}] of the investigated triarylboranes. Experimental radiative fluorescence rate constants measured in hexane solution at RT and phosphorescence rate constants measured in the crystal at RT are given in red.

The absorption spectra show two broad bands and analysis of the vertical excitations at the ground state reveals that up to five excited singlet states are populated upon excitation. The spectra have similar features in the low energy region and exhibit a bathochromic shift moving from **1** to **4** in hexane at RT. All four triarylboranes emit blue/violet fluorescence, while greenish-yellow phosphorescence can be observed additionally in the crystalline state at RT for components **1** and **3**. Like the absorption, the fluorescence spectra exhibit the same features and bathochromic shifts in hexane. A similar situation is seen in the time-gated phosphorescence spectra measured in a frozen methylcyclohexane glass. The phosphorescence

bands of the components show a similar fine structure except in component **1** which is broadened by a low-frequency vibrational mode in the ground state. This low frequency vibrational motion is prohibited as soon as one methyl group is added to the unsubstituted aryl ring as present in the molecular structures of **2** to **4**.
Since fluorescence and phosphorescence are clearly visible in **1** and **3**, fluorescence is expected to compete with ISC on the same timescale. Phosphorescence has to be faster in these compounds or the non-radiative deactivation channels are inhibited strongly enough such that emission becomes visible. To shed some light on the reason why RTP is only visible in those two compounds, rate constants for the excited state transitions (Fig. 3.1) were evaluated. The rate constants agree well between experiment and theory and show that in each component an ISC channel exists that competes with fluorescence at about $10^7\,\mathrm{s}^{-1}$. The fastest ISC channel in these compounds is $S_1 \rightsquigarrow T_2$ with SOCMEs of about $1\,\mathrm{cm}^{-1}$, while the $S_1 \rightsquigarrow T_1$ channel is very slow with a vanishing SOCME. Following El-Sayed,[93] the $\langle S_1|\hat{\mathcal{H}}_{SO}|T_1\rangle$ SOCME is small due to the missing difference in electronic character of the S_1 and T_1 states, while for $S_1 \rightsquigarrow T_2$ the electronic character changes strongly visible in two aspects.

- The S_1 state is distributed over all three aryl substituents, while the T_2 excitation involves only two of the aryl rings. This difference in excitation character has only a small effect on the SOCME as it involves mainly π-type orbitals at different atom centers.
- The SOCME's strength originates from the σ-type density connecting the boron to the aryl ring in the T_2 state's difference density.

Therefore, the driving factors in the triarylboranes are $(\sigma, B\,p) \rightarrow (\pi, B\,p)$ and $(\pi, B\,p) \rightarrow (\sigma, B\,p)$ transitions generating SOCMEs of $1\,\mathrm{cm}^{-1}$ sufficient for ISC to progress at $10^7\,\mathrm{s}^{-1}$. As ISC can efficiently populate the T_2 state, phosphorescence from the T_1 state proceeds at about $0.13\,\mathrm{s}^{-1}$ up to $0.20\,\mathrm{s}^{-1}$ in all four components.

The measured and computed rate constants can explain the observed behavior of the four components, and show that the RTP of **1** and **3** does not originate from faster ISC or phosphorescence rate constants. Moreover, the longer RTP lifetime of **3** is explained, as it can convert singlet excitons more efficiently to triplet excitons than component **1**. The reason why **2** and **4** do not show RTP is founded in efficient non-radiative deactivation processes that quench the phosphorescence emission at RT. In **1** and **3** these processes are slower and allow phosphorescence to compete. As RTP is only observed in the crystalline state and in highly doped PMMA films, aggregation effects are expected to play a critical role in quenching the non-radiative deactivation processes. An analysis of the crystal structure by X-ray diffraction and the Hirshfeld[98] method by our cooperation partners in Würzburg revealed that the interactions in the crystal are stronger for **1** and **3**, while **2** shows the densest packing. The stronger interactions can be the cause for RTP as they may lead to quenching of the non-radiative deactivation channels. This study has shown that triarylboranes can pose as efficient RTP emitters without the need of lone pairs to facilitate fast ISC rate constants. The molecular environment is critical for the design of RTP emitters as non-radiative deactivation processes need to be inhibited to allow phosphorescence to compete.

3.2 Aggregation-induced dual phosphorescence from o-BrTAB

[Paper 2] Aggregation-induced dual phosphorescence from (o-bromophenyl)bis-(2,6-dimethylphenyl)borane at room temperature[19]

The previous study investigated four triarylboranes with respect to their ISC and emission mechanisms where two components showed RTP. Component **1** exhibits efficient ISC, which could be further improved by introducing heavy atoms into the system and utilizing the heavy atom effect to increase SOC and speed up the ISC process. Therefore, bromine was introduced into component **1**, which will from now on be referred to as triarylborane (TAB), in ortho- (o-BrTAB), meta- (m-BrTAB) and para-position (p-BrTAB) (Fig. 3.2). Interestingly, the bromine substitution did not only enhance ISC, moreover o-BrTAB showed DRTP, a rare process where phosphorescence is observed at RT from two distinct emission channels. DRTP was observed for this compound only in low temperature experiments and in crystalline state or embedded in highly doped PMMA films. Mechanistically, DRTP stems from two emissive triplet states within the same molecule or from more complex intramolecular interactions as intramolecular CT states and aggregates.[19] With this finding the scope broadened from investigating the bromine substitution effects onto the ISC processes in BrTAB to additionally understanding the origin of the DRTP in o-BrTAB and why it was not observed in m-BrTAB and p-BrTAB.

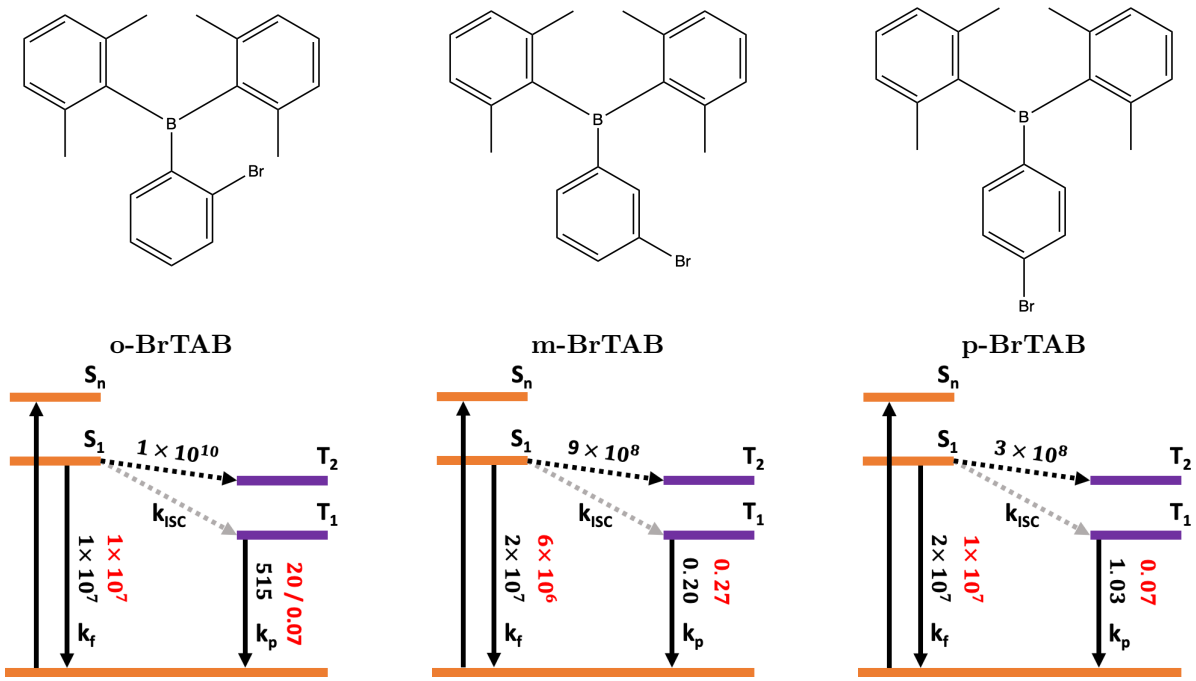

Figure 3.2: Structures and rate constants [s^{-1}] of the **o-BrTAB**, **m-BrTAB** and **p-BrTAB** monomers. Experimental radiative fluorescence rate constants measured in hexane solution at RT and phosphorescence rate constants measured in the crystal at RT are given in red.

The DRTP mechanism, as will be explained later, is believed to stem from a highly environment dependent aggregate state T_1^A. Therefore, the superscript M will denote monomer

states while the aggregate state will be referred to with superscript A. Absorption spectra of the compounds in hexane solution at RT show two broad bands at 300 nm and $260-270$ nm, where the band at lower energies is attributed to the $S_1^M \leftarrow S_0^M$ and $S_4^M \leftarrow S_0^M$ excitations, while the band at higher energy corresponds to the $S_6^M \leftarrow S_0^M$ excitation. The bromine position affects the absorption spectra only slightly such that moving from o-BrTAB to p-BrTAB the intensity of the band at higher energies is increased. As observed in the previous project the components emit blue fluorescence and, similar to the absorption, fluorescence is alike in all three compounds with an overlapping λ_{max} at 358 nm showing that bromine has no effect on the fluorescence behavior.
Green-yellowish RTP is observed in all three compounds where the phosphorescence spectra in a frozen methylcyclohexane glass at 77 K overlap similar to the fluorescence spectra and differ only slightly in their features. Interestingly, these spectra reveal residual fluorescence for m-BrTAB and p-BrTAB indicating, that in these compound's fluorescence can compete with the ISC channels. Time gated phosphorescence spectra in the crystalline state are red-shifted relative to the ones in frozen methylcyclohexane glass at 77 K, but still overlap for all three compounds. O-BrTAB differs from m-BrTAB and p-BrTAB by a smaller red-shift and a stronger resolved fine structure. The fine structure reveals four signals at 446, 477, 517 and 562 nm of which only the latter two stay visible after about 3 ms in time gated measurements. This behavior suggests that two triplet states are involved in the emission process, where one triplet has a short lifetime of about 0.8 ms and the other one a longer lifetime of about 234 ms. The computational phosphorescence spectrum of monomeric o-BrTAB reproduces the fine structure nicely showing that the initial phosphorescence signal belongs to the T_1^M state. The emission after 3 ms originates from a triplet state that is lower in energy indicated by a stronger red-shifted spectrum. The phenomenon is only observed in crystals and highly doped PMMA films suggesting an aggregate state T_1^A to be responsible for the slower phosphorescence channel. The meta- and para-compounds show dual phosphorescence only in low temperature experiments (77 K) indicating that with raising temperature non-radiative deactivation channels quench the emission of the short-lived triplet state.

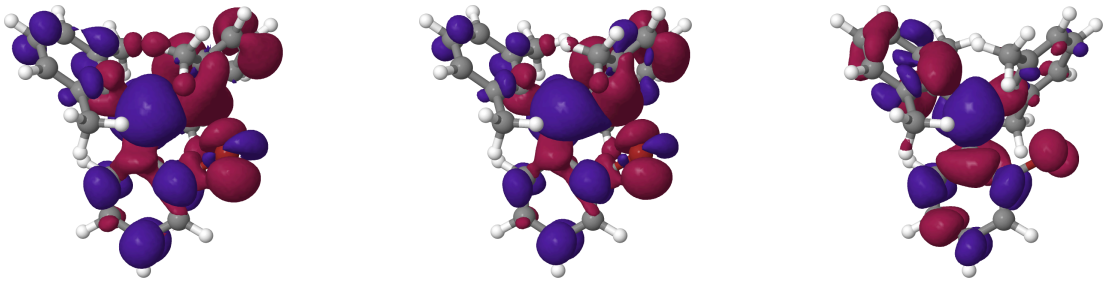

Figure 3.3: Difference densities of the S_1^M, T_1^M and T_2^M states in **o-BrTAB** relative to the S_0^M state at the S_1^M state geometry. Red areas indicate a loss of electron density, while blue areas indicate a gain.

To understand the mechanistic origin of the DRTP and why m-BrTAB and p-BrTAB are efficiently quenched at RT the rate constants were evaluated (Fig. 3.2). Fluorescence proceeds with a rate constant of 10^7 s^{-1} in all three compounds and therefore similar to the unsubstituted components. ISC is expected to be of the same order of magnitude in m-BrTAB and

p-BrTAB as residual fluorescence is visible in the spectra. In contrast, o-BrTAB does not show residual fluorescence indicating that at least one ISC channel exists which can convert singlet excitons into triplet excitons faster than fluorescence can depopulate the S_1^M state. The fastest ISC channel in o-BrTAB proceeds at 1×10^{10} s^{-1}, three orders of magnitude faster than the fluorescence. In m-BrTAB and p-BrTAB the ISC rate constants are 9×10^8 s^{-1} and 3×10^8 s^{-1}, respectively, close to the order of magnitude of the fluorescence rate constants explaining the observed residual fluorescence. Nevertheless, these ISC channels allow for efficient population of the triplet moiety even faster than in the unsubstituted components. As the ISC rate constants indicate, SOC is strongest in o-BrTAB followed by m-BrTAB and p-BrTAB which is the case due to a stronger involvement of bromine in the excited states. As shown in the previous work and following the El-Sayed rules,[93] SOC depends strongly on the change of orbital character along the transition. In o-BrTAB the $S_1^M \rightsquigarrow T_1^M$ transition is slower than $S_1^M \rightsquigarrow T_2^M$ as both states are similar in orbital character which is already seen for the unsubstituted compound. Still, compared to TAB the heavy atom effect increases the SOCME tremendously from 1 cm^{-1} to 25 cm^{-1}. The $S_1^M \rightsquigarrow T_2^M$ channel exhibits a SOCME sum of squares of immense 18639 cm^{-2} mainly caused by the rotation of the $(Br\,p)$ orbital moving between the S_1^M and T_2^M states (Fig. 3.3). In m-BrTAB the fastest ISC channel is found to be $S_1^M \rightsquigarrow T_3^M$ with a SOCME of 122 cm^{-1} while in p-BrTAB the fastest ISC channel is $S_1^M \rightsquigarrow T_1^M$ with about 1×10^7 s^{-1}. The cause for the decreasing SOCMEs moving from o-BrTAB to p-BrTAB is the vanishing bromine involvement in the excited states which can be seen in the difference densities of the publications supplementary information.

The phosphorescence rate constants show that emission from the T_1^M state in o-BrTAB is fast, while in m-BrTAB and p-BrTAB phosphorescence is a lot slower and of the order of magnitude as found for TAB. The stronger SOC in o-BrTAB allows efficient intensity borrowing from the bright $S_1^M \leftarrow S_0^M$ and $S_4^M \leftarrow S_0^M$ transitions through the large $\langle S_2^M|\hat{\mathcal{H}}_{SO}|T_1^M\rangle$ and $\langle S_4^M|\hat{\mathcal{H}}_{SO}|T_1^M\rangle$ SOCMEs. In m-BrTAB and p-BrTAB these SOCMEs are small rendering intensity borrowing inefficient and the phosphorescence rate constant slower than in o-BrTAB. These findings agree well with the experimental observations and show that for DRTP to be visible in m-BrTAB and p-BrTAB non-radiative deactivation processes quenching the slow phosphorescence have to be inhibited by low temperatures. The long-lived phosphorescence component is not observed in the monomer calculations and even the calculation of dimers did not show an aggregate state that could be responsible for the emission. As the DRTP phenomenon is only visible in crystals and highly doped PMMA films the T_1^A state is expected to be delocalized over multiple monomer units. The X-Ray diffraction and Hirshfeld[98] experiments of the Würzburg group indicate, that in o-BrTAB multiple molecular contacts inhibit the non-radiative deactivation processes allowing the short-lived component to be observed even at RT.

In conclusion, RTP in triarylboranes can be substantially increased by including heavy atoms like bromine into the molecular structure improving the efficiency of the ISC and phosphorescence channels. The position of the bromine substitution has a heavy impact on ISC and phosphorescence rate constants rendering these processes orders of magnitudes faster in o-BrTAB than in m-BrTAB and p-BrTAB. The environment plays a crucial role to allow RTP and DRTP to be visible as non-radiative deactivation processes have to be inhibited to reduce phosphorescence quenching.

4 Reduced One-Electron Density Matrices

Reduced one-electron (transition) density matrices which will be named in the following simply as (transition) density matrices, pose important tools in quantum chemistry. On one hand, they offer easy and efficient access to expectation values of quantum mechanical operators while on the other they are used to visualize the character of wave functions and their respective transitions. Properties of wave functions like (transition) dipole moments, their corresponding oscillator strengths and SOCMEs can be obtained utilizing (transition) density matrices following Eq. 2.59. Moreover, methods like the MTD approach utilize (transition) density matrices to obtain the ECME between two states located on different fragments.
Another important use for (transition) density matrices is to visualize transitions between electronic states and characterize them.[99]

$$\Delta_{FI} = \langle \Psi_I | \hat{\mathcal{D}} | \Psi_I \rangle - \langle \Psi_F | \hat{\mathcal{D}} | \Psi_F \rangle \tag{4.1}$$

Difference densities Δ_{FI} plotted on a 3D grid show spaces of positive and negative difference painting a clear picture about the electronic changes happening when moving from initial to final state. To visualize electron transfer processes (Sec. 7.2) difference densities can be converted to attachment and detachment densities showing only spaces where electron density is added or removed.[99] TheoDORE, a toolbox for automated analysis of excited states developed by F. Plasser[100] offers a fragment based analysis procedure to aid in the character assignment utilizing density matrices as foundation for the analysis.

Due to their advantages, the evaluation of density matrices is widely available in quantum chemical software packages as intermediate properties for various methodologies. Linear response TDDFT supplies singlet-singlet $\langle {}^1\Psi_F | \hat{\mathcal{S}} | {}^1\Psi_0 \rangle$ and singlet-triplet $\langle {}^3\Psi_F | \hat{\mathcal{T}}_0 | {}^1\Psi_0 \rangle$ (transition) density matrices between the excited states and the ground state, while density matrices between excited states are not evaluated. The DFT/MRCI and DFT/MRSOCI methods supply density matrices for the $\hat{\mathcal{S}}$ operator (Eq. 2.40) between all employed states $\langle \Psi_F | \hat{\mathrm{S}} | \Psi_I \rangle$ where the DFT/MRCI program was additionally restricted to matrices between states of the same multiplicity. Density matrices for operators involving spin-flips ($\hat{\mathcal{T}}_{+1}$, $\hat{\mathcal{T}}_0$ and $\hat{\mathcal{T}}_{-1}$) were not available at the beginning of my PhD project. The SPOCK program package utilizes the spin-flip operators to obtain SOCMEs by direct contraction of the wave functions in the basis of CSFs with their corresponding SOMF integrals. Density matrices of the form $\langle {}^3\Psi_F | \hat{\mathcal{T}}_\gamma | {}^1\Psi_I \rangle$ are in principle evaluated during the calculation of SOCMEs, but diagonal matrix elements are ignored during the contraction as they vanish. Additionally, employing AMEWs as done within Spoiler (Chapter 6) requires the evaluation of density

matrices with similar forms as mentioned above.

Within this thesis, densities employing the $\hat{\mathcal{S}}$, $\hat{\mathcal{T}}_{+1}$, $\hat{\mathcal{T}}_0$ and $\hat{\mathcal{T}}_{-1}$ operators are required to obtain electric (transition) dipole moments, SOCMEs and ECMEs for the evaluation of radiative as well as non-radiative rate constants. An extension of Spoiler for phosphorescence rate constants required the evaluation of $\langle {}^1\Psi_F|\hat{\mathcal{S}}|{}^1\Psi_I\rangle$ and $\langle {}^3\Psi_F|\hat{\mathcal{T}}_{+1}|{}^1\Psi_I\rangle$ type density matrices employing AMEWs to obtain (transition) dipole moments. These transition moments are in turn employed in combination with the already available SOCMEs to obtain mixed-spin wave functions and their properties by the SOCQDPT approach (Sec. 2.9.2). DFT/MRCI singlet-triplet density matrices $\langle {}^3\Psi_F|\hat{\mathcal{T}}_{+1}|{}^1\Psi_I\rangle$ build the foundation for the calculation of TEET couplings in the MTD approach and are required to apply the TheoDORE wave function analysis to DFT/MRCI triplet states.

To supply the density matrices by post-processing wave functions obtained within the different methodologies, the DensityEngine was implemented to centralize the density matrix evaluation and offer optimizations for DFT/MRCI wave functions and AMEWs. The DensityEngine is a C++ library created to offer density matrices for arbitrary density operators with modularity and reusability in mind. Additionally, the library was parallelized utilizing a shared memory scheme to offer scalability and improve the old serial DFT/MRCI implementations. The library is used in the Densomat and Spoiler programs to access densities for DFT/MRCI wave functions and AMEWs respectively, but can easily be incorporated in future projects.
In the following the computational procedures, implementations and usage of the DensityEngine as well as the Densomat are discussed while usage of the DensityEngine within Spoiler is part of chapter 6. Additionally, the extension of TheoDORE with DFT/MRCI singlet-triplet density matrices is presented.

4.1 The DensityEngine

The DensityEngine is a C++ framework to compute (transition) density matrices. It offers access to density matrices employing wave functions containing only singly excited configurations in relation to a reference configuration as well as truncated wave functions with arbitrary excitation orders. Density matrices for CIS and AMEWs of TDDFT amplitudes utilize the former, while the latter is used in combination with DFT/MRCI wave functions. The wave functions can exhibit arbitrary S and M_s quantum numbers and are required to be expanded in the basis of CSFs. Currently, the four density operators $\hat{\mathcal{S}}$, $\hat{\mathcal{T}}_{+1}$, $\hat{\mathcal{T}}_0$ and $\hat{\mathcal{T}}_{-1}$ are implemented, but since the DensityEngine was developed with modern software principle in mind the density operators work as a plugin to the application and allow for easy extension. Recently, two new density operators $\hat{\mathcal{D}}^A = \hat{a}^\dagger$ and $\hat{\mathcal{D}}^C = \hat{a}$ were implemented under my supervision by Simon Metz. These operators are used for the calculation of Dyson orbitals[101] which are typically employed to describe ionization processes. The implementation required only small changes of the code basis underlining the easy to extend framework structure for future projects. Moreover, the DensityEngine is a library that can be embedded in future programs eliminating unnecessary data conversions for external routines.

To obtain the density matrix, the density operator $\hat{\mathcal{D}}$ has to be applied to the initial state's wave function Ψ_I followed by integrating the final Ψ_F and now altered $\Psi_I^{'}$ wave functions.

$$\langle \Psi_F | \hat{\mathcal{D}} | \Psi_I \rangle = \langle \Psi_F | \Psi_I^{'} \rangle \tag{4.2}$$

Since the density operator represents a single excitation (Eq. 2.40), contributions arise only from equal configurations ($\hat{a}_i^\dagger \hat{a}_i$) as well as configurations exhibiting a relative single excitation ($\hat{a}_i^\dagger \hat{a}_j$). Equal configurations contribute to the diagonal elements $\mathbf{D}_{ii}$ of the density matrix, while couplings of relative single excitations are accumulated in the off-diagonal elements $\mathbf{D}_{ij}$.

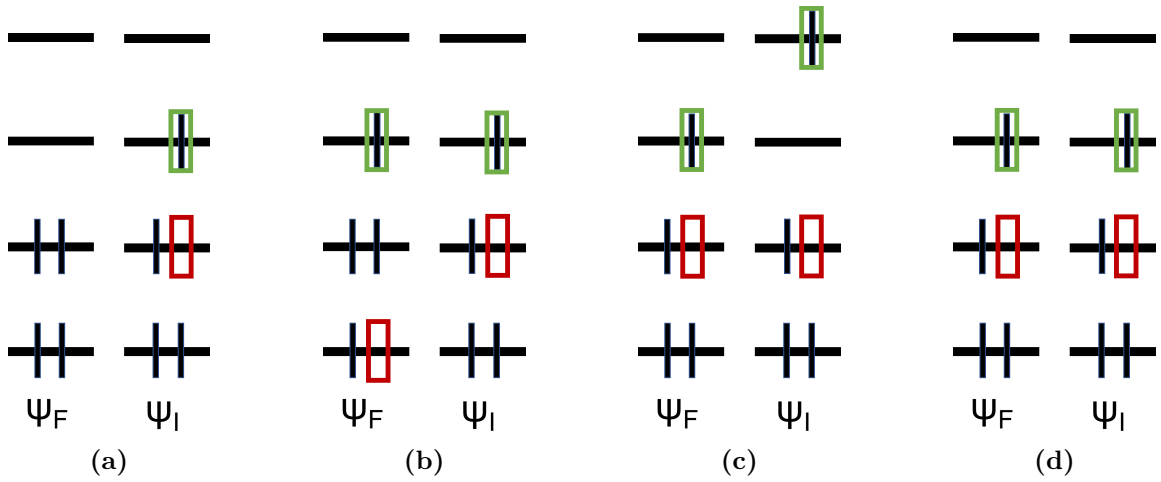

Figure 4.1: Selected coupling cases contributing to density matrices. Annihilators (red) and creators (green) mark the excitations with respect to the closed shell reference configuration.

Therefore, the evaluation procedure requires to find equal configurations and relative single excitations between the wave functions and to calculate the spin-coupling coefficients η for

the respective CSFs (Eq. 2.43). Figure 4.1 shows typical coupling cases between singly and doubly excited configurations with respect to the closed shell reference where couplings arise in the following cases:

- If the annihilators of both compared configurations are equal, density contributions arise for equal (Fig. 4.1(d)) creators or one creator differences in the creator space (Fig. 4.1(c)).
- If the annihilators show a one annihilator difference, the creators need to differ by one creator to contribute (Fig. 4.1(a)).
- If the annihilators show a two annihilator difference, the creators need to be equal to contribute (Fig. 4.1(b)).

Utilizing the coupling cases the evaluation process can be formulated primitively in pseudocode as:

Listing 4.1: Calculation of density matrices.

```
for finalConfiguration in finalWavefunction {
    for initialConfiguration in initialWavefunction {
        if (finalConfiguration == initialConfiguration)
            finalConfiguration.integrateEqualConfigurations(initialConfiguration)
        else if (finalConfiguration.isSingleExcitation(initialConfiguration))
            finalConfiguration.integrateSingleExcitation(initialConfiguration)
    }
}
```

Here all configurations of the final and initial wave functions are compared, and only in the case of equal configurations and relative single excitations the integration is performed. To ensure efficient evaluation procedures the actual implementation differs between the wave functions types utilizing the wave function structure to ease the configuration comparison.

- **Truncated wave functions with arbitrary excitation orders**:
  Truncated wave functions with arbitrary excitation orders require a more complex approach to reduce the computational effort of the configuration comparison. First, the configurations are collected in configuration blocks exhibiting the same excitation order relative to one reference configuration. This reduces the number of configuration comparisons drastically, since only configuration blocks with neighboring excitation orders ($|ex_F - ex_I| <= 1$) have to be considered.

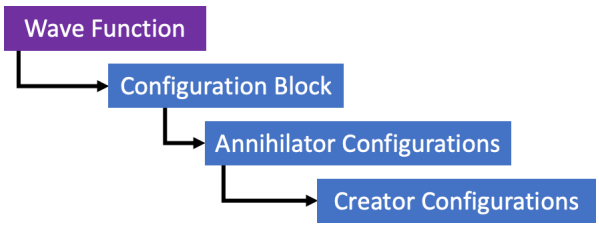

Figure 4.2: Structure of truncated wave functions with arbitrary excitation orders.

Additionally, each configuration is separated as done in the DFT/MRCI code into an annihilator and creator configuration containing only the respective annihilators and

creators. This subdivision allows clustering of multiple configurations sharing the same annihilator configuration, but differing in their creator configurations. Moreover, the configuration comparison can be skipped if the annihilator configurations differ by more than a single excitation. The annihilator and creator configurations are ordered with respect to their annihilators and creators enabling the utilization of efficient search algorithms like *Binary Search* to find configurations with $\mathcal{O}(log(n))$ complexity instead in $\mathcal{O}(n)$ for linear searches.

- **Wave functions with singly excited configurations**:
  Single excited configurations correspond to exactly one CSF allowing to save the coefficients of the wave function's linear combinations in a matrix $\mathbf{C}$ utilizing the position $\mathbf{C}_{ia}$ as indicator for the configurations annihilator and creator. Since all single excitations are contained within the wave function, the configuration comparison reduces to simple loops over these coefficients.

Computing density matrices requires additionally to the efficient configuration comparison the CSF spin-couplings η. The DFT/MRCI and SPOCK programs calculate the spin-couplings once for a given number of open shells and store them utilizing a pattern approach introduced by Wetmore and Segal[43] for the $\hat{\mathcal{S}}$ operator and extended by Kleinschmidt *et al.*[45] for the $\hat{\mathcal{T}}_0$ and $\hat{\mathcal{T}}_{+1}$ operators. The DensityEngine utilizes for this purpose the CsfEngine (Sec. 4.2), another C++ library which supplies routines and structures to obtain and manipulate CSFs. The CsfEngine allows the DensityEngine to implement arbitrary density operators with minimal effort. Spin-couplings obtained from these CSFs are cached dynamically within a hash map utilizing a similar pattern approach to generate the hash map's keys. The hash map allows looking up the spin-couplings in constant time ($\mathcal{O}(1)$) rendering this approach very efficient.

The top level structure of the DensityEngine (Fig. 4.3) shows the most important entities supplied to users (applications) of the library.

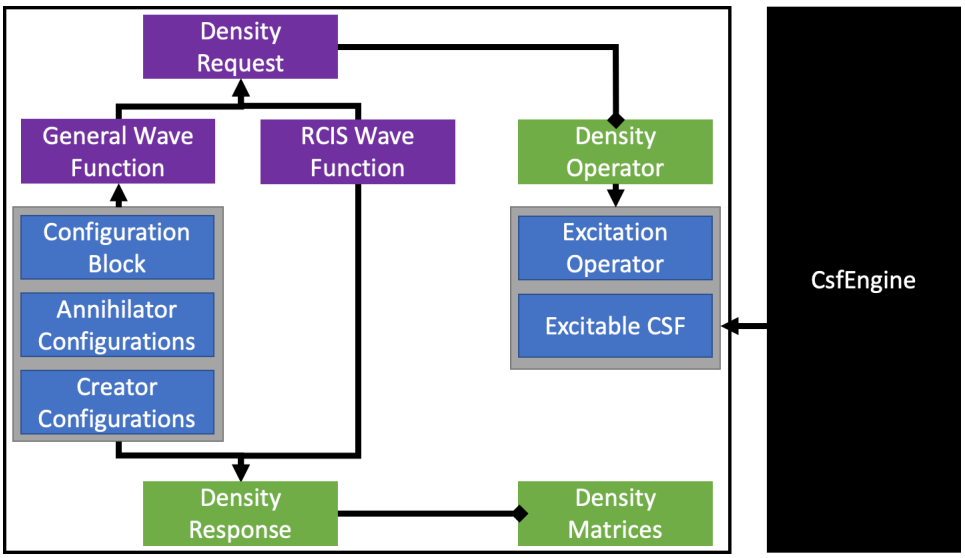

Figure 4.3: The DensityEngine.

To evaluate density matrices, the user has to instantiate one of the wave function structures and add the coefficient weighted configurations to the structure. The **GeneralWaveFunction**, which represents the truncated wave function branch, inserts the added configurations into the more complex block structures. The **DensityRequest** structure allows requesting a batch of density matrices and setting the density operator for the evaluation process. The wave function structures offer integration routines, which require a density request to be supplied and yield a **DensityResponse** containing the requested density matrices.

4.2 The CsfEngine

The CsfEngine is a C++ library which offers routines and data structures to construct and manipulate CSFs. CSFs are required in this thesis to evaluate the spin-couplings η for DFT/MRCI wave functions and AMEWs. To follow modular design principles, the CSF construction and manipulation was separated from the DensityEngine to utilize the routines and structures in multiple applications. CSFs can be constructed in the CsfEngine following the genealogical approach and by combination of already known CSFs from two subsystems. The latter can be used to obtain CSFs for wave functions represented in a product ansatz ($\Psi = \psi_A\psi_B$) by creating the proper linear combinations of the subsystem A's and B's Slater determinants. While the genealogical construction of CSFs is already implemented in the ETAGEN program providing η-Fields for the DFT/MRCI and SPOCK program packages, the DensityEngine required manipulable CSF structures instead of the implicitly handled CSFs within ETAGEN to support the spin-couplings for arbitrary density operators.

A helpful tool when dealing with CSFs is the *Branching Diagram*:

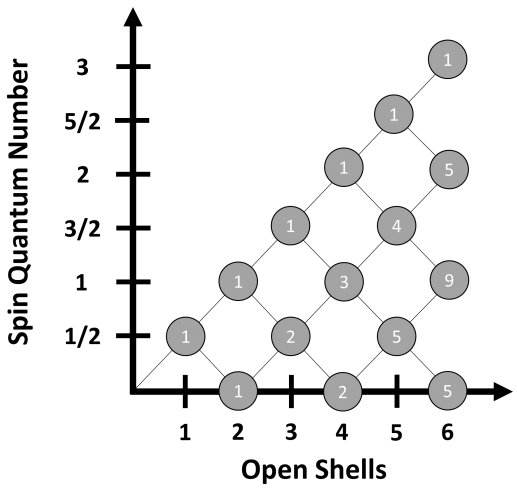

Figure 4.4: The Branching Diagram.

The *Branching Diagram* shows the number of constructible CSFs corresponding to a given spin quantum number S and number of open shells. Moreover, the *Branching Diagram* offers aid in the construction of CSFs supplying so-called path functions. Path functions define routes through the *Branching Diagram* that can be utilized to add electrons with their respective spin to the CSF to obtain the final CSF at the end of the path. The number of

CSFs for a given spin quantum number S and number of open shells corresponds directly to the number of possible path functions.

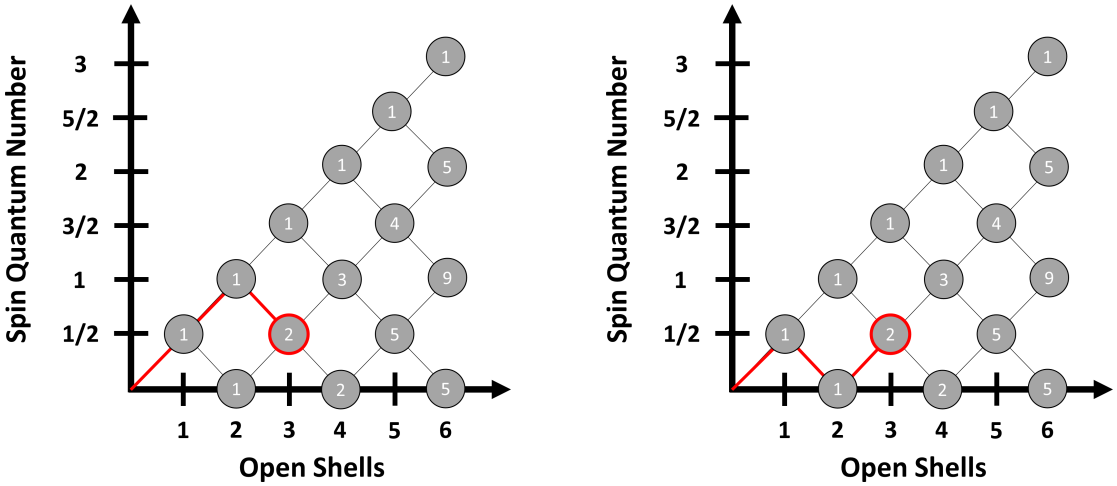

Figure 4.5: Path function in the Branching Diagram.

The genealogical approach to CSF construction utilizes the path functions in a recursive scheme to obtain the appropriate linear combinations of Slater determinants, while the CSF construction from CSFs of subsystems in principle combines all path functions in each possible permutations to yield a similar result. In the following both approaches are presented following R. Pauncz.[46]

4.2.1 Genealogical CSF Construction

The genealogical approach constructs CSFs utilizing the path functions to add electrons in sequence following the path recursively. Corresponding to raising and falling path segments, two equations exist for the addition and subtraction of electron spins respectively:

Addition

$$\begin{aligned}\psi(N,S,M_S;k) = &\Big[(S+M)^{\frac{1}{2}}\psi\Big(N-1,S-\frac{1}{2},M_S-\frac{1}{2};k'\Big)\alpha(N)\\ &+(S-M)^{\frac{1}{2}}\psi\Big(N-1,S-\frac{1}{2},M_S+\frac{1}{2};k'\Big)\beta(N)\Big]\\ &\times(2S)^{-\frac{1}{2}}\end{aligned} \tag{4.3}$$

Subtraction

$$\begin{aligned}\psi(N,S,M_S;k) = &\Big[-(S-M+1)^{\frac{1}{2}}\psi\Big(N-1,S+\frac{1}{2},M_S-\frac{1}{2};k'\Big)\alpha(N)\\ &+(S+M+1)^{\frac{1}{2}}\psi\Big(N-1,S+\frac{1}{2},M_S+\frac{1}{2};k'\Big)\beta(N)\Big]\\ &\times(2S+2)^{-\frac{1}{2}}\end{aligned} \tag{4.4}$$

Here $\psi(N,S,M;k)$ is the CSF with number of electrons N, spin quantum number S, magnetic spin quantum number M_S and path function k. To construct a CSF for a singlet configuration

with two open shells one path function ($up - down$) starting from the lower left of the *Branching Diagram* exists. To apply the recursive equations the path function is inverted ($down - up$) starting at $S = 0, N = 2$. For the first descending path segment the subtraction equation (Eq. 4.4) has to be applied:

$$\psi(2,0,0;k) = \left[-\psi\left(1,\frac{1}{2},-\frac{1}{2};k'\right)\alpha(2) + \psi\left(1,\frac{1}{2},\frac{1}{2};k'\right)\beta(2)\right] \times \frac{1}{\sqrt{2}} \tag{4.5}$$

To solve the given expression knowledge of the doublet CSFs $\psi(1,\frac{1}{2},-\frac{1}{2};k')$ and $\psi(1,\frac{1}{2},\frac{1}{2};k')$ is required which can be obtained by applying the addition equation to the remaining path $k' = up$:

$$\begin{aligned} \psi\left(1,\frac{1}{2},\frac{1}{2};k'\right) &= \psi\left(0,0,0;k''\right)\alpha(1) = \alpha(1) \\ \psi\left(1,\frac{1}{2},-\frac{1}{2};k'\right) &= \psi\left(0,0,0;k''\right)\beta(1) = \beta(1) \end{aligned} \tag{4.6}$$

Since closed shells do not contribute to the CSFs, $\psi(0,0,0;k'')$ vanishes leaving the CSFs for two doublets with $M = \frac{1}{2}$ and $M = -\frac{1}{2}$. Filling in the results into the expression obtained for Eq. 4.5 yields the singlet CSF for two open shells:

$$\begin{aligned} \psi(2,0,0;k) &= \left[-\beta(1)\alpha(2) + \alpha(1)\beta(2)\right] \times \frac{1}{\sqrt{2}} \\ &= \frac{1}{\sqrt{2}}\left(\alpha(1)\beta(2) - \beta(1)\alpha(2)\right) \end{aligned} \tag{4.7}$$

4.2.2 CSF Construction from Subsystems

Another way to construct a CSFs with a given number of open shells and quantum numbers S and M_S is by using CSFs of subsystems A and B with a lesser number of open shells obeying the following relations:

$$\begin{aligned} S^A + S^B \leq S \leq |S^A - S^B| \qquad & N = N^A + N^B \\ & M_S = M_S^A + M_S^B \end{aligned} \tag{4.8}$$

The CSF can then be obtained as linear combination of the subsystem CSFs following

$$\begin{aligned} \psi(N,S,M_S;S^A,S^B,k^A,k^B) = \sum_{M_S^A M_S^B} & \langle S^A,S^B,M_S^A,M_S^B|S,M_S\rangle \\ & \times \psi(N^A,S^A,M_S^A;k^A)\psi(N^B,S^B,M_S^B;k^B) \end{aligned} \tag{4.9}$$

where $\langle S^A,S^B,M_s^A,M_s^B|S,M_S\rangle$ are the Clebsch–Gordan coefficients. The CSF for a singlet configuration with two open shells as given above can then be obtained utilizing the doublet CSFs $\psi(1,\frac{1}{2},\frac{1}{2};k^A) = \alpha$ and $\psi(1,\frac{1}{2},-\frac{1}{2};k^B) = \beta$.

$$\begin{aligned} \psi\left(2,0,0;\frac{1}{2},\frac{1}{2},k_1,k_2\right) &= \left\langle \frac{1}{2},\frac{1}{2},\frac{1}{2},-\frac{1}{2}\middle|0,0\right\rangle \times \psi\left(1,\frac{1}{2},-\frac{1}{2};k_1\right)\psi\left(1,\frac{1}{2},\frac{1}{2};k_2\right) \\ &+ \left\langle \frac{1}{2},\frac{1}{2},-\frac{1}{2},\frac{1}{2}\middle|0,0\right\rangle \times \psi\left(1,\frac{1}{2},\frac{1}{2};k_1\right)\psi\left(1,\frac{1}{2},-\frac{1}{2};k_2\right) \\ &= -\frac{1}{\sqrt{2}}\beta\alpha + \frac{1}{\sqrt{2}}\alpha\beta = \frac{1}{\sqrt{2}}\left(\alpha\beta - \beta\alpha\right) \end{aligned} \tag{4.10}$$

The two approaches to CSF construction are implemented in the CsfEngine of which the top level entities are show in Fig. 4.6. The **CSFEngine** interface exposes both approaches to the user (application) passing collections of **CSF** structures, which allow for further manipulations like insertion and removal of electrons taking care of the necessary sign flips in the linear combinations Slater determinants. The **CSFFactory** coordinates the construction of CSFs by obtaining path functions for the genealogical construction (**Branch**) and subsystem approach (**CombinedBranch**). The generation functions for both approaches are integrated into the path function structures. A hash map is used to cache generated CSFs such that frequent requests for the same CSFs reduce to a simple constant time hash map look up ($\mathcal{O}(1)$).

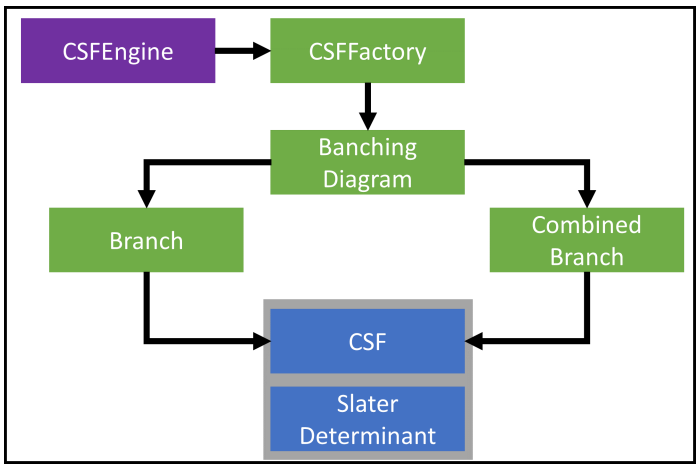

Figure 4.6: The CsfEngine.

4.3 The Densomat : DFT/MRCI Density Matrices

The Densomat is a C++ program that was created to supply (transition) density matrices utilizing the DensityEngine for DFT/MRCI wave functions. Herein, the DFT/MRCI program evaluates singlet-singlet and triplet-triplet density matrices, but does not supply singlet-triplet densities required for the evaluation of triplet-triplet ECMEs within the MTD approach as well as the analysis of triplet states using TheoDORE. Moreover, the density matrix evaluation in the DFT/MRCI program is not parallelized, while the DensityEngine offers shared memory parallelized routines employing OpenMP[102] yielding a better CPU utilization if more than one CPU is used for the DFT/MRCI run. The steps performed by the Densomat are in more detail:

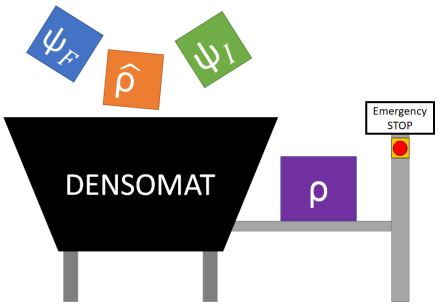

Figure 4.7: Densomat Logo.

- **Preprocessing of the DFT/MRCI wave functions**:
  The multireference wave functions are converted to a single reference wave function and appended to the DensityEngine wave function structure. The construction of the wave functions is performed utilizing Abelian point group symmetry such that

the symmetry employed in the DFT/MRCI calculation can be reused to reduce the computational effort.

- **Evaluating of density matrices**:
  The DensityEngine is utilized to obtain the density matrices $\langle\Psi_F|\hat{\mathcal{D}}|\Psi_F\rangle$ and $\langle\Psi_R|\hat{\mathcal{D}}|\Psi_I\rangle$ while the latter are obtained only between the reference state Ψ_R and all initial states. The density operator, reference state as well as the employed wave functions are specified in the input file.

- **Creation of density matrix files**:
  The obtained density matrices are written to files, where the user can specify the format (*DFTMRCI*, *DENSOMAT*). The *DFTMRCI* format is utilized by applications of the DFT/MRCI program package but is not usable for singlet-triplet density matrices which require the new *DENSOMAT* format.

The BoysOV diabatization implemented in the EET program, requires the density matrices separated into occupied-occupied and virtual-virtual orbital blocks where the separation can be performed with the Densomat. Additional to the evaluation of density matrices, the Densomat can be utilized to obtain Dyson orbitals implemented into the DensityEngine by Simon Metz and supervised as well as connected to the Densomat by me.

The Densomat is used by supplying the required parameters in an input file.

```
1    densomat [input] > [output]
```

The desired input file can be generated utilizing one of the following commands:

```
1    densomat -g DFTMRCI
2    densomat --generateInput DFTMRCI
```

The Densomat was mainly used for the evaluation of triplet-triplet couplings by the MTD approach and has otherwise been utilized so far in some publications[103–105] to supply singlet-triplet densities for the analysis of excited triplet states with TheoDORE.

4.4 TheoDORE Extension – Analysis of Triplet States

TheoDORE[100] is a tool to analyze excited-state calculations. It provides a fast and easy way to extract and visualize the important information about the excited state's character and composition. Popular analyses that can be performed are fragment-based approaches to evaluate the excited state's character, estimations of exciton sizes to measure CT and natural transition orbitals to investigate excited states with multiconfiguration character. TheoDORE is interfaced to multiple quantum chemical packages and utilizes (transition) density matrices obtained in the packages' format.

In 2020, TheoDORE was interfaced by the maintainer Felix Plasser to the DFT/MRCI code using singlet-singlet and singlet-triplet (transition) density matrices to analyze the excited singlet and triplet states. Instead of the DFT/MRCI's singlet-triplet transition densities, that were in a development state at that time, triplet-triplet densities were employed resulting in wrong results for the analyses of triplet states. Therefore, TheoDORE was changed by me to process the newly developed singlet-triplet transition density matrices available through the Densomat.
The adapted implementation was used together with the new density matrices to perform analyses for triplet states.[103–105]

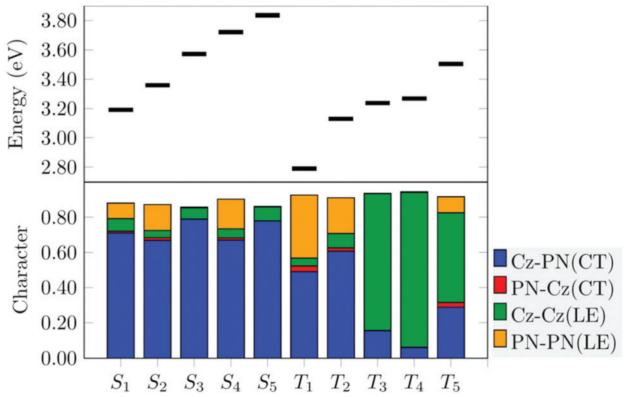

Figure 4.8: Example of a typical excited state fragment analysis performed with TheoDORE used in the analysis of 2CzPN (Sec. 5.5).

5 Vibronic Coupling

The consideration of vibronic coupling effects is very important to properly describe systems and their behavior. Investigating a molecular system computationally requires deciding on a suited tool set that supplies the needed accuracy while keeping the cost of the calculations at bay. One way to conduct such an investigation, is to optimize the equilibrium geometries of the system and obtain its properties at those chosen geometries. This 'static' computation protocol allows employing more sophisticated quantum chemical methods, as the number of calculations is small and more effort and time can be spent on each one. A 'dynamic' approach uses methods like molecular dynamics simulations which imitate the movement of the molecule while the system's properties are evaluated utilizing less expensive methodologies at the cost of accuracy. From an experimental point of view, the 'dynamic' approach represents the experiment better if the simulation meets the experiment's time range since movements and structural changes of the system are taken into account while the measurement is conducted. If the accuracy is crucial to describe the system properly, 'static' calculations are the tool of choice and a way has to be found to incorporate at least some dynamic effects into the calculations. Employing the HT approximation[68] (Sec. 2.10) allows to include some dynamic effects with respect to the vibrations ν by a Taylor expansion of the property along the dimensionless normal coordinates $\mathcal{Q}_k$ of the equilibrium geometry or reference geometry $\mathcal{Q}_0$.

$$\begin{aligned}\sum_b \langle \Psi_F \nu_b | \hat{\mathcal{O}} | \Psi_I \nu_a \rangle = \langle \Psi_F | \hat{\mathcal{O}} | \Psi_I \rangle \Big|_{\mathcal{Q}_0} \sum_b \langle \nu_b | \nu_a \rangle \\ + \sum_k^N \frac{\delta \langle \Psi_F | \hat{\mathcal{O}} | \Psi_I \rangle}{\delta \mathcal{Q}_k} \Big|_{\mathcal{Q}_0} \sum_b \langle \nu_b | \mathcal{Q}_k | \nu_a \rangle \\ + \dots\end{aligned} \tag{5.1}$$

The matrix element $\langle \Psi_F | \hat{\mathcal{O}} | \Psi_I \rangle$ is obtained from a single point calculation at the reference geometry, while the gradients $\frac{\delta \langle \Psi_F | \hat{\mathcal{O}} | \Psi_I \rangle}{\delta \mathcal{Q}_k}$ have to be evaluated analytically or numerically.

5.1 Numerical Gradients

Analytical gradients are highly accurate and come at low cost, but require solving very difficult mathematical problems to obtain analytic expressions if they exist at all. Numerical gradients in contrast are easily available but require one or two additional single point calculations per mode increasing the overall computational cost. It is important to note here that deriving these gradients numerically poses a problem as the computed matrix elements at different geometries are allowed to have an arbitrary phase. Typically, this means no harm because the matrix elements are employed in their quadratic form but for the gradient

evaluation the phases have to be corrected. The used correction procedures in this work are explained in section 5.2.

The simplest way to evaluate the numerical gradients is to use two-point finite-difference techniques like the forward difference requiring one computation at the reference and one point at a displaced geometry.

$$\frac{\delta\langle\Psi_F|\hat{\mathcal{O}}|\Psi_I\rangle|_{\mathcal{Q}_0}}{\delta\mathcal{Q}_k} = \frac{\langle\Psi_F|\hat{\mathcal{O}}|\Psi_I\rangle|_{\mathcal{Q}_0\pm s\vec{e}} - \langle\Psi_F|\hat{\mathcal{O}}|\Psi_I\rangle|_{\mathcal{Q}_0}}{s} \tag{5.2}$$

The numerical error of the gradient can be reduced by averaging over a forward and backward difference namely constructing the central difference.

$$\begin{aligned} 2\cdot\frac{\delta\langle\Psi_F|\hat{\mathcal{O}}|\Psi_I\rangle|_{\mathcal{Q}_0}}{\delta\mathcal{Q}_k} &= \frac{\langle\Psi_F|\hat{\mathcal{O}}|\Psi_I\rangle|_{\mathcal{Q}_0+s\vec{e}} - \langle\Psi_F|\hat{\mathcal{O}}|\Psi_I\rangle|_{\mathcal{Q}_0}}{s} \\ &\quad - \frac{\langle\Psi_F|\hat{\mathcal{O}}|\Psi_I\rangle|_{\mathcal{Q}_0-s\vec{e}} - \langle\Psi_F|\hat{\mathcal{O}}|\Psi_I\rangle|_{\mathcal{Q}_0}}{s} \\ \frac{\delta\langle\Psi_F|\hat{\mathcal{O}}|\Psi_I\rangle|_{\mathcal{Q}_0}}{\delta\mathcal{Q}_k} &= \frac{\langle\Psi_F|\hat{\mathcal{O}}|\Psi_I\rangle|_{\mathcal{Q}_0+s\vec{e}} - \langle\Psi_F|\hat{\mathcal{O}}|\Psi_I\rangle|_{\mathcal{Q}_0-s\vec{e}}}{2s} \end{aligned} \tag{5.3}$$

Evaluating numerical gradients for (complex) transition dipole moments and SOCMEs as well as employing these properties to calculate rate constants for vibronic fluorescence, phosphorescence and ISC is a major part of this thesis. Therefore, multiple technical developments that finally eclipsed in the creation of the GRADIENATOR, a sophisticated tool to derive numerical gradients and perform scans along molecular distortions, have been achieved. In the following these developments are presented showing their use cases and foundations including the crucial phase corrections.

5.2 Phase Corrections

Correcting the phases of the matrix elements is a crucial part in the computation of numerical gradients. In this work the following three phase corrections were used:

- A phase correction utilizing reference matrix elements to infer the phase of the matrix element of interest. This method was already used by Tatchen *et al.*[72]
- A general phase correction for pure-spin wave functions utilizing the overlap matrix to correct the molecular orbital phases in combination with realigning the wave functions.
- A general phase correction for mixed-spin wave functions employing the general phase correction for pure-spin wave functions and realigning additionally the mixed-spin wave function in the complex space.

5.2.1 Phase Correction Utilizing Reference Matrix Elements

Following Tatchen *et al.*,[72] the phases of the matrix elements can be corrected by choosing a reference state Ψ_R which exhibits two large reference matrix elements $\langle\Psi_R|\hat{\mathcal{O}}|\Psi_I\rangle$ and $\langle\Psi_F|\hat{\mathcal{O}}|\Psi_R\rangle$ with the states of interest Ψ_F and Ψ_I. Figure 5.1 illustrates the procedure.

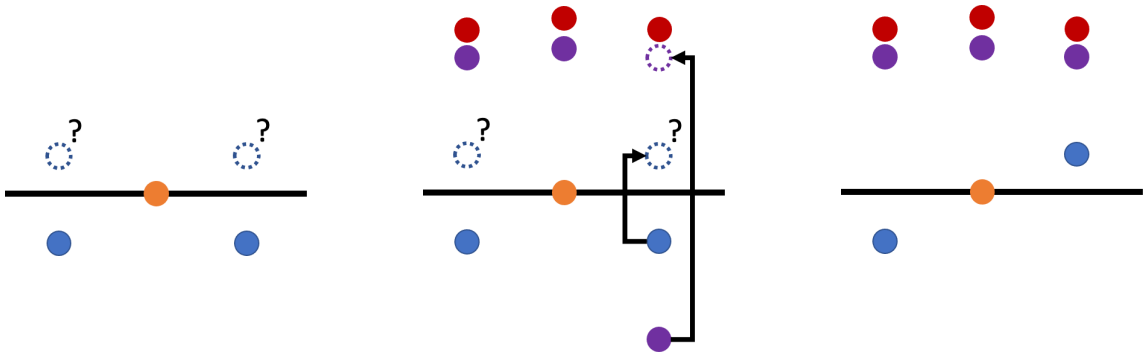

(a) **Unknown phases** (b) **Reference matrix elements** (c) **Corrected phases**

Figure 5.1: Procedure used to correct the matrix element phases utilizing large reference matrix elements.

The idea is to infer whether a nonphysical sign change occurred by comparing the reference matrix elements at the reference geometry and the distorted one. For small matrix elements the correct phase is unknown as the change of the matrix element can be large enough to physically induce a sign change (Figure 5.1 (a)). In contrast, for large matrix elements one can assume that moving between both geometries, no physical sign change should occur as the displacement and the change of the matrix element is typically small. Therefore, a nonphysical sign change of a large matrix element is easily detected and corrected (Figure 5.1 (b)). If only one sign change occurs in the reference matrix elements (Figure 5.1 (c)) the matrix element of interest has to change its sign:

- Phase change in $\langle \Psi_R | \hat{\mathcal{O}} | \Psi_I \rangle$:
  If a phase change occurs in this reference matrix element either Ψ_R swapped its sign or Ψ_I. A sign change in Ψ_R causes the reference matrix element $\langle \Psi_R | \hat{\mathcal{O}} | \Psi_F \rangle$ to change its sign, as long as the sign of Ψ_F did not change. If only $\langle \Psi_R | \hat{\mathcal{O}} | \Psi_I \rangle$ changed its sign, one sign change in either Ψ_I or Ψ_F has occurred and therefore the phase of $\langle \Psi_F | \hat{\mathcal{O}} | \Psi_I \rangle$ has to be swapped.

- Phase change in $\langle \Psi_F | \hat{\mathcal{O}} | \Psi_R \rangle$:
  If the phase is changed in this reference matrix element either Ψ_R or Ψ_F changed its sign. Again, if a sign change happened in Ψ_R the matrix element $\langle \Psi_R | \hat{\mathcal{O}} | \Psi_I \rangle$ needs to flip its sign otherwise the sign change stems from Ψ_I. Therefore, if only $\langle \Psi_F | \hat{\mathcal{O}} | \Psi_R \rangle$ changed its sign, the phase of $\langle \Psi_F | \hat{\mathcal{O}} | \Psi_I \rangle$ has to be swapped.

- Phase hange in $\langle \Psi_R | \hat{\mathcal{O}} | \Psi_I \rangle$ and $\langle \Psi_F | \hat{\mathcal{O}} | \Psi_R \rangle$:
  If a sign change occurred in both reference matrix elements Ψ_R swapped its sign or both states of interest Ψ_I and Ψ_F did undergo a sign change. In either case the sign change cancels out and $\langle \Psi_F | \hat{\mathcal{O}} | \Psi_I \rangle$ has the correct phase.

Table 5.1: Possible phase relations and their impact on the phase of the matrix element.

Phase at Reference Geometry		Phase at Displaced Geometry		Phase Change
$\langle\Psi_R\|\hat{O}\|\Psi_I\rangle$	$\langle\Psi_F\|\hat{O}\|\Psi_R\rangle$	$\langle\Psi_R\|\hat{O}\|\Psi_I\rangle$	$\langle\Psi_F\|\hat{O}\|\Psi_R\rangle$	$\langle\Psi_F\|\hat{O}\|\Psi_I\rangle$
+	+	+	+	no
+	+	+	-	yes
+	+	-	+	yes
+	+	-	-	no
+	-	+	+	yes
+	-	+	-	no
+	-	-	+	no
+	-	-	-	yes
-	+	+	+	yes
-	+	+	-	no
-	+	-	+	no
-	+	-	-	yes
-	-	+	+	no
-	-	+	-	yes
-	-	-	+	yes
-	-	-	-	no

Using reference matrix elements to correct the phases is an easy solution as it can be applied after all computations are done, as long as large reference matrix elements exist. In molecular systems with particular small matrix elements it is very difficult to find suitable reference matrix elements. Often larger numbers of excited states have to be computed increasing the computational cost of each single point calculation. In case of pyrazine,[53] the phases of transition dipole matrix elements between the ground state (A_g) and the lowest excited singlet and triplet state (B_{3u}) needed to be corrected. Due to symmetry selection rules there exists no reference state Ψ_R that has large matrix elements with gerade and ungerade states at the same time rendering the correction method useless under these circumstances. To still enable the correction of matrix elements in these kinds of situations a more sophisticated phase correction was developed, which corrects the phase relation at the root of the problem in the molecular orbitals and wave functions.

5.2.2 Phase Correction of Pure-Spin Wave Functions

The matrix element of an (effective) one-electron operator, such as the electric transition dipole operator $\hat{\mu_{el}}$ or the spin–orbit coupling operator $\hat{\mathcal{H}}_{SO}$ can be computed by the means of density matrix theory:

$$\langle\Psi_F|\hat{\mathcal{O}}|\Psi_I\rangle = tr\left(D^{F\leftarrow I}\cdot\mathcal{O}\right) \tag{5.4}$$

Here $D^{F\leftarrow I}$ is the transition density matrix between the states Ψ_F and Ψ_I, which is contracted with the operator's integrals. The phase of the integrals depends on the phase of the molecular orbitals, while the phase of the density matrix is dependent on the phases of Ψ_F and Ψ_I in addition to the molecular orbital phases. Therefore, relating the molecular orbital phases at the distorted geometry to the molecular orbitals at the reference geometry fixes phase changes rooted in the integrals $\mathcal{O}$. Computing the density matrix $D^{F\leftarrow R}$ with phase corrected

molecular orbitals removes phase switches induced by the molecular orbitals and leaves only phase changes in the linear combination of the wave functions Ψ_F and Ψ_I. If in addition to the largest coefficient of the wave functions linear combinations are aligned to the ones at the reference geometry, all roots of phase instabilities are removed. Therefore, a general phase correction for the matrix elements splits into two parts:

- **Phase correction of the molecular orbitals**:
  The orbital phases can be corrected by superimposing the reference and distorted molecular geometries and calculating the overlap matrix.

$$\mathbf{S} = \begin{pmatrix} S_{1,1} & S_{1,2} & \dots & S_{1,n} \\ S_{2,1} & S_{2,2} & \dots & S_{2,n} \\ \vdots & \vdots & \ddots & \vdots \\ S_{n,1} & S_{n,2} & \dots & S_{n,n} \end{pmatrix} \overset{\delta_{ij}}{=} \begin{pmatrix} 1 & 0 & \dots & 0 \\ 0 & 1 & \dots & 0 \\ \vdots & \vdots & \ddots & \vdots \\ 0 & 0 & \dots & 1 \end{pmatrix} \tag{5.5}$$

  The overlap matrix describes the deviations of the molecular orbitals from an orthonormal basis. Computational methods typically require the molecular orbitals as an orthonormal basis, in which case the overlap matrix simplifies to a unit matrix. The overlap matrix is therefore a good quantity to measure the closeness of the molecular orbitals at different geometries. If the molecular orbitals i and j are similar, the overlap matrix will contain a value of $S_{ij} \approx 1$, while for unrelated orbitals a value of $S_{ij} \approx 0$ will be obtained. In case of similar orbitals with a sign change at one geometry the overlap is $S_{ij} \approx -1$.

  Creating an overlay of the reference and the distorted geometry as well as their respective molecular orbitals creates a new set of localized molecular orbitals. The molecular orbital coefficients of the reference geometry are herein C^R and the ones of the distorted geometry C^D.

$$\mathbf{C}_{superposition} = \begin{pmatrix} C^R_{1,1} & C^R_{1,2} & \dots & 0 & 0 & 0 \\ C^R_{2,1} & C^R_{2,2} & \dots & 0 & 0 & 0 \\ \vdots & \vdots & \ddots & 0 & 0 & 0 \\ 0 & 0 & 0 & C^D_{1,1} & C^D_{1,2} & \dots \\ 0 & 0 & 0 & C^D_{2,1} & C^D_{1,2} & \dots \\ 0 & 0 & 0 & \vdots & \vdots & \ddots \end{pmatrix} \tag{5.6}$$

  The overlap matrix for such a constructed orbital basis is easily calculable within standard quantum chemistry packages and has the following structure:

$$\mathbf{S}_{superposition} = \begin{pmatrix} S_R & S_{RD} \\ S_{DR} & S_D \end{pmatrix} \tag{5.7}$$

  The S_R and S_D blocks are the overlap matrices of the reference and distorted geometries, which both are unit matrices because of the orthonormality of each set of molecular orbitals. The blocks S_{RD} and S_{DR} are used to correct the phase relations and will also show if orbital rotations happened moving from the reference to the distorted geometry or vice versa. Only one of the blocks is needed since they are related by a transposition ($S^T_{RD} = S_{DR}$). Utilizing the overlap matrix to correct the molecular orbital phases is a suitable approach as long as the compared geometries are not too far from each other and therefore the step length for the evaluation of the gradients has to be rather small.

- **Phase correction of the wave functions**:
  After the excited states are obtained utilizing the corrected molecular orbitals, the largest coefficient of the wave function's linear combination at the reference geometry is compared to the corresponding coefficient at the distorted geometry. If the phases differ the sign of the linear combination at the distorted geometry is inverted.

5.2.3 Phase Corrections for Mixed-Spin Wave Functions

Correcting matrix element phases of mixed-spin wave functions is slightly more complex than correcting the phases of pure-spin wave functions. The phase of mixed-spin wave functions depends on the phases of the molecular orbitals as well as the phases of the pure-spin wave functions it is a mixture of. Therefore, the correction is based on the phase corrections for pure-spin wave functions and molecular orbitals as discussed above.
Matrix element phases of mixed-spin wave functions are complex valued and therefore, not only a sign change can occur between the reference and distorted geometries but also rotations in the complex space expressed as an imaginary phase factor are possible. This imaginary phase factor becomes visible when expressing a complex matrix element $a + ib$ using Euler's formula.

$$(a+ib) = |(a+ib)| \cdot (\cos\phi + i\sin\phi) = re^{i\phi} \quad \text{where} \quad \phi = \begin{cases} \text{if } a > 0 : \arctan(\frac{b}{a}) \\ \text{if } b > 0 : \frac{\pi}{2} - \arctan(\frac{a}{b}) \\ \text{if } b < 0 : -\frac{\pi}{2} - \arctan(\frac{a}{b}) \\ \text{if } a < 0 : \arctan(\frac{b}{a}) \pm \pi \\ \text{if } a, b = 0 : \text{undefined} \end{cases} \tag{5.8}$$

The imaginary phase factor $e^{i\phi}$ has to be aligned between the mixed-spin wave functions at the reference and distorted geometry. One way to achieve this is to choose the imaginary phase factor of the largest wave function coefficient at the reference geometry and the corresponding coefficient at the distorted geometry as e^{i0} such that the coefficient is a positive real number. This will fix the wave function's phase and rotate the matrix elements (Fig 5.2 (a)) such that numerical gradients are obtainable. With mixed-spin wave functions root swapping does happen more often due to degeneracies and the wave functions at the reference and the distorted geometry have to be matched up to perform the phase corrections. For this purpose, one can compute the scalar product between both wave functions. If the wave functions match, the scalar product is $\langle \Psi_R | \Psi_D \rangle \approx 1$ because the geometric difference between the reference and the distortion is small.
In some applications the complex matrix elements have to be transformed to real valued ones. One of these applications are computations of spectra or rate constants utilizing the VIBES program, which due to technical limitations does only accept real valued matrix elements and gradients.
To obtain real valued matrix elements while maintaining the phase relation between the reference and distorted geometries, all matrix elements have to be moved in unison. To perform the transformation, the reference matrix element is rotated by $e^{-i\phi}$, which will turn it into a positive real valued number. The matrix element at the distorted geometry is rotated equally (Fig. 5.2 (b)). This rotation will most likely not convert the distorted geometry into a purely real valued number, but it maintains the phase relation and will maximize the real

valued component of the complex number. Conversion to a purely real value can then be achieved by projection (Fig. 5.2 (c)).

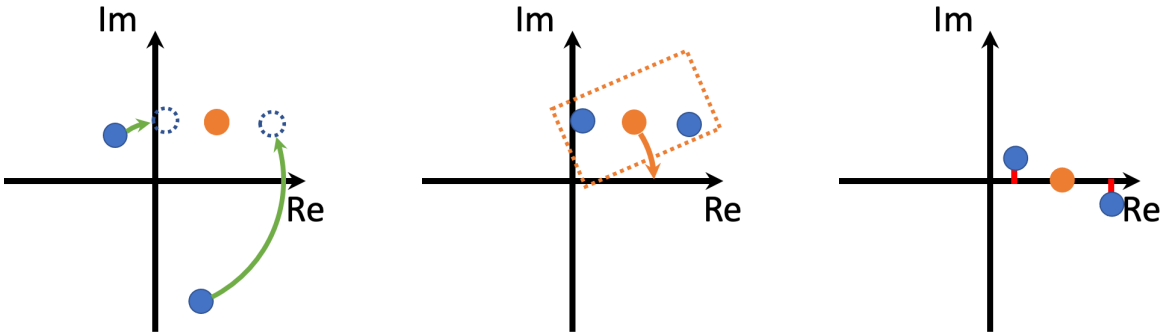

(a) **Align wave functions** (b) **Rotate matrix elements** (c) **Project onto real space**

Figure 5.2: Procedure used to transform complex valued matrix elements into real valued elements, while correcting their arbitrary phases.

5.3 Implementations

5.3.1 Extension of the SNF Program for SPOILER

The project on vibronic coupling started with the 2017 version of SPOILER[53] which offers inexpensive SOCMEs from linear response TDDFT close to the accuracy achieved at DFT/MRCI and SPOCK level of theory. As the computation of SOCME gradients is tedious, SPOILER should be used to supply the SOCMEs instead of the SPOCK program lowering the computational cost tremendously. At that time TDDFT frequency analyses were performed numerically utilizing the SNF[97] program in our department, which in principle generates Cartesian displacements, computes the gradient of the energy analytically to construct a numerical Hessian. Diagonalization of the Hessian decouples the Cartesian displacements and transforms them into a set of independent movements known as normal coordinates and their respective frequencies.

$$H^q = T^\dagger M^{-\frac{1}{2}} H^c M^{-\frac{1}{2}} T \tag{5.9}$$

Here H^c is the Cartesian Hessian that is mass-weighted by $M^{-\frac{1}{2}}$, a diagonal matrix containing the atomic masses $M_{ij}^{-\frac{1}{2}} = \frac{\delta_{ij}}{\sqrt{m_i}}$. The transformation Matrix T diagonalizes H^c into the Hessian in the basis of normal coordinates H^q, which contains the frequencies on its diagonal. The matrix T contains the normal coordinates and defines the transition between the Cartesian and normal mode basis. As the SNF already generated the Cartesian distortions and performed a TDDFT calculation for the spin state to be analyzed, it was extended to run another TDDFT calculation to supply SPOILER with singlet and triplet states at each distorted geometry. To compute the numerical gradients from the SOCMEs, the SOMEGRAD program was developed to collect the SOCMEs, fix their phases, apply the center difference and transform the Cartesian SOCME gradients into the basis of dimensionless normal coordinates $\mathcal{Q}$.

$$\frac{\delta\langle\Psi_F|\hat{\mathcal{H}}_{SO}|\Psi_I\rangle}{\delta\mathcal{Q}_k} = \sum_i \frac{\hbar}{\sqrt{m_i\hbar\omega_k}} T_{ik} \cdot \frac{\delta\langle\Psi_F|\hat{\mathcal{H}}_{SO}|\Psi_I\rangle}{\delta x} \tag{5.10}$$

The phase correction implemented in SOMEGRAD follows the reference matrix approach in Sec. 5.2. The SNF extension has the advantage that computations are reused where possible to lower the computational cost while still an additional TDDFT calculation has to be performed. If a molecular system is investigated where equilibrium structures are difficult to optimize multiple SNF runs have to be conducted and the advantage is turned into a disadvantage. To offer the evaluation of SOCME gradients after the frequency analysis was performed a set of Python scripts was developed.

5.3.2 Python Scripts for Vibronic Coupling

Starting from Pearl scripts that were already used by Tatchen *et. al*,[72] a set of Python scripts was developed offering the computation of numerical gradients utilizing displacements along dimensionless normal coordinates. The scripts contain routines to obtain the gradients from TDDFT and SPOILER or DFT/MRCI and SPOCK calculations. The displacements along dimensionless normal coordinates are generated by DISTORT, a program used for various geometry manipulations. The scripts take care of setting up and conducting the calculations

for each geometry, while SOMEGRAD is used to compute the gradients. SOMEGRAD omits in combination with the scripts the transformation of SOCMEs into dimensionless normal coordinates. This approach was used to supply the SOCME gradients in the publications regarding fluoroflavins[106] and pyrazine,[107] while in the latter the approach was extended for gradients of electric transition dipole moments to describe vibronic fluorescence and phosphorescence in addition to ISC. The scripts got more and more important as the Gaussian[21] program package offered analytical Hessians rendering usage of the SNF program a less favorable approach. As the DISTORT program did not offer support for normal coordinates in the format of Gaussian, the scripts needed to be improved. Mario Bracker developed his DELTA program to compute NACMEs utilizing scripts that were based on the ones presented here which required for the sake of usability a system that unifies the evaluation of the numerical gradients.

5.3.3 The GRADIENATOR

The Gradienator was built to offer efficient and easy to use gradient computations for SOCMEs, NACMEs and electric transition dipole moments as well as conducting scans along coordinate displacement vectors. It was developed, improved and used extensively to investigate 2CzPN,[103] Heptazines[108] and TpAT-tFFO.[104,105] At its core, it is a system allowing to set up molecular geometries along a displacement vector and conducting a set of computations at these geometries as well as their automatic evaluation and presentation. To create the molecular geometries one of the following modes can be chosen:

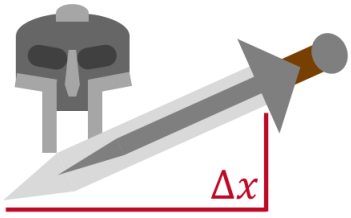

Figure 5.3: Gradienator Logo.

- **Normal mode scan**: A reference geometry and its frequency analysis are supplied to distort the molecule along its vibrational normal modes.
- **Cartesian scan**: A reference geometry is supplied, and all $3N$ Cartesian displacements are generated similar to the SNF approach.
- **Interpolation**: An initial and final geometry are supplied, which are used to create a linear interpolated path between both geometries.
- **User defined**: A folder containing geometry files is supplied.

For all modes the user can decide between the Gaussian, Turbomole, Mopac and XYZ geometry formats as well as formats of Gaussian and Mopac normal coordinates. The **Normal mode scan** and **Cartesian scan** modes require additionally the number of steps and the length of each step for the generation of the displaced geometries. To perform computations at each generated geometry, the following calculations can be added to the configuration:

- **Gaussian PCM**: A Gaussian calculation utilizing the polarizable continuum model (PCM)[109] to simulate solvent effects. The obtained solvent model is converted into point charges, that can be employed in consecutive direct self-consistent field (DSCF) calculations to model solvent effects.

- **Gaussian DSCF / Turbomole DSCF**: A DSCF calculation utilizing the Gaussian or Turbomole program package to supplying the ground state energy, its properties as well as converged molecular orbitals. This calculation type can depend on a **Gaussian PCM** calculation.
- **Gaussian TDDFT / Turbomole TDDFT**: A TDDFT calculation utilizing the Gaussian or Turbomole program package to compute the excited states yielding energies, amplitudes and properties.
- **Gaussian TDDFT-OPT / Turbomole TDDFT-OPT**: A TDDFT calculation used to perform a TDDFT geometry optimization at each geometry with Gaussian or Turbomole yielding a relaxed scan.
- **Spoiler**: A Spoiler calculation yielding electric transition dipole moments of pure-spin and mixed-spin wave functions and SOCMEs from a previous Gaussian or Turbomole TDDFT calculation which can be used to compute gradients.
- **DFT/MRCI**: A DFT/MRCI calculation yielding wave functions, their corresponding energies and properties. Prior to the DFT/MRCI calculation a Turbomole DSCF calculations has to be performed. With this calculation type electric transition dipole moment gradients of DFT/MRCI wave functions are accessible.
- **SPOCK**: A SPOCK calculation which can be used to obtain electric transition dipole moments of mixed-spin wave functions and SOCMEs from a previous DFT/MRCI calculation.
- **DELTA**: A DELTA calculation to obtain NACMEs from a previous DFT/MRCI calculation utilizing the new developed program by Mario Bracker.

The necessary phase corrections (Sec. 5.2) are included by default. The Gradienator is designed such that calculations can depend on preceeding calculations which is illustrated in Figure 5.4.

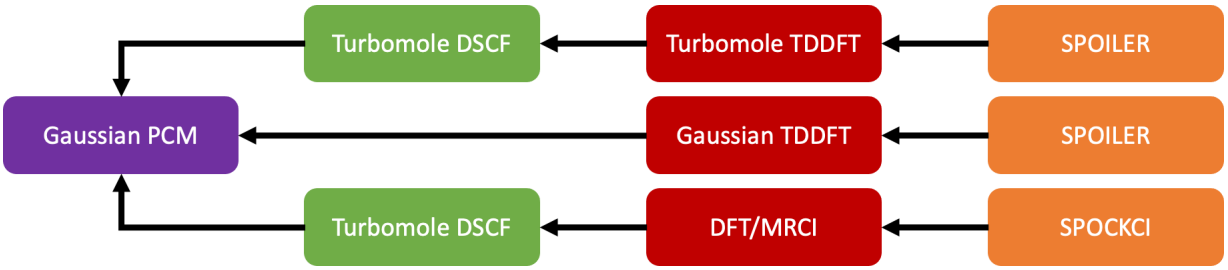

Figure 5.4: Example dependency tree of three Gradienator computations.

If a calculation is run, the Gradienator checks recursively that its predecessors or its dependencies were run properly. This dependency tree allows for an incremental computation scheme, without the need to recompute data that is already present. Additionally, the memory impact can be reduced, as only new unique computation data has to be saved. The initial Python scripts started the computations for all generated geometries right away, which when run can submit a very large amount of jobs to the computer cluster blocking other users from starting computations on their own. The Gradienator introduced a batch protocol

such that only a specified number of jobs is run at the same time. As soon as one job finishes the next job is started. The GRADIENATOR offers evaluators for its calculations allowing to create input for the use in follow-up calculations. Additionally, the implementation allows for easy and fast extension to new calculations, formats, and scan modes.

The GRADIENATOR is used with the command

```
1  gradienator <command> [folder]
```

where the ⟨command⟩ parameter can be one of the following:

- **new**
  The new command is used to set up a new gradient calculation and requires coordinates and a frequency analysis to be successful.
- **add** [**folder**]
  The add command is used to add a new calculation to the gradient calculation. Dependencies have to be added in advance and can be selected in the calculation specific menu.
- **batch** [**folder**]
  The batch command is used to run the calculations. When batching, one can select normal modes to batch and configure the parameters for the cluster. Additionally, a limit can be set of how many computations should be processed at the same time.
- **evaluate** [**folder**]
  The evaluate command is used to collect the results of the calculations and present them in a compressed format creating files for viewing or input files for follow-up calculations.
- **validate** [**folder**]
  The validate command is used to check if the gradient calculation is missing any files that might have been deleted by the user manually.
- **update** [**folder**]
  The update command is used to update the scripts inside the gradient calculation. This makes it easy to upgrade old calculation configurations to the newest standard.

5.4 Vibronic and Spin–Orbit Coupling Effects in Pyrazine

[Paper 3] Vibronic and spin–orbit coupling effects in the absorption spectra of pyrazine: A quantum chemical approach[107]

Pyrazine (1,4-diabenzene) is a well known system exhibiting strong vibronic coupling contributions in its $S_1 \leftarrow S_0$ absorption spectrum, while the $T_1 \leftarrow S_0$ absorption spectrum shows close to no indication of vibronic activity. Experimental studies on pyrazine reported contradicting results regarding the interpretations of the absorption spectra as well as the location of the T_2 state and its influences on the spectra. Theoretical studies on pyrazine were mainly limited to the singlet moiety,[110,111] while the T_1 state was investigated utilizing an approximate treatment of SOC by means of fitting parameters[112,113] or without accounting for spin–forbidden transitions at all.[114]
To resolve the contradictions and shed some light on the T_2 origin, extensive DFT/MRCI and SPOCK calculations were conducted including vibronic SOC effects on top of geometric structures obtained at DFT and TDDFT level of theory. The S_1 (1^1B_{3u}) and T_1 (1^3B_{3u}) states are $n_{HOMO} \rightarrow \pi^*_{LUMO}$ excitations which yield $\mathcal{C}_{2h}$ and $\mathcal{D}_{2h}$-symmetric structures respectively if optimized. When the S_1 state is optimized under $\mathcal{D}_{2h}$ symmetry constraints in TDDFT, a shallow double minimum is obtained with a $3b_g$ mode exhibiting an imaginary frequency while DFT/MRCI calculations show a true minimum instead. To acquire a good estimate of the force constant of this mode the fitting procedure developed together with Mario Bracker in a previous project on fluoroflavins[106] was employed. Herein, a scan of the TDDFT potential surface along the $3b_g$ mode was performed to utilize the outer branches of the potential and fit the mode's harmonic frequency yielding 1025 cm^{-1} close to the value for the same vibration in the T_1 state at 1075 cm^{-1}.

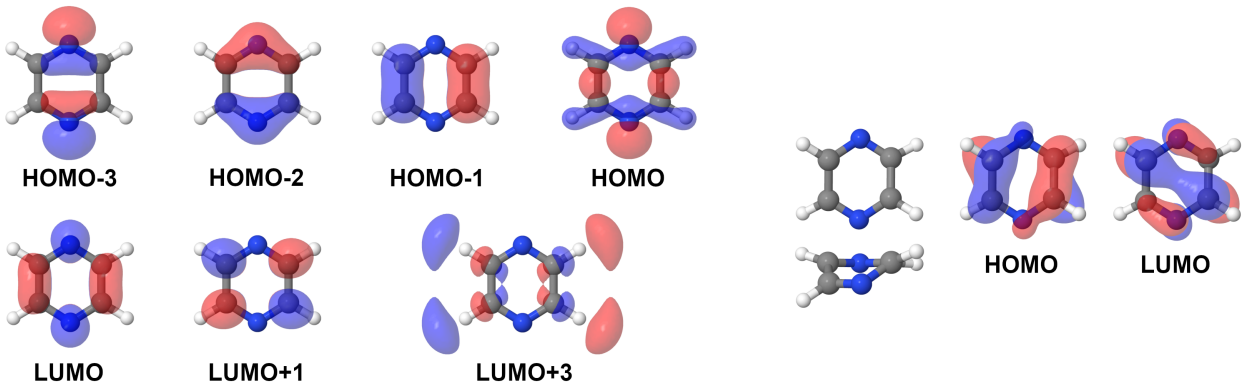

Figure 5.5: Structure and molecular orbitals at (a) the $\mathcal{D}_{2h}$-symmetric ground state minimum, (b) the Jahn–Teller distorted T_2 state minimum.

The T_2 state which exhibits $\pi\pi^*$ character has been subject to heavy debate in the literature[115–117] as it was unclear whether its location is above or below the S_1 state's minimum. A sudden increase in bandwidth was observed by Hochstrasser and Marzzacco[116] in the $T_1 \leftarrow S_0$ absorption spectrum of pyrazine crystals at low temperature, which was interpreted as a perturbation caused by a close-by $\pi\pi^*$ state about 1600 cm^{-1} ($\approx$ 0.2 eV) above the T_1 origin. The state observed by Hochstrasser and Marzzacco was the T_2 state according to our calculations, which is located adiabatically 0.2 eV below the S_1 and 0.24 eV above the

T_1 states minimum in the DFT/MRCI calculations. The geometry of the T_2 state is heavily Jahn–Teller distorted caused by a strong mixing of B_{1u} and B_{2u} symmetry leading to an intersection between the T_2 and S_0 potentials far away from the FC region.
The $S_1 \leftarrow S_0$ absorption spectrum (Fig. 5.6) is dominated by the $^1B_{3u} \leftarrow {}^1A_g$ absorption rooted in a moderately strong electric transition dipole moment. The ν_{10a} $(1b_{1g})$ mode allows the 1^1B_{3u} state to borrow intensity from the bright $1^1B_{2u} \leftarrow 1^1A_g$ and $2^1B_{2u} \leftarrow 1^1A_g$ transitions, where both states are higher lying $\pi\pi^*$ states. Additionally, the ν_{4a} $(1b_{2g})$ and ν_{5a} $(2b_{2g})$ modes borrow intensity, but less strongly than ν_{10a}, from $B_{1u} \leftarrow 1^1A_g$ transitions.

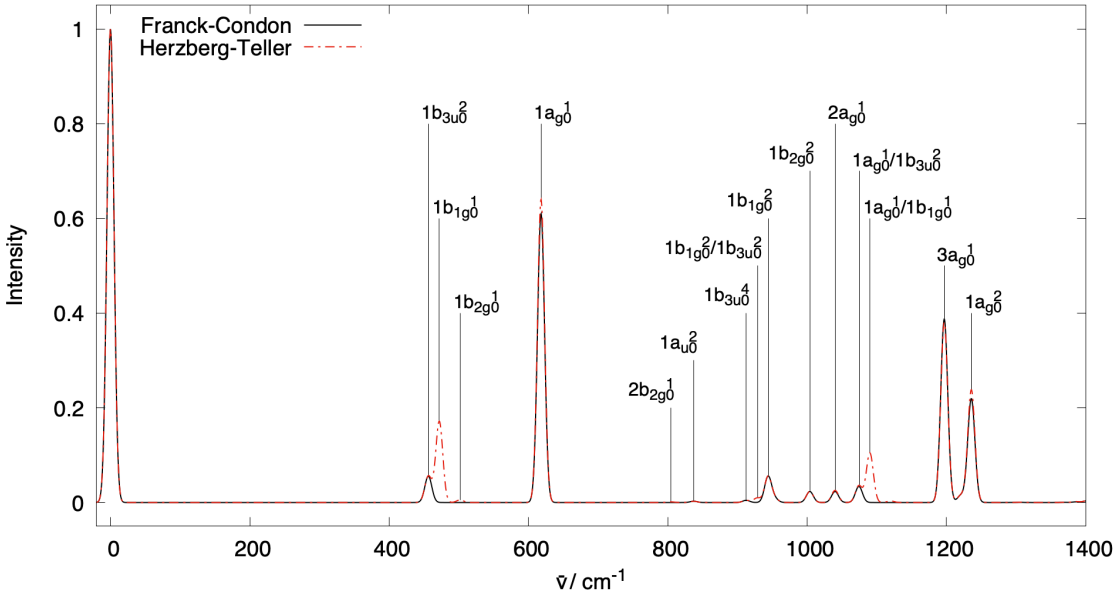

Figure 5.6: FC and HT $S_1 \leftarrow S_0$ absorption spectrum.

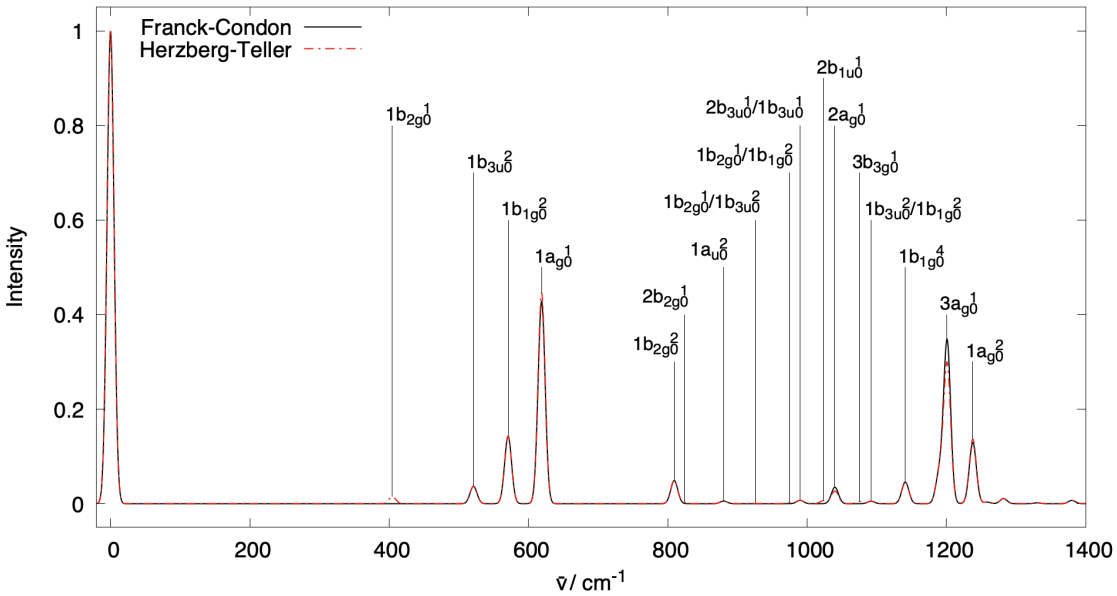

Figure 5.7: FC and HT $T_1 \leftarrow S_0$ absorption spectrum.

The $T_1 \leftarrow S_0$ absorption spectrum does not show large vibronic contributions, as the FC and HT spectra look in principle the same. From the $S_1 \leftarrow S_0$ absorption spectrum it was expected that ν_{10a} ($1b_{1g}$) vibration mediates vibronic coupling as well, but SOC between $\langle 1^3B_{3u}|\hat{\mathcal{H}}_{SO}|1^1B_{2u}\rangle$ and $\langle 1^3B_{3u}|\hat{\mathcal{H}}_{SO}|2^1B_{2u}\rangle$ is small. Thus, the vibronic intensity gain is not allowed into the spin–forbidden transition. Instead of vibronic coupling effects, the T_1 (1^3B_{3u}) state draws its intensity from the bright $1^1B_{1u} \leftarrow 1^1A_g$ and $1^2B_{1u} \leftarrow 1^1A_g$ transitions by direct SOC.

The calculation of vibronic absorption spectra in this project required the implementation of a new phase correction. The phase correction utilizing reference matrix elements proposed by Tatchen *et al.* (Sec. 5.2.1) could not be applied because no large suitable reference matrix elements exist between B_{3u} and A_g due to symmetry selection rules. To circumvent this problem the phase corrections were performed in a more fundamental approach correcting the phases in the molecular orbitals and the respective wave functions (Sec. 5.2.2).

5.5 Intersystem Crossing in the 2CzPN Emitter

[Paper 4] Intersystem crossing processes in the 2CzPN emitter: a DFT/MRCI study including vibrational spin–orbit interactions[103]

2CzPN is a molecule of the CDCB family, which is a group of components that is heavily studied for the use as TADF emitters in OLEDs yielding high efficiencies and operational stability. CDCB compounds are composed of carbazole (Cz) units acting as donors and dicyanobenzene (DCB) units acting as acceptors and known for emission from strong intermolecular charge-transfer (ICT) states.
In this study we aimed at understanding the driving force for (R)ISC in 2CzPN by means of extensive DFT/MRCI calculations. The investigation of CT states poses a difficult task especially for methods like TDDFT which is usually used for geometry optimization in our department and known to perform poorly for CT states involving double excitations and Rydberg states. To find good geometries that can be employed as basis for more sophisticated DFT/MRCI calculations multiple density functionals and methods like RI-CC2 and ADC2 were evaluated, where the calculated absorption spectrum at DFT/MRCI level is compared against experimental spectra to find the best fitting geometries. The best agreement was found for TDDFT in combination with PBE0 and the def-SV(P) basis set and employed for further investigations.
Optimization of the ground state yields two minima S_0 and S_0' differing in the orientation of the Cz ligands where the opening angle connecting the Cz units to the phthalonitrile (PN) is widened in the S_0' geometric structure.

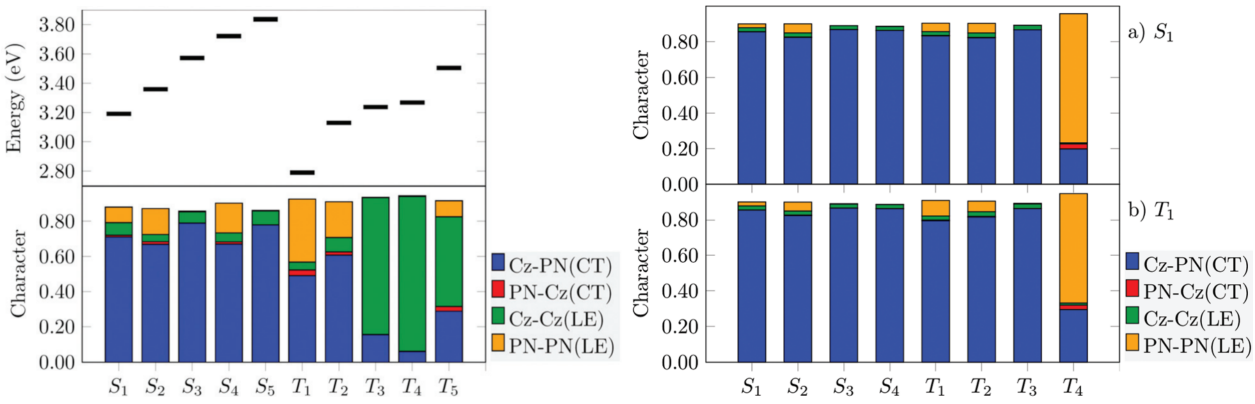

Figure 5.8: TheoDORE analysis of the vertical excitations at the S_0 geometry (left) and the adiabatic S_1 and T_1 geometries (right).

The TheoDORE analysis of the vertically excited states shows that the low-lying singlet states are mainly composed of Cz to PN CT excitations, while the corresponding triplet states contain more PN to PN local excitation (LE) character. Vertically, the T_1 (2.79 eV) and T_2 (3.13 eV) states are found below the S_1 (3.19 eV) state resulting in singlet-triplet gaps of 0.40 eV and 0.06 eV respectively. The S_1 state has lesser LE character than the S_2 (3.36 eV) state, which is reversed for the corresponding triplet, where T_1 exhibits larger LE character than T_2.
Optimization of the S_1, S_2, T_1 and T_2 states leads to structures that mainly differ in the relative orientation of the Cz groups. In comparison to the ground state geometries, the excited

states show a more parallel Cz group orientation. During the optimizations two enantiomeric structures were found. Linear interpolated paths of these excited states show that no substantial barrier exist between the enantiomers and interconversion is easily achieved by alteration of the Cz torsion angles. The more parallel orientation of the Cz groups reduces the amount of Cz to Cz character and increases the Cz to PN CT character in the adiabatic picture.
Energetically, the S_1 state relaxes by 0.28 eV while the T_1 stabilization is reduced resulting in a smaller singlet-triplet gap of 0.13 eV comparable to experimental estimated $S_1 - T_1$ gaps which range from 0.09[118] to 0.31 eV.[119] In contrast to the vertical picture, the T_2 state is located 0.10 eV above the adiabatic S_1 state forcing ISC from $S_1 \rightsquigarrow T_2$ to require thermal activation.
SOC is small for these $\pi\pi^*$ CT states and is attributed to small amounts of LE character. In the FC picture the $\langle S_1|\hat{\mathcal{H}}_{SO}|T_1\rangle$ and $\langle S_1|\hat{\mathcal{H}}_{SO}|T_2\rangle$ SOCMEs are rather small (about 0.2 cm^{-1}). Moving from the ground state to the excited states the amount of LE character is reduced due to a more parallel orientation of the Cz groups, which suggests that vibrational movements along the torsion angle of the Cz groups can cause substantial SOC and drive the ISC process. The SOCME gradients required for the HT treatment of vibronic ISC are small for $S_1 \rightsquigarrow T_1$ and $T_1 \rightsquigarrow S_1$ with values in the second decimal place. For $S_1 \rightsquigarrow T_2$, a few larger gradients are obtained ranging from 0.2 cm^{-1} to 0.4 cm^{-1}. Utilizing the SOCME gradients, ISC rate constants of 7.6×10^6 s^{-1} for $S_1 \rightsquigarrow T_1$ ISC, 2.7×10^4 s^{-1} for $T_1 \rightsquigarrow S_1$ RISC and 9.3×10^4 for $S_1 \rightsquigarrow T_2$ ISC are calculated indicating a speed-up through vibronic coupling by a factor of 2.

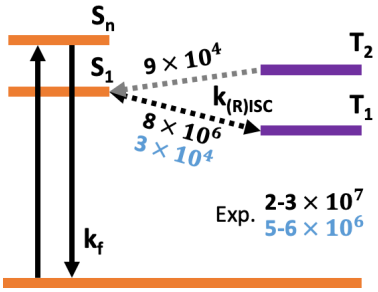

Figure 5.9: Schematic of ISC (black) and RISC (blue) processes in 2CzPN.

The $T_2 \rightsquigarrow S_1$ RISC process is not expected to contribute to TADF as it requires population of the T_2 state by ISC or IC from higher triplet states. Experimentally, rate constants of the order of $2 - 3 \times 10^7$ s^{-1} for $S_1 \rightsquigarrow T_1$ ISC and $5 - 6 \times 10^6$ s^{-1} for $T_1 \rightsquigarrow S_1$ RISC are estimated. The computed ISC rate constant is smaller than the experimental findings, while the RISC rate constant depends strongly on the singlet-triplet gap which varies in the experiments between 0.09 eV up to 0.31 eV and lowers the rate constant by about 4 orders of magnitude. While vibronic contributions slightly enhance RISC in 2CzPN, the $T_1 \rightsquigarrow S_1$ transition remains the main (R)ISC channel.
Within this publication, Angela Rodriguez Serrano conducted most of the calculations while development of the GRADIENATOR and evaluation of the derivatives for vibronic (R)ISC as well as development of the singlet-triplet reduced one-electron transition densities for the triplet wave function analysis utilizing THEODORE was my responsibility.

5.6 Intersystem Crossing in Heptazine Derivatives

[Paper 5] Large Inverted Singlet–Triplet Energy Gaps Are Not Always Favorable for Triplet Harvesting: Vibronic Coupling Drives the (Reverse) Intersystem Crossing in Heptazine Derivatives[108]

TADF emitter pose efficient systems for applications in OLEDs, as they can access triplet excitons by thermal activation. Favorable for the TADF process are systems that exhibit a small singlet-triplet gap and therefore require only weak thermal activation to harvest triplet excitons. Besides the small gap, strong SOC is required to allow the spin–forbidden RISC process to happen efficiently. Recent studies[120,121] on heptazine (Hz) and its derivates found a negative singlet-triplet gap, that inverts the typical singlet-triplet ordering. The inverted singlet-triplet (IST) gap removes the need for thermal energy as RISC is a 'downhill' process in these systems and therefore promises efficient harvesting of triplet excitons. However, these studies did not estimate rate constants showing that IST is actually favorable for the RISC process and that Hz or its derivatives are indeed well suited for OLED applications.
The typical positive singlet-triplet gap depends on the exchange interaction, which decreases with smaller overlap of the involved molecular orbitals. Therefore, disjunct molecular orbitals cause a smaller singlet-triplet gap, but SOC as well as transition dipole moments depend on the spatial overlap of the molecular orbitals. Since a small singlet-triplet gap and large SOC contradict each other in this kind of systems, one has to establish a good balance between both within the molecular design of TADF emitters. Besides its IST gap, Hz shows emissive properties that are unexpected at a first glance as the inherent $\mathcal{D}_{3h}$ symmetry enforces strong constraints that forbid emission and (R)ISC in first order proposing that vibronic coupling is the driving force for fluorescence and ISC. A strong dependence on vibronic coupling effects lessens the importance of the IST gap as these processes would be too slow to compete with deactivation channels without sufficient vibronic coupling.

To understand the excited state kinetics in Hz and its derivative HAP-3MF both systems were investigated with extensive quantum chemical calculations moving past the FC approximation to incorporate vibronic coupling effects by means of HT coupling. Hz and HAP-3MF are both highly symmetric systems exhibiting $\mathcal{D}_{3h}$ and $\mathcal{C}_{3h}$ symmetry in the ground and first excited singlet and triplet states. TDDFT optimization of the excited states yields first-order transition states which are actually minimum structures within the DFT/MRCI method as already found in previously discussed projects. The vibrational mode exhibiting the imaginary frequency displaces the central nitrogen atom out of plane reducing the symmetry to $\mathcal{C}_{3v}$ and $\mathcal{C}_3$ respectively. Similar to previous projects, the TDDFT imaginary frequencies were fitted utilizing the outer branches of the TDDFT scan's potential well to yield a good approximation for the minima's harmonic potentials. The first excited singlet and triplet states are $\pi \rightarrow \pi^*$ excitations moving electron density from nitrogen atoms located at the molecule's edges to the neighbouring carbon atoms and central nitrogen atom. For HAP-3MF additionally charge is transferred from the Hz core to the surrounding phenyl rings.
As reported by Sobolewski, Domcke and co-workers,[122] an IST gap is found for the vertical excitation energies at the ground state geometry of Hz (S_1: 2.59 eV, T_1: 2.60 eV). Within the DFT/MRCI calculations this gap (−0.01 eV) is almost vanishing in contrast to results at ADC2 level (−0.24 eV). Adiabatically, the gap is also present at DFT/MRCI level (−0.02 eV), but vanishes as soon as zero-point vibrational energy corrections are considered. In HAP-

3MF, the IST gap is present at the ground state geometry, but vanishes for the adiabatic S_1 and T_1 states. Whether heptazines are IST or TADF emitters is less important as the gap is very small and the effect of the IST gap is put into perspective by vibronic effects.
Vibronic effects are the driving force in Hz and HAP-3MF for the absorption, fluorescence and ISC processes. In Hz, S_1 and T_1 are $A_2^{'}$ states rendering absorption ($A_2^{'} \leftarrow A_1^{'}$) into and emission ($A_2^{'} \rightarrow A_1^{'}$) from the S_1 state symmetry forbidden as the product of the irreducible representation yields $A_2^{'} \otimes A_1^{'} = A_2^{'}$ and no component of the electric transition dipole operator transforms according to the same irreducible representation. ISC between S_1 and T_1 is symmetry forbidden for a similar reason as the direct product of the spatial symmetries yields $A_2^{'} \otimes A_2^{'} = A_1^{'}$ and no component of the angular momentum operator transforms accordingly.

Table 5.2: Character Table $\mathcal{D}_{3h}$.

$\mathcal{D}_{3h}$	E	$2C_3(z)$	$3C_2^{'}$	$\sigma_h(xy)$	$2S_3$	$3\sigma_v$	
$A_1^{'}$	1	1	1	1	1	1	
$A_2^{'}$	1	1	-1	1	1	-1	R_z
$E^{'}$	2	-1	0	2	-1	0	x, y
$A_1^{''}$	1	1	1	-1	-1	-1	
$A_2^{''}$	1	1	-1	-1	-1	1	z
$E^{''}$	2	-1	0	-2	1	0	R_x, R_y

In HAP-3MF both states exhibit $A^{'}$ symmetry rendering absorption into or emission from the S_1 state forbidden by symmetry too. ISC in contrast is in principle allowed for the operator's z component.

Table 5.3: Character Table $\mathcal{C}_{3h}$.

$\mathcal{C}_{3h}$	E	$C_3(z)$	C_3^2	σ_h	S_3	S_3^5	
$A^{'}$	1	1	1	1	1	1	R_z
$E^{'}$	1	ϵ	ϵ^*	1	ϵ	ϵ^*	$x+iy$
	1	ϵ^*	ϵ	1	ϵ^*	ϵ	$x-iy$
$A^{''}$	1	1	1	-1	-1	-1	z
$E^{''}$	1	ϵ	ϵ^*	1	ϵ	ϵ^*	R_x+iR_y
	1	ϵ^*	ϵ	1	ϵ^*	ϵ	R_x-iR_y

Vibronic rate constants were obtained utilizing the GRADIENATOR and the phase corrections discussed in Sec. 5.2 in combination with the VIBES program. Fluorescence proceeds in Hz at a rate of 3×10^5 s^{-1} about two orders of magnitude slower that ISC with 1×10^7 s^{-1} and RISC with 3×10^6 if the DFT/MRCI's singlet-triplet gap is employed. Utilizing the IST gap from ADC2 (-0.24 eV) the ISC and RISC rate constants are reduced to 3×10^2 s^{-1} and 5×10^5 s^{-1} respectively showing, that a large IST gap is not necessarily favorable for the interconversion of singlet and triplet states. IC between $S_1 \rightarrow S_0$ is expected to quench the fluorescence in Hz, as it proceeds at 3×10^8 s^{-1}. HAP-3MF shows a fluorescence rate constant of 9×10^5 s^{-1} in good agreement with experimental measurements estimating a rate constant of 1×10^6 s^{-1}. Interestingly, Li *et al.*[123] assigned in their experimental analysis of the excited states an $n\pi^*$ character to the S_1 state due to its low oscillator strength, while

the first $n\pi^*$ state is the S_3 state found at 3.92 eV in our calculations. ISC and RISC are slower than in Hz yielding rate constants of 7×10^6 s^{-1} and 3×10^5 s^{-1}, respectively. The IC process in HAP-3MF is a lot more favorable than in Hz as it proceeds at the same speed as fluorescence forming a competing process. Cause for the reduction of the IC rate constant are the toluene substituents which inhibit vibrations leading to rotations in the Hz core and slow down the non-radiative deactivation processes.
Besides a concrete kinetic picture of the excited state processes the origin of the vibronic effects (Fig. 5.10) are very interesting in Hz and HAP-3MF.

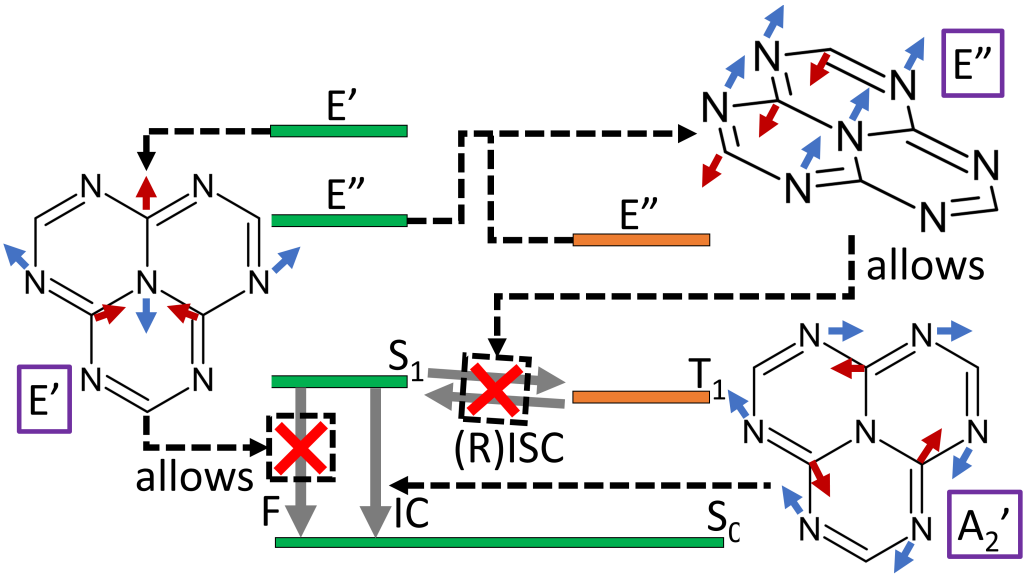

Figure 5.10: Schematic of the fluorescence and (R)ISC processes in Hz.

For the S_1 state to be emissive, bright $\pi\pi^*$ states have to be mixed into the wave function to allow intensity borrowing. This is achieved by in-plane vibrations of $E^{'}$ modes blending bright $E^{'}$ symmetric states into the S_1 wave function. A similar process is necessary for ISC, which is symmetry forbidden in Hz and in principle allowed but of vanishing size in HAP-3MF. Following El-Sayed's rule, ISC between the S_1 and T_1 states which are both $\pi\pi^*$ states can be increased greatly by introducing $n\pi^*$ character into the wave function. Vibrational modes of $E^{''}$ symmetry mix higher lying $E^{''}$ states of $n\pi^*$ character into the wave functions driving the ISC and RISC processes.

6 Spin–Orbit Coupling from Linear Response TDDFT (SPOILER)

The ability to investigate spin–forbidden processes is crucial to understand the system's excited state transitions and find relaxation pathways to explain the emissive behavior after photoexcitation. Ab initio methods like MRCI, multi-configuration self-consistent field (MCSCF) and MRMP2 are well established methods for SOC calculations. Due to their computational cost these methods are confined to studies of small systems. The semi-empirical DFT/MRCI method achieved to push the computational boundary from small to medium-sized systems by clever combination of DFT and MRCI yielding comparable results to the mentioned ab initio methods. The investigation of spin-forbidden processes in large systems however, is limited to low-cost methods like CIS imposing large drawbacks on the accuracy of the results.
To fill the need for inexpensive SOC calculations, Wang and Ziegler[49] developed an approximate relativistic linear response TDDFT formalism utilizing the ZORA Hamiltonian[124] for transition metal compounds. Linear response TDDFT is a single reference method, that allows very cost-efficient calculations of excited states rendering it the tool of choice for many computational scientists. SOC is inaccessible within the linear response TDDFT methodology and more costly quadratic response TDDFT calculations have to be carried out to describe phosphorescence. Interstate couplings, however, are missing for the description of ISC processes. The computation of SOC is straight forward in wave function based methods which makes the conversion from the linear response picture into a wave function picture desirable. Wang and Ziegler adapted AMEWs which were typically utilized to ease the computation of NACMEs[47,48] to facilitate the transition incorporating scalar relativistic effects to evaluate SOCMEs. Other groups devised and applied similar schemes.[50–52,125–129]
In 2016, the Spoiler program was developed as the product of my master's thesis and offers inexpensive SOCMEs computed from linear response TDDFT to fill the need for SOC calculations applicable to large systems.[53] Spoiler utilizes the SOMF integrals to compute SOCMEs and was interfaced to Turbomole. At the same time PySOC was developed by Gao *et al.*[130] following a similar route utilizing an effective charge approximation within the effective one-electron operator instead.[130] In 2019 de Souza *et al.* followed the approach of Spoiler and PySOC allowing in addition to evaluate phosphorescence rate constants and utilization of different operators including the RI-SOMF operator which handles the two-electron integrals within the resolution-of-the-identity (RI) approximation.[131]
Within the scope of this thesis, Spoiler received a major overhaul to improve the 2016/2017 computation scheme and implement extensions for obtaining phosphorescence rate constants by the means of SOCQDPT. The discussion of Spoiler is split into the following parts:

- The 2016/2017 state of Spoiler is reviewed and the improvements of the 2021 ver-

sion as well as the extension to evaluate electric transition dipole moments and finally emissive rate constants by the means of AMEWs are presented.

- The 2017 Benchmark[53] will be presented and key findings regarding the application and choice of amplitudes will be reviewed.
- A new Benchmark will be presented, which compares SPOILER to PySOC.[130] Additionally, examples utilizing the extensions of SPOILER to evaluate ISC and vibronic ISC are discussed.

6.1 Implementation

SPOILER was developed in 2016[53] to obtain SOCMEs and ISC rate constants from linear response TDDFT amplitudes. The central equation to obtain SOCMEs utilizing the SOMF approach and wave function methodology is:

$$\langle \Psi_{\mathrm{F}} | \hat{\mathcal{H}}_{\mathrm{SO}} | \Psi_{\mathrm{I}} \rangle = \mathrm{tr}\left(D^{\mathrm{F}\leftarrow\mathrm{I}} H_{\mathrm{SO}}^{\mathrm{mf}} \right) \tag{6.1}$$

AMEWs are employed to translate between the TDDFT and wave function picture such that the density matrix $D^{F\leftarrow I}$ can be calculated and the contraction with the SOMF integrals H_{SO}^{mf} can be performed. The 2016 SPOILER version was developed as a FORTRAN program interfaced to the Turbomole program package to utilize the amplitudes of time-dependent Hartree–Fock (TDHF), TDDFT, CIS and TDDFT/TDA calculations.

Figure 6.1: SPOILER version of 2016.

Herein, the SOMF program a part of the SPOCK program package that implements the SOMF operator is utilized to supply the spin–orbit integrals. SOCMEs obtained with this approach can be employed in consecutive VIBES calculations yielding ISC rate constants.

The computational scheme contracted the density contributions of the AMEWs directly with their respective spin–orbit integrals. To perform this direct contraction between two AMEWs one has to compare each configuration of the final wave function to the initial wave function and determine the coupling. Contributions arise between all configurations where a relative single excitation connects both configurations (Fig. 6.2(a-c)). Equal configurations (Fig. 6.2(d)) contribute to diagonal elements of the density matrix, but the contraction of these matrix elements with the spin–orbit integrals is zero and therefore diagonal elements can be ignored for the evaluation of SOCMEs.

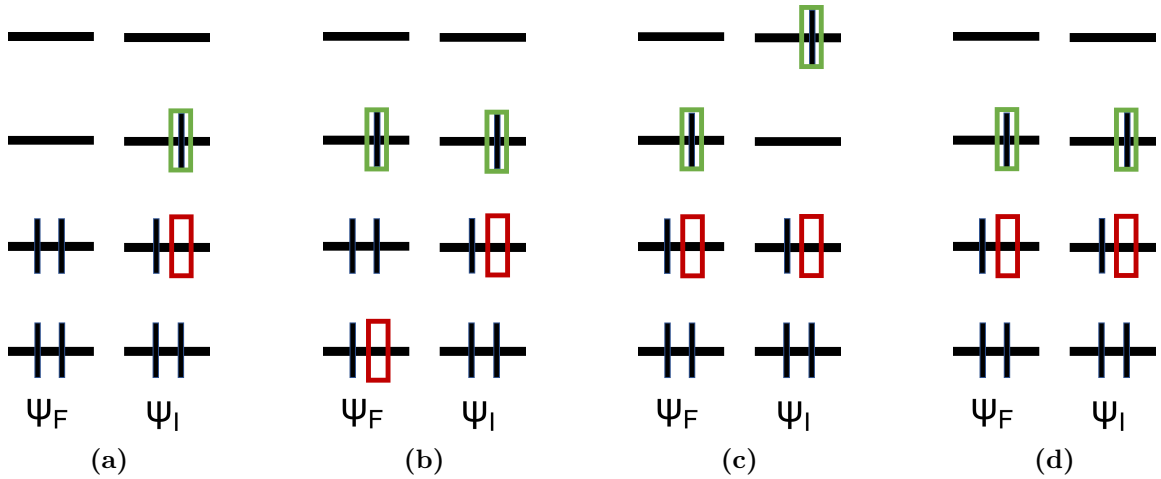

Figure 6.2: Coupling cases contributing to reduced one-electron density matrices.

Relative single excitations occur between the ground state configuration and all singly excited configurations (Fig. 6.2(a)) as well as between singly excited configurations exhibiting the same annihilators (Fig. 6.2(b)) or the same creators (Fig. 6.2(c)) instead.
The evaluation procedure can be written in pseudocode the following way:

```
1     for csfA in finalAMEW:
2         for csfB in initialAMEW:
3             if areCreatorsEqual(csfA, csfB):
4                 a1, a2 = getAnihilators(csfA, csfB)
5                 SOCME += Hso(a1, a2) * spinCoupling
6                       * csfA.amplitude * csfB.amplitude
7             else areAnihilatorsEqual(csfA, csfB):
8                 c1, c2 = getCreators(csfA, csfB)
9                 SOCME += Hso(c1, c2) * spinCoupling
10                      * csfA.amplitude * csfB.amplitude
```

Instead of utilizing the annihilators and creators directly, all amplitudes are saved ordered according to their respective creator and annihilator pair in a one-dimensional array reducing the *areCreatorsEqual* and *areAnihilatorsEqual* routines to a simple matter of iteration over the arrays of the final and initial AMEWs. The spin couplings (Sec. 4.2) for the different coupling cases were evaluated in advance and used in the appropriate situations.

The 2017 publication showed very good agreement between SPOILER and SPOCK SOCMEs, such that the idea arose to utilize SPOILER to supply SOCMEs and their gradients with respect to the normal modes of vibration for the calculation of vibronic ISC rate constants. Through this approach the computational cost for vibronic ISC rate constant could be lowered tremendously. This kind of calculation involves typically one DFT/MRCI and a consecutive SPOCK calculation at two distorted points along each $3N - 6$ ($3N - 5$ if linear) normal coordinate, where N is the number of atoms in the system. Since a TDDFT and SPOILER calculation costs just a fraction of a DFT/MRCI and SPOCK calculation for large systems, huge time savings can be obtained as long as TDDFT AMEWs pose as a proper approximation to the DFT/MRCI wave functions. The implementation and procedure to obtain numerical SOCME gradients is discussed further in the section on vibronic coupling (Sec. 5),

while the benchmarks and performance will be discussed here (Sec. 6.4).

Besides the calculation of vibronic ISC rate constants, SPOILER was extended to obtain static and vibronic emission rate constants. Electric transition dipole moments are only accessible between the ground and excited states in linear response TDDFT, allowing the direct computation of fluorescence rate constants in pure TDDFT methodology. For consistent results within the AMEW approximation however, transition dipole moments between the ground and excited states have to be evaluated employing AMEWs. Phosphorescence rate constants can be obtained utilizing the SOCQDPT approach (Sec. 2.9.2), which requires next to the SOCMEs the singlet-singlet and triplet-triplet (transition) dipole moments between the ground and excited states as well as between the excited states themselves. As TDDFT does not supply these transition dipole moments, SPOILER was extended to supply these quantities.

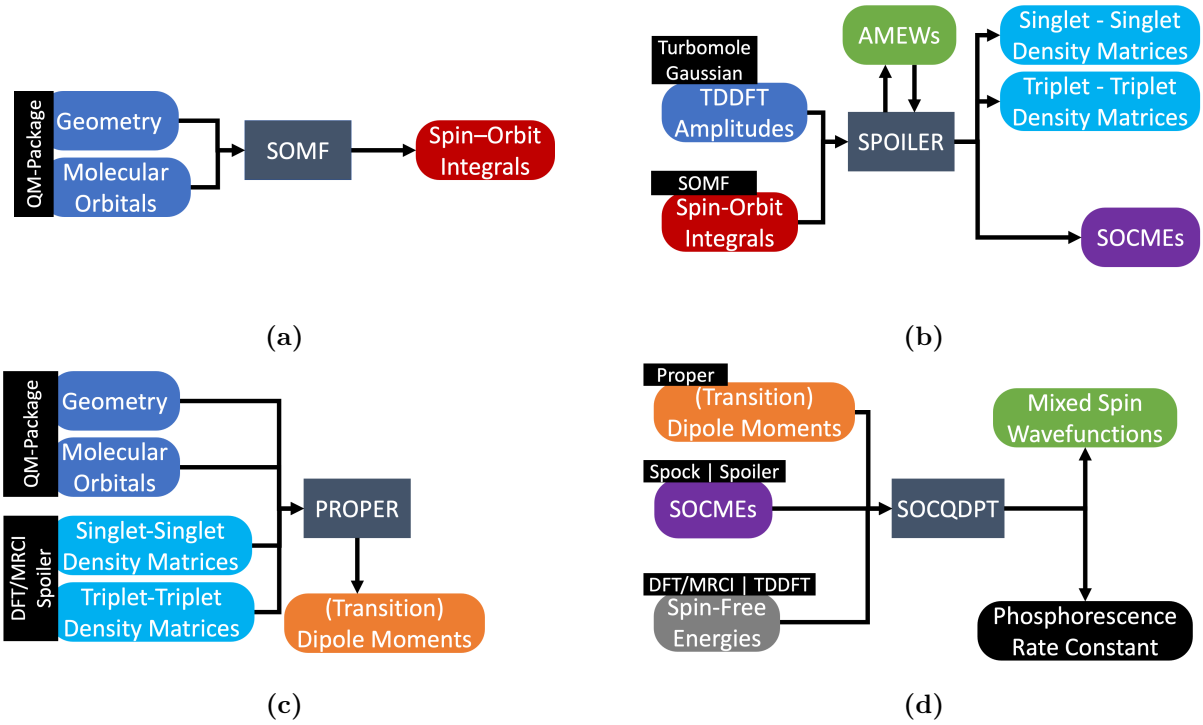

Figure 6.3: The SPOILER version of 2021.

For this purpose, SPOILER (Fig. 6.3(b)) was redesigned in C++ to calculate singlet-singlet, singlet-triplet and triplet-triplet reduced one-electron transition density matrices utilizing the efficient parallel implementation of the DENSITYENGINE. The SOMF program (Fig. 6.3(a)) is still used to supply SOMF integrals for the evaluation of SOCMEs, which in the new implementation are obtained by computing the trace of the density matrix product with the spin–orbit integrals. The singlet-singlet and triplet-triplet transition densities are used in a consecutive PROPER (Fig. 6.3(c)) calculation to obtain the corresponding transition dipole moments. PROPER is a part of the DFT/MRCI program package, that evaluates singlet-singlet and triplet-triplet transition dipole moments among multiple wave function properties requiring next to the molecular geometry, the basis set and molecular orbitals only the transition density matrices. SOCQDPT, a part of SPOCK, utilizes the singlet-singlet and triplet-triplet (transition) dipole moments as well as the spin-free energies and

the SOCMEs to obtain mixed-spin AMEWs and their respective transition dipole moments. The phosphorescence rate constant can then finally be obtained from the transition dipole moments of the mixed-spin AMEWs by Eq. 2.91.
The redesign of SPOILER follows modern software principles treating the quantum chemical program packages as plugins, such that a new interface can be added without the need to adapt parts of the core functionalities. To make SPOILER accessible for a broader audience of users an interface to Gaussian was created such that TDHF, TDDFT, CIS, and TDDFT/TDA calculations from Turbomole and Gaussian can be processed.
The main entities of the SPOILER implementation (Fig. 6.4) are the **QMPackage** interface, its respective implementation for **Turbomole** and **Gaussian** as well as the **Calculation** class.

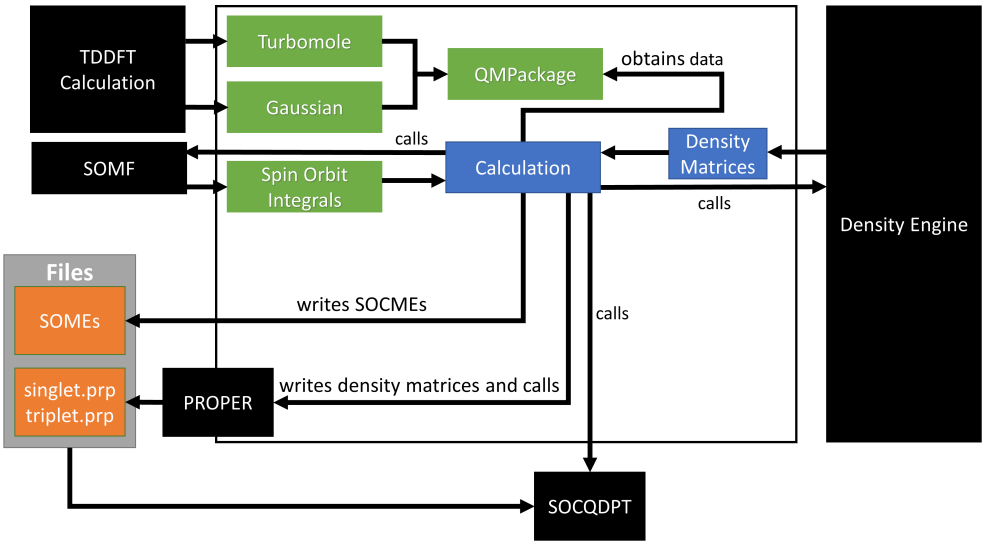

Figure 6.4: Important entities of the SPOILER implementation.

The **QMPackage** interface offers standardized access to the calculation data obtained with different quantum chemical program packages to the **Calculation** class. The actual implementation of the **QMPackage**, may it be **Turbomole** or **Gaussian** is injected at runtime by dependency injection such that the **Calculation** class is decoupled from code specific to the quantum chemical programs. This procedure is known as dependency inversion, where **Turbomole** or **Gaussian** are dependent on the code in the **QMPackage** as they derive from it and have to implement the data access routines, while the calculation also depends on the **QMPackage**. New quantum chemical program packages can be easily interfaced to SPOILER by utilizing this plugin structure by generating the quantum chemical specific code in a class deriving from the **QMPackage** class and injection at runtime.
The **Calculation** class obtains the TDDFT data via the **QMPackage** interface and orchestrates the density matrix calculation utilizing the DENSITYENGINE as well as supplying required files to PROPER, SOMF and SOCQDPT and calling these external systems. The **Calculation** class is the super class of the **LLCalculation**, **LRCalculation**, **RLCalculation**, **RRCalculation** and **MixedCalculation** classes and supplies methods that are equal for all different calculation types. The subclasses of the **Calculation** class implement only the specific behavior to employ the requested amplitude combinations.

6.2 Usage

The usage of SPOILER is straight forward. After the TDDFT computation with Turbomole or Gaussian was conducted SPOILER can be started using:

```
spoiler [input] > [output]
```

SPOILER will start by converting the Turbomole or Gaussian geometry and molecular orbital information to the TWFN Format (*mos.bin*) needed for SOMF. SOMF supplies the spin–orbit integrals (*SQUARE-igls*) and SPOILER computes the required density matrices by calling into the DENSITYENGINE writing them to files (*singlet.cidens*, *triplet.cidens*) for PROPER or contracting them directly with the spin–orbit integrals to SOCMEs (*SOMEs*). PROPER is invoked to generated transition dipole moments (*singlet.prp*, *triplet.prp*), which are in turn read by SOCQDPT in combination with the SOCMEs (*SOMEs*) to obtain phosphorescence rate constants.
Since the number of configuration parameters in SPOILER exceeds the limit of comfortably manageable parameters in a command line interface, the configuration is read from file. The default input file for a given quantum chemistry program package can be generated by:

```
1    spoiler -g QMPackage
2    spoiler --generateInput QMPackage
```

The input file defines parameters such as the choice of amplitudes and file names for the designated quantum chemistry package. Besides the quantum chemistry specific files the SOMF program requires an input file, by default called *somf.input*, to be supplied. The amplitude combination is given by the **CALCULATION_TYPE** parameter (LL, LR, RL, RR, MIXED) and the normalization can be turned on or off by setting **NORMALIZE** appropriately. The **SOC_PHASER** parameter is used to correct the phases of the mixed-spin wave functions in the SOCQDPT invocation, a feature needed to compute numerical gradients in chapter 5. In the following some specific input parameters for Turbomole and Gaussian are presented.

Turbomole

The default input for Turbomole can be generated using:

```
1  spoiler -g Turbomole
2  spoiler --generateInput Turbomole
```

For a successful SPOILER run the *coord*, *control*, *basis* and *mos* files and the output files of the singlet and triplet TDHF, TDDFT, CIS or TDDFT/TDA calculations obtained with the **ESCF** program of the Turbomole package have to be specified. TDDFT calculations are often carried out utilizing full TDDFT for singlets and TDDFT/TDA for triplets to obtain more accurate excitation energies.[36,132,133]

The energies and amplitudes can be chosen in SPOILER by setting the following parameters.

```
1    TURBOMOLE_SINGLET_ESCF_FILE
2    TURBOMOLE_TRIPLET_ESCF_FILE
3    TURBOMOLE_SINGLET_ENERGY_FILE
4    TURBOMOLE_TRIPLET_ENERGY_FILE
```

Gaussian

The default input for Gaussian can be generated using:

```
3  spoiler -g Gaussian
4  spoiler --generateInput Gaussian
```

For a SPOILER computation with Gaussian the **.log*, **.rwf* and **.chk* files of a Gaussian TDHF, TDDFT, CIS or TDDFT computation for singlet and triplet are required. The Gaussian **formchk** and **rwfdump** commands have to be included in the user's shell path and are utilized to convert the **.chk* file and the amplitudes on the binary **.rwf* files into a readable format.

6.3 2017 Benchmark

The 2017 version of SPOILER was benchmarked against DFT/MRCI calculations of a subset of polyatomic molecules (Fig. 6.5) from the previous work of Jovanović *et al.*.[134] Jovanović *et al.* determined multi-reference wave functions utilizing the DFT/MRCI and MRMP2 methods, their respective energies and SOCMEs and found good agreement with experimental gas phase data and CASSCF/CASPT2 calculations. The subset for the SPOILER benchmark was formed by excluding methionine as it was not possible to find the corresponding states between TDDFT, TDDFT/TDA and the multi-reference calculations. In total 241 SOCMEs from 121 electronic excitations were selected for the benchmark incorporating $n \rightarrow \pi^*$, $\pi \rightarrow \pi^*$, $\pi \rightarrow \sigma^*$, $\sigma \rightarrow \pi^*$ and a few Rydberg states. The computational protocol was kept as close as possible to the calculations by Jovanović *et al.*, employing the same basis sets i.e. the TZVP[135] basis set on all atoms except for sulfur where the TZVPP[95] basis set was utilized. In some cases the basis sets were augmented with diffuse functions to improve the description of low-lying Rydberg states. For the TDDFT and TDDFT/TDA calculations the B3-LYP and PBE0 density functionals were used, which are known to yield good excitation energies for singlet and triplet states of organic compounds respectively.[136–138]

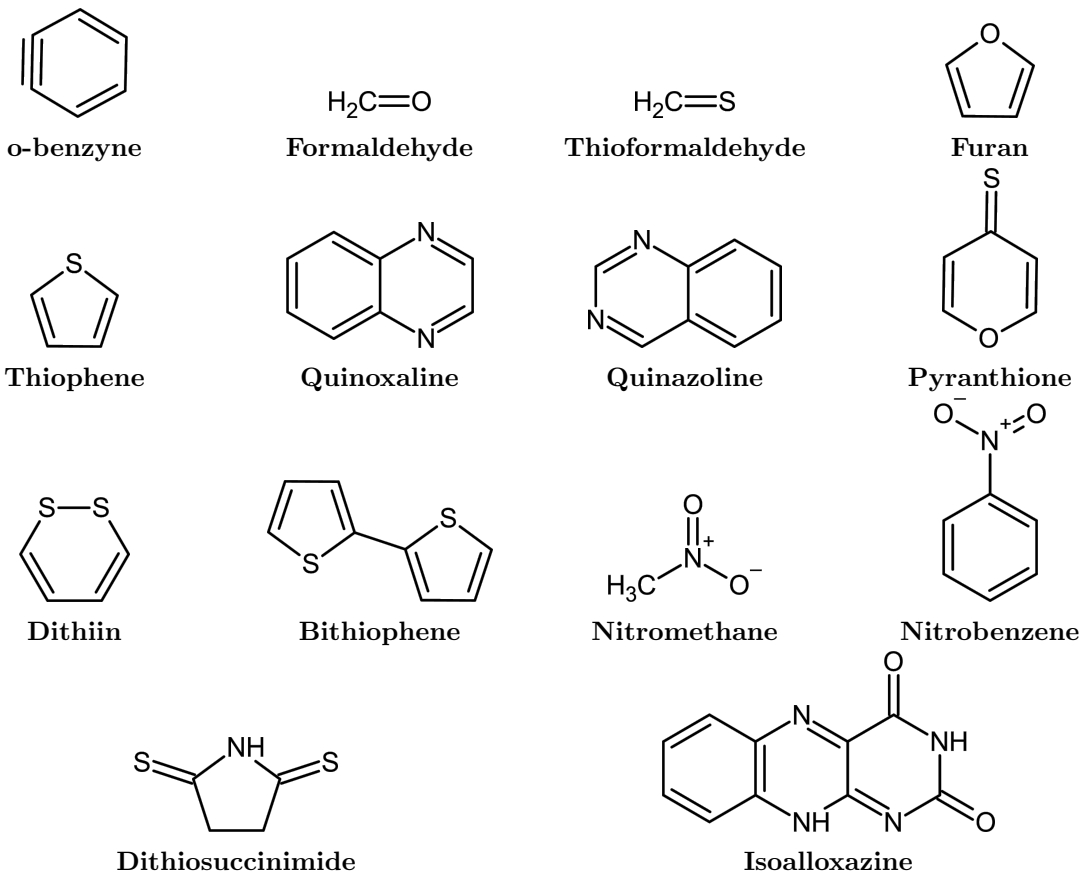

Figure 6.5: 2017 Benchmark Set.

In the benchmark, vertical excitation energies as well as SOCMEs were compared between TDDFT, TDDFT/TDA and the DFT/MRCI method. Overall a good agreement was found between the excitation energies of the three methods visible in correlation coefficients about

0.96 and root-mean-square deviation (RMSD) values of $0.24 - 0.27$ eV. Looking closer at the excitation energies, TDDFT seems to perform better in the higher energy spectrum, while the energies of low-lying triplet states are systematically underestimated. Employing the TDA improves the description of the low-lying states at the cost of stronger deviations in the high energy range. To obtain usable singlet-triplet gaps between low-lying states the use of TDA for the triplet moiety is crucial. Additionally, TDDFT employing B3-LYP and PBE0 has problems to describe Rydberg states and states with doubly excited configurations, where the former exhibit very diffuse electron distributions and the latter configurations not included in the TDDFT methodology. For SOCMEs obtained at the TDDFT level all amplitude combinations (Eq. 2.46) of the left and right eigenvectors were employed. For SOCMEs, the correlation graphs yield correlation coefficients above 0.96 and RMSDs between $6.1 - 7.5$ cm^{-1} showing, that the choice of amplitudes has only a minor effect. Nevertheless, utilizing A_{MN}^{RL}-AMEWs yields the lowest RMSDs for this set of molecules. The SOCMEs were found to be rather insensitive to the encountered energetic problems, except when doubly excited configurations are encountered, which can contribute indirectly through the SOMF operator by coupling to singly excited configurations. TDDFT as a method incorporating purely singly excited configurations is not able to account for these contributions. Therefore, the SPOILER approach should be applied only for low-lying states without substantial double excitation character.

6.4 2022 Benchmark

The promising results of the 2017 benchmark led to new use cases of the SPOILER approach. Next to ISC as a spin–forbidden process, the phosphorescence process plays an important role when investigating the kinetics of a molecule's excited states. Phosphorescence rate constants in the regime of DFT methodology are typically evaluated by quadratic response TDDFT, at a much higher cost as a linear response TDDFT calculation imposes. Within wave function methods, the same rate constant can be obtained easily from methods like SOCQDPT requiring the knowledge of singlet-singlet and triplet-triplet (transition) dipole couplings as well as SOCMEs. The latter were supplied by SPOILER already and an extension was required to evaluate singlet-singlet and triplet-triplet transition dipole couplings within the AMEW framework. Next to obtaining a more complete picture of the spin–forbidden processes, SPOILER was utilized in combination with the GRADIENATOR to obtain vibronic rate constants. The inclusion of vibrational effects on rate constants requires the calculation of costly numerical gradients if inexpensive analytical gradients are absent. Numerical gradients require the evaluation of at least $3N - 6$ ($3N - 5$ if the molecule is linear) calculations, where N is the number of atoms, which skyrockets the computational costs and suggests to use SPOILER as a particular inexpensive method to drastically reduce them.

6.4.1 Extended SOCME Benchmark

In 2017, Gao *et al.* published PYSOC,[130] a Python implementation that utilizes linear response TDDFT amplitudes of Gaussian or DFTB+[139] calculations employing a semi-empirical one-electron spin–orbit operator with effective nuclear charges. The PYSOC performance benchmark (Fig. 6.6) showed substantial SOCME deviations from the reference data and the question arose, where these deviations originate from and whether SPOILER showed similar results employing the SOMF operator. To answer the question the PYSOC benchmark set was re-computed with SPOILER and investigated similarly to the 2017 benchmark augmenting the reference data with new DFT/MRCI and SPOCK calculations. Additionally, a set of molecules (Fig. 6.8) was benchmarked against experimental ISC rate constants in comparison to DFT/MRCI and SPOCK to test the implementation extension for (vibronic) spin–forbidden transitions. The application of SPOILER to phosphorescence, however, is still subject to research.

The PYSOC benchmark set contains similar organic systems as the molecules used for the 2017 SPOILER benchmark where formaldehyde as a typical quantum chemical guinea pig is contained in both sets. Computationally, an equivalent protocol to Gao *et al.*[130] was employed for the SPOILER calculations utilizing the geometric structures from their supplementary information in combination with the B3-LYP density functional and the TZVP atomic basis set to perform Turbomole[22] TDDFT calculations. The DFT/MRCI and SPOCK calculations are conducted employing Kohn–Sham BH-LYP orbitals as one-particle basis for the R2016[59] DFT/MRCI operator.
Overall, the benchmark shows good agreement between SPOILER and SOCMEs obtained at DFT/MRCI and SPOCK level of theory visible in correlation coefficients of about 0.96 (Fig. 6.7). As found in the 2017 benchmark, the choice of AMEWs has only a minor effect on the performance varying the RMSD (Tab. 6.1) between $9.2 - 9.9$ cm^{-1}. From the publication of Gao *et al.*, the chosen linear response TDDFT amplitudes for AMEW construction were

unclear, but the SPOILER calculations show almost perfect agreement if A^{LL}_{MN}-AMEWs are employed suggesting that Gao *et al.* made a similar choice.

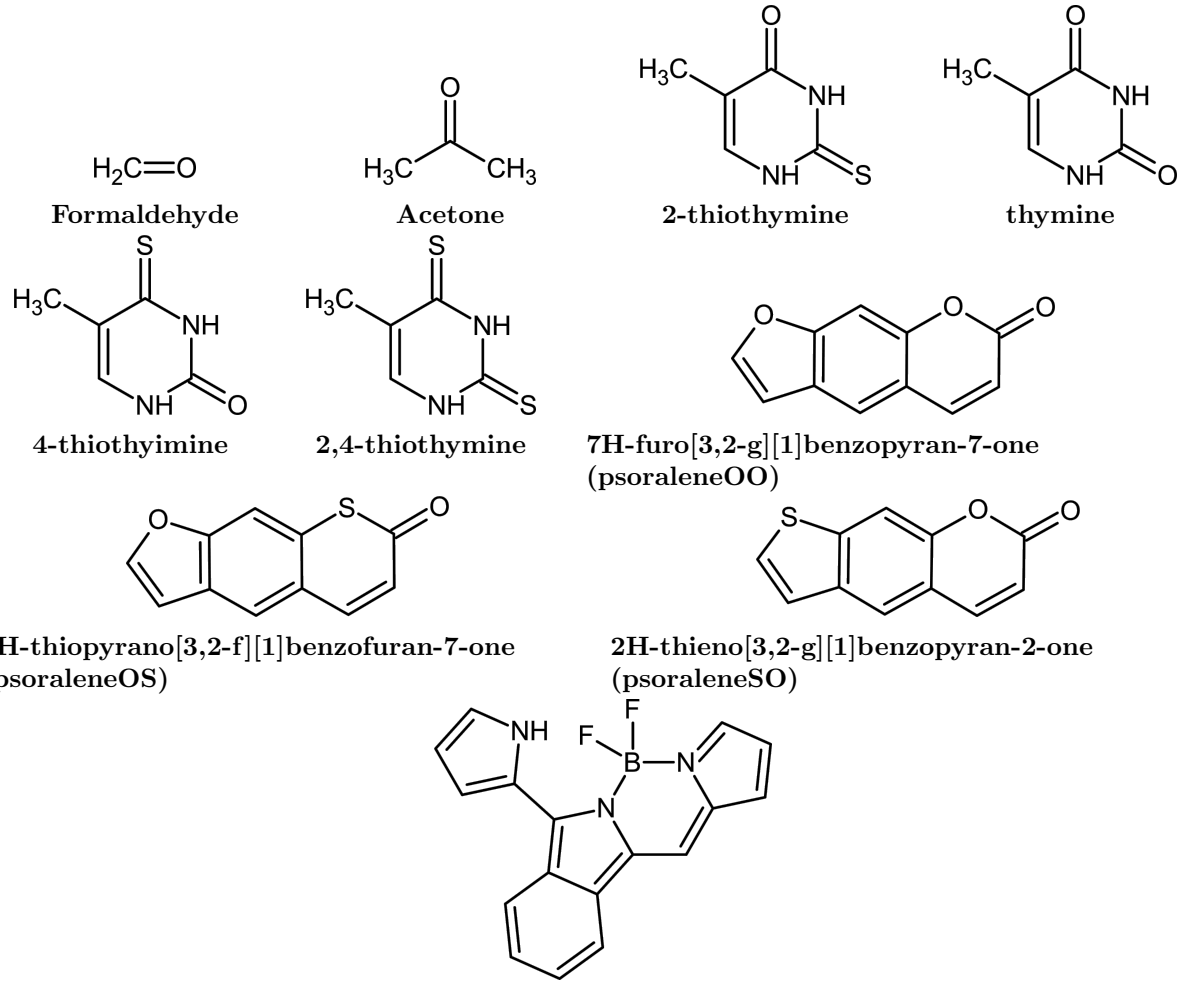

Figure 6.6: PySOC Benchmark Set.

Table 6.1: SOCME Statistics employing different TDDFT-AMEWs on the PySOC benchmark set.

Method	RMSD [cm^{-1}]	NRMSD [%]	max(+) [cm^{-1}]	max(-) [cm^{-1}]
A^{LL}_{MN}	9.7	7	26.8	-32.8
A^{LR}_{MN}	9.9	7	26.8	-32.8
A^{RL}_{MN}	9.2	6	35.1	-24.2
A^{RR}_{MN}	9.4	6	35.1	-25.4
A^{aver}_{MN}	9.3	6	30.8	-27.3
TDA	9.9	7	37.9	-25.5

The significant deviations observed in the benchmark of Gao *et al.* are reproduced by SPOILER showing that the deviations are not rooted in the semi-empirical one-electron spin–orbit operator with effective nuclear charges as the SOMF operator yields similar results.

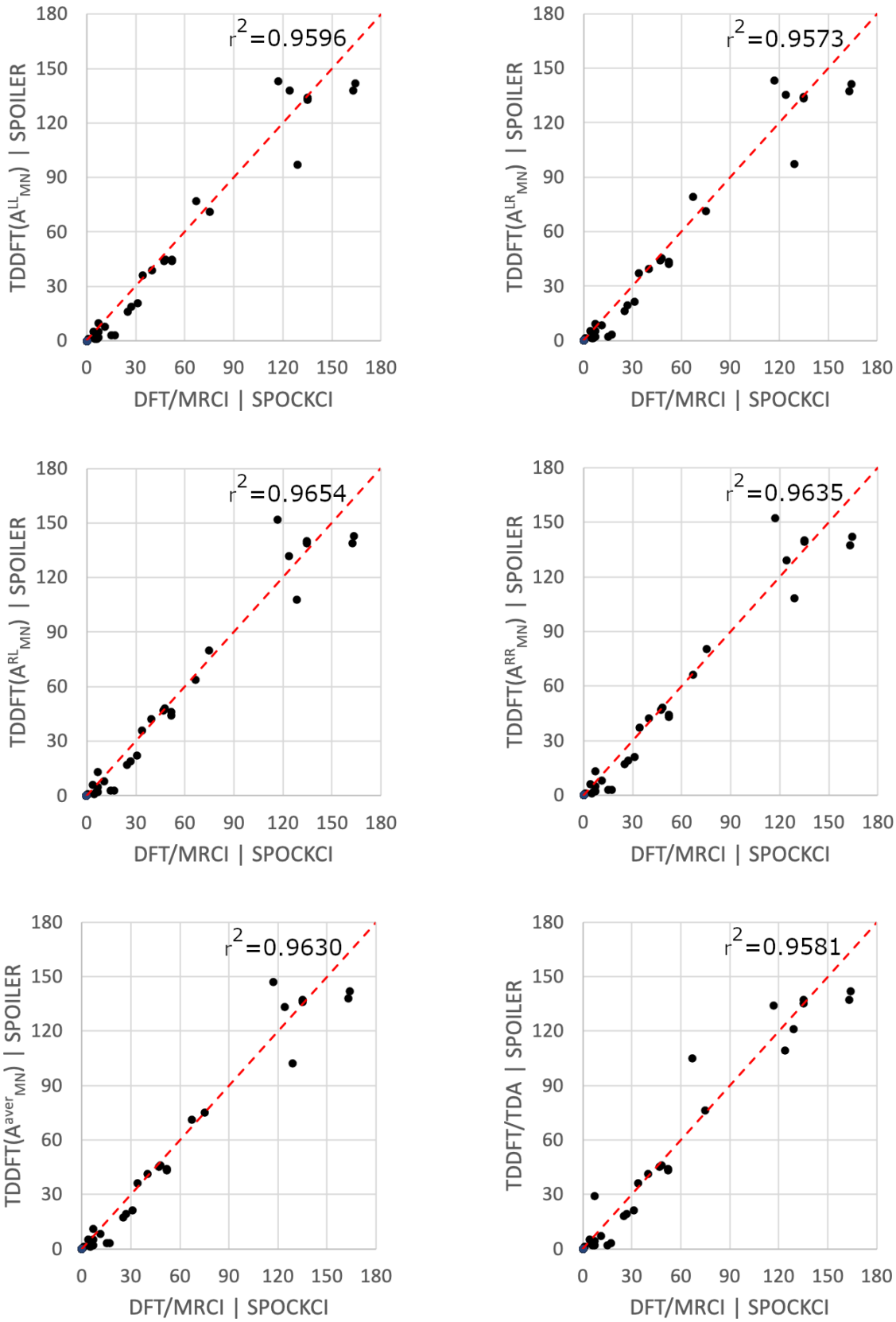

Figure 6.7: SOCME correlation graphs in cm^{-1} obtained with CI and Spoiler for the PySOC benchmark set.

For more complicated systems however, the effective spin–orbit operator should be used with caution. Investigation of the detailed contributions to each SOCME showed that the deviations originate mostly from differences between the DFT/MRCI wave functions and TDDFT/TDA AMEW compositions (Sec. A.1).
In some cases doubly excited configurations in the DFT/MRCI wave functions yield non-negligible contributions to the SOCME causing a substantial difference between DFT/MRCI and TDDFT results as doubly excited configurations are completely absent from the TDDFT AMEWs. The lack of doubly excited configurations is slightly counteracted by increased weights of contributing singly excited configurations in the TDDFT AMEWs. Contributions of doubly excited configurations of the DFT/MRCI wave functions have to be taken with a grain of salt as the R2016 operator has lately been known to be susceptible to artificial double excitations.[140]

The largest deviations in the correlation plots occur for 2-thiothymine. The structure of 2-thiothymine is particularly interesting, as it exhibits a mostly planar structure while the sulfur substituent is in an angled out of plane position. This circumstance renders the electronic states of 2-thiothymine a mixture between n and π character and increases the SOCMEs with respect to transitions between pure $\pi \rightarrow \pi^*$ states in the other investigated thymine compounds (Tab. A.6). In 2-thiothymine the S_1 and S_2 states are composed of a mixture of the $n/\pi_H \rightarrow \pi_L^*$ and $n/\pi_{H-1} \rightarrow \pi_L^*$ excitations, where the former contributes stronger to S_2 and the latter to S_1. Within the DFT/MRCI wave functions the mixture is quite balanced at about 40 %, while in TDDFT and TDDFT/TDA the excited states are mainly described by the leading configuration with admixtures of about 20 % of the other. Additional to the large differences between the excited state descriptions, the S_1 and S_2 states are reversed in relation to the DFT/MRCI order. The triplet states however do not encounter similar problems and are mainly composed $n/\pi_H \rightarrow \pi_L^*$ and $n/\pi_{H-1} \rightarrow \pi_L^*$ single excitations, where the former corresponds to the T_1 and the latter to the T_2 state. It is important to note here that TDDFT/TDA AMEWs are closer related to the DFT/MRCI wave function with about 80 % contribution of the main configuration, while in TDDFT the mixing is closer to the singlet case with contributions of 60 % and 30 % respectively. The largest SOCME deviations between TDDFT and DFT/MRCI are encountered for $\langle T_1|\hat{\mathcal{H}}_{SO}|S_0\rangle$ (TDDFT: 97-102 cm^{-1}, TDA: 121 cm^{-1}, DFT/MRCI: 129 cm^{-1}) and $\langle T_2|\hat{\mathcal{H}}_{SO}|S_0\rangle$ (TDDFT: 143-152 cm^{-1}, TDA: 138 cm^{-1}, DFT/MRCI: 117 cm^{-1}).

Investigating the SOCME components more closely reveals that the x and y component exhibit the largest deviations.
Utilizing A_{MN}^{RL}, the $\langle T_1|\hat{\mathcal{H}}_{SO}|S_0\rangle$ matrix element vanishes, while TDA seems to be closer to the DFT/MRCI results. A closer look at the wave function coefficients and the weighted SOC contributions (Tab. 6.3) to the $\langle T_1|\hat{\mathcal{H}}_{SO}|S_0\rangle$ and $\langle T_2|\hat{\mathcal{H}}_{SO}|S_0\rangle$ matrix elements shows that the TDDFT wave functions exhibit a sign-change compared to the DFT/MRCI wave function and therefore the contributions to the SOCME do not add up, but compensate. In case of A_{MN}^{RL} this circumstance causes the $\langle T_1|\hat{\mathcal{H}}_{SO,y}|S_0\rangle$ component to almost vanish.
The sign-flip in the wave functions may be caused due to the non-planar arrangement of the sulfur atom. Even at DFT level the molecular orbitals show large differences within their SOMF integrals. Herein, the integral of $\langle n/\pi_H|\hat{\mathcal{H}}_{SO,y}|\pi_L^*\rangle$ does contribute less to the SOCME utilizing BH-LYP than with B3-LYP orbitals (Tab. 6.4).
Ignoring the diverging descriptions of 2-thiothymine with DFT/MRCI and TDDFT, the

benchmark shows a very good agreement between the SOCMEs and therefore that SPOILER can be used within the bounds of TDDFT. To obtain SOCMEs closest to SPOCK the A^{RL}_{MN} amplitudes should be utilized as the have proven in the 2017 and 2022 benchmark to yield the lowest RMSD values.

Table 6.2: SOCME contributions in cm^{-1} for selected methods in 2-thiothymine.

Method	$\hat{\mathcal{H}}_{SO,x}$	$\hat{\mathcal{H}}_{SO,y}$	$\hat{\mathcal{H}}_{SO,z}$
	$\langle T_1\|\hat{\mathcal{H}}_{SO}\|S_0\rangle$		
SPOCK	108.58	68.48	16.91
A^{RL}_{MN}	107.54	6.65	9.74
TDA	112.00	43.20	11.01
	$\langle T_2\|\hat{\mathcal{H}}_{SO}\|S_0\rangle$		
SPOCK	3.41	116.22	9.32
A^{RL}_{MN}	51.44	142.07	14.29
TDA	15.31	132.95	8.38

Table 6.3: Leading wave functions configurations and weighted SOMF integrals in cm^{-1} for selected methods in 2-thiothymine.

Method	$c_{n/\pi_H\rightarrow\pi^*_L}$	$c_{n/\pi_{H-1}\rightarrow\pi^*_L}$	$\langle n/\pi_H\|\hat{\mathcal{H}}_{SO,y}\|\pi^*_L\rangle$	$\langle n/\pi_{H-1}\|\hat{\mathcal{H}}_{SO,y}\|\pi^*_L\rangle$
			T_1	
SPOCK	0.9002	-0.2682	-21.85	-31.30
A^{RL}_{MN}	-0.7035	-0.4582	62.07	-56.73
TDA	-0.9380	-0.3087	70.36	-32.49
			T_2	
SPOCK	-0.2683	-0.9182	6.51	-107.13
A^{RL}_{MN}	0.5686	-0.7259	-46.00	-82.41
TDA	0.3192	-0.9372	-31.56	-98.65

Table 6.4: SOMF integrals in cm^{-1} of the leading configurations for BH-LYP (SPOCK) and B3-LYP (TDDFT).

Method	$\langle n/\pi_H\|\hat{\mathcal{H}}_{SO,y}\|\pi^*_L\rangle$	$\langle n/\pi_{H-1}\|\hat{\mathcal{H}}_{SO,y}\|\pi^*_L\rangle$
BH-LYP	34.919222	-167.857330
B3-LYP	106.078137	-148.855615

6.4.2 Applications for ISC Rate Constants

Benchmarking Spoiler for the evaluation of SOCMEs, as important as it is to establish the validity and boundaries of the approach, does not resemble the typical use case in which Spoiler is applied. Typically, the user is interested in the excited state kinetics and in the context of Spoiler the rate constants of spin-forbidden radiative and non-radiative processes.

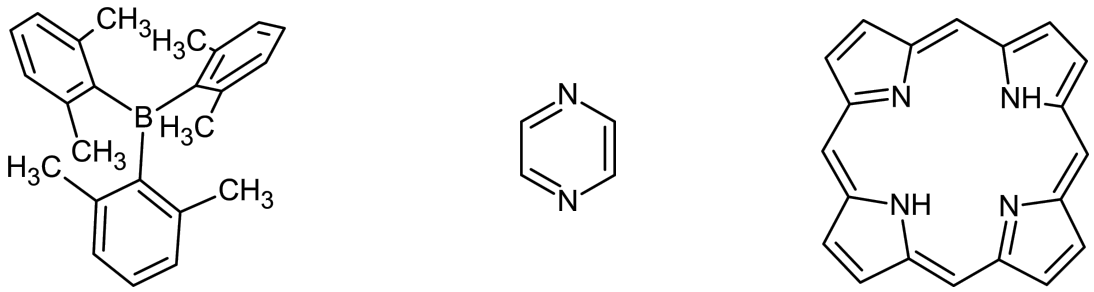

Tris(2,6-dimethylphenyl)-borane (TXB) **Pyrazine** **Porphyrin**

Figure 6.8: Benchmark molecules for ISC rate constants.

To benchmark Spoiler for this application, ISC rate constants were calculated for tris(2,6-dimethylphenyl)borane (TXB), pyrazine and porphyrin (Fig. 6.8).

Tris(2,6-dimethylphenyl)borane (TXB)

Triarylboranes have been shown to emit fluorescence and long-lasting phosphorescence where the latter occurs even at RT if employed in rigid environments. The emissive properties and excited state kinetics of TXB are in detail discussed in section 3.1 where TXB is the studied compound 3 showing blue/violet fluorescence and greenish-yellow phosphorescence. Fluorescence and ISC were found to proceed at the same timescale rendering fluorescence and phosphorescence competing processes.
The important states involved in the emission mechanism are the S_1, T_1 and T_2 states, where ISC was found to proceed mainly via $S_1 \rightsquigarrow T_2$ ISC. Adiabatically, these states are located at 3.77 eV, 2.93 eV and 3.17 eV within the DFT/MRCI method agreeing well with experimental findings, while TDDFT places them at 3.40 eV, 2.76 eV, 2.96 eV respectively. TDDFT locates the states systematically about 0.2 eV below the DFT/MRCI level. Employing the TDA lifts the triplet states into good agreement, while the S_1 state is still located 0.3 eV below the corresponding DFT/MRCI energy.
The lower S_1 excitation energy does not affect the fluorescence rate constants much in TDDFT/TDA where a rate constant of $2 - 3 \times 10^7$ s^{-1} is obtained in good agreement with the rate constant of 3×10^7 s^{-1} at DFT/MRCI level. ISC as competing process proceeds for the $S_1 \rightsquigarrow T_2$ channel at DFT/MRCI level with 5×10^7 s^{-1} and at TDDFT/TDA level with $1 - 4 \times 10^7$ s^{-1}.
The slow $S_1 \rightsquigarrow T_1$ channel yields rate constants of 5×10^6 s^{-1} within the DFT/MRCI and $0.8 - 2 \times 10^7$ s^{-1} within TDDFT/TDA. The ISC rate constants for $S_1 \rightsquigarrow T_2$ agree well between the methods and contain some fluctuations depending on the choice of amplitudes. For the $S_1 \rightsquigarrow T_1$ ISC channel TDDFT/TDA yields rate constants up to an order of magnitude

larger than obtained with the DFT/MRCI. The enlargement originates from the $\langle T_1|\hat{\mathcal{H}}_{SO}|S_1\rangle$ SOCME that differs by a factor of up to 4 between both methods.

Table 6.5: ISC rate constants in TXB.

Method	$\Delta E_{DFT/MRCI}$		ΔE_{TDDFT}	
	$S_1 \rightsquigarrow T_1$ [10^7 s^{-1}]	$S_1 \rightsquigarrow T_2$ [10^7 s^{-1}]	$S_1 \rightsquigarrow T_1$ [10^7 s^{-1}]	$S_1 \rightsquigarrow T_2$ [10^7 s^{-1}]
SPOCK	0.49	5.21	-	-
A_{MN}^{LL}	2.30	3.29	1.94	4.60
A_{MN}^{LR}	1.94	3.25	1.64	4.55
A_{MN}^{RL}	1.20	3.58	1.01	5.00
A_{MN}^{RR}	0.82	3.53	0.69	4.93
A_{MN}^{aver}	1.52	3.41	1.29	4.77
TDA	5.09	1.08	4.31	5.09

Table 6.6: SOCMEs (sum of squares) between the low-lying excited states in TXB.

SOCME [cm^{-2}]	SPOCK	A_{MN}^{LL}	A_{MN}^{LR}	A_{MN}^{RL}	A_{MN}^{RR}	A_{MN}^{aver}	TDA
$\langle T_1|\hat{H}_{SO}|S_1\rangle$	0.05	0.19	0.16	0.10	0.08	0.13	0.42
$\langle T_2|\hat{H}_{SO}|S_1\rangle$	1.28	1.13	1.12	1.23	1.21	1.17	1.25

If A_{MN}^{RR}-AMEWs are chosen, the closest agreement for $\langle T_1|\hat{\mathcal{H}}_{SO}|S_1\rangle$ is obtained with the DFT/MRCI results. The lower energy of the S_1 state in the TDDFT/TDA calculations increases the rate constant of the $S_1 \rightsquigarrow T_2$ channel, while the $S_1 \rightsquigarrow T_1$ channel is subject to decrease. Utilizing the DFT/MRCI energy gaps ($\Delta E_{DFT/MRCI}$) instead of the TDDFT ones (ΔE_{TDDFT}) improves the agreement between the methods.

Pyrazine

Pyrazine was already studied by means of DFT/MRCI calculations (Sec. 5.4) showing the importance of vibronic interactions in the $S_1 \leftarrow S_0$ absorption spectrum. The $T_1 \leftarrow S_0$ absorption spectrum, however, remains mostly unaffected by vibronic coupling effects and the $T_1(n\pi^*)$ phosphorescence intensity is directly borrowed from higher lying bright singlet states ($\pi\pi^*$). The ISC channel between the lowest singlet and triplet state $S_1 \rightsquigarrow T_1$ is a symmetry forbidden process as both states exhibit B_{3u} symmetry in the $\mathcal{D}_{2h}$ point group prohibiting ISC in FC approximation. Vibrations corresponding to the b_{3g}, b_{2g} and b_{1g} irreducible representations can break the $\mathcal{D}_{3h}$ symmetry and mix in close lying $\pi\pi^*$ states allowing the spin-forbidden process.
Adiabatically, the S_1 state is located in the DFT/MRCI calculations at 3.95 eV, while the T_1 state is placed at 3.50 eV. TDDFT positions both states at 3.91 eV and 3.00 eV while employing TDA yields energies of 3.96 eV and 3.08 eV. In both cases the energies are close to the experiment which locates both states at 3.83 eV and 3.33 eV, where DFT/MRCI overestimates the T_1 energy and TDDFT/TDA underestimates it by about 0.2 eV. The different energetic location of the T_1 state causes strongly diverging adiabatic energy gaps (DFT/MRCI: 0.45 eV, TDDFT: 0.8 eV) that can influence the outcome of rate constant calculations quite drastically. Following section 5, SOCME gradients (Tab. 6.7) for the evaluation of HT

rate constants were obtained for both methods along the TDDFT vibrational normal modes and the appropriate phase corrections were applied.

Table 6.7: Pyrazine SOCME gradients in cm^{-1} along dimensionless normal modes.

Mode	Symmetry	SPOCK	A^{LL}_{MN}	A^{LR}_{MN}	A^{RL}_{MN}	A^{RR}_{MN}	A^{aver}_{MN}	TDA
			$\hat{\mathcal{H}}_{\mathbf{SO,x}}$					
ν_5	b_{3g}	3.15	2.15	1.90	1.34	1.14	1.59	0.98
ν_{11}	b_{3g}	0.72	0.37	0.38	0.23	0.26	0.30	0.17
			$\hat{\mathcal{H}}_{\mathbf{SO,y}}$					
ν_4	b_{2g}	0.09	0.00	0.00	0.00	0.00	0.00	0.22
			$\hat{\mathcal{H}}_{\mathbf{SO,z}}$					
ν_1	b_{1g}	0.08	0.23	0.14	0.22	0.13	0.17	0.20
ν_8	b_{1g}	0.00	0.01	0.01	0.01	0.00	0.01	0.00
ν_{16}	b_{1g}	0.04	0.08	0.06	0.07	0.04	0.06	0.00
ν_{21}	b_{1g}	0.06	0.10	0.08	0.08	0.06	0.08	0.08

The SOCME gradients show that most vibronic coupling is mediated by ν_5 and to a smaller extent by ν_{11}. The gradients vary between DFT/MRCI and TDDFT/TDA strongly showing the best agreement when A^{LL}_{MN}-AMEWs are employed with still 1 cm^{-1} per displacement unit difference for ν_5 and about 0.5 cm^{-1} per displacement unit for ν_{11}. The large SOCME gradient within DFT/MRCI is caused by doubly excited configurations contributing about 2/3 of the SOCMEs value. Without the contributions of the doubly excited configurations a value close to TDDFT/TDA of about 1 cm^{-1} is obtained. TDDFT shows the largest SOCME gradient when A^{LL}_{MN}-AMEWs are employed and reduces from left to right in table 6.7 with its lowest value at the TDDFT/TDA level. The origin of the differences between the amplitude choices are rather complex. The main contributions to the SOCMEs arise from couplings of the $\pi_{H-2} \rightarrow \pi^*_L$ and $\pi_H \rightarrow \pi^*_L$ configurations, which exhibit the largest coefficient when the A^{LL}_{MN}-AMEWs are chosen explaining the larges SOCME gradients in this case. The other amplitude choices yield a lower SOCME gradient as the coefficients of these two configurations are reduced when mixtures of the $(X-Y)$ and $(X+Y)$ amplitudes are used up to the point, where the lowest full TDDFT SOCME is achieved for A^{RR}_{MN}-AMEWs.

Table 6.8: ISC rate constants [s^{-1}] in pyrazine.

Method	$\Delta E_{DFT/MRCI}$ $S_1 \rightsquigarrow T_1$	ΔE_{TDDFT} $S_1 \rightsquigarrow T_1$
SPOCK	3.30×10^7	-
A^{LL}_{MN}	1.56×10^7	1.36×10^5
A^{LR}_{MN}	1.22×10^7	1.00×10^5
A^{RL}_{MN}	6.16×10^6	5.95×10^4
A^{RR}_{MN}	4.49×10^6	3.96×10^4
A^{aver}_{MN}	8.63×10^6	7.57×10^4
TDA	3.43×10^6	1.35×10^4

Employing the SOCME gradients HT ISC rate constants of 3×10^7 s^{-1} for DFT/MRCI and $0.1 - 1 \times 10^5$ s^{-1} for TDDFT/TDA are obtained for the $S_1 \rightsquigarrow T_1$ transition. The

TDDFT/TDA rate constants are about two orders of magnitude lower than the ones obtained at DFT/MRCI level which is caused mostly by the strongly varying energy gap and slightly attributed to the difficulties observed for the SOCME gradients. If the DFT/MRCI energy gap is employed within the TDDFT/TDA calculations instead rate constants of $0.3 - 2 \times 10^7$ s^{-1} are obtained which lie within the same ballpark as the DFT/MRCI results.
Pyrazine is a great example of the problems that can be encountered utilizing TDDFT for a system, where double excitations play an important role. The doubly excited configurations have non-negligable contributions to the SOCMEs and their gradients. Next to the compositions of the wave functions, the estimation of energy gaps requires more sophisticated methods than TDDFT to obtain accurate rate constants. Besides the encountered problems, however, TDDFT yields qualitative results for pyrazine that are in the ballpark with DFT/MRCI calculations if an appropriate energy gap is supplied.

Porphyrin

Vibronic interactions play a decisive role in the radiative and non-radiative processes of porphyrin. The low-lying electronic states exhibit $\pi \rightarrow \pi^*$ character which following El-Sayed's rule renders ISC weak, while in a planar nuclear arrangement the SOCME $\langle T_1|\hat{\mathcal{H}_{SO}}|S_1\rangle$ is close to zero and $\langle T_2|\hat{\mathcal{H}_{SO}}|S_1\rangle$ vanishes due to the molecular symmetry. Vibronic contributions were shown to enhance computational ISC rate constants obtained at DFT/MRCI level of theory from about 10^5 s^{-1} in FC approximation to 10^7 s^{-1} utilizing the HT-type expansion.[141] In contrast to TXB, where a nearly constant red shift of the low-lying singlet and triplet is observed moving from DFT/MRCI to TDDFT, the $S_1(^1B_{3u})$ state is shifted by about 0.4 eV whereas the $T_1(^3B_{2u})$ state is lowered in energy by about the same amount. Utilizing TDDFT/TDA the T_1 state is shifted into good agreement with the DFT/MRCI method. It is important to note here, that the DFT/MRCI excitation energies (T_1 : 1.62 eV, S_1 : 1.92 eV)[141] are in excellent agreement with experimental 0-0 transition energies (T_1 : 1.58[142] eV, S_1 : 1.98[143] eV). Utilizing the TDDFT potentials will therefore yield significantly different results in comparison with the DFT/MRCI method. The calculation of numerical SOCME gradients poses a problem in porphyrin due to triplet-instabilities in TDDFT, rendering TDDFT/TDA the only method applicable in this case.
The SPOCK and Spoiler calculations show in very good agreement, that HT ISC is driven by out-of-plane vibrations corresponding to the b_{1g} and b_{2g} irreducible representations (Tab. 6.9). While the SOCME gradients are very similar (Fig. 6.9), the ISC rate constants (Tab. 6.10) are about one order of magnitude smaller in TDDFT than at DFT/MRCI level due to the lower S_1 state's energy.
If the DFT/MRCI energy gap is employed instead similar rate constants are obtained in both methods. Therefore, utilization of Spoiler can lower the costs for HT-type calculation schemes obtaining results similar to more sophisticated methods, while it can be necessary to obtain energies by more reliable methods.

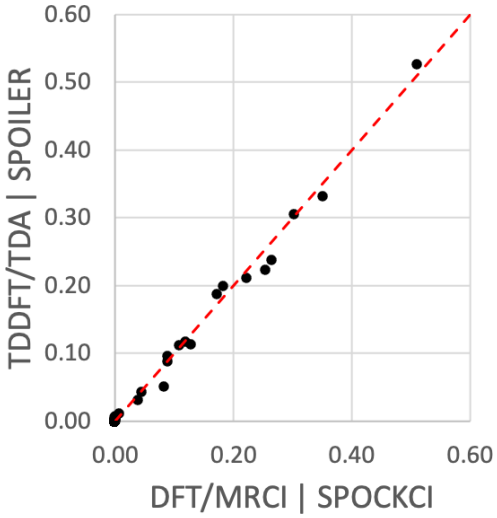

Figure 6.9: SOCME gradient correlation graph in cm^{-1} obtained with SPOCK and SPOILER in porphyrin.

Table 6.9: Porphyrin SOCME gradients in cm^{-1} along dimensionless normal modes.

Mode	Symmetry	$S_1 \rightarrow T_1$	
		SPOCK	TDA
	$\hat{\mathcal{H}}_{\mathbf{SO,x}}$		
6	b_{1g}	0.1180	0.1189
10	b_{1g}	0.0438	0.0449
21	b_{1g}	0.2118	0.2227
25	b_{1g}	0.2232	0.2538
30	b_{1g}	0.2000	0.1824
37	b_{1g}	0.1872	0.1728
46	b_{1g}	0.1137	0.1288
51	b_{1g}	0.1120	0.1085
	$\hat{\mathcal{H}}_{\mathbf{SO,y}}$		
5	b_{2g}	0.0112	0.0066
8	b_{2g}	0.0310	0.0394
19	b_{2g}	0.5264	0.5103
23	b_{2g}	0.0512	0.0829
26	b_{2g}	0.0963	0.0896
29	b_{2g}	0.3316	0.3507
39	b_{2g}	0.0887	0.0888
47	b_{2g}	0.2380	0.2642
50	b_{2g}	0.3050	0.3026

Table 6.10: ISC rate constants $[s^{-1}]$ for the $S_1 \rightsquigarrow T_1$ transition in porphyrin.

Method	$\Delta E_{DFT/MRCI}$	ΔE_{TDA}
SPOCK	$6.74 \cdot 10^7$	
TDA	$6.81 \cdot 10^7$	$3.25 \cdot 10^6$

7 Excitation Energy Transfer

Excitation energy transfer (EET) is a photophysical process that describes the non-radiative transfer of an exciton. The exciton is transferred from the excited donor (D^*) to the unexcited acceptor (A), de-exciting the donor (D) and exciting the acceptor (A^*) in the process.

$$D^* + A \rightarrow D + A^* \tag{7.1}$$

The transfer can occur intra- and intermolecular such that the exciton donor and acceptor can be separate molecules or fragments of a larger system. EET can follow three principle processes:

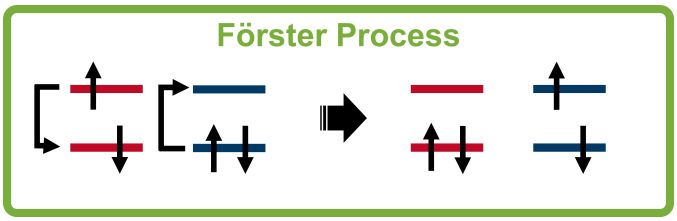

Figure 7.1: The Förster process facilitates the simultaneous de-excitation of the donor (red) and excitation of the acceptor (blue).

The Förster process, also known as FRET, is named after Theodore Förster[10,11] and describes the excitation energy transfer through a simultaneous donor de-excitation and acceptor excitation. The process is highly dependent on the relative orientation of the donor and acceptor molecules and requires the donor emission and acceptor absorption spectra to overlap. It is important to note, that throughout the transfer process no particles are exchanged and that the excitation energy transfer is merely a result of the Coulomb interaction of the donor and acceptor systems. The Coulomb force drives this transfer with typical transfer ranges of up to 100 Å.[144] The Förster process is used to describe energy transfer reactions between singlet states, but as Förster proposed in 1959[11] it can occur even between singlet and triplet states (TSEET). Herein, the Coulomb operator as a spin–independent entity can not mediate the transfer between different spin states such that the partial singlet character mixed into the triplet's wave function by SOC is responsible. Occurrences of FRET are widely investigated employing Förster's theory (Sec. 2.11.1) to obtain transfer rate constants and determine Förster radii for pairings of chromophores. Herein Förster's theory offers an easy and inexpensive approach to obtain transfer rate constants. While it is based on the IDA, which is known to break down at short distances, it has been found in molecular dynamics simulations that the deviations due to short chromophore distances do not matter statistically. For static computations however one has to go beyond the IDA.[145]

The Dexter process is named after David L. Dexter[12] and describes a simultaneous ET, where the donor is de-excited by exchanging an excited electron with the acceptor, exciting the latter in the process. As an ET process, the Dexter mechanism is highly dependent on the distance between the chromophores rendering it a short-range process decaying fast with increasing distance. The simultaneous exchange of electrons allows transferring excitation energy between singlets and triplets such that it contributes to SEET, TSEET and TEET.

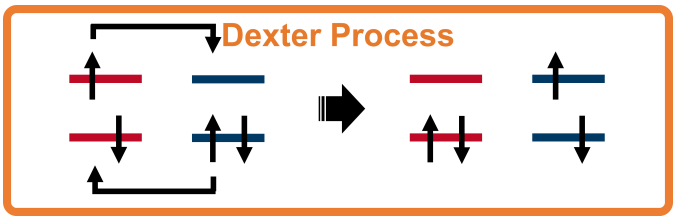

Figure 7.2: The Dexter process facilitates the simultaneous de-excitation of the donor (red) and excitation of the acceptor (blue).

Next to the simultaneous ET described by the Dexter process, the excitation energy can be transferred by consecutive ET processes involving intermediate CT states.[23,86,89] Typically, this kind of transfer processes are ascribed to the Dexter process, but they will be treated as separate processes here to distinguish the different computational treatment of their contributions to the transfer rate.

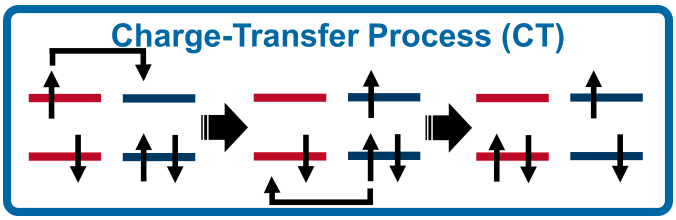

Figure 7.3: The CT processes facilitate the de-excitation of the donor (red) and excitation of the acceptor (blue).

The EET rate constants for the mentioned processes can be evaluated utilizing Fermi's Golden Rule (Sec. 2.10.1) where the ECME poses the computational challenge. While the ECME for a homo-dimer is accessible from the Davydov splitting, more computational effort has to be invested to describe the coupling in complex systems. The approaches to obtain the excitonic couplings can be split into super-molecular and fragment approaches:

- **Super-molecular approaches**: Super-molecular approaches treat the ECME evaluation in a top-down fashion by first conducting quantum chemical calculations on the whole system and applying a picture change to extract the ECME from the system's properties. The picture change is typically performed by diabatization of the system's adiabatic states. Diabatization techniques try to obtain or approximate the nonadiabatic coupling between the electronic states to transform the adiabatic states by a unitary transformation and obtain the ECME as an off-diagonal element of the Hamiltonian matrix. Two of the these approaches for EET and ET, the ER, Boys and BoysOV diabatization schemes have already been presented in the theory section

(Sec. 2.11.3). Other representatives of these methods are the fragment charge difference (FCD) and fragment excitation difference (FED) methods,[146–148] which utilize differences between reduced one-electron density matrices to obtain the unitary rotation. While these diabatization approaches allow going beyond the two-state model, one major problem of diabatization approaches is the blurry picture of the transfer process they may deliver.[149]

- **Monomer or fragment approaches**: Next to super-molecular methods, fragmentation approaches exist which aim at constructing the ECME in a bottom-up fashion from fragment properties. One representative of these methods is the transition density cube (TDC)[150] method which divides the transition density of the donor and acceptor into sets of volume elements called transition density cubes and integrates them on a 3D grid. Another is the MTD method which expands the transition densities in the basis of molecular orbitals and contracts the densities with the appropriate two-electron integrals (Sec. 2.11.4). As will be shown, extending the MTD method for short-range ET contributions is crucial. Fujimoto's extension of the TDFI method, a very close relative of the MTD method, obtains a very good agreement with a lot more costly super-molecular approaches for the ethylene dimer, while it is strongly limited by the treatment of CT contributions in a HOMO-LUMO picture. Fragment approaches can reduce the computational costs drastically allowing the investigation of larger systems.

The MTD approach was central to the work of Dr. Dominik Spiegel, a former PhD student who investigated excitonic SEET and applied the method to transfer processes in biological systems[145] and BODIPY cassettes.[82,151] Within this project Dominik's work was extended to TEET including short-range overlap corrections as well as usability improvements of the existing programs. Additionally, the Boys and BoysOV as well as the ER diabatization procedures were implemented to supply reference values for the extension of the MTD approach to short-range ET processes involving CT states.

7.1 Redesign and Extension of the Programs

Dominik Spiegel created during his studies multiple programs bundled in the program package *ExETracKt*, where each one fulfilled its own use case. These use cases range from simple manipulations of the molecule's coordinates to the contraction of reduced one-electron (transition) density matrices with two-electron integrals to obtain the ECME. To perform a MTD calculation multiple programs needed to be invoked, each with its own command line options rendering the operation of the program package complex. To simplify the system and improve the usability, the programs were merged into one executable offering structured input files. The input files for each execution mode can be generated via a command line option.

```
1    EET -g [mode]
2    EET --generateInput [mode]
```

The *mode* parameter determines the performed calculation type which will be explained in more detail in following:

7.1.1 IDA Mode

The IDA mode is an implementation of the FRET theory (Sec. 2.11.1) utilizing the IDA approximation to determine the ECME from the strength and orientation of the donor's and acceptor's electric transition dipole moments. The transition dipole moments are supplied via the input file and utilized to derive the orientation factor κ if it is not supplied too.

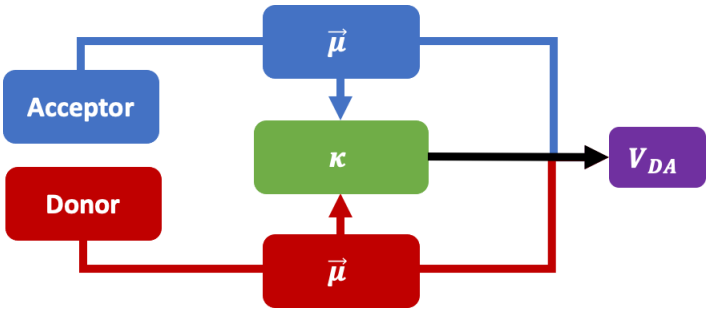

Figure 7.4: The IDA approach.

7.1.2 MTD Modes

The MTD mode is an implementation of the MTD approach (Sec. 2.11.4) utilizing the system's RI-integrals in combination with the donor's and acceptor's transition density matrices to determine the ECME. This mode requires donor and acceptor monomer calculations performed with the DFT/MRCI method employing the Turbomole[22] program package to obtain one- and two-electron integrals, structures as well as molecular orbitals.

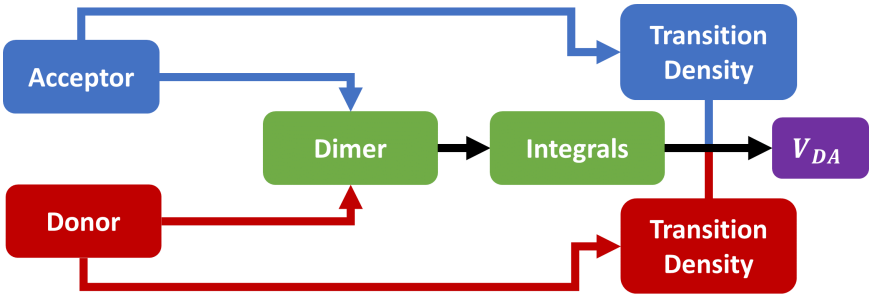

Figure 7.5: The MTD approach.

In a first step, the monomer calculations are combined to form the dimer for which the ECME should be determined. The dimer construction is taken from the *ExETracKt* program package, where a new set of Turbomole files is generated from the monomer calculations employing the product ansatz for the dimer wave functions. The full system's molecular orbitals are constructed by extending the orbital basis of each monomer to the full system, keeping the local monomer orbitals and padding the extended orbital's coefficients by zeros. Within *ExETracKt*, the monomer systems could be translated and rotated prior to the dimer construction as well as aligned to a reference structure using a quaternion approach to determine the rotation between both structures. Rotating a molecule invalidates the obtained reduced one-electron (transition) density matrices requiring to rerun the quantum chemical calculations of the monomers. To circumvent the costly calculations, the molecular orbitals, which represent the basis of the reduced one-electron (transition) density matrices, can be

rotated with the molecule. Dominik performed these rotations for up to spherical d-functions, which in turn was extended to f-functions in this work. Additionally, the dimer creation was extended throughout the redesign. The new dimer generator allows to define an initial rotation of the donor and acceptor molecules either by defining the rotation angles and rotation order or by utilizing the quaternion approach with a reference geometry. After the initial rotation is set, the fragments are placed in one coordinate system at a fixed distance, where the donor is located at the center of the coordinate system. To define the orientation of both fragments towards each other the acceptor can be moved on a sphere around the donor.

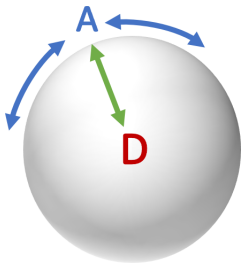

Figure 7.6: Dimer construction on a sphere.

With this improvement scans for optimal donor-acceptor orientations become simple. After dimer construction the RI-integrals are evaluated with Turbomole and contracted with the donor and acceptor transition densities exploiting the two-electron integral symmetry to obtain the ECME. Herein, the computational costs of the MTD mode are determined by the speed of the two-electron RI-integral calculation. A threshold can be applied to the transition density matrices to omit the integral contraction for negligible density contributions and speed up the ECME evaluation tremendously.

While the *ExETracKt* program package allowed to obtain the ECME only for SEET, the redesign extends the approach for TSEET and TEET[85] employing complex valued transition density matrices of SOC wave functions and the newly implemented singlet-triplet transition density matrices obtained with the Densomat (Sec. 4.3). Additionally, overlap corrections were introduced to account for the non-orthogonal orbital basis utilized in the product approach. At long distances the overlap between the basis functions located on the donor and acceptor fragments vanishes and does not pose a problem. At shorter distances the non-orthogonality of the molecular orbitals may lead to unreasonable RI-integrals and transition densities. One way to restore orthogonality of the fragment's molecular orbitals is to perform a Löwdin orthogonalization,[152] which rotates the molecular orbitals symmetrically and ensures to find orthogonal molecular orbitals with the least distance to the initial orbital basis. The procedure constructs a new set of molecular orbitals ϕ^{ortho} by a linear transformation $\phi^{ortho} = S^{\frac{1}{2}}\phi^{nonortho}$ of the old molecular orbitals. To apply the transformation the matrix $S^{-\frac{1}{2}}$ has to be known. To obtain this matrix the overlap matrix $S_{ij} = \langle\phi_i|\phi_j\rangle$ is diagonalized in a first step.

$$S_{diag} = U^T S U \tag{7.2}$$

Here the matrices U^T and U form an orthogonal transformation which follows $U^T U = UU^T = 1$. Taking the invers square root of S_{diag} with $-\frac{1}{\sqrt{S_{ii}}}$ yields $S_{diag}^{-\frac{1}{2}}$. In a last step, the $S_{diag}^{-\frac{1}{2}}$ has to be transformed back to its non-diagonal form in the basis of the molecular orbitals.

$$S^{-\frac{1}{2}} = U S_{diag}^{-\frac{1}{2}} U^T \tag{7.3}$$

The overlap corrections are employed in the MTD approach after the dimer has been constructed leading to a new orbital basis utilized to evaluate the two-electron integrals.

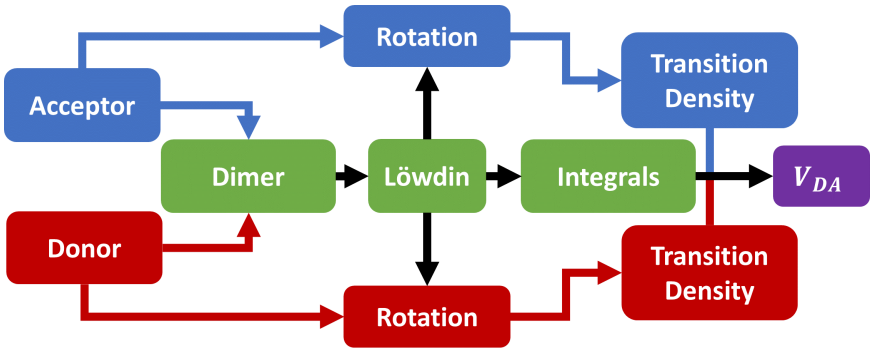

Figure 7.7: The MTD approach extended with the Löwdin overlap correction.

Applying the re-orthogonalization within the MTD approach corrects the molecular orbitals and the two-electron integrals derived from them. The (transition) densities of the fragments however exist still in the non-orthogonal basis and need to be transformed to the new orbitals.

$$D_{ortho}^{F\leftarrow I} = C^T D_{nonortho}^{F\leftarrow I} C \tag{7.4}$$

This transformation poses in principle a rotation of the (transition) density matrices, where density is transferred from one fragment to the other and vice versa. The so transformed density matrices are expanded in the orbital basis of the full system increasing the number of required integrals and therefore raising the computational costs for the RI-integral contraction.

Another extension of the MTD approach is the MTDTI mode which implements the MTD approach extended by short-range CT contributions following Fujimoto's TDFI-TI method. Fujimoto extended the perturbative approach to the ECME of Harcourt *et al.*[86] (Eq. 2.129) for SEET to incorporate contributions by short-range ET via CT states. Similar expressions can be derived for TEET.

$$\begin{aligned} V_{DA} &= \langle \psi_{DA^*} | \hat{\mathcal{H}} | \psi_{D^*A} \rangle \\ &+ \Bigg[- \frac{\langle \psi_{DA^*} | \hat{\mathcal{H}} | \psi_{D^+A^-} \rangle \langle \psi_{D^+A^-} | \hat{\mathcal{H}} | \psi_{D^*A} \rangle}{E_{D^+A^-} - E_{DA^*}} - \frac{\langle \psi_{DA^*} | \hat{\mathcal{H}} | \psi_{D^-A^+} \rangle \langle \psi_{D^-A^+} | \hat{\mathcal{H}} | \psi_{D^*A} \rangle}{E_{D^-A^+} - E_{DA^*}} \\ &+ \frac{\langle \psi_{DA^*} | \hat{\mathcal{H}} | \psi_{D^+A^-} \rangle \langle \psi_{D^+A^-} | \hat{\mathcal{H}} | \psi_{D^-A^+} \rangle \langle \psi_{D^-A^+} | \hat{\mathcal{H}} | \psi_{D^*A} \rangle}{(E_{D^-A^+} - E_{DA^*})(E_{D^+A^-} - E_{DA^*})} \\ &+ \frac{\langle \psi_{DA^*} | \hat{\mathcal{H}} | \psi_{D^-A^+} \rangle \langle \psi_{D^-A^+} | \hat{\mathcal{H}} | \psi_{D^+A^-} \rangle \langle \psi_{D^+A^-} | \hat{\mathcal{H}} | \psi_{D^*A} \rangle}{(E_{D^-A^+} - E_{DA^*})(E_{D^+A^-} - E_{DA^*})} \Bigg] \end{aligned} \tag{7.5}$$

The latter two contributions involving ET between CT configurations are omitted as they are rather small and do only matter at very short distances.[23] To obtain expressions for the Hamiltonian matrix elements, the involved singlet and triplet dimer states can be formulated in a CSF basis assuming orthogonal molecular orbitals between the donor and acceptor fragments. The assumption of orthogonal molecular orbitals holds true, as long as orthogonality

corrections like a proper molecular orbital re-orthogonalization are applied.

$$
\begin{aligned}
{}^1\Psi_{DA} &= \phi_i\bar{\phi}_i\phi_k\bar{\phi}_k \\
{}^1\Psi_{D^*A} &= \frac{1}{\sqrt{2}}(\phi_i\bar{\phi}_j\phi_k\bar{\phi}_k - \bar{\phi}_i\phi_j\phi_k\bar{\phi}_k) \qquad {}^3\Psi_{D^*A} = \frac{1}{\sqrt{2}}(\phi_i\bar{\phi}_j\phi_k\bar{\phi}_k + \bar{\phi}_i\phi_j\phi_k\bar{\phi}_k) \\
{}^1\Psi_{DA^*} &= \frac{1}{\sqrt{2}}(\phi_i\bar{\phi}_i\phi_k\bar{\phi}_l - \phi_i\bar{\phi}_i\bar{\phi}_k\phi_l) \qquad {}^3\Psi_{DA^*} = \frac{1}{\sqrt{2}}(\phi_i\bar{\phi}_i\phi_k\bar{\phi}_l + \phi_i\bar{\phi}_i\bar{\phi}_k\phi_l) \\
{}^1\Psi_{D^+A^-} &= \frac{1}{\sqrt{2}}(\phi_i\phi_k\bar{\phi}_k\bar{\phi}_l - \bar{\phi}_i\phi_k\bar{\phi}_k\phi_l) \qquad {}^3\Psi_{D^+A^-} = \frac{1}{\sqrt{2}}(\phi_i\phi_k\bar{\phi}_k\bar{\phi}_l + \bar{\phi}_i\phi_k\bar{\phi}_k\phi_l) \\
{}^1\Psi_{D^-A^+} &= \frac{1}{\sqrt{2}}(\phi_i\bar{\phi}_i\phi_j\bar{\phi}_k - \phi_i\bar{\phi}_i\bar{\phi}_j\phi_k) \qquad {}^3\Psi_{D^-A^+} = \frac{1}{\sqrt{2}}(\phi_i\bar{\phi}_i\phi_j\bar{\phi}_k + \phi_i\bar{\phi}_i\bar{\phi}_j\phi_k)
\end{aligned}
\tag{7.6}
$$

The Hamiltonian matrix elements are derived in detail in the appendix (Sec. A.2) and only the results will be shown here:

$$
\begin{aligned}
\langle {}^1\Psi_{DA^*}|\hat{\mathcal{H}}|{}^1\Psi_{D^*A}\rangle &= 2V_{ikjl} - V_{iklj} \\
\langle {}^1\Psi_{D^+A^-}|\hat{\mathcal{H}}|{}^1\Psi_{D^*A}\rangle &= h_{lj} + V_{ilij} + V_{ilji} + 2V_{klkj} - V_{kljk} \\
\langle {}^1\Psi_{DA^*}|\hat{\mathcal{H}}|{}^1\Psi_{D^+A^-}\rangle &= -h_{ik} - V_{iiik} - V_{ikkk} + 2V_{likl} - V_{ilkl} \\
\langle {}^1\Psi_{D^-A^+}|\hat{\mathcal{H}}|{}^1\Psi_{D^*A}\rangle &= -h_{ik} - V_{iiik} - V_{ikkk} + 2V_{jikj} - V_{ijkj} \\
\langle {}^1\Psi_{DA^*}|\hat{\mathcal{H}}|{}^1\Psi_{D^-A^+}\rangle &= h_{lj} + V_{klkj} + V_{kljk} + 2V_{ilij} - V_{ilji}
\end{aligned}
\tag{7.7}
$$

$$
\begin{aligned}
\langle {}^3\Psi_{DA^*}|\hat{\mathcal{H}}|{}^3\Psi_{D^*A}\rangle &= -V_{lijk} \\
\langle {}^3\Psi_{D^+A^-}|\hat{\mathcal{H}}|{}^3\Psi_{D^*A}\rangle &= h_{lj} + V_{ilij} - V_{ilji} - V_{kljk} + 2V_{klkj} \\
\langle {}^3\Psi_{DA^*}|\hat{\mathcal{H}}|{}^3\Psi_{D^+A^-}\rangle &= -h_{ik} - V_{iiik} - V_{ikkk} - V_{ilkl} \\
\langle {}^3\Psi_{D^-A^+}|\hat{\mathcal{H}}|{}^3\Psi_{D^*A}\rangle &= h_{ik} + V_{iiik} + V_{ikkk} + V_{jijk} \\
\langle {}^3\Psi_{DA^*}|\hat{\mathcal{H}}|{}^3\Psi_{D^-A^+}\rangle &= -h_{lj} - 2V_{ilij} + V_{ilji} + V_{kljk} - V_{klkj}
\end{aligned}
\tag{7.8}
$$

For SEET the direct ECME $\langle {}^1\Psi_{DA^*}|\hat{\mathcal{H}}|{}^1\Psi_{D^*A}\rangle$ is given by the Coulomb interaction between the dimer states. The exchange contribution to the coupling, which has to be reintroduced into the MTD method is present here due to the chosen CSFs including proper anti-symmetrization. For TEET the direct ECME $\langle {}^3\Psi_{DA^*}|\hat{\mathcal{H}}|{}^3\Psi_{D^*A}\rangle$ is given solely by the exchange interaction. The indirect couplings via CT contributions mediate the transfer of one electron between the donor and acceptor fragments. Utilizing the definition of the Fock matrix $\mathbf{F}$ (Eq. 2.52), the involved ionization processes can be simplified.

$$
\begin{aligned}
F_{lj} &= h_{lj} + 2V_{liji} + 2V_{lkjk} - V_{liij} - V_{lkkj} \\
F_{ik} &= h_{ik} + V_{iiki} + V_{ikkk}
\end{aligned}
\tag{7.9}
$$

Substituting the one electron integrals h_{lj} and h_{ik} by their Fock matrix counterparts yields the following expressions:

$$
\begin{aligned}
\langle {}^1\Psi_{D^+A^-}|\hat{\mathcal{H}}|{}^1\Psi_{D^*A}\rangle &= F_{lj} - V_{liji} + 2V_{ilji} \\
\langle {}^1\Psi_{DA^*}|\hat{\mathcal{H}}|{}^1\Psi_{D^+A^-}\rangle &= -F_{ik} - V_{ilkl} + 2V_{likl} \\
\langle {}^1\Psi_{D^-A^+}|\hat{\mathcal{H}}|{}^1\Psi_{D^*A}\rangle &= -F_{ik} - V_{ijkj} + 2V_{jikj} \\
\langle {}^1\Psi_{DA^*}|\hat{\mathcal{H}}|{}^1\Psi_{D^-A^+}\rangle &= F_{lj} - V_{lkjk} + 2V_{kljk}
\end{aligned}
\tag{7.10}
$$

$$
\begin{aligned}
\langle {}^3\Psi_{D^+A^-}|\hat{\mathcal{H}}|{}^3\Psi_{D^*A}\rangle &= F_{lj} - V_{liji} \\
\langle {}^3\Psi_{DA^*}|\hat{\mathcal{H}}|{}^3\Psi_{D^+A^-}\rangle &= -F_{ik} - V_{ilkl} \\
\langle {}^3\Psi_{D^-A^+}|\hat{\mathcal{H}}|{}^3\Psi_{D^*A}\rangle &= F_{ik} + V_{ijkj} \\
\langle {}^3\Psi_{DA^*}|\hat{\mathcal{H}}|{}^3\Psi_{D^-A^+}\rangle &= -F_{lj} + V_{lkjk}
\end{aligned}
\tag{7.11}
$$

Casting the equations into a HOMO-LUMO model, weighting the coupling by the wave function's HOMO-LUMO excitation and converting the two-electron integrals into chemist's notation yields the equations obtained by Fujimoto.[23] Additionally, the newly derived TEET expressions are obtained.

$$
\begin{aligned}
\langle {}^1\Psi_{D^+A^-}|\hat{\mathcal{H}}|{}^1\Psi_{D^*A}\rangle &= {}^1c^I_{H\to L}\Big(\langle\phi^I_L|\hat{F}|\phi^J_L\rangle - (\phi^I_L\phi^J_L|\phi^I_H\phi^I_H) + 2(\phi^I_L\phi^I_H|\phi^I_H\phi^J_L)\Big) \\
\langle {}^1\Psi_{DA^*}|\hat{\mathcal{H}}|{}^1\Psi_{D^+A^-}\rangle &= {}^1c^J_{H\to L}\Big(-\langle\phi^I_H|\hat{F}|\phi^J_H\rangle - (\phi^I_H\phi^J_H|\phi^J_L\phi^J_L) + 2(\phi^I_H\phi^J_L|\phi^J_L\phi^J_H)\Big) \\
\langle {}^1\Psi_{D^-A^+}|\hat{\mathcal{H}}|{}^1\Psi_{D^*A}\rangle &= {}^1c^I_{H\to L}\Big(-\langle\phi^I_H|\hat{F}|\phi^J_H\rangle - (\phi^I_H\phi^J_H|\phi^I_L\phi^I_L) + 2(\phi^I_H\phi^I_L|\phi^I_L\phi^J_H)\Big) \\
\langle {}^1\Psi_{DA^*}|\hat{\mathcal{H}}|{}^1\Psi_{D^-A^+}\rangle &= {}^1c^J_{H\to L}\Big(\langle\phi^I_L|\hat{F}|\phi^J_L\rangle - (\phi^I_L\phi^J_L|\phi^J_H\phi^J_H) + 2(\phi^I_L\phi^J_H|\phi^J_H\phi^J_L)\Big)
\end{aligned}
\tag{7.12}
$$

$$
\begin{aligned}
\langle {}^3\Psi_{D^+A^-}|\hat{\mathcal{H}}|{}^3\Psi_{D^*A}\rangle &= {}^3c^I_{H\to L}\Big(\langle\phi^I_L|\hat{F}|\phi^J_L\rangle - (\phi^I_L\phi^J_L|\phi^I_H\phi^I_H)\Big) \\
\langle {}^3\Psi_{DA^*}|\hat{\mathcal{H}}|{}^3\Psi_{D^+A^-}\rangle &= {}^3c^J_{H\to L}\Big(-\langle\phi^I_H|\hat{F}|\phi^J_H\rangle - (\phi^I_H\phi^J_H|\phi^J_L\phi^J_L)\Big) \\
\langle {}^3\Psi_{D^-A^+}|\hat{\mathcal{H}}|{}^3\Psi_{D^*A}\rangle &= {}^3c^I_{H\to L}\Big(\langle\phi^I_H|\hat{F}|\phi^J_H\rangle + (\phi^I_H\phi^J_H|\phi^I_L\phi^I_L)\Big) \\
\langle {}^3\Psi_{DA^*}|\hat{\mathcal{H}}|{}^3\Psi_{D^-A^+}\rangle &= {}^3c^J_{H\to L}\Big(-\langle\phi^I_L|\hat{F}|\phi^J_L\rangle + (\phi^I_L\phi^J_L|\phi^J_H\phi^J_H)\Big)
\end{aligned}
\tag{7.13}
$$

Evaluating equation 7.5 requires next to the Hamiltonian matrix elements the proper energy scaling involving the energies of the dimer states. The energies of the locally excited states Ψ_{D^*A} and Ψ_{DA^*} can be obtained following Fujimoto by embedding each fragment in the other fragments potential:

$$
\begin{aligned}
E_{D^*A} &= \langle\Psi_{D^*A}|\hat{\mathcal{H}} - E_0|\Psi_{D^*A}\rangle \\
&= E^{D^*}_{ex} + \sum_{ij\in A}(D^{A^*\to A} - D^A)_{ij} \times \left(V^{nuc,A}_{ij} + \sum_{kl\in D} D^{D^*\to D}\left[(ij|kl) - \frac{1}{2}(il|kj)\right]\right)
\end{aligned}
\tag{7.14}
$$

$$
\begin{aligned}
E_{DA^*} &= \langle\Psi_{DA^*}|\hat{\mathcal{H}} - E_0|\Psi_{DA^*}\rangle \\
&= E^{A^*}_{ex} + \sum_{ij\in D}(D^{D^*\to D} - D^D)_{ij} \times \left(V^{nuc,D}_{ij} + \sum_{kl\in A} D^{A^*\to A}\left[(ij|kl) - \frac{1}{2}(il|kj)\right]\right)
\end{aligned}
\tag{7.15}
$$

Here $E^{D^*}_{ex}$ and $E^{A^*}_{ex}$ are the monomer excitation energies while V^{nuc} are the nuclear attraction integrals of the respective fragment. The V^{nuc} are evaluated using an adapted ONEINT program, which is typically used to precalculate one-electron integrals for MRCI calculations.

The energies of the singlet and triplet CT states ${}^{1,3}E_{D^+A^-}$ and ${}^{1,3}E_{D^-A^+}$ can be expressed as:

$$\begin{aligned}
\langle {}^1\Psi_{D^+A^-}|\hat{\mathcal{H}} - E_0|{}^1\Psi_{D^+A^-}\rangle &= -h_{ii} + h_{ll} - 2V_{ikik} + V_{ilil} + V_{ikki} + V_{illi} + 2V_{klkl} - V_{kllk} - V_{iiii} \\
\langle {}^3\Psi_{D^+A^-}|\hat{\mathcal{H}} - E_0|{}^3\Psi_{D^+A^-}\rangle &= -h_{ii} + h_{ll} - 2V_{ikik} + V_{ilil} + V_{ikki} - V_{illi} + 2V_{klkl} - V_{kllk} - V_{iiii} \\
\langle {}^1\Psi_{D^-A^+}|\hat{\mathcal{H}} - E_0|{}^1\Psi_{D^-A^+}\rangle &= h_{jj} - h_{kk} + 2V_{ijij} - 2V_{ikik} - V_{ijji} + V_{ikki} + V_{jkjk} + V_{jkkj} - V_{kkkk} \\
\langle {}^3\Psi_{D^-A^+}|\hat{\mathcal{H}} - E_0|{}^3\Psi_{D^-A^+}\rangle &= h_{jj} - h_{kk} + 2V_{ijij} - 2V_{ikik} - V_{ijji} + V_{ikki} + V_{jkjk} - V_{jkkj} - V_{kkkk}
\end{aligned} \tag{7.16}$$

Utilizing the Fock matrix elements, the expressions can be converted to integral corrected orbital energies:

$$\begin{aligned}
F_{ii} &= h_{ii} + V_{iiii} + 2V_{ikik} - V_{ikki} \\
F_{jj} &= h_{jj} + 2V_{jiji} - V_{jiij} + 2V_{jkjk} - V_{jkkj} \\
F_{kk} &= h_{kk} + 2V_{kiki} - V_{kiik} + V_{kkkk} \\
F_{ll} &= h_{ll} + 2V_{lili} - V_{liil} + 2V_{lklk} - V_{lkkl}
\end{aligned} \tag{7.17}$$

$$\begin{aligned}
{}^1E_{D^+A^-} &= \langle {}^1\Psi_{D^+A^-}|\hat{\mathcal{H}} - E_0|{}^1\Psi_{D^+A^-}\rangle = -F_{ii} + F_{ll} - V_{lili} + 2V_{liil} \\
{}^3E_{D^+A^-} &= \langle {}^3\Psi_{D^+A^-}|\hat{\mathcal{H}} - E_0|{}^3\Psi_{D^+A^-}\rangle = -F_{ii} + F_{ll} - V_{lili} \\
{}^1E_{D^-A^+} &= \langle {}^1\Psi_{D^-A^+}|\hat{\mathcal{H}} - E_0|{}^1\Psi_{D^-A^+}\rangle = F_{jj} - F_{kk} - V_{jkjk} + 2V_{jkkj} \\
{}^3E_{D^-A^+} &= \langle {}^3\Psi_{D^-A^+}|\hat{\mathcal{H}} - E_0|{}^3\Psi_{D^-A^+}\rangle = F_{jj} - F_{kk} - V_{jkjk}
\end{aligned} \tag{7.18}$$

The extension of the MTD approach by the transfer integral (TI) approximation allows to recover the short-range ET contribution to EET (Sec. 7.3), while its major downside is the limitation to a HOMO-LUMO model.

7.1.3 Diabatization Modes

The program was extended by the Boys/BoysOV and ER diabatization schemes. Both schemes obtain the ECME by a unitary rotation of the diagonal Hamiltonian matrix while they utilize different physical properties. The general procedure following Pipek[78] and Edmiston–Ruedenberg[81] requires to minimize a cost function by consecutive two-by-two rotations of the involved electronic states. The two-by-two rotations can be obtained by so-called Jacobi sweeps:

1. Calculate the gain G, where the matrices A and B depend on the diabatization property:

$$G_{ij} = A_{ij} + \sqrt{A_{ij}^2 + B_{ij}^2} \tag{7.19}$$

   If the largest gain is below a given threshold the Jacobi sweeps are accepted as converged and the procedure is stopped.

2. Otherwise, obtain the pair of states (i, j) which has the largest gain:

$$G_{max,ij} = max(G) \tag{7.20}$$

3. Calculate $sin(4\alpha)$ and $cos(4\alpha)$ for the states (i, j):

$$\begin{aligned}
sin(4\alpha) &= \frac{B_{ij}}{\sqrt{(A_{ij}^2 + B_{ij}^2)}} \\
cos(4\alpha) &= \frac{-A_{ij}}{\sqrt{(A_{ij}^2 + B_{ij}^2)}}
\end{aligned} \tag{7.21}$$

4. Obtain the rotation angle for the unitary rotation by solving:

$$x_{1,2}^2 = \frac{1}{2}\left(1 \pm \sqrt{[1 - \frac{1}{2}(1 - cos(4a))]}\right) \tag{7.22}$$

Where two sets of angles (x_1, y_1) and (x_2, y_2) are obtained for:

$$x = \sqrt{x^2}, \qquad y = \sqrt{[1 - x^2]} \tag{7.23}$$

The correct pair of angles for the unitary rotation has to satisfy:

$$4x_i y_i (x_i^2 - y_i^2) = sin(4\alpha) \tag{7.24}$$

5. Update the unitary transformation matrix U by applying the rotation:

$$U' = \begin{pmatrix} x_i & y_i \\ -y_i & x_i \end{pmatrix} U \tag{7.25}$$

6. Update the diabatization scheme specific matrices A and B by applying the new unitary transformation and repeat from the top.

After convergence of the procedure the ECME can be obtained as the off-diagonal Hamiltonian matrix element applying the final unitary rotation to the adiabatic Hamiltonian.

$$H_{diab} = U^\dagger H_{adia} U \tag{7.26}$$

- **BoysETDiabatization and BoysEETDiabatization Modes**: The Boys diabatization modes employ the (transition) dipole moments between the adiabatic states to obtain the proper unitary transformation of the Hamiltonian matrix. For this purpose the matrices A and B are defined in terms of the electric dipole operator $\hat{\mu}_{el}$:

$$\begin{aligned} A_{ij} &= \langle i|\hat{\mu}_{el}|j\rangle^2 - \frac{1}{4}\left[\langle i|\hat{\mu}_{el}|i\rangle - \langle j|\hat{\mu}_{el}|j\rangle\right]^2 \\ B_{ij} &= \langle i|\hat{\mu}_{el}|j\rangle\left[\langle i|\hat{\mu}_{el}|i\rangle - \langle j|\hat{\mu}_{el}|j\rangle\right] \end{aligned} \tag{7.27}$$

In the case of the BoysEETDiabatization mode, the BoysOV scheme is utilized, which treats the occ-occ and virt-virt blocks of the (transition) dipole moment matrix differently.

$$\begin{aligned} A_{ij} &= \sum_{k \in occ,virt}\left(\langle i|\hat{\mu}_{el}|j\rangle^2 - \frac{1}{4}\left[\langle i|\hat{\mu}_{el}|i\rangle - \langle j|\hat{\mu}_{el}|j\rangle\right]^2\right)_k \\ B_{ij} &= \sum_{k \in occ,virt}\left(\langle i|\hat{\mu}_{el}|j\rangle\left[\langle i|\hat{\mu}_{el}|i\rangle - \langle j|\hat{\mu}_{el}|j\rangle\right]\right)_k \end{aligned} \tag{7.28}$$

- **ERDiabatization Mode**: The ERDiabatization Mode performs the ER diabatization utilizing the two-electron integrals to maximize the self interaction. The matrices A and B are defined as follows:

$$\begin{aligned} A_{ij} &= \langle ij|\hat{r}_{12}^{-1}|ij\rangle - \frac{1}{4}\left(\langle ii|\hat{r}_{12}^{-1}|ii\rangle + \langle jj|\hat{r}_{12}^{-1}|jj\rangle - 2\langle ii|\hat{r}_{12}^{-1}|jj\rangle\right) \\ B_{ij} &= \langle ii|\hat{r}_{12}^{-1}|ij\rangle - \langle jj|\hat{r}_{12}^{-1}|ij\rangle \end{aligned} \tag{7.29}$$

Both expressions involve the contraction of the two-electron integrals with the reduced one-electron (transition) density matrices of the involved states rendering the approach rather costly.

The Jacobi sweeps are implemented as a general scheme to allow the addition of further diabatization approaches by extension of the **SweepableFunction** interface. The **SweepableFunction** defines methods to obtain the gains and the matrix elements of A and B to abstract the diabatization approaches. The Jacobi sweep algorithm can then be used to perform the sweeps on the **SweepableFunction** and return the optimized unitary transformation.

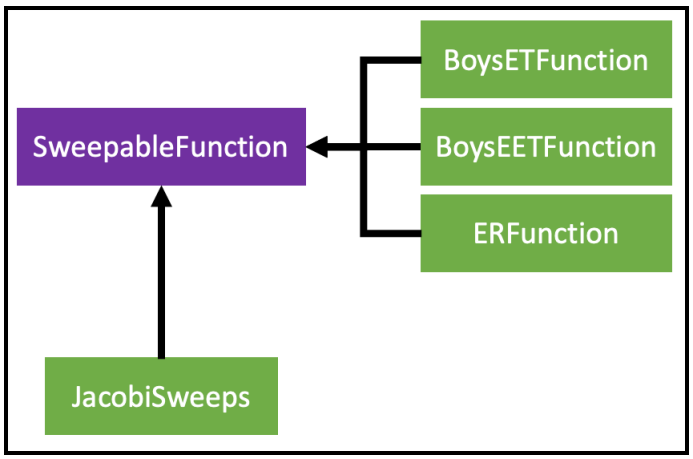

Figure 7.8: SweepableFunction interface.

The different diabatization modes prepare the required data, like the adiabatic Hamiltonian matrix and the transition dipole operator matrix or the two-electron integrals and construct a **SweepableFunction**. The **SweepableFunction** is then handed to the Jacobi Sweep implementation and processed until convergence.

7.1.4 SpectralOverlap Mode

The SpectralOverlap mode allows to evaluate the spectral overlap integral employing the donor's emission and acceptor's absorption spectra. Since the absorption and emission spectra are obtained in different calculations, the grid of both spectra may not be aligned. Therefore, a polynomial spline is fitted to the spectra to align the grids as well as ease the construction of the product spectrum and its integration. The polynomial splines are constructed in an adaptive manner, adding more spline segments in regions, that require additional flexibility to obtain an accurate fit. The normalized root-mean-square deviation (NRMSD) between the polynomial spline and the original data and a maximum number of iterations is utilized to define convergence criteria. In the construction of the polynomial spline, a segment is defined as:[153]

$$S_i(x) = a_i + b_i(x - x_i) + c_i(x - x_i)^2 + d_i(x - x_i)^3 \tag{7.30}$$

In a first step a system of linear equations is solved defining the boundary conditions of each spline segment to obtain a contiguous function. The equation for the first interval is given by:

$$2(d_0 + d_1)c_1 + d_1c_2 = 3\frac{y_2 - y_1}{d_1} - 3\frac{y_1 - y_0}{d_0} - d_0c_0 \tag{7.31}$$

For the intervals $i = 2, ..., n-2$ and $n \geq 4$:

$$d_{i-1}c_{i-1} + 2(d_{i-1} + d_i)c_i + d_i c_{i+1} = 3\frac{y_{i+1} - y_i}{d_i} - 3\frac{y_i - y_{i-1}}{d_{i-1}} \tag{7.32}$$

And the last interval equation is:

$$d_{n-2}c_{n-2} + 2(d_{n-2} - d_{n-1})c_{n-1} = 3\frac{y_n - y_{n-1}}{d_{n-1}} - 3\frac{y_{n-1} - y_{n-2}}{d_{n-2}} - d_{n-1}c_n \tag{7.33}$$

Where c_i are the coefficients, $d_i = x_{i+1} - x_i$ the distance between the interval start and end x-coordinates, and y_i the y-coordinates of each fulcrum of the original function. The system of linear equations can be expressed in matrix form as:

$$A = \begin{pmatrix} 2(d_0 + d_1) & d_1 & & & & & \\ d_1 & 2(d_1 + d_2) & d_2 & & & & \\ & d_2 & 3(d_2 + d_3) & d_3 & & & \\ & \ddots & \ddots & \ddots & & & \\ & & d_{n-3} & 2(d_{n-3} + d_{n-2}) & d_{n-2} & & \\ & & & d_{n-2} & 2(d_{n-2} + d_{n-1}) & d_{n-1} \end{pmatrix} \tag{7.34}$$

With the solution vector a:

$$a = \begin{pmatrix} 3\frac{y_2 - y_1}{d_1} - 3\frac{y_1 - y_0}{d_0} - d_0 c_0 \\ 3\frac{y_3 - y_2}{d_2} - 3\frac{y_2 - y_1}{d_1} \\ \vdots \\ 3\frac{y_n - y_{n-1}}{d_{n-1}} - 3\frac{y_{n-1} - y_{n-2}}{d_{n-2}} - d_{n-1}c_n \end{pmatrix} \tag{7.35}$$

Since the symmetric sparse matrix A is trigonal diagonal dominant, it is always invertible and therefore linear equation systems of such matrices are always solvable. A solution for the coefficient c is obtained easily by a Cholesky decomposition for trigonal matrices. The spline segment coefficients a_i, b_i, c_i and d_i are then calculated from the solutions c:

$$\begin{aligned} a_i &= y_i \\ b_i &= \frac{y_{i+1} - y_i}{d_i} - \frac{d_i}{3}(c_{i+1} + 2c_i) \\ c_i &= c_i \\ d_i &= \frac{1}{3d_i}(c_{i+1} - c_i) \end{aligned} \tag{7.36}$$

7.2 TEET Donor–Bridge–Acceptor Systems

To test the implementation of the MTD method involving overlap corrections as well as the diabatization schemes for TEET, a set of molecules was required where experimentally obtained TEET rate constants are known. In addition, these molecules should constrain the distance and orientation between the donor and acceptor moieties to circumvent complex sampling procedures. A suitable set of molecules was found in experiments of Closs *et al.*,[154] who measured long distance intramolecular TEET rate constants for a set of donor-acceptor

systems separated by a bridge (Fig. 7.9) where 4-benzophenoneyl was utilized as a donor and 2-naphthyl as acceptor. The bridge is given by cyclohexane or decalin rings denoted by **C** and **D** in the structure's identifier. These bridges create rigid systems with multiple stereo- and conformational isomers, where the donor's and acceptor's location is denoted by the first and second number and the axial and equatorial orientation with **a** and **e** respectively. Closs *et al.* measured the TEET rate constants in benzene using flash photolysis to excite the benzophenone chromophore and utilizing the $T_n \rightarrow T_1$ benzophenone decay or the increase of the naphthalene $T_n \leftarrow T_1$ absorption.

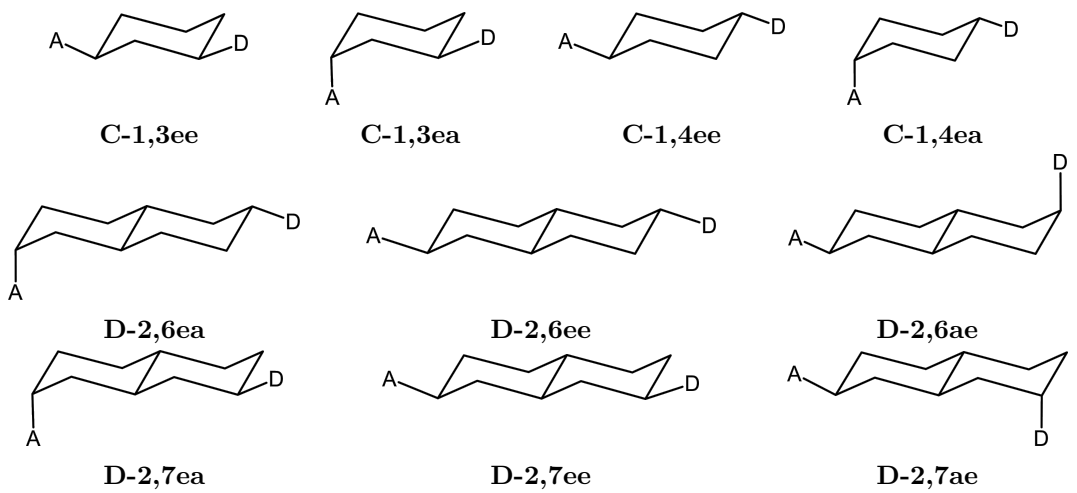

Figure 7.9: TEET donor–bridge–acceptor systems with naphthalene as the acceptor and benzaldehyde as the donor.

In 2010, Subotnik *et al.*[79] used the same set of molecules to test their implementations of the BoysOV and ER diabatization schemes to obtain ECMEs. Additionally, they estimated the spectral overlap integrals utilizing Marcus theory. Computationally, benzophenone was replaced by benzaldehyde to simplify the calculations and the CIS method was utilized in combination with the 6-31G** basis set to obtain the excited triplet states of the full system at the ground state geometry. To compare the MTD method and the implementation of the diabatization schemes a similar protocol was followed. Sadly, Subotnik *et al.* did not include the molecular geometries they based their CIS calculations on in their publication. This circumstance required to perform the geometry optimizations to obtain similar minima. Therefore, the geometry of the electronic ground state was optimized utilizing DFT employing the PBE0 density functional in combination with the 6-31G** atomic basis set (Tab A.16 - A.25). For the diabatization schemes, the excited triplet states of the full system are calculated employing the CIS branch of the DFT/MRCI program. The obtained CIS wave functions are then utilized to obtain the triplet-triplet transition density matrices between the coupling triplet states and are separated in case of the BoysOV scheme into their occupied-occupied and virtual-virtual blocks within the Densomat. The (transition) density matrices are then used to perform the Jacobi sweeps to obtain the rotated adiabatic Hamiltonian.
For the MTD calculations, the optimized ground state geometries of the full system are utilized to obtain the donor and acceptor structures by removing all atoms except the ones belonging to the naphthalene and benzaldehyde fragments. To complete the formerly bridged structures again, connections to the bridge are capped with hydrogen atoms and a geometry optimization was conducted fixing all centers from the original geometry except the newly

added hydrogens. Since the ECMEs reported by Subotnik *et al.* are of the order of a few meV, geometric differences between the calculations of Subotnik *et al.* and the ones presented here are expected to cause some deviance.

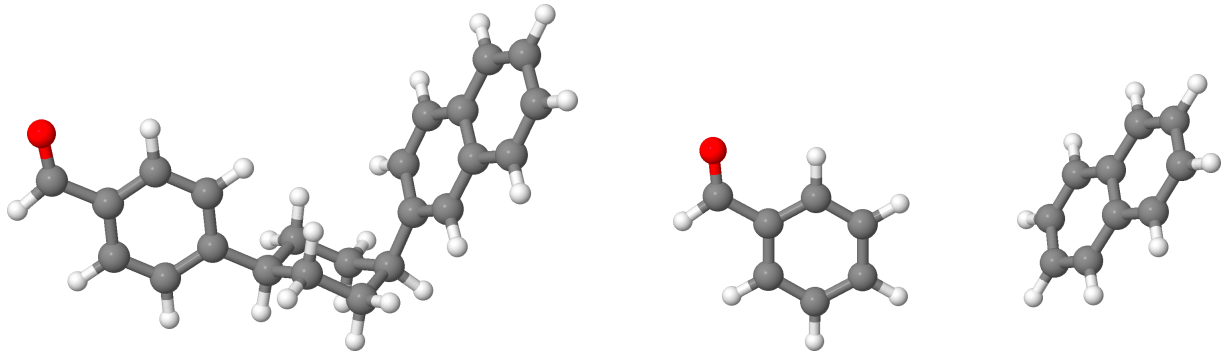

Figure 7.10: C-1,4ea geometry utilized in the quantum chemical calculations of the full system and dimer constructed from the fragmented donor-acceptor system.

The TEET process takes place between the lowest $\pi\pi^*$ localized triplet states of benzaldehyde and naphthalene, which are mainly composed of the following configurations:

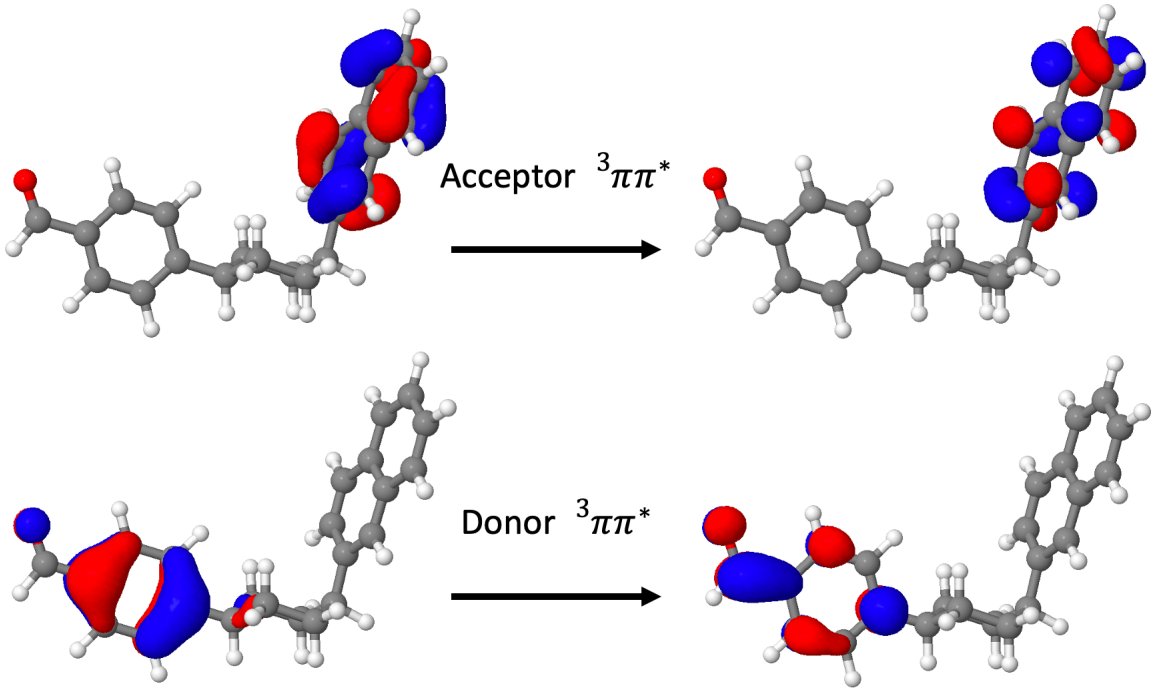

Figure 7.11: Leading configurations of the lowest excited triplet states in C-1,4ea.

Both excited states are in principle local excitations while small CT contributions are involved in the excited states moving charge between benzaldehyde and naphthalene.
Evaluating the ECME with the diabatization approaches shows a good agreement to couplings obtained by Subotnik *et al.* supporting the correctness of the implementations. The small deviations can be caused by small geometric differences to the structures obtained by Subotnik *et al.*. Even if the systems are mostly rigid the orientations of the chromophores can

differ depending on the optimized minimum. The strongest couplings are found for conformers where the chromophores are separated by the smallest distance and located in equatorial positions.

Table 7.1: TEET couplings [meV] of the donor–bridge–acceptor systems from Fig. 7.9

Molecule	BoysOV		ER		MTD	MTD-ORTHO
	Reference[79]	MRCI/CIS	Reference[79]	MRCI/CIS		
C-1,3ea	0.56	0.48	0.51	0.42	0.01	0.01
C-1,3ee	1.40	1.58	1.5	1.58	0.00	0.00
C-1,4ea	0.037	0.052	0.026	0.045	0.001	0.001
C-1,4ee	0.57	0.62	0.56	0.52	0.00	0.00
D-2,6ea	0.0019	0.0061	0.0022	0.0005	0.0000	0.0000
D-2,6ee	0.019	0.021	0.020	0.013	0.000	0.000
D-2,6ae	0.0011	0.0024	0.0010	0.0012	0.0000	0.0000
D-2,7ea	0.045	0.013	0.047	0.011	0.000	0.000
D-2,7ee	0.16	0.17	0.17	0.12	0.00	0.00
D-2,7ae	0.053	0.013	0.049	0.015	0.000	0.000

In contrast to the diabatization schemes, the MTD method predicts, even with enabled orthogonalization corrections, vanishing ECMEs. These findings lead to the suspicion, that important short-range contributions, namely CT contributions, were missing to obtain accurate results. To understand the origin of these contributions and extend the MTD approach, the ethylene dimer, a much simpler system, was investigated.

7.3 The Ethylene Dimer

The vanishing TEET couplings for the donor-bridge-acceptor systems suggested that short-range contributions are missing in the MTD description. To understand the origin of the contributions and incorporate them in an extended MTD approach, the ethylene dimer, was investigated. The ethylene dimer was already analyzed in previous works of Spiegel *et al.*[82] to show the correct long-range behavior of the MTD approach and the increased midrange accuracy compared to the IDA utilized in FRET for SEET. To visualize the range dependent behavior, the ECME of a π-stacked ethylene dimer was evaluated at CIS/SVP level of theory with inter-fragment distances ranging from 3 Å to 10 Å in 0.25 Å steps. The theoretically expected ECME is obtained from the Davydov splitting of the full system's quantum chemical calculations.

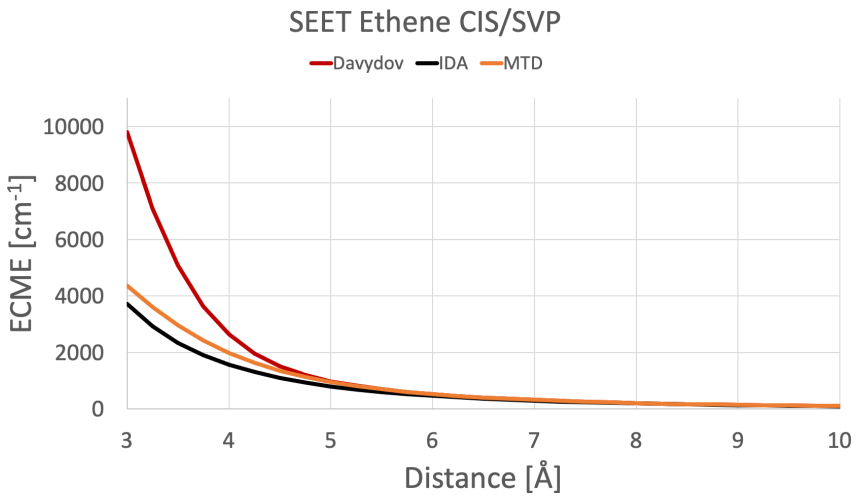

Figure 7.12: SEET excitonic coupling in the ethylene dimer utilizing the MTD approach (orange) and IDA approach (black) in comparison to the Davydov splitting of the dimer states (red) at the CIS/SVP level of theory.

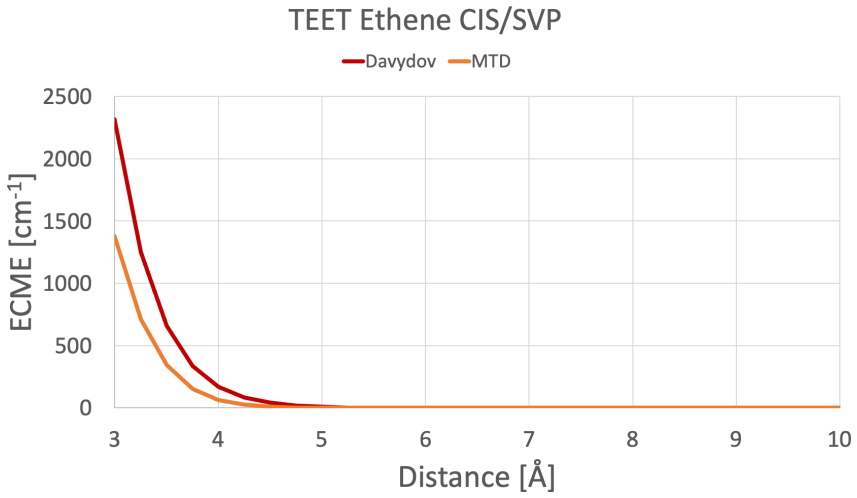

Figure 7.13: TEET excitonic coupling in the ethylene dimer utilizing the MTD approach (orange) in comparison to the Davydov splitting of the dimer states (red) at the CIS/SVP level of theory.

At long distances the MTD and IDA approaches recover the Davydov splitting showing, that for long-range SEET the typically applied FRET approach is valid. At mid-range inter-fragment distances (about 4 - 5 Å), a growing difference can be seen between the MTD and IDA approach, indicating that the IDA approximation at these distances underestimates the coupling stronger than the MTD approach does. Compared to the Davydov splitting, the MTD and IDA approaches underestimate the excitonic coupling from the mid-range to the short-range regime. A similar situation is visible for TEET, where the excitonic coupling in the MTD method is solely given by the exchange interaction. Starting at 4.5 Å, the Davydov splitting is non-vanishing while the exchange contribution is still negligible. This case was encountered for the donor-bridge-acceptor systems, where a small ECME is present, but the exchange interaction does not recover the full coupling.

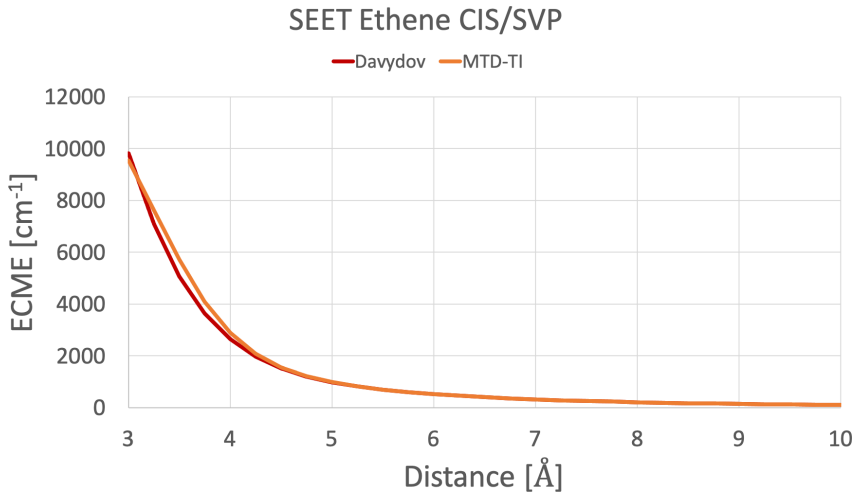

Figure 7.14: SEET excitonic coupling in the ethylene dimer utilizing the monomer transition density combined with transfer integral (MTD-TI) approach (orange) in comparison to the Davydov splitting of the dimer states (red) at the CIS/SVP level of theory.

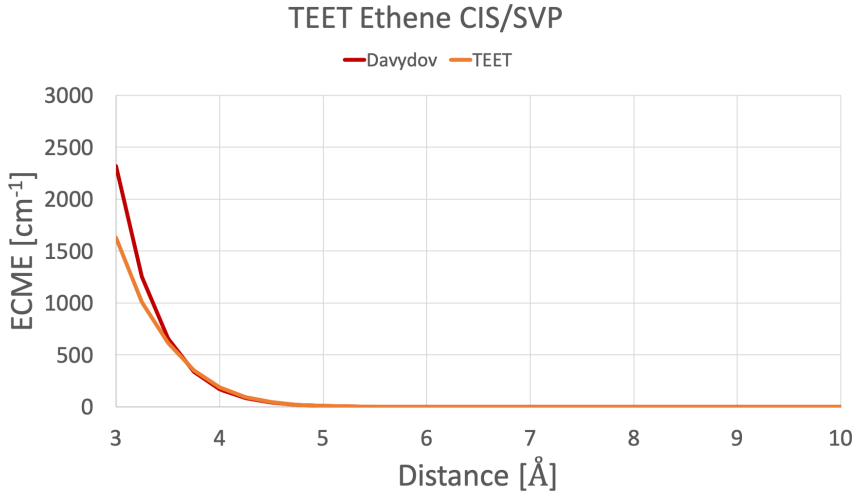

Figure 7.15: TEET excitonic coupling in the ethylene dimer utilizing the MTD-TI approach (orange) in comparison to the Davydov splitting of the dimer states (red) at the CIS/SVP level of theory.

Utilizing the extended MTD-TI approach instead, the SEET and TEET Davydov splitting is

almost fully recovered where small differences between the Davydov splitting and the MTD-TI couplings are expected to originate from the energy scaling of the short-range CT contributions which is to steep around 4 Å and to flat at 3.5 Å. Additional deviations below a distance of 3.5 Å can be caused by the neglect of the $\langle\psi_{DA^*}|\hat{\mathcal{H}}|\psi_{D^+A^-}\rangle\langle\psi_{D^+A^-}|\hat{\mathcal{H}}|\psi_{D^-A^+}\rangle\langle\psi_{D^-A^+}|\hat{\mathcal{H}}|\psi_{D^*A}\rangle$ and $\langle\psi_{DA^*}|\hat{\mathcal{H}}|\psi_{D^-A^+}\rangle\langle\psi_{D^-A^+}|\hat{\mathcal{H}}|\psi_{D^+A^-}\rangle\langle\psi_{D^+A^-}|\hat{\mathcal{H}}|\psi_{D^*A}\rangle$ couplings.

7.4 Generalization of the MTD-TI Approach

The MTD-TI method allows to obtain short-range CT contributions to EET while its major downside is the limitation to HOMO-LUMO excitations. Generalizing the MTD-TI approach beyond the HOMO-LUMO restriction requires to evaluate the Hamiltonian matrix elements and the excitation energies of the CT states. Fujimoto weighted the Hamiltonian matrix elements with the wave function's HOMO-LUMO coefficient to scale the interaction appropriately assuming all population is transferred to the corresponding CT configuration. Employing more than one excited state requires to evaluate the Hamiltonian matrix elements for all reasonable CT states utilizing the respective reduced one- and two-electron (transition) density matrices.

$$\begin{aligned} V_{CT} = \sum_m \Bigg(&- \frac{\langle\Psi_{DA^*}|\hat{\mathcal{H}}|\Psi_{D^+A^-,m}\rangle\langle\Psi_{D^+A^-,m}|\hat{\mathcal{H}}|\Psi_{D^*A}\rangle}{E_{D^+A^-,k} - E_{D^*A}} \\ &- \frac{\langle\Psi_{DA^*}|\hat{\mathcal{H}}|\Psi_{D^-A^+,m}\rangle\langle\Psi_{D^-A^+,m}|\hat{\mathcal{H}}|\Psi_{D^*A}\rangle}{E_{D^-A^+,k} - E_{D^*A}} \Bigg) \end{aligned} \tag{7.37}$$

The dimer wave functions $\Psi_{D^+A^-,m}$ and $\Psi_{D^-A^+,m}$ can be constructed in a product approach utilizing all combinations of the charged monomer states $\psi_{D_m^+}$, $\psi_{D_m^-}$,$\psi_{A_m^+}$ and $\psi_{A_m^-}$ obtained by adding or removing one electron from the uncharged fragment. Herein, the molecular orbital basis of the uncharged fragment can be retained allowing the evaluation of density matrices without complex orbital transformations.

In principle, the Hamiltonian matrix elements can be solved directly utilizing their respective reduced one- and two-electron density matrices. The latter scales with $(N_{DONOR} + N_{ACCEPTOR})^4$ where N are the fragment's number of molecular orbitals rendering this approach only applicable to small systems. Investigating the expressions of the reduced one- and two-electron (transition) density matrices further allows for simplifications. The reduced one-electron (transition) density matrices can be reformulated in terms of Dyson orbitals $\langle\psi|\hat{a}^\dagger|\psi^+\rangle$ and $\langle\psi|\hat{a}|\psi^-\rangle$.

$$\begin{aligned} \langle\Psi_{DA^*}|\hat{E}_i^j|\Psi_{D^+A^-,m}\rangle &= \langle\psi_D\psi_{A^*}|\hat{E}_i^j|\psi_{D_m^+}\psi_{A_m^-}\rangle \\ &= \langle\psi_D\psi_{A^*}|\hat{a}_i^\dagger\hat{a}_j|\psi_{D_m^+}\psi_{A_m^-}\rangle \\ &= \langle\psi_D|\hat{a}_i^\dagger|\psi_{D_m^+}\rangle\langle\psi_{A^*}|\hat{a}_j|\psi_{A_m^-}\rangle \end{aligned} \tag{7.38}$$

$$\begin{aligned} \langle\Psi_{D^+A^-,m}|\hat{E}_i^j|\Psi_{D^*A}\rangle &= \langle\psi_{D_m^+}\psi_{A_m^-}|\hat{E}_i^j|\psi_{D^*}\psi_A\rangle \\ &= \langle\psi_{D_m^+}\psi_{A_m^-}|\hat{a}_i^\dagger\hat{a}_j|\psi_{D^*}\psi_A\rangle \\ &= \langle\psi_{D_m^+}|\hat{a}_j|\psi_{D^*}\rangle\langle\psi_{A_m^-}|\hat{a}_i^\dagger|\psi_A\rangle \end{aligned} \tag{7.39}$$

$$\begin{aligned}\langle\Psi_{DA^*}|\hat{E}_i^j|\Psi_{D^-A^+,m}\rangle &= \langle\psi_D\psi_{A^*}|\hat{E}_i^j|\psi_{D_m^-}\psi_{A_m^+}\rangle \\ &= \langle\psi_D\psi_{A^*}|\hat{a}_i^\dagger\hat{a}_j|\psi_{D_m^-}\psi_{A_m^+}\rangle \\ &= \langle\psi_D|\hat{a}_j|\psi_{D_m^-}\rangle\langle\psi_{A^*}|\hat{a}_i^\dagger|\psi_{A_m^+}\rangle\end{aligned} \tag{7.40}$$

$$\begin{aligned}\langle\Psi_{D^-A^+,m}|\hat{E}_i^j|\Psi_{D^*A}\rangle &= \langle\psi_{D_m^-}\psi_{A_m^+}|\hat{E}_i^j|\psi_{D^*}\psi_A\rangle \\ &= \langle\psi_{D_m^-}\psi_{A_m^+}|\hat{a}_i^\dagger\hat{a}_j|\psi_{D^*}\psi_A\rangle \\ &= \langle\psi_{D_m^-}|\hat{a}_i^\dagger|\psi_{D^*}\rangle\langle\psi_{A_m^+}|\hat{a}_j|\psi_A\rangle\end{aligned} \tag{7.41}$$

In this case the excitation operator $\hat{E}$ mediates always between the neutral and cationic as well as the neutral and anionic configurations allowing to apply the creator and annihilator to the separate fragments. This separation allows to split the reduced one-electron (transition) density matrix into a product of Dyson orbitals.
A similar separation can be applied to the reduced two-electron (transition) density matrices:

$$\begin{aligned}\langle\Psi_{DA^*}|\hat{E}_i^j\hat{E}_k^l|\Psi_{D^+A^-,m}\rangle = &\sum_{i\in D}\sum_{j,k,l\in A}\langle\psi_D|\hat{a}_i^\dagger|\psi_{D_m^+}\rangle\langle\psi_{A^*}|\hat{a}_j\hat{a}_k^\dagger\hat{a}_l|\psi_{A_m^-}\rangle \\ &+\sum_{k\in D}\sum_{i,j,l\in A}\langle\psi_D|\hat{a}_k^\dagger|\psi_{D_m^+}\rangle\langle\psi_{A^*}|\hat{a}_i^\dagger\hat{a}_j\hat{a}_l|\psi_{A_m^-}\rangle \\ &+\sum_{i,j,k\in D}\sum_{l\in A}\langle\psi_D|\hat{a}_i^\dagger\hat{a}_j\hat{a}_k^\dagger|\psi_{D_m^+}\rangle\langle\psi_{A^*}|\hat{a}_l|\psi_{A_m^-}\rangle \\ &+\sum_{i,k,l\in D}\sum_{j\in A}\langle\psi_D|\hat{a}_i^\dagger\hat{a}_k^\dagger\hat{a}_l|\psi_{D_m^+}\rangle\langle\psi_{A^*}|\hat{a}_j|\psi_{A_m^-}\rangle\end{aligned} \tag{7.42}$$

$$\begin{aligned}\langle\Psi_{D^+A^-,m}|\hat{E}_i^j\hat{E}_k^l|\Psi_{D^*A}\rangle = &\sum_{j\in D}\sum_{i,k,l\in A}\langle\psi_{D_m^+}|\hat{a}_j|\psi_{D^*}\rangle\langle\psi_{A_m^-}|\hat{a}_i^\dagger\hat{a}_k^\dagger\hat{a}_l|\psi_A\rangle \\ &+\sum_{l\in D}\sum_{i,j,k\in A}\langle\psi_{D_m^+}|\hat{a}_l|\psi_{D^*}\rangle\langle\psi_{A_m^-}|\hat{a}_i^\dagger\hat{a}_j\hat{a}_k^\dagger|\psi_A\rangle \\ &+\sum_{i,j,l\in D}\sum_{k\in A}\langle\psi_{D_m^+}|\hat{a}_i^\dagger\hat{a}_j\hat{a}_l|\psi_{D^*}\rangle\langle\psi_{A_m^-}|\hat{a}_k^\dagger|\psi_A\rangle \\ &+\sum_{j,k,l\in D}\sum_{i\in A}\langle\psi_{D_m^+}|\hat{a}_j\hat{a}_k^\dagger\hat{a}_l|\psi_{D^*}\rangle\langle\psi_{A_m^-}|\hat{a}_i^\dagger|\psi_A\rangle\end{aligned} \tag{7.43}$$

$$\begin{aligned}\langle\Psi_{DA^*}|\hat{E}_i^j\hat{E}_k^l|\Psi_{D^-A^+,m}\rangle = &\sum_{j\in D}\sum_{i,k,l\in A}\langle\psi_D|\hat{a}_j|\psi_{D_m^-}\rangle\langle\psi_{A^*}|\hat{a}_i^\dagger\hat{a}_k^\dagger\hat{a}_l|\psi_{A_m^+}\rangle \\ &+\sum_{l\in D}\sum_{i,j,k\in A}\langle\psi_D|\hat{a}_l|\psi_{D_m^-}\rangle\langle\psi_{A^*}|\hat{a}_i^\dagger\hat{a}_j\hat{a}_k^\dagger|\psi_{A_m^+}\rangle \\ &+\sum_{i,j,l\in D}\sum_{k\in A}\langle\psi_D|\hat{a}_i^\dagger\hat{a}_j\hat{a}_l|\psi_{D_m^-}\rangle\langle\psi_{A^*}|\hat{a}_k^\dagger|\psi_{A_m^+}\rangle \\ &+\sum_{j,k,l\in D}\sum_{j\in A}\langle\psi_D|\hat{a}_j\hat{a}_k^\dagger\hat{a}_l|\psi_{D_m^-}\rangle\langle\psi_{A^*}|\hat{a}_i^\dagger|\psi_{A_m^+}\rangle\end{aligned} \tag{7.44}$$

$$
\begin{aligned}
\langle \Psi_{D^- A^+,m} | \hat{E}_i^j \hat{E}_k^l | \Psi_{D^* A} \rangle = & \sum_{i \in D} \sum_{j,k,l \in A} \langle \psi_{D_m^-} | \hat{a}_i^\dagger | \psi_{D^*} \rangle \langle \psi_{A_m^+} | \hat{a}_j \hat{a}_k^\dagger \hat{a}_l | \psi_A \rangle \\
& + \sum_{k \in D} \sum_{i,j,l \in A} \langle \psi_{D_m^-} | \hat{a}_k^\dagger | \psi_{D^*} \rangle \langle \psi_{A_m^+} | \hat{a}_i^\dagger \hat{a}_j \hat{a}_l | \psi_A \rangle \\
& + \sum_{i,j,k \in D} \sum_{l \in A} \langle \psi_{D_m^-} | \hat{a}_i^\dagger \hat{a}_j \hat{a}_k^\dagger | \psi_{D^*} \rangle \langle \psi_{A_m^+} | \hat{a}_l | \psi_A \rangle \\
& + \sum_{i,k,l \in D} \sum_{j \in A} \langle \psi_{D_m^-} | \hat{a}_i^\dagger \hat{a}_k^\dagger \hat{a}_l | \psi_{D^*} \rangle \langle \psi_{A_m^+} | \hat{a}_j | \psi_A \rangle
\end{aligned}
\tag{7.45}
$$

Here each expression can be split into four terms, where an additional single excitation can change the configuration prior or post to the ionization on each fragment. The expressions can be simplified even more utilizing the RI approximation, employing the basis of the uncharged ($\sum_n |\psi\rangle\langle\psi|$) and charged ($\sum_n |\psi^\pm\rangle\langle\psi^\pm|$) excited states.

$$
\begin{aligned}
\langle \Psi_{DA^*} | \hat{E}_i^j \hat{E}_k^l | \Psi_{D^+ A^-,m} \rangle = & \sum_{i \in D} \sum_{j,k,l \in A} \langle \psi_D | \hat{a}_i^\dagger | \psi_{D_m^+} \rangle \sum_n \left(\langle \psi_{A^*} | \hat{a}_j | \psi_{A_n^-} \rangle \langle \psi_{A_n^-} | \hat{E}_k^l | \psi_{A_m^-} \rangle \right) \\
& + \sum_{k \in D} \sum_{i,j,l \in A} \langle \psi_D | \hat{a}_k^\dagger | \psi_{D_m^+} \rangle \sum_n \left(\langle \psi_{A^*} | \hat{E}_i^j | \psi_{A_n^*} \rangle \langle \psi_{A_n^*} | \hat{a}_l | \psi_{A_m^-} \rangle \right) \\
& + \sum_{i,j,k \in D} \sum_{l \in A} \sum_n \left(\langle \psi_D | \hat{E}_i^j | \psi_{D_n^*} \rangle \langle \psi_{D_n^*} | \hat{a}_k^\dagger | \psi_{D_m^+} \rangle \right) \langle \psi_{A^*} | \hat{a}_l | \psi_{A_m^-} \rangle \\
& + \sum_{i,k,l \in D} \sum_{j \in A} \sum_n \left(\langle \psi_D | \hat{a}_i^\dagger | \psi_{D_n^+} \rangle \langle \psi_{D_n^+} | \hat{E}_k^l | \psi_{D_m^+} \rangle \right) \langle \psi_{A^*} | \hat{a}_j | \psi_{A_m^-} \rangle
\end{aligned}
\tag{7.46}
$$

$$
\begin{aligned}
\langle \Psi_{D^+ A^-,m} | \hat{E}_i^j \hat{E}_k^l | \Psi_{D^* A} \rangle = & \sum_{j \in D} \sum_{i,k,l \in A} \langle \psi_{D_m^+} | \hat{a}_j | \psi_{D^*} \rangle \sum_n \left(\langle \psi_{A_m^-} | \hat{a}_i^\dagger | \psi_{A_n^*} \rangle \langle \psi_{A_n^*} | \hat{E}_k^l | \psi_A \rangle \right) \\
& + \sum_{l \in D} \sum_{i,j,k \in A} \langle \psi_{D_m^+} | \hat{a}_l | \psi_{D^*} \rangle \sum_n \left(\langle \psi_{A_m^-} | \hat{E}_i^j | \psi_{A_n^-} \rangle \langle \psi_{A_n^-} | \hat{a}_k^\dagger | \psi_A \rangle \right) \\
& + \sum_{i,j,l \in D} \sum_{k \in A} \sum_n \left(\langle \psi_{D_m^+} | \hat{E}_i^j | \psi_{D_n^+} \rangle \langle \psi_{D_n^+} | \hat{a}_l | \psi_{D^*} \rangle \right) \langle \psi_{A_m^-} | \hat{a}_k^\dagger | \psi_A \rangle \\
& + \sum_{j,k,l \in D} \sum_{i \in A} \sum_n \left(\langle \psi_{D_m^+} | \hat{a}_j | \psi_{D_n^*} \rangle \langle \psi_{D_n^*} | \hat{E}_k^l | \psi_{D^*} \rangle \right) \langle \psi_{A_m^-} | \hat{a}_i^\dagger | \psi_A \rangle
\end{aligned}
\tag{7.47}
$$

$$
\begin{aligned}
\langle \Psi_{DA^*} | \hat{E}_i^j \hat{E}_k^l | \Psi_{D^- A^+,m} \rangle = & \sum_{j \in D} \sum_{i,k,l \in A} \langle \psi_D | \hat{a}_j | \psi_{D_m^-} \rangle \sum_n \left(\langle \psi_{A^*} | \hat{a}_i^\dagger | \psi_{A_n^+} \rangle \langle \psi_{A_n^+} | \hat{E}_k^l | \psi_{A_m^+} \rangle \right) \\
& + \sum_{l \in D} \sum_{i,j,k \in A} \langle \psi_D | \hat{a}_l | \psi_{D_m^-} \rangle \sum_n \left(\langle \psi_{A^*} | \hat{E}_i^j | \psi_{A_n^*} \rangle \langle \psi_{A_n^*} | \hat{a}_k^\dagger | \psi_{A_m^+} \rangle \right) \\
& + \sum_{i,j,l \in D} \sum_{k \in A} \sum_n \left(\langle \psi_D | \hat{E}_i^j | \psi_{D_n^*} \rangle \langle \psi_{D_n^*} | \hat{a}_l | \psi_{D_m^-} \rangle \right) \langle \psi_{A^*} | \hat{a}_k^\dagger | \psi_{A_m^+} \rangle \\
& + \sum_{j,k,l \in D} \sum_{j \in A} \sum_n \left(\langle \psi_D | \hat{a}_j | \psi_{D_n^-} \rangle \langle \psi_{D_n^-} | \hat{E}_k^l | \psi_{D_m^-} \rangle \right) \langle \psi_{A^*} | \hat{a}_i^\dagger | \psi_{A_m^+} \rangle
\end{aligned}
\tag{7.48}
$$

$$
\begin{aligned}
\langle \Psi_{D^- A^+,m} | \hat{E}_i^j \hat{E}_k^l | \Psi_{D^* A} \rangle = & \sum_{i \in D} \sum_{j,k,l \in A} \langle \psi_{D_m^-} | \hat{a}_i^\dagger | \psi_{D^*} \rangle \sum_n \Big(\langle \psi_{A_m^+} | \hat{a}_j | \psi_{A_n^*} \rangle \langle \psi_{A_n^*} | \hat{E}_k^l | \psi_A \rangle \Big) \\
& + \sum_{k \in D} \sum_{i,j,l \in A} \langle \psi_{D_m^-} | \hat{a}_k^\dagger | \psi_{D^*} \rangle \sum_n \Big(\langle \psi_{A_m^+} | \hat{E}_i^j | \psi_{A_n^+} \rangle \langle \psi_{A_n^+} | \hat{a}_l | \psi_A \rangle \Big) \\
& + \sum_{i,j,k \in D} \sum_{l \in A} \sum_n \Big(\langle \psi_{D_m^-} | \hat{E}_i^j | \psi_{D_n^-} \rangle \langle \psi_{D_n^-} | \hat{a}_k^\dagger | \psi_{D^*} \rangle \Big) \langle \psi_{A_m^+} | \hat{a}_l | \psi_A \rangle \\
& + \sum_{i,k,l \in D} \sum_{j \in A} \sum_n \Big(\langle \psi_{D_m^-} | \hat{a}_i^\dagger | \psi_{D_n^*} \rangle \langle \psi_{D_n^*} | \hat{E}_k^l | \psi_{D^*} \rangle \Big) \langle \psi_{A_m^+} | \hat{a}_j | \psi_A \rangle
\end{aligned}
\tag{7.49}
$$

Utilizing the RI approximation requires a large enough set of uncharged and charged excited states to converge the calculation.
Next to the expressions of the Hamiltonian matrix elements the energies of the CT states are required. The extension of the MTD-TI approach and its application is subject to a follow-up PhD project handled by my successor on the EET project.

8 Conclusions

The aim of this thesis was to extend and supply new tools and methods for the evaluation of electronic matrix elements as well as their gradients for radiative and non-radiative rate constants. Herein the focus resided on the fluorescence, phosphorescence, ISC and EET processes. These rate constants are particularly interesting for the investigation of OLED emitters. Typical TADF and phosphorescent emitters allow theoretically harvesting of all singlet and triplet excitons leading to an IQE of 100%. The weakness of such emitters is exciton loss due to non-radiative deactivation processes which are allowed to compete with slow emission pathways. To circumvent the exciton loss, a fluorophore is introduced into the emitter system to supply a fast emission channel that can be populated by EET. To find suitable molecules, it is crucial to obtain a reliable picture of the excited state kinetics within and between the sensitizer and emitter molecules.

The first two publications within this work, were concerned with RTP emitters which are presently a 'hot' topic with many applications in daily life. Herein a group of four triarylboranes of which two showed RTP of up to four seconds were investigated in cooperation with researchers from Würzburg, Manchester and Xi'an. Triarylboranes are purely organic systems without atoms introducing lone pairs where ISC and phosphorescence are expected to be slow. To understand the emission mechanism and its driving force in these systems experimental and theoretical studies were conducted. It was found that $(\sigma, B\,p) \rightarrow (\pi, B\,p)$ and $(\pi, B\,p) \rightarrow (\sigma, B\,p)$ transitions involving the boron's σ orbital at the systems center drive SOC and allow ISC from $S_1 \rightsquigarrow T_2$ to progress at a rate constant of about 10^7 s^{-1} in competition to fluorescence. The emission mechanism was found to populate the T_2 state via ISC followed by phosphorescence from the T_1 state at up to 0.20 s^{-1}. RTP is observed only in the crystalline state and in highly doped films and therefore aggregation effects are expected to play a critical role in suppressing the non-radiative deactivation channels that otherwise efficiently quench the emission. One of the investigated RTP components was selected for a subsequent study with the aim to introduce bromine in ortho-, meta- and para position to enhance ISC. While the introduction of bromine speeds up ISC in all three compounds ISC in the ortho compound is enhanced the most. Unexpectedly, the ortho substituted compound showed DRTP in rigid environments revealing a second emissive triplet state within the same molecule or formed by more complex intramolecular interactions.

Reduced one-electron (transition) density matrices pose useful tools to obtain expectation values of quantum mechanical operators and to visualize the character of wave functions as well as their respective transitions. Due to their importance, density matrices are widely available in quantum chemical software packages. Within this thesis, electric transition dipole moments, SOCMEs and ECMEs are obtained utilizing these matrices to determine radia-

tive and non-radiative rate constants. To evaluate electric transition dipole moments and SOCMEs, SPOILER requires triplet-triplet and singlet-triplet transition densities in addition to the density matrices supplied by TDDFT. Employing DFT/MRCI wave functions to calculate ECMEs within the MTD approach as well as analyzing excited triplet states with THEODORE lacked singlet-triplet transition densities in the beginning of this thesis. The DENSITYENGINE, a C++ library, was developed to evaluate density matrices efficiently in parallel for CIS and DFT/MRCI wave functions where for the latter the DENSOMAT program is utilized as a driver. In future projects, the DENSITYENGINE can be easily extended to new density operators which was proven by the extension to Dyson orbitals performed by Simon Metz under my supervision. Herein the modular design required only small portions of the code to be altered.

Vibronic interactions can play an important role for a system's radiative and non-radiative properties. Within this thesis vibronic effects are treated utilizing the HT approximation employing first-order derivatives of the quantum chemical operator's matrix elements. The GRADIENATOR, a Python program, was developed to supply these derivatives in a numerical fashion. Herein the GRADIENATOR applies phase corrections to fix the arbitrary phases at each calculation step. An early version of this program was applied to investigate vibronic effects in pyrazine. Pyrazine shows vibronic interactions in its singlet-singlet absorption spectrum, while similar effects are absent for singlet-triplet absorption. In addition to deeper insights into pyrazine's vibronic interactions, contradicting assumptions on the T_2 state's location were clarified. Another publication investigated vibronic coupling in the 2CzPN molecule, a system heavily studied for TADF applications in OLEDs where vibronic effects speed up RISC by a factor of 2. The GRADIENATOR was in addition utilized to investigate Hz and HAP-3MF, two IST systems, where triplet-singlet conversion is expected to be fast as RISC is a downhill process. In these systems emission and ISC is actually mainly driven by vibronic effects and IST was found to be not always favorable. The GRADIENATOR offers an efficient incremental computation scheme, that can easily be extended to supply derivatives for methods available in arbitrary quantum chemical packages. This allows the GRADIENATOR to be applied in many future studies investigating vibronic effects for radiative and non-radiative processes.

The SPOILER program, which was initially developed in 2017 to supply SOCMEs for linear response TDDFT, was extended during this work to calculate phosphorescence rate constants within the FC and HT approximation. Herein the DENSITYENGINE is utilized to evaluate the density matrices for electric transition dipole moments as well as SOCMEs. To enable users outside the Turbomole community to use SPOILER, the program was interfaced to the Gaussian program package. The benchmark of 2017 was extended to additional systems presented in the PYSOC publication,[130] a similar approach to SPOILER. The PYSOC benchmark showed large deviations between SOCMEs at TDDFT level and the reference values. Performing the PYSOC benchmark with SPOILER and SPOCK shows good agreement between both methods with correlation coefficients of about 0.96. Significant deviations within the PYSOC benchmark can be reproduced with SPOILER utilizing the A^{LL}_{MN} AMEWs. The largest deviations occur for 2-thiothymine, where the excited state descriptions of DFT/MRCI and TDDFT differ strongly due to the extraordinary structure of the system. Moreover, TXB, pyrazine and porphyrin are added to the benchmark set to investigate the performance of ISC at TDDFT level. TXB and porphyrin show good agreement for ISC rate constants

at DFT/MRCI and TDDFT level of theory as long as DFT/MRCI excitation energies are utilized. Herein, rate constants with TDDFT and DFT/MRCI are of the same order of magnitude in TXB, while TDDFT rate constants are slightly smaller due to a lower S_1 excitation energy. In porphyrin the S_1 state is located 0.4 eV below the DFT/MRCI state in TDDFT, causing a lower ISC rate constant of about one order of magnitude. Pyrazine represents a cautionary tale, as non-negligible double excitation character causes the SOCMEs and their gradients to differ between the DFT/MRCI and TDDFT calculations. In summary, the SPOILER approach proves to be an inexpensive route to accurate ISC rate constants as long as TDDFT is able to properly describe the system. States that can typically not be described by TDDFT are charge-transfer states, Rydberg states and states with important double excitations.

Long- and short-range EET processes as well as methodologies to obtain EET rate constants were discussed. Herein FRET is a long-range EET process transfering excitons between singlet states or mediating triplet-singlet EET. At small distances Dexter and short-range electron transfer processes contribute additionally to EET. Within this work the existing EET programs were redesigned into one system improving their usability and new program components were developed to allow an easier manipulation of fragment and dimer geometries. Additionally, diabatization approaches like Boys, BoysOV and ER diabatization were implemented as well as the extension of the MTD method to TEET incorporating short-range orthogonality corrections. The MTD and diabatization approaches were tested against experimental[154] and theoretical[79] TEET studies of a group of bridged donor-acceptor systems. In contrast to the diabatization approaches, which agreed very well with the experiment, the MTD approach suggested, that short-range contributions were missing in the methodology. The missing contributions turned out to originate from short-range electron transfer processes which are difficult to obtain within a fragment approach. To treat these contributions the MTD-TI approach was implemented following the TDFI-TI method by Fujimoto.[23] Within the MTD-TI approach, the Davydov splitting can be reproduced for SEET and TEET in simple systems like the ethylene dimer. While the MTD-TI approach can in principle be applied to more complex systems, determination of the charge-transfer state's excitation energies is limited to a HOMO-LUMO picture. To move beyond the MTD-TI approach, the excitation energies have to be obtained outside of Koopman's theorem and the electronic couplings need to be evaluated more efficiently. Currently, the follow-up PhD project investigates the use of Dyson orbitals for this purpose. Besides the excitonic coupling, the EET rate constant draws its strength from the FC weighted density of states which is typically determined by the spectral overlap integral. Theoretical determination of the spectral overlap integral requires very accurate spectra to hinder small errors in the spectra to have tremendous effects on the EET rate constant.

Bibliography

(*1*) In *OLED Display Fundamentals and Applications*; John Wiley & Sons, Ltd: 2017; Chapter 2, pp 7–59.

(*2*) Tang, C. W., and VanSlyke, S. A. (1987). Organic electroluminescent diodes. *Appl. Phys. Lett. 51*, 913–915.

(*3*) Rothberg, L. J., and Lovinger, A. J. (1996). Status of and prospects for organic electroluminescence. *J. Mater. Res. 11*, 3174.

(*4*) Baldo, M. A., O'Brien, D. F., Thompson, M. E., and Forrest, S. R. (1999). Excitonic singlet-triplet ratio in a semiconducting organic thin film. *Phys. Rev. B 60*, 14422–14428.

(*5*) Kasha, M. (1950). Characterization of electronic transitions in complex molecules. *Discuss. Faraday Soc. 9*, 14–19.

(*6*) Nakanotani, H., Higuchi, T., Furukawa, T., Masui, K., Morimoto, K., Numata, M., Tanaka, H., Sagara, Y., Yasuda, T., and Adachi, C. (2014). High-efficiency organic light-emitting diodes with fluorescent emitters. *Nat. Commun. 5*, 4016.

(*7*) Baldo, M. A., Thompson, M. E., and Forrest, S. R. (2000). High-efficiency fluorescent organic light-emitting devices using a phosphorescent sensitizer. *Nature 403*, 750–753.

(*8*) Delcanale, P., Galstyan, A., Daniliuc, C. G., Grecco, H. E., Abbruzzetti, S., Faust, A., Viappiani, C., and Strassert, C. A. (2018). Oxygen-Insensitive Aggregates of Pt(II) Complexes as Phosphorescent Labels of Proteins with Luminescence Lifetime-Based Readouts. *ACS Appl. Mater. Interfaces 10*, 24361–24369.

(*9*) Clegg, R. M. In *DNA Structures Part A: Synthesis and Physical Analysis of DNA*; Meth. Enzymol, Vol. 211; Academic Press: 1992, pp 353–388.

(*10*) Förster, T. (1948). Zwischenmolekulare Energiewanderung und Fluoreszenz. *Ann. Phys. 437*, 55–75.

(*11*) Förster, T. (1959). 10th Spiers Memorial Lecture. Transfer mechanisms of electronic excitation. *Discuss. Faraday Soc. 27*, 7–17.

(*12*) Dexter, D. L. (1953). A Theory of Sensitized Luminescence in Solids. *J. Chem. Phys. 21*, 836–850.

(*13*) Sauer, M., Hofkens, J., and Enderlein, J., *Handbook of Fluorescence Spectroscopy and Imaging*; Wiley-VCH Verlag GmbH & Co. KGaA: Weinheim, 2011.

(*14*) Hai-Wei, C., Jiun-Haw, L., Bo-Yen, L., Stanley, C., and Shin-Tson, W. (2018). Liquid crystal display and organic light-emitting diode display: present status and future perspectives. *Light Sci. Appl. 7*, 17168.

(*15*) Adachi, C. (2014). Third-generation organic electroluminescence materials. *Jpn. J. Appl. Phys. 53*, 060101.

(*16*) Higuchi, T., Nakanotani, H., and Adachi, C. (2015). High-Efficiency White Organic Light-Emitting Diodes Based on a Blue Thermally Activated Delayed Fluorescent Emitter Combined with Green and Red Fluorescent Emitters. *Adv. Mater. 27*, 2019–2023.

(*17*) Baldo, M. A., O'Brien, D. F., You, Y., Shoustikov, A., Sibley, S., Thompson, M. E., and Forrest, S. R. (1998). Highly efficient phosphorescent emission from organic electroluminescent devices. *Nature 395*, 151–154.

(*18*) Wu, Z., Nitsch, J., Schuster, J., Friedrich, A., Edkins, K., Loebnitz, M., Dinkelbach, F., Stepanenko, V., Würthner, F., Marian, C., Ji, L., and Marder, T. (2020). Persistent Room Temperature Phosphorescence from Triarylboranes: A Combined Experimental and Theoretical Study. *Angew. Chem. Int. Ed. Engl. 39*, 17137–17144.

(*19*) Wu, Z., Dinkelbach, F., Kerner, F., Friedrich, A., Ji, L., Stepanenko, V., Würthner, F., Marian, C. M., and Marder, T. B. (2022). Aggregation-Induced Dual Phosphorescence from (o-Bromophenyl)-Bis(2,6-Dimethylphenyl)Borane at Room Temperature. *Chem. Eur. J. 28*, e202200525.

(*20*) Geffroy, B., le Roy, P., and Prat, C. (2006). Organic light-emitting diode (OLED) technology: materials, devices and display technologies. *Polym. Int. 55*, 572–582.

(*21*) Frisch, M. J. et al. Gaussian 16 Revision C.01, Gaussian Inc. Wallingford CT, 2016.

(*22*) TURBOMOLE V7.5 2021, a development of University of Karlsruhe and Forschungszentrum Karlsruhe GmbH, 1989-2007, TURBOMOLE GmbH, since 2007; available from `http://www.turbomole.com`.

(*23*) Fujimoto, K. J. (2012). Transition-density-fragment interaction combined with transfer integral approach for excitation-energy transfer via charge-transfer states. *J. Chem. Phys. 137*, 034101.

(*24*) March, N. (1957). The Thomas-Fermi approximation in quantum mechanics. *Adv. Phys. 6*, 1–101.

(*25*) Dirac, P. A. M. (1930). Note on Exchange Phenomena in the Thomas Atom. *Math. Proc. Camb. Philos. Soc. 26*, 376–385.

(*26*) Hohenberg, P., and Kohn, W. (1964). Inhomogeneous Electron Gas. *Phys. Rev. 136*, B864–B871.

(*27*) Kohn, W., and Sham, L. J. (1965). Self-Consistent Equations Including Exchange and Correlation Effects. *Phys. Rev. 140*, A1133–A1138.

(*28*) Becke, A. D. (1993). Density-functional thermochemistry. III. The role of exact exchange. *J. Chem. Phys. 98*, 5648–5652.

(*29*) Lee, C., Yang, W., and Parr, R. G. (1988). Development of the Colle-Salvetti correlation-energy formula into a functional of the electron density. *Phys. Rev. B 37*, 785–789.

(*30*) Vosko, S. H., Wilk, L., and Nusair, M. (1980). Accurate spin-dependent electron liquid correlation energies for local spin density calculations: a critical analysis. *Can J. Phys. 58*, 1200–1211.

(*31*) Perdew, J. P., Burke, K., and Ernzerhof, M. (1996). Generalized Gradient Approximation Made Simple. *Phys. Rev. Lett. 77*, 3865–3868.

(*32*) Perdew, J. P., Burke, K., and Ernzerhof, M. (1997). Generalized Gradient Approximation Made Simple [Phys. Rev. Lett. 77, 3865 (1996)]. *Phys. Rev. Lett. 78*, 1396–1396.

(*33*) Becke, A. D. (1993). A new mixing of Hartree-Fock and local density-functional theories. *J. Chem. Phys. 98*, 1372–1377.

(*34*) Dreuw, A., and Head-Gordon, M. (2005). Single-Reference ab Initio Methods for the Calculation of Excited States of Large Molecules. *Chem. Rev. 105*, 4009–4037.

(*35*) Runge, E., and Gross, E. K. U. (1984). Density-Functional Theory for Time-Dependent Systems. *Phys. Rev. Lett. 52*, 997–1000.

(*36*) Hirata, S., and Head-Gordon, M. (1999). Time-dependent density functional theory within the Tamm–Dancoff approximation. *Chem. Phys. Lett. 314*, 291–299.

(*37*) Grimme, S., and Waletzke, M. (1999). A combination of Kohn–Sham density functional theory and multi-reference configuration interaction methods. *J. Chem. Phys. 111*, 5645–5655.

(*38*) Dreuw, A., and Head-Gordon, M. (2004). Failure of Time-Dependent Density Functional Theory for Long-Range Charge-Transfer Excited States: The Zincbacteriochlorin–Bacteriochlorin and Bacteriochlorophyll–Spheroidene Complexes. *J. Am. Chem. Soc. 126*, 4007–4016.

(*39*) Cave, R. J., Zhang, F., Maitra, N. T., and Burke, K. (2004). A dressed TDDFT treatment of the 21Ag states of butadiene and hexatriene. *Chem. Phys. Lett. 389*, 39–42.

(*40*) Maitra, N. T., Zhang, F., Cave, R. J., and Burke, K. (2004). Double excitations within time-dependent density functional theory linear response. *J. Chem. Phys. 120*, 5932–5937.

(*41*) Olsen, J. In *European Summerschool in Quantum Chemistry: Book I*; Simen Reine and Trond Saue, Eds.: 2017, pp 81–93.

(*42*) Szabo, A., and Ostlund, N. S., *Modern Quantum Chemistry*; Dover Publications: Mineola, New York, 1996.

(*43*) Wetmore, R. W., and Segal, G. A. (1975). Efficient generation of configuration interaction matrix elements. *Chem. Phys. Lett. 36*, 478–483.

(*44*) Kleinschmidt, M., Tatchen, J., and Marian, C. M. (2006). SPOCK.CI: A multireference spin-orbit configuration interaction method for large molecules. *J. Chem. Phys. 124*, 124101.

(*45*) Kleinschmidt, M., and Marian, C. M. (2005). Efficient generation of matrix elements for one-electron spin–orbit operators. *Chem. Phys. 311*, 71–79.

(*46*) Pauncz, R., *Spin Eigenfunctions: Construction and Use*; Springer Science+Business Media: New York, 1979.

(*47*) Tapavicza, E., Tavernelli, I., and Rothlisberger, U. (2007). Trajectory Surface Hopping within Linear Response Time-Dependent Density-Functional Theory. *Phys. Rev. Lett. 98*, 023001.

(*48*) Tavernelli, I., Curchod, B. F. E., Laktionov, A., and Rothlisberger, U. (2010). Nonadiabatic coupling vectors for excited states within time-dependent density functional theory in the Tamm–Dancoff approximation and beyond. *J. Chem. Phys. 133*, 194104.

(*49*) Wang, F., and Ziegler, T. (2005). A simplified relativistic time-dependent density-functional theory formalism for the calculations of excitation energies including spin-orbit coupling effect. *J. Chem. Phys. 123*, 154102.

(*50*) Franco de Carvalho, F., Curchod, B. F. E., Penfold, T. J., and Tavernelli, I. (2014). Derivation of spin-orbit couplings in collinear linear-response TDDFT: A rigorous formulation. *J. Chem. Phys. 140*, 144103.

(*51*) Ou, Q., and Subotnik, J. E. (2013). Electronic Relaxation in Benzaldehyde Evaluated via TD-DFT and Localized Diabatization: Intersystem Crossings, Conical Intersections, and Phosphorescence. *J. Phys. Chem. C 117*, 19839–19849.

(*52*) Franco de Carvalho, F., and Tavernelli, I. (2015). Nonadiabatic dynamics with intersystem crossings: A time-dependent density functional theory implementation. *J. Chem. Phys. 143*, 224105.

(*53*) Dinkelbach, F., Kleinschmidt, M., and Marian, C. M. (2017). Assessment of Interstate Spin–Orbit Couplings from Linear Response Amplitudes. *J. Chem. Theory Comput. 13*, 749–766.

(*54*) Christiansen, O., Gauss, J., and Schimmelpfennig, B. (2000). Spin-orbit coupling constants from coupled-cluster response theory. *Phys. Chem. Chem. Phys. 2*, 965–971.

(*55*) Epifanovsky, E., Klein, K., Stopkowicz, S., Gauss, J., and Krylov, A. I. (2015). Spin-orbit couplings within the equation-of-motion coupled-cluster framework: Theory, implementation, and benchmark calculations. *J. Chem. Phys. 143*, 064102.

(*56*) Werner, H. J., and Knowles, P. J. (1988). An efficient internally contracted multiconfiguration–reference configuration interaction method. *J. Chem. Phys. 89*, 5803–5814.

(*57*) Fock, V. (1932). Konfigurationsraum und zweite Quantelung. *Z. Physik. 75*, 622–647.

(*58*) Marian, C. M., Heil, A., and Kleinschmidt, M. (2019). The DFT/MRCI method. *WIREs Comput Mol Sci. 9*, e1394.

(*59*) Lyskov, I., Kleinschmidt, M., and Marian, C. M. (2016). Redesign of the DFT/MRCI Hamiltonian. *J. Chem. Phys. 144*, 034104.

(*60*) Heil, A., and Marian, C. M. (2017). DFT/MRCI Hamiltonian for odd and even numbers of electrons. *J. Chem. Phys. 147*, 194104.

(*61*) McWeeny, R. In *Methods in Computational Molecular Physics*, Wilson, S., and Diercksen, G. H. F., Eds.; Springer US: Boston, MA, 1992, pp 3–17.

(*62*) Kleinschmidt, M., Tatchen, J., and Marian, C. M. (2002). Spin-orbit coupling of DFT/MRCI wave functions: Method, test calculations, and application to thiophene. *J. Comput. Chem. 23*, 824–833.

(*63*) Danovich, D., Marian, C. M., Neuheuser, T., Peyerimhoff, S. D., and Shaik, S. (1998). Spin–Orbit Coupling Patterns Induced by Twist and Pyramidalization Modes in C2H4: A Quantitative Study and a Qualitative Analysis. *J. Phys. Chem. A 102*, 5923–5936.

(*64*) Tatchen, J., and Marian, C. M. (1999). On the performance of approximate spin–orbit Hamiltonians in light conjugated molecules: the fine-structure splitting of HC6H+, NC5H+, and NC4N+. *Chem. Phys. Lett. 313*, 351–357.

(*65*) Neese, F. (2005). Efficient and accurate approximations to the molecular spin-orbit coupling operator and their use in molecular g-tensor calculations. *J. Chem. Phys. 122*, 034107.

(*66*) Marian, C. M. In *Reviews in Computational Chemistry*; John Wiley & Sons, Ltd: 2001; Chapter 3, pp 99–204.

(*67*) Atkins, P. W., and de Paula, J., *Physikalische Chemie (Fifth German Edition)*; Wiley-VCH: 2013.

(*68*) Herzberg, G., and Teller, E. (1933). Schwingungsstruktur der Elektronenübergänge bei mehratomigen Molekülen. *Z. Phys. Chem. 21B*, 410–446.

(*69*) Etinski, M., Tatchen, J., and Marian, C. M. (2011). Time-dependent approaches for the calculation of intersystem crossing rates. *J. Chem. Phys. 134*, 154105.

(*70*) Etinski, M. (2011). The role of Duschinsky rotation in intersystem crossing: A case study of uracil. *J. Serb. Chem. Soc. 76*, 1694–1660.

(*71*) Etinski, M., Tatchen, J., and Marian, C. M. (2014). Thermal and solvent effects on the triplet formation in cinnoline. *Phys. Chem. Chem. Phys. 16*, 4740–4751.

(*72*) Tatchen, J., Gilka, N., and Marian, C. M. (2007). Intersystem crossing driven by vibronic spin–orbit coupling: a case study on psoralen. *Phys. Chem. Chem. Phys. 9*, 5209–5221.

(*73*) Cupellini, L., Corbella, M., Mennucci, B., and Curutchet, C. (2019). Electronic energy transfer in biomacromolecules. *WIREs Comput Mol Sci. 9*, e1392.

(*74*) Duschinsky, F. (1937). *Acta Physiochim. USSR*, 551.

(*75*) You, Z.-Q., and Hsu, C.-P. (2011). Ab Inito Study on Triplet Excitation Energy Transfer in Photosynthetic Light-Harvesting Complexes. *J. Phys. Chem. A 115*, 4092–4100.

(*76*) Banerjee, S., Baiardi, A., Bloino, J., and Barone, V. (2016). Temperature Dependence of Radiative and Nonradiative Rates from Time-Dependent Correlation Function Methods. *J. Chem. Theory Comput. 12*, 774–786.

(*77*) Lyskov, I., Etinski, M., Marian, C. M., and Russo, S. P. (2018). Exciton energy transfer in organic light emitting diodes with thermally activated delayed fluorescence dopants. *J. Mater. Chem. C 6*, 6860–6868.

(*78*) Pipek, J., and Mezey, P. G. (1989). A fast intrinsic localization procedure applicable for ab initio and semiempirical linear combination of atomic orbital wave functions. *J. Chem. Phys. 90*, 4916–4926.

(*79*) Subotnik, J. E., Vura-Weis, J., Sodt, A. J., and Ratner, M. A. (2010). Predicting Accurate Electronic Excitation Transfer Rates via Marcus Theory with Boys or Edmiston–Ruedenberg Localized Diabatization. *J. Phys. Chem. A 114*, 8665–8675.

(*80*) Subotnik, J. E., Cave, R. J., Steele, R. P., and Shenvi, N. (2009). The initial and final states of electron and energy transfer processes: Diabatization as motivated by system-solvent interactions. *J. Chem. Phys. 130*, 234102.

(*81*) Edmiston, C., and Ruedenberg, K. (1963). Localized Atomic and Molecular Orbitals. *Rev. Mod. Phys. 35*, 457–464.

(*82*) Spiegel, J. D., Kleinschmidt, M., Larbig, A., Tatchen, J., and Marian, C. M. (2015). Quantum-Chemical Studies on Excitation Energy Transfer Processes in BODIPY-Based Donor–Acceptor Systems. *J. Chem. Theory Comput. 11*, 4316–4327.

(*83*) Fink, R. F., Pfister, J., Zhao, H. M., and Engels, B. (2008). Assessment of quantum chemical methods and basis sets for excitation energy transfer. *Chem. Phys. 346*, 275–285.

(*84*) Fink, R., Pfister, J., Schneider, A., Zhao, H., and Engels, B. (2008). Ab initio configuration interaction description of excitation energy transfer between closely packed molecules. *Chem. Phys. 343*, 353–361.

(*85*) Nagae, H., Kakitani, T., Katoh, T., and Mimuro, M. (1993). Calculation of the excitation transfer matrix elements between the S2 or S1 state of carotenoid and the S2 or S1 state of bacteriochlorophyll. *J. Chem. Phys. 98*, 8012–8023.

(*86*) Harcourt, R. D., Scholes, G. D., and Ghiggino, K. P. (1994). Rate expressions for excitation transfer. II. Electronic considerations of direct and through–configuration exciton resonance interactions. *J. Chem. Phys. 101*, 10521–10525.

(*87*) Scholes, G. D., and Ghiggino, K. P. (1994). Rate expressions for excitation transfer I. Radiationless transition theory perspective. *J. Chem. Phys. 101*, 1251–1261.

(*88*) Scholes, G. D., Harcourt, R. D., and Ghiggino, K. P. (1995). Rate expressions for excitation transfer. III. An ab initio study of electronic factors in excitation transfer and exciton resonance interactions. *J. Chem. Phys. 102*, 9574–9581.

(*89*) May, V., and Oliver, K., *Charge and Energy Transfer Dynamics in Molecular Systems*; John Wiley & Sons, Ltd: 2011.

(*90*) Fujimoto, K. J., and Hayashi, S. (2009). Electronic Coulombic Coupling of Excitation-Energy Transfer in Xanthorhodopsin. *J. Am. Chem. Soc. 131*, 14152–14153.

(*91*) Fujimoto, K. J. (2010). Transition-density-fragment interaction approach for exciton-coupled circular dichroism spectra. *J. Chem. Phys. 133*, 124101.

(*92*) Koopmans, T. (1934). Über die Zuordnung von Wellenfunktionen und Eigenwerten zu den einzelnen Elektronen eines Atoms. *Physica 1*, 104–113.

(*93*) El-Sayed, M. A. (1963). Origin of the Phosphorescence Radiation in Aromatic Hydrocarbons. *Nature 197*, 481–482.

(*94*) Schäfer, A., Horn, H., and Ahlrichs, R. (1992). Fully optimized contracted Gaussian basis sets for atoms Li to Kr. *J. Chem. Phys. 97*, 2571–2577.

(*95*) Weigend, F., Häser, M., Patzelt, H., and Ahlrichs, R. (1998). RI-MP2: optimized auxiliary basis sets and demonstration of efficiency. *Chem. Phys. Lett. 294*, 143–152.

(*96*) Peterson, K. A., Figgen, D., Goll, E., Stoll, H., and Dolg, M. (2003). Systematically convergent basis sets with relativistic pseudopotentials. II. Small-core pseudopotentials and correlation consistent basis sets for the post-d group 16-18 elements. *J. Chem. Phys. 119*, 11113–11123.

(*97*) Neugebauer, J., Reiher, M., Kind, C., and Hess, B. A. (2002). Quantum chemical calculation of vibrational spectra of large molecules—Raman and IR spectra for Buckminsterfullerene. *J. Comput. Chem. 23*, 895–910.

(*98*) Spackman, M. A., and Jayatilaka, D. (2009). Hirshfeld surface analysis. *Cryst. Eng. Comm. 11*, 19–32.

(*99*) Head-Gordon, M., Grana, A. M., Maurice, D., and White, C. A. (1995). Analysis of Electronic Transitions as the Difference of Electron Attachment and Detachment Densities. *J. Phys. Chem. 99*, 14261–14270.

(*100*) Plasser, F. (2020). TheoDORE: a Toolbox for a Detailed and Automated Analysis of Electronic Excited State Computations. *J. Chem. Phys. 152*.

(*101*) Ortiz, J. V. (2020). Dyson-orbital concepts for description of electrons in molecules. *J. Chem. Phys. 153*, 070902.

(*102*) Dagum, L., and Menon, R. (1998). OpenMP: an industry standard API for shared-memory programming. *IEEE Computational Science and Engineering 5*, 46–55.

(*103*) Rodriguez-Serrano, A., Dinkelbach, F., and Marian, C. M. (2021). Intersystem crossing processes in the 2CzPN emitter: a DFT/MRCI study including vibrational spin–orbit interactions. *Phys. Chem. Chem. Phys. 23*, 3668–3678.

(*104*) Kaminski, J. M., Rodríguez-Serrano, A., Dinkelbach, F., Miranda-Salinas, H., Monkman, A. P., and Marian, C. M. (2022). Vibronic effects accelerate the intersystem crossing processes of the through-space charge transfer states in the triptycene bridged acridine-triazine donor-acceptor molecule TpAT-tFFO. *Chem. Sci. 13*, 7057–7066.

(*105*) Miranda-Salinas, H., Rodriguez-Serrano, A., Kaminski, J., Dinkelbach, F., Nakagawa, H., Kusakabe, Y., Kaji, H., Marian, C. M., and Monkman, A. P. (2022). Conformational and host influences on the photophysics and dynamic TADF of the through-space charge transfer states in triptycene bridged acridinetriazine donor acceptor molecule TpAT-tFFO. *J. Phys. Chem C.*, submitted.

(*106*) Bracker, M., Dinkelbach, F., Weingart, O., and Kleinschmidt, M. (2019). Impact of fluorination on the photophysics of the flavin chromophore: a quantum chemical perspective. *Phys. Chem. Chem. Phys. 21*, 9912–9923.

(*107*) Dinkelbach, F., and Marian, C. M. (2019). Vibronic and spin–orbit coupling effects in the absorption spectra of pyrazine: A quantum chemical approach. *J. Serb. Chem. Soc. 84*, 819–836.

(*108*) Dinkelbach, F., Bracker, M., Kleinschmidt, M., and Marian, C. M. (2021). Large Inverted Singlet–Triplet Energy Gaps Are Not Always Favorable for Triplet Harvesting: Vibronic Coupling Drives the (Reverse) Intersystem Crossing in Heptazine Derivatives. *J. Phys. Chem. A 125*, 10044–10051.

(*109*) Tomasi, J., Mennucci, B., and Cammi, R. (2005). Quantum Mechanical Continuum Solvation Models. *Chem. Rev. 105*, 2999–3094.

(*110*) Woywod, C., Domcke, W., Sobolewski, A. L., and Werner, H.-J. (1994). Characterization of the S1-S2 conical intersection in pyrazine using ab initio multiconfiguration self-consistent-field and multireference configuration-interaction methods. *J. Chem. Phys. 100*, 1400–1413.

(*111*) Berger, R., Fischer, C., and Klessinger, M. (1998). Calculation of the Vibronic Fine Structure in Electronic Spectra at Higher Temperatures. 1. Benzene and Pyrazine. *J. Phys. Chem. A 102*, 7157–7167.

(*112*) Siebrand, W., and Zgierski, M. Z. (1979). Interaction between vibronic coupling and spin—orbit coupling in pyrazine. *Chem. Phys. Lett. 67*, 13–16.

(*113*) Fischer, G. (1993). An analysis of vibronic coupling in the triplet absorption spectrum of pyrazine. *Can. J. Chem. 71*, 1537–1547.

(*114*) Weber, P., and Reimers, J. R. (1999). Ab Initio and Density-Functional Calculations of the Vibrational Structure of the Singlet and Triplet Excited States of Pyrazine. *J. Phys. Chem. A 103*, 9830–9841.

(*115*) Tomer, J. L., Holtzclaw, K. W., Pratt, D. W., and Spangler, L. H. (1988). Phosphorescence excitation spectroscopy in supersonic jets. The lowest triplet state of pyrazine. *J. Chem. Phys. 88*, 1528–1538.

(*116*) Hochstrasser, R. M., and Marzzacco, C. (1968). Perturbations between Electronic States in Aromatic and Heteroaromatic Molecules. *J. Chem. Phys. 49*, 971–984.

(*117*) Villa, E., Terazima, M., and Lim, E. (1986). Mpi detection of singlet $\rightarrow$ triplet transitions in a supersonic jet: Evidence for T1 potential energy distortion in pyrazine and related molecules. *Chem. Phys. Lett. 129*, 336–341.

(*118*) Masui, K., Nakanotani, H., and Adachi, C. (2013). Analysis of exciton annihilation in high-efficiency sky-blue organic light-emitting diodes with thermally activated delayed fluorescence. *Org. Electron. 14*, 2721–2726.

(*119*) Zhang, Y., Zhang, D., Tsuboi, T., Qiu, Y., and Duan, L. (2019). Simultaneous enhancement of efficiency and stability of OLEDs with thermally activated delayed fluorescence materials by modifying carbazoles with peripheral groups. *Sci. China Chem. 62*, 393–402.

(*120*) de Silva, P. (2019). Inverted Singlet–Triplet Gaps and Their Relevance to Thermally Activated Delayed Fluorescence. *J. Phys. Chem. Lett. 10*, 5674–5679.

(*121*) Ehrmaier, J., Rabe, E. J., Pristash, S. R., Corp, K. L., Schlenker, C. W., Sobolewski, A. L., and Domcke, W. (2019). Singlet–Triplet Inversion in Heptazine and in Polymeric Carbon Nitrides. *J. Phys. Chem. A 123*, 8099–8108.

(*122*) Sobolewski, A. L., and Domcke, W. (2021). Are Heptazine-Based Organic Light-Emitting Diode Chromophores Thermally Activated Delayed Fluorescence or Inverted Singlet–Triplet Systems? *J. Phys. Chem. Lett. 12*, 6852–6860.

(*123*) Li, J., Zhang, Q., Nomura, H., Miyazaki, H., and Adachi, C. (2014). Thermally activated delayed fluorescence from $3n\pi^*$ to $1n\pi^*$ up-conversion and its application to organic light-emitting diodes. *Appl. Phys. Lett. 105*, 013301.

(*124*) Lenthe, E. v., Baerends, E. J., and Snijders, J. G. (1993). Relativistic regular two-component Hamiltonians. *J. Chem. Phys. 99*, 4597–4610.

(*125*) Chiodo, S., and Russo, N. (2008). Determination of spin-orbit coupling contributions in the framework of density functional theory. *J. Comput. Chem. 29*, 912–920.

(*126*) Chiodo, S. G., and Russo, N. (2010). DFT spin-orbit coupling between singlet and triplet excited states: A case of psoralen compounds. *Chem. Phys. Lett. 490*, 90–96.

(*127*) Capano, G., Chergui, M., Rothlisberger, U., Tavernelli, I., and Penfold, T. J. (2014). A Quantum Dynamics Study of the Ultrafast Relaxation in a Prototypical Cu(I)-Phenanthroline. *J. Phys. Chem. A 118*, 9861–9869.

(*128*) Gibson, J., Monkman, A. P., and Penfold, T. J. (2016). The Importance of Vibronic Coupling for Efficient Reverse Intersystem Crossing in Thermally Activated Delayed Fluorescence Molecules. *Chem. Phys. Chem. 17*, 2956–2961.

(*129*) Li, Z., Suo, B., Zhang, Y., Xiao, Y., and Liu, W. (2013). Combining spin-adapted open-shell TD-DFT with spin-orbit coupling. *Mol. Phys. 111*, 3741–3755.

(*130*) Gao, X., Bai, S., Fazzi, D., Niehaus, T., Barbatti, M., and Thiel, W. (2017). Evaluation of spin–orbit couplings with linear-response TDDFT, TDA, and TD-DFTB. *J. Chem. Theory Comput. 13*, 515–524.

(*131*) de Souza, B., Farias, G., Neese, F., and Izsák, R. (2019). Predicting Phosphorescence Rates of Light Organic Molecules Using Time-Dependent Density Functional Theory and the Path Integral Approach to Dynamics. *J. Chem. Theory Comput. 15*, 1896–1904.

(*132*) Peach, M. J. G., Williamson, M. J., and Tozer, D. J. (2011). Influence of Triplet Instabilities in TDDFT. *J. Chem. Theory Comput. 7*, 3578–3585.

(*133*) Peach, M. J. G., and Tozer, D. J. (2012). Overcoming Low Orbital Overlap and Triplet Instability Problems in TDDFT. *J. Phys. Chem. A 116*, 9783–9789.

(*134*) Jovanović, V., Lyskov, I., Kleinschmidt, M., and Marian, C. M. (2017). On the performance of DFT/MRCI-R and MR-MP2 in spin–orbit coupling calculations on diatomics and polyatomic organic molecules. *Mol. Phys. 115*, 109–137.

(*135*) Schäfer, A., Huber, C., and Ahlrichs, R. (1994). Fully optimized contracted Gaussian basis sets of triple zeta valence quality for atoms Li to Kr. *J. Chem. Phys. 100*, 5829–5835.

(*136*) Silva-Junior, M. R., Schreiber, M., Sauer, S. P. A., and Thiel, W. (2008). Benchmarks for electronically excited states: Time-dependent density functional theory and density functional theory based multireference configuration interaction. *J. Chem. Phys. 129*, 104103.

(*137*) Jacquemin, D., Wathelet, V., Perpète, E. A., and Adamo, C. (2009). Extensive TD-DFT Benchmark: Singlet-Excited States of Organic Molecules. *J. Chem. Theory Comput. 5*, 2420–2435.

(*138*) Bousquet, D., Fukuda, R., Jacquemin, D., Ciofini, I., Adamo, C., and Ehara, M. (2014). Benchmark Study on the Triplet Excited-State Geometries and Phosphorescence Energies of Heterocyclic Compounds: Comparison Between TD-PBE0 and SAC-CI. *J. Chem. Theory Comput. 10*, 3969–3979.

(*139*) Hourahine, B. et al. (2020). DFTB+, a software package for efficient approximate density functional theory based atomistic simulations. *J. Chem. Phys. 152*, 124101.

(*140*) Dombrowski, D. R., Schulz, T., Kleinschmidt, M., and Marian, C. M. (2023). R2022: A DFT/MRCI Ansatz with Improved Performance for Double Excitations. *J. Phys. Chem. A 127*, 2011–2025.

(*141*) Perun, S., Tatchen, J., and Marian, C. M. (2008). Singlet and Triplet Excited States and Intersystem Crossing in Free-Base Porphyrin: TDDFT and DFT/MRCI Study. *ChemPhysChem 9*, 282–292.

(*142*) Radziszewski, J. G., Waluk, J., Nepraš, M., and Michl, J. (1991). Fourier transform fluorescence and phosphorescence of porphine in rare gas matrices. *J. Phys. Chem. 95*, 1963.

(*143*) Edwards, L., Dolphin, D. H., Gouterman, M., and Adler, A. D. (1971). Porphyrins XVII. Vapor absorption spectra and redox reactions: tetraphenyl porphins and porphin. *J. Molec. Struct. 38*, 16.

(*144*) Didenko, V. V. (2001). DNA Probes Using Fluorescence Resonance Energy Transfer (FRET): Designs and Applications. *BioTechniques 31*, 1106–1121.

(*145*) Spiegel, J. D., Fulle, S., Kleinschmidt, M., Gohlke, H., and Marian, C. M. (2016). Failure of the IDA in FRET Systems at Close Inter-Dye Distances Is Moderated by Frequent Low κ^2 Values. *J. Phys. Chem. B 120*, 8845–8862.

(*146*) Voityuk, A. A., and Rösch, N. (2002). Fragment charge difference method for estimating donor–acceptor electronic coupling: Application to DNA π-stacks. *J. Chem. Phys. 117*, 5607–5616.

(*147*) Hsu, C.-P., You, Z.-Q., and Chen, H.-C. (2008). Characterization of the Short-Range Couplings in Excitation Energy Transfer. *J. Phys. Chem. C 112*, 1204–1212.

(*148*) You, Z.-Q., and Hsu, C.-P. (2010). The fragment spin difference scheme for triplet-triplet energy transfer coupling. *J. Chem. Phys. 133*, 074105.

(*149*) Vura-Weis, J., Newton, M. D., Wasielewski, M. R., and Subotnik, J. E. (2010). Characterizing the Locality of Diabatic States for Electronic Excitation Transfer By Decomposing the Diabatic Coupling. *J. Phys. Chem. C 114*, 20449–20460.

(*150*) Krueger, B. P., Scholes, G. D., and Fleming, G. R. (1998). Calculation of Couplings and Energy-Transfer Pathways between the Pigments of LH2 by the ab Initio Transition Density Cube Method. *J. Phys. Chem. B 102*, 5378–5386.

(*151*) Spiegel, J. D., Lyskov, I., Kleinschmidt, M., and Marian, C. M. (2017). Charge-transfer contributions to the excitonic coupling matrix element in BODIPY-based energy transfer cassettes. *Chem. Phys. 482*, 265–276.

(*152*) Piela, L. In *Ideas of Quantum Chemistry (Second Edition)*, Piela, L., Ed., Second Edition; Elsevier: Oxford, 2014, e99–e103.

(*153*) Engeln-Müllges, G., Niederdrenk, K., and Wodicka, R., *Numerik-Algorithmen: Verfahren, Beispiele, Anwendungen*, 10th ed.; Springer Berlin, Heidelberg: 2011, 410ff.

(*154*) Closs, G. L., Piotrowiak, P., MacInnis, J. M., and Fleming, G. R. (1988). Determination of long-distance intramolecular triplet energy-transfer rates. Quantitative comparison with electron transfer. *J. Am. Chem. Soc. 110*, 2652–2653.

A Appendix

A.1 Spoiler 2022 Benchmark: Computational Data

Table A.1: SOCME Benchmark in cm^{-1}

Transition	DFT/MRCI	TDDFT					TDA	PySOC
		A_{MN}^{LL}	A_{MN}^{LR}	A_{MN}^{RL}	A_{MN}^{RR}	A_{MN}^{aver}		
formaldehyde								
$^1n\pi^*/^3\pi\pi^*$	52	45	43	46	44	44	44	45
$^1n\pi^*/^3n\pi^*$	0	0	0	0	0	0	0	0
acetone								
$^1n\pi^*/^3\pi\pi^*$	52	44	42	44	43	43	43	44
$^1n\pi^*/^3n\pi^*$	0	0	0	0	0	0	0	0
thymine								
$^1gs/^3\pi\pi^*$	4	5	5	6	6	5	5	4
$^1gs/^3n\pi^*$	40	39	39	42	42	41	41	38
$^1n\pi^*/^3\pi\pi^*$	31	21	21	22	21	21	21	21
$^1n\pi^*/^3n\pi^*$	5	1	1	1	1	1	3	1
2-thiothymine								
$^1gs/^3\pi\pi^*$	129	97	97	108	108	102	121	97
$^1gs/^3n\pi^*$	117	143	143	152	152	147	134	143
$^1n\pi^*/^3\pi\pi^*$	124	138	135	132	129	133	109	137
$^1n\pi^*/^3n\pi^*$	67	77	79	64	66	71	105	78
4-thiothymine								
$^1gs/^3\pi\pi^*$	6	1	1	2	2	2	2	2
$^1gs/^3n\pi^*$	135	133	133	139	139	136	135	133
$^1n\pi^*/^3\pi\pi^*$	164	142	141	143	142	142	142	142
$^1n\pi^*/^3n\pi^*$	7	2	2	2	2	2	2	2
2,4-thiothymine								
$^1gs/^3\pi\pi^*$	15	3	2	3	3	3	2	2
$^1gs/^3n\pi^*$	135	134	134	140	140	137	137	134
$^1n\pi^*/^3\pi\pi^*$	163	138	137	139	137	138	137	138
$^1n\pi^*/^3n\pi^*$	17	3	3	3	3	3	3	4

Table A.2: SOCME Benchmark in cm^{-1} [cont.]

Transition	DFT/MRCI	TDDFT					TDA	PySOC
		A_{MN}^{LL}	A_{MN}^{LR}	A_{MN}^{RL}	A_{MN}^{RR}	A_{MN}^{aver}		
psoralenOO								
S_0/T_1	0	0	0	0	0	0	0	1
S_0/T_4	48	45	45	48	48	46	46	43
S_1/T_1	0	0	0	0	0	0	0	1
S_1/T_2	0	0	0	0	0	0	0	0
S_1/T_3	0	0	0	0	0	0	0	0
S_1/T_4	11	8	8	8	8	8	7	8
S_3/T_1	27	19	19	19	19	19	19	19
psoralenOS								
S_0/T_1	0	0	0	0	0	0	0	1
S_0/T_4	75	71	71	80	80	75	76	70
S_1/T_1	0	0	0	0	0	0	0	0
S_1/T_2	0	0	0	0	0	0	0	0
S_1/T_3	0	0	0	0	0	0	0	0
S_1/T_4	34	36	37	36	37	36	36	37
S_2/T_1	7	10	9	13	13	11	29	10
psoralenSO								
S_0/T_1	0	0	0	0	0	0	0	0
S_0/T_5	47	44	44	47	47	45	45	42
S_1/T_1	0	0	0	0	0	0	0	1
S_1/T_2	0	0	0	0	0	0	0	0
S_1/T_3	0	0	0	0	0	0	0	0
S_1/T_5	7	5	5	5	5	5	4	4
S_3/T_1	25	16	16	17	17	17	18	16
BODIPY								
S_0/T_1	1	1	1	1	1	1	1	1
S_1/T_1	0	0	0	0	0	0	0	0
S_1/T_2	0	0	0	0	0	0	0	0

Table A.3: Wave function coefficients and amplitudes of the low-lying states in formaldehyde

State	DFT/MRCI			TDDFT			TDA		
	E [eV]	Excitations		E [eV]	Excitations		E [eV]	Excitations	
S_1	3.97	94.5	$n_H \rightarrow \pi_L^*$	4.02	99.7	$n_H \rightarrow \pi_L^*$	4.04	99.7	$n_H \rightarrow \pi_L^*$
		2.4	$\pi_{H-1} n_H \rightarrow {\pi_L^*}^2$						
		1.4	$n_H \rightarrow \pi_{L+5}^*$						
		1.1	$n_{H-3} \rightarrow \pi_L^*$						
T_1	3.62	95.6	$n_H \rightarrow \pi_L^*$	3.29	98.5	$n_H \rightarrow \pi_L^*$	3.35	98.6	$n_H \rightarrow \pi_L^*$
		1.5	$\pi_{H-1} n_H \rightarrow {\pi_L^*}^2$						
		1.5	$n_H \rightarrow \pi_{L+5}^*$						
T_2	5.83	97.5	$\pi_{H-1} \rightarrow \pi_L^*$	5.60	99.5	$\pi_{H-1} \rightarrow \pi_L^*$	6.00	99.5	$\pi_{H-1} \rightarrow \pi_L^*$
		2.1	$\pi_{H-1} \rightarrow \pi_{L+5}^*$						

Table A.4: Wave function coefficients and amplitudes of the low-lying states in acetone

State	DFT/MRCI			TDDFT			TDA		
	E [eV]	Excitations		E [eV]	Excitations		E [eV]	Excitations	
S_1	4.50	92.0	$n_H \rightarrow \pi_L^*$	4.48	99.3	$n_H \rightarrow \pi_L^*$	4.50	99.2	$n_H \rightarrow \pi_L^*$
		1.9	$\pi_{H-1}n_H \rightarrow {\pi_L^*}^2$						
		1.6	$n_{H-7} \rightarrow \pi_L^*$						
		1.2	$n_H \rightarrow Ry_{L+4}^*$						
T_1	4.20	93.3	$n_H \rightarrow \pi_L^*$	3.84	99.1	$n_H \rightarrow \pi_L^*$	3.89	99.0	$n_H \rightarrow \pi_L^*$
		1.3	$n_{H-7} \rightarrow \pi_L^*$						
		1.2	$n_H \rightarrow Ry_{L+4}^*$						
		1.2	$\pi_{H-1}n_H \rightarrow {\pi_L^*}^2$						
T_2	6.07	89.4	$\pi_{H-1} \rightarrow \pi_L^*$	5.72	92.6	$\pi_{H-1} \rightarrow \pi_L^*$	6.04	93.5	$\pi_{H-1} \rightarrow \pi_L^*$
		6.8	$\pi_{H-6} \rightarrow \pi_L^*$		3.8	$n_{H-6} \rightarrow \pi_L^*$		3.3	$n_{H-6} \rightarrow \pi_L^*$
		1.1	$\pi_{H-1} \rightarrow Ry_{L+4}^*$		1.8	$n_{H-7} \rightarrow \pi_L^*$		1.5	$n_{H-7} \rightarrow \pi_L^*$

Table A.5: Wave function coefficients and amplitudes of the low-lying states in thymine

State	DFT/MRCI			TDDFT			TDA		
	E [eV]	Excitations		E [eV]	Excitations		E [eV]	Excitations	
S_1	3.81	66.4	$n_{H-1} \rightarrow \pi_L^*$	3.93	96.1	$n_{H-1} \rightarrow \pi_L^*$	3.94	97.0	$n_{H-1} \rightarrow \pi_L^*$
		5.1	$n_{H-1}\pi_H \rightarrow {\pi_L^2}^*$		1.3	$\pi_H \rightarrow \pi_L^*$			
		4.6	$\pi_{H-2} \rightarrow \pi_L^*$						
		4.5	$n_{H-3} \rightarrow \pi_L^*$						
		3.8	$\pi_H \rightarrow \pi_L^*$						
		2.0	$n_{H-1} \rightarrow \pi_{L+1}^*$						
		1.3	$n_{H-1}\pi_H \rightarrow \pi_L^*\pi_{L+1}^*$						
		1.1	$n_{H-1}\pi_H \rightarrow \pi_L^*\pi_{L+1}^*$						
		1.0	$n_{H-3}\pi_H \rightarrow {\pi_L^*}^2$						
		1.0	$n_{H-1} \rightarrow \pi_{L+6}^2$						
T_1	2.19	95.3	$\pi_H \rightarrow \pi_L^*$	1.87	97.0	$\pi_H \rightarrow \pi_L^*$	2.15	97.5	$\pi_H \rightarrow \pi_L^*$
		1.0	$\pi_{H-4} \rightarrow \pi_L^*$						
		1.0	$\pi_{H-8} \rightarrow \pi_L^*$						
T_2	3.69	71.3	$n_{H-1} \rightarrow \pi_L^*$	3.60	93.3	$n_{H-1} \rightarrow \pi_L^*$	3.63	94.0	$n_{H-1} \rightarrow \pi_L^*$
		4.7	$n_{H-3} \rightarrow \pi_L^*$		1.9	$n_{H-1} \rightarrow \pi_{L+1}^*$		1.8	$n_{H-1} \rightarrow \pi_{L+1}^*$
		4.5	$n_{H-1}\pi_H \rightarrow {\pi_L^2}^*$		1.4	$\pi_{H-2} \rightarrow \pi_L^*$		1.0	$n_{H-3} \rightarrow \pi_L^*$
		3.8	$\pi_{H-2} \rightarrow \pi_L^*$						
		2.1	$n_{H-1} \rightarrow \pi_{L+1}^*$						
		1.6	$n_{H-1}\pi_H \rightarrow \pi_L^*\pi_{L+1}^*$						
		1.5	$n_{H-1} \rightarrow \pi_{L+6}^2$						

Table A.6: Wave function coefficients and amplitudes of the low-lying states in 2-thiothymine

State	DFT/MRCI			TDDFT			TDA		
	E [eV]	Excitations		E [eV]	Excitations		E [eV]	Excitations	
S_1	2.09	47.3	$n/\pi_{H-1} \rightarrow \pi_L^*$	3.13	73.8	$n/\pi_{H-1} \rightarrow \pi_L^*$	3.36	63.8	$n/\pi_{H-1} \rightarrow \pi_L^*$
		41.2	$n/\pi_H \rightarrow \pi_L^*$		18.7	$n/\pi_H \rightarrow \pi_L^*$		18.0	$n/\pi_H \rightarrow \pi_L^*$
		1.5	$\pi/n_{H-2} \rightarrow \pi_L^*$		3.2	$n/\pi_H \rightarrow \pi_{L+1}^*$		7.7	$n/\pi_{H-1} \rightarrow \pi_{L+1}^*$
		1.3	$\pi/n_{H-2}n/\pi_H \rightarrow {\pi_L^*}^2$					2.5	$n/\pi_{H-2} \rightarrow \pi_L^*$
		1.2	$n/{\pi_{H-1}}^2 \rightarrow {\pi_L^*}^2$					1.7	$n/\pi_H \rightarrow \pi_{L+1}^*$
		1.0	$n/{\pi_H}^2 \rightarrow {\pi_L^*}^2$					1.3	$n/\pi_{H-3} \rightarrow \pi_L^*$
								1.1	$n_{H-5} \rightarrow \pi_L^*$
S_2	2.84	43.0	$n/\pi_H \rightarrow \pi_L^*$	2.26	77.9	$n/\pi_H \rightarrow \pi_L^*$	2.29	75.4	$n/\pi_H \rightarrow \pi_L^*$
		41.2	$n/\pi_{H-1} \rightarrow \pi_L^*$		21.1	$n/\pi_{H-1} \rightarrow \pi_L^*$		23.4	$n/\pi_{H-1} \rightarrow \pi_L^*$
		1.9	$\pi/n_{H-2}\pi/nH \rightarrow {\pi_L^*}^2$						
		1.5	$n/\pi_H \rightarrow \pi_{L+1}^*$						
		1.2	$n/\pi_{H-1}n/\pi_H \rightarrow {\pi_L^*}^2$						
T_1	1.79	81.0	$n/\pi_H \rightarrow \pi_L^*$	1.67	64.3	$n/\pi_H \rightarrow \pi_L^*$	1.80	88.0	$n/\pi_H \rightarrow \pi_L^*$
		7.2	$n/\pi_{H-1} \rightarrow \pi_L^*$		32.2	$n/\pi_{H-1} \rightarrow \pi_L^*$		9.5	$n/\pi_{H-1} \rightarrow \pi_L^*$
		3.9	$\pi/n_{H-2} \rightarrow \pi_L^*$		2.0	$\pi/n_{H-2} \rightarrow \pi_L^*$		1.2	$\pi/n_{H-2} \rightarrow \pi_L^*$
		1.3	$n/\pi_{H-1}n/\pi_H \rightarrow {\pi_L^*}^2$						
T_2	2.05	84.3	$n/\pi_{H-1} \rightarrow \pi_L^*$	1.88	64.5	$n/\pi_{H-1} \rightarrow \pi_L^*$	1.96	87.8	$n/\pi_{H-1} \rightarrow \pi_L^*$
		7.2	$n/\pi_H \rightarrow \pi_L^*$		33.9	$n/\pi_H \rightarrow \pi_L^*$		10.2	$n/\pi_H \rightarrow \pi_L^*$
		1.2	$\pi/n_{H-2} \rightarrow \pi_L^*$						

Table A.7: Wave function coefficients and amplitudes of the low-lying states in 4-thiothymine

State	DFT/MRCI			TDDFT			TDA		
	E [eV]	Excitations		E [eV]	Excitations		E [eV]	Excitations	
S_1	2.41	87.5	$n_H \rightarrow \pi_L^*$	2.51	99.3	$n_H \rightarrow \pi_L^*$	2.52	99.3	$n_H \rightarrow \pi_L^*$
		6.7	$\pi_{H-1} n_H \rightarrow {\pi_L^*}^2$						
		1.1	$n_H \rightarrow \pi_{L+1}$						
T_1	2.27	94.7	$\pi_{H-1} \rightarrow \pi_L^*$	2.10	98.0	$\pi_{H-1} \rightarrow \pi_L^*$	2.29	98.4	$\pi_{H-1} \rightarrow \pi_L^*$
T_2	2.30	88.5	$n_H \rightarrow \pi_L^*$	2.20	98.4	$n_H \rightarrow \pi_L^*$	2.22	98.2	$n_H \rightarrow \pi_L^*$
		5.3	$\pi_{H-1} n_H \rightarrow {\pi_L^*}^2$		1.1	$n_H \rightarrow \pi_{L+1}$			
		1.4	$n_H \rightarrow \pi_{L+1}$						

Table A.8: Wave function coefficients and amplitudes of the low-lying states in 2,4-thiothymine

State	DFT/MRCI			TDDFT			TDA		
	E [eV]	Excitations		E [eV]	Excitations		E [eV]	Excitations	
S_1	2.28	56.7	$n_H \rightarrow \pi_L^*$	2.48	85.7	$n_H \rightarrow \pi_L^*$	2.49	86.0	$n_H \rightarrow \pi_L^*$
		28.5	$n_{H-3} \rightarrow \pi_L^*$		13.3	$n_{H-3} \rightarrow \pi_L^*$		13.0	$n_{H-3} \rightarrow \pi_L^*$
		3.0	$\pi_{H-2} n_H \rightarrow {\pi_L^*}^2$						
		1.9	$n_{H-3} \pi_{H-2} \rightarrow {\pi_L^*}^2$						
		1.4	$\pi_{H-1} \rightarrow \pi_L^*$						
T_1	2.17	55.2	$n_H \rightarrow \pi_L^*$	2.17	78.3	$n_H \rightarrow \pi_L^*$	2.19	78.7	$n_H \rightarrow \pi_L^*$
		28.4	$n_{H-3} \rightarrow \pi_L^*$		19.3	$n_{H-3} \rightarrow \pi_L^*$		19.1	$n_{H-3} \rightarrow \pi_L^*$
		2.9	$\pi_{H-1} \rightarrow \pi_L^*$		1.0	$n_H \rightarrow \pi_{L+1}$			
		2.3	$\pi_{H-2} n_H \rightarrow {\pi_L^*}^2$						
		1.6	$\pi_{H-2} \rightarrow \pi_L^*$						
		1.5	$n_{H-3} \pi_{H-2} \rightarrow {\pi_L^*}^2$						
T_2	2.25	71.9	$\pi_{H-2} \rightarrow \pi_L^*$	2.08	86.0	$\pi_{H-2} \rightarrow \pi_L^*$	2.28	84.9	$\pi_{H-2} \rightarrow \pi_L^*$
		18.6	$\pi_{H-1} \rightarrow \pi_L^*$		11.5	$\pi_{H-1} \rightarrow \pi_L^*$		12.9	$\pi_{H-1} \rightarrow \pi_L^*$
		2.2	$n_H \rightarrow \pi_L^*$						
		1.4	$n_{H-3} \rightarrow \pi_L^*$						

Table A.9: Wave function coefficients and amplitudes of the low-lying states in psoralenOO

State	DFT/MRCI			TDDFT			TDA		
	E [eV]	Excitations		E [eV]	Excitations		E [eV]	Excitations	
S_1	3.85	77.6	$\pi_H \rightarrow \pi_L$	3.82	91.5	$\pi_H \rightarrow \pi_L$	3.91	85.1	$\pi_H \rightarrow \pi_L$
		6.3	$\pi_{H-1} \rightarrow \pi_{L+1}$		4.0	$\pi_{H-1} \rightarrow \pi_{L+1}$		7.2	$\pi_{H-1} \rightarrow \pi_{L+1}$
		1.3	$\pi_H \pi_H \rightarrow {\pi_L}^2$		3.3	$\pi_{H-1} \rightarrow \pi_L$		5.5	$\pi_{H-1} \rightarrow \pi_L$
S_3	4.48	69.4	$n_{H-2} \rightarrow \pi_L$	4.51	94.9	$n_{H-2} \rightarrow \pi_L$	4.52	95.0	$n_{H-2} \rightarrow \pi_L$
		9.2	$n_{H-2} \rightarrow \pi_{L+2}$		2.9	$n_{H-2} \rightarrow \pi_{L+2}$		2.8	$n_{H-2} \rightarrow \pi_{L+2}$
		2.7	$n_{H-2} \rightarrow \pi_{L+1}$		1.1	$n_{H-2} \rightarrow \pi_{L+1}$		1.0	$n_{H-2} \rightarrow \pi_{L+1}$
		2.5	$n_{H-2} \rightarrow \pi_{L+3}$						
		1.9	$n_{H-2} \rightarrow \pi_{L+12}$						
		1.4	$n_{H-2}\pi_{H-1} \rightarrow {\pi_L}^2$						
T_1	2.99	47.7	$\pi_{H-1} \rightarrow \pi_L$	2.85	61.5	$\pi_{H-1} \rightarrow \pi_L$	3.20	47.1	$\pi_{H-1} \rightarrow \pi_L$
		33.7	$\pi_H \rightarrow \pi_L$		25.0	$\pi_H \rightarrow \pi_L$		31.1	$\pi_H \rightarrow \pi_L$
		3.8	$\pi_H \rightarrow \pi_{L+1}$		6.4	$\pi_H \rightarrow \pi_{L+1}$		14.7	$\pi_H \rightarrow \pi_{L+1}$
		3.5	$\pi_{H-4} \rightarrow \pi_L$		2.9	$\pi_{H-4} \rightarrow \pi_L$		2.0	$\pi_{H-1} \rightarrow \pi_{L+1}$
		1.1	$\pi_{H-3} \rightarrow \pi_L$					1.1	$\pi_{H-4} \rightarrow \pi_L$
								1.0	$\pi_{H-1} \rightarrow \pi_{L+2}$
T_2	3.30	39.5	$\pi_H \rightarrow \pi_L$	3.03	62.2	$\pi_H \rightarrow \pi_L$	3.02	60.8	$\pi_H \rightarrow \pi_L$
		21.8	$\pi_H \rightarrow \pi_{L+1}$		16.8	$\pi_H \rightarrow \pi_{L+1}$		33.9	$\pi_{H-1} \rightarrow \pi_L$
		17.6	$\pi_{H-1} \rightarrow \pi_L$		12.5	$\pi_{H-1} \rightarrow \pi_L$		1.4	$\pi_{H-4} \rightarrow \pi_L$
		8.6	$\pi_{H-1} \rightarrow \pi_{L+1}$		3.4	$\pi_{H-1} \rightarrow \pi_{L+1}$			
		2.1	$\pi_{H-3} \rightarrow \pi_{L+3}$		1.3	$\pi_{H-3} \rightarrow \pi_{L+3}$			
					1.2	$\pi_{H-1} \rightarrow \pi_{L+2}$			
T_3	3.78	54.1	$\pi_H \rightarrow \pi_{L+1}$	3.68	63.9	$\pi_H \rightarrow \pi_{L+1}$	3.78	75.1	$\pi_H \rightarrow \pi_{L+1}$
		18.1	$\pi_{H-1} \rightarrow \pi_L$		17.4	$\pi_{H-1} \rightarrow \pi_L$		12.5	$\pi_{H-1} \rightarrow \pi_L$
		7.8	$\pi_H \rightarrow \pi_L$		7.9	$\pi_H \rightarrow \pi_L$		3.9	$\pi_H \rightarrow \pi_L$
		3.0	$\pi_H \rightarrow \pi_{L+2}$		2.5	$\pi_H \rightarrow \pi_{L+2}$		1.8	$\pi_{H-1} \rightarrow \pi_{L+1}$
		2.2	$\pi_{H-3} \rightarrow \pi_L$		2.1	$\pi_{H-1} \rightarrow \pi_{L+1}$		1.8	$\pi_H \rightarrow \pi_{L+2}$
		1.2	$\pi_{H-1} \rightarrow \pi_{L+2}$		1.3	$\pi_{H-4} \rightarrow \pi_L$		1.1	$\pi_{H-3} \rightarrow \pi_{L+3}$
		1.0	$\pi_{H-3} \rightarrow \pi_{L+3}$		1.2	$\pi_{H-3} \rightarrow \pi_{L+3}$			
T_4	4.31	68.5	$n_{H-2} \rightarrow \pi_L$	4.15	89.7	$n_{H-2} \rightarrow \pi_L$	4.18	90.2	$n_{H-2} \rightarrow \pi_L$
		10.7	$n_{H-2} \rightarrow \pi_{L+2}$		6.3	$n_{H-2} \rightarrow \pi_{L+2}$		5.9	$n_{H-2} \rightarrow \pi_{L+2}$
		3.0	$n_{H-2} \rightarrow \pi_{L+3}$		1.4	$n_{H-2} \rightarrow \pi_{L+3}$		1.3	$n_{H-2} \rightarrow \pi_{L+3}$
		2.6	$n_{H-2} \rightarrow \pi_{L+1}$		1.1	$n_{H-2} \rightarrow \pi_{L+1}$		1.1	$n_{H-2} \rightarrow \pi_{L+1}$
		2.5	$n_{H-2} \rightarrow \pi_{L+12}$		1.0	$n_{H-2} \rightarrow \pi_{L+9}$			
		1.0	$n_{H-2}\pi_{H-1} \rightarrow {\pi_L}^2$						

Table A.10: Wave function coefficients and amplitudes of the low-lying states in psoralenOS

State	DFT/MRCI			TDDFT			TDA		
	E [eV]	Excitations		E [eV]	Excitations		E [eV]	Excitations	
S_1	3.52	79.7	$\pi_H \rightarrow \pi_L$	3.56	95.0	$\pi_H \rightarrow \pi_L$	3.66	90.2	$\pi_H \rightarrow \pi_L$
		3.8	$\pi_{H-1} \rightarrow \pi_{L+1}$		2.5	$\pi_{H-1} \rightarrow \pi_{L+1}$		4.9	$\pi_{H-1} \rightarrow \pi_{L+1}$
		1.4	$\pi_{H-3} \rightarrow \pi_L$					1.9	$\pi_{H-1} \rightarrow \pi_L$
		1.0	${\pi_H}^2 \rightarrow {\pi_L}^2$						
S_2	3.83	72.7	$n_{H-2} \rightarrow \pi_L$	3.91	95.3	$n_{H-2} \rightarrow \pi_L$	3.92	95.3	$n_{H-2} \rightarrow \pi_L$
		8.9	$n_{H-2} \rightarrow \pi_{L+2}$		3.3	$n_{H-2} \rightarrow \pi_{L+2}$		3.2	$n_{H-2} \rightarrow 12a'$
		1.4	$n_{H-2}\pi_{H-1} \rightarrow {\pi_L}^2$						
		1.3	$n_{H-2} \rightarrow \pi_{L+4}$						
		1.1	$n_{H-6} \rightarrow \pi_L$						
		1.1	$n_{H-2} \rightarrow \pi_{L+1}$						
		1.1	$n_{H-2} \rightarrow \pi_{L+11}$						
T_1	2.89	44.2	$\pi_H \rightarrow \pi_L$	2.76	48.7	$\pi_{H-1} \rightarrow \pi_L$	3.09	62.9	$\pi_{H-1} \rightarrow \pi_L$
		38.6	$\pi_{H-1} \rightarrow \pi_L$		40.2	$\pi_H \rightarrow \pi_L$		14.5	$\pi_H \rightarrow \pi_L$
		3.6	$\pi_{H-4} \rightarrow \pi_L$		5.1	$\pi_H \rightarrow \pi_{L+1}$		14.3	$\pi_H \rightarrow \pi_{L+1}$
		2.4	$\pi_H \rightarrow \pi_{L+1}$		2.7	$\pi_{H-4} \rightarrow \pi_L$		2.0	$\pi_{H-4} \rightarrow \pi_L$
								1.2	$\pi_{H-1} \rightarrow \pi_{L+2}$
T_2	3.15	34.2	$\pi_H \rightarrow \pi_L$	2.90	50.9	$\pi_H \rightarrow \pi_L$	2.88	80.4	$\pi_H \rightarrow \pi_L$
		27.9	$\pi_{H-1} \rightarrow \pi_L$		22.5	$\pi_{H-1} \rightarrow \pi_L$		16.0	$\pi_{H-1} \rightarrow \pi_L$
		17.6	$\pi_H \rightarrow \pi_{L+1}$		17.2	$\pi_H \rightarrow \pi_{L+1}$			
		4.1	$\pi_{H-1} \rightarrow \pi_{L+1}$		1.8	$\pi_{H-1} \rightarrow \pi_{L+2}$			
		1.7	$\pi_{H-3} \rightarrow \pi_{L+1}$		1.7	$\pi_{H-1} \rightarrow \pi_{L+1}$			
		1.4	$\pi_{H-1} \rightarrow \pi_{L+2}$		1.7	$\pi_{H-3} \rightarrow \pi_{L+1}$			
		1.3	$\pi_{H-3} \rightarrow \pi_{L+4}$						
T_3	3.47	58.3	$\pi_H \rightarrow \pi_{L+1}$	3.37	63.9	$\pi_H \rightarrow \pi_{L+1}$	3.49	74.9	$\pi_H \rightarrow \pi_{L+1}$
		16.4	$\pi_{H-1} \rightarrow \pi_L$		19.1	$\pi_{H-1} \rightarrow \pi_L$		13.7	$\pi_{H-1} \rightarrow \pi_L$
		4.9	$\pi_H \rightarrow \pi_L$		5.0	$\pi_H \rightarrow \pi_L$		2.1	$\pi_{H-1} \rightarrow \pi_{L+1}$
		3.3	$\pi_{H-3} \rightarrow \pi_L$		2.3	$\pi_{H-4} \rightarrow \pi_L$		2.1	$\pi_{H-3} \rightarrow \pi_L$
		1.8	$\pi_{H-1} \rightarrow \pi_{L+1}$		2.2	$\pi_{H-1} \rightarrow \pi_{L+1}$		1.8	$\pi_H \rightarrow \pi_L$
		1.5	$\pi_{H-4} \rightarrow \pi_L$		2.2	$\pi_{H-3} \rightarrow \pi_L$		1.1	$\pi_{H-4} \rightarrow \pi_L$
		1.1	$\pi_{H-3} \rightarrow \pi_{L+4}$		1.0	$\pi_{H-3} \rightarrow \pi_{L+3}$		1.0	$\pi_{H-3} \rightarrow \pi_{L+1}$
		1.0	$\pi_{H-3} \rightarrow \pi_{L+1}$		1.0	$\pi_{H-3} \rightarrow \pi_{L+1}$			
T_4	3.65	72.1	$n_{H-2} \rightarrow \pi_L$	3.55	90.7	$n_{H-2} \rightarrow \pi_L$	3.59	91.1	$n_{H-2} \rightarrow \pi_L$
		10.5	$n_{H-2} \rightarrow \pi_{L+2}$		6.7	$n_{H-2} \rightarrow \pi_{L+2}$		6.3	$n_{H-2} \rightarrow \pi_{L+2}$
		1.6	$n_{H-2} \rightarrow \pi_{L+4}$						
		1.4	$n_{H-2} \rightarrow \pi_{L+11}$						
		1.1	$n_{H-6} \rightarrow \pi_L$						
		1.0	$n_{H-2} \rightarrow \pi_{L+1}$						

Table A.11: Wave function coefficients and amplitudes of the low-lying states in psoralenSO

State	DFT/MRCI			TDDFT			TDA		
	E [eV]	Excitations		E [eV]	Excitations		E [eV]	Excitations	
S_1	3.71	68.3	$\pi_H \rightarrow \pi_L$	3.64	96.1	$\pi_H \rightarrow \pi_L$	3.72	93.0	$\pi_H \rightarrow \pi_L$
		7.6	$\pi_{H-1} \rightarrow \pi_{L+1}$		2.6	$\pi_{H-1} \rightarrow \pi_{L+1}$		4.4	$\pi_{H-1} \rightarrow \pi_{L+1}$
		6.3	$\pi_{H-1} \rightarrow \pi_L$						
		1.7	$\pi_{H-1}\pi_H \rightarrow {\pi_L}^2$						
		1.4	$\pi_H \rightarrow \pi_{L+1}$						
		1.0	$\pi_H \rightarrow \pi_{L+2}$						
S_3	4.45	69.1	$n_{H-3} \rightarrow \pi_L$	4.47	94.3	$n_{H-3} \rightarrow \pi_L$	4.48	95.3	$n_{H-3} \rightarrow \pi_L$
		10.0	$n_{H-3} \rightarrow \pi_{L+2}$		3.1	$n_{H-3} \rightarrow \pi_{L+2}$		3.0	$n_{H-3} \rightarrow \pi_{L+2}$
		3.7	$n_{H-3} \rightarrow \pi_{L+4}$						
		1.9	$n_{H-3} \rightarrow \pi_{L+12}$						
		1.6	$n_{H-3}\pi_{H-1} \rightarrow {\pi_L}^2$						
T_1	2.95	71.6	$\pi_{H-1} \rightarrow \pi_L$	2.76	64.5	$\pi_{H-1} \rightarrow \pi_L$	2.98	76.2	$\pi_{H-1} \rightarrow \pi_L$
		6.7	$\pi_{H-2} \rightarrow \pi_L$		11.4	$\pi_H \rightarrow \pi_{L+1}$		7.9	$\pi_H \rightarrow \pi_L$
		4.5	$\pi_H \rightarrow \pi_{L+1}$		10.2	$\pi_H \rightarrow \pi_L$		5.4	$\pi_H \rightarrow \pi_{L+1}$
		3.0	$\pi_{H-4} \rightarrow \pi_L$		5.7	$\pi_{H-2} \rightarrow \pi_L$		4.5	$\pi_{H-2} \rightarrow \pi_L$
		2.2	$\pi_H \rightarrow \pi_L$		1.7	$\pi_{H-4} \rightarrow \pi_L$		1.5	$\pi_{H-4} \rightarrow \pi_L$
		1.8	$\pi_{H-4} \rightarrow \pi_{L+2}$		1.4	$\pi_{H-1} \rightarrow \pi_{L+1}$			
		1.3	$\pi_{H-1} \rightarrow \pi_{L+1}$		1.2	$\pi_{H-4} \rightarrow \pi_{L+2}$			
T_2	3.19	57.9	$\pi_H \rightarrow \pi_L$	2.99	65.3	$\pi_H \rightarrow \pi_L$	3.07	78.6	$\pi_H \rightarrow \pi_L$
		20.1	$\pi_H \rightarrow \pi_{L+1}$		20.4	$\pi_{H-1} \rightarrow \pi_L$		12.6	$\pi_{H-1} \rightarrow \pi_L$
		6.2	$\pi_{H-1} \rightarrow \pi_L$		8.8	$\pi_H \rightarrow \pi_{L+1}$		4.7	$\pi_H \rightarrow \pi_{L+1}$
		1.3	$\pi_H \rightarrow \pi_{L+2}$						
		1.1	$\pi_{H-4} \rightarrow \pi_L$						
T_3	3.54	57.3	$\pi_H \rightarrow \pi_{L+1}$	3.42	68.9	$\pi_H \rightarrow \pi_{L+1}$	3.54	81.8	$\pi_H \rightarrow \pi_{L+1}$
		20.2	$\pi_H \rightarrow \pi_L$		18.4	$\pi_H \rightarrow \pi_L$		8.3	$\pi_H \rightarrow \pi_L$
		4.7	$\pi_{H-1} \rightarrow \pi_{L+1}$		3.3	$\pi_{H-1} \rightarrow \pi_L$		2.5	$\pi_{H-1} \rightarrow \pi_L$
		2.0	$\pi_H \rightarrow \pi_{L+2}$		2.1	$\pi_{H-1} \rightarrow \pi_{L+1}$		1.8	$\pi_{H-1} \rightarrow \pi_{L+1}$
		1.3	$\pi_{H-2} \rightarrow \pi_L$		1.1	$\pi_H \rightarrow \pi_{L+2}$			
		1.2	$\pi_{H-1} \rightarrow \pi_L$		1.1	$\pi_{H-2} \rightarrow \pi_L$			
T_5	4.27	68.0	$n_{H-3} \rightarrow \pi_L$	4.11	89.8	$n_{H-3} \rightarrow \pi_L$	4.15	90.3	$n_{H-3} \rightarrow \pi_L$
		11.5	$n_{H-3} \rightarrow \pi_{L+2}$		6.4	$n_{H-3} \rightarrow \pi_{L+2}$		6.1	$n_{H-3} \rightarrow \pi_{L+2}$
		4.5	$n_{H-3} \rightarrow \pi_{L+4}$		2.2	$n_{H-3} \rightarrow \pi_{L+4}$		2.1	$n_{H-3} \rightarrow \pi_{L+4}$
		2.4	$n_{H-3} \rightarrow \pi_{L+12}$		1.0	$n_{H-3} \rightarrow \pi_{L+9}$			
		1.1	$n_{H-3}\pi_{H-1} \rightarrow {\pi_L}^2$						

Table A.12: Wave function coefficients and amplitudes of the low-lying states in BODIPY

State	DFT/MRCI			TDDFT			TDA		
	E [eV]	Excitations		E [eV]	Excitations		E [eV]	Excitations	
S_1	2.27	85.3	$\pi_H \rightarrow \pi_L$	2.58	96.4	$\pi_H \rightarrow \pi_L$	2.88	88.3	$\pi_H \rightarrow \pi_L$
		1.3	$\pi_{H-1}\pi_H \rightarrow {\pi_L}^2$		1.2	$\pi_{H-2} \rightarrow \pi_L$		3.6	$\pi_H \rightarrow \pi_{L+1}$
					1.0	$\pi_H \rightarrow \pi_{L+1}$		3.6	$\pi_{H-2} \rightarrow \pi_L$
T_1	1.42	89.9	$\pi_H \rightarrow \pi_L$	1.34	97.7	$\pi_H \rightarrow \pi_L$	1.46	98.1	$\pi_H \rightarrow \pi_L$
T_2	2.77	70.4	$\pi_{H-1} \rightarrow \pi_L$	2.70	86.7	$\pi_{H-1} \rightarrow \pi_L$	2.76	89.2	$\pi_{H-1} \rightarrow \pi_L$
		6.6	$\pi_H \rightarrow \pi_{L+1}$		3.5	$\pi_H \rightarrow \pi_{L+1}$		3.7	$\pi_H \rightarrow \pi_{L+1}$
		2.8	$\pi_{H-5} \rightarrow \pi_L$		2.1	$\pi_{H-5} \rightarrow \pi_L$		1.6	$\pi_{H-5} \rightarrow \pi_L$
		2.7	$\pi_{H-1} \rightarrow \pi_{L+2}$		1.3	$\pi_H \rightarrow \pi_{L+2}$		1.0	$\pi_H \rightarrow \pi_{L+2}$
		2.6	$\pi_H \rightarrow \pi_{L+2}$		1.1	$\pi_{H-1} \rightarrow \pi_{L+2}$			
		1.7	$\pi_H \rightarrow \pi_{L+3}$		1.0	$\pi_{H-2} \rightarrow \pi_L$			
		1.6	$\pi_{H-4} \rightarrow \pi_L$		1.0	$\pi_{H-4} \rightarrow \pi_L$			

Table A.13: Wave function coefficients and amplitudes of the low-lying states in TXB at the S_0 geometry

State	DFT/MRCI			TDDFT			TDA		
	E [eV]	Excitations		E [eV]	Excitations		E [eV]	Excitations	
S_1	3.46	88.2	$\pi_H \rightarrow \pi_L$	3.11	98.8	$\pi_H \rightarrow \pi_L$	3.14	98.2	$\pi_H \rightarrow \pi_L$
T_1	2.91	63.5	$\pi_H \rightarrow \pi_L$	2.69	78.7	$\pi_H \rightarrow \pi_L$	2.80	89.2	$\pi_H \rightarrow \pi_L$
		19.3	$\pi_H \rightarrow \pi_{L+1}$		12.3	$\pi_H \rightarrow \pi_{L+1}$		6.2	$\pi_H \rightarrow \pi_{L+1}$
		2.2	$\pi_{H-5} \rightarrow \pi_{L+1}$		1.5	$\pi_{H-3} \rightarrow \pi_{L+5}$			
		1.7	$\pi_{H-4} \rightarrow \pi_{L+1}$		1.3	$\pi_{H-5} \rightarrow \pi_{L+1}$			
		1.2	$\pi_{H-5} \rightarrow \pi_L$						
T_2	3.01	55.1	$\pi_{H-1} \rightarrow \pi_L$	2.85	67.6	$\pi_{H-1} \rightarrow \pi_L$	3.00	76.3	$\pi_{H-1} \rightarrow \pi_L$
		10.4	$\pi_{H-2} \rightarrow \pi_L$		11.0	$\pi_{H-3} \rightarrow \pi_{L+1}$		10.6	$\pi_{H-3} \rightarrow \pi_L$
		9.7	$\pi_{H-5} \rightarrow \pi_{L+2}$		5.8	$\pi_{H_5} \rightarrow \pi_{L+2}$		3.9	$\pi_{H-5} \rightarrow \pi_{L+2}$
		8.2	$\pi_{H-3} \rightarrow \pi_L$		3.7	$\pi_{H-2} \rightarrow \pi_L$		3.3	$\pi_{H-2} \rightarrow \pi_L$
		2.6	$\pi_{H-1} \rightarrow \pi_{L+1}$		2.6	$\pi_{H-2} \rightarrow \pi_{L+3}$		1.1	$\pi_{H-1} \rightarrow \pi_{L+1}$
		1.5	$\pi_{H-2} \rightarrow \pi_{L+3}$		1.9	$\pi_{H-1} \rightarrow \pi_{L+1}$			
		1.4	$\pi_H \rightarrow \pi_{L+2}$		1.8	$\pi_{H-4} \rightarrow \pi_{L+4}$			
					1.0	$\pi_H \rightarrow \pi_{L+2}$			

Table A.14: Wave function coefficients and amplitudes of the low-lying states in pyrazine at the S_0 geometry

State	DFT/MRCI			TDDFT			TDA		
	E [eV]	Excitations		E [eV]	Excitations		E [eV]	Excitations	
S_1	3.84	92.2	$n_H \rightarrow \pi_L$	3.79	99.6	$n_H \rightarrow \pi_L$	3.84	99.5	$n_H \rightarrow \pi_L$
		3.0	$n_{H-3}\pi_{H-2} \rightarrow {\pi_L}^2$		4.2	$n_{H-2} \rightarrow \pi_{L+7}$			
		1.1	$n_{H-3} \rightarrow \pi_{L+7}$						
T_1	3.39	92.2	$n_H \rightarrow \pi_L$	3.00	98.0	$n_H \rightarrow \pi_L$	3.08	98.0	$n_H \rightarrow \pi_L$
		2.0	$n_{H-3} \rightarrow \pi_{L+7}$		1.6	$n_{H-2} \rightarrow \pi_{L+7}$		1.5	$n_{H-2} \rightarrow \pi_{L+7}$
		1.6	$n_{H-3}\pi_{H-2} \rightarrow {\pi_L}^2$						
T_2	4.15	72.3	$\pi_{H-1} \rightarrow \pi_{L+1}$	3.83	64.8	$\pi_{H-1} \rightarrow \pi_{L+1}$	4.29	99.5	$\pi_{H-1} \rightarrow \pi_L$
		22.4	$\pi_{H-2} \rightarrow \pi_L$		31.9	$\pi_{H-3} \rightarrow \pi_L$			
		1.6	$\pi_{H-5} \rightarrow \pi_{L+7}$		2.2	$\pi_{H-5} \rightarrow \pi_{L+7}$			

Table A.15: Wave function coefficients and amplitudes of the low-lying states in porphyrin at the S_0 geometry

State	DFT/MRCI			TDDFT			TDA		
	E [eV]	Excitations		E [eV]	Excitations		E [eV]	Excitations	
S_1	1.94	44.6	$\pi_H \rightarrow \pi_L$	2.29	61.6	$\pi_H \rightarrow \pi_L$	2.35	57.2	$\pi_H \rightarrow \pi_L$
		35.0	$\pi_{H-1} \rightarrow \pi_{L+1}$		37.3	$\pi_{H-1} \rightarrow \pi_{L+1}$		41.2	$\pi_{H-1} \rightarrow \pi_{L+1}$
		1.4	$\pi_{H-1}\pi_H \rightarrow \pi_L\pi_{L+2}$						
		1.3	$\pi_{H-6}\pi_{H-1} \rightarrow \pi_L\pi_{L+1}$						
T_1	1.63	80.3	$\pi_H \rightarrow \pi_L$	1.28	74.5	$\pi_H \rightarrow \pi_L$	1.69	86.3	$\pi_H \rightarrow \pi_L$
		5.2	$\pi_{H-1} \rightarrow \pi_{L+1}$		20.7	$\pi_{H-1} \rightarrow \pi_{L+1}$		10.3	$\pi_{H-1} \rightarrow \pi_{L+1}$
		1.1	$\pi_{H-6} \rightarrow \pi_{L+2}$		1.9	$\pi_{H-6} \rightarrow \pi_{L+2}$		1.3	$\pi_{H-6} \rightarrow \pi_{L+2}$
		1.1	$\pi_{H-6}\pi_H \rightarrow \pi_L\pi_{L+1}$						
T_2	1.74	66.9	$\pi_H \rightarrow \pi_{L+1}$	1.69	92.6	$\pi_H \rightarrow \pi_{L+1}$	1.83	98.1	$\pi_H \rightarrow \pi_{L+1}$
		19.5	$\pi_{H-1} \rightarrow \pi_L$		4.7	$\pi_{H-1} \rightarrow \pi_L$			
		1.6	$\pi_{H-1}\pi_H \rightarrow \pi_{L+1}\pi_{L+2}$						

A.2 Derivation Of Matrix Elements For Excitonic Couplings

$$\left\langle {}^{1,3}\Psi_{DA^*}\middle|\sum_{ij} h_{ij}\hat{E}_i^j + \frac{1}{2}\sum_{ijkl} V_{ikjl}(\hat{E}_i^j\hat{E}_k^l - \delta_{jk}\hat{E}_i^l)\middle|{}^{1,3}\Psi_{D^*A}\right\rangle \tag{A.1}$$
$$= \frac{1}{2}\Big\langle {}^{1,3}\Psi_{DA^*}\Big| V_{iljk}(\hat{E}_i^j\hat{E}_l^k - \delta_{jl}\hat{E}_k^i) + V_{lijk}(\hat{E}_l^j\hat{E}_i^k - \delta_{ji}\hat{E}_l^k)$$
$$+ V_{ilkj}(\hat{E}_i^k\hat{E}_l^j - \delta_{kl}\hat{E}_i^j) + V_{likj}(\hat{E}_l^k\hat{E}_i^j - \delta_{ki}\hat{E}_l^j)\Big|{}^{1,3}\Psi_{D^*A}\Big\rangle$$

$$\left\langle {}^{1}\Psi_{DA^*}\middle|\sum_{ij} h_{ij}\hat{E}_i^j + \frac{1}{2}\sum_{ijkl} V_{ikjl}(\hat{E}_i^j\hat{E}_k^l - \delta_{jk}\hat{E}_i^l)\middle|{}^{1}\Psi_{D^*A}\right\rangle \tag{A.2}$$
$$= \frac{1}{2}\Big(2V_{iljk} - V_{lijk} - V_{ilkj} + 2V_{likj}\Big)$$
$$= 2V_{ikjl} - V_{iklj}$$

$$\left\langle {}^{3}\Psi_{DA^*}\middle|\sum_{ij} h_{ij}\hat{E}_i^j + \frac{1}{2}\sum_{ijkl} V_{ikjl}(\hat{E}_i^j\hat{E}_k^l - \delta_{jk}\hat{E}_i^l)\middle|{}^{3}\Psi_{D^*A}\right\rangle \tag{A.3}$$
$$= \frac{1}{2}\Big(-V_{ilkj} - V_{lijk}\Big)$$
$$= -V_{ilkj}$$

$$\left\langle {}^{1,3}\Psi_{D^+A^-}\middle|\sum_{ij} h_{ij}\hat{E}_i^j + \frac{1}{2}\sum_{ijkl} V_{ikjl}(\hat{E}_i^j\hat{E}_k^l - \delta_{jk}\hat{E}_i^l)\middle|{}^{1,3}\Psi_{D^*A}\right\rangle \tag{A.4}$$
$$= h_{lj} + \frac{1}{2}\Big\langle {}^{1,3}\Psi_{D^+A^-}\Big| V_{ilij}(\hat{E}_i^i\hat{E}_l^j - \delta_{il}\hat{E}_i^j) + V_{liji}(\hat{E}_l^j\hat{E}_i^i - \delta_{ji}\hat{E}_l^i)$$
$$+ V_{kljk}(\hat{E}_k^j\hat{E}_l^k - \delta_{jl}\hat{E}_k^k) + V_{klkj}(\hat{E}_k^k\hat{E}_l^j - \delta_{kl}\hat{E}_k^j)$$
$$+ V_{liij}(\hat{E}_l^i\hat{E}_i^j - \delta_{ii}\hat{E}_l^j) + V_{liji}(\hat{E}_l^j\hat{E}_i^i - \delta_{ji}\hat{E}_l^i)$$
$$+ V_{lkjk}(\hat{E}_l^j\hat{E}_k^k - \delta_{jk}\hat{E}_l^k) + V_{lkkj}(\hat{E}_l^k\hat{E}_k^j - \delta_{kk}\hat{E}_l^j)\Big|{}^{1,3}\Psi_{D^*A}\Big\rangle$$

$$\left\langle {}^{1}\Psi_{D^+A^-}\middle|\sum_{ij} h_{ij}\hat{E}_i^j + \frac{1}{2}\sum_{ijkl} V_{ikjl}(\hat{E}_i^j\hat{E}_k^l - \delta_{jk}\hat{E}_i^l)\middle|{}^{1}\Psi_{D^*A}\right\rangle \tag{A.5}$$
$$= h_{lj} + \frac{1}{2}\Big(V_{ilij} + V_{liji} - V_{kljk} + 2V_{klkj} + V_{liij} + V_{liji} + 2V_{lkjk} - V_{lkkj}\Big)$$
$$= h_{lj} + V_{ilij} + V_{ilji} - V_{kljk} + 2V_{klkj}$$

$$\left\langle {}^3\Psi_{D^+A^-}\middle|\sum_{ij}h_{ij}\hat{E}_i^j+\frac{1}{2}\sum_{ijkl}V_{ikjl}(\hat{E}_i^j\hat{E}_k^l-\delta_{jk}\hat{E}_i^l)\middle|{}^3\Psi_{D^*A}\right\rangle \tag{A.6}$$
$$=h_{lj}+\frac{1}{2}\Big(V_{ilij}-V_{ilji}+V_{kljk}+2V_{klkj}-V_{liij}+V_{liji}+2V_{lkjk}-V_{lkkj}\Big)$$
$$=h_{lj}+V_{ilij}-V_{ilji}-V_{kljk}+2V_{klkj}$$

$$\left\langle {}^{1,3}\Psi_{DA^*}\middle|\sum_{ij}h_{ij}\hat{E}_i^j+\frac{1}{2}\sum_{ijkl}V_{ikjl}(\hat{E}_i^j\hat{E}_k^l-\delta_{jk}\hat{E}_i^l)\middle|{}^{1,3}\Psi_{D^+A^-}\right\rangle \tag{A.7}$$
$$=-h_{ik}+\frac{1}{2}\Big\langle {}^{1,3}\Psi_{D^+A^-}\Big|V_{iiik}(\hat{E}_i^i\hat{E}_i^k-\delta_{ii}\hat{E}_i^k)+V_{iiki}(\hat{E}_i^k\hat{E}_i^i-\delta_{ki}\hat{E}_i^i)$$
$$+V_{ikkk}(\hat{E}_i^k\hat{E}_k^k-\delta_{kk}\hat{E}_i^k)+V_{ilkl}(\hat{E}_i^k\hat{E}_l^l-\delta_{kl}\hat{E}_i^l)$$
$$+V_{illk}(\hat{E}_i^l\hat{E}_l^k-\delta_{ll}\hat{E}_i^k)+V_{kikk}(\hat{E}_k^k\hat{E}_i^k-\delta_{ki}\hat{E}_k^k)$$
$$+V_{likl}(\hat{E}_l^k\hat{E}_i^l-\delta_{ki}\hat{E}_l^l)+V_{lilk}(\hat{E}_l^l\hat{E}_i^k-\delta_{li}\hat{E}_l^k)\Big|{}^{1,3}\Psi_{D^+A^-}\Big\rangle$$

$$\left\langle {}^1\Psi_{DA^*}\middle|\sum_{ij}h_{ij}\hat{E}_i^j+\frac{1}{2}\sum_{ijkl}V_{ikjl}(\hat{E}_i^j\hat{E}_k^l-\delta_{jk}\hat{E}_i^l)\middle|{}^1\Psi_{D^+A^-}\right\rangle \tag{A.8}$$
$$=-h_{ik}+\frac{1}{2}\Big(-V_{iiik}-V_{iiki}-V_{ikkk}-V_{ilkl}+2V_{illk}-V_{kikk}+2V_{likl}-V_{lilk}\Big)$$
$$=-h_{ik}-V_{iiik}-V_{ikkk}+2V_{likl}-V_{ilkl}$$

$$\left\langle {}^3\Psi_{DA^*}\middle|\sum_{ij}h_{ij}\hat{E}_i^j+\frac{1}{2}\sum_{ijkl}V_{ikjl}(\hat{E}_i^j\hat{E}_k^l-\delta_{jk}\hat{E}_i^l)\middle|{}^3\Psi_{D^+A^-}\right\rangle \tag{A.9}$$
$$=-h_{ik}+\frac{1}{2}\Big(-V_{iiik}-V_{iiki}-V_{ikkk}-V_{ilkl}-V_{kikk}-V_{lilk}\Big)$$
$$=-h_{ik}-V_{iiik}-V_{ikkk}-V_{ilkl}$$

$$\left\langle {}^{1,3}\Psi_{D^-A^+}\middle|\sum_{ij}h_{ij}\hat{E}_i^j+\frac{1}{2}\sum_{ijkl}V_{ikjl}(\hat{E}_i^j\hat{E}_k^l-\delta_{jk}\hat{E}_i^l)\middle|{}^{1,3}\Psi_{D^*A}\right\rangle \tag{A.10}$$
$$=-h_{ik}+\frac{1}{2}\Big\langle {}^{1,3}\Psi_{D^-A^+}\Big|V_{iiik}(\hat{E}_i^i\hat{E}_i^k-\delta_{ii}\hat{E}_i^k)+V_{ijjk}(\hat{E}_i^j\hat{E}_j^k-\delta_{jj}\hat{E}_i^k)$$
$$+V_{iiki}(\hat{E}_i^k\hat{E}_i^i-\delta_{ki}\hat{E}_i^i)+V_{ijkj}(\hat{E}_i^k\hat{E}_j^j-\delta_{kj}\hat{E}_i^j)$$
$$+V_{ikkk}(\hat{E}_i^k\hat{E}_k^k-\delta_{kk}\hat{E}_i^k)+V_{jijk}(\hat{E}_j^j\hat{E}_i^k-\delta_{ji}\hat{E}_j^k)$$
$$+V_{jikj}(\hat{E}_j^k\hat{E}_i^j-\delta_{ki}\hat{E}_j^j)+V_{kikk}(\hat{E}_k^k\hat{E}_i^k-\delta_{ki}\hat{E}_k^k)\Big|{}^{1,3}\Psi_{D^*A}\Big\rangle$$

$$\left\langle {}^1\Psi_{D^-A^+}\middle|\sum_{ij}h_{ij}\hat{E}_i^j+\frac{1}{2}\sum_{ijkl}V_{ikjl}(\hat{E}_i^j\hat{E}_k^l-\delta_{jk}\hat{E}_i^l)\middle|{}^1\Psi_{D^*A}\right\rangle \tag{A.11}$$
$$=-h_{ik}+\frac{1}{2}\Big(-V_{iiik}+2V_{ijjk}-V_{iiki}-V_{ijkj}-V_{ikkk}-V_{jiik}+2V_{jikj}-V_{kikk}\Big)$$
$$=-h_{ik}-V_{iiik}-V_{ikkk}+2V_{jikj}-V_{ijkj}$$

$$\left\langle {}^3\Psi_{D^-A^+}\middle|\sum_{ij}h_{ij}\hat{E}_i^j+\frac{1}{2}\sum_{ijkl}V_{ikjl}(\hat{E}_i^j\hat{E}_k^l-\delta_{jk}\hat{E}_i^l)\middle|{}^3\Psi_{D^*A}\right\rangle \tag{A.12}$$
$$=h_{ik}+\frac{1}{2}\Big(V_{iiik}+V_{iiki}+V_{ijkj}+V_{ikkk}+V_{jiik}+V_{kikk}\Big)$$
$$=h_{ik}+V_{iiik}+V_{ikkk}+V_{jiik}$$

$$\left\langle {}^{1,3}\Psi_{DA^*}\middle|\sum_{ij}h_{ij}\hat{E}_i^j+\frac{1}{2}\sum_{ijkl}V_{ikjl}(\hat{E}_i^j\hat{E}_k^l-\delta_{jk}\hat{E}_i^l)\middle|{}^{1,3}\Psi_{D^-A^+}\right\rangle \tag{A.13}$$
$$=h_{lj}+\frac{1}{2}\Big\langle {}^{1,3}\Psi_{DA^*}\Big|V_{ilij}(\hat{E}_i^i\hat{E}_l^j-\delta_{il}\hat{E}_i^j)+V_{ilji}(\hat{E}_i^j\hat{E}_l^i-\delta_{jl}\hat{E}_i^i)$$
$$+V_{kljk}(\hat{E}_k^j\hat{E}_l^k-\delta_{jl}\hat{E}_k^k)+V_{klkj}(\hat{E}_k^k\hat{E}_l^j-\delta_{kl}\hat{E}_k^j)$$
$$+V_{liij}(\hat{E}_l^i\hat{E}_i^j-\delta_{ii}\hat{E}_k^j)+V_{liji}(\hat{E}_l^j\hat{E}_i^i-\delta_{ji}\hat{E}_l^i)$$
$$+V_{lkjk}(\hat{E}_l^j\hat{E}_k^k-\delta_{jk}\hat{E}_l^k)+V_{lkkj}(\hat{E}_l^k\hat{E}_j^k-\delta_{kk}\hat{E}_l^j)\Big|{}^{1,3}\Psi_{D^-A^+}\Big\rangle$$

$$\left\langle {}^1\Psi_{DA^*}\middle|\sum_{ij}h_{ij}\hat{E}_i^j+\frac{1}{2}\sum_{ijkl}V_{ikjl}(\hat{E}_i^j\hat{E}_k^l-\delta_{jk}\hat{E}_i^l)\middle|{}^1\Psi_{D^-A^+}\right\rangle \tag{A.14}$$
$$=h_{lj}+\frac{1}{2}\Big(+2V_{ilij}-V_{ilji}+V_{kljk}+V_{klkj}-V_{liij}+2V_{liji}+V_{lkjk}+V_{lkkj}\Big)$$
$$=h_{lj}+2V_{ilij}-V_{ilji}+V_{kljk}+V_{klkj}$$

$$\left\langle {}^3\Psi_{DA^*}\middle|\sum_{ij}h_{ij}\hat{E}_i^j+\frac{1}{2}\sum_{ijkl}V_{ikjl}(\hat{E}_i^j\hat{E}_k^l-\delta_{jk}\hat{E}_i^l)\middle|{}^3\Psi_{D^-A^+}\right\rangle \tag{A.15}$$
$$=-h_{lj}+\frac{1}{2}\Big(-2V_{ilij}+V_{ilji}+V_{kljk}-V_{klkj}+V_{liij}-2V_{liji}-V_{lkjk}+V_{lkkj}\Big)$$
$$=-h_{lj}-2V_{ilij}+V_{ilji}+V_{kljk}-V_{klkj}$$

$$\left\langle {}^1\Psi_{DA}\middle|\sum_{ij} h_{ij}\hat{E}_i^j+\frac{1}{2}\sum_{ijkl}V_{ikjl}(\hat{E}_i^j\hat{E}_k^l-\delta_{jk}\hat{E}_i^l)\middle|{}^1\Psi_{DA}\right\rangle = E_0 \tag{A.16}$$

$$\begin{aligned}
&= 2h_{ii}+2h_{kk}+\frac{1}{2}\Big\langle {}^1\Psi_{DA}\Big| V_{iiii}(\hat{E}_i^i\hat{E}_i^i-\delta_{ii}\hat{E}_i^i)+V_{ikik}(\hat{E}_i^i\hat{E}_k^k-\delta_{ik}\hat{E}_i^k)\\
&\qquad +V_{ijji}(\hat{E}_i^j\hat{E}_j^i-\delta_{jj}\hat{E}_i^i)+V_{ikik}(\hat{E}_i^k\hat{E}_k^i-\delta_{kk}\hat{E}_i^i)\\
&\qquad +V_{illi}(\hat{E}_i^l\hat{E}_l^i-\delta_{ll}\hat{E}_i^i)+V_{kiik}(\hat{E}_k^i\hat{E}_i^k-\delta_{ii}\hat{E}_k^k)\\
&\qquad +V_{kjjk}(\hat{E}_k^j\hat{E}_j^k-\delta_{jj}\hat{E}_k^k)+V_{kiki}(\hat{E}_k^k\hat{E}_i^i-\delta_{ki}\hat{E}_k^i)\\
&\qquad +V_{kkkk}(\hat{E}_k^k\hat{E}_k^k-\delta_{kk}\hat{E}_k^k)+V_{kllk}(\hat{E}_k^l\hat{E}_l^k-\delta_{ll}\hat{E}_k^k)\Big|{}^1\Psi_{DA}\Big\rangle\\
&= 2h_{ii}+2h_{kk}+\frac{1}{2}\Big(2V_{iiii}+4V_{ikik}-2V_{ikki}-2V_{kiik}+4V_{kiki}+2V_{kkkk}\Big)\\
&= 2h_{ii}+2h_{kk}+V_{iiii}+4V_{ikik}-2V_{ikki}+V_{kkkk}
\end{aligned}$$

$$\left\langle {}^{1,3}\Psi_{D^+A^-}\middle|\sum_{ij} h_{ij}\hat{E}_i^j+\frac{1}{2}\sum_{ijkl}V_{ikjl}(\hat{E}_i^j\hat{E}_k^l-\delta_{jk}\hat{E}_i^l)\middle|{}^{1,3}\Psi_{D^+A^-}\right\rangle \tag{A.17}$$

$$\begin{aligned}
&= h_{ii}+2h_{kk}+h_{ll}+\frac{1}{2}\Big\langle {}^{1,3}\Psi_{D^+A^-}\Big| V_{iiii}(\hat{E}_i^i\hat{E}_i^i-\delta_{ii}\hat{E}_i^i)+V_{ikik}(\hat{E}_i^i\hat{E}_k^k-\delta_{ik}\hat{E}_i^k)\\
&\qquad +V_{ilil}(\hat{E}_i^i\hat{E}_l^l-\delta_{il}\hat{E}_i^l)+V_{ijji}(\hat{E}_i^j\hat{E}_j^i-\delta_{jj}\hat{E}_i^i)\\
&\qquad +V_{ikki}(\hat{E}_i^k\hat{E}_k^i-\delta_{kk}\hat{E}_i^i)+V_{illi}(\hat{E}_i^l\hat{E}_l^i-\delta_{ll}\hat{E}_i^i)\\
&\qquad +V_{kiik}(\hat{E}_k^i\hat{E}_i^k-\delta_{ii}\hat{E}_k^k)+V_{kjjk}(\hat{E}_k^j\hat{E}_j^k-\delta_{jj}\hat{E}_k^k)\\
&\qquad +V_{kiki}(\hat{E}_k^k\hat{E}_i^i-\delta_{ki}\hat{E}_k^i)+V_{kkkk}(\hat{E}_k^k\hat{E}_k^k-\delta_{kk}\hat{E}_k^k)\\
&\qquad +V_{klkl}(\hat{E}_k^k\hat{E}_l^l-\delta_{kl}\hat{E}_k^l)+V_{kllk}(\hat{E}_k^l\hat{E}_l^k-\delta_{ll}\hat{E}_k^k)\\
&\qquad +V_{liil}(\hat{E}_l^i\hat{E}_i^l-\delta_{ii}\hat{E}_l^l)+V_{ljjl}(\hat{E}_l^j\hat{E}_j^l-\delta_{jj}\hat{E}_l^l)\\
&\qquad +V_{lkkl}(\hat{E}_l^k\hat{E}_k^l-\delta_{kk}\hat{E}_l^l)+V_{lili}(\hat{E}_l^l\hat{E}_i^i-\delta_{li}\hat{E}_l^i)\\
&\qquad +V_{lklk}(\hat{E}_l^l\hat{E}_k^k-\delta_{lk}\hat{E}_l^k)+V_{llll}(\hat{E}_l^l\hat{E}_l^l-\delta_{ll}\hat{E}_l^l)\Big|{}^{1,3}\Psi_{D^+A^-}\Big\rangle
\end{aligned}$$

$$\left\langle {}^1\Psi_{D^+A^-}\middle|\sum_{ij} h_{ij}\hat{E}_i^j+\frac{1}{2}\sum_{ijkl}V_{ikjl}(\hat{E}_i^j\hat{E}_k^l-\delta_{jk}\hat{E}_i^l)\middle|{}^1\Psi_{D^+A^-}\right\rangle \tag{A.18}$$

$$\begin{aligned}
&= h_{ii}+2h_{kk}+h_{ll}+\frac{1}{2}\Big(2V_{ikik}+V_{ilil}-V_{ikik}+V_{illi}-V_{kiik}+2V_{kiki}+2V_{kkkk}\\
&\qquad +2V_{klkl}-V_{kllk}+V_{liil}-V_{lkkl}+V_{lili}+2V_{lklk}\Big)\\
&= h_{ii}+2h_{kk}+h_{ll}+2V_{ikik}+V_{ilil}-V_{ikki}+V_{illi}+V_{kkkk}+2V_{klkl}-V_{kllk}
\end{aligned}$$

$$\left\langle {}^3\Psi_{D^+A^-}\middle|\sum_{ij}h_{ij}\hat{E}_i^j+\frac{1}{2}\sum_{ijkl}V_{ikjl}(\hat{E}_i^j\hat{E}_k^l-\delta_{jk}\hat{E}_i^l)\middle|{}^3\Psi_{D^+A^-}\right\rangle \tag{A.19}$$
$$\begin{aligned}&=h_{ii}+2h_{kk}+h_{ll}+\frac{1}{2}\Big(2V_{ikik}+V_{ilil}-V_{ikki}-V_{illi}-V_{kiik}+2V_{kiki}+2V_{kkkk}\\&\qquad+2V_{klkl}-V_{kllk}-V_{liil}-V_{lkkl}+V_{lili}+2V_{lklk}\Big)\\&=h_{ii}+2h_{kk}+h_{ll}+2V_{ikik}+V_{ilil}-V_{ikki}-V_{illi}+V_{kkkk}+2V_{klkl}-V_{kllk}\end{aligned}$$

$$\left\langle {}^{1,3}\Psi_{D^-A^+}\middle|\sum_{ij}h_{ij}\hat{E}_i^j+\frac{1}{2}\sum_{ijkl}V_{ikjl}(\hat{E}_i^j\hat{E}_k^l-\delta_{jk}\hat{E}_i^l)\middle|{}^{1,3}\Psi_{D^-A^+}\right\rangle \tag{A.20}$$
$$\begin{aligned}&=2h_{ii}+h_{jj}+h_{kk}+\frac{1}{2}\Big\langle {}^{1,3}\Psi_{D^-A^+}\Big|V_{iiii}(\hat{E}_i^i\hat{E}_i^i-\delta_{ii}\hat{E}_i^i)+V_{ijij}(\hat{E}_i^i\hat{E}_j^j-\delta_{ij}\hat{E}_i^j)\\&\qquad+V_{ikik}(\hat{E}_i^i\hat{E}_k^k-\delta_{ik}\hat{E}_i^k)+V_{ijji}(\hat{E}_i^j\hat{E}_j^i-\delta_{jj}\hat{E}_i^i)\\&\qquad+V_{ikki}(\hat{E}_i^k\hat{E}_k^i-\delta_{kk}\hat{E}_i^i)+V_{illi}(\hat{E}_i^l\hat{E}_l^i-\delta_{ll}\hat{E}_i^i)\\&\qquad+V_{jiij}(\hat{E}_j^i\hat{E}_i^j-\delta_{ii}\hat{E}_j^j)+V_{jiji}(\hat{E}_j^j\hat{E}_i^i-\delta_{ji}\hat{E}_j^i)\\&\qquad+V_{jjjj}(\hat{E}_j^j\hat{E}_j^j-\delta_{jj}\hat{E}_j^j)+V_{jkjk}(\hat{E}_j^j\hat{E}_k^k-\delta_{jk}\hat{E}_j^k)\\&\qquad+V_{jkkj}(\hat{E}_j^k\hat{E}_j^k-\delta_{kk}\hat{E}_j^j)+V_{jllj}(\hat{E}_j^l\hat{E}_l^j-\delta_{ll}\hat{E}_j^j)\\&\qquad+V_{kiik}(\hat{E}_k^i\hat{E}_i^k-\delta_{ii}\hat{E}_k^k)+V_{kjjk}(\hat{E}_k^j\hat{E}_j^k-\delta_{jj}\hat{E}_k^k)\\&\qquad+V_{kiki}(\hat{E}_k^k\hat{E}_i^i-\delta_{ki}\hat{E}_k^i)+V_{kjkj}(\hat{E}_k^k\hat{E}_j^j-\delta_{kj}\hat{E}_k^j)\Big|{}^{1,3}\Psi_{D^-A^+}\Big\rangle\end{aligned}$$

$$\left\langle {}^1\Psi_{D^-A^+}\middle|\sum_{ij}h_{ij}\hat{E}_i^j+\frac{1}{2}\sum_{ijkl}V_{ikjl}(\hat{E}_i^j\hat{E}_k^l-\delta_{jk}\hat{E}_i^l)\middle|{}^1\Psi_{D^-A^+}\right\rangle \tag{A.21}$$
$$\begin{aligned}&=2h_{ii}+h_{jj}+h_{kk}+\frac{1}{2}\Big(2V_{iiii}+2V_{ijij}+2V_{ikik}-V_{ijji}-V_{ikki}-V_{jiij}+2V_{jiji}\\&\qquad+V_{jkjk}+V_{jkkj}-V_{kiik}+V_{kjjk}+2V_{kiki}+V_{kjkj}\Big)\\&=2h_{ii}+h_{jj}+h_{kk}+V_{iiii}+2V_{ijij}+2V_{ikik}-V_{ijji}-V_{ikki}+V_{jkjk}+V_{jkkj}\end{aligned}$$

$$\left\langle {}^3\Psi_{D^-A^+}\middle|\sum_{ij}h_{ij}\hat{E}_i^j+\frac{1}{2}\sum_{ijkl}V_{ikjl}(\hat{E}_i^j\hat{E}_k^l-\delta_{jk}\hat{E}_i^l)\middle|{}^3\Psi_{D^-A^+}\right\rangle \tag{A.22}$$
$$\begin{aligned}&=2h_{ii}+h_{jj}+h_{kk}+\frac{1}{2}\Big(2V_{iiii}+2V_{ijij}+2V_{ikik}-V_{ijji}-V_{ikki}-V_{jiij}+2V_{jiji}\\&\qquad+V_{jkjk}-V_{jkkj}-V_{kiik}-V_{kjjk}+2V_{kiki}+V_{kjkj}\Big)\\&=2h_{ii}+h_{jj}+h_{kk}+V_{iiii}+2V_{ijij}+2V_{ikik}-V_{ijji}-V_{ikki}+V_{jkjk}-V_{jkkj}\end{aligned}$$

A.3 TEET Donor-Bridge-Acceptor Systems: Computational Data

Table A.16: C-1,3ea ground state geometry [Å] optimized at PBE0/6-31G** level of theory.

Element	x	y	z
C	-0.8351260	-2.8486990	-0.5209900
C	-0.3837950	-3.4416390	0.8166770
C	-3.0371000	-4.0414650	-0.2629390
C	-2.5438190	-4.6585780	1.0403510
C	-1.0217890	-4.8097830	1.0951630
H	-3.0374300	-5.6155470	1.2293170
H	-2.8382460	-4.0046830	1.8695950
H	-0.6693240	-2.7587330	1.6252240
H	0.7059700	-3.5039980	0.8429240
C	-0.1371510	-1.5501880	-0.8259590
C	-0.2994240	-0.4304330	-0.0104640
C	0.3453070	0.7574880	-0.3052440
C	1.1685080	0.8546610	-1.4230890
C	1.3393510	-0.2577470	-2.2437200
C	0.6932020	-1.4410340	-1.9437760
H	1.9830190	-0.1704460	-3.1117280
H	-0.9383830	-0.4869590	0.8639920
H	0.2120740	1.6247290	0.3349990
C	1.8437510	2.1271370	-1.7218810
O	2.5750890	2.3194920	-2.6601260
H	1.6290100	2.9414290	-0.9955830
C	-0.4491860	-5.9184760	0.2213530
H	-0.7611830	-5.0769430	2.1274080
C	-1.2708020	-6.8772560	-0.4167680
C	-0.7419160	-7.8978880	-1.1591820
C	0.6512930	-8.0384130	-1.3177660
C	1.4948050	-7.0933720	-0.6753040
C	0.9119720	-6.0560550	0.0818860
C	1.2339540	-9.0757590	-2.0792760
C	2.5924590	-9.1751480	-2.1987600
C	3.4312840	-8.2398190	-1.5599520
C	2.8955170	-7.2249390	-0.8166300
H	0.5839340	-9.7941200	-2.5682350
H	3.0303710	-9.9746930	-2.7853550
H	4.5069690	-8.3286680	-1.6616180
H	3.5408020	-6.5038140	-0.3253830
H	1.5838090	-5.3586780	0.5721490
H	-2.3468490	-6.8134670	-0.3185620
H	-1.3991920	-8.6170030	-1.6375600
H	0.8283410	-2.3062950	-2.5848390
C	-2.3591900	-2.7076560	-0.5417170
H	-4.1222210	-3.9073300	-0.2218270
H	-2.8403610	-4.7204380	-1.0992930
H	-2.6632540	-1.9759200	0.2167150
H	-2.6824800	-2.3081660	-1.5073610
H	-0.5566960	-3.5607270	-1.3073850

Table A.17: C-1,3ee ground state geometry [Å] optimized at PBE0/6-31G** level of theory.

Element	x	y	z
C	-1.2777240	-1.2645940	-0.9075230
C	-0.3805520	-2.3981850	-0.4018260
C	-3.2651490	-2.4153510	0.1314320
C	-2.3693250	-3.5429130	0.6227110
C	-1.1445680	-3.7191180	-0.2771510
H	-2.9268020	-4.4826520	0.6734410
H	-2.0359330	-3.3248770	1.6444010
H	0.0326150	-2.1276450	0.5767780
H	0.4740010	-2.5248990	-1.0730410
C	-0.5182450	0.0246000	-1.0759730
C	0.0774590	0.6621780	0.0118760
C	0.7722360	1.8463560	-0.1573880
C	0.8880420	2.4222750	-1.4189460
C	0.2972160	1.7944030	-2.5126750
C	-0.3947120	0.6120740	-2.3369280
H	0.3941870	2.2520420	-3.4906840
H	-0.0021110	0.2278450	1.0023900
H	1.2334740	2.3354450	0.6956850
C	1.6307630	3.6822800	-1.5797680
O	1.7891300	4.2637180	-2.6232420
H	2.0581290	4.0863350	-0.6360640
C	-0.2503660	-4.8479460	0.1720740
H	-1.5116680	-3.9778360	-1.2793300
C	-0.0043410	-5.9379250	-0.6931390
C	0.8025560	-6.9774060	-0.3214000
C	1.4203610	-6.9954800	0.9467550
C	1.1839710	-5.9063740	1.8292770
C	0.3451200	-4.8523300	1.4093630
C	2.2599170	-8.0506330	1.3678410
C	2.8406120	-8.0312200	2.6057140
C	2.6072770	-6.9522830	3.4815070
C	1.7991940	-5.9165480	3.1019610
H	2.4368310	-8.8793750	0.6899440
H	3.4833150	-8.8462870	2.9183080
H	3.0728560	-6.9470610	4.4605700
H	1.6189580	-5.0852620	3.7759580
H	0.1780640	-4.0305910	2.0997660
H	-0.4709050	-5.9429380	-1.6733240
H	0.9771930	-7.8047020	-1.0017150
H	-0.8535030	0.1253060	-3.1916910
C	-2.5004930	-1.1064070	0.0000910
H	-4.1143470	-2.2866190	0.8089490
H	-3.6870820	-2.6867070	-0.8443380
H	-2.1718160	-0.7748820	0.9924570
H	-3.1508060	-0.3184240	-0.3909760
H	-1.6437600	-1.5556790	-1.9007940

Table A.18: C-1,4ea ground state geometry [Å] optimized at PBE0/6-31G** level of theory.

Element	x	y	z
C	-0.7899970	-3.0564190	-0.5165160
C	-2.1298470	-2.6382010	0.0946320
C	-0.3072500	-4.3769770	0.0644420
C	-3.1616600	-3.7532700	-0.0988950
C	-2.6580740	-5.0868510	0.4409060
H	-3.3910070	-3.8381260	-1.1657070
H	-4.0972590	-3.4792390	0.3980530
C	-1.3135520	-5.5156110	-0.1508560
H	-3.4131900	-5.8649190	0.2995870
H	-2.5259360	-4.9967710	1.5253930
H	-0.1518140	-4.2590360	1.1436500
H	0.6672010	-4.6339620	-0.3559370
C	-2.6194190	-1.3185130	-0.4380000
C	-2.8199130	-0.2403730	0.4196520
C	-3.2745590	0.9762170	-0.0619080
C	-3.5387280	1.1391060	-1.4166050
C	-3.3408760	0.0662540	-2.2856210
C	-2.8879740	-1.1427680	-1.7999440
H	-3.5499680	0.2070510	-3.3400500
H	-2.6157400	-0.3599920	1.4787490
H	-3.4274920	1.8106010	0.6163850
C	-4.0220630	2.4366780	-1.9133340
O	-4.2823930	2.6847500	-3.0634960
H	-4.1391890	3.2134920	-1.1262030
C	-1.3655410	-5.9938470	-1.5956740
H	-0.9625110	-6.3731780	0.4371830
C	-2.5849630	-6.2107770	-2.2792180
C	-2.6157930	-6.6851610	-3.5626010
C	-1.4272160	-6.9829030	-4.2585740
C	-0.1920060	-6.7850990	-3.5856050
C	-0.2016790	-6.2936960	-2.2638790
C	-1.4188320	-7.4716210	-5.5839590
C	-0.2398010	-7.7549220	-6.2157690
C	0.9867900	-7.5622780	-5.5486790
C	1.0095580	-7.0896230	-4.2659070
H	-2.3658540	-7.6193610	-6.0928380
H	-0.2435700	-8.1296110	-7.2329750
H	1.9153360	-7.7907530	-6.0595120
H	1.9537110	-6.9401610	-3.7520980
H	0.7571620	-6.1662530	-1.7711340
H	-3.5242000	-6.0048220	-1.7820860
H	-3.5677180	-6.8397550	-4.0605230
H	-2.7378320	-1.9685890	-2.4870710
H	-0.0452920	-2.2740760	-0.3429560
H	-0.8961890	-3.1513900	-1.6028150
H	-1.9732820	-2.5159860	1.1746540

Table A.19: C-1,4ee ground state geometry [Å] optimized at PBE0/6-31G** level of theory.

Element	x	y	z
C	-1.0386040	-1.9346140	-0.8544640
C	-2.2192060	-1.7192230	0.0964820
C	-0.3055090	-3.2343890	-0.5559520
C	-3.1599230	-2.9263480	0.0475570
C	-2.4246960	-4.2251250	0.3451690
H	-3.6176520	-2.9862740	-0.9471270
H	-3.9806890	-2.7846280	0.7569140
C	-1.2438570	-4.4422600	-0.6036190
H	-3.1134700	-5.0723140	0.2782150
H	-2.0563820	-4.2080110	1.3779060
H	0.1525940	-3.1752900	0.4386040
H	0.5154990	-3.3757460	-1.2648870
C	-2.9379830	-0.4237750	-0.1696880
C	-2.9879930	0.5696760	0.8043580
C	-3.6471520	1.7648450	0.5680810
C	-4.2721290	1.9912190	-0.6523870
C	-4.2288830	1.0034970	-1.6360270
C	-3.5708170	-0.1844210	-1.3943590
H	-4.7205180	1.1930150	-2.5835250
H	-2.5023730	0.4003920	1.7599380
H	-3.6795630	2.5326650	1.3355510
C	-4.9685710	3.2652770	-0.8897320
O	-5.5413630	3.5616210	-1.9076490
H	-4.9354510	3.9723570	-0.0321590
C	-0.5247660	-5.7416590	-0.3410930
H	-1.6509960	-4.4977960	-1.6221530
C	-0.4844450	-6.7385770	-1.3419430
C	0.1578190	-7.9288100	-1.1400210
C	0.8058050	-8.2023280	0.0828570
C	0.7749350	-7.2102560	1.1006060
C	0.1019860	-5.9947680	0.8542960
C	1.4797270	-9.4190030	0.3301310
C	2.0960560	-9.6462150	1.5294710
C	2.0662880	-8.6637940	2.5392160
C	1.4218000	-7.4762360	2.3291330
H	1.4999780	10.1725920	-0.4504890
H	2.6103120	10.5835970	1.7083190
H	2.5582310	-8.8543890	3.4863440
H	1.3984740	-6.7191530	3.1063570
H	0.0910530	-5.2510930	1.6459120
H	-0.9771530	-6.5473490	-2.2901850
H	0.1760940	-8.6802040	-1.9228570
H	-3.5452910	-0.9436310	-2.1686020
H	-0.3499220	-1.0872170	-0.7869340
H	-1.4066060	-1.9525660	-1.8873040
H	-1.8128680	-1.6621250	1.1148590

Table A.20: D-2,6ea ground state geometry [Å] optimized at PBE0/6-31G** level of theory.

Element	x	y	z
C	-1.6912750	-0.6892360	-0.8303250
C	-2.7889630	-1.1367700	0.1590480
C	-2.2528100	-1.0855220	1.6041740
C	-1.0163870	-1.9839290	1.7477230
C	0.0872120	-1.5593470	0.7587430
C	-0.4529690	-1.5977800	-0.6911150
H	-1.4023460	0.3667570	-0.6331440
H	-2.0827020	-0.7564660	-1.8692980
H	-3.0369850	-1.4346710	2.3108110
H	-1.9778340	-0.0430180	1.8767230
H	-1.3109720	-3.0388560	1.5507270
H	-0.6367700	-1.9187610	2.7905390
C	1.3176230	-2.4949200	0.8918510
H	0.3675640	-0.5120690	0.9887260
C	0.6588340	-1.1862030	-1.6739710
H	-0.7660920	-2.6393410	-0.9361270
C	1.8417820	-2.1561670	-1.5473910
H	0.9960760	-0.1451970	-1.4735700
H	0.2680080	-1.2331130	-2.7137090
C	2.4466760	-2.1564600	-0.1183270
H	2.6069400	-1.9190270	-2.3135040
H	1.4714600	-3.1797420	-1.7792280
H	0.9747760	-3.5325580	0.6788560
H	1.7168070	-2.4973790	1.9288450
C	-4.0473200	-0.3011500	0.0105550
H	-3.0385110	-2.1981040	-0.0705920
C	-5.2541280	-0.9194580	-0.3614420
C	-6.4252810	-0.1703160	-0.4993940
C	-6.4151880	1.2119820	-0.2687000
C	-5.2123710	1.8362260	0.1023020
C	-4.0394970	1.0871280	0.2406660
H	-3.1277580	1.5937710	0.5286510
H	-5.1780440	2.9027710	0.2863860
H	-5.2933840	-1.9860320	-0.5451230
H	-7.3414030	-0.6725750	-0.7861900
C	-7.6666130	1.9837630	-0.4189400
O	-7.6921480	3.1890100	-0.2244630
H	-8.5838250	1.4784860	-0.7060170
C	3.2640110	-0.8910810	0.1816230
H	3.1883530	-2.9843210	-0.0673770
C	3.0317080	-0.0512160	1.2942120
C	3.8320020	1.0700010	1.5303630
C	4.8932130	1.3773730	0.6721230
C	5.1536660	0.5437870	-0.4378280
C	4.3443760	-0.5771680	-0.6704570
C	5.7071670	2.4967080	0.9083010
C	6.7713880	2.7840750	0.0485110
C	7.0302410	1.9592180	-1.0491330
C	6.2262400	0.8424800	-1.2940190
H	5.5232280	3.1453610	1.7564250
H	7.3981710	3.6467110	0.2343540
H	7.8565300	2.1849420	-1.7109440
H	6.4432420	0.2135260	-2.1492870
H	4.5682940	-1.2144740	-1.5167130
H	2.2485540	-0.2472120	2.0073270
H	3.6257850	1.6924000	2.3932460

Table A.21: D-2,6ee ground state geometry [Å] optimized at PBE0/6-31G** level of theory.

Element	x	y	z
C	2.2014940	-0.1842970	-0.7920650
C	2.9646260	0.6746360	0.2197620
C	2.4629890	0.3906710	1.6384960
C	0.9566640	0.5766580	1.7437210
C	0.2014950	-0.2748740	0.7318780
C	0.6942010	0.0061820	-0.6877240
H	2.4406630	-1.2422970	-0.6250000
H	2.5399170	0.0513950	-1.8066050
H	2.9807120	1.0408200	2.3500200
H	2.7230140	-0.6385800	1.9129790
H	0.7063850	1.6327330	1.5768540
H	0.6198720	0.3375000	2.7578120
C	-1.3058720	-0.0851950	0.8352510
H	0.4246900	-1.3318500	0.9491190
C	-0.0607480	-0.8451460	-1.7000450
H	0.4713980	1.0631790	-0.9050050
C	-1.5670300	-0.6592320	-1.5930700
H	0.1898070	-1.9011990	-1.5329500
H	0.2768840	-0.6058280	-2.7140020
C	-2.0707290	-0.9422770	-0.1757320
H	-2.0850920	-1.3083920	-2.3051470
H	-1.8282180	0.3700390	-1.8666880
H	-1.5465040	0.9725240	0.6678170
H	-1.6447290	-0.3201320	1.8497950
C	4.4559120	0.5090850	0.0977220
H	2.7357520	1.7247430	-0.0038970
C	5.2622390	1.5920390	-0.2417750
C	6.6352050	1.4483460	-0.3563120
C	7.2317960	0.2132450	-0.1326160
C	6.4344980	-0.8791230	0.2083410
C	5.0679770	-0.7291820	0.3207580
H	4.4600130	-1.5873250	0.5862250
H	6.9126510	-1.8368620	0.3801170
H	4.8037850	2.5597060	-0.4180460
H	7.2541710	2.3004000	-0.6218980
C	8.6909960	0.0751440	-0.2581990
O	9.3070440	-0.9462810	-0.0867260
H	9.2180420	1.0146140	-0.5342140
C	-3.5653240	-0.7816750	-0.0515350
H	-1.8393750	-1.9922930	0.0475630
C	-4.3669650	-1.8924970	0.2960400
C	-5.7246650	-1.7845900	0.4186770
C	-6.3744530	-0.5515500	0.2006490
C	-5.5831850	0.5762050	-0.1502370
C	-4.1852380	0.4245850	-0.2671380
C	-7.7739210	-0.3987400	0.3180190
C	-8.3663030	0.8140850	0.0987150
C	-7.5833390	1.9328210	-0.2492280
C	-6.2263370	1.8157460	-0.3704180
H	-8.3727670	-1.2631590	0.5861540
H	-9.4411790	0.9197320	0.1916920
H	-8.0632350	2.8897090	-0.4209250
H	-5.6226320	2.6768890	-0.6383600
H	-3.6000850	1.2993170	-0.5358920
H	-3.8857620	-2.8503170	0.4680000
H	-6.3204280	-2.6512340	0.6866840

Table A.22: D-2,6ae ground state geometry [Å] optimized at PBE0/6-31G** level of theory.

Element	x	y	z
C	2.4003110	-2.2983560	-0.7443640
C	3.5230950	-2.0273920	0.2924230
C	2.9238490	-2.2120410	1.7121920
C	1.6790720	-1.3288130	1.9488220
C	0.6025430	-1.6144570	0.8885360
C	1.1788920	-1.3822300	-0.5295600
H	2.0686960	-3.3557440	-0.6361450
H	2.7815370	-2.1938950	-1.7802710
H	3.6952190	-2.0319600	2.4905670
H	2.6040560	-3.2724930	1.8200930
H	1.9331200	-0.2526080	1.9082740
H	1.2738950	-1.5398700	2.9621920
C	-0.6369460	-0.7257960	1.1123860
H	0.2915360	-2.6804600	0.9860000
C	0.0949180	-1.6766360	-1.5830800
H	1.4969530	-0.3200180	-0.6381430
C	-1.1449030	-0.8011180	-1.3547810
H	-0.2057930	-2.7467530	-1.5260930
H	0.4963050	-1.4833010	-2.6016840
C	-1.7301800	-1.0300080	0.0592340
H	-1.8906120	-1.0560690	-2.1367580
H	-0.8716860	0.2707410	-1.4764850
H	-0.3340000	0.3432940	1.0451840
H	-1.0411960	-0.9238840	2.1296000
C	4.2565220	-0.6995570	0.0431370
H	4.3003760	-2.8113530	0.1547960
C	4.8415470	-0.4786300	-1.2213010
C	5.5381500	0.6994760	-1.5013650
C	5.6813550	1.6889300	-0.5228250
C	5.1216410	1.4788310	0.7451550
C	4.4235870	0.3010640	1.0275100
H	4.0398720	0.1931090	2.0282420
H	5.2289260	2.2231480	1.5246490
H	4.7686150	-1.2217200	-2.0035180
H	5.9710680	0.8348760	-2.4852070
C	6.4265960	2.9258400	-0.8376010
O	6.5731230	3.8043520	-0.0020870
H	6.8556710	3.0637600	-1.8252540
C	-3.0201680	-0.2298140	0.2443370
H	-2.0015240	-2.1043570	0.1705560
C	-3.1649140	0.7913040	1.2097650
C	-4.3704110	1.4851030	1.3443650
C	-5.4619000	1.1746390	0.5249270
C	-5.3381540	0.1527190	-0.4437090
C	-4.1244360	-0.5373090	-0.5754860
C	-6.6774480	1.8643690	0.6574610
C	-7.7608870	1.5405360	-0.1643200
C	-7.6396180	0.5295570	-1.1211850
C	-6.4340300	-0.1634830	-1.2628860
H	-6.7899190	2.6501930	1.3949190
H	-8.6968930	2.0736980	-0.0587300
H	-8.4819730	0.2821740	-1.7543020
H	-6.3589090	-0.9446070	-2.0100540
H	-4.0412610	-1.3250510	-1.3150990
H	-2.3563720	1.0695050	1.8694080
H	-4.4491960	2.2644760	2.0932340

Table A.23: D-2,7ea ground state geometry [Å] optimized at PBE0/6-31G** level of theory.

Element	x	y	z
C	0.6228300	2.0565910	-1.6558520
C	2.1550780	0.2859800	-0.6526340
C	1.4600980	0.5050380	0.7131550
C	0.0001930	0.9650970	0.5308080
C	-0.0394830	2.2797030	-0.2841800
H	2.0252870	1.2694360	1.2927070
H	1.4566200	-0.4378380	1.2998360
C	-0.6699390	1.1846150	1.9004620
H	-0.5527990	0.1659370	-0.0140610
C	-1.4881380	2.7671760	-0.4500660
H	0.5277990	3.0654530	0.2663160
C	-2.1779830	2.9296790	0.9255860
H	-2.0239490	2.0400450	-1.0876480
H	-1.4975370	3.7437190	-0.9808210
C	-2.1536220	1.6149050	1.7522470
H	-3.2171860	3.3027350	0.8089070
H	-1.6232170	3.7112270	1.4912740
H	-0.1166830	1.9825210	2.4456210
H	-0.5824050	0.2692360	2.5191080
C	3.5827810	-0.2229850	-0.4385720
C	3.7740230	-1.4538420	0.2201450
C	5.0577990	-1.9543690	0.4525760
C	6.1854370	-1.2407530	0.0287500
C	6.0097340	-0.0197680	-0.6387440
C	4.7271160	0.4835340	-0.8717320
H	6.8648880	0.5506890	-0.9795650
H	2.9260090	-2.0346360	0.5594920
H	5.1695790	-2.9012900	0.9668450
C	7.5350330	-1.7827690	0.2910110
O	8.5365900	-1.1814480	-0.0649390
H	7.6477320	-2.7283600	0.8120350
C	-3.0464600	0.4795230	1.2167230
H	-2.5362140	1.8411040	2.7718760
C	-3.0293090	-0.7695270	1.8734300
C	-3.8060680	-1.8388360	1.4210960
C	-4.6363270	-1.6865200	0.3068050
C	-4.6959140	-0.4383630	-0.3510490
C	-3.9119880	0.6299010	0.1082710
C	-5.4154400	-2.7569960	-0.1609640
C	-6.2467350	-2.5866160	-1.2716640
C	-6.3099890	-1.3503600	-1.9194100
C	-5.5392460	-0.2781420	-1.4623000
H	-5.3806310	-3.7218540	0.3305220
H	-6.8447150	-3.4141150	-1.6309000
H	-6.9561570	-1.2223480	-2.7780780
H	-5.5999870	0.6725570	-1.9789800
H	-4.0026770	1.5699320	-0.4115120
H	-2.4074900	-0.9325520	2.7421480
H	-3.7551060	-2.7860810	1.9449300
H	4.6534720	1.4294750	-1.3870330
C	2.0741410	1.5956390	-1.4767800
H	0.6114710	3.0017840	-2.2407970
H	0.0598080	1.2858070	-2.2287530
H	1.6020400	-0.4987300	-1.2169880
H	2.6317720	2.4061700	-0.9575920
H	2.5218350	1.4363500	-2.4820820

Table A.24: D-2,7ee ground state geometry [Å] optimized at PBE0/6-31G** level of theory.

Element	x	y	z
C	-1.7843800	3.0675750	-0.4627510
C	-2.8590070	0.7986820	-0.5551340
C	-1.6323320	0.1155060	0.0761780
C	-0.4753040	1.0808560	0.3755900
C	-0.4802000	2.2657130	-0.5876910
H	-1.2850080	-0.6757360	-0.5969900
H	-1.9298880	-0.3876070	1.0013070
C	0.8572240	0.3403820	0.3570430
H	-0.6153590	1.4903100	1.3868770
C	0.7359150	3.1597330	-0.3772620
H	-0.4162740	1.8524690	-1.6052500
C	2.0478580	2.3936150	-0.4263730
H	0.6431650	3.6479980	0.6020960
H	0.7364340	3.9646110	-1.1202470
C	2.0577890	1.2574400	0.5970710
H	2.8906210	3.0665610	-0.2428410
H	2.1959770	1.9775560	-1.4299180
H	0.9767560	-0.1464000	-0.6195080
H	0.8473040	-0.4650190	1.0993060
C	-4.1150870	-0.0096730	-0.3736430
C	-4.7762190	-0.5472270	-1.4743490
C	-5.9359820	-1.2881230	-1.3154260
C	-6.4611270	-1.5047060	-0.0472240
C	-5.8080650	-0.9701680	1.0635070
C	-4.6521750	-0.2363570	0.8985290
H	-6.2290880	-1.1457710	2.0470220
H	-4.3735780	-0.3803420	-2.4681530
H	-6.4424040	-1.7040580	-2.1815590
C	-7.6944060	-2.2916530	0.1061780
O	-8.2329680	-2.5373290	1.1558850
H	-8.1216760	-2.6647160	-0.8503030
C	3.3576690	0.4926640	0.6152730
H	1.9353810	1.7112740	1.5895040
C	4.1049290	0.4023100	1.8115160
C	5.2825510	-0.2904030	1.8689140
C	5.7941050	-0.9425040	0.7272620
C	5.0552040	-0.8616480	-0.4845210
C	3.8442400	-0.1376400	-0.5035490
C	7.0062310	-1.6677420	0.7453490
C	7.4685310	-2.2862640	-0.3832480
C	6.7372670	-2.2069490	-1.5851460
C	5.5606370	-1.5119190	-1.6335090
H	7.5659340	-1.7260190	1.6732820
H	8.3999170	-2.8403650	-0.3577300
H	7.1129430	-2.7010040	-2.4740740
H	4.9968810	-1.4503110	-2.5588230
H	3.2959890	-0.0898520	-1.4399150
H	3.7285530	0.8979420	2.7010340
H	5.8399830	-0.3457850	2.7984480
H	-4.1532700	0.1725340	1.7707480
C	-2.9796570	2.2231430	-0.0147730
H	-2.0060180	3.5410620	-1.4245160
H	-1.6358100	3.8860640	0.2497170
H	-2.6870440	0.8786300	-1.6348850
H	-3.9151380	2.6803850	-0.3472700
H	-3.0287940	2.1863630	1.0786920

Table A.25: D-2,7ae ground state geometry [Å] optimized at PBE0/6-31G** level of theory.

Element	x	y	z
C	2.2433060	-2.4243920	1.0291850
C	2.9400100	-1.5616680	-1.2817780
C	1.4626770	-1.1534830	-1.5234620
C	0.7260310	-0.8252090	-0.1977880
C	0.7755150	-2.0429700	0.7552540
H	0.9372790	-2.0081290	-2.0061000
H	1.4122070	-0.3055490	-2.2393280
C	-0.7307000	-0.4114600	-0.4719340
H	1.2181400	0.0226790	0.3180340
C	0.0352670	-1.7252400	2.0697920
H	0.2658680	-2.9073350	0.2699100
C	-1.4186510	-1.3139800	1.7880960
H	0.5515570	-0.8934710	2.5990270
H	0.0427130	-2.6159780	2.7349600
C	-1.4521260	-0.0880640	0.8533030
H	-1.9177170	-1.0683780	2.7506810
H	-1.9578760	-2.1687860	1.3240270
H	-1.2551810	-1.2342900	-1.0058610
H	-0.7381520	0.4898690	-1.1237920
C	3.8779910	-0.4159660	-0.8624820
C	3.4646290	0.9325570	-0.7507250
C	4.3667110	1.9353140	-0.3878700
C	5.7077130	1.6294000	-0.1354060
C	6.1381910	0.3008530	-0.2589170
C	5.2374770	-0.7045220	-0.6225910
H	7.1732040	0.0377920	-0.0795320
H	2.4537410	1.2457770	-0.9535990
H	4.0145410	2.9572280	-0.3112530
C	6.6425450	2.7097510	0.2428280
O	7.8205190	2.4765110	0.4642200
H	6.2845380	3.7314700	0.3264170
C	-2.8698910	0.3883420	0.5973440
H	-0.8882680	0.7308550	1.3562610
C	-3.2493020	1.6807960	1.0011370
C	-4.5419440	2.1523570	0.7666180
C	-5.4820260	1.3407900	0.1197370
C	-5.1162760	0.0364460	-0.2912120
C	-3.8155300	-0.4317160	-0.0477670
C	-6.7814170	1.8100090	-0.1267790
C	-7.7101440	0.9931280	-0.7771150
C	-7.3504860	-0.2944700	-1.1837830
C	-6.0595810	-0.7741730	-0.9426830
H	-7.0771570	2.8061240	0.1807070
H	-8.7107280	1.3595640	-0.9669140
H	-8.0740760	-0.9219120	-1.6878760
H	-5.7989810	-1.7747280	-1.2664200
H	-3.5382530	-1.4294150	-0.3657210
H	-2.5414790	2.3320210	1.4989070
H	-4.8044550	3.1534100	1.0878490
H	5.6150060	-1.7131040	-0.7196400
C	2.9530320	-2.7565980	-0.2901670
H	2.2772740	-3.3163360	1.6920410
H	2.7743940	-1.5904460	1.5392000
H	3.3515220	-1.9292690	-2.2476940
H	2.4217910	-3.6152440	-0.7582950
H	3.9862590	-3.1014910	-0.0847650

A.4 The Ethylene Dimer: Computational Data

Table A.26: SEET excitonic couplings in cm^{-1} at CIS/def-SVP level of theory.

Distance [Å]	Coulomb	Exchange	MTD	ET1-HT2	HT1-ET2	MTD-TI	Davydov
3.00	5052.40	-1379.92	3672.48	2935.83	2935.83	9544.15	9811.61
3.25	3972.62	-712.49	3260.14	2176.60	2176.60	7613.33	7088.37
3.50	3138.23	-341.86	2796.36	1466.31	1466.31	5728.98	5075.57
3.75	2500.62	-152.86	2347.76	871.57	871.57	4090.91	3637.02
4.00	2014.54	-63.66	1950.89	466.02	466.02	2882.92	2640.72
4.25	1642.39	-24.59	1617.81	228.78	228.78	2075.37	1965.51
4.50	1355.00	-8.75	1346.24	104.37	104.37	1554.98	1510.31
4.75	1130.57	-2.86	1127.71	44.43	44.43	1216.57	1199.65
5.00	953.18	-0.85	952.33	17.64	17.64	987.61	981.38
5.25	811.26	-0.23	811.02	6.51	6.51	824.05	821.71
5.50	696.39	-0.06	696.33	2.23	2.23	700.79	699.69
5.75	602.42	-0.01	602.41	0.70	0.70	603.82	603.23
6.00	524.78	-0.00	524.78	0.21	0.21	525.19	524.76
6.25	460.05	-0.00	460.05	0.06	0.06	460.16	459.80
6.50	405.64	-0.00	405.64	0.01	0.01	405.67	405.37
6.75	359.56	-0.00	359.56	0.00	0.00	359.57	359.39
7.00	320.27	-0.00	320.27	0.00	0.00	320.27	320.10
7.25	286.54	-0.00	286.54	0.00	0.00	286.54	286.41
7.50	257.43	-0.00	257.43	0.00	0.00	257.43	257.33
7.75	232.17	-0.00	232.17	0.00	0.00	232.17	232.09
8.00	210.13	-0.00	210.13	0.00	0.00	210.13	210.04
8.25	190.82	-0.00	190.82	0.00	0.00	190.82	190.72
8.50	173.82	-0.00	173.82	0.00	0.00	173.82	173.71
8.75	158.79	-0.00	158.79	0.00	0.00	158.79	158.79
9.00	145.46	-0.00	145.46	0.00	0.00	145.46	145.40
9.25	133.59	-0.00	133.59	0.00	0.00	133.59	133.55
9.50	122.99	-0.00	122.99	0.00	0.00	122.99	122.91
9.75	113.48	-0.00	113.48	0.00	0.00	113.48	113.47
10.00	104.94	-0.00	104.94	0.00	0.00	104.94	104.91

Table A.27: TEET excitonic couplings in cm^{-1} at CIS/def-SVP level of theory.

Distance [Å]	Exchange	MTD	ET1-HT2	HT1-ET2	MTD-TI	Davydov
3.00	-472.01	-472.01	-577.96	-577.96	-1627.94	-2316.34
3.25	-235.24	-235.24	-385.80	-385.80	-1006.84	-1250.90
3.50	-109.72	-109.72	-252.49	-252.49	-614.70	-656.56
3.75	-47.98	-47.98	-152.75	-152.75	-353.47	-337.33
4.00	-19.63	-19.63	-84.93	-84.93	-189.49	-169.98
4.25	-7.47	-7.47	-43.71	-43.71	-94.89	-83.73
4.50	-2.62	-2.62	-20.93	-20.93	-44.49	-39.83
4.75	-0.84	-0.84	-9.33	-9.33	-19.51	-18.00
5.00	-0.25	-0.25	-3.86	-3.86	-7.98	-7.68
5.25	-0.07	-0.07	-1.48	-1.48	-3.03	-2.96
5.50	-0.02	-0.02	-0.52	-0.52	-1.06	-1.10
5.75	-0.00	-0.00	-0.17	-0.17	-0.34	-0.33
6.00	-0.00	-0.00	-0.05	-0.05	-0.10	-0.11
6.25	-0.00	-0.00	-0.01	-0.01	-0.03	-0.00
6.50	-0.00	-0.00	-0.00	-0.00	-0.01	-0.00
6.75	-0.00	-0.00	-0.00	-0.00	-0.00	-0.00
7.00	-0.00	-0.00	-0.00	-0.00	-0.00	-0.00
7.25	-0.00	-0.00	-0.00	-0.00	-0.00	-0.00
7.50	-0.00	-0.00	-0.00	-0.00	-0.00	-0.00
7.75	-0.00	-0.00	-0.00	-0.00	-0.00	-0.00
8.00	-0.00	-0.00	-0.00	-0.00	-0.00	-0.00
8.25	-0.00	-0.00	-0.00	-0.00	-0.00	-0.00
8.50	-0.00	-0.00	-0.00	-0.00	-0.00	-0.00
8.75	-0.00	-0.00	-0.00	-0.00	-0.00	-0.00
9.00	-0.00	-0.00	-0.00	-0.00	-0.00	-0.00
9.25	-0.00	-0.00	-0.00	-0.00	-0.00	-0.00
9.50	-0.00	-0.00	-0.00	-0.00	-0.00	-0.00
9.75	-0.00	-0.00	-0.00	-0.00	-0.00	-0.00
10.00	-0.00	-0.00	-0.00	-0.00	-0.00	-0.00

B Included Papers

Phosphorescence Very Important Paper

How to cite: *Angew. Chem. Int. Ed.* **2020**, *59*, 17137–17144
International Edition: doi.org/10.1002/anie.202007610
German Edition: doi.org/10.1002/ange.202007610

Persistent Room Temperature Phosphorescence from Triarylboranes: A Combined Experimental and Theoretical Study

Zhu Wu, Jörn Nitsch, Julia Schuster, Alexandra Friedrich, Katharina Edkins, Marcel Loebnitz, Fabian Dinkelbach, Vladimir Stepanenko, Frank Würthner, Christel M. Marian, Lei Ji,* and Todd B. Marder**

Abstract: *Achieving highly efficient phosphorescence in purely organic luminophors at room temperature remains a major challenge due to slow intersystem crossing (ISC) rates in combination with effective non-radiative processes in those systems. Most room temperature phosphorescent (RTP) organic materials have O- or N-lone pairs leading to low lying (n, π*) and (π, π*) excited states which accelerate k_{isc} through El-Sayed's rule. Herein, we report the first persistent RTP with lifetimes up to 0.5 s from simple triarylboranes which have no lone pairs. RTP is only observed in the crystalline state and in highly doped PMMA films which are indicative of aggregation induced emission (AIE). Detailed crystal structure analysis suggested that intermolecular interactions are important for efficient RTP. Furthermore, photophysical studies of the isolated molecules in a frozen glass, in combination with DFT/MRCI calculations, show that (σ, B p)→(π, B p) transitions accelerate the ISC process. This work provides a new approach for the design of RTP materials without (n, π*) transitions.*

Introduction

Luminophores with ultralong room temperature phosphorescence (RTP) have attracted much attention because of a variety of applications in time-gated biological imaging,[1] anti-counterfeiting,[2] watch dials, safety signs, and optoelectronic devices.[3] Unlike metal-containing materials, in which the heavy atom effect can efficiently accelerate the intersystem crossing (ISC) process from singlet to triplet excited states,[4] RTP from purely organic molecules is relatively rare because the formation of the triplet states is usually not efficient as ISC is slow. In addition, radiative decay from T_1 to the S_0 ground state is also spin forbidden, and is very slow compared to the non-radiative relaxation from T_1 in an unrestricted environment.[5] Designing purely organic systems showing ultralong RTP is a challenge.[6] Key approaches involve reducing the nonradiative decay rate ($k_{nr}(T_1)$) from T_1 by avoiding collisions with quenching species such as oxygen, and minimizing vibrational relaxation (Figure 1 a).[7] For example, Tang and co-workers reported purely organic luminophores which phosphoresce in the crystalline state.[8] Huang and colleagues proposed that effective stabilization of triplet excited states through strong coupling in H-aggregated molecules enables their lifetimes to become orders of magnitude longer than those of conventional organic fluorophores.[9] Adachi and co-workers developed efficient persistent RTP materials by minimizing nonradiative decay rates in organic amorphous host–guest materials.[10] Very recently, Wang and co-workers have achieved ultralong RTP from *N*-phenyl-2-naphthylamine by confining it in a crystalline dibromobiphenyl matrix.[11] To increase the population of triplet excitons, heteroatoms with lone pairs are usually introduced into organic systems to enhance spin–orbit coupling (El-Sayed's rule),[12] which is why most RTP phosphors are limited to phenothiazine, carbazole, and naphthylimide derivatives (Figure 1 b).[1b,4d,13] Thus, intersystem crossing usually involves $^1(n, \pi^*)\rightarrow{}^3(\pi, \pi^*)$ transitions. Recently, arylboronic acids and esters, which also contain lone pairs on their hydroxy or alkoxy groups, have been reported to show RTP with lifetimes up to several seconds in the solid state.[14] Thus far, ultralong RTP from purely organic

[*] Z. Wu, Dr. J. Nitsch, Dr. J. Schuster, Dr. A. Friedrich, Dr. K. Edkins, Prof. Dr. L. Ji, Prof. Dr. T. B. Marder
Institut für Anorganische Chemie and Institute for Sustainable Chemistry & Catalysis with Boron, Julius-Maximilians-Universität Würzburg
Am Hubland, 97074 Würzburg (Germany)
E-mail: todd.marder@uni-wuerzburg.de

Dr. K. Edkins
School of Health Sciences, The University of Manchester, Oxford Road, Manchester M13 9PL (UK)

M. Loebnitz, F. Dinkelbach, Prof. Dr. C. M. Marian
Institut für Theoretische Chemie und Computerchemie, Heinrich-Heine-Universität Düsseldorf, Universitätsstr. 1, 40225 Düsseldorf (Germany)
E-mail: Christel.Marian@hhu.de

Dr. V. Stepanenko, Prof. Dr. F. Würthner
Institut für Organische Chemie, Julius-Maximilians-Universität Würzburg
Am Hubland, 97074 Würzburg (Germany)

Prof. Dr. L. Ji
Frontiers Science Center for Flexible Electronics (FSCFE) & Shaanxi Institute of Flexible Electronics (SIFE), Northwestern Polytechnical University, 127 West Youyi Road, 710072 Xi'an (China)
E-mail: iamlji@nwpu.edu.cn

Supporting information and the ORCID identification number(s) for the author(s) of this article can be found under: https://doi.org/10.1002/anie.202007610.

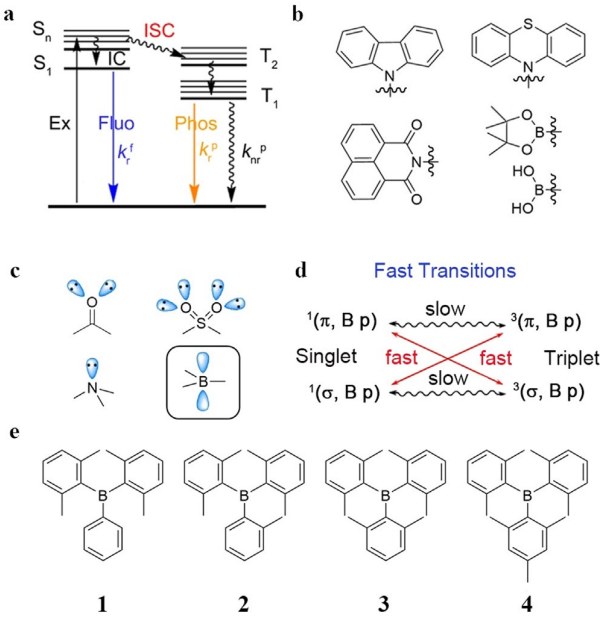

Figure 1. a) Jablonski-diagram. b) The structural features of reported RTP materials. c) Typical functional groups having lone pairs in organic phosphors, and the empty p_z orbital on three-coordinate boron. d) Fast transitions between (σ, B p) and (π, B p). e) Molecular structures of compounds **1**–**4**.

phosphors without lone pairs has rarely been reported,[15] as k_{isc} is slow.

In fact, organic compounds without lone pairs,[16] such as triarylboranes, can show phosphorescence in a frozen optical glass at 77 K (Figure 1c).[17] This indicates that k_{isc} in a photoexcited triarylborane molecule can compete with fluorescence, for which the rate constant is usually on the order of $10^7\ s^{-1}$. Therefore, we propose that k_{isc} can also be accelerated by (σ, B p)→(π, B p) transitions, which would be the inversion of the normally observed $^1(n, \pi^*)\rightarrow{}^3(\pi, \pi^*)$ ISC process (Figure 1d). However, probably due to the fact that the nonradiative decay rate from T_1 k_{nr}^P at RT is usually much faster than the phosphorescence, RTP from triarylboranes has not been reported. Only if k_{nr}^P is suppressed to a large extent, might we observe RTP from triarylboranes. In 1955, Wittig et al. reported that some triarylboranes, including tris(2-methylphenyl)borane, showed a yellowish-white emission under UV light.[18] However, no lifetimes were reported and, when we prepared tris(2-methylphenyl)borane, it showed only blue fluorescence; in other words, no phosphorescence at room temperature was detected (Supporting Information, Figures S14 and S15). Given our interest in the linear and nonlinear optical properties of 3-coordinate organoboron compounds,[19] we examined the triarylboranes **1**–**4** (Figure 1e). Crystalline samples of **3** (tris(2,6-dimethylphenyl)borane) show ultralong ($\tau_p = 478$ ms), intense, yellow phosphorescence under ambient conditions, and it is thus, to the best of our knowledge, the first triarylboron compound without lone pairs to display ultralong RTP.

Results and Discussion

The synthesis and characterization of all compounds are given in the Supporting Information and the photophysical properties of **1**–**4** are summarized in Table 1. The important results of our quantum chemical studies are shown in brackets, and complete data are given in Tables S2 and S4 in the Supporting Information. The UV/Vis absorption and emission spectra were first measured in hexane. Compounds **1**–**4** all show a broad first absorption band between 280–350 nm in hexane, which can be assigned to B←π transitions, that is, a transition from the aryl ring π-systems to the empty *p*-orbital on the boron atom (Figure 2a). Our calculations reveal that this band is formed by up to five electronic transitions, $S_1\leftarrow S_0$ to $S_4\leftarrow S_0$ in the D_3-symmetric compound **3** and $S_1\leftarrow S_0$ to $S_5\leftarrow S_0$ in the less symmetric compounds **1**, **2**, and **4** (Supporting Information, Figures S1–S5). The energies

Table 1: Experimental and calculated (in brackets) photophysical properties of compounds **1**–**4** in hexane and the crystalline state at RT, and in a frozen methylcyclohexane glass at 77 K.

	State	λ_f [nm]	Φ_f [%]	k_r^f [$\times 10^7\ s^{-1}$]	k_{nr}^f [$\times 10^8\ s^{-1}$]	k_{isc} [s^{-1}]	λ_p [nm]	Φ_p [%]	τ_p [s]
1	Crystalline[a]	369	3.4	2	6.0		524	0.3	0.09 (21%), 0.68 (79%)
	Crystalline[b]	368					471, 502, 541		2.27
	Frozen glass[b]	349 {383}				{1×10^7}	404, 427 {425, 597}		1.45 {8}
2	Crystalline[a]	369	6.9	4	5.8		nd[c]		nd
	Crystalline[b]	352, 366					426, 449		0.22 (39%), 1.22 (61%)
	Frozen glass[b]	373 {391}				{6×10^6}	417, 442 {448, 476}		1.57 {8}
3	Crystalline[a]	371, 390	17.0	10	5.9		540, 575	1.2	0.48
	Crystalline[b]	372, 392, 415					488, 538, 582, 630		0.52 (23%), 1.64 (77%)
	Frozen glass[b]	375 {404}				{5×10^7}	421, 446 {456, 486}		1.48 {7}
4	Crystalline[a]	381	6.3	4	6.2		nd[c]		nd
	Crystalline[b]	370					456, 485		0.08 (32%), 1.32 (68%)
	Frozen glass[b]	374 {430}				{3×10^7}	425, 452 {458, 489}		1.36 {5}

[a] Measured at RT. [b] Measured at 77 K. [c] Not detected (nd).

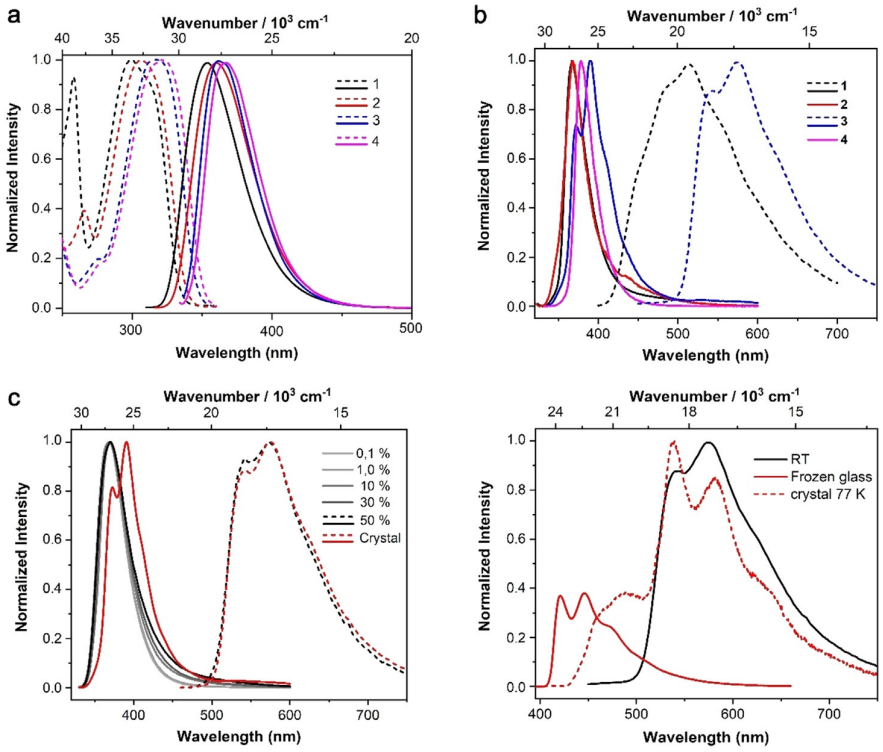

Figure 2. a) Normalized UV/Vis absorption (dashed lines) and fluorescence emission (solid lines) spectra of **1**–**4** in hexane solution at room temperature (λ_{exc} = 290 nm). b) Photoluminescence (PL) emission spectra (solid lines) of crystalline **1**–**4**, and time-gated phosphorescence emission (dashed lines) spectra at room temperature (λ_{exc} = 305 nm). c) Total PL emission (solid lines) and time-gated phosphorescence emission (dashed lines) spectra of **3** at 0.1, 1.0, 10, 30, and 50% loadings in PMMA films and in the crystalline state at room temperature (λ_{exc} = 305 nm). d) Time-gated phosphorescence emission spectra of compound **3** in the crystalline state at room temperature (solid black), frozen methylcylohexane glass matrix (solid red), and crystalline state (dashed line) at 77 K.

of the absorption maxima decrease in the order **1** > **2** > **3** > **4**. This indicates that introducing each methyl substituent, a weak σ-donor, on the phenyl ring, redshifts the absorption spectra by 6–12 nm (580–1230 cm^{-1}). The fluorescence spectra of the compounds in hexane show the same trend; their maxima redshift 2–7 nm (150–530 cm^{-1}) for each methyl group added to the phenyl ring (Figure 2a). However, the emission spectra of crystalline **1**–**4** are not related to their chemical structures in an obvious way (Figure 2b). In general, the fluorescence spectra of the solid, crystalline samples of compounds **1**–**4** are all redshifted compared with those in hexane solution. The bathochromic shift of **3** (2060 cm^{-1}) is considerably larger than those of **1**, **2**, and **4**. The bathochromic shifts of **2** (750 cm^{-1}) and **4** (930 cm^{-1}) are smaller than that of **1** (1150 cm^{-1}). This indicates that intermolecular interactions in crystalline **1** and **3** are larger than those in **2** and **4**, which is one possible explanation for the slower nonradiative decay (k_{nr}) from both S_1 and T_1, see below. In addition, compounds **1** and **3** may also have a higher probability of showing excimer emissions.

We noticed that upon exposure to a hand-held UV-lamp (λ = 365 nm), crystalline **3** showed violet fluorescence which disappears immediately when the lamp is turned off. Persistent greenish-yellow phosphorescence emission was then observed, which is visible to the naked eye for almost 4 s (Figure 3). Time-gated emission spectroscopy revealed long-lived (τ = 478 ms) phosphorescence from crystalline **3**, with an emission maximum at 575 nm and a shoulder at 540 nm (Figures 2b and S13 in the Supporting Information). To the best of our knowledge, this is the first triarylborane without any heavy atom[6j] to show long-lived RTP, and one of the rare examples where free electron pairs are absent. In addition to the RTP from **3**, RTP was also observed from crystalline **1**, with a phosphorescence emission maximum at 515 nm and a lifetime of τ = 680 ms. Compared to compound **3**, the phosphorescence quantum yield (Φ_P) of **1** is 0.26%, which is lower than that of **3** (1.14%). We did not observe any phosphorescence from compounds **2** and **4** at room temperature.

Interestingly, we found that the photoluminescence behavior of **3** largely depends on its aggregation state. We investigated two different kinds of aggregation states, crystalline sample **A** and ball-milled sample **B**. SEM pictures and powder X-ray diffraction (pXRD) patterns clearly revealed the difference between the samples. In the SEM pictures of the ball-milled powder, we can see smaller size particles with a larger surface area (Supporting Information, Figure S21). This is in agreement with the powder X-ray diffraction pattern of the ball-milled sample, which shows broader reflections compared to the diffraction pattern obtained from

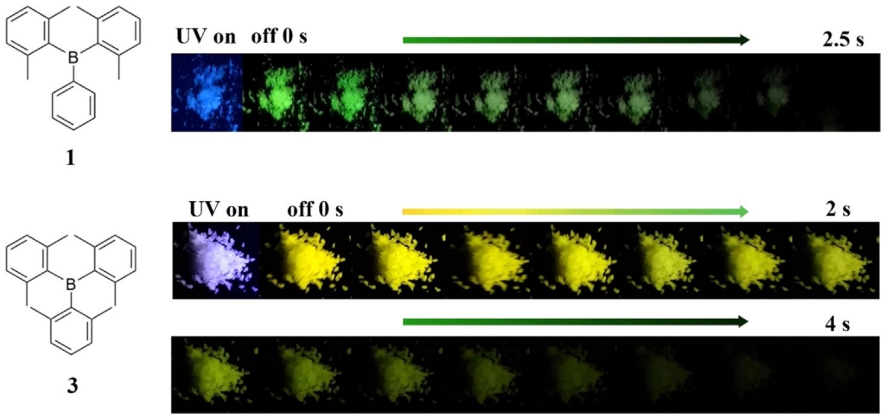

Figure 3. Photographs of crystalline **1** and **3** taken during and after irradiation (365 nm) under ambient conditions.

the crystalline sample **A** (Supporting Information, Figure S29), and this indicates that sample **B** contains much smaller crystallites than the sample **A**. We find that the emission maxima differ by 25 nm (1760 cm^{-1}) and that the peak at 350 nm in the excitation spectrum of sample **A** decreases in intensity as the crystalline domains increase (Supporting Information, Figures S23 and S24). Although the fluorescence lifetime and the time-gated phosphorescence emission spectra remained the same, the phosphorescence lifetime and quantum yield decreased significantly for the ball-milled sample **B** compared with crystalline **A**, from 478 to 340 ms and 1.12 % to 0.2 %, respectively. In the ball-milled powder, the exposed surface area is much larger, and phosphorescence is more sensitive to oxygen quenching, compared to the crystalline state. This hypothesis is supported by phosphorescence lifetime measurements under argon, for which the difference between the two samples disappears (Supporting Information, Figures S27 and S28).

To understand further the relationship between molecular structure and phosphorescence, we measured the emission spectra of **1**–**4** in a frozen methylcyclohexane optical glass at 77 K (Supporting Information, Figures S30 and S31), where we can assume that there are no intermolecular interactions present ($c < 10^{-5}$ mol L^{-1}). All four compounds show two well-separated emission bands. We observed phosphorescence emissions (400–600 nm), which are all hypsochromically shifted in comparison to the emission from the solid at room temperature (by 5230–5670 cm^{-1}). All compounds show similar vibrational fine structures except compound **1**, because **1** has low-frequency vibrational modes according to our calculations, which broaden the emission bands. In addition, there are high energy fluorescence emission bands (330–400 nm), which show less vibrational fine structure (Supporting Information, Figure S30). The maxima of the computed emission spectra (Supporting Information, Figures S8 and S11) are redshifted (by 1220–1820 cm^{-1}) with respect to the experimental spectra in a frozen glass while the energies of the 0-0 transitions agree well. The redshifts of the maxima are partially attributed to the harmonic oscillator approximation, which overestimates the intensities at the long wavelength tail of the emission spectrum that stems from electric dipole transitions between the vibrational ground state of the electronically excited state and vibrationally excited levels of the electronic ground state. The calculated values for k_{isc} of **1**–**4** are circa 10^7 s^{-1}, thus ISC can compete with fluorescence. Noticeably, the major components of the phosphorescence lifetimes of all four compounds are similar, with a value of circa 1.5 s (Supporting Information, Figure S32). Up to six triplet states are located energetically below or very close to the S_1 state as shown in Figures S6 and S7 in the Supporting Information. Some of the triplet potential energy surfaces cross the S_1 energy profile along the linear interpolated path connecting the Franck–Condon point with the minimum of the S_1 state. ISC is nevertheless fastest for a transition between S_1 and T_2 in **1**, **2**, **3**, and **4**. To understand the origin of the non-negligible spin–orbit coupling (SOC) between these states, we computed and plotted the differences of the electron densities between the ground and excited-state wave functions. S_1 and T_1 of compound **3**, for example (Figure 4), result from similar (π, B p) excitations, with T_1 showing additional contributions from local (π, π^*) excitations on xylyl ring a. For this transition,[12] the SOC is very small. Comparing the difference densities of S_1 and T_2 instead, we see two major differences. First, in T_2, most of the electron density has been transferred from the other two xylyl rings b and c. As the largest SOCs result from one-center terms, excitations from different π systems to the same boron orbital yield negligible interaction matrix elements. The second, and more important, difference with regard to SOC is a contribution to the T_2 wave function in which charge is transferred from a σ-type orbital connecting xylyl ring a with boron. The change of orbital angular momentum on this carbon atom leads to stronger SOC than expected in the absence of (n, π^*) excitations. This evidence clearly demonstrates that k_{isc} can also be accelerated by (σ, B p)→(π, B p) and (π, B p)→(σ, B p) transitions. An electronic matrix element $|<T_2|H_{SO}|S_1>| \approx 1$ cm^{-1} is sufficient for ISC to proceed at a rate of circa 10^7 s^{-1} (for more details, see Tables S1 and S2 in the Supporting Information). As the calculated fluorescence and ISC rate constants are of the same order of magnitude, the competition between the two processes is easily explained. T_2 and T_1 form a Jahn–Teller pair which is degenerate in D_3-symmetric geometries.

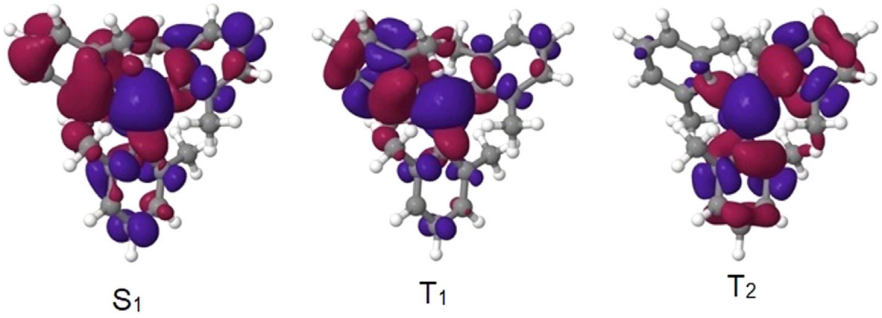

Figure 4. Difference densities (|isovalue| = 0.001 [e Å^{-3}]$^{1/2}$) of low-lying excited states of compound **3** at the TD-DFT-optimized geometry of the S_1 state. The loss of electron density with respect to the S_0 state is indicated in red and the gain in blue.

The states are thus coupled by strong vibronic interactions that facilitate fast $T_2 \rightarrow T_1$ internal conversion. Although triplet formation is likely to occur in all compounds, no phosphorescence was detected in solution at room temperature, likely due to rapid nonradiative decay $k_{nr}(T_1)$ compared to slow k_p. Our data indicate that triplet excited states are formed in all compounds **1**–**4** after excitation.

We further noticed that the RTP emission in crystalline samples of **3** is noticeably redshifted by 5230 cm^{-1} when compared to that in the frozen glass (Figure 2d). Such a large shift makes it unlikely that it results from the suppression of the internal conversion (temperature effect) in the excited state, or by a less polar environment (environment effect) in the frozen glass. To examine how temperature influences the luminescent behavior of crystalline samples, we also measured the emission spectra of crystalline **1**–**4** at 77 K (Supporting Information, Figure S33). In crystalline **3**, a sharp fluorescence peak appears at 415 nm at 77 K, which is almost identical to the fluorescence in the frozen glass. However, a very broad phosphorescent emission ranging from 430 to 720 nm (Figure 2d) is observed, which we assign to two phosphorescence bands, one at 488 nm and a second ranging from 500 to 720 nm. We noticed that the band at 488 nm is only visible at low temperature and is most likely not a vibrational band of the 500–720 nm emission, for which the range is identical to the spectrum at room temperature (Figure 2d). We observe two lifetimes, one of 1.64 s, and a second of 0.52 s, which further support the existence of two independent triplet states. We note that the longer lifetime is almost identical to the lifetime in the frozen glass, in which we can assume the absence of any intermolecular interaction except with solvent matrix molecules. We assume that the band at 488 nm is phosphorescence which is caused by the population of the T_1 state of the triarylboranes and which is only visible when the non-radiative decay is suppressed. Therefore, it cannot be observed at higher temperatures, at which $k_{nr}(T_1)$ dominate. This emission is also found in the frozen glass in which it is shifted by 67 nm (3260 cm^{-1}), which is a reasonable shift if one considers the different environments of the frozen glass matrix and the crystalline sample. The emission between 500–720 nm, however, is the real RTP emission which is an aggregation induced phenomenon, in contrast to the phosphorescence at 488 nm. It is important to note that this emission is absent in the dilute frozen glass, in which we can assume that the emission resembles that of the isolated molecules. Furthermore, when **3** is embedded in a poly(methyl methacrylate) (PMMA) matrix, RTP is only observed in very highly doped films ($\geq$ 50 wt %, Figure 2c), further confirming the critical role of aggregation for this emission (Supporting Information, Figures S16–S20).

To understand the effect of the solid-state structures and the intermolecular packing on the luminescence properties, the crystal structures of compounds **1**–**4** were obtained by single-crystal X-ray diffraction (Supporting Information, Figures S39–S42). If we compare the molecular geometries of compounds **1**–**4** in their crystal structures, we can observe the influence of additional methyl groups on the phenyl rings close to the central boron atom. While the B–C bond distances lie in a similar range for the bulkier *m*-xylyl and mesityl groups (1.576–1.587 Å), the B–C (aryl) distances to the *o*-tolyl group (B–C = 1.570(2) Å in compound **2**) and the phenyl ring (B–C = 1.569(2) Å in compound **1**) are slightly shorter (Supporting Information, Table S7). The effect of the bulkiness of the substituent and, hence, repulsion between methyl groups is further observed in the torsion angles between the aryl groups and the BC3 planes. While the torsion angles are in a similar range (50.0–54.9°) for the *m*-xylyl and mesityl groups in compounds **3** and **4**, a significantly smaller torsion angle (41.9°) is observed for the *o*-tolyl group in compound **2**, and a very small torsion angle of only 16.1° is observed for the phenyl group in compound **1**. These smaller torsion angles are compensated by larger torsion angles (56.7–65.3°) for the *m*-xylyl groups in compounds **1** and **2** compared to those of compounds **3** and **4** (Table S7).

In order to compare and classify the types and magnitudes of the intermolecular interactions within single crystals of these four triarylboranes, which organize in a complex three-dimensional arrangement, the concept of Hirshfeld surface analysis was applied (see Supporting Information for more details).[20] The Hirshfeld surface is a special isosurface defined by the weighting function $w(\mathbf{r}) = 0.5$ for a particular molecule. This means that the Hirshfeld surface envelops the volume within which the particular molecule contributes more than half of the electron density. Hence, it also includes information on the nearest neighbors and closest contacts to the molecule. The molecules are most densely packed in compound **2**, as is clear from both the crystal packing coefficient c_k, which corresponds to the ratio of volume

occupied by all molecules in the unit cell to the unit cell volume, and the surface of the crystal's void per formula unit, which is obtained from the Hirshfeld analysis (Supporting Information, Table S8).[21] Interestingly, compounds **1** and **3** show similar, intermediate packing densities, while compound **4** seems to have the loosest packing. While the surfaces of the voids seem to be spread well throughout the unit cells of compounds **1**, **2**, and **4**, a larger void of 9 $Å^3$ is present in compound **3** around the origin of the unit cell (Figure 5). From comparison of the fluorescence emissions of compounds **1**–**4**, we can conclude that the RTP is not correlated with the packing density, as compound **2** is the densest packed compound. A deeper insight into the intermolecular interactions is required in order to provide an interpretation of the observed differences in emission behavior. Fingerprint analysis of the Hirshfeld surface and its breakdown into the individual relative contributions in crystals of **1**–**4**,[22] exhibited a strong contribution of H···H interactions (75–83%), followed by a significant amount of C···H interactions (17–25%) in all four compounds (Supporting Information, Figures S4 and S44). Only a very weak contribution of C···C interactions is observed for compound **3** (0.2%). While this analysis shows the relative contributions of the different types of intermolecular interactions, we are now interested in their strengths in the individual crystal structures. Compounds **1** and **3** exhibit several significant intermolecular C–H···C interactions, including strong, nearly linear interactions (C···H = 2.835–2.841 Å, C–H···C = 164–168°, Table S9 in the Supporting Information). In addition, compound **1** has a short H···H contact (2.241 Å) between two aryl rings, which is also demonstrated by the spike in the bottom left corner of its fingerprint plot (Supporting Information, Figure S44).

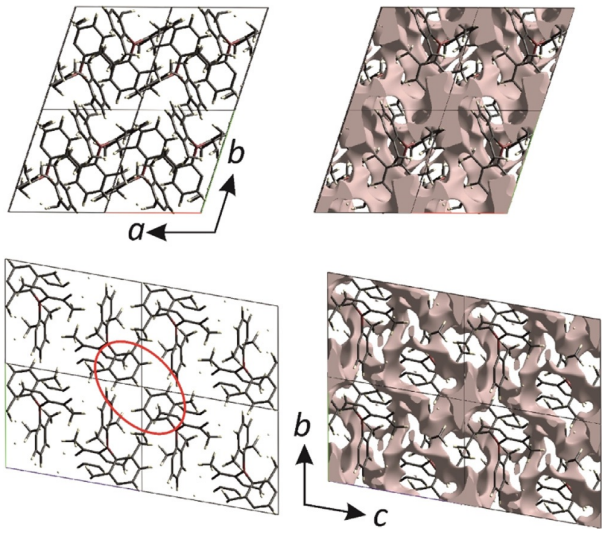

Figure 5. Crystal structure of compound **3** (left) projected along the *c* axis (top) and along the *a* axis (bottom), and plot of the surface of the crystal voids (0.002 au) from the Hirshfeld analysis (right). Four unit cells are shown in each case. Note the larger voids around the origin of the unit cell, as best observed in the centers of the drawings. The red ellipse encloses the aryl rings that are involved in a weak π···π interaction.

Compound **2**, although more densely packed than **1** and **3**, shows significantly fewer and weaker intermolecular C–H···C interactions. In addition, it shows a nearly linear, weak C–H···π interaction towards the centroid of an *m*-xylyl ring (H···π = 2.907 Å) and two close C···C contacts (C···C = 3.334 and 3.384 Å), a strong one between two aryl rings, and a weak one between the same aryl and a methyl group (Table S9). These results are consistent with our analysis of the fluorescence emission in the crystalline states, wherein compounds **1** and **2** have the same emission maxima although one more methyl group is introduced to the phenyl ring in compound **2**. This may be explained by the presence of more and stronger interactions in **1** than in **2**. In crystals of compound **4**, intermolecular interactions are the weakest (Table S9). This is in agreement with the loosest packing mode. In addition to the strong C–H···C interactions, compound **3** also has a strong C···C interaction (C6···C6 = 3.319 Å) between two aryl rings with an approximately parallel alignment of their planes. This is the shortest nearest-neighbor (nn) C···C distance in all of the compounds. The interplanar separation between the aryl planes is only 2.980 Å; however, the offset shift is large (4.221 Å), resulting in a centroid-to-centroid distance of 5.167 Å, the latter two values being too large for a typical offset face-to-face π···π stacking interaction between two arenes (Supporting Information, Table S10), which typically have values ranging from 3.3–3.8 Å for the interplanar separation, < 4.0 Å for the offset, and < 5.0 Å for the centroid-to-centroid distance.[23] There is another arrangement of nearly parallel aryl rings, which has a longer C···C distance (3.495 Å) and interplanar separation (3.397 Å), but a smaller shift (3.493 Å) and, hence, a smaller centroid-to-centroid distance of 4.872 Å, all of those values being within the typical range of weak π···π interactions. The aryl rings, and hence the π···π interaction, are situated close to the voids, which are around the origin (Figure 5). It is proposed that, on compression of the crystal structure, the voids may shrink and, hence, the offset may also be reduced, enhancing the π···π interaction between these aryl rings. On the other hand, expansion of the molecule may also bring the rings closer together and enhance the π···π interaction. We assume that the aggregation of molecules forming C–H···C and π···π interactions is important for effective RTP in compounds **1** and **3**. A C···C offset aryl–aryl interaction is also present in both compounds **2** and **4** (Supporting Information, Table S10); however, the C–H···C interactions are much weaker in these compounds. In summary, the presence of both strong C–H···C and C···C contacts as well as weak π···π interactions in compound **3**, together with the void accumulation at the origin of the unit cell (Figure 5) may be the reason for the strong redshift and persistence of the aggregation-induced phosphorescence emission of these crystals at room temperature and in highly doped PMMA-films.

Conclusion

We have prepared triarylboranes without lone pairs which exhibit long-lived room-temperature phosphorescence in the crystalline state and in highly doped PMMA films. Theoret-

ical calculations revealed that the ISC process can be accelerated by transitions between local σ and π excitation, which is consistent with photophysical studies of the isolated molecules in a frozen glass and is an extension of El-Sayed's rule. Moreover, the phosphorescent compounds **1** and **3** have the strongest interactions, especially when considering C–H···C interactions, which appear to play an important role in achieving persistent RTP and, at the same time, suppressing nonradiative decay. However, compounds **2** and **4** have fewer and weaker contacts in their crystalline states, and their nonradiative decay is fast, even though compound **2** has the densest packing. Thus, we do not observe RTP from crystals of compounds **2** and **4**. This study on triarylboranes provides an interesting example of how to expand the scope of purely organic phosphorescent materials.

Acknowledgements

Funding from the Julius-Maximilians-Universität Würzburg, and the Deutsche Forschungsgemeinschaft (DFG) (GRK 2112, and 396890929/GRK 2482) is gratefully acknowledged. We are grateful to the China Scholarship Council for providing a scholarship to Z.W. Open access funding enabled and organized by Project DEAL.

Conflict of interest

The authors declare no conflict of interest.

Keywords: AIE · boron · El-Sayed's rule · non-radiative transition · RTP

[1] a) T. Maldiney, A. Lecointre, B. Viana, A. Bessiere, M. Bessodes, D. Gourier, C. Richard, D. Scherman, *J. Am. Chem. Soc.* **2011**, *133*, 11810 – 11815; b) J. Yang, X. Zhen, B. Wang, X. Gao, Z. Ren, J. Wang, Y. Xie, J. Li, Q. Peng, K. Pu, Z. Li, *Nat. Commun.* **2018**, *9*, 840 – 849; c) G. Zhang, G. M. Palmer, M. W. Dewhirst, C. L. Fraser, *Nat. Mater.* **2009**, *8*, 747 – 751; d) K. Y. Zhang, Q. Yu, H. Wei, S. Liu, Q. Zhao, W. Huang, *Chem. Rev.* **2018**, *118*, 1770 – 1839; e) X. F. Wang, H. Y. Xiao, P. Z. Chen, Q. Z. Yang, B. Chen, C. H. Tung, Y. Z. Chen, L. Z. Wu, *J. Am. Chem. Soc.* **2019**, *141*, 5045 – 5050.

[2] a) M. Baroncini, G. Bergamini, P. Ceroni, *Chem. Commun.* **2017**, *53*, 2081 – 2093; b) S. Cai, H. Shi, J. Li, L. Gu, Y. Ni, Z. Cheng, S. Wang, W. W. Xiong, L. Li, Z. F. An, W. Huang, *Adv. Mater.* **2017**, *29*, 1701244; c) C. Li, X. Tang, L. Zhang, C. Li, Z. Liu, Z. Bo, Y. Q. Dong, Y. H. Tian, Y. Dong, B. Z. Tang, *Adv. Opt. Mater.* **2015**, *3*, 1184 – 1190.

[3] L. Dou, J. You, Z. Hong, Z. Xu, G. Li, R. A. Street, Y. Yang, *Adv. Mater.* **2013**, *25*, 6642 – 6671.

[4] a) A. Fermi, G. Bergamini, M. Roy, M. Gingras, P. Ceroni, *J. Am. Chem. Soc.* **2014**, *136*, 6395 – 6400; b) T. J. Penfold, E. Gindensperger, C. Daniel, C. M. Marian, *Chem. Rev.* **2018**, *118*, 6975 – 7025; c) J. Zhao, W. Wu, J. Sun, S. Guo, *Chem. Soc. Rev.* **2013**, *42*, 5323 – 5351; d) S. Xu, R. Chen, C. Zheng, W. Huang, *Adv. Mater.* **2016**, *28*, 9920 – 9940.

[5] a) O. Bolton, D. Lee, J. Jung, J. Kim, *Chem. Mater.* **2014**, *26*, 6644 – 6649; b) S. Cai, H. Shi, Z. Zhang, X. Wang, H. Ma, N. Gan, Q. Wu, Z. Cheng, K. Ling, M. Gu, C. Ma, L. Gu, Z. An, W. Huang, *Angew. Chem. Int. Ed.* **2018**, *57*, 4005 – 4009; *Angew. Chem.* **2018**, *130*, 4069 – 4073; c) P. Ceroni, *Chem* **2016**, *1*, 524 – 526; d) M. A. El-Sayed, *J. Chem. Phys.* **1963**, *38*, 2834 – 2838; e) R. M. Hochstrasser, *J. Chem. Phys.* **1963**, *39*, 3153 – 3154; f) R. Joshi, O. R. Meitei, M. Jadhao, H. Kumar, S. K. Ghosh, *Phys. Chem. Chem. Phys.* **2016**, *18*, 27910 – 27920; g) H. Matsuoka, M. Retegan, L. Schmitt, S. Hoger, F. Neese, O. Schiemann, *J. Am. Chem. Soc.* **2017**, *139*, 12968 – 12975; h) G. Q. Zhang, J. B. Chen, S. J. Payne, S. E. Kooi, J. N. Demas, C. L. Fraser, *J. Am. Chem. Soc.* **2007**, *129*, 8942 – 8943.

[6] a) S. M. A. Fateminia, Z. Mao, S. Xu, Z. Yang, Z. Chi, B. Liu, *Angew. Chem. Int. Ed.* **2017**, *56*, 12160 – 12164; *Angew. Chem.* **2017**, *129*, 12328 – 12332; b) K. Jiang, Y. Wang, C. Cai, H. Lin, *Adv. Mater.* **2018**, *30*, 1800783; c) Y. Katsurada, S. Hirata, K. Totani, T. Watanabe, M. Vacha, *Adv. Opt. Mater.* **2015**, *3*, 1726 – 1737; d) M. S. Kwon, D. Lee, S. Seo, J. Jung, J. Kim, *Angew. Chem. Int. Ed.* **2014**, *53*, 11177 – 11181; *Angew. Chem.* **2014**, *126*, 11359 – 11363; e) Q. Li, M. Zhou, Q. Yang, Q. Wu, J. Shi, A. Gong, M. Yang, *Chem. Mater.* **2016**, *28*, 8221 – 8227; f) S. Mukherjee, P. Thilagar, *Chem. Commun.* **2015**, *51*, 10988 – 11003; g) M. Shimizu, R. Shigitani, M. Nakatani, K. Kuwabara, Y. Miyake, K. Tajima, H. Sakai, T. Hasobe, *J. Phys. Chem. C* **2016**, *120*, 11631 – 11639; h) Y. Yu, M. S. Kwon, J. Jung, Y. Zeng, M. Kim, K. Chung, J. Gierschner, J. H. Youk, S. M. Borisov, J. Kim, *Angew. Chem. Int. Ed.* **2017**, *56*, 16207 – 16211; *Angew. Chem.* **2017**, *129*, 16425 – 16429; i) Z. Xu, Q. T. Liu, X. Z. Wang, Q. Liu, D. Hean, K. C. Chou, M. O. Wolf, *Chem. Sci.* **2020**, *11*, 2729 – 2734; j) J. L. Ma, H. Liu, S. Y. Li, Z. Y. Li, H. Y. Zhang, Y. Wang, C. H. Zhao, *Organometallics* **2020**, https://doi.org/10.1021/acs.organomet.0c00068.

[7] a) M. S. Kwon, Y. Yu, C. Coburn, A. W. Phillips, K. Chung, A. Shanker, J. Jung, G. Kim, K. Pipe, S. R. Forrest, J. H. Youk, J. Gierschner, J. Kim, *Nat. Commun.* **2015**, *6*, 8947; b) D. Lee, O. Bolton, B. C. Kim, J. H. Youk, S. Takayama, J. Kim, *J. Am. Chem. Soc.* **2013**, *135*, 6325 – 6329; c) H. Shi, Z. An, P. Z. Li, J. Yin, G. Xing, T. He, H. Chen, J. Wang, H. Sun, W. Huang, Y. Zhao, *Cryst. Growth Des.* **2016**, *16*, 808 – 813; d) X. G. Wu, C. Y. Huan, D. G. Chen, D. H. Liu, C. C. Wu, K. J. Chou, B. Zhang, Y. F. Wang, Y. Liu, E. Y. Li, W. G. Zhu, P. T. Chou, *Nat. Commun.* **2020**, *11*, 2145; e) J. F. Wang, Z. F. Chai, J. Q. Wang, C. Wang, M. M. Han, Q. Y. Liao, A. R. Huang, P. X. Lin, C. G. Li, Q. Q. Li, Z. Li, *Angew. Chem. Int. Ed.* **2019**, *58*, 17297 – 17302; *Angew. Chem.* **2019**, *131*, 17457 – 17462.

[8] a) Y. Gong, G. Chen, Q. Peng, W. Z. Yuan, Y. Xie, S. Li, Y. Zhang, B. Z. Tang, *Adv. Mater.* **2015**, *27*, 6195 – 6201; b) Y. Gong, L. Zhao, Q. Peng, D. Fan, W. Z. Yuan, Y. Zhang, B. Z. Tang, *Chem. Sci.* **2015**, *6*, 4438 – 4444; c) Z. He, W. Zhao, J. W. Y. Lam, Q. Peng, H. Ma, G. Liang, Z. Shuai, B. Z. Tang, *Nat. Commun.* **2017**, *8*, 416; d) W. Zhao, Z. He, J. W. Y. Lam, Q. Peng, H. Ma, Z. Shuai, G. Bai, J. Hao, B. Z. Tang, *Chem* **2016**, *1*, 592 – 602.

[9] Z. F. An, C. Zheng, Y. Tao, R. Chen, H. Shi, T. Chen, Z. Wang, H. Li, R. Deng, X. Liu, W. Huang, *Nat. Mater.* **2015**, *14*, 685 – 690.

[10] S. Hirata, K. Totani, J. Zhang, T. Yamashita, H. Kaji, S. R. Marder, T. Watanabe, C. Adachi, *Adv. Funct. Mater.* **2013**, *23*, 3386 – 3397.

[11] J. Wei, B. Liang, R. Duan, Z. Cheng, C. Li, T. Zhou, Y. Yi, Y. Wang, *Angew. Chem. Int. Ed.* **2016**, *55*, 15589 – 15593; *Angew. Chem.* **2016**, *128*, 15818 – 15822.

[12] M. A. El-sayed, *Nature* **1963**, *197*, 481 – 482.

[13] a) X. F. Chen, C. Xu, T. Wang, C. Zhou, X. P. Zhang, J. N. Demas, C. O. Trindle, G. Q. Zhang, *Angew. Chem. Int. Ed.* **2016**, *55*, 9872 – 9876; *Angew. Chem.* **2016**, *128*, 10026 – 10030; b) S. Hirata, *Adv. Opt. Mater.* **2017**, *5*, 1700116; c) D. Li, F. Lu, J. Wang, W. Hu, X. M. Cao, X. Ma, H. Tian, *J. Am. Chem. Soc.* **2018**, *140*, 1916 – 1923; d) P. K. Samanta, D. Kim, V. Coropceanu, J. L. Bredas, *J. Am. Chem. Soc.* **2017**, *139*, 4042 – 4051; e) Y. Xiong, Z. Zhao, W. J. Zhao, H. L. Ma, Q. Peng, Z. K. He, X. P. Zhang, Y. C. Chen, X. W. He, J. W. Y. Lam, B. Z. Tang, *Angew.*

Chem. Int. Ed. **2018**, *57*, 7997 – 8001; *Angew. Chem.* **2018**, *130*, 8129 – 8133; f) J. Yang, X. Gao, Z. Xie, Y. Gong, M. Fang, Q. Peng, Z. Chi, Z. Li, *Angew. Chem. Int. Ed.* **2017**, *56*, 15299 – 15303; *Angew. Chem.* **2017**, *129*, 15501 – 15505; g) Z. Yang, Z. Mao, X. Zhang, D. Ou, Y. Mu, Y. Zhang, C. Zhao, S. Liu, Z. Chi, J. Xu, Y. C. Wu, P. Y. Lu, A. Lien, M. R. Bryce, *Angew. Chem. Int. Ed.* **2016**, *55*, 2181 – 2185; *Angew. Chem.* **2016**, *128*, 2221 – 2225.

[14] a) Z. Chai, C. Wang, J. Wang, F. Liu, Y. Xie, Y. Z. Zhang, J. R. Li, Q. Li, Z. Li, *Chem. Sci.* **2017**, *8*, 8336 – 8344; b) S. Kuno, T. Kanamori, Z. Yijing, H. Ohtani, H. Yuasa, *ChemPhotoChem* **2017**, *1*, 102 – 106; c) Y. Shoji, Y. Ikabata, Q. Wang, D. Nemoto, A. Sakamoto, N. Tanaka, J. Seino, H. Nakai, T. Fukushima, *J. Am. Chem. Soc.* **2017**, *139*, 2728 – 2733; d) Q. Sun, L. Tang, Z. Zhang, K. Zhang, Z. Xie, Z. Chi, H. Zhang, W. Yang, *Chem. Commun.* **2018**, *54*, 94 – 97; e) J. Yang, Z. Ren, Z. Xie, Y. Liu, C. Wang, Y. Xie, Q. Peng, B. Xu, W. Tian, F. Zhang, Z. Chi, Q. Li, Z. Li, *Angew. Chem. Int. Ed.* **2017**, *56*, 880 – 884; *Angew. Chem.* **2017**, *129*, 898 – 902.

[15] a) M. Zander, *Naturwissenschaften* **1962**, *49*, 7; b) D. B. Clapp, *J. Am. Chem. Soc.* **1939**, *61*, 523 – 524; c) C. A. M. Salla, G. Farias, M. Rouzieres, P. Dechambenoit, F. Durola, H. Bock, B. de Souza, I. H. Bechtold, *Angew. Chem. Int. Ed.* **2019**, *58*, 6982 – 6986; *Angew. Chem.* **2019**, *131*, 7056 – 7060.

[16] a) C. Dou, S. Saito, S. Yamaguchi, *J. Am. Chem. Soc.* **2013**, *135*, 9346 – 9349; b) Z. M. Hudson, S. Wang, *Acc. Chem. Res.* **2009**, *42*, 1584 – 1596; c) F. Jäkle, *Chem. Rev.* **2010**, *110*, 3985 – 4022; d) W. L. Jia, D. T. Song, S. N. Wang, *J. Org. Chem.* **2003**, *68*, 701 – 705; e) C. Reus, S. Weidlich, M. Bolte, H. W. Lerner, M. Wagner, *J. Am. Chem. Soc.* **2013**, *135*, 12892 – 12907; f) S. Saito, K. Matsuo, S. Yamaguchi, *J. Am. Chem. Soc.* **2012**, *134*, 9130 – 9133; g) C. R. Wade, A. E. J. Broomsgrove, S. Aldridge, F. P. Gabbai, *Chem. Rev.* **2010**, *110*, 3958 – 4022; h) S. Yamaguchi, A. Wakamiya, *Pure Appl. Chem.* **2006**, *78*, 1413 – 1424.

[17] a) X. Wang, S. L. Gong, D. Song, Z. H. Lu, S. Wang, *Adv. Funct. Mater.* **2014**, *24*, 7257 – 7271; b) Z. L. Zhang, R. M. Edkins, N. Jörn, K. Fucke, A. Steffen, L. E. Longobardi, D. W. Stephan, C. Lambert, T. B. Marder, *Chem. Sci.* **2015**, *6*, 308 – 321.

[18] G. Wittig, W. Herwig, *Chem. Ber.* **1955**, *88*, 962 – 976.

[19] a) C. D. Entwistle, T. B. Marder, *Chem. Mater.* **2004**, *16*, 4574 – 4585; b) L. Ji, S. Griesbeck, T. B. Marder, *Chem. Sci.* **2017**, *8*, 846 – 863.

[20] a) J. J. McKinnon, A. S. Mitchell, M. A. Spackman, *Chem. Eur. J.* **1998**, *4*, 2136 – 2141; b) J. J. McKinnon, M. A. Spackman, A. S. Mitchell, *Acta Crystallogr. Sect. B* **2004**, *60*, 627 – 668; c) M. A. Spackman, D. Jayatilaka, *CrystEngComm* **2009**, *11*, 19 – 32; d) M. A. Spackman, P. G. Byrom, *Chem. Phys. Lett.* **1997**, *267*, 215 – 220.

[21] M. J. Turner, J. J. McKinnon, D. Jayatilaka, M. A. Spackman, *CrystEngComm* **2011**, *13*, 1804 – 1813.

[22] a) J. J. McKinnon, D. Jayatilaka, M. A. Spackman, *Chem. Commun.* **2007**, 3814 – 3816; b) A. Parkin, G. Barr, W. Dong, C. J. Gilmore, D. Jayatilaka, J. J. McKinnon, M. A. Spackman, C. C. Wilson, *CrystEngComm* **2007**, *9*, 648 – 652; c) M. A. Spackman, J. J. McKinnon, *CrystEngComm* **2002**, *4*, 378 – 392.

[23] a) T. Dahl, *Acta Chem. Scand.* **1994**, *48*, 95 – 106; b) C. A. Hunter, J. K. M. Sanders, *J. Am. Chem. Soc.* **1990**, *112*, 5525 – 5534; c) M. O. Sinnokrot, C. D. Sherrill, *J. Phys. Chem. A* **2004**, *108*, 10200 – 10207; d) M. O. Sinnokrot, E. F. Valeev, C. D. Sherrill, *J. Am. Chem. Soc.* **2002**, *124*, 10887 – 10893; e) L. Loots, L. J. Barbour, *The Importance of Pi-Interactions in Crystal Engineering: Frontiers in Crystal Engineering*, Wiley, Chichester, **2012**, pp. 109 – 124.

Manuscript received: May 27, 2020
Accepted manuscript online: June 23, 2020
Version of record online: August 4, 2020

Angewandte Chemie
Eine Zeitschrift der Gesellschaft Deutscher Chemiker

Supporting Information

Persistent Room Temperature Phosphorescence from Triarylboranes: A Combined Experimental and Theoretical Study

Zhu Wu, Jörn Nitsch, Julia Schuster, Alexandra Friedrich, Katharina Edkins, Marcel Loebnitz, Fabian Dinkelbach, Vladimir Stepanenko, Frank Würthner, Christel M. Marian, Lei Ji,* and Todd B. Marder**

anie_202007610_sm_miscellaneous_information.pdf

Supporting Information

Table of Contents

I. General information.....S2

II. Experimental procedures and characterization.....S5

III. DFT calculations.....S9

IV. Experimental photophysical spectra.....S24

V. Single-crystal X-ray diffraction.....S40

VI. ^{1}H, $^{13}C\{^{1}H\}$, ^{11}B NMR spectra, GC-MS and HRMS.....S57

VII. References.....S71

I. General information

Compounds **1-4** were prepared according to reported literature procedures.[1] Details are shown below. All starting materials were purchased from commercial sources and were used without further purification. The organic solvents for synthetic reactions and for photophysical measurements were HPLC grade, further treated to remove trace water using an Innovative Technology Inc. Pure-Solv Solvent Purification System and deoxygenated using the freeze-pump-thaw method. All synthetic reactions were performed in an Innovative Technology Inc. glovebox or under an argon atmosphere using standard Schlenk techniques. ^{1}H, ^{13}C and ^{11}B NMR spectra were measured on a Bruker Avance 500 MHz (^{1}H, 500 MHz; ^{13}C, 126 MHz; ^{11}B, 160 MHz) or Bruker Avance III 400 MHz (^{1}H, 400 MHz; ^{13}C, 101 MHz; ^{11}B, 128 MHz) NMR spectrometer. Mass spectra were recorded on Agilent 7890A/5975C Inert GC/MSD systems operating in EI mode. Elemental analyses were performed on a Leco CHNS-932 Elemental Analyser.

General photophysical measurements. All measurements were performed in standard quartz cuvettes (1 cm × 1 cm cross-section) except for ball-milled powder samples. They were prepared on 1 x 5 cm quartz plate (in air) or in a sealed cuvette (under argon). The emission signal showed no decrease in intensity or shape even after continuous irradiation over a period of 4 h. Samples recovered after each measurement showed the same photophysical properties when measured again, so there was no evidence for (photo)decomposition. UV-visible absorption spectra were recorded using an S6 Agilent 8453 diode array UV-visible spectrophotometer. The molar extinction coefficients were calculated from three independently prepared samples in hexane solutions. The emission spectra were recorded using an Edinburgh Instruments FLSP920 spectrometer equipped with a double monochromator for both excitation and emission, operating in right angle geometry mode, and all spectra were fully corrected for the spectral response of the instrument. All solutions used in photophysical measurements had concentrations lower than 10^{-5} M to minimize inner filter effects during fluorescence measurements.

Quantum yield measurements. The photoluminescent quantum yields were measured using a calibrated integrating sphere (inner diameter: 150 mm) from Edinburgh Instruments combined with the FLSP920 spectrometer described above.

For solution-state measurements, the longest-wavelength absorption maximum of the compound in the hexane was chosen as the excitation wavelength. For solid-state measurements, the excitation wavelength was 305 nm. The phosphorescence quantum yield of compounds **1** and **3** were obtained using the equation:

$$\boldsymbol{\Phi}_{\mathrm{P}} = \frac{B}{A} \times \boldsymbol{\Phi}_{\mathrm{PL}}$$

where A and B represent the integrated areas of the total photoluminescence and phosphorescence spectra, respectively. For the phosphorescence quantum yields, the phosphorescence component was separated from the total photoluminescence (PL) spectrum based on the phosphorescence spectrum obtained separately. $\boldsymbol{\Phi}_{\mathrm{PL}}$ represents the absolute photoluminescence quantum yields of compounds in solid state.

Lifetime measurements. Fluorescence lifetimes were recorded using the time-correlated single-photon counting (TCSPC) method using an Edinburgh Instruments FLSP920 spectrometer equipped with a high speed photomultiplier tube positioned after a single emission monochromator. Measurements were made in right-angle geometry mode, and the emission was collected through a polarizer set to the magic angle. Solutions were excited with a pulsed diode laser at a wavelength of 316 nm at repetition rates of 10 or 20 MHz. The instrument response functions (IRF) were *ca.* 230 ps FWHM. The phosphorescence lifetimes were measured using a μF920 pulsed 60 W Xenon microsecond flashlamp, with a repetition rate of 0.2 Hz at room temperature and 0.1 Hz at 77 K. Decays were recorded to 10000 counts in the peak channel with a record length of at least 2000 channels. Iterative reconvolution of the IRF with one decay function and non-linear least-squares analysis were used to analyze the data. The quality of all decay fits was judged to be satisfactory, based on the calculated values of the reduced χ^2 and Durbin-Watson parameters and visual inspection of the weighted residuals.

Scanning Electron Microscopy SEM images were recorded using a Zeiss Ultra Plus field emission scanning electron microscope equipped with GEMINI e-Beam column operated at 1-3 kV with an aperture size set to 10 or 30 μm to avoid excessive charging and radiation damage of the areas imaged.

Powder X-ray diffraction and Phase analysis Compound **3** was ground into a powder using an agate mortar until almost no room-temperature phosphorescence was observed (sample **A**). In addition, compound **3** was placed in a stainless steel vial (2 mL) and ground with 5 steel balls (3 mm diameter) for 5 minutes at a frequency of 15 Hz in a Lab Wizz LMLW 320/2 ball mill (sample **B**). Powder X-ray diffraction patterns were collected from two parts of each of the manually ground and the ball-milled powder samples in reflection geometry on a Bruker D8 Discover powder diffractometer with Da Vinci design and linear Lynx-Eye detector. X-ray radiation (Cu-Kα_1; λ = 1.5406 Å) was focused with a Goebel mirror and Cu-Kα_2 radiation was eliminated by a Ni-absorber. Data were collected from 5 – 60° 2θ in steps of 0.025° at ambient temperature. They were corrected for an offset in 2θ and exported using the Bruker AXS Diffrac-Suite. The diffraction patterns were then converted using CMPR software[2] for further processing with the GSAS program.[3] Cell parameters, background, scaling factor, zero shift and profile parameters were refined using the LeBail method. The starting values for the refinement were taken from the single-crystal structure refinement at 100 K.

Crystal structure determination Crystals suitable for single-crystal X-ray diffraction were selected, coated in perfluoropolyether oil, and mounted on MiTeGen sample holders. For the data collection at room temperature, a crystal was glued onto the holder. Diffraction data were collected on Bruker X8 Apex II 4-circle diffractometers with CCD area detectors using Mo-Kα radiation monochromated by graphite or multi-layer focusing mirrors. The crystals were cooled using an Oxford Cryostream low-temperature device. Data for compounds **1**, **2**, **3**, and **4** were collected at 100 K. Additional data for compound **3** were collected at 293, 240, 180, 120, and 83 K. The images were processed and corrected for Lorentz-polarization effects and absorption as implemented in the Bruker software packages. The structures were solved using the intrinsic phasing method (SHELXT)[4] and Fourier expansion technique. All non-hydrogen atoms were refined in anisotropic approximation, with hydrogen atoms 'riding' in idealized positions, by full-matrix least squares against F^2 of all data, using SHELXL[5] software and the SHELXLE graphical user interface.[6] Diamond[7] software was used for graphical representation. Other structural information was extracted using Mercury[8] and OLEX2[9] software. Hirshfeld surfaces were calculated and analyzed using the Crystal Explorer[10] program. Crystal

data and experimental details are listed in Table S6 for all compounds at 100 K and in Table S11 for compound **3** at other temperatures; full structural information has been deposited with Cambridge Crystallographic Data Centre. CCDC-1940099 (**1**), CCDC-1940100 (**2**), CCDC-1940101 – 1940106 (**3**), and CCDC-1940107 (**4**).

II. Experimental procedures and characterization

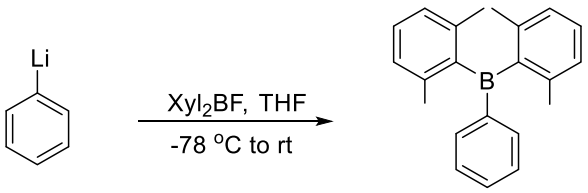

1

Bis(2,6-dimethylphenyl)(phenyl)borane (1): To a solution of bis(2,6-dimethylphenyl)-fluoroborane[11] (720 mg, 3.0 mmol) in anhydrous THF (20 mL) a hexane solution of PhLi (1.9 mL, 1.6 M, 3.1 mmol) was added dropwise by syringe at -78 °C. The reaction mixture was warmed to room temperature and stirred overnight. The reaction was quenched with a saturated solution of NaCl and the aqueous layer was extracted with Et_2O. The combined organic layer was dried over anhydrous Na_2SO_4, filtered, and concentrated under reduced pressure. The resulting crude material was subjected to silica gel column chromatography using *n*-hexane as eluent to afford 518 mg (1.74 mmol, 58%) of **1** as a white solid. Compound **1** (0.2 g) was dissolved in 2 mL of hexane. The solution was then transferred to two 1 mL GC vials into which hexane vapor was diffused at room temperature. Block-shaped crystals suitable for single-crystal X-ray diffraction formed after 48 h.

^{1}H NMR (400 MHz, $CDCl_3$, r.t., ppm): δ 7.53-7.47 (m, 3H), 7.38-7.34 (m, 2H), 7.24 (t, *J* = 8 Hz, 2H), 6.99 (d, *J* = 8 Hz, 4H), 2.05 (s, 12H). ^{13}C NMR (126 MHz, $CDCl_3$, r.t., ppm): δ 145.4 (br), 144.5 (br), 140.7, 136.5, 132.3, 129.0, 128.1, 127.3, 23.6. ^{11}B NMR (160 MHz, $CDCl_3$, r.t., ppm): δ 75 (br). MS (EI^+) m/z: 298 $[M]^+$. HRMS ($ASAP^+$): m/z calcd for $[C_{22}H_{23}B]$: 298.1887; found: 298.1882 (|Δ| = 1.68 ppm); Elem. Anal. Calcd (%) for $C_{22}H_{23}B$: C, 88.60; H 7.77; Found: C, 88.71; H, 7.92.

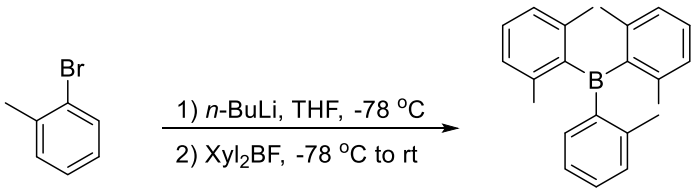

2

Bis(2,6-dimethylphenyl)(o-tolyl)borane (2): To a solution of 1-bromo-2-methylbenzene (462 mg, 2.7 mmol) in anhydrous THF (20 mL) a hexane solution of *n*-BuLi (1.7 mL, 1.6 M, 2.7 mmol) was added dropwise by syringe at -78 °C. The mixture was stirred at the same temperature for 1 h. A solution of bis(2,6-dimethylphenyl)fluoroborane (624 mg, 2.6 mmol) in anhydrous THF (5 mL) was added to the reaction mixture via syringe. The reaction mixture was warmed to room temperature and stirred overnight. The reaction was quenched with saturated solution of NaCl and the aqueous layer was extracted with Et_2O. The combined organic layer was dried over anhydrous Na_2SO_4, filtered, and concentrated under reduced pressure. The resulting crude material was subjected to silica gel column chromatography using *n*-hexane as eluent to afford 508 mg (1.63 mmol, 64%) of **2** as a white solid.

Compound **2** (0.2 g) was dissolved in 2 mL of hexane. The solution was then transferred to two 1 mL GC vials into which hexane vapor was diffused at room temperature. Block-shaped crystals suitable for single-crystal X-ray diffraction formed after 48 h.

^{1}H NMR (500 MHz, $CDCl_3$, r.t., ppm): δ 7.33-7.29 (t, J = 8 Hz, 1H), 7.21 (d, J = 8 Hz, 1H), 7.18-7.14 (m, 4H), 6.94 (d, J = 8 Hz, 4H), 2.08 (s, 3H), 2.02 (s, 12H). ^{13}C{^{1}H} NMR (126 MHz, $CDCl_3$, r.t., ppm): δ 147.4 (br), 146.0 (br), 142.7, 140.3, 135.0, 131.2, 130.0, 129.3, 127.5, 125.7, 23.2, 22.5. ^{11}B NMR (160 MHz, $CDCl_3$, r.t., ppm): δ 76 (br). MS (EI^+) m/z: 312 $[M]^+$. HRMS ($ASAP^+$): m/z calcd for $[C_{23}H_{25}B]$: 312.2158; found: 312.2145 (|Δ| = 4.16 ppm); Elem. Anal. Calcd (%) for $C_{23}H_{25}B$: C, 88.47; H, 8.07; Found: C, 88.72; H, 8.23.

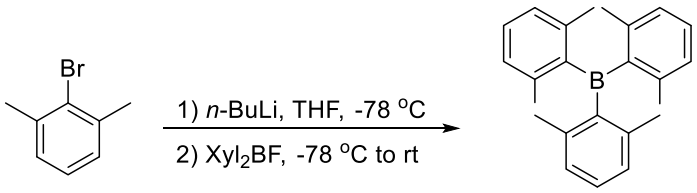

3

Tris(2,6-dimethylphenyl)borane (3): A solution of 2-bromo-m-xylene (1.1 mL, 8.3 mmol) in THF (10 mL) was treated with *t*-BuLi (1.7 M in pentane, 8.8 mL, 15 mmol) under argon at –78 °C. Then it was stirred at RT for 3 h before a solution of Xyl_2BF (1.8 g, 7.5 mmol) in THF (5 mL) was added at –78 °C and the reaction was allowed to warm to room temperature and stirred overnight. After 16 h, the reaction was quenched by adding 1 mL of water under argon. After removing the solvent and recrystallisation of the yellow solid from EtOH, the title compound was obtained as a white crystalline material (1.6 g, 64 %).

Compound **3** (0.2 g) was dissolved in 2 mL of hexane. The solution was then transferred to two 1 mL GC vials into which hexane vapor was diffused at room temperature. Block-shaped crystals suitable for single-crystal X-ray diffraction formed after 48 h.

^{1}H NMR (500 MHz, $CDCl_3$, r.t., ppm): δ 7.14 (t, J = 8 Hz, 3H), 6.91 (d, J = 8 Hz, 6H), 2.02 (s, 18H); $^{13}C\{^1H\}$ NMR: (75 MHz, $CDCl_3$) δ 147.2 (br), 140.9, 130.0, 128.2, 23.3. ^{11}B NMR (160 MHz, $CDCl_3$, r.t., ppm): δ 77 (br). MS (EI) m/z: 326. HRMS ($ASAP^+$): m/z calcd for $[C_{24}H_{27}B]$: 326.2200; found: 326.2194 (|Δ| = 1.84 ppm); Elem. Anal. calcd for $C_{24}H_{27}B$: C, 88.35; H, 8.34; Found C 88.51, H 7.86.

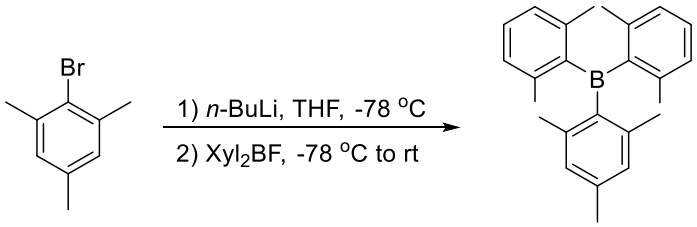

4

Bis(2,6-dimethylphenyl)(mesityl)borane (**4**): To a solution of 2-bromo-1,3,5-trimethylbenzene (617 mg, 3.1 mmol) in anhydrous THF (20 mL) a hexane solution of *n*-BuLi (1.9 mL, 1.6 M, 3.1 mmol) was added dropwise by syringe at -78 °C. The mixture was stirred at the same temperature for 1 h. A solution of bis(2,6-dimethylphenyl)fluoroborane (720 mg, 3.0 mmol) in anhydrous THF (5 mL) was added to the reaction mixture via syringe. The reaction mixture was warmed to room temperature and stirred overnight. The reaction was quenched with saturated solution of NaCl and the aqueous layer was extracted with Et_2O. The combined organic layer was dried over anhydrous Na_2SO_4, filtered, and concentrated under reduced pressure. The resulting crude material was subjected to silica gel column chromatography using *n*-hexane as eluent to afford 715 mg (2.1 mmol) of **4** in 71% yield as a white solid.

Compound **4** (0.2 g) was dissolved in 2 mL of hexane. The solution was then transferred to two 1 mL GC vials into which hexane vapor was diffused at room temperature. Block-shaped crystals suitable for single-crystal X-ray diffraction formed after 48 h.

^{1}H NMR (400 MHz, $CDCl_3$, r.t., ppm): δ 7.13 (t, J = 8 Hz, 2H), 6.91 (s, 2H), 6.90 (s, 2H), 6.75 (d, J = 1 Hz, 2H), 2.27 (s, 3H), 2.03 (s, 6H), 2.01 (s, 6H), 1.98 (s, 6H). ^{13}C{^{1}H} NMR (126 MHz, $CDCl_3$, r.t., ppm): δ 147.2 (br), 143.9 (br), 140.9, 140.5, 140.4, 139.6, 129.4, 128.8, 127.8, 127.8, 23.1, 22.9, 22.9, 21.4 ppm. ^{11}B NMR (160 MHz, $CDCl_3$, r.t., ppm): δ 78 (br). MS (EI^+) m/z: 340 $[M]^+$. HRMS ($ASAP^+$): m/z calcd for $[C_{25}H_{29}B]$: 340.2357; found: 340.2350 (|Δ| = 2.06 ppm); Elem. Anal. Calcd (%) for $C_{25}H_{29}B$: C, 88.23; H, 8.59; Found: C, 87.90; H, 8.74.

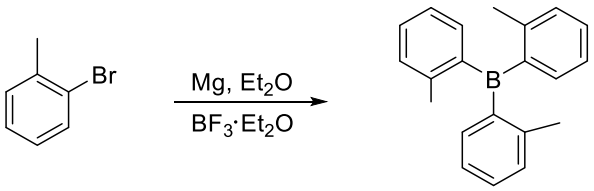

Tris(2-methylphenyl)borane: In a 200-mL, three-necked, round-bottomed flask maintained under argon and equipped with a reflux condenser, whose top was connected to an argon inlet and a pressure-equalizing dropping funnel, were placed 0.14 g (5.8 mmol) of magnesium turnings. With stirring, 50 mL of 3 g (17.5 mmol) of 1-bromo-2-methylbenzene anhydrous ether solution was added in one portion. The mixture was warmed to initiate the reaction and was then heated under reflux for another 2 h. Subsequently, 0.72 ml (5.8 mmol) $BF_3 \cdot Et_2O$ was added to the mixture. After 24 h, 150 mL of dry ether was added, while maintaining an argon atmosphere. The mixture was filtered and the filtrate was evaporated to dryness. The crude material was crystallized from pentane at –35 °C to afford 1.26 g (4.4 mmol, 76 %) of tris(2-methylphenyl)borane as white solids: ^{1}H NMR (500 MHz, $CDCl_3$, r.t., ppm): δ 7.34 (m, 3H), 7.18 (m, 9H), 2.10 (s, 9H). $^{13}C\{^{1}H\}$ NMR (126 MHz, $CDCl_3$, r.t., ppm): δ 146.3 (br.), 142.4, 134.8, 130.4, 129.8, 125.0, 23.1. ^{11}B NMR (160 MHz, $CDCl_3$, r.t., ppm): δ 73 (br). HRMS ($ASAP^+$): m/z calcd for $[C_{22}H_{21}B]$: 284.1731; found: 284.1723 (|Δ| = 2.82 ppm); Elem. Anal. Calcd (%) for $C_{22}H_{21}B$: C, 88.75; H, 7.45; Found: C, 88.51; H, 7.45.

III. DFT calculations

Computational methods and technical details for the quantum chemical calculations

The Turbomole program package was used for all geometry optimizations.[12] The equilibrium geometry of the electronic ground state was optimized with Kohn-Sham density functional theory (DFT)[13] employing the B3-LYP functional.[14] For the singlet excited state geometries, full linear response time dependent DFT (TD-DFT)[15] calculations were performed whereas the Tamm-Dancoff approximation was employed for the triplet states. Atomic orbitals were represented by split-valence basis sets with polarization functions (SVP) from the Turbomole basis set library.[16] Electronic excitation energies and transition dipole moments were calculated with a

redesigned variant of the DFT/MRCI[17] method. DFT/MRCI is a semi-empirical multireference configuration interaction approach based on Kohn-Sham orbitals and orbital energies of a closed shell BH-LYP[14b, 18] functional determinant. To avoid double counting of electron correlation, high-lying configurations with energies more than 1 E_h above the highest root in the reference space are discarded. The reference space was determined iteratively, starting with single and double excitations of 12 electrons within an active window of 12 frontier orbitals. At all geometries, 11 singlet and 10 triplet roots were determined. Absorption line spectra were broadened with Gaussians of 1000 cm^{-1} full width at half maximum (FWHM). Electronic spin–orbit coupling matrix elements (SOCMEs) and phosphorescence lifetimes were obtained with the SPOCK program.[19] Harmonic vibrational frequencies were determined numerically at the TDDFT or TDA level using the SNF code.[20] The FC profiles of the emission spectra were obtained using the Fourier transform approach implemented in the Vibes program.[21] Herein, a time interval of 300 fs and a grid of 16384 points were chosen. The correlation function was damped with a Gaussian function of 200 cm^{-1} FWHM and the temperature was set to 77 K. All spectra were normalized to one. Rate constants for intersystem crossing (ISC) of the respective S_1 states to the T_1 states of all compounds and a few other triplet states were computed for a temperature of 300 K using the Condon approximation. For the integration of the time correlation function in the VIBES program a time interval of 250 fs, an integration grid of 1000 points and smaller damping of width 0.3 cm^{-1} were chosen. The electronic SOCME is largest for the ISC from S_1 to T_2, but harmonic vibrational wavefunctions of the latter state could unfortunately not be determined due to (near) degeneracy of the T_1 and T_2 potentials at the T_2 minimum. For that reason, we used the modes of the T_1 (compounds **1** and **2**) or T_3 potentials (compounds **3** and **4**) to estimate the vibrational density of final states at the energies of the initial singlet states which are required in addition to the sum over squared SOCMEs to determine the ISC rate constants in the Condon approximation.[22]

Table S1. Spin–orbit coupling matrix elements (absolute values, cm^{-1}) of the S_1, T_1, and T_2 states at the respective S_1 minimum geometry.

SOCME	x	y	z	$(x^2 + y^2 + z^2)$
		Compound 1		
$\langle T_1 \vert \hat{H}_{SO} \vert S_1 \rangle$	0.039	0.149	0.232	0.078
$\langle T_2 \vert \hat{H}_{SO} \vert S_1 \rangle$	0.524	0.999	0.022	1.273
		Compound 2		
$\langle T_1 \vert \hat{H}_{SO} \vert S_1 \rangle$	0.154	0.167	0.147	0.073
$\langle T_2 \vert \hat{H}_{SO} \vert S_1 \rangle$	0.403	0.883	0.159	0.967
		Compound 3		
$\langle T_1 \vert \hat{H}_{SO} \vert S_1 \rangle$	0.024	0.039	0.002	0.002
$\langle T_2 \vert \hat{H}_{SO} \vert S_1 \rangle$	0.005	1.270	0.038	1.614
		Compound 4		
$\langle T_1 \vert \hat{H}_{SO} \vert S_1 \rangle$	0.048	0.060	0.030	0.007
$\langle T_2 \vert \hat{H}_{SO} \vert S_1 \rangle$	0.317	1.067	0.706	1.737

Table S2. Photophysical properties of compounds **1**-**4** in vacuum as obtained from quantum chemical calculations.

Compound	λ_{abs} /nm [a]	k_{isc} /s^{-1} [b]	λ_f /nm [c]	k_f/ s^{-1}	τ_f /ns [d]	λ_p /nm [c]	k_p / s^{-1}	τ_p /s [d]
1	303	≈$1*10^7$	(335), 383	$2*10^7$	45	(425), 597	0.13	8
2	308	≈$6*10^6$	368, 391	$2*10^7$	45	448, 476	0.13	8
3	314	≈$5*10^7$	367, 404	$3*10^7$	38	456, 486	0.14	7
4	316	≈$3*10^7$	381, 430	$4*10^7$	25	458, 489	0.20	5

[a] Absorption maximum of line spectrum broadened by Gaussian function of 1000 cm^{-1} full width at half maximum; [b] rate constant for the fastest of the open ISC channels; [c] maximum of 0-0 band, maximum of Franck-Condon spectrum at 77 K, entries given in parentheses indicate the position of a shoulder; [d] pure radiative lifetime assuming a quantum yield of **1**.

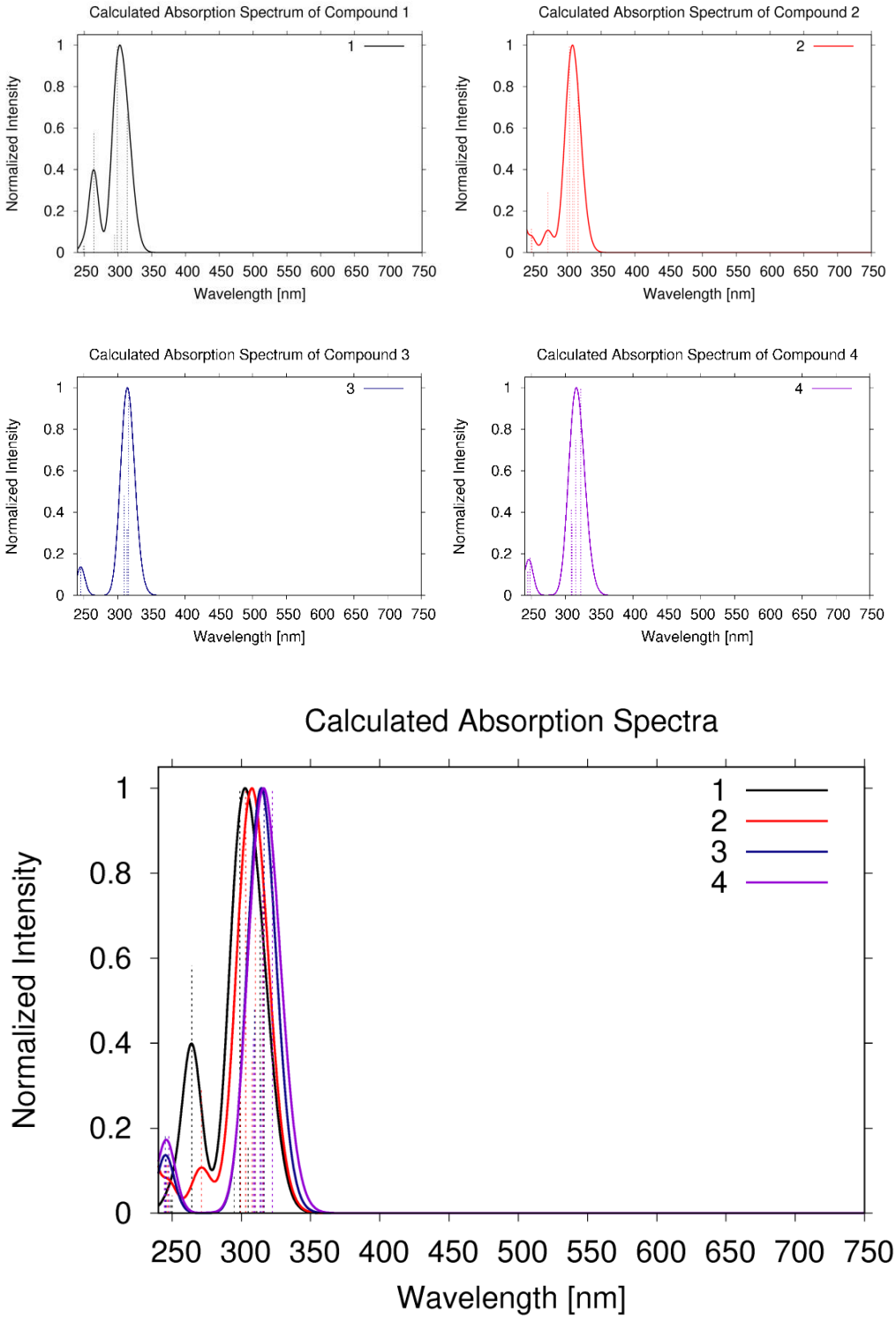

Figure S1. Calculated absorption spectra of the isolated compounds **1**, **2**, **3**, and **4**.

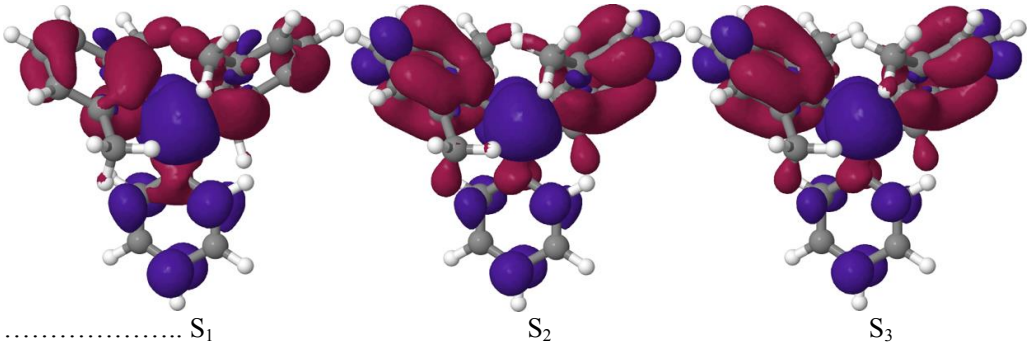

…….. S_1 S_2 S_3

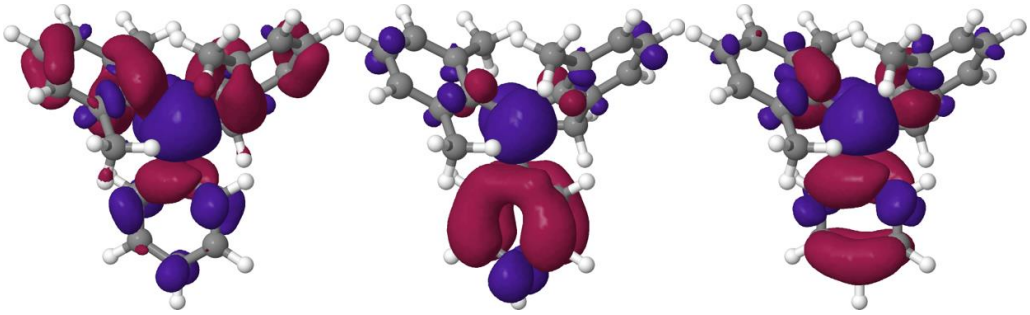

…….. S_4 S_5 S_6

Figure S2. Difference densities (|isovalue| = 0.001) of low-lying singlet excited states of compound **1** at the DFT-optimized ground-state geometry. A loss of electron density with respect to the S_0 state is indicated in red, a gain in blue.

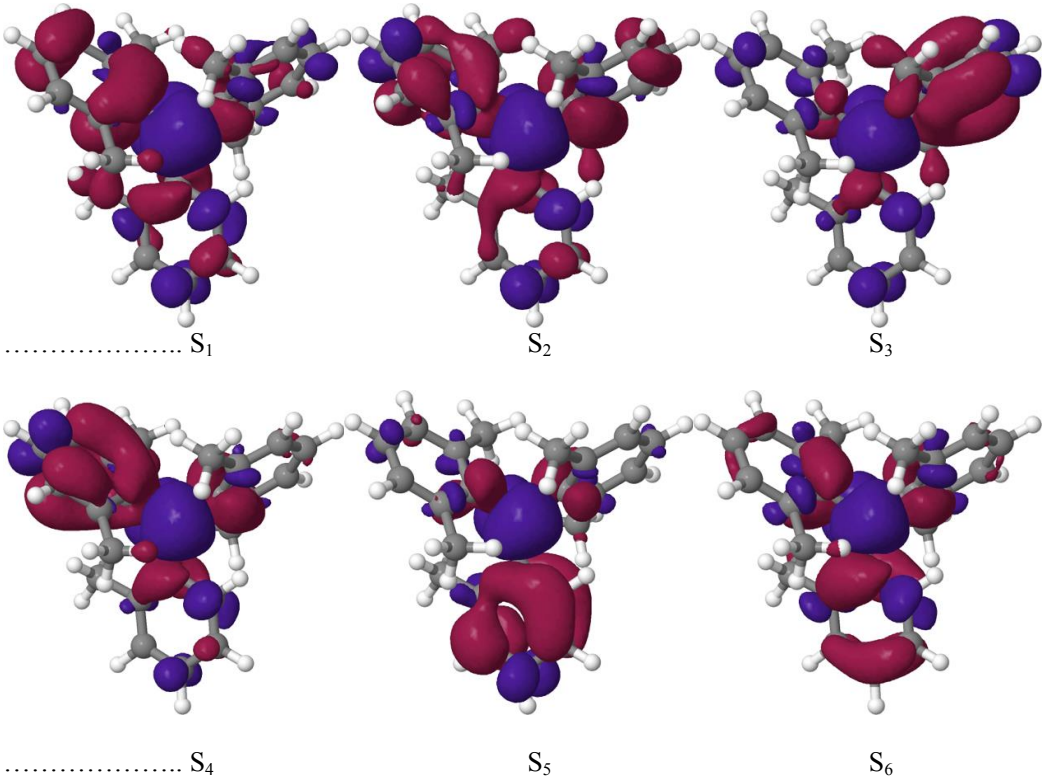

Figure S3. Difference densities (|isovalue| = 0.001) of low-lying singlet excited states of compound **2** at the DFT-optimized ground-state geometry. A loss of electron density with respect to the S_0 state is indicated in red, a gain in blue.

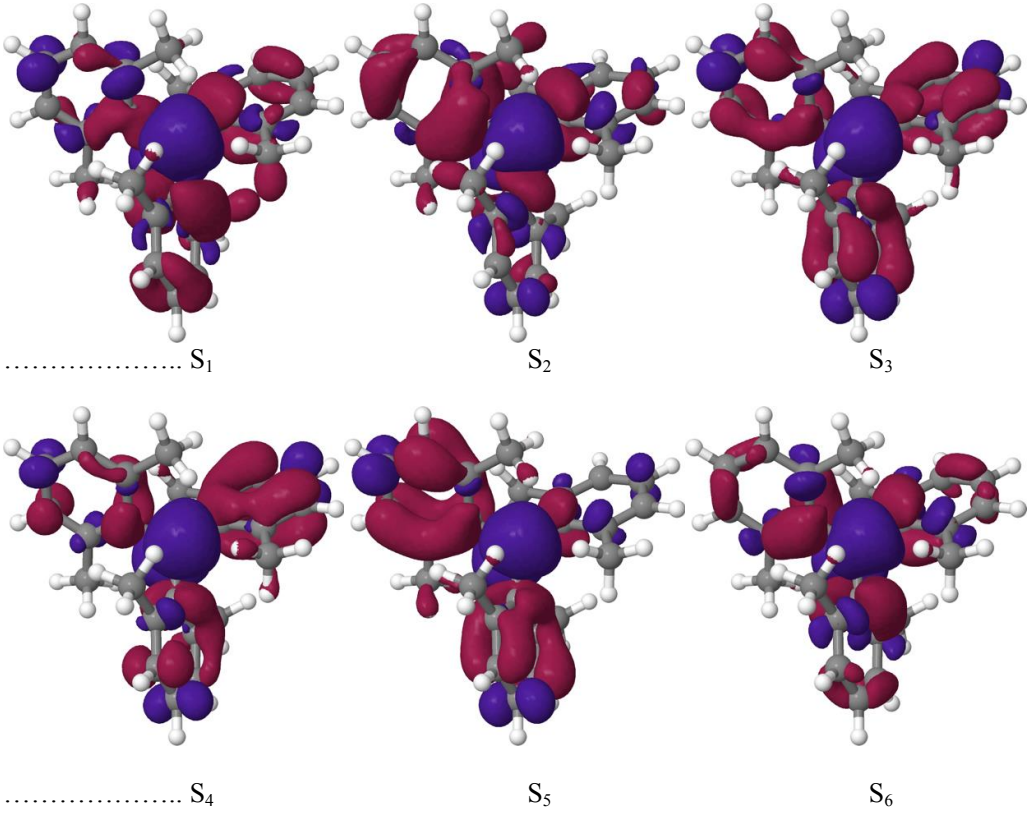

Figure S4. Difference densities (|isovalue| = 0.001) of low-lying singlet excited states of compound **3** at the DFT-optimized ground-state geometry. A loss of electron density with respect to the S_0 state is indicated in red, a gain in blue.

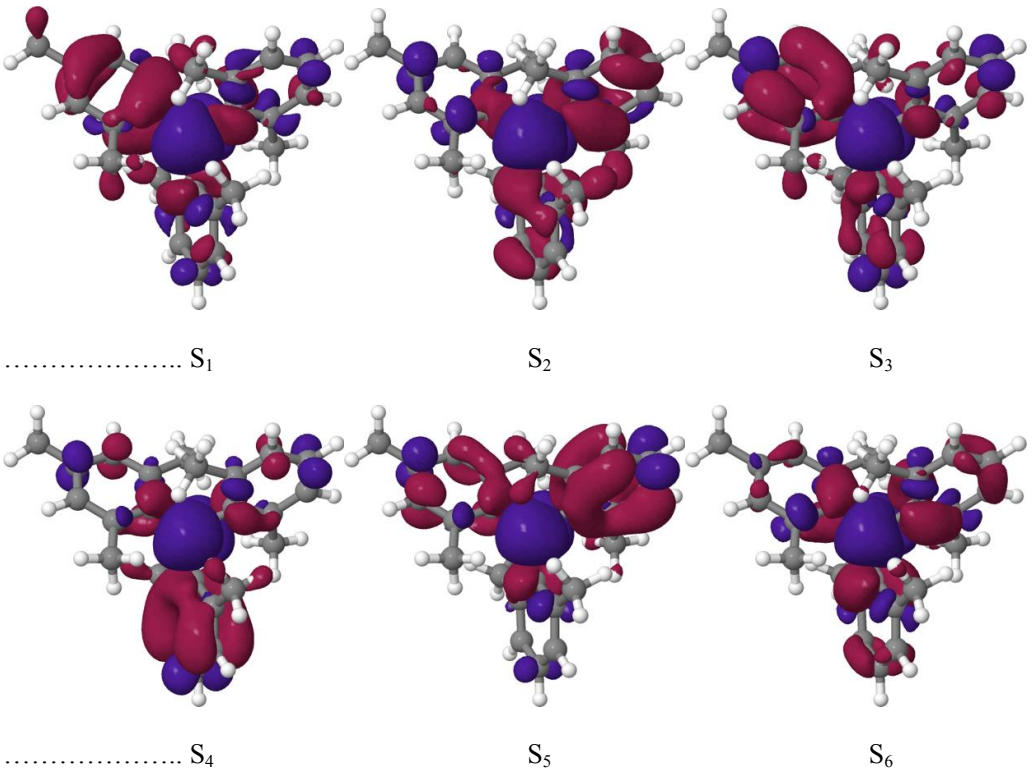

Figure S5. Difference densities (|isovalue| = 0.001) of low-lying singlet excited states of compound **4** at the DFT-optimized ground-state geometry. A loss of electron density with respect to the S_0 state is indicated in red, a gain in blue.

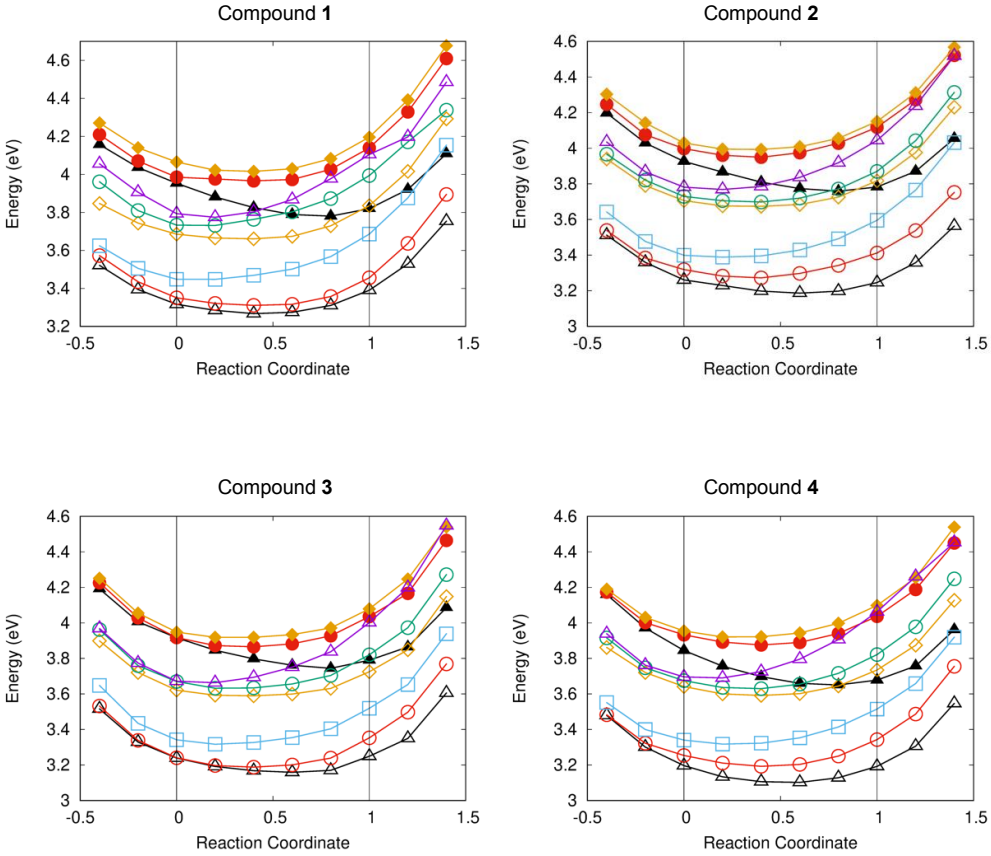

Figure S6. DFT/MRCI potential energy profiles of low-lying singlet (filled symbols) and triplet (open symbols) states of compounds **1**, **2**, **3**, and **4**. The reaction coordinate connects the DFT-optimized S_0 geometry (RC = 0) and the TDDFT-optimized geometry of the first excited singlet state S_1 (RC = 1) and is extrapolated on both sides. Potential energy curve crossings are observed between the S_1 state (full black triangles) and excited triplet states along the relaxation path from the Franck-Condon geometry.

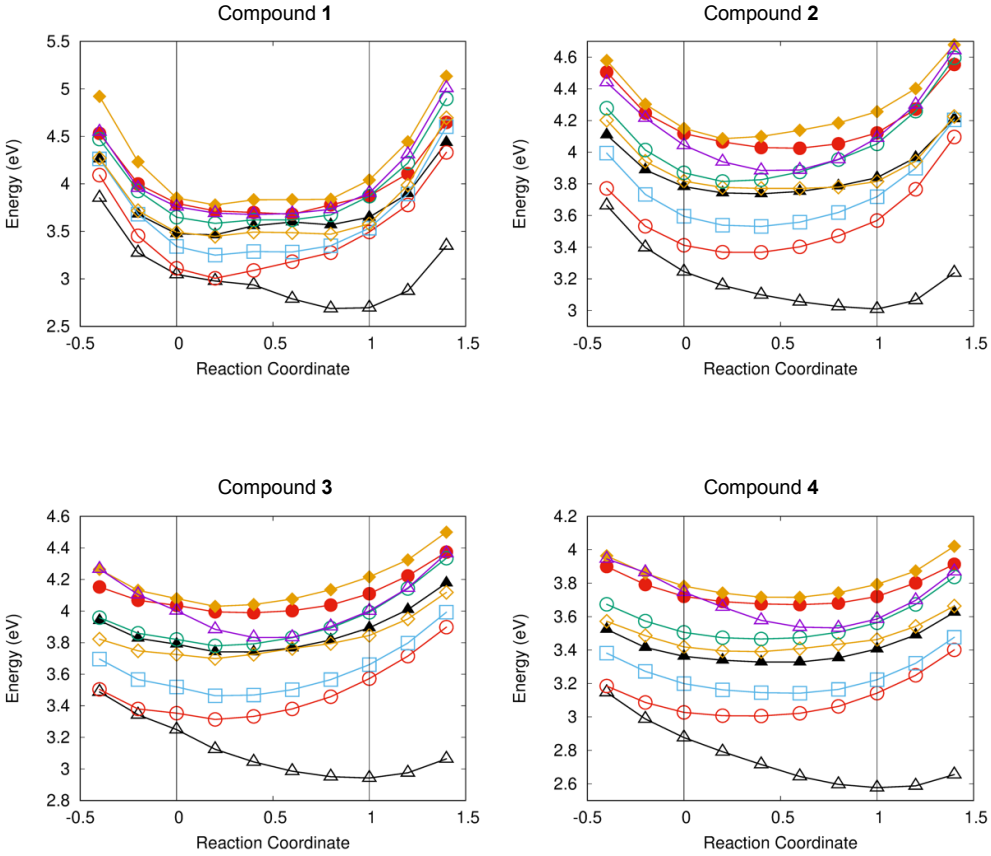

Figure S7. DFT/MRCI potential energy profiles of low-lying singlet (filled symbols) and triplet (open symbols) states of compounds **1**, **2**, **3**, and **4**. The reaction coordinate connects the TDDFT-optimized geometries of the S_1 (RC = 0) and T_1 (RC = 1) states and is extrapolated on both sides.

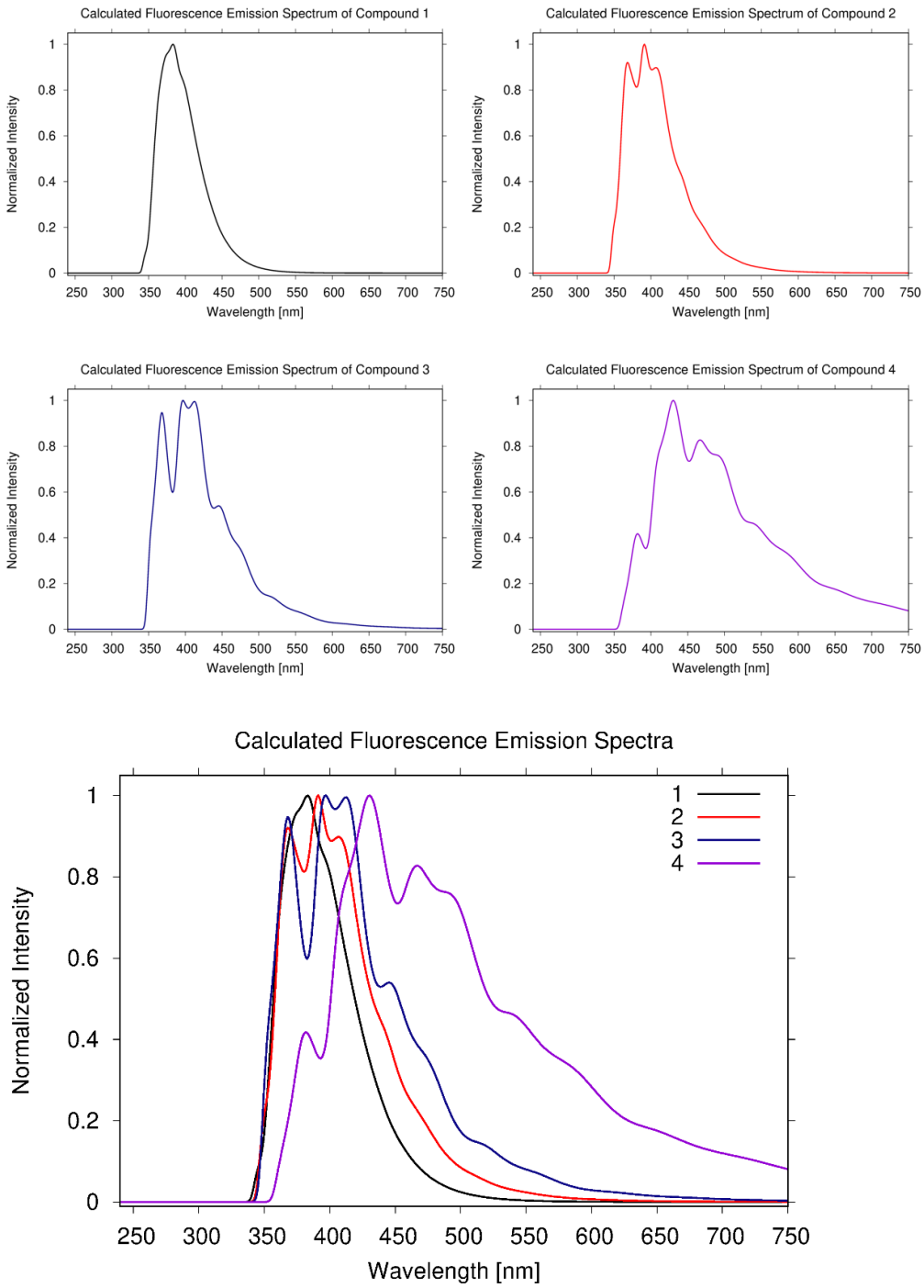

Figure S8. Calculated fluorescence spectra of the isolated compounds **1**, **2**, **3**, and **4** at 77 K.

Table S3. Selected bond lengths (Å) and angles (°) of the isolated compounds **1**, **2**, **3**, and **4** as obtained from geometry optimizations of the S_0, S_1, and T_1 states. The electronic excitation in the S_1 and T_1 states mainly involves residue R2.

1: R1=phenyl, R2=R3=xylyl
2: R1=tolyl, R2=R3=xylyl
3: R1=R2=R3=xylyl
4: R1=R3=xylyl, R2=mesityl

Compound **1**	S_0	S_1	T_1
B-R1	1.574	1.532	1.568
B-R2	1.589	1.620	1.567
B-R3	1.589	1.592	1.602
∠R1(C)-B-(C-C)R2	55.3	70.5	38.4
∠R2(C)-B-(C-C)R3	55.4	49.8	61.5
∠R3(C)-B-(C-C)R1	28.3	20.3	20.6
∠R2(C)-B-(C-C)R1	28.3	13.2	25.5
∠R3(C)-B-(C-C)R2	55.5	67.1	43.4
∠R1(C)-B-(C-C)R3	55.2	48.4	62.0
Compound **2**	S_0	S_1	T_1
B-R1	1.580	1.546	1.574
B-R2	1.588	1.610	1.562
B-R3	1.591	1.597	1.605
∠R1(C)-B-(C-C)R2	51.9	59.2	39.0
∠R2(C)-B-(C-C)R3	53.0	46.8	55.5
∠R3(C)-B-(C-C)R1	38.1	25.3	31.5
∠R2(C)-B-(C-C)R1	38.7	24.2	36.9
∠R3(C)-B-(C-C)R2	54.2	60.9	44.1
∠R1(C)-B-(C-C)R3	55.4	51.6	58.5
Compound **3**	S_0	S_1	T_1
B-R1	1.590	1.581	1.596
B-R2	1.590	1.611	1.557
B-R3	1.590	1.579	1.595
∠R1(C)-B-(C-C)R2	50.1	56.4	43.4
∠R2(C)-B-(C-C)R3	49.9	38.9	48.8
∠R3(C)-B-(C-C)R1	49.8	43.6	47.8
∠R2(C)-B-(C-C)R1	49.9	40.3	49.2
∠R3(C)-B-(C-C)R2	50.3	56.8	43.6
∠R1(C)-B-(C-C)R3	49.6	42.3	47.5
Compound **4**	S_0	S_1	T_1
B-R1	1.591	1.575	1.593
B-R2	1.587	1.619	1.564
B-R3	1.591	1.577	1.596
∠R1(C)-B-(C-C)R2	49.4	58.9	43.9
∠R2(C)-B-(C-C)R3	49.6	39.3	48.1
∠R3(C)-B-(C-C)R1	49.8	42.2	46.1
∠R2(C)-B-(C-C)R1	49.9	38.6	47.1
∠R3(C)-B-(C-C)R2	49.4	59.0	44.3
∠R1(C)-B-(C-C)R3	49.7	42.8	47.6

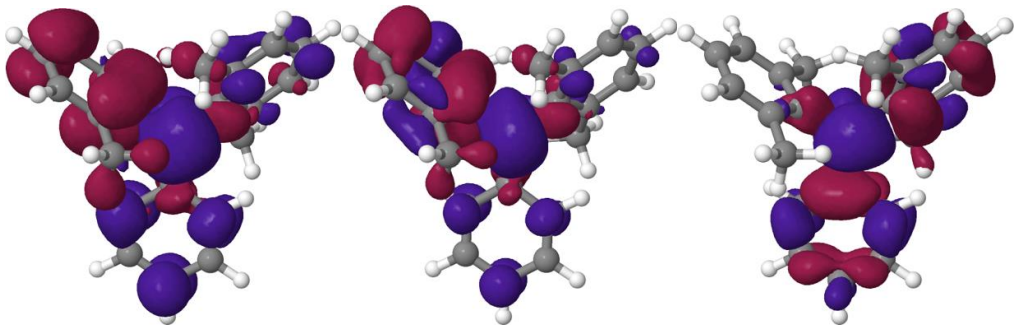

Compound **1** S_1 T_1 T_2

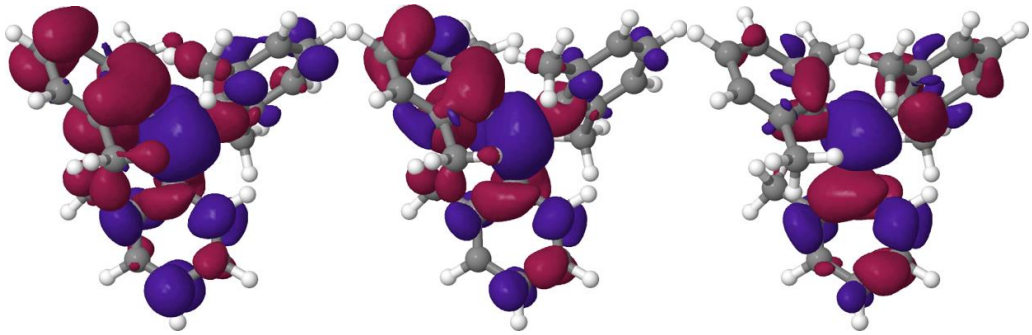

Compound **2** S_1 T_1 T_2

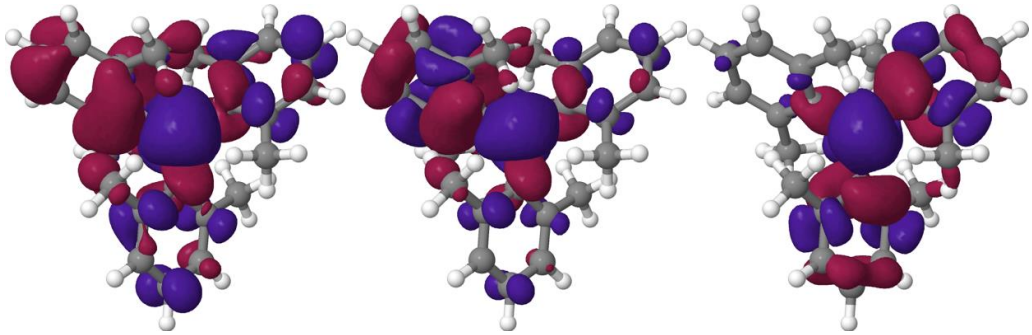

Compound **3** S_1 T_1 T_2

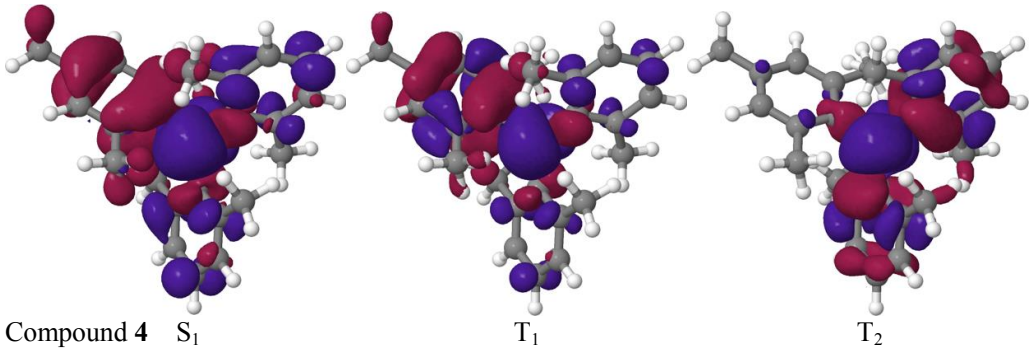

Compound **4** S_1 T_1 T_2

Figure S9. Difference densities (|isovalue| = 0.001) of low-lying excited states of compounds **1**, **2**, **3**, and **4** at the TDDFT-optimized geometry of the S_1 state. A loss of electron density with respect to the S_0 state is indicated in red, a gain in blue.

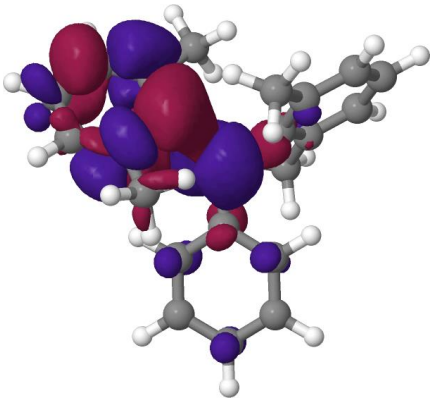

Compound **1** T_1

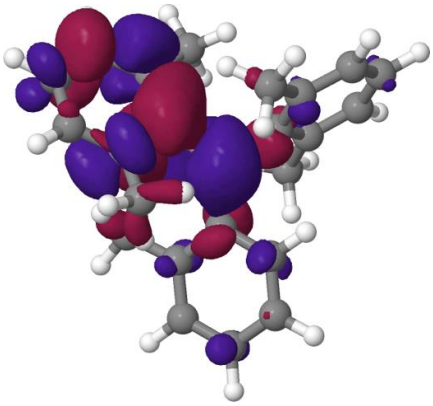

Compound **2** T_1

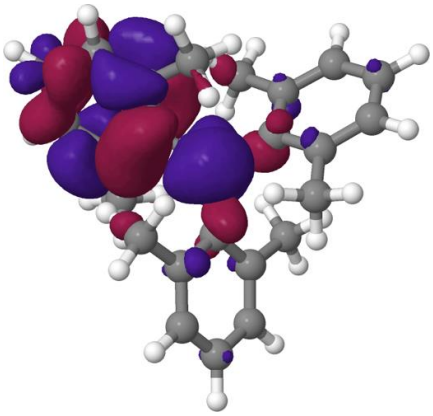

Compound **3** T_1

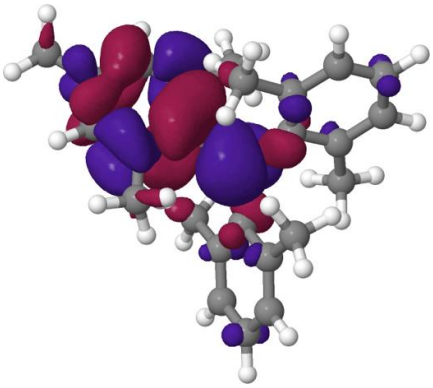

Compound **4** T_1

Figure S10. Difference densities (|isovalue| = 0.001) of the T_1 state of compounds **1**, **2**, **3**, and **4** at its TDDFT-TDA-optimized minimum geometry. A loss of electron density with respect to the S_0 state is indicated in red, a gain in blue.

Calculated minimum energy structures of the S_1 and T_1 states reveal opposite trends of the B–C bond lengths. In the S_1 state, the bond connecting boron and the aryl group from which electron density is transferred to boron (B-R2 in Table S3) is elongated upon excitation while the other two B–C bonds shorten with respect to the electronic ground-state structure. In the T_1 state, which exhibits more local (π, π^*) contributions to the excitations than S_1, the first B–C bond shortens and the other two are elongated (Figures S9 and S10). In compounds 3 and 4, with methyl groups in the ortho positions of all aryl rings, the dihedral angles change by 10° at most in the S_1 state, and by less than 7° in T_1. Corresponding displacements of the minimum dihedral angles in compound 1 reach values up to 15° and 17°, respectively, and up to 14° and 13°, respectively, in compound 2.

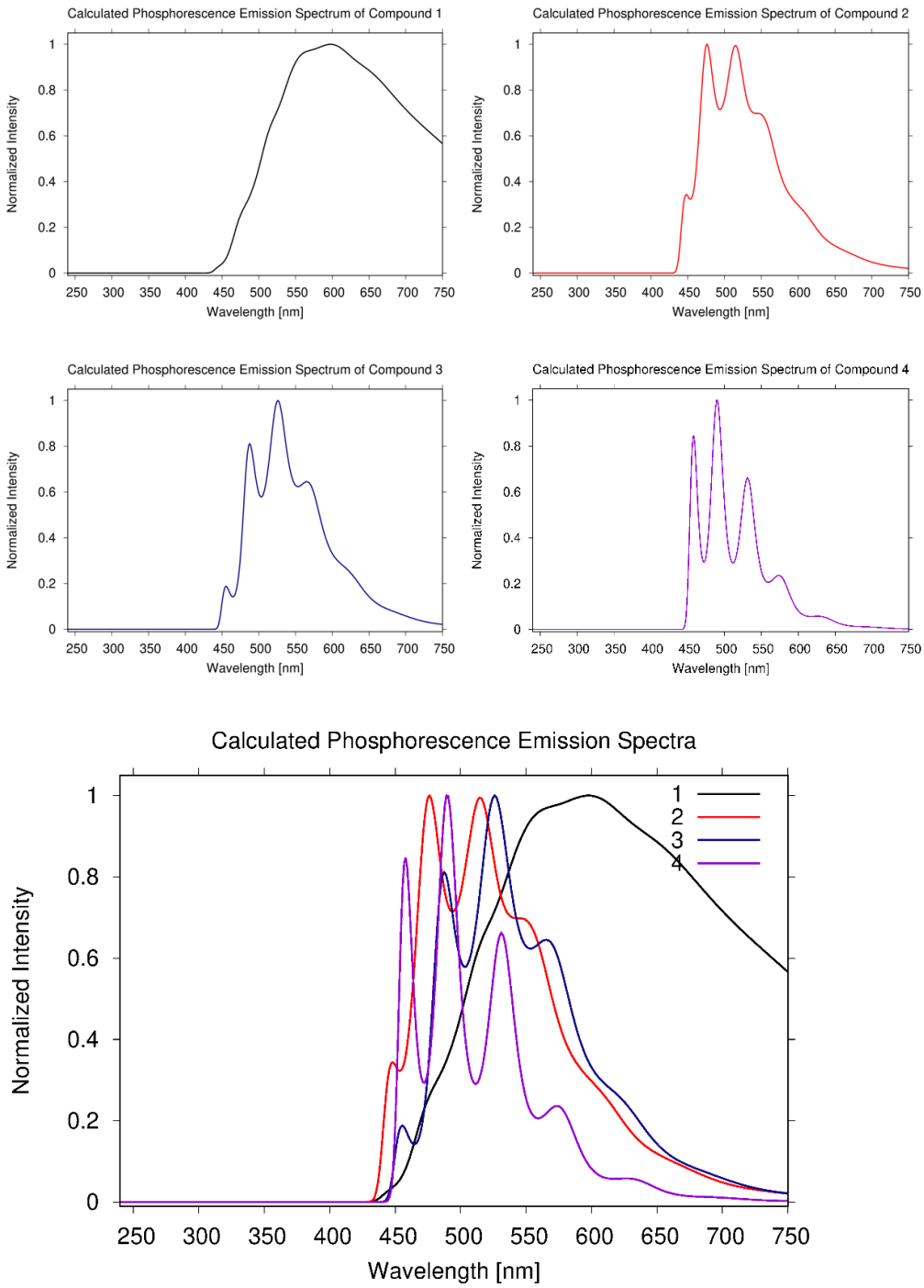

Figure S11. Calculated phosphorescence spectra of the isolated compounds **1**, **2**, **3**, and **4** at 77 K.

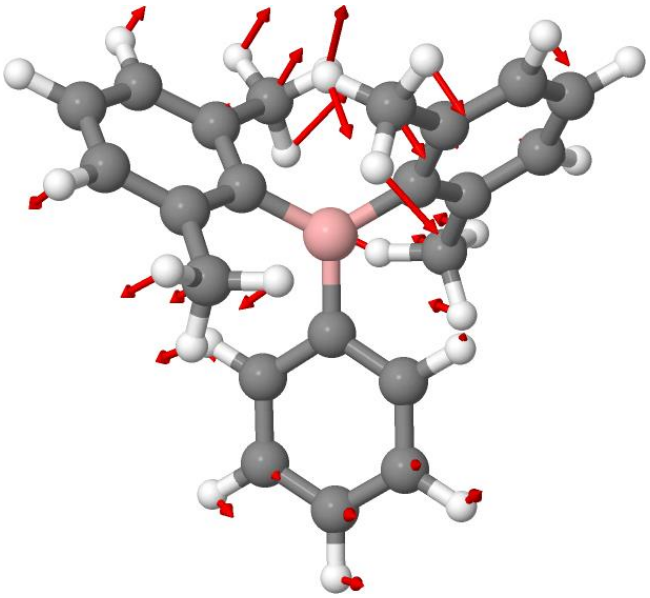

Figure S12. Low-frequency vibrational mode in the S_0 state of compound **1** showing the largest displacement with respect to the corresponding mode in the T_1 state. Excitation of this mode causes the extraordinary breadth of the phosphorescence emission of this compound. One methyl group in ortho-position of residue R3 is sufficient to prevent similar large-amplitude motions along in compound **2**.

IV. Experimental photophysical spectra

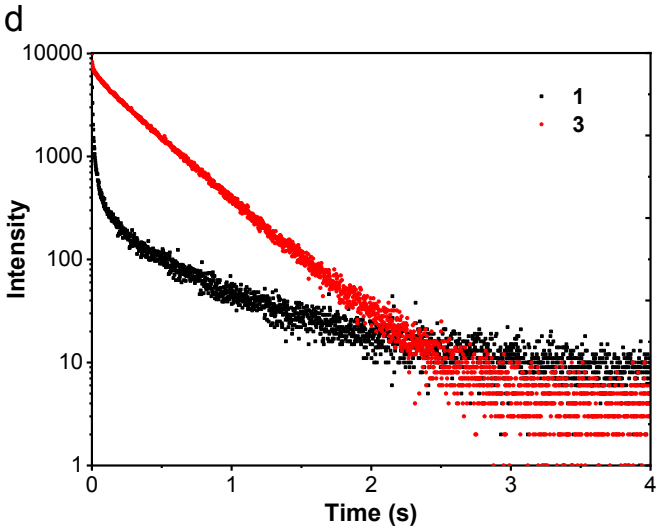

Figure S13. Decays of the phosphorescence emission from crystalline **1** (520 nm) and 3 (575 nm) at room temperature.

Table S4. Experimental photophysical properties of compounds **1**-**4** in hexane and crystalline state at RT, and in methylcyclohexane at 77 K.

Compound	State (T)	λ_{abs} nm	ε $M^{-1}cm^{-1}$	Φ_{PL} %	λ_f nm	Φ_f %	τ_f ns	τ_0^f ns	k_r^f s^{-1}	k_{nr}^f s^{-1}	λ_p nm	Φ_p %	τ_p s	τ_0^p s	k_r^p s^{-1}	k_{nr}^p s^{-1}
1	Solution (RT)[a]	299	14500	3.5	354	3.5	1.3	37.1	$3*10^7$	$7*10^8$	nd[b]		nd			
	Crystalline (RT)[c]			3.7	369	3.4	1.6	47.1	$2*10^7$	$6*10^8$	524	0.3	0.68 (79%)[d]	107	0.01	3.1
	Crystalline (77 K)	-		-	368		-	-			471, 502, 541		2.27			
	Frozen glass (77 K)[e]	-		-	349						404, 427		1.45			
2	Solution (RT) [a]	306	15600	6.6	359	6.6	2.0	30.0	$3*10^7$	$5*10^8$	nd		nd			
	Crystalline (RT) [c]	-		6.9	369	6.9	1.6	23.2	$4*10^7$	$6*10^8$	nd		nd			
	Crystalline (77 K)			-	352, 366		-	-			426, 449		1.22 (61%)[d]			
	Frozen glass (77 K)[e]	-		-	373		-	-			417, 442		1.57			
3	Solution (RT) [a]	318	15800	6.3	361	6.3	1.7	30.0	$3*10^7$	$6*10^8$	nd		nd			
	Crystalline (RT) c	-		18.2	371, 390	17.0	1.4	8.2	$1*10^8$	$6*10^8$	540, 575	1.2	0.47	16	0.06	5.1
	Crystalline (77 K)				372, 392, 415		1.4				488, 538, 582, 630		1.54			
	Frozen glass (77 K)[e]	-		-	375		-	-			421, 446		1.48			
	PMMA Film (RT)[f]			-	365		-	-								
	PMMA Film (77 K)			-	367		1.6	-			422, 447		1.57			
4	Solution (RT) [a]	324	16800	8.0	368	8.0	1.5	18.8	$5*10^7$	$6*10^8$	nd		nd			
	Crystalline (RT)[c]	-		6.3	381	6.3	1.5	23.8	$4*10^7$	$6*10^8$	nd		nd			
	Crystalline (77 K)	-		-	370			-			428,465		1.32 (68%)[d]			
	Frozen glass (77 K)[e]	-		-	374		-	-			425, 452		1.36			

[a] Measured in hexane at RT; [b] not detected (nd); [c] measured in the crystalline state at RT; [d] major component of lifetimes; [e] measured in methylcyclohexane at 77 K; the phosphorescence maxima of different vibrational levels have the same lifetimes; [f] measured in a PMMA (poly(methyl methacrylate) film at room temperature.

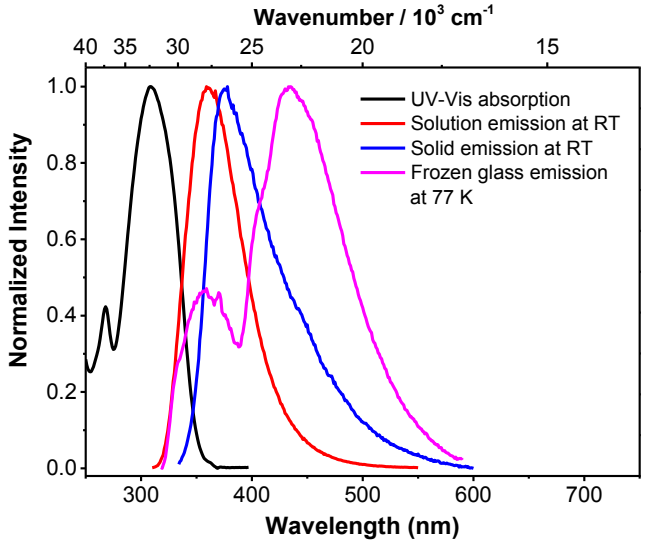

Figure S14. Normalized absorption and emission spectra of tris(2-methylphenyl)borane (E_x = 305 nm) in hexane.

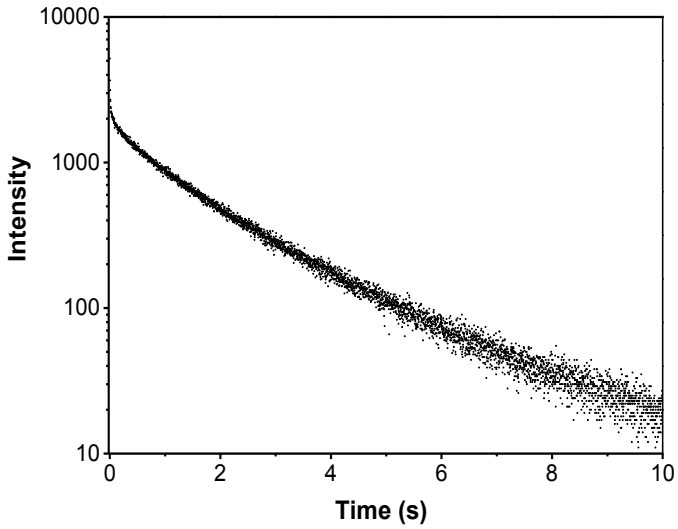

Figure S15. Decay of the 450 nm emission from tris(2-methylphenyl)borane in a frozen methylcyclohexane glass at 77 K.

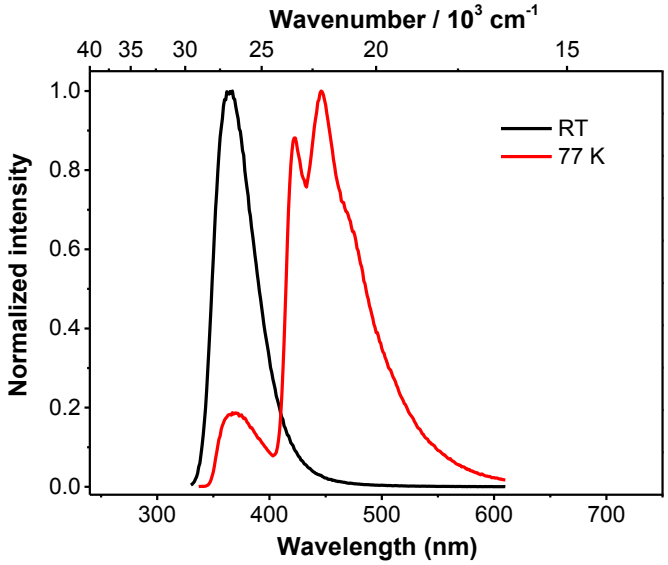

Figure S16. Normalized emission spectra of **3** in a PMMA film (1 %) at room temperature and 77 K (E_x = 305 nm).

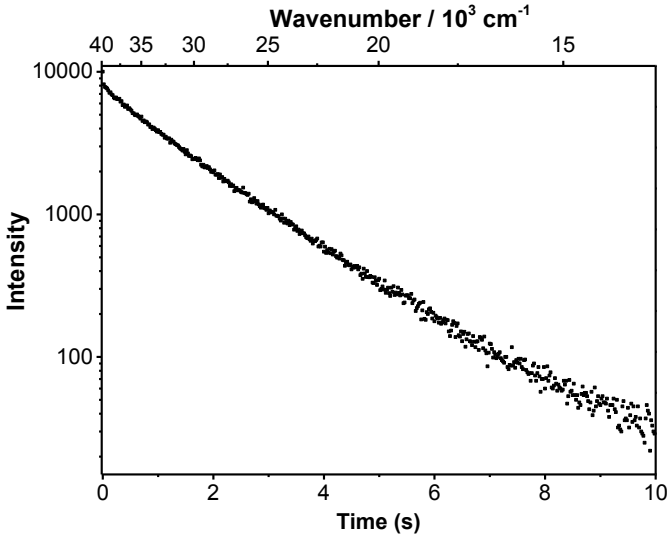

Figure S17. Decay of the 450 nm emission from **3** in a PMMA film (1 %) at 77 K.

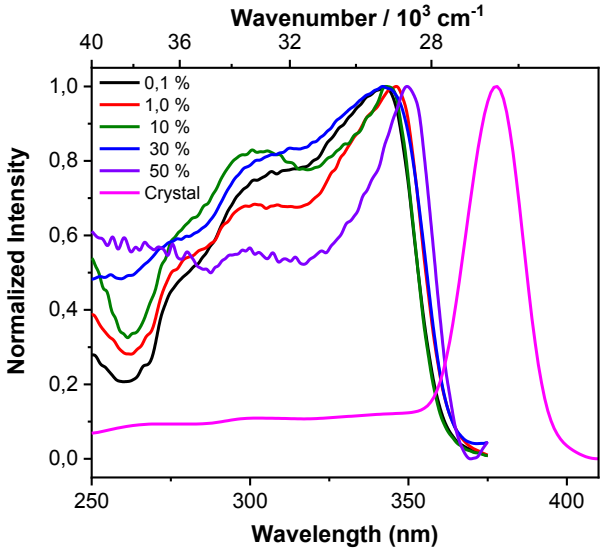

Figure S18. Normalized excitation spectra of compound **3** in 0.1, 1.0, 10, 30 and 50 % PMMA film and the crystalline state.

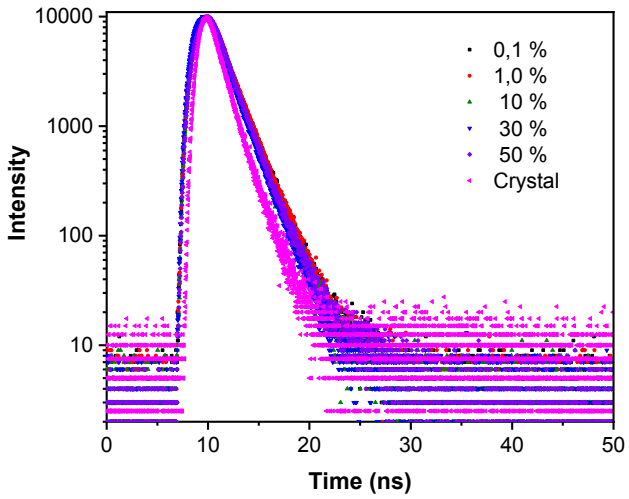

Figure S19. Decays of fluorescence at maximum emission wavelength of compound **3** in 0.1, 1.0, 10, 30 and 50 % PMMA film and the crystalline state.

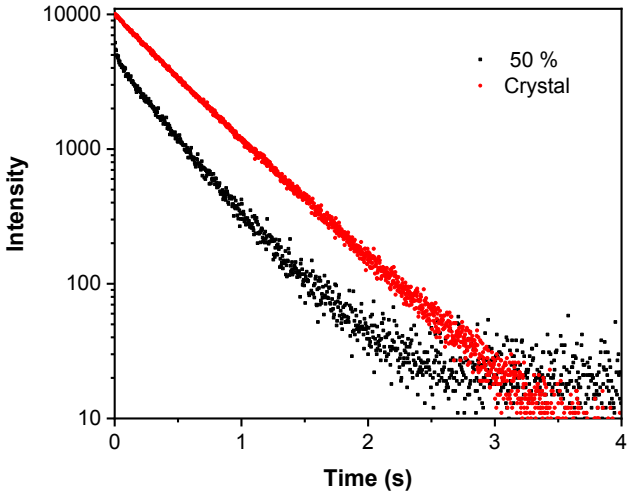

Figure S20. Decays of phosphorescence emission at 550 nm of compound **3** in 50 % PMMA film (407 ms) and the crystalline state (478 ms) at room temperature in air.

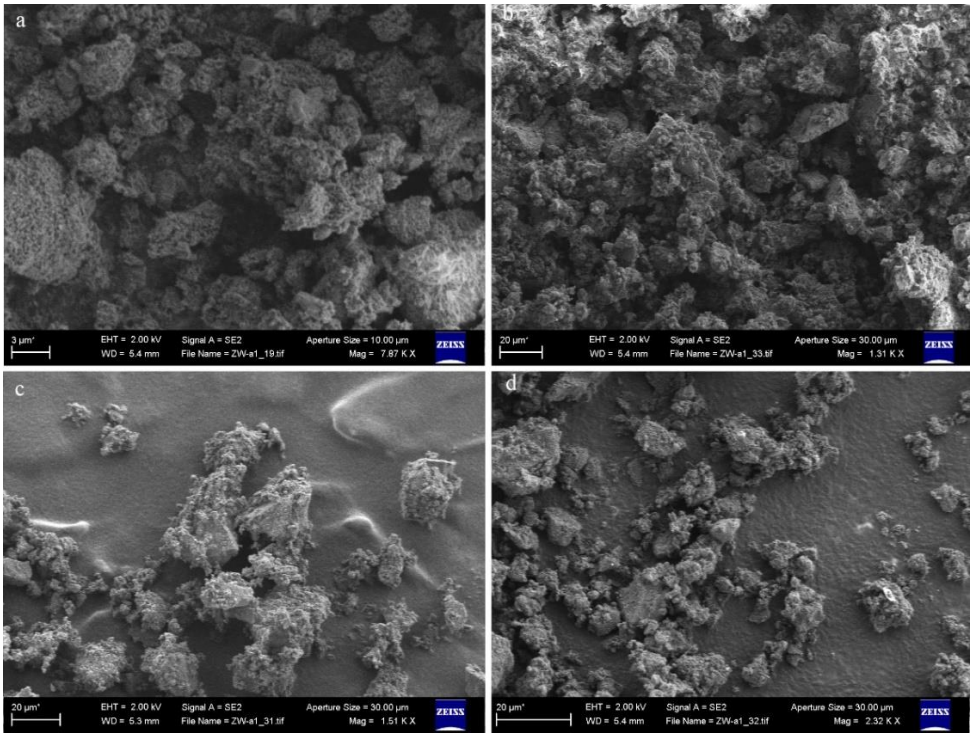

Figure S21. (a)-(d) SEM pictures of **3** in ball-milled powder state.

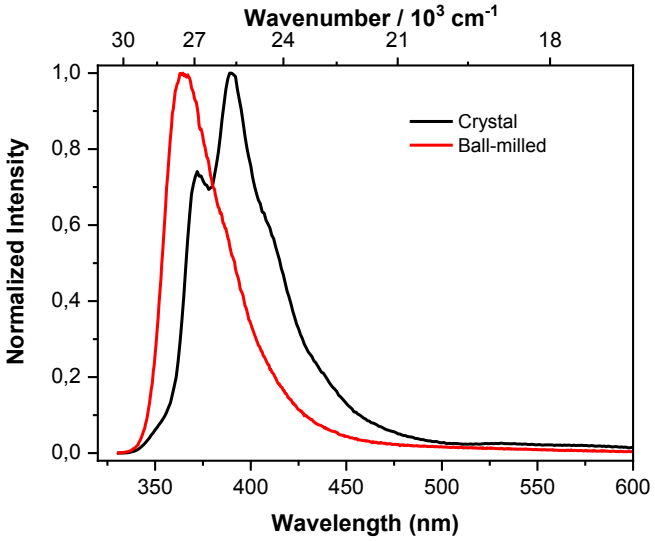

Figure S22. Normalized PL emission spectra of **3** in the crystalline state and ball-milled powder state at room temperature (E_x = 305 nm).

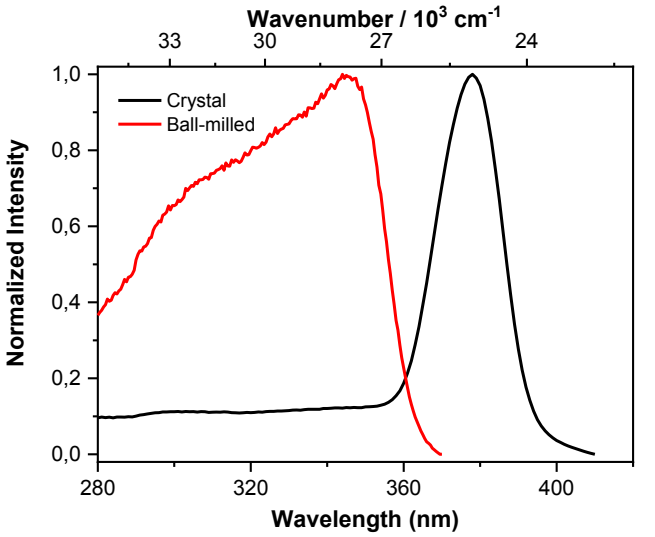

Figure S23. Normalized excitation spectra of **3** in the crystalline state and ball-milled powder state at room temperature.

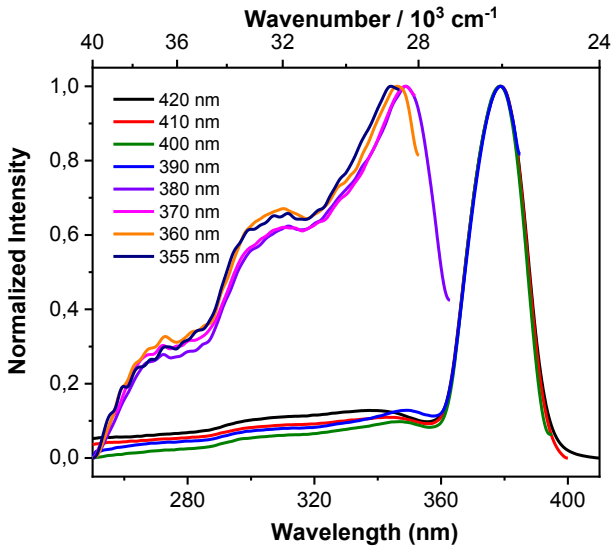

Figure S24. Normalized emission dependent excitation spectra of compound **3** in the crystalline state from 420 to 355 nm.

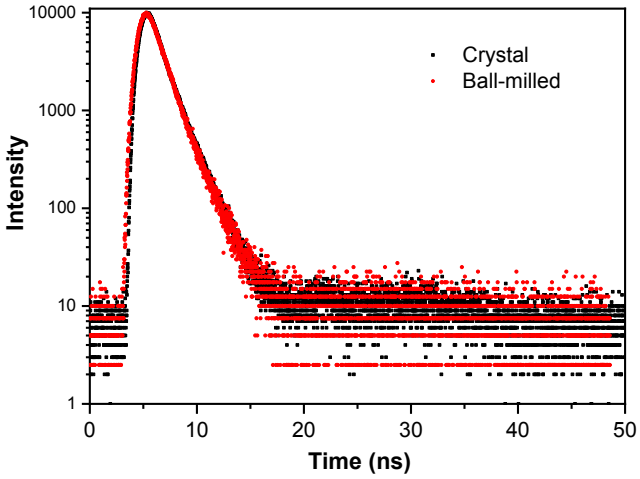

Figure S25. Fluorescence decay of **3** in the crystalline state and ball-milled powder state at room temperature.

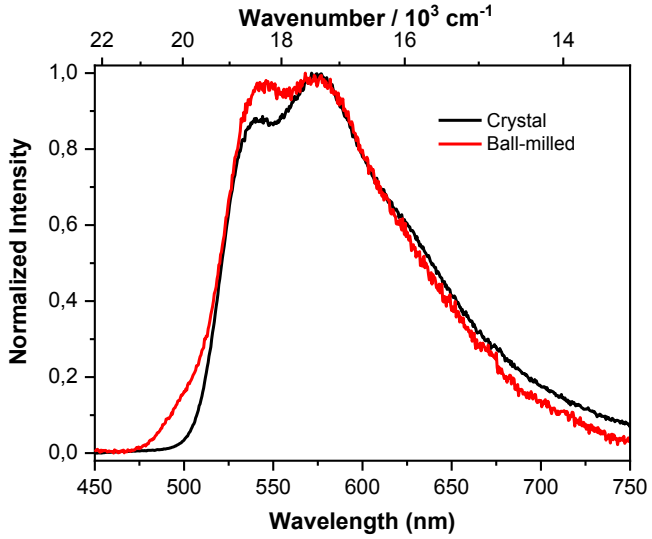

Figure S26. Normalized time-gated phosphorescence emission spectra of **3** in the crystalline state and ball-milled powder state at room temperature (E_x = 305 nm).

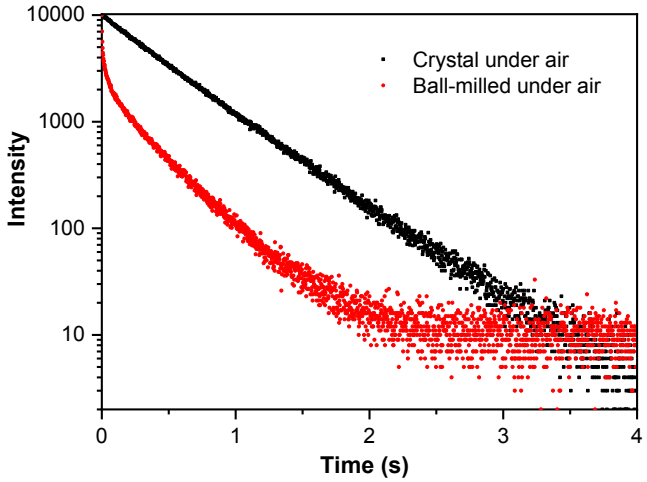

Figure S27. Phosphorescence decay of **3** in the crystalline state (470 ms) and ball-milled powder state (340 ms) at room temperature under air.

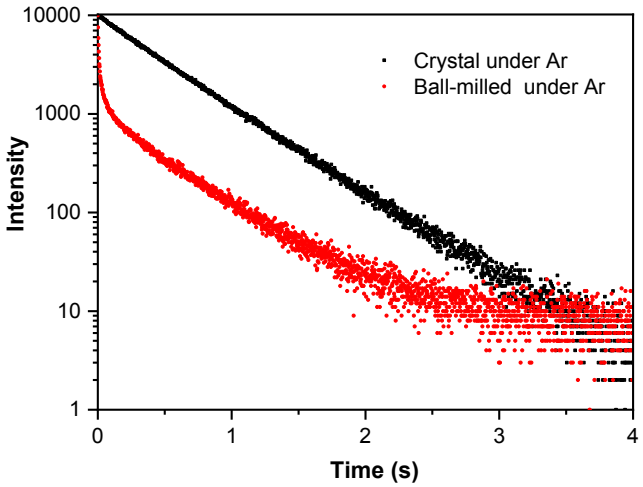

Figure S28. Phosphorescence decay of **3** in the crystalline state (478 ms) and ball-milled powder state (481 ms) at room temperature under argon.

Powder X-ray diffraction

Table S5. Unit cell parameters of **3** obtained from the LeBail refinement of powder X-ray diffraction data at room temperature. Ball-milled samples were obtained by placing compound **3** in a stainless steel vial (2 mL) and grinding with 5 steel balls (3 mm diameter) for 5 minutes at a frequency of 15 Hz in a Lab Wizz LMLW 320/2 ball mill.

Data	**# manually ground** (sample **A**)	**# ball-milled** (sample **B**)
λ / Å, radiation	1.5406, Cu-Kα_1	1.5406, Cu-Kα_1
θ range / °	5 – 60	5 – 60
a / Å	8.6841(9)	8.6437(9)
b / Å	9.7658(9)	9.7390(9)
c / Å	12.3669(8)	12.3531(14)
α / °	98.548(7)	98.497(8)
β / °	90.992(7)	90.908(7)
γ / °	107.646(7)	107.648(5)
Volume / Å^3	986.19(10)	978.0(2)
R_p	0.0525	0.0264
wR_p	0.1519	0.0387

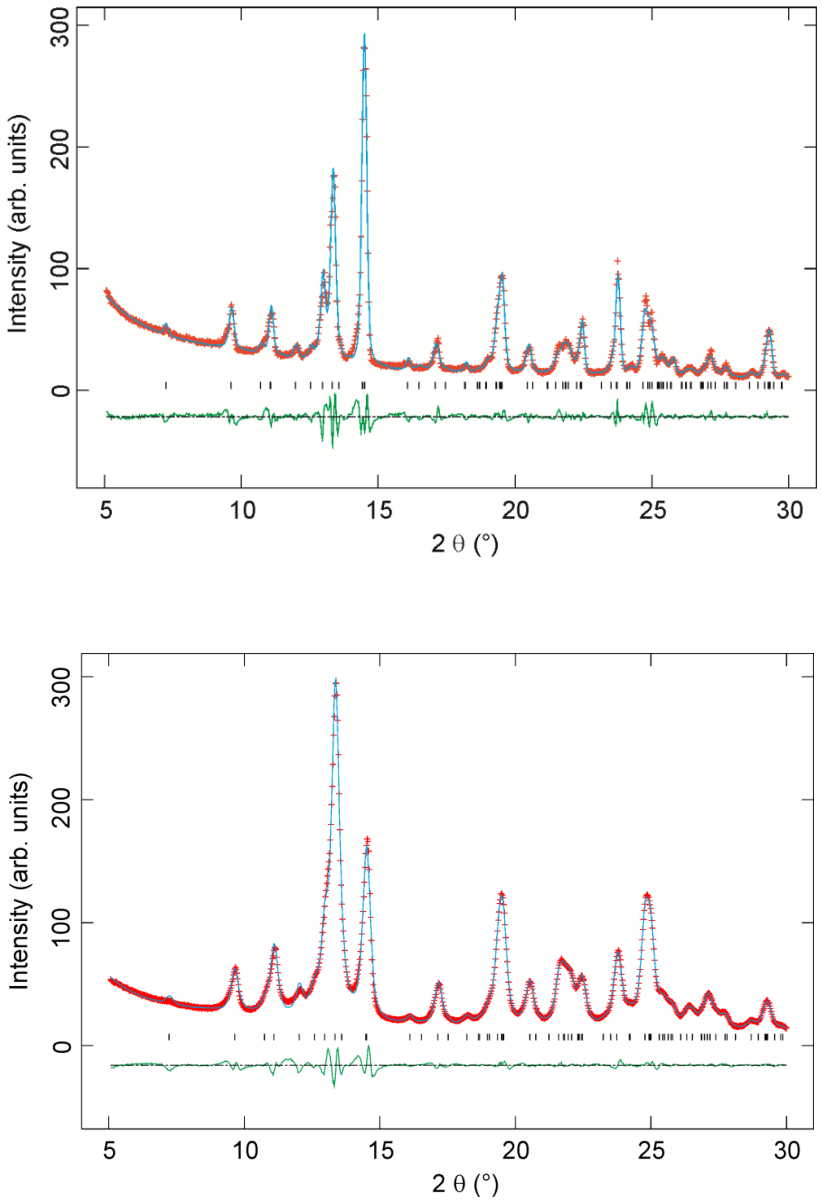

Figure S29. Powder X-ray diffraction patterns of compound **3** after grinding crystals in an agate mortar (sample **A**, top) and after ball-milling (sample **B**, bottom) in the selected range from 5 – 30° 2θ. Bottom: The increased reflection width is due to a smaller particle size after ball milling. Red crosses represent the experimental values. The continuous blue line shows the results of the Le Bail fit to the data. The difference between experimental data and LeBail fit is represented by the green line at the bottom of the plot. Vertical bars show the positions of the Bragg reflections of compound **3**.

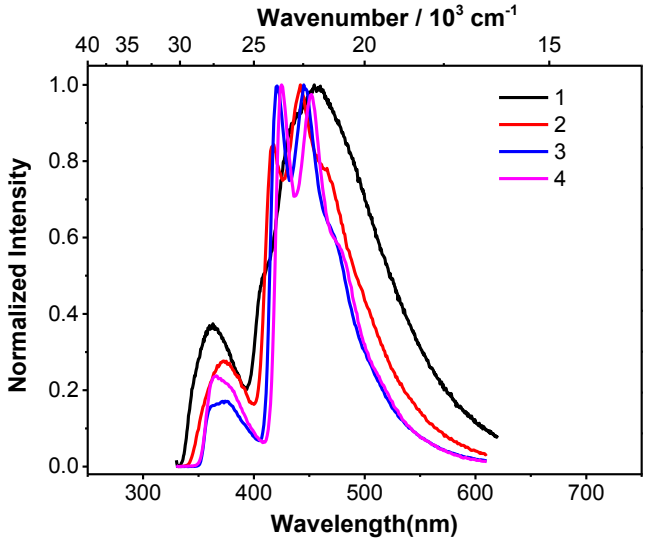

Figure S30. Normalized photoluminescence emission spectra of **1**-**4** in a frozen methylcyclohexane glass at 77 K (E_x = 305 nm).

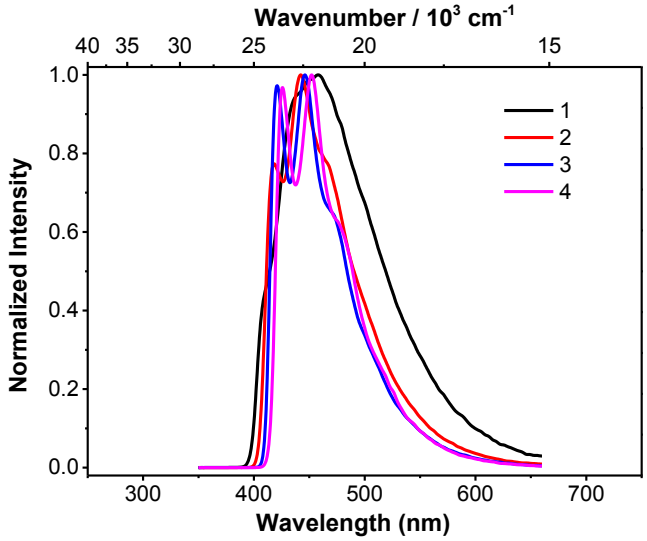

Figure S31. Normalized time-gated phosphorescence emission spectra of compounds **1**-**4** in a frozen methylcyclohexane glass at 77 K (E_x = 305 nm).

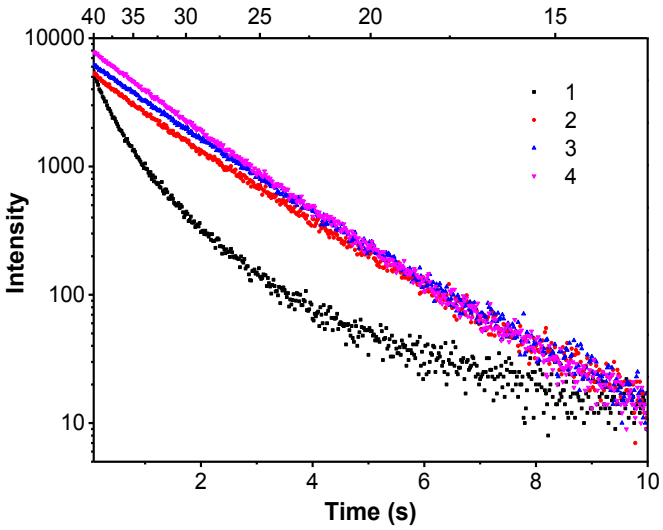

Figure S32. Decays of the phosphorescent emissions of **1-4** in a frozen methylcyclohexane glass at 77 K.

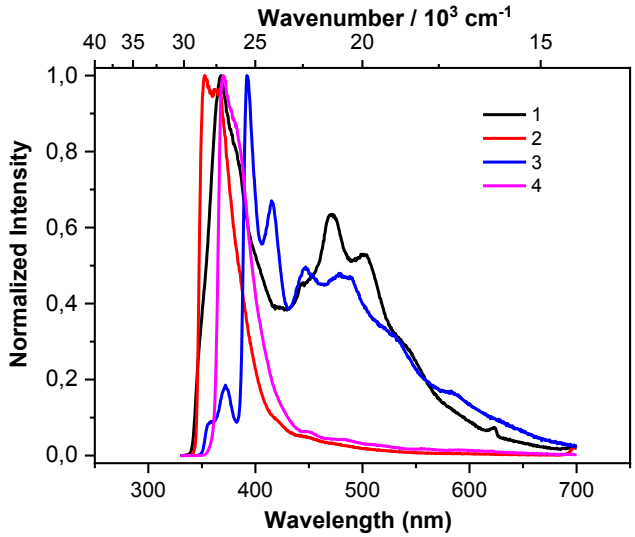

Figure S33. Normalized photoluminescent emission spectra of crystalline **1-4** at 77 K (E_x = 305 nm).

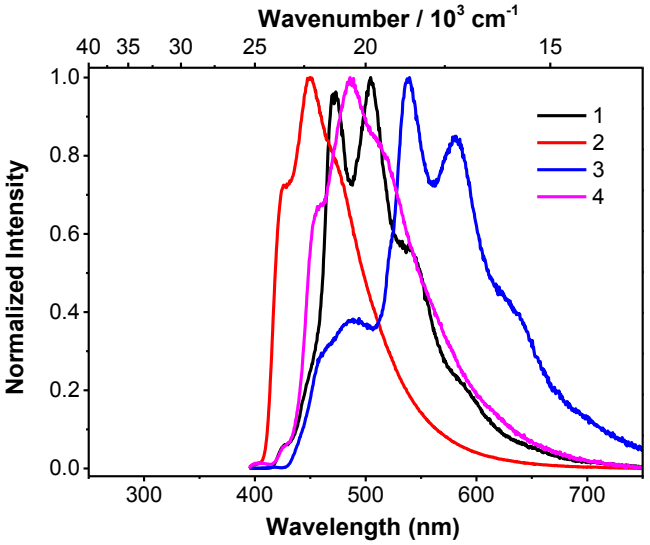

Figure S34. Normalized time-gated phosphorescence emission spectra of crystalline **1-4** at 77 K (E_x = 305 nm).

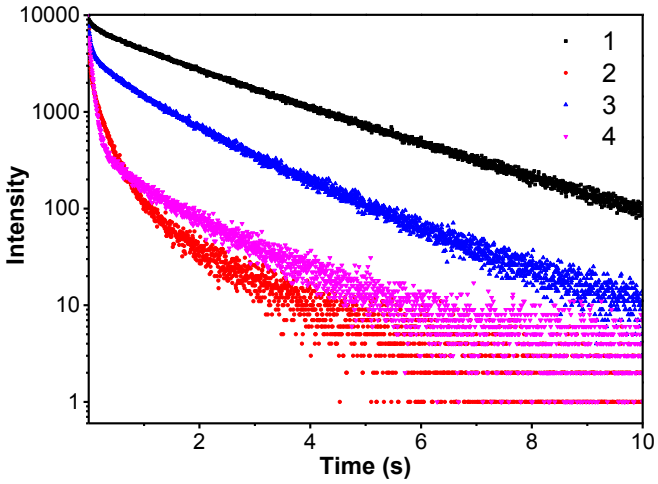

Figure S35. Decays of the maximum phosphorescent emissions of crystalline **1-4** at 77 K.

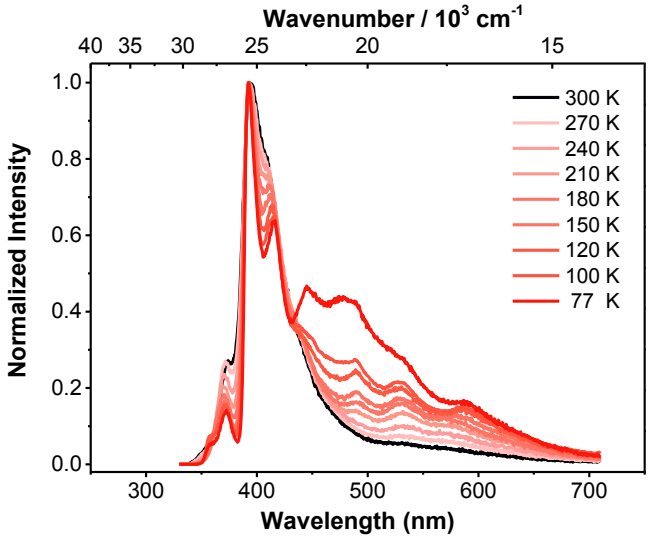

Figure S36. Normalized photoluminescent emission spectra of crystalline **3** at different temperatures (E_x = 305 nm).

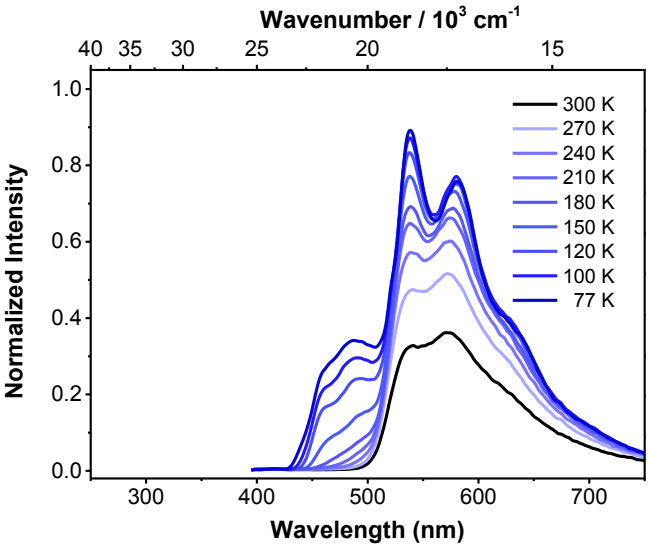

Figure S37. Normalized time-gated phosphorescence emission spectra of crystalline **3** at different temperatures (E_x = 305 nm).

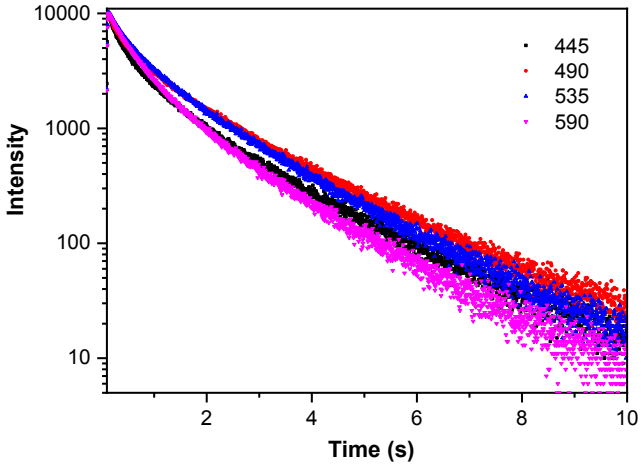

Figure S38. Decays of the phosphorescent emission of crystalline **3** at 445, 490, 535 and 590 nm at 77 K.

V. Single-crystal X-ray diffraction

Table S6. Single-crystal X-ray diffraction data and structure refinements for **1**, **2**, **3**, and **4**.

Data	**1**	**2**	**3**	**4**
CCDC number	1940099	1940100	1940101	1940107
Empirical formula	$C_{22}H_{23}B$	$C_{23}H_{25}B$	$C_{24}H_{27}B$	$C_{25}H_{29}B$
Formula weight / $g \cdot mol^{-1}$	298.21	312.24	326.26	340.29
T / K	100(2)	100(2)	100(2)	100(2)
radiation, λ / Å	MoKα 0.71073	MoKα 0.71073	MoKα 0.71073	MoKα 0.71073
Crystal size / mm^3	0.23×0.29×0.78	0.28×0.35×0.41	0.23×0.36×0.41	0.12×0.42×0.48
Crystal color, habit	colorless block	colorless block	colorless block	colorless plate
μ / mm^{-1}	0.063	0.064	0.063	0.063
Crystal system	Monoclinic	Monoclinic	Triclinic	Triclinic
Space group	$P2_1/c$	$P2_1/n$	$P\ \bar{1}$	$P\ \bar{1}$
a / Å	8.148(6)	8.138(5)	8.511(4)	8.445(3)
b / Å	10.828(3)	18.060(10)	9.675(2)	9.647(3)
c / Å	19.832(9)	12.161(7)	12.241(4)	12.890(5)
α / °	90	90	99.28(2)	99.166(15)
β / °	97.06(4)	90.293(11)	90.87(4)	91.49(3)
γ / °	90	90	107.44(2)	105.371(15)
Volume / $Å^3$	1736.5(16)	1787.4(17)	946.9(6)	997.1(6)
Z	4	4	2	2
ρ_{calc} / $g \cdot cm^{-3}$	1.141	1.160	1.144	1.133
F(000)	640	672	352	368
θ range / °	2.069 - 28.310	2.019 - 28.338	2.514 - 26.732	1.604 - 28.441
Reflections collected	19166	19909	16834	24532
Unique reflections	4300	4440	4009	5019
Parameters / restraints	212 / 0	222 / 0	232 / 0	253 / 0
GooF on F^2	1.054	1.029	1.035	1.050
R_1 [I>2σ(I)]	0.0469	0.0501	0.0437	0.0480
wR^2 (all data)	0.1256	0.1350	0.1174	0.1316
Max. / min. residual electron density / $e \cdot Å^{-3}$	0.364 / –0.236	0.382 / –0.207	0.365 / –0.230	0.366 / –0.244

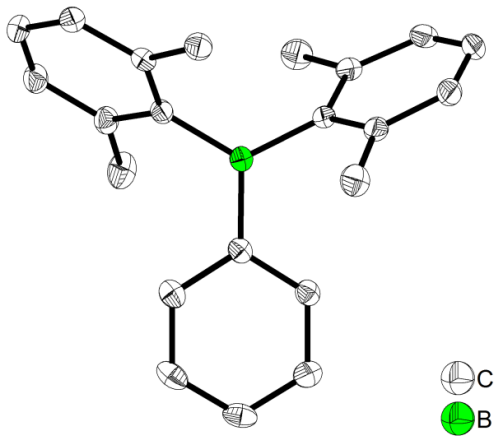

Figure S39. The solid-state molecular structure of **1** determined by single-crystal X-ray diffraction at 100 K. All ellipsoids are drawn at the 50% probability level, and H atoms are omitted for clarity.

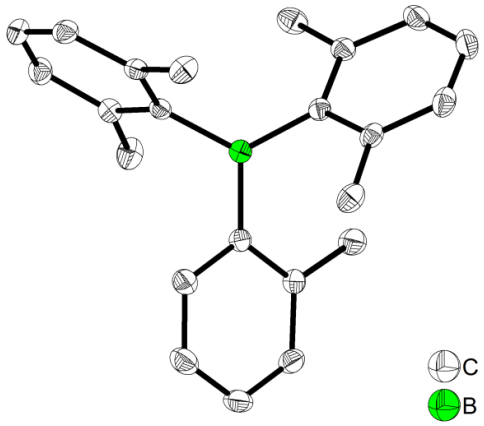

Figure S40. The solid-state molecular structure of **2** determined by single-crystal X-ray diffraction at 100 K. All ellipsoids are drawn at the 50% probability level, and H atoms are omitted for clarity.

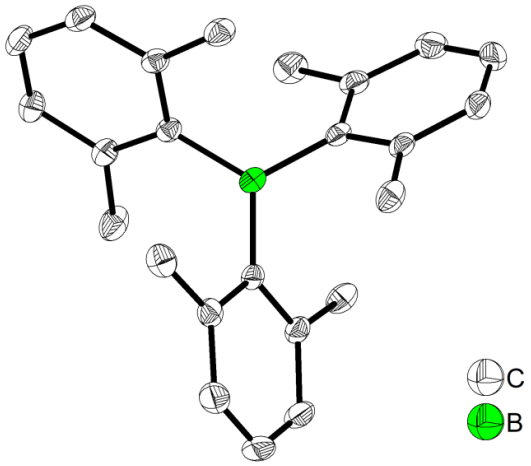

Figure S41. The solid-state molecular structure of **3** determined by single-crystal X-ray diffraction at 100 K. All ellipsoids are drawn at the 50% probability level, and H atoms are omitted for clarity.

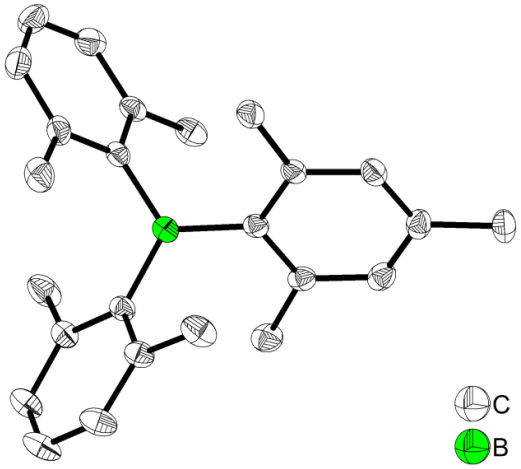

Figure S42. The solid-state molecular structure of **4** determined by single-crystal X-ray diffraction at 100 K. All ellipsoids are drawn at the 50% probability level, and H atoms are omitted for clarity. The major structural conformation with a refined occupancy of 0.809(4) is shown here.

Hirshfeld surface analysis and intermolecular interactions in detail

In order to compare and classify the types and magnitudes of the intermolecular interactions within single crystals of these four triarylboranes, which organize in a complex three-dimensional arrangement, the concept of Hirshfeld surface analysis was applied.[23] The molecules are most densely packed in compound **2**, as is clear from both the crystal packing coefficient c_k, which corresponds to the ratio of volume occupied by all molecules in the unit cell to the unit cell volume, and the surface of the crystal's void per formula unit, which is obtained from the Hirshfeld analysis (Table S8).[24] In order to quantify the nature and type of intermolecular interactions from the Hirshfeld surface analysis in a two-dimensional, graphical way, fingerprint plots and their breakdown to the individual contributions can be used.[25] This separation of relative contributions in crystals of **1**-**4** exhibited a strong contribution of H···H interactions (75 – 83 %), followed by a significant amount of C···H interactions (17 – 25 %) (Figures S43-S44). Only a very weak contribution of C···C interactions is observed for compound **3** (0.2 %). The similarity of the amounts and types of interactions in the four compounds is demonstrated in the two-dimensional fingerprint plots, which plot the distances from points on the surface to the nearest nuclei outside the surface, d_e, as a function of the distance to the nearest nucleus inside the surface, d_i.[23c] The largest differences in these plots are observed for compound **1**, which has close H···H contacts as demonstrated by the spike in the bottom left corner, and for compound **3**, which has a small percentage of C···C interactions. While this analysis shows the relative contributions of the different types of intermolecular interactions, we are now interested in their strengths in the individual crystal structures. Compound **1** exhibits several significant intermolecular interactions. Two strong C−H···C interactions (C···H = 2.835 and 2.839 Å, C−H···C = 168 and 166°) exist, three of intermediate strength (C−H···C = 138 – 160°), and one weak one (C−H···C = 127°). In addition, there is a short H···H contact (2.241 Å) between two aryl rings (Table S9). Compound **2**, although more densely packed than **1**, shows significantly fewer and weaker intermolecular interactions, i.e. three C−H···C interactions of intermediate strength (C−H···C = 145 – 155°), and one weak one (C−H···C = 114°). It is the only compound that has a nearly linear, weak C−H···π interaction towards the centroid of an m-xylyl ring with H···π = 2.907 Å. In addition, two close C···C contacts (C···C = 3.334 and 3.384 Å) are present, a strong one between two aryl rings, and a weak one

between the same aryl and a methyl group (Table S9). Compound **3** shows three linear intermolecular C−H···C interactions with C−H···C angles ranging from 164 to 172° which are strong, intermediate and weak according to their C···H distances of 2.841, 2.871, and 2.897 Å, respectively. This is quite similar to compound **1**. However, in addition to the C−H···C interactions, compound **3** also has a strong C···C interaction (C6···C6 = 3.319 Å) between two aryl rings with an approximately parallel alignment of their planes. This is the shortest nearest-neighbor (nn) C···C distance in all of the compounds. The interplanar separation between the aryl planes is only 2.980 Å; however, the offset shift is large (4.221 Å), resulting in a centroid-to-centroid distance of 5.167 Å, the latter two values being too large for a typical offset face-to-face π···π stacking interaction between two arenes (Table S10), which typically have values ranging from 3.3–3.8 Å for the interplanar separation, < 4.0 Å for the offset, and < 5.0 Å for the centroid-to-centroid distance.[26] There exists another arrangement of nearly parallel aryl rings, which has a longer C···C distance (3.495 Å) and interplanar separation (3.397 Å), but a smaller shift (3.493 Å) and, hence, a smaller centroid-to-centroid distance of 4.872 Å, all of those values being within the typical range of weak π···π interactions. The aryl rings, and hence the π···π interaction, are situated close to the voids, which are around the origin (Figure 5). A C···C offset aryl-aryl interaction is also present in compounds **2** and **4**; however, the C−H···C interactions are much weaker in these compounds. In crystals of compound **4**, intermolecular interactions are the weakest. This is in agreement with the loosest packing mode. There is a relatively close H···H contact (2.311 Å) between two methyl groups, one weak C−H···C interaction, and the weak C···C offset aryl-aryl interaction (Table S9).

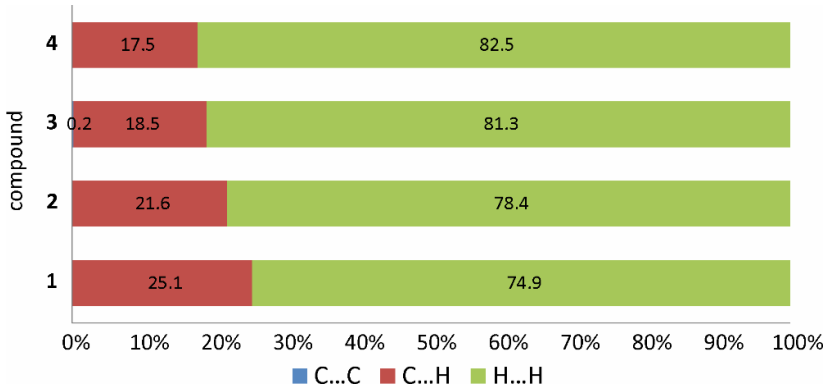

Figure S43. Percentage contributions to the Hirshfeld surface area for the various close intermolecular contacts in compounds **1**, **2**, **3**, and **4** at 100 K.

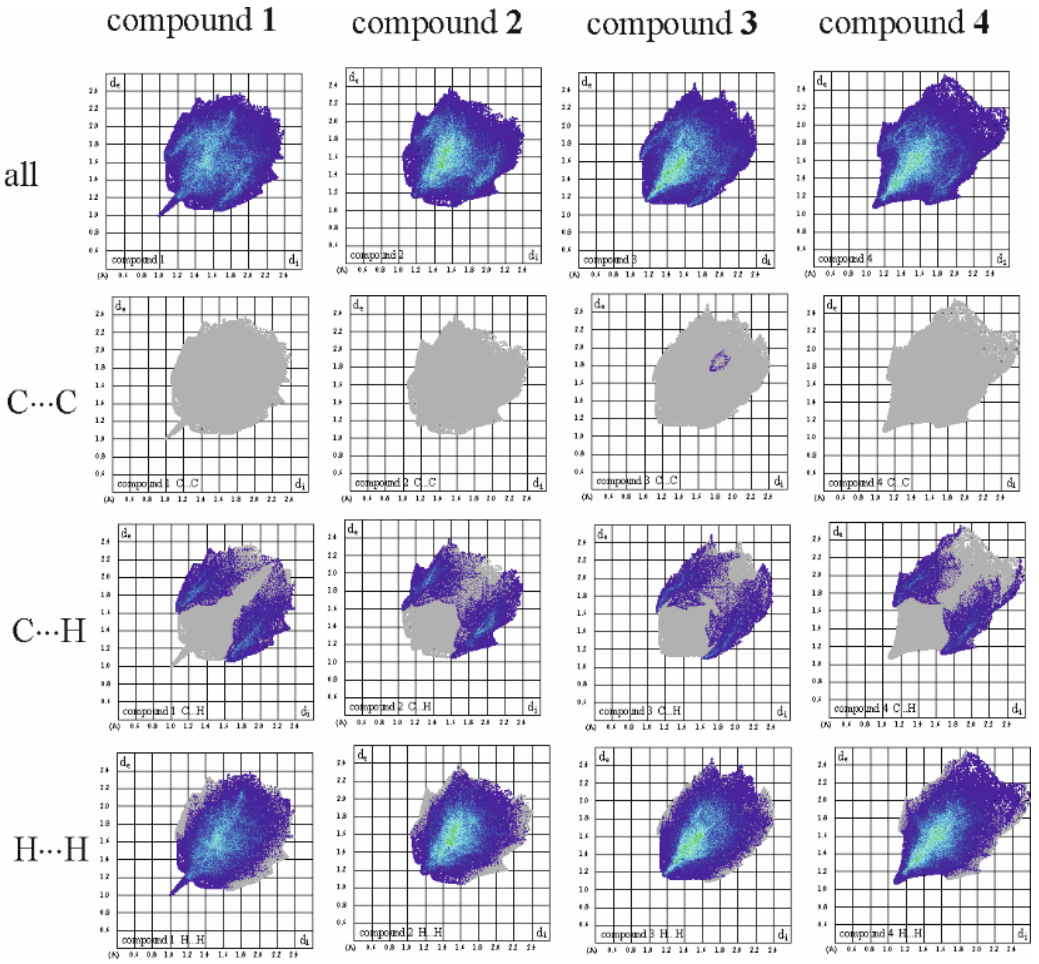

Figure S44. Two-dimensional fingerprint plots of molecules **1**, **2**, **3**, and **4** calculated from the Hirshfeld surfaces. The top row shows the complete fingerprint plots, while the other plots indicate the contributions of the individual intermolecular interactions (C···C, C···H, and H···H from top to bottom) within the grey area of all contributions.

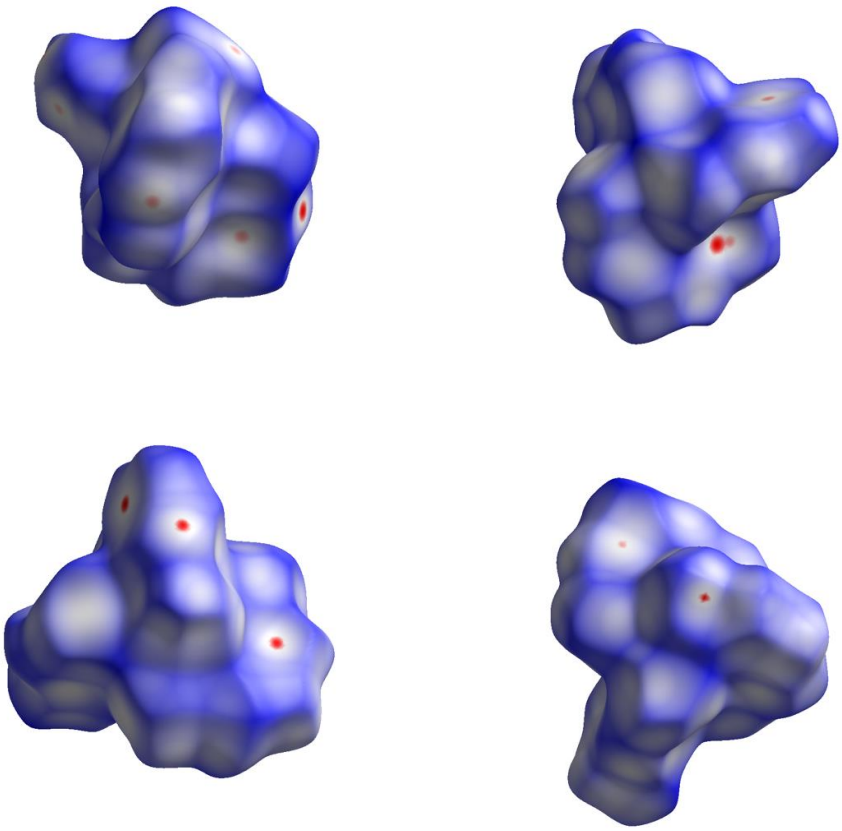

Figure S45. Hirshfeld surfaces of compounds **1** (top left), **2** (top right), **3** (bottom left), and **4** (bottom right) at 100 K mapped with d_{norm} over the range -0.16 to 1.40. Close contacts are shown red on the surface.

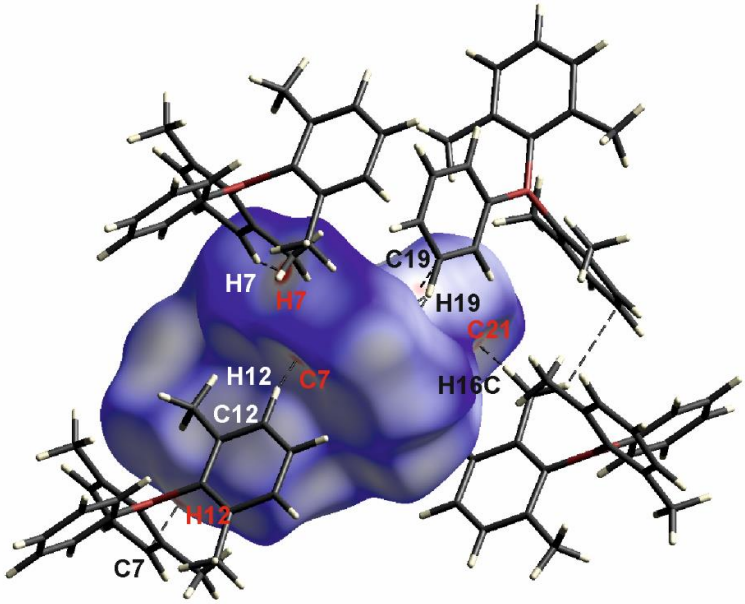

Figure S46. Hirshfeld surface of compound **1** mapped with d_{norm} over the range -0.16 to 1.40 at 100 K. Neighbouring molecules associated with close contacts are shown.

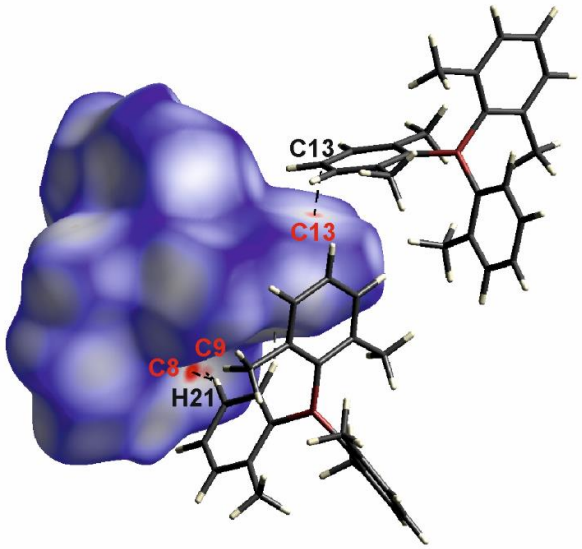

Figure S47. Hirshfeld surface of compound **2** mapped with d_{norm} over the range -0.16 to 1.40 at 100 K. Neighbouring molecules associated with close contacts are shown.

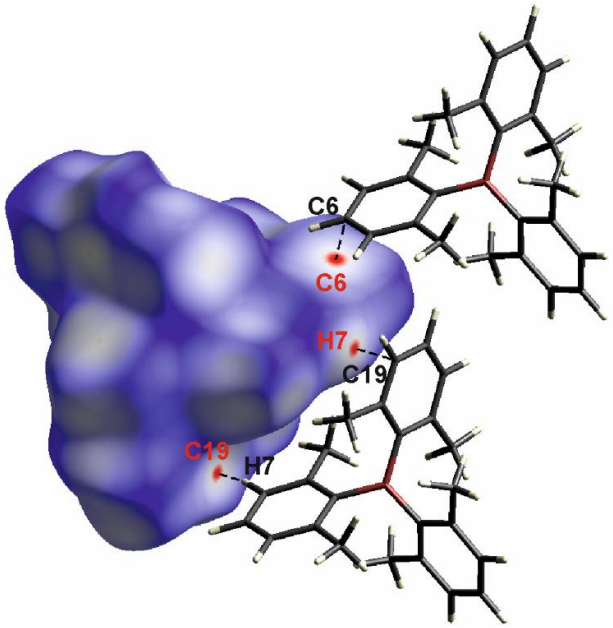

Figure S48. Hirshfeld surface of compound **3** mapped with d_{norm} over the range -0.16 to 1.40 at 100 K. Neighbouring molecules associated with close contacts are shown.

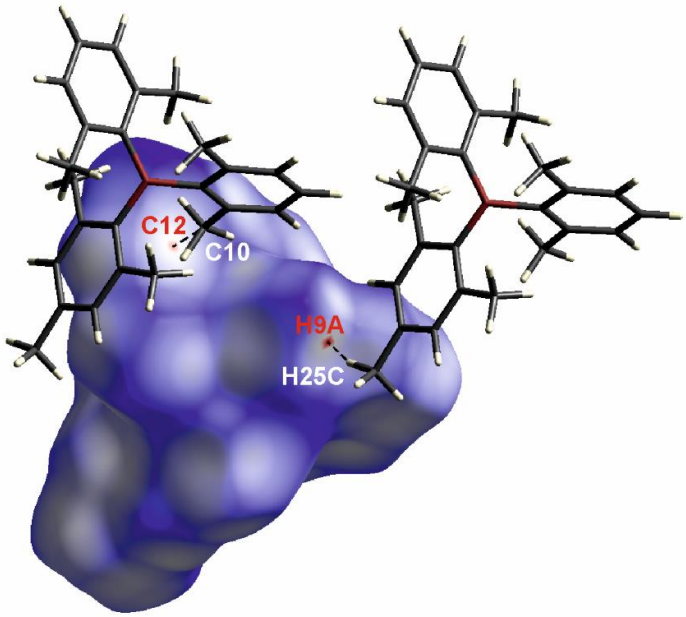

Figure S49. Hirshfeld surface of compound **4** mapped with d_{norm} over the range -0.16 to 1.40 at 100 K. Neighbouring molecules associated with close contacts are shown.

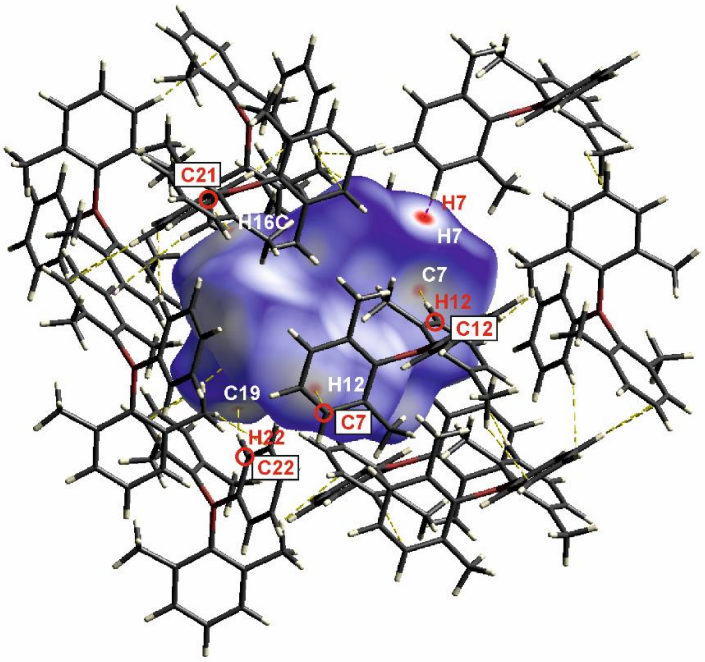

Figure S50. Hirshfeld surface of compound **1** mapped with d_{norm} over the range -0.16 to 1.40 at 100 K. Neighbouring molecules associated with close contacts are shown. Closest contacts are labelled.

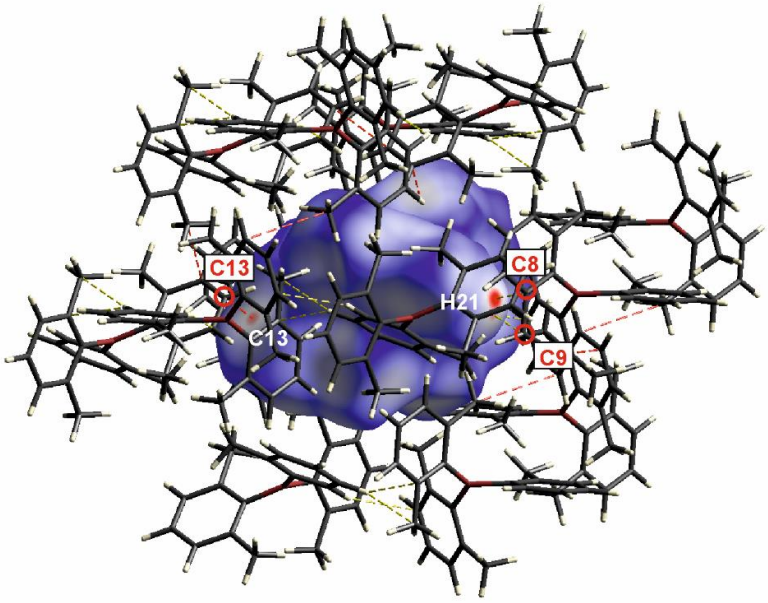

Figure S51. Hirshfeld surface of compound **2** mapped with d_{norm} over the range -0.16 to 1.40. Neighbouring molecules associated with close contacts are shown. Closest contacts are labelled.

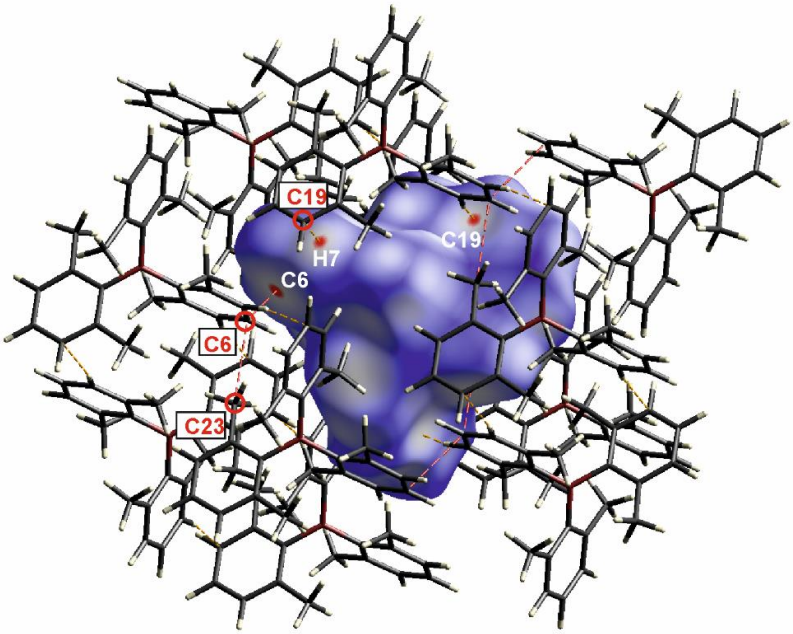

Figure S52. Hirshfeld surface of compound **3** mapped with d_{norm} over the range -0.16 to 1.40 at 100 K. Neighbouring molecules associated with close contacts are shown. Closest contacts are labelled.

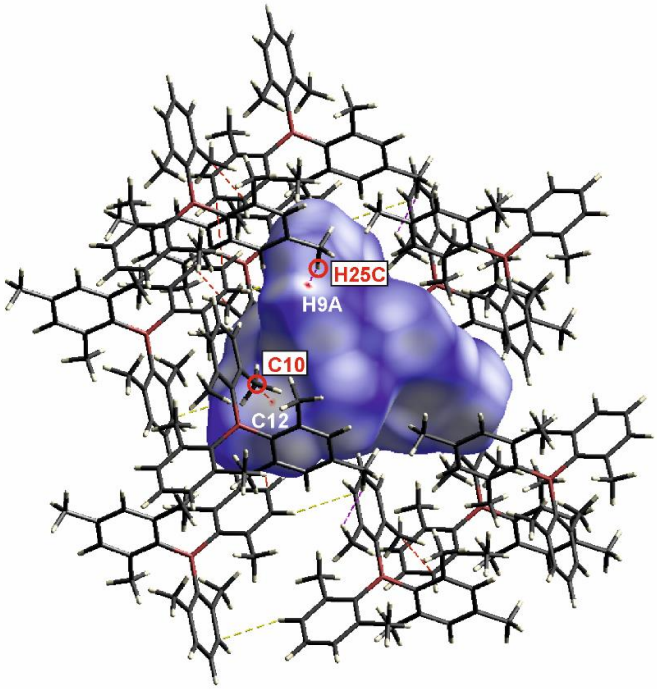

Figure S53. Hirshfeld surface of compound **4** mapped with d_{norm} over the range -0.16 to 1.40 at 100 K. Neighbouring molecules associated with close contacts are shown. Closest contacts are labelled.

Table S7. Selected bond lengths (Å) and angles (°) in compounds **1**, **2**, **3**, and **4** at 100 K**.**

	1	**2**	**3**	**4** [a]
Sum ∠ CBC	360.0(1)	359.9(1)	360.0(1)	360.0(1)
B–C	1.5867(18)	1.583(2)	1.5795(19)	1.5848(18)
	1.5819(18)	1.581(2)	1.5826(18)	1.5794(18)
	1.5686(19)	1.570(2)	1.5858(18)	1.5763(18)
∠ BC3 – aryl	65.28(6)	60.53(5)	53.52(7)	49.96(5)
	57.45(6)	56.67(6)	52.91(7)	54.85(6)
	16.09(9)	41.91(6)	53.92(6)	51.15(6)

[a] The mesityl group is disordered with one of the m-xylyl groups.

Table S8. Properties of crystals of compounds **1**, **2**, **3**, and **4** at 100 K: volume within van der Waals (V_m), Hirshfeld (V_H), and surface of the crystal voids (V_v), crystal packing coefficient (c_k), solvent accessible volume (V_{solv}), and percentage of intermolecular contacts.

	1	**2**	**3**	**4** [a]
V_m / Å³	283.36	298.60	312.20	323.94
V_H / Å³	427.11	440.18	466.68	491.63
V_v / Å³	211.86	169.00	103.82	111.40
V_v / Å³ per formula unit	52.97	42.25	51.91	55.70
c_k	0.654	0.668	0.659	0.650
V_{solv} / Å³	0.0	0.0	9.0	0.0
C···C / %	0.0	0.0	0.2	0.0
C···H / %	25.1	21.6	18.5	17.5
H···H / %	74.9	78.4	81.3	82.5

[a] The mesityl group is disordered with one of the m-xylyl groups. The configuration with the major occupancy (80%) is considered in this comparison.

Table S9. Intermolecular C−H···C(π), C···C, and H···H interaction distances (Å) and angles (°) in compounds **1**, **2**, **3**, and **4** at 100 K. Distances and angles of strong interactions are in bold type.

Compound	C−H···C	H···C/H	C···C	∠(CHC)
1	H7···H7	**2.2413(12)**		
	C12−H12···C7	**2.8346(16)**	**3.770(2)**	**168.04(8)**
	C19−H19···C5	**2.8388(15)**	**3.767(2)**	**166.02(8)**
	C19−H19···C6	2.8866(19)	3.650(2)	138.19(8)
	C22−H22···C19	2.8555(15)	3.761(2)	159.93(8)
	C16(methyl)−H16C···C21	2.792(2)	3.634(3)	144.47(10)
	C16(methyl)−H16B···C13	2.8509(16)	3.532(2)	127.27(9)
2	C21−H21···C8	2.7521(17)	3.572(3)	144.95(10)
	C21−H21···C9(methyl)	2.859(2)	3.742(3)	155.05(10)
	C22−H22···C12	2.877(2)	3.756(3)	154.27(10)
	C10(methyl)−H10B···C14	2.8608(19)	3.385(2)	114.33(9)
	C12-H12···**π** (centroid of aryl#1)	2.9068(16)	3.830(3)	168.10(7)
	C13···C13		3.334(3)	
	C10(methyl)···C14		3.385(2)	
3	C7−H7···C19	**2.8407(17)**	**3.765(2)**	**164.41(9)**
	C14−H14···C21	2.8714(17)	3.815(2)	**171.96(9)**
	C5−H5···C12	2.897(2)	3.832(3)	168.18(9)
	C6···C6		**3.319(2)**	
	C6···C23(methyl)		3.392(2)	
4	H9A(methyl)···H25C (methyl)	2.3105(7)		
	C14−H14···C7	2.8931(18)	3.745(3)	149.84(9)
	C13A···C13A		3.392(2)	
	C10(methyl)···C12		3.3785(19)	

Table S10. Aryl···aryl (π···π) distances (Å) and angles (°) in crystals of **1**, **2**, **3**, and **4** at 100 K: nearest-neighbor (nn) C···C distances, centroid-centroid distances, interplanar separations, shifts, and slip angles. Aryl rings are numbered 1, 2, or 3 according to the C1, C2, or C3 atom being present and bonding to the boron atom, respectively. The closest interactions are in bold type.

Compound	Aryl···Aryl	nn C···C	Centroid-centroid distance	Interplanar separation	Shift	Slip angle
1	#1···#1	3.857(5)	6.123(3)	2.513(6)	5.583(4)	65.7
	#2···#2	4.315(5)	6.275(3)	3.507(5)	5.203(5)	56.0
	#1···#2	4.526(4)	6.587(3)	3.886(5) / 2.982(6)	5.319(5) / 5.874(4)	53.8/ 63.1
2	#2···#2	**3.3338(17)**	**5.000(2)**	**3.1607(13)**	**3.8745(19)**	**50.8**
	#3···#3	3.5833(12)	5.489(2)	3.0270(15)	4.578(3)	56.5
	#1···#1	4.1070(16)	6.348(3)	3.0521(15)	5.566(3)	61.3
3	#1···#1	**3.319(3)**	**5.1671(17)**	**2.980(3)**	**4.221(3)**	**54.8**
	#2···#2	**3.495(3)**	**4.8718(16)**	**3.397(3)**	**3.493(3)**	**45.8**
4	#2···#2	**3.392(3)**	**5.1873(18)**	**3.096(3)**	**4.162(2)**	**53.4**
	#3···#3	3.768(3)	5.2472(18)	3.550(3)	3.864(3)	47.4
	#2···#2	4.396(3)	6.077(2)	3.613(3)	4.887(3)	53.5

Table S11. Temperature-dependent single-crystal X-ray diffraction data and structure refinements of **3**, $C_{24}H_{27}B$. Formula weight = 326.26 g·mol^{-1}; F(000) = 352; Z = 2.

T / K	293(2)	240(2)	180(2)	120(2)	83(2)
CCDC number	1940102	1940103	1940104	1940105	1940106
λ / Å, radiation	0.71073, MoKα				
Crystal color, habit	Colorless, block				
Crystal size / mm³	0.28×0.40×0.48	0.27×033×0.34	0.27×033×0.34	0.27×033×0.34	0.27×033×0.34
Crystal system	Triclinic				
Space group	$P\ \bar{1}$				
a / Å	8.661(2)	8.604(2)	8.549(2)	8.507(3)	8.511(3)
b / Å	9.7587(15)	9.718(2)	9.7014(13)	9.6857(13)	9.6752(16)
c / Å	12.379(2)	12.330(3)	12.2995(16)	12.2513(17)	12.207(2)
α / °	98.602(7)	98.854(7)	99.073(6)	99.278(7)	99.373(8)
β / °	90.91(2)	90.760(13)	90.765(12)	90.929(18)	91.212(19)
γ / °	107.622(7)	107.483(16)	107.392(18)	107.37(2)	107.48(3)
Volume / Å^3	983.9(3)	969.6(4)	959.3(3)	948.6(4)	943.4(4)
ρ_{calc} / g·cm^{-3}	1.101	1.117	1.130	1.142	1.149
μ / mm^{-1}	0.061	0.062	0.062	0.063	0.063
θ range / °	2.473 – 26.022	2.487 – 26.020	2.502 – 26.021	2.810 – 26.022	2.516 – 26.011
Reflections collected	14499	16739	16620	16349	16202
Unique reflections	3876	3811	3773	3726	3710
Parameters / restraints	232 / 0	232 / 0	232 / 0	307 / 0	307 / 0
GooF on F^2	1.027	1.047	1.028	1.029	1.057
R_1 [I>2σ(I)]	0.0525	0.0549	0.0513	0.0465	0.0448
wR^2 (all data)	0.1519	0.1542	0.1377	0.1247	0.1149
Max. / min. residual electron density / e·Å^{-3}	0.215 / –0.147	0.211 / –0.163	0.225 / –0.178	0.213 / –0.202	0.268 / –0.209

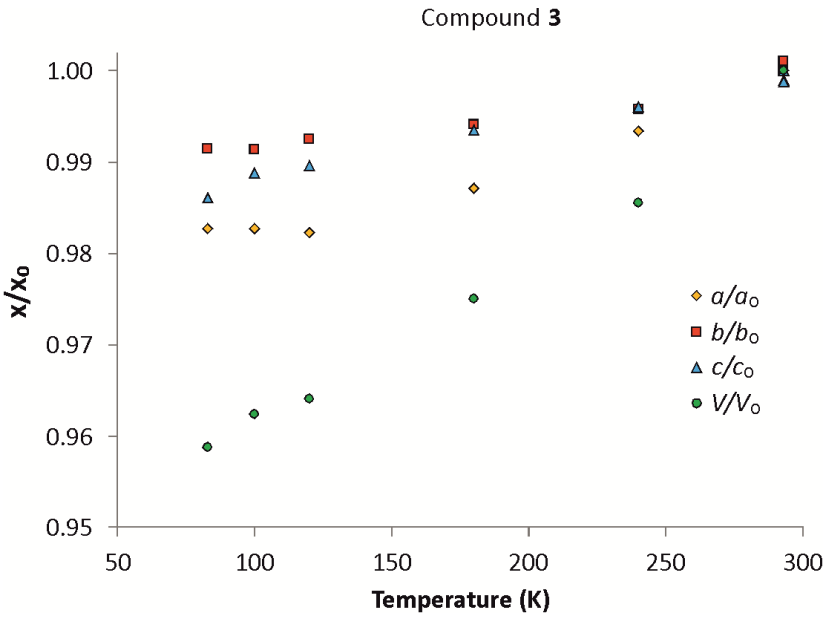

Figure S54. Temperature dependence of the normalized unit cell lengths and volume of compound **3**.

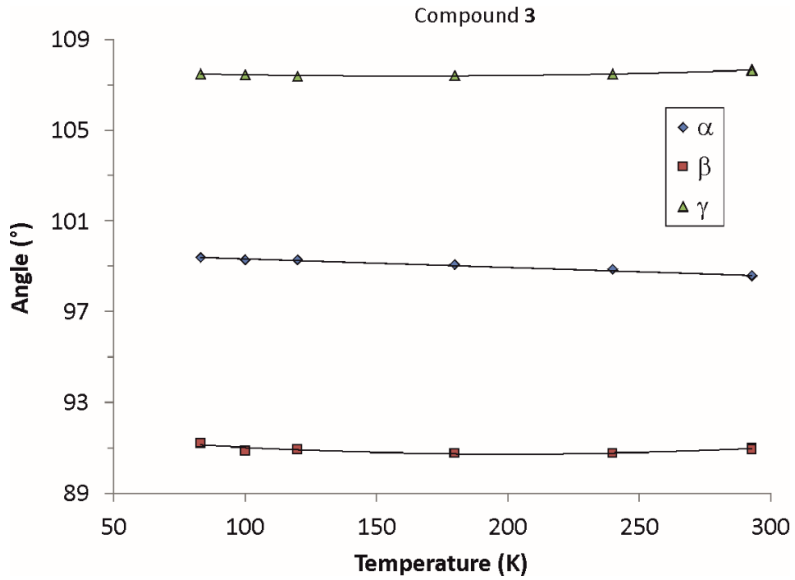

Figure S55. Temperature dependence of the unit cell angles (°) of compound **3**.

Table S12. Temperature dependence of **s**elected bond lengths (Å) and angles (°) of compound **3.**

T (K)	**293**	**240**	**180**	**120**	**100**	**83**
Sum ∠ CBC	360.0(2)	360.0(2)	360.0(2)	360.0(1)	360.0(1)	360.0(1)
B–C	1.577(3) 1.579(3) 1.587(3)	1.574(3) 1.583(3) 1.585(3)	1.576(3) 1.581(3) 1.590(3)	1.579(2) 1.584(2) 1.589(2)	1.5795(19) 1.5826(18) 1.5858(18)	1.579(2) 1.584(2) 1.588(2)
∠ BC3 – aryl	53.68(9) 53.06(8) 52.74(6)	53.66(9) 53.07(8) 53.15(6)	53.57(8) 52.91(7) 53.69(5)	53.46(7) 52.89(7) 53.91(5)	53.52(7) 52.91(7) 53.92(6)	53.30(7) 53.01(6) 53.86(5)

Table S13. Temperature dependence of the properties of crystals of compound **3**: Volume within van der Waals (V_m), Hirshfeld (V_H), and surface of the crystal voids (V_v), crystal packing coefficient (c_k), solvent accessible volume (V_{solv}), and percentage of intermolecular contacts. pfu…per formula unit.

T (K)	**293**	**240**	**180**	**120**	**100**	**83**
V_m / Å³	309.49	309.73	311.79	312.64	312.20	312.92
V_H / Å³	485.16	478.07	472.87	467.55	466.68	464.92
V_v / Å³	140.13	126.45	115.58	104.17	103.82	98.90
V_v / Å³ pfu	70.07	63.23	57.79	52.09	51.91	49.45
c_k	0.629	0.639	0.650	0.659	0.659	0.663
V_{solv} / Å³	11.0	10.9	9.1	9.0	9.0	9.0
C···C / %	0.2	0.2	0.2	0.3	0.2	0.2
C···H / %	17.0	17.6	18.1	18.6	18.5	18.8
H···H / %	82.8	82.2	81.7	81.1	81.3	81.0

Table S14. Temperature dependence of the intermolecular C–H···C and C···C interaction distances (Å) and angles (°) in compound **3**.

T (K)	293	240	180	120	100	83
H7···C19	2.924(2)	2.881(2)	2.860(2)	2.80(2)	2.841(2)	2.815(2)
C7···C19	3.816(4)	3.787(3)	3.779(3)	3.768(3)	3.765(2)	3.771(2)
∠(C7-H7-C19)	161.3(2)	162.0(2)	163.1(1)	162(1)	164.41(9)	162(1)
H14···C21	2.971(2)	2.929(2)	2.897(2)	2.86(2)	2.871(2)	2.85(2)
C14···C21	3.897(3)	3.865(3)	3.842(3)	3.823(3)	3.815(2)	3.815(2)
∠(C14-H14-C21)	174.1(2)	173.7(2)	172.9(1)	169(1)	171.96(9)	170(1)
H5···C12	3.028(3)	2.982(3)	2.934(2)	2.85(2)	2.897(2)	2.88(2)
C5···C12	3.943(4)	3.907(4)	3.870(3)	3.831(3)	3.832(3)	3.817(3)
∠(C5-H5-C12	168.4(2)	168.5(2)	168.5(1)	170(1)	168.18(9)	167(1)
C6···C6	3.421(4)	3.376(3)	3.343(3)	3.324(2)	3.319(2)	3.318(2)
C6···C23(methyl)	3.488(3)	3.460(3)	3.430(2)	3.402(2)	3.392(2)	3.376(2)

Table S15. Temperature dependence of the aryl···aryl (π···π) distances (Å) and angles (°) in crystals of **3**: nearest-neighbour (nn) C···C distances, centroid-centroid distances, interplanar separations, shifts, and slip angles. Aryl rings are numbered 1, 2, or 3 according to the C1, C2, or C3 atom being present and bonding to the boron atom, respectively.

T (K)	Aryl···Aryl	nn C···C	Centroid-centroid distance	Interplanar separation	Shift	Slip angle
293	#1···#1	3.421(5)	5.3311(19)	2.996(4)	4.409(3)	55.8
	#2···#2	3.633(6)	4.9301(19)	3.523(4)	3.449(4)	44.4
240	#1···#1	3.375(4)	5.2606(19)	2.995(4)	4.325(3)	55.3
	#2···#2	3.587(5)	4.9088(19)	3.479(4)	3.463(4)	44.9
180	#1···#1	3.343(4)	5.2075(16)	2.991(4)	4.263(3)	54.9
	#2···#2	3.544(4)	4.8973(16)	3.440(4)	3.486(3)	45.4
120	#1···#1	3.3239(7)	5.1722(6)	2.9827(9)	4.2255(10)	54.8
	#2···#2	3.4938(8)	4.8779(5)	3.3963(9)	3.5013(10)	45.9
100	#1···#1	3.319(3)	5.1671(17)	2.980(3)	4.221(3)	54.8
	#2···#2	3.495(3)	4.8718(16)	3.397(3)	3.493(3)	45.8
83	#1···#1	3.318(3)	5.1715(14)	2.973(3)	4.231(2)	54.9
	#2···#2	3.469(3)	4.8633(14)	3.375(3)	3.502(3)	46.1

VI. ^{1}H, $^{13}C\{^{1}H\}$, ^{11}B NMR spectra, GC-MS and HRMS

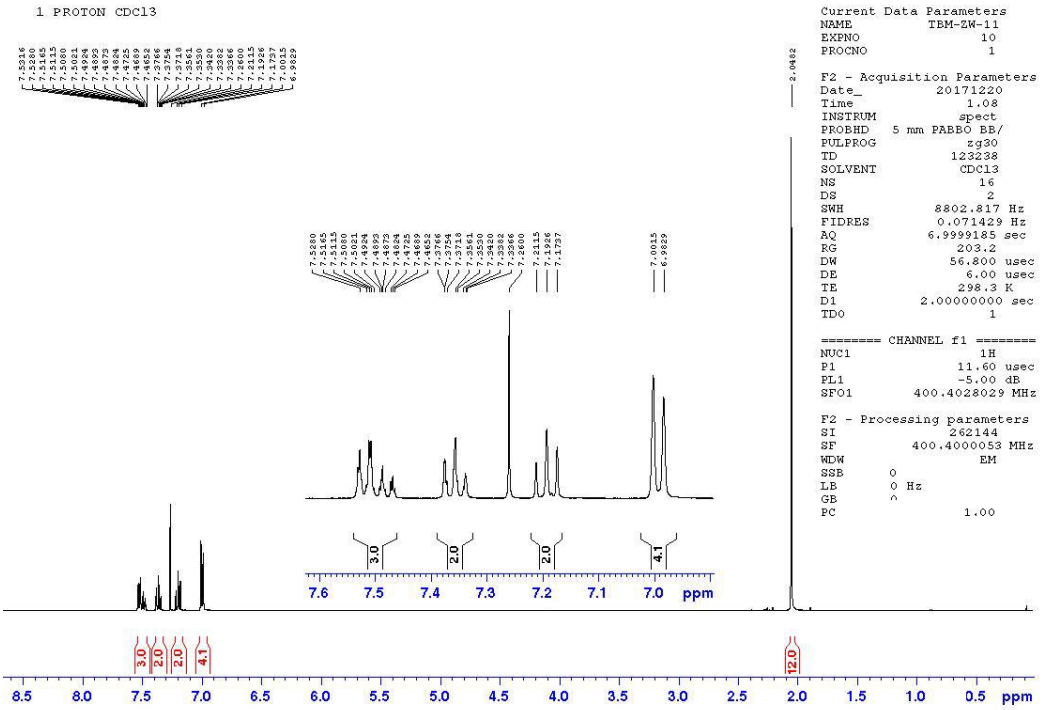

Figure S56. ^{1}H NMR spectrum (400 MHz, $CDCl_3$) of **1**.

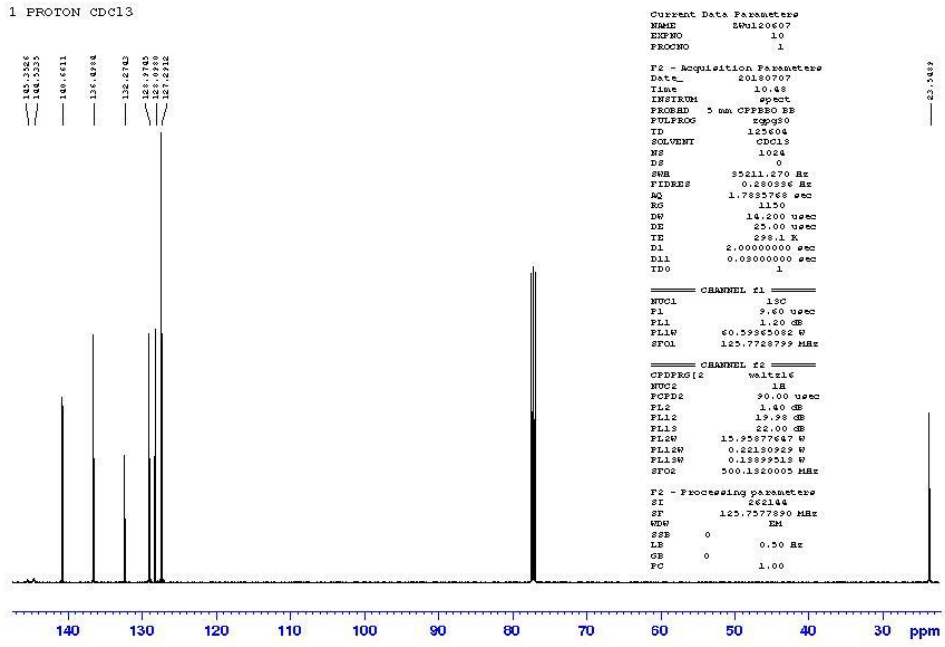

Figure S57. $^{13}C\{^{1}H\}$ NMR spectrum (126 MHz, $CDCl_3$) of **1**.

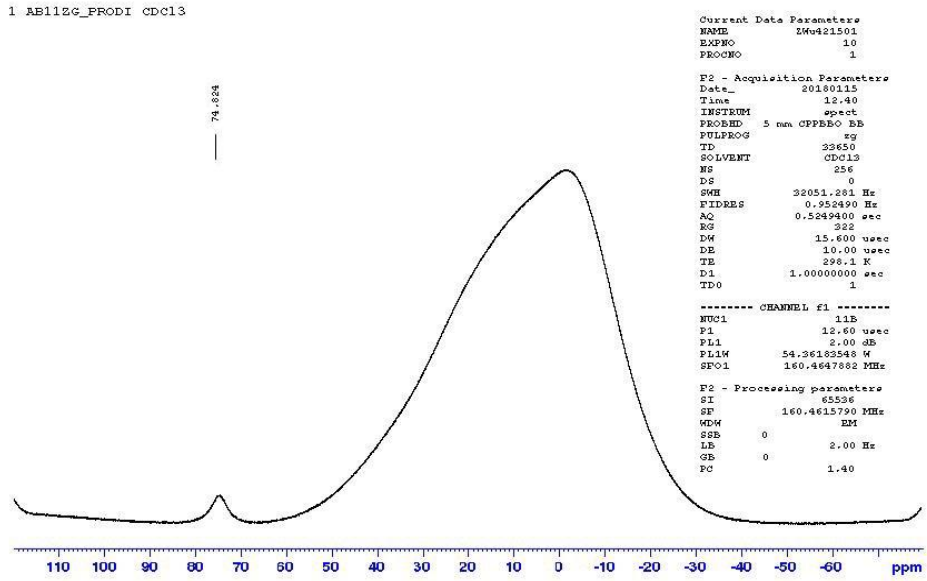

Figure S58. ^{11}B NMR spectrum (160 MHz, $CDCl_3$) of **1**.

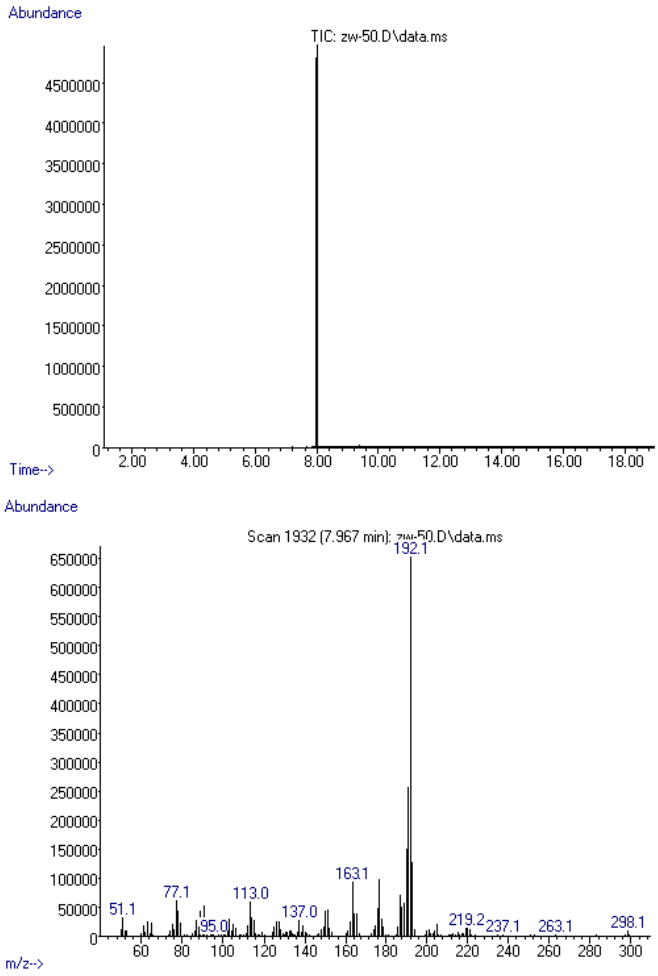

Figure S59. GC-MS total ion chromatogram (TIC) and MS $(EI)_{m/z}$ of **1**.

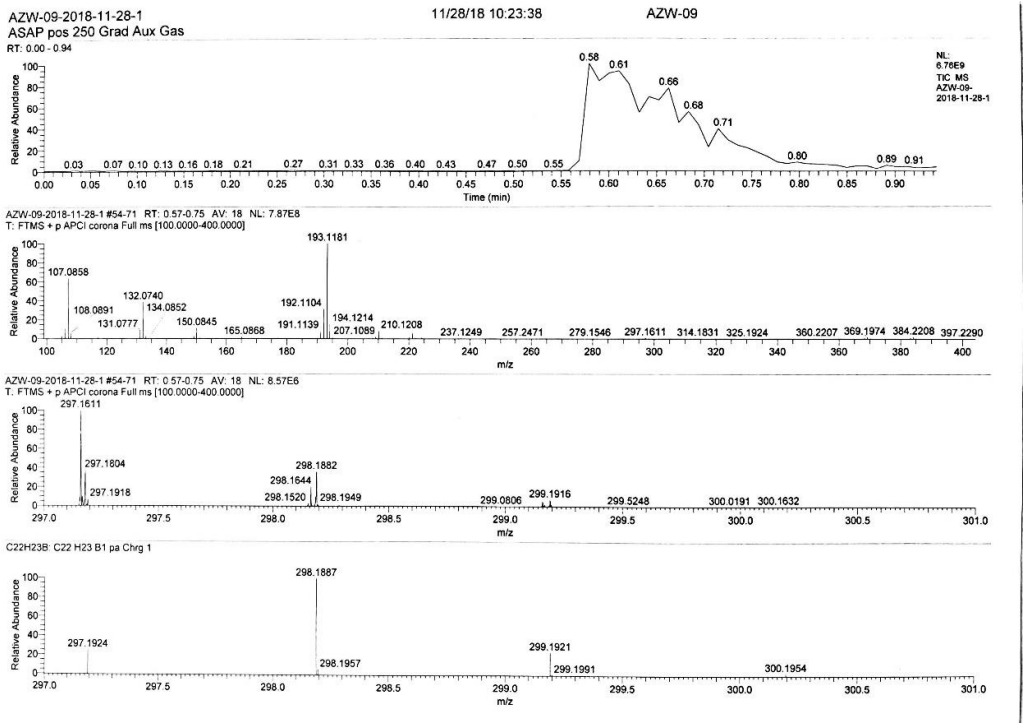

Figure S60. ESI-HRMS of **1**.

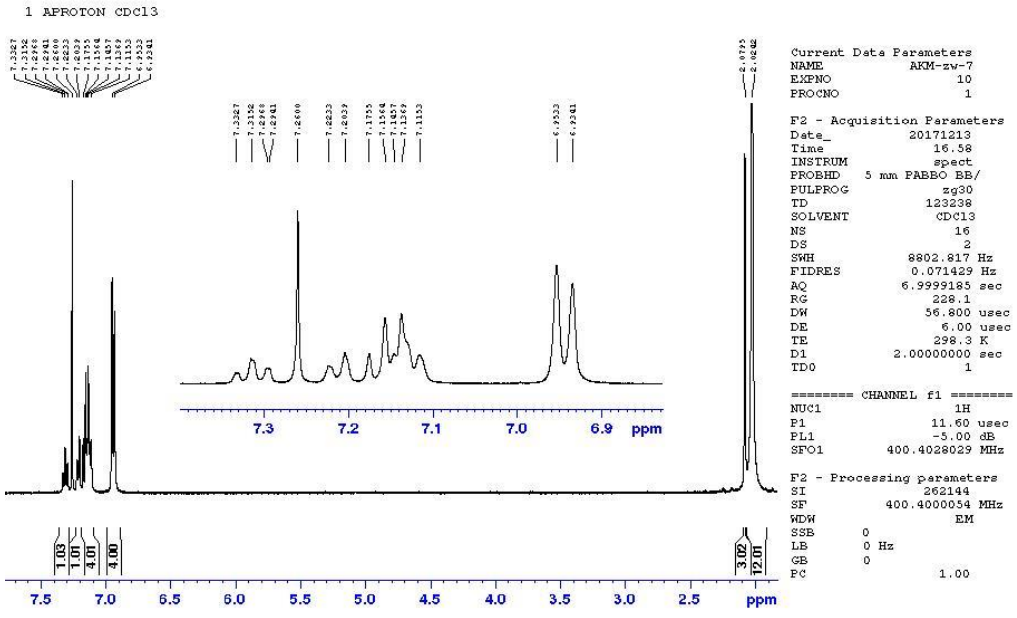

Figure S61. ^{1}H NMR spectrum (400 MHz, $CDCl_3$) of **2**.

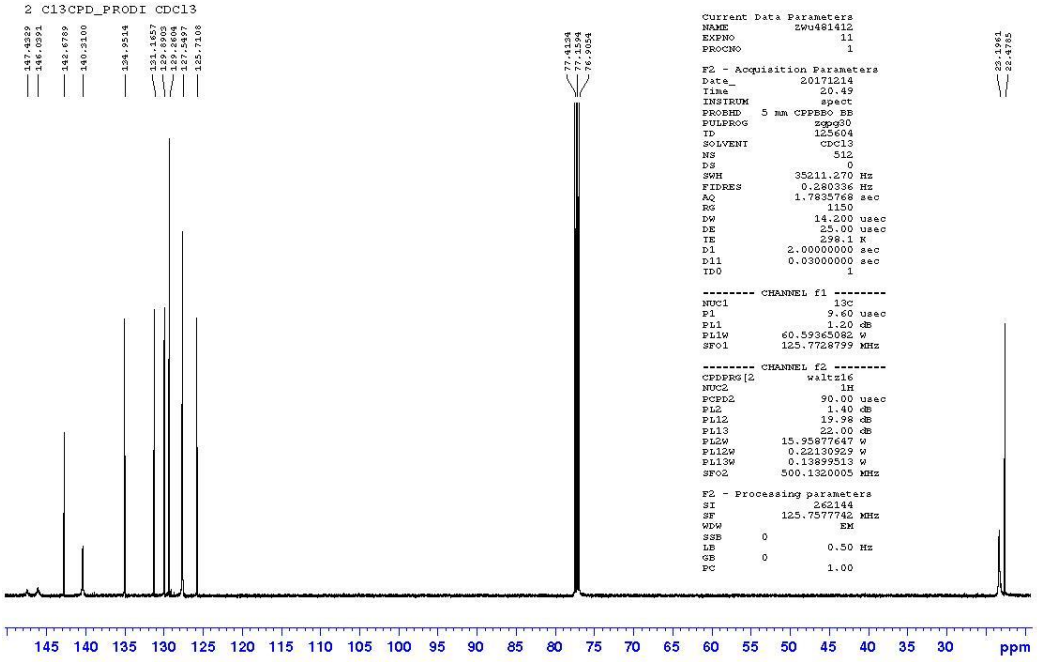

Figure S62. $^{13}C\{^{1}H\}$ NMR spectrum (126 MHz, $CDCl_3$) of **2**.

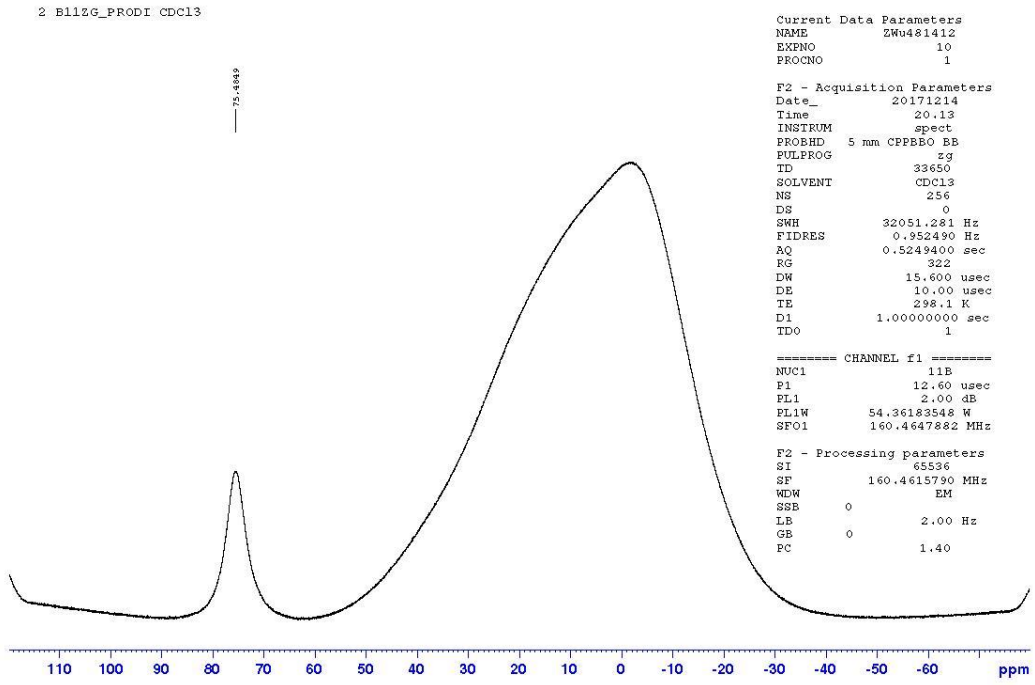

Figure S63. ^{11}B NMR spectrum (160 MHz, $CDCl_3$) of **2**.

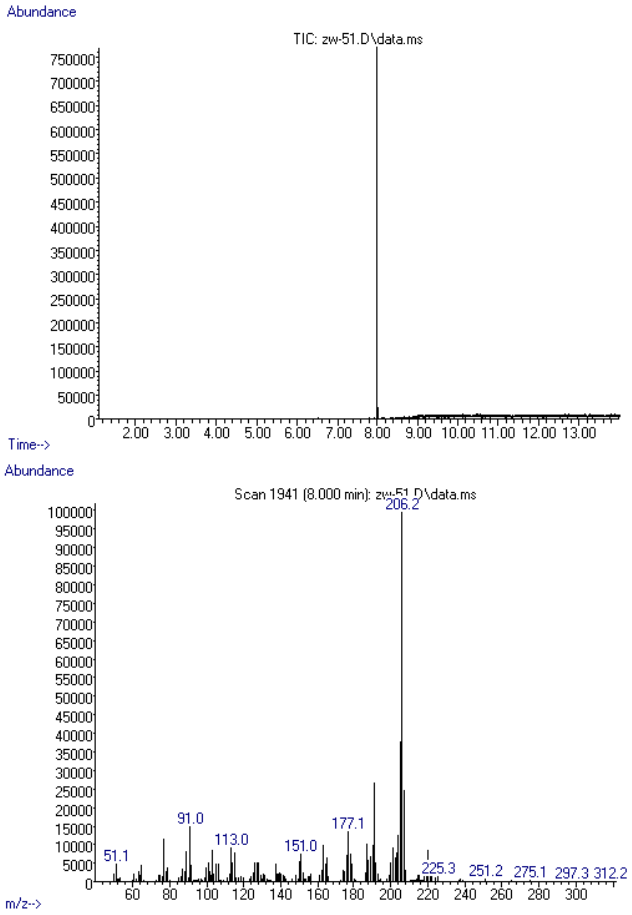

Figure S64. GC-MS total ion chromatogram (TIC) and MS $(EI)_{m/z}$ of **2**.

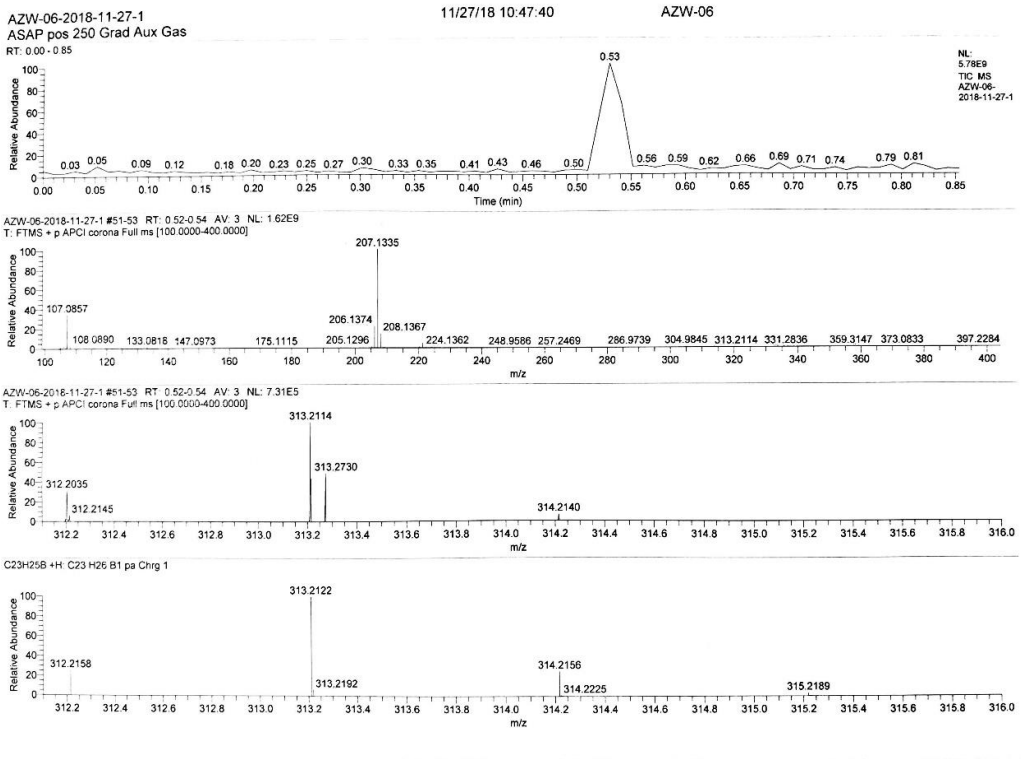

Figure S65. ESI-HRMS of **2**.

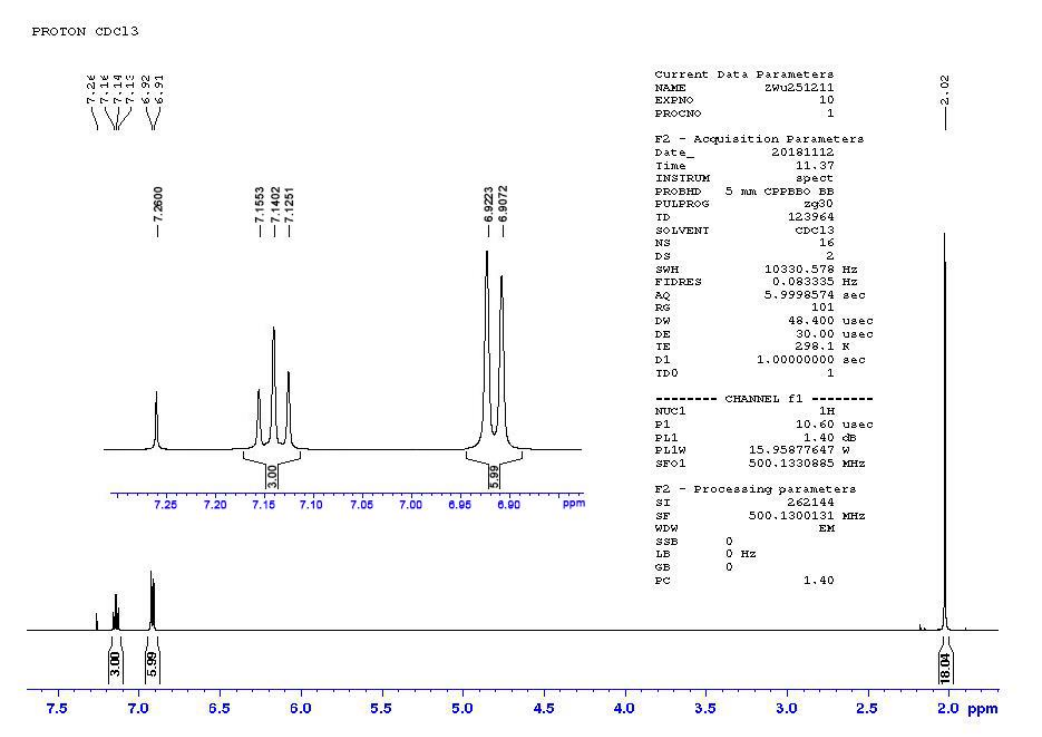

Figure S66. ^{1}H NMR spectrum (500 MHz, $CDCl_3$) of **3**.

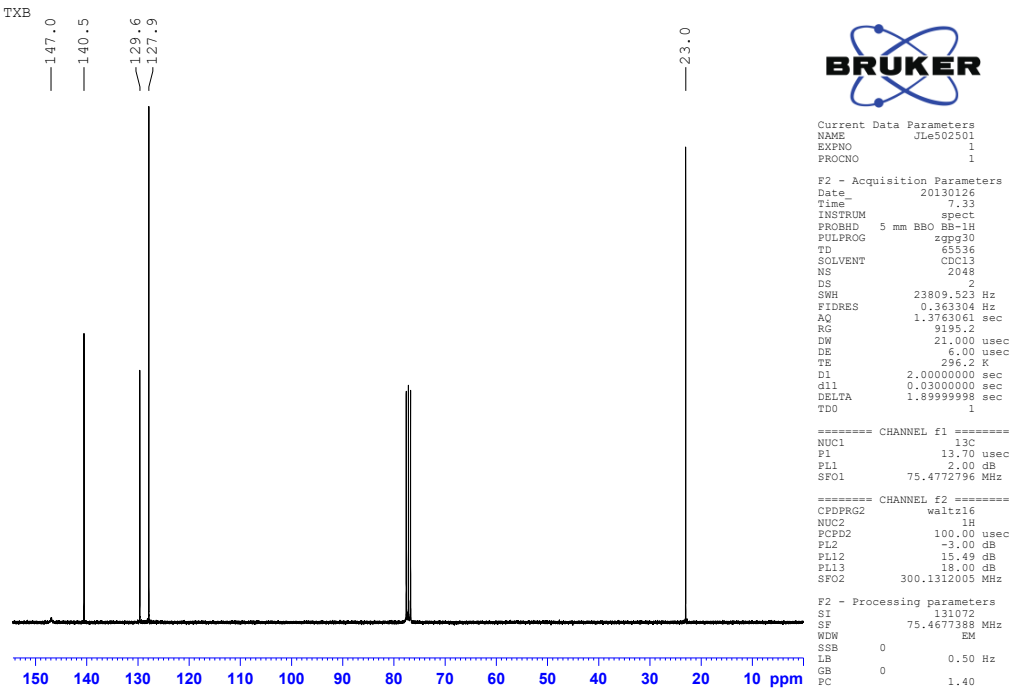

Figure S67. $^{13}C\{^{1}H\}$ NMR spectrum (126 MHz, $CDCl_3$) of **3**.

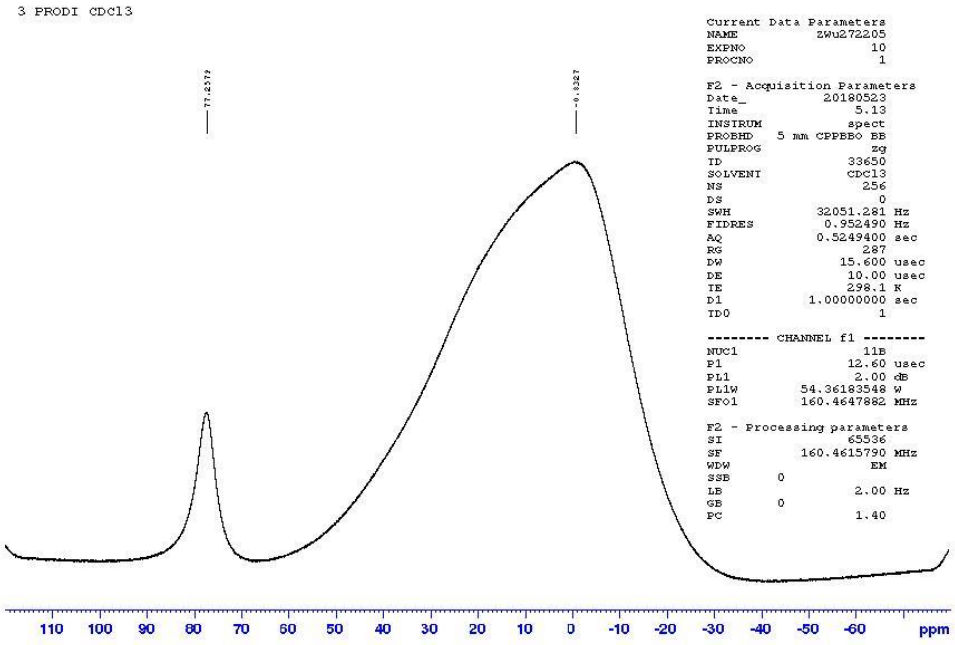

Figure S68. ^{11}B NMR spectrum (160 MHz, $CDCl_3$) of **3**.

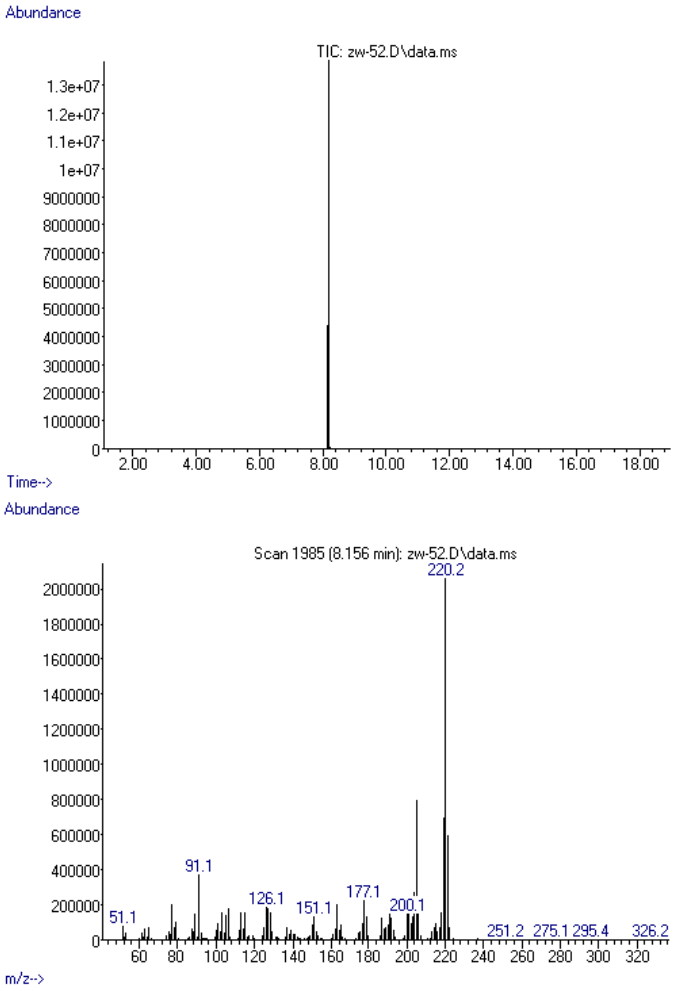

Figure S69. GC-MS total ion chromatogram (TIC) and MS $(EI)_{m/z}$ of **3**.

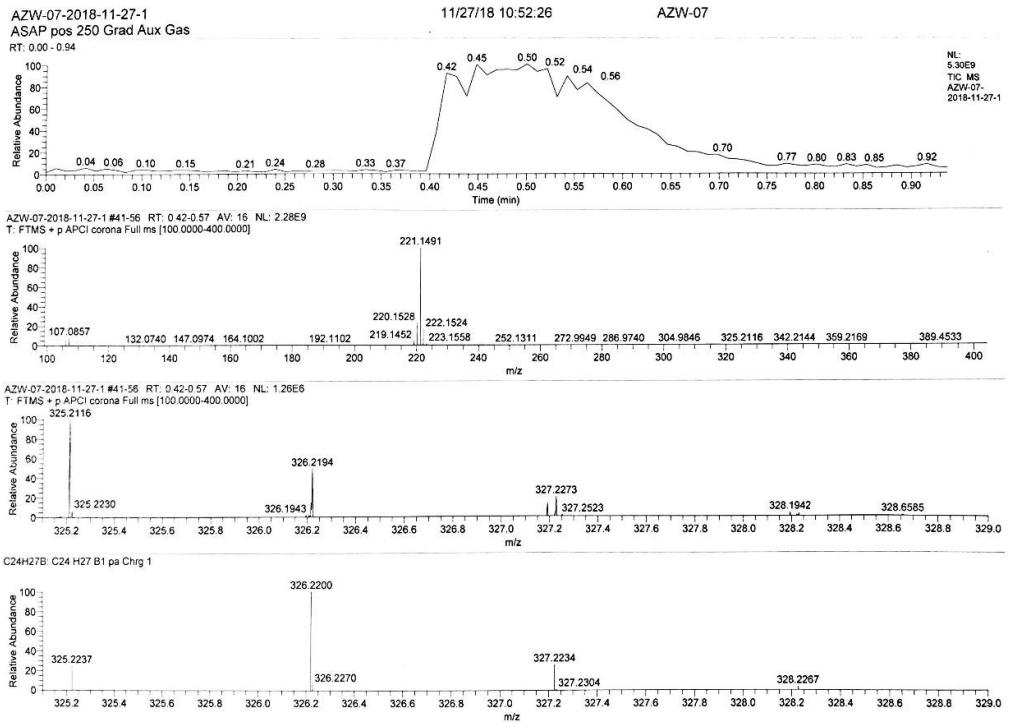

Figure S70. ESI-HRMS of **3**.

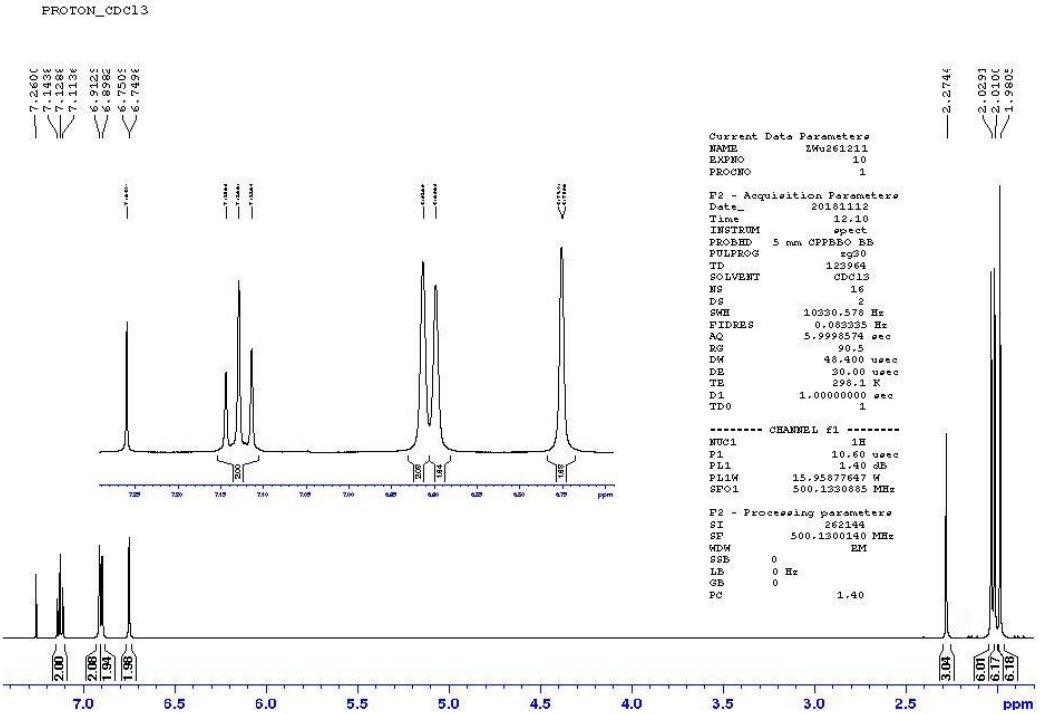

Figure S71. ^{1}H NMR spectrum (500 MHz, $CDCl_3$) of **4**.

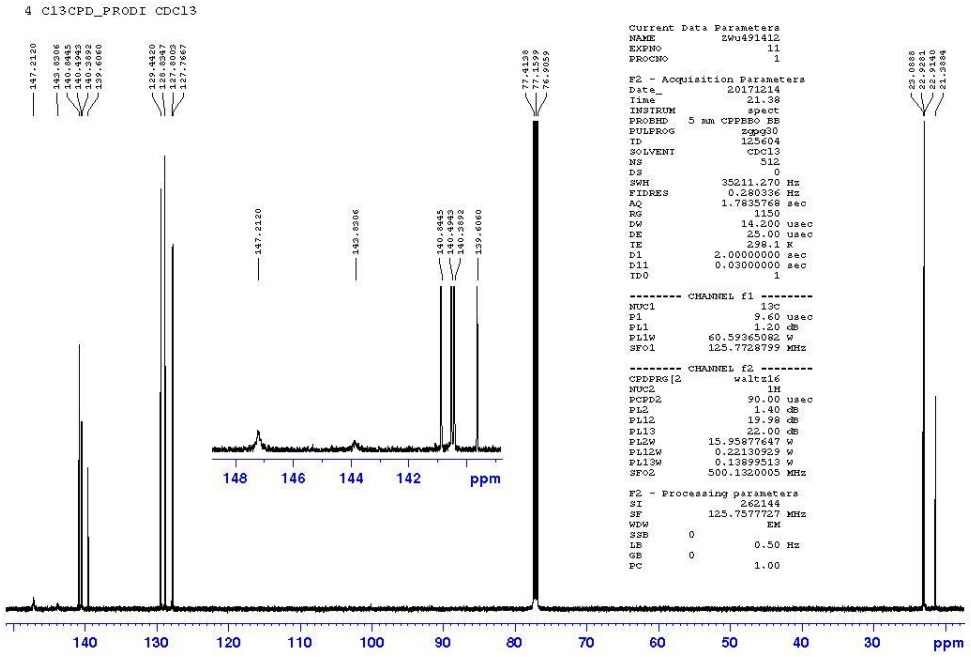

Figure S72. $^{13}C\{^{1}H\}$ NMR spectrum (126 MHz, $CDCl_3$) of **4**.

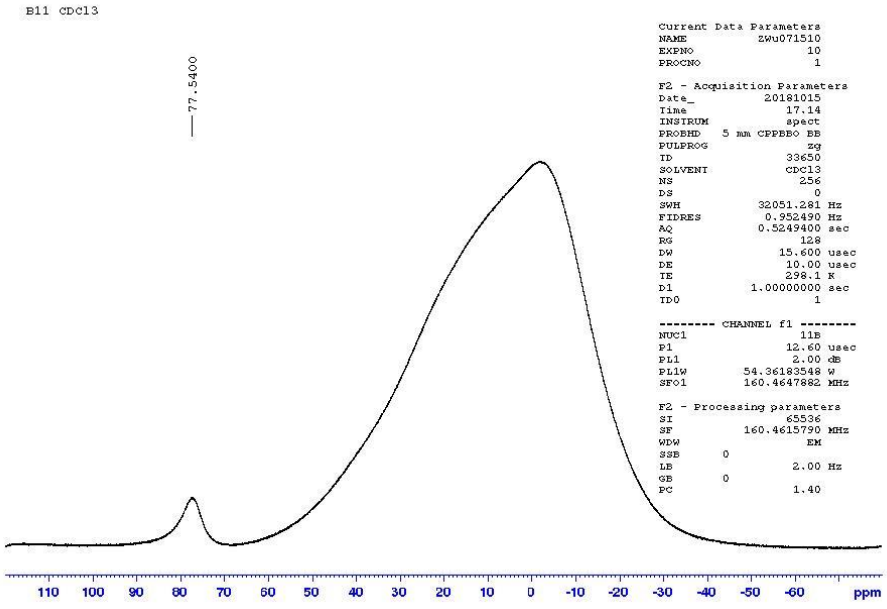

Figure S73. ^{11}B NMR spectrum (160 MHz, $CDCl_3$) of **4**.

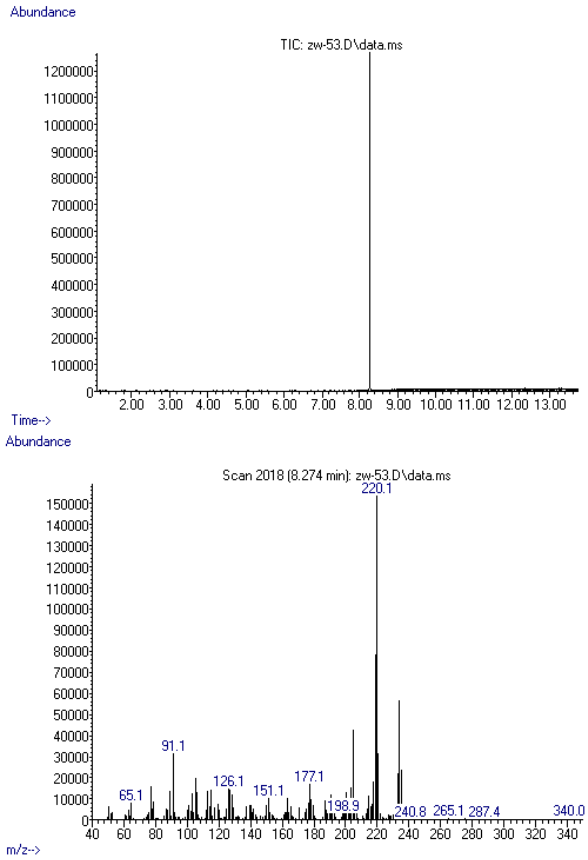

Figure S74. GC-MS total ion chromatogram (TIC) and MS $(EI)_{m/z}$ of **4**.

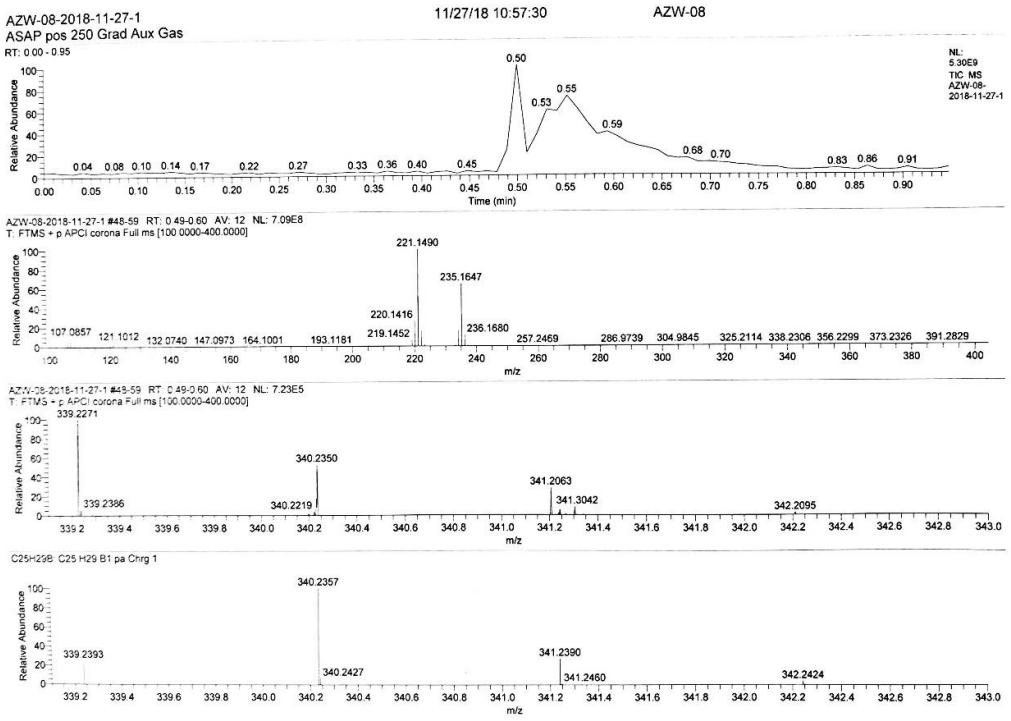

Figure S75. ESI-HRMS of **4**.

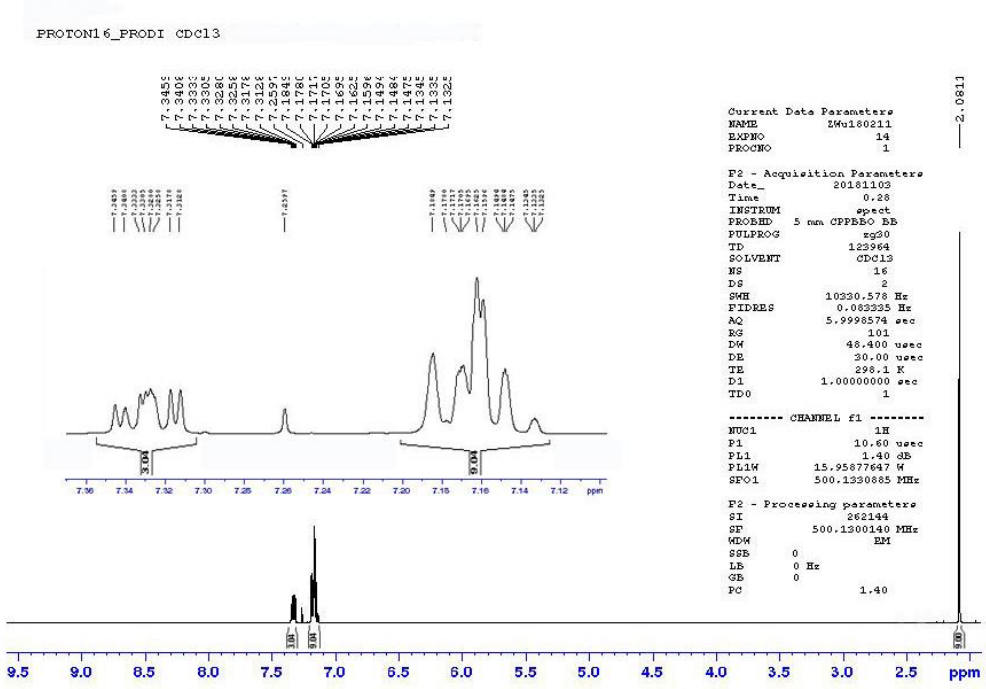

Figure S76. ^{1}H NMR spectrum (500 MHz, $CDCl_3$) of **tris(2-methylphenyl)borane**.

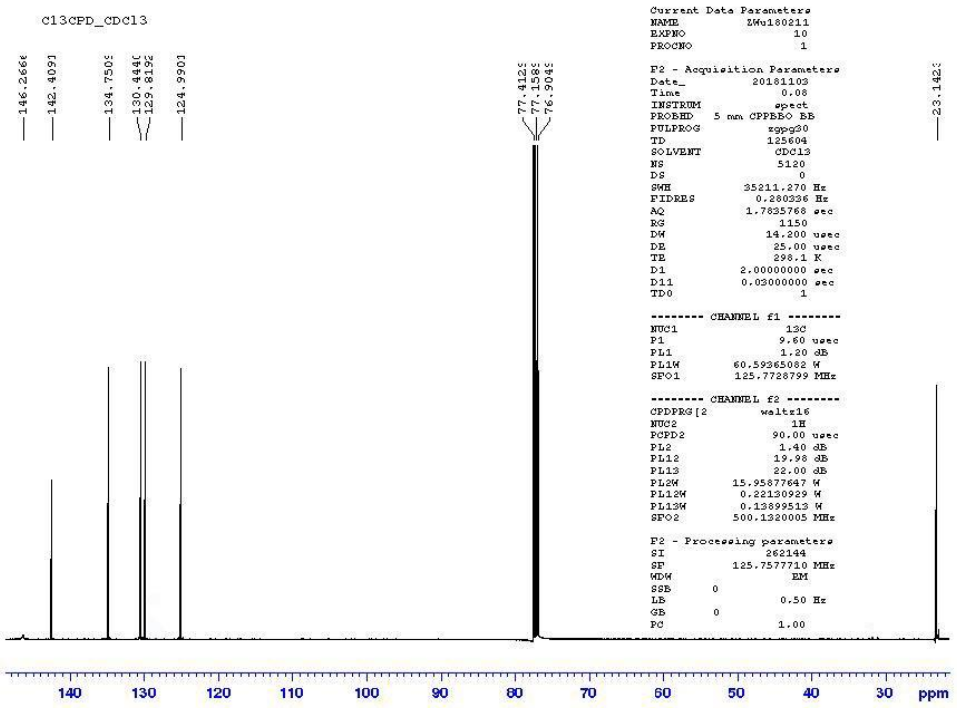

Figure S77. $^{13}C\{^{1}H\}$ NMR spectrum (126 MHz, $CDCl_3$) of **tris(2-methylphenyl)borane**.

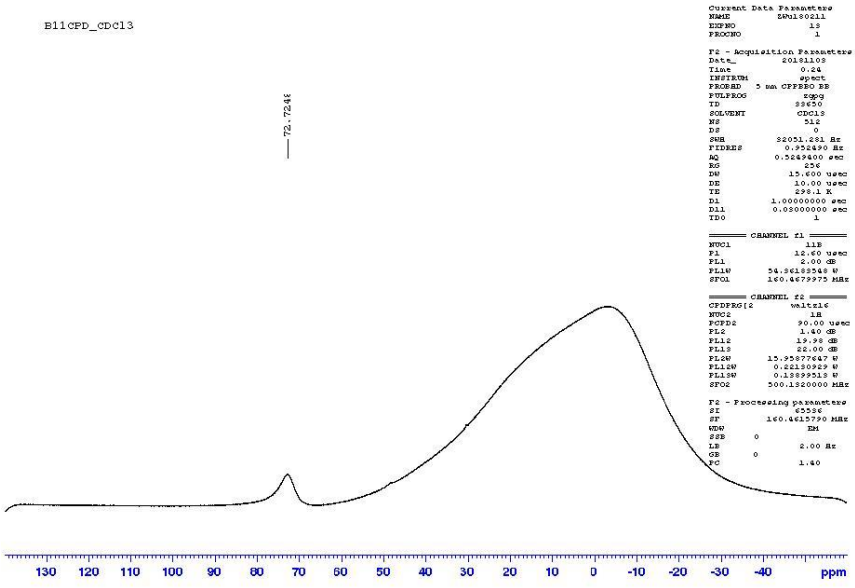

Figure S78. ^{11}B NMR spectrum (160 MHz, $CDCl_3$) of **tris(2-methylphenyl)borane**.

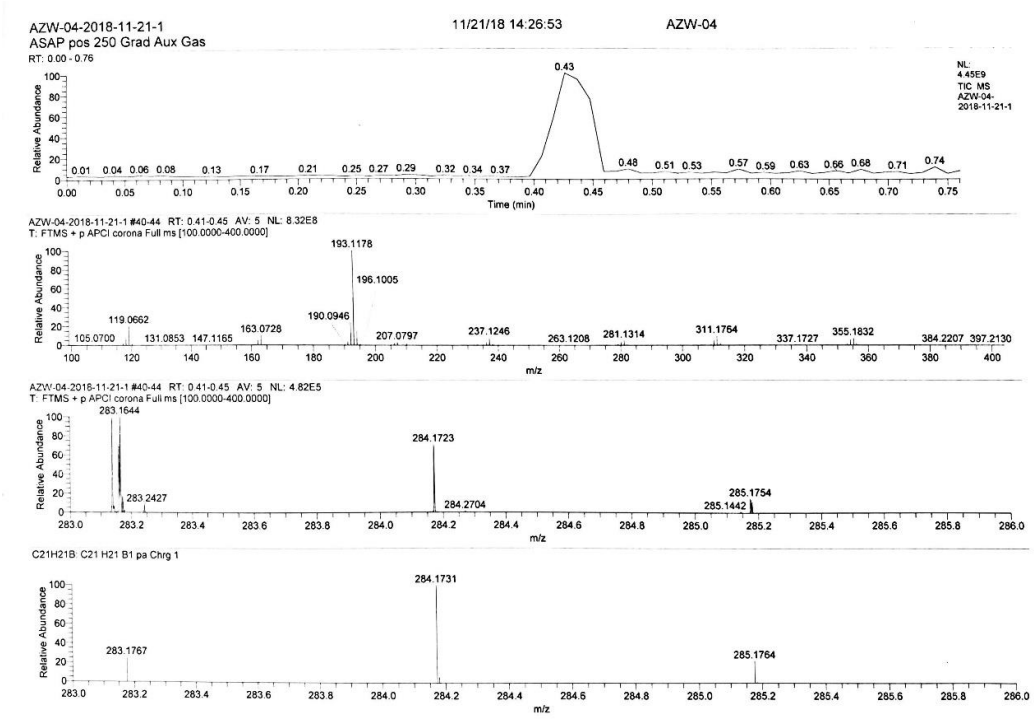

Figure S79. ESI-HRMS of **tris(2-methylphenyl)borane**.

VII. References

[1] H. Pan, G. L. Fu, Y. H. Zhao, C. H. Zhao, *Org. Lett.* **2011**, *13*, 4830-4833.

[2] B. H. Toby, *J. Appl. Crystallogr.* **2005**, *38*, 1040-1041.

[3] A. C. Larson, R. B. Von Dreele, Los Alamos National Laboratory Report LAUR, **2004**, pp. 86-748.

[4] G. M. Sheldrick, *Acta. Crystallogr. A Found. Adv.* **2015**, *71*, 3-8.

[5] G. M. Sheldrick, *Acta. Crystallogr. A Found. Adv.* **2008**, *64*, 112-122.

[6] C. B. Hübschle, G. M. Sheldrick, B. Dittrich, *J. Appl. Crystallogr.* **2011**, *44*, 1281-1284.

[7] K. D. Brandenburg, Crystal and Molecular Structure Visualization, Crystal Impact H. Putz & K. Brandenburg GbR, Bonn (Germany), **2017**.

[8] C. F. Macrae, I. J. Bruno, J. A. Chisholm, P. R. Edgington, P. McCabe, E. Pidcock, L. R. Monge, R. Taylor, J. van de Streek, P. A. Wood, *J. Appl. Crystallogr.* **2008**, *41*, 466-470.

[9] O. V. Dolomanov, L. J. Bourhis, R. J. Gildea, J. A. K. Howard, H. Puschmann, *J. Appl. Crystallogr.* **2009**, *42*, 339-341.

[10] M. J. Turner, J. J. McKinnon, S. K. Wolff, D. J. Grimwood, P. R. Spackman, D. Jayatilaka, M. A. Spackman, CrystalExplorer17 (2017), University of Western Australia, http://hirshfeldsurface.net.

[11] I. R. Morgan, A. E. J. Broomsgrove, P. Fitzpatrick, D. Vidovic, A. L. Thompson, I. A. Fallis, S. Aldridge, *Organometallics* **2010**, *29*, 4762-4765.

[12] TURBOMOLE V7.0, a development of University of Karlsruhe and Forschungszentrum Karlsruhe GmbH, 1989-2007; TURBOMOLE GmbH, since 2007; available from **http://www.turbomole.com.**

[13] M. von Arnim, R. Ahlrichs, *J. Comput. Chem.* **1998**, *19*, 1746-1757.

[14] a) A. D. Becke, *J. Chem. Phys.* **1993**, *98*, 5648-5652; b) C. Lee, W. Yang, R. G. Parr, *Phys. Rev. B: Condens. Matter Mater. Phys.* **1988**, *37*, 785-789; c) P. J. Stephens, F. J. Devlin, C. F. Chabalowski, M. J. Frisch, *J. Phys. Chem. A* **1994**, *98*, 11623-11627.

[15] G. Scalmani, M. J. Frisch, B. Mennucci, J. Tomasi, R. Cammi, V. Barone, *J. Chem. Phys.* **2006**, *124*, 94107.

[16] A. Schäfer, H. Horn, R. J. Ahlrichs, *J. Chem. Phys.* **1992**, *97*, 2571-2577.

[17] a) I. Lyskov, M. Kleinschmidt, C. M. Marian, *J. Chem. Phys.* **2016**, *144*, 034104; b) C. M. Marian, A. Heil, M. Kleinschmidt, *WIREs Comput. Mol. Sci.* **2019**, *9*, e1394.
[18] A. D. Becke, *J. Chem. Phys.* **2014**, *140*, 1372.
[19] a) M. Kleinschmidt, C. M. Marian, *Chem. Phys.* **2005**, *311*, 71-79; b) M. Kleinschmidt, J. Tatchen, C. M. Marian, *J. Comput. Chem.* **2002**, *23*, 824-833; c) M. Kleinschmidt, J. Tatchen, C. M. Marian, *J. Chem. Phys.* **2006**, *124*, 124101.
[20] J. Neugebauer, M. Reiher, C. Kind, B. A. Hess, *J. Comput. Chem.* **2002**, *23*, 895-910.
[21] a) M. Etinski, J. Tatchen, C. M. Marian, *J. Chem. Phys.* **2011**, *134*, 154105; b) M. Etinski, J. Tatchen, C. M. Marian, *Phys. Chem. Chem. Phys.* **2014**, *16*, 4740-4751.
[22] T. J. Penfold, E. Gindensperger, C. Daniel, C. M. Marian, *Chem. Rev.* **2018**, *118*, 6975-7025.
[23] a) J. J. McKinnon, A. S. Mitchell, M. A. Spackman, *Chem. Eur. J.* **1998**, *4*, 2136-2141; b) J. J. McKinnon, M. A. Spackman, A. S. Mitchell, *Acta Crystallogr B* **2004**, *60*, 627-668; c) M. A. Spackman, D. Jayatilaka, *CrystEngComm* **2009**, *11*, 19-32; d) M. A. Spackman, P. G. Byrom, *Chem. Phys. Lett.* **1997**, *267*, 215-220.
[24] M. J. Turner, J. J. McKinnon, D. Jayatilaka, M. A. Spackman, *CrystEngComm* **2011**, *13*, 1804-1813.
[25] a) J. J. McKinnon, D. Jayatilaka, M. A. Spackman, *Chem. Commun.* **2007**, *0*, 3814–3816; b) A. Parkin, G. Barr, W. Dong, C. J. Gilmore, D. Jayatilaka, J. J. McKinnon, M. A. Spackman, C. C. Wilson, *CrystEngComm* **2007**, *9*; c) M. A. Spackman, J. J. McKinnon, *CrystEngComm* **2002**, *4*, 378-392.
[26] a) T. Dahl, *Acta Chem. Scand.* **1994**, *48*, 95-106; b) C. A. Hunter, J. K. M. Sanders, *J. Am. Chem. Soc.* **1990**, *112*, 5525-5534; c) M. O. Sinnokrot, C. D. Sherrill, *J. Phys. Chem. A* **2004**, *108*, 10200-10207; d) M. O. Sinnokrot, E. F. Valeev, C. D. Sherrill, *J. Am. Chem. Soc.* **2002**, *124*, 10887-10893; e) L. Loots, L. J. Barbour, *John Wiley & Sons*, Chichester, UK, **2012**, 109-124.

Chemistry–A European Journal
Research Article
doi.org/10.1002/chem.202200525
Chemistry Europe
European Chemical Societies Publishing
www.chemeurj.org

Aggregation-Induced Dual Phosphorescence from (*o*-Bromophenyl)-Bis(2,6-Dimethylphenyl)Borane at Room Temperature

Zhu Wu,[a] Fabian Dinkelbach,[b] Florian Kerner,[a] Alexandra Friedrich,[a] Lei Ji,[a, c] Vladimir Stepanenko,[d] Frank Würthner,[d] Christel M. Marian,*[b] and Todd B. Marder*[a]

Abstract: Designing highly efficient purely organic phosphors at room temperature remains a challenge because of fast non-radiative processes and slow intersystem crossing (ISC) rates. The majority of them emit only single component phosphorescence. Herein, we have prepared 3 isomers (*o*, *m*, *p*-bromophenyl)-bis(2,6-dimethylphenyl)boranes. Among the 3 isomers (***o***-, ***m***- and ***p*-BrTAB**) synthesized, the *ortho*-one is the only one which shows dual phosphorescence, with a short lifetime of 0.8 ms and a long lifetime of 234 ms in the crystalline state at room temperature. Based on theoretical calculations and crystal structure analysis of ***o*-BrTAB**, the short lifetime component is ascribed to the T_1^M state of the monomer which emits the higher energy phosphorescence. The long-lived, lower energy phosphorescence emission is attributed to the T_1^A state of an aggregate, with multiple intermolecular interactions existing in crystalline ***o*-BrTAB** inhibiting nonradiative decay and stabilizing the triplet states efficiently.

Introduction

Purely organic phosphors have received considerable research interest in optoelectronic devices,[1] bioimaging, molecular sensing,[3] and security printing,[4] due to efficient utilization of their triplet states. So far, most luminophores displaying room temperature phosphorescence (RTP) are restricted to inorganics containing noble transition metals such as iridium (Ir) and platinum (Pt), as transition-metal complexes are characterized by strong spin-orbit coupling (SOC) induced by heavy metal ions and an intrinsic conformational rigidity which can theoretically harvest 100% of the electrically generated singlet and triplet excitons.[5] In addition, the phosphorescence emission spectra and quantum efficiencies can be tuned by modification of the ligand system. On the other hand, purely organic phosphors generally show inefficient intersystem crossing (ISC) and slow radiative decay rates from the lowest triplet state (T_1) to the ground singlet state (S_0).[6] In addition, the long-lived triplet excitons in metal-free luminophores can interact with environmental quenchers such as O_2, which quench the phosphorescence to a great extent.[7] In order to achieve RTP, one prerequisite is to enhance SOC to accelerate the ISC process, typically by utilizing heteroatoms, heavy atoms, or particular functional groups containing heteroatoms with lone pairs such as C=O, C=S or NR_2.[8] At the same time, it is also important to suppress nonradiative pathways and to isolate the chromophores from oxygen by host-guest doping,[9] crystallization,[10] or incorporation in a polymer matrix or on carbon dots.[11] Unlike trapped organic phosphors which emit only single component phosphorescence,[12] dual phosphorescence emission results from two different triplet states and was observed previously in a frozen glass matrix at low temperature.[13] More recently, dual room temperature phosphorescence (DRTP) in aggregated states was reported by several groups. For example, Tang's group developed a single-molecule white light phosphor which emits from both T_1 and T_2 states at room temperature.[14] Huang et al. reported a series of indole derivatives which show DRTP via inter-/intramolecular charge transfer.[15] Zhang et al. designed a number of D-sp^3-linker-A-type triphenylamine (TPA) luminophores, which showed a TPA-localized triplet state T_1^L and an acceptor centered triplet state T_1^H simultaneously in a PMMA film.[16] Ma's group observed dual phosphorescence from pyridine-modified

[a] *Z. Wu, Dr. F. Kerner, Dr. A. Friedrich, Prof. Dr. L. Ji, Prof. Dr. T. B. Marder*
Institut für Anorganische Chemie and
Institute for Sustainable Chemistry & Catalysis with Boron
Julius-Maximilians-Universität Würzburg
Am Hubland, 97074 Würzburg (Germany)
E-mail: todd.marder@uni-wuerzburg.de

[b] *F. Dinkelbach, Prof. Dr. C. M. Marian*
Institut für Theoretische Chemie und Computerchemie
Heinrich-Heine-Universität Düsseldorf
Universitätsstr. 1, 40225 Düsseldorf (Germany)
E-mail: Christel.Marian@hhu.de

[c] *Prof. Dr. L. Ji*
Frontiers Science Center for Flexible Electronics (FSCFE) &
Shaanxi Institute of Flexible Electronics (SIFE),
Northwestern Polytechnical University
Xi An Shi, 127 West Youyi Road, 710072 Xi'an (P. R. China)

[d] *Dr. V. Stepanenko, Prof. Dr. F. Würthner*
Institut für Organische Chemie and Center for Nanosystems Chemistry
Julius-Maximilians-Universität Würzburg
Am Hubland, 97074 Würzburg (Germany)

Supporting information for this article is available on the WWW under https://doi.org/10.1002/chem.202200525

carbazole derivatives originating from T_1 and T_1* states.[17] Although several DRTP luminophores have been reported, research on this topic and the types of DRTP systems are still quite limited,[18] and there is no reliable design concept and strategy to achieve DRTP luminophores with high performance.

Based on our long standing interest in 3-coordinate organoboron materials and their optical and electronic properties,[19,20] we successfully designed persistent triarylboron phosphors with efficient ISC via (σ, B p)→(π, B p) transitions.[21] However, it seemed likely that the SOC and, thus, the ISC rate constant could be improved. It is proposed that introducing heavy atoms (Br or I) into existing persistent RTP luminophores to enhance the SOC may greatly improve the performance of RTP phosphors. Br or I atoms can also provide multiple efficient intermolecular interactions to restrict nonradiative pathways, which is crucial to stabilize triplet states.[22] More importantly, the dense crystalline matrix provides a favorable environment for delocalization of the excitation and the formation of energy dispersed band structures.[23] Herein, we introduced the heavy atom Br into phenyl-bis(2,6-dimethylphenyl)borane at different positions on the phenyl ring to obtain 3 isomers (***o***-, ***m***- and ***p***-**BrTAB**, Figure 1c). Interestingly, (2-bromophenyl)bis(2,6-dimethylphenyl)borane (***o***-**BrTAB**) exhibits DRTP in the crystalline state under ambient conditions (Figure 1b). The faster, higher energy phosphorescence ranging from 430 to 490 nm with a short lifetime of 0.8 ms is ascribed to the T_1^M state of the monomer while the long-lived, lower energy phosphorescence emission in the range of 490–700 nm with a lifetime of up to 234 ms is attributed to the T_1^A state of an aggregate in the crystalline material.

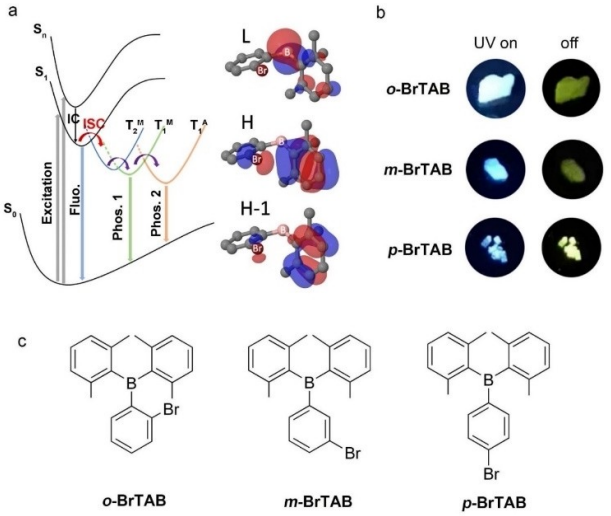

Figure 1. (a) Proposed mechanism of the dual phosphorescent emission in ***o***-**BrTAB** and essential parts of the molecular orbitals involved in the transitions; T_1^M and T_2^M represent monomer states, T_1^A an aggregate state (b) afterglow photographs taken before and after irradiation (λ_{ex} = 365 nm) under ambient conditions; (c) molecular structures of the three isomeric compounds described in the paper.

Results and Discussion

The compound ***o***-**BrTAB** was synthesized[24] by reaction of the Grignard reagent (2,6-Me_2-C_6H_3)MgBr with *o*-Br-$C_6H_4BF_3K$, whereas ***m***- and ***p***-**BrTAB** were prepared by the reaction of bis(2,6-dimethylphenyl)fluoroborane with the respective aryllithium species generated by mono lithium-halogen exchange of *m*- or *p*-dibromobenzene with *n*-BuLi (for synthetic details and characterization data, see the Supporting Information). All three compounds showed absorption bands between 270 and 350 nm in hexane which are attributed to B←π transitions with extinction coefficients of ε = 10000-16000 $M^{-1}cm^{-1}$ (Figure 2a and Table 1). Placement of the Br atoms at the *ortho*, *meta* and *para* positions of the phenyl group had no obvious effect on the molecular energy levels of the three triarylboranes.

The spectra are composed of two absorption bands, where the lower energy band, around 300 nm, is more intense than the one at 260–270 nm. DFT/MRCI (multireference configuration interaction) calculations (Figure S10) show that the band at 300 nm is an overlay of the $S_0 \rightarrow S_1$ and $S_0 \rightarrow S_4$ absorptions, while the band at higher energy arises from the $S_0 \rightarrow S_6$ absorption. They also reveal that irradiation of the compounds with UV light in the 310–320 nm wavelength regime predominantly populates the S_1 state. The experimental fluorescence spectra of the 3 isomers in solution almost overlap, with emission maxima at 358 nm. Our calculations show the onsets of the fluorescence to occur at 348 nm for ***o***-**BrTAB**, 328 nm for ***m***-**BrTAB** and 324 nm for ***p***-**BrTAB**, while experimentally, the onset is located at 328 nm for all three compounds. The computed fluorescence rate constants for ***o***-, ***m***-, and ***p***-**BrTAB** are 1×10^7, 2×10^7 and 2×10^7 s^{-1}, respectively, (Table S3) while their corresponding experimental fluorescence rate constants are 1×10^7, 6×10^6 and 1×10^7 s^{-1}, respectively, showing good agreement between calculated and experimental values (Table 1 and Table S3).

We also measured the PL emission spectra in a frozen methylcyclohexane optical glass at 77 K (Figure 3). Compared to ***m***- and ***p***-**BrTAB**, which still show some residual fluorescence at higher energies (330-400 nm), only phosphorescence with a lifetime of 23 ms (57%) was observed in the spectrum of ***o***-**BrTAB**, which indicates that ISC is very efficient and the phosphoresce quantum yield is much higher than that of fluorescence. Note that, as indicated in the footnote to Table 1, % values in parentheses are the larger of two contributions to a bi-exponential fit of the decays. Comparison of both experimental and computed fluorescence rate constants (ca. 10^7 s^{-1}) with the fastest ISC rate constants for ***o***-, ***m***-, and ***p***-**BrTAB** obtained from our theoretical calculations (see below) of 1×10^{10}, 9×10^8 and 3×10^8 s^{-1} (Table S3), respectively, supports the above observations at 77 K in the frozen matrices. Thus, in the bromo-substituted triarylboranes, most of the excited state population is transferred to the triplet manifold, especially in ***o***-**BrTAB**. The heavy atom effect of Br on the monomer phosphorescence radiative lifetimes is in the order ***o***-**BrTAB** > ***p***-**BrTAB** > ***m***-**BrTAB** (Table S3), in agreement with the experimental trends listed in Table 1. The absence of DRTP in the frozen glass at 77 K suggests that the longer-lived phosphorescence component must originate from an aggregated state.

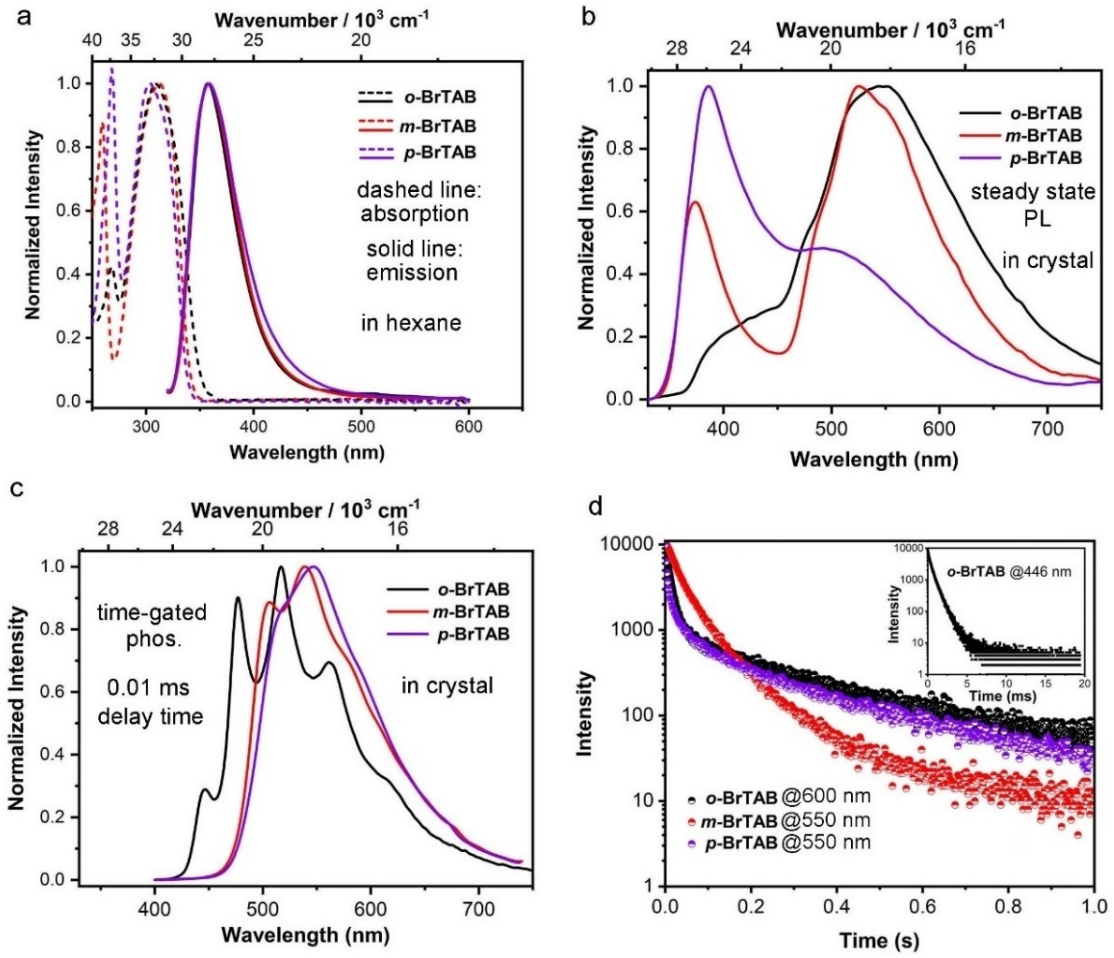

Figure 2. Normalized (a) UV/Vis absorption and fluorescence in hexane, (b) PL and (c) time-gated (0.01 ms delay) phosphorescence spectra of crystalline ***o***-, ***m***- and ***p*-BrTAB** (λ_{ex} = 305 nm). (d) Decays of the phosphorescence (600 nm for ***o*-BrTAB** and 550 nm for ***m***- and ***p*-BrTAB**) in the crystalline state. Insert: decay of the phosphorescence (446 nm) of crystalline ***o*-BrTAB**. All above measurements were conducted at room temperature in air.

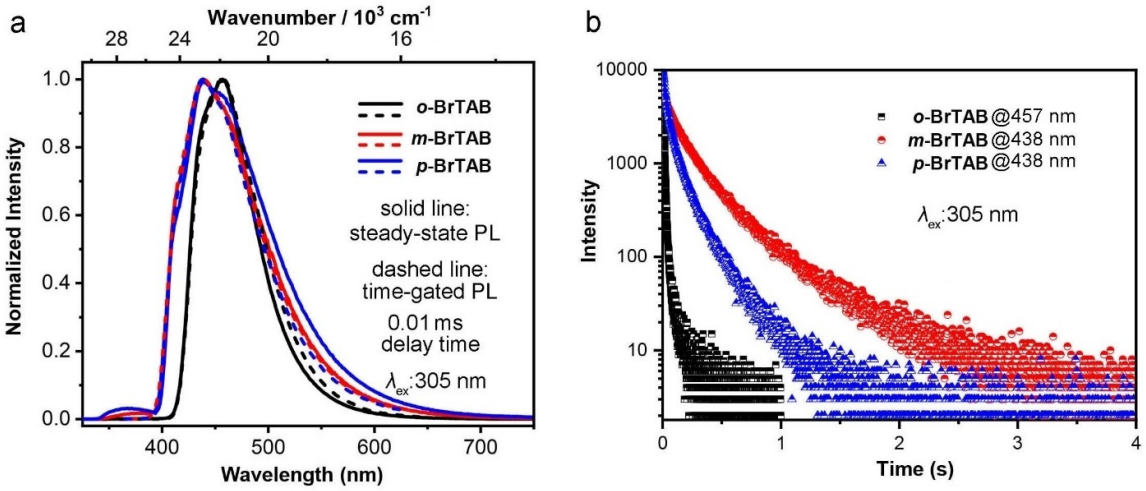

Figure 3. (a) Normalized photoluminescence (solid line) and time-gated phosphorescence (dashed line) spectra and (b) decays of the phosphorescence of ***o***-, ***m***- and ***p*-BrTAB** at their maximum emission wavelength in a frozen methylcyclohexane glass at 77 K (λ_{ex} = 305 nm).

Table 1. Photophysical properties of ***o***-, ***m***- and ***p*-BrTAB** in hexane and the crystalline state at RT, and in frozen methylcyclohexane and in the crystalline state at 77 K.

Compound	State [T]	λ_{abs} [nm]	E [$_M^{-1}$cm^{-1}]	Φ_{PL} [%]	λ_f [nm]	Φ_f [%]	τ_f ns	τ_0^f [ns]	k_r^f [s^{-1}]	λ_p [nm]	Φ_p [%]	τ_p (T_1^M) [ms]	τ_p (T_1^A) [ms]
o-BrTAB	Solution (RT)[a]	312	10900	3.5	358	3.5	2.8	80	1*10^7	nd[b]		nd	nd
	Crystalline (RT)[c]			1.5	-[d]	0.2	3.2	8*10^3	1*10^5	446, 477, 517, 562[e]	1.3	0.3 (34%), 0.8 (66%)	13 (22%), 234 (78%)
	Crystalline (77 K)	–		–	–		–	–		431, 455		0.3 (28%), 2.1 (72%)	161 (42%), 453 (58%)
	Frozen glass (77 K)[f]	–		–	–					457		23 (57%), 92 (43%)	–
m-BrTAB	Solution (RT)[a]	310	11300	1.4	358	1.4	2.3	164	6*10^6	nd		-	nd
	Crystalline (RT)[c]	–		3.8	374	0.7	6.0	3*10^3	3*10^5	506, 539	3.1	-	64 (67%), 215 (33%)
	Crystalline (77 K)			–	374		–	–		430, 458, 483, 510		51 (54%), 153 (45%)	45 (28%), 512 (72%)
	Frozen glass (77 K)[f]	–		–	–		–	–		438		154 (55%), 486 (45%)	–
p-BrTAB	Solution (RT)[a]	304	15200	1.2	358	1.2	1.7	77	1*10^7	nd		–	nd
	Crystalline (RT)[c]	–		4.4	386	2.4	2.9	121	8*10^6	547	2.0	–	90 (30%), 378 (70%)
	Crystalline (77 K)	–		–	386			–		427, 458, 510		18 (69%), 59 (31%)	166 (19%), 581 (81%)
	Frozen glass (77 K)[f]	–		–	367		–	–		438		53 (48%), 201 (52%)	–

[a] Measured in hexane at room temperature (RT); [b] not detected (nd); [c] measured in the crystalline state at RT; [d] The maximum fluorescence emission wavelength of ***o*-BrTAB** is estimated to occur at ca. 400–405 nm, but cannot be more accurately determined due to the overlap of fluorescence and phosphorescence; [e] 446 and 477 nm are ascribed to T_1^M and 517 and 562 nm are ascribed to T_1^A; [f] measured in frozen methylcyclohexane at 77 K. For the phosphorescence lifetimes, the value given in % in parentheses is the larger of two contributions to a bi-exponential fit of the decay.

Recently, Sarkar, Hendrickson et al. reported on the three isomeric *o*-, *m*-, and *p*-bromobenzaldehydes.[25] When Br is *ortho* to the aldehyde, SOC is greatly enhanced, consistent with our observations. Looking at Table S3, the heavy Br atom effect leads to efficient ISC for all three compounds. However, while the fluorescence rate constant has the same order of magnitude (10^7 s^{-1}) for all three isomers, the ISC rate constants decrease in the order ***o***-$>$***m***-$>$***p*-BrTAB**. For ***p*-BrTAB** and ***m*-BrTAB**, ISC is 15 and 45 times faster, respectively, than fluorescence, so that residual fluorescence might be expected from those 2 isomers. For ***o*-BrTAB**, however, ISC is 1000 times faster than fluorescence, so nearly all excited molecules rapidly form triplet states. As can be seen in the difference densities in Figures S13-15, bromine is involved the stronger in the excitation the closer it is located to the boron center. Following El-Sayed's rule,[27] a change in orbital character is required for a fast ISC process. This orbital change is visible in all three isomers, but most dominant in the ***o*-BrTAB** compound, where the Br p-orbital changes its orientation moving from the S_1 to the T_2 state (Figure 4) causing the squared SOCME to increase markedly to 18640 cm^{-2}. Despite the similarity of the electron distributions in both states (Figure 4), even the S_1^M and T_1^M states experience

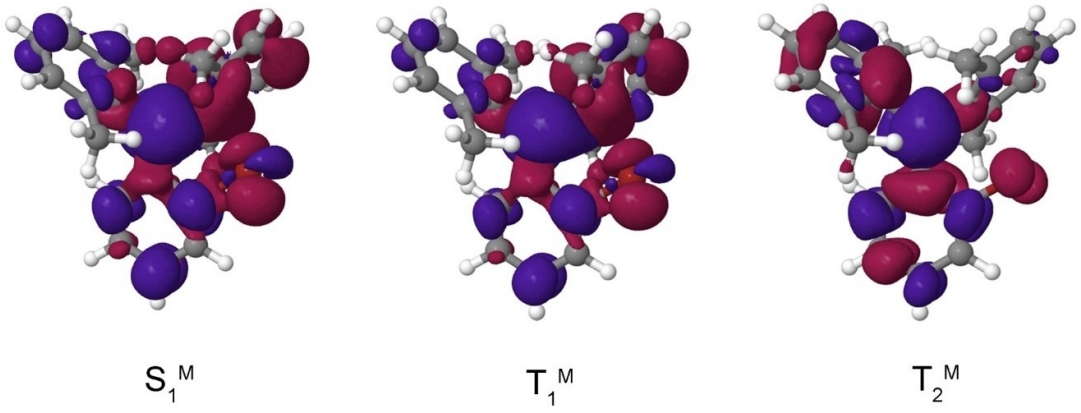

Figure 4. Difference of electron density distributions in the S_1^M, T_1^M and T_2^M states of the ***o*-BrTAB** monomer with regard to the electronic ground state, S_0^M, at the S_1^M geometry. Red areas indicate a loss of electron density upon excitation, blue areas a gain. Note the reorientation of the p orbital hole on the bromine atom when proceeding from S_1^M to T_2^M.

substantial mutual SOC in ***o*-BrTAB**. With a squared sum of SOCMEs of 25 cm^{-2}, the $S_1^M \rightarrow T_1^M$ transition is significantly faster ($k_{ISC} = 2 \times 10^9\ s^{-1}$) than in the unsubstituted compound. Nevertheless, with a rate constant of ca. $1 \times 10^{10}\ s^{-1}$, the $S_1^M \rightarrow T_2^M$ ISC is five times faster than the direct $S_1^M \rightarrow T_1^M$ ISC. Besides ISC, internal conversion (IC) plays an important role for the population of the emissive T_1 state from higher triplet states. In ***o*-BrTAB** we found a conical intersection allowing a very efficient population transfer from T_2 to T_1 without the necessity to surmount a large energy barrier in the process.

In ***m*-BrTAB**, the largest SOCMEs arise between the $S_1^M \rightarrow T_2^M$ and $S_1^M \rightarrow T_3^M$ pair of states. Both target states are similar in character except that the bromine involvement is more pronounced in the T_3^M state, yielding a rate constant of $9 \times 10^8\ s^{-1}$ for the $S_1^M \rightarrow T_3^M$ ISC in this isomer. In ***p*-BrTAB**, the bromine substitution primarily enhances the probabilities of the $S_1^M \rightarrow T_1^M$ and $S_1^M \rightarrow T_3^M$ ISCs. Here we find the T_2^M state to be more similar in character to the S_1^M state than the T_1^M state. The fastest ISC is found for the $S_1^M \rightarrow T_3^M$ channel with $k_{ISC} = 3 \times 10^8\ s^{-1}$. A comparison of the ISC rate constants with the fluorescence rate constants of ca. $10^7\ s^{-1}$ (Table S3) suggests that the fluorescence quantum yield is low and that most of the excited state population is transferred to the triplet manifold in the bromo-substituted triarylboranes, in particular in the ***o*-BrTAB** isomer, which is consistent with the low fluorescence intensities observed in a frozen glass at 77 K.

The phosphorescence rate constant of T_1 depends essentially on three factors: the magnitude of the SOC matrix element (SOCME) between T_1 and singlet states S_n, the energy difference between T_1 and S_n, and the brightness of the S_n-S_0 transition. Interference effects aside, the larger the T_1-S_n SOC, the smaller the T_1-S_n energy difference, and the larger the S_n-S_0 transition dipole, the larger the phosphorescence probability.[26] Because of the large T_1-S_2 SOC and T_1-S_4 SOC, ***o*-BrTAB** can borrow substantial intensity from the spin-allowed bright transitions (S_2-S_0 and S_4-S_0, respectively). In ***m*-BrTAB** and ***p*-BrTAB**, SOC between T_1 and the low-lying singlet states is small and, therefore, the intensity borrowing is not very efficient. Hence, ***o*-BrTAB** is the only compound with a phosphorescence rate constant in the millisecond regime; the other two have rate constants of 5 s (***m*-BrTAB**) and 1 s (***p*-BrTAB**) according to the calculations.

However, the photoluminescence spectra at room temperature in the crystalline state are much different from the results in solution (Figure 2b). First, in addition to the fluorescence peaks attributed to the monomer excited state at short wavelength, broad peaks between 450 and 750 nm result from phosphorescence. The longer-lived (phosphorescence) emission lifetimes measured for ***o*-**, ***m*-** and ***p*-BrTAB** at room temperature are 234 (78%), 64 (67%) and 378 (70%) ms, respectively, where the percentages given are those of the larger component of a bi-exponential fit to the decay curves (Figure 2d). Second, the fluorescence emissions from crystalline samples of ***o*-**, ***m*-** and ***p*-BrTAB** are all redshifted compared with those in hexane solution. The bathochromic shift of ***p*-BrTAB** (2026 cm^{-1}) is approximately twice that of ***m*-BrTAB** (1194 cm^{-1}). Third, ***o*-BrTAB** has a larger ratio of phosphorescence to fluorescence intensity, indicating that ISC in ***o*-BrTAB** is the most efficient of the three isomers. The time-gated phosphorescence spectrum of crystalline ***o*-BrTAB** at room temperature shows four fine structured bands at 446, 477, 517 and 562 nm, respectively (Figure 2c). The vibrational fine structure is also present in the computed Franck-Condon (FC) spectrum of the T_1^M emission, though less pronounced. We attribute it to a progression of a vibrational mode with a frequency of 1673 cm^{-1} in the electronic ground state which corresponds to an asymmetric C–C stretching motion of the xylyl ring closest to the Br atom.

The aggregation state of **o-BrTAB** has a large influence on the photoluminescence behavior. A ground solid sample of **o-BrTAB** exhibited multiple small size particles with increased surface area as observed by SEM (Figure S1). The powder X-ray diffraction pattern of the ground **o-BrTAB** sample shows its crystalline nature (Figure S3). In the ground sample, the exposed surface area is much larger than in the single crystal and, as slower phosphorescence is more sensitive to oxygen quenching, the ratio of phosphorescence to fluorescence dramatically decreased (Figure S2). The longer phosphorescence lifetime decreases significantly from 234 to 191 ms and the quantum yield is too small to be measured. The shorter phosphorescence lifetime also drops slightly to 0.7 ms, further indicating the important role of the aggregation state in the photoluminescence behavior. In addition, **o-BrTAB** was embedded in a poly(methyl methacrylate) (PMMA) matrix at different loading levels. In a highly doped film (40 wt%, Figure S4), the time-gated phosphorescence emission blueshifts (ca. 600 cm^{-1}) compared to that in the crystalline state, and only the short lifetime (0.8 ms) component was detected, while in an even more concentrated PMMA film (60 wt%, Figure S5), the long lifetime (226 ms) component emerged. The experimental results clearly indicate that longer-lived component of the DRTP is induced by aggregation.

The DRTP was confirmed by time-gated phosphorescence spectroscopy of ***o*-BrTAB** at room temperature (Figure 5a). Upon increasing the delay time, the intensity of peaks of the shorter wavelength emission components at 446 and 477 nm decreased gradually. When the delay time was set at 3 ms, the short-lived monomer T_1^M emission of ***o*-BrTAB** almost disappeared, and the remaining long lifetime component is ascribed to phosphorescence from the T_1^A state of an aggregate. We performed time-gated excitation spectroscopy of crystalline ***o*-BrTAB** at 480 and 560 nm, respectively (Figures 5c and 5d). Upon increasing the delay time from 0.1 to 3 ms, the overall excitation intensity gradually decreases. We stress that the spectra at each delay time are identical in the range of 300 to 450 nm, indicating that one absorption leads to all excited states. We also measured time-gated phosphorescence spectra at different excitation wavelengths (Figure 5b). The two triplet excited states always appear at the same time which further indicates that T_1^M and T_1^A originate from the same absorption ($S_0 \rightarrow S_1$ and $S_0 \rightarrow S_n$). Furthermore, we measured the time-gated phosphorescence spectra of ***o*-BrTAB** in the crystalline state at different excitation wavelengths (300, 370 and 420 nm) and different delay times (0.1, 1.0, and 3.0 ms) (Figure 6). When a delay time of 0.1 ms was used to measure the time-gated

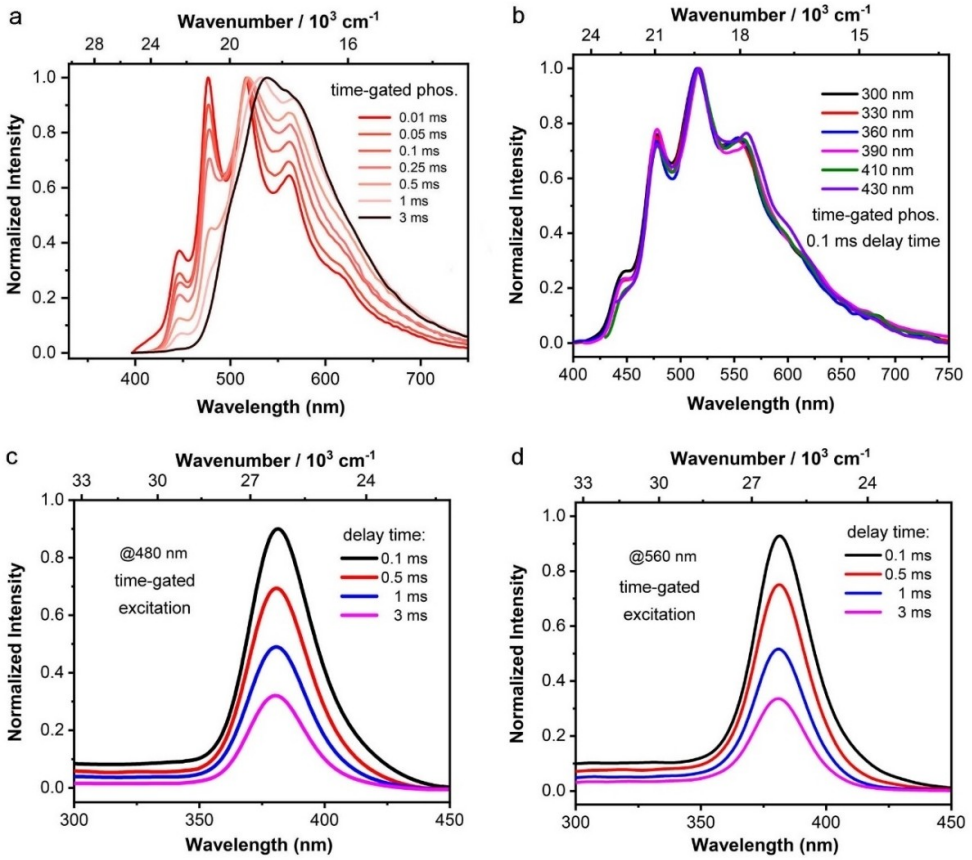

Figure 5. Normalized time-gated phosphorescence spectra of crystalline ***o*-BrTAB** (a) with different delay times and (b) with 0.1 ms delay at different excitation wavelengths. Time-gated excitation spectra (c, λ_{em} = 480 nm) and (d, λ_{em} = 560 nm) of crystalline ***o*-BrTAB** at different delay times at room temperature.

spectra of crystalline ***o*-BrTAB** at different excitation wavelengths (Figure 6a), the short-lived component T_1^M and long-lived component T_1^A are both apparent and the spectra at the three different excitation wavelengths are identical. When a longer delay time of 1.0 ms was used at different excitation wavelength (Figure 6b), T_1^M and T_1^A also appear with a smaller relative intensity of the short-lived T_1^M component due to the time-gating effect. With a 3.0 ms delay time (Figure 6c), the relative intensity of the T_1^M component becomes even smaller, but it is still apparent. These results clearly indicate that the short-lived T_1^M and long-lived T_1^A components originate from the same absorption.

Therefore, we propose that first, the single molecule of ***o*-BrTAB** is excited into its S_1^M or S_n^M state. Then it undergoes ISC to T_2^M which undergoes IC to a short-lived T_1^M state. At the same time, T_1^A evolves into a T_1^M state, emitting more slowly and at lower energy. The process going from T_1^M to T_1^A was confirmed by temperature-dependent, time-gated spectroscopic study of crystalline ***o*-BrTAB** (Figure 7b). Upon decreasing the temperature from 298 to 77 K, the phosphorescence peaks belonging to T_1^M at 446 and 477 nm blueshift to ca. 431 and 455 nm, respectively, which become dominant at 77 K with a lifetime ca. 2.1 ms. At 77 K, the long-lived T_1^A emission at longer wavelength still exists with a lifetime of ca. 453 ms (58%), but in a much lower ratio compared to the short-lived component. Thus, there is a thermal barrier for the conversion of T_1^M to T_1^A, and lowering the temperature makes it harder to cross the barrier.

For crystalline **m**- and **p**-**BrTAB**, we did not observe dual phosphorescence at room temperature, but only at low temperature. At 77 K, new emission peaks at 431 and 455 nm appeared in the time-gated spectra with the phosphorescence lifetimes of crystalline **m**- and **p**-**BrTAB** of 51 (54%) and 18 (69%) ms, respectively, being much shorter than the lifetimes 512 (72%) and 581 (81%) ms of the longer-wavelength emissions (Figures S6–S9). As the strength of intermolecular interactions is especially distinct between the three compounds at room temperature, only ***o*-BrTAB** exhibits strong intermolecular interactions, effectively suppressing the nonradiative decay rate k_{nr}, which plays an important role in stabilizing the triplet states. Hence, a nonradiative decay channel is opened for ***m***- and ***p*-BrTAB** going from 77 K to RT. In ***o*-BrTAB**, the radiative channel can compete with the nonradiative one even at RT. This may be the reason that dual phosphorescence is only observed in ***o*-BrTAB** at room temperature and a detailed discussion of

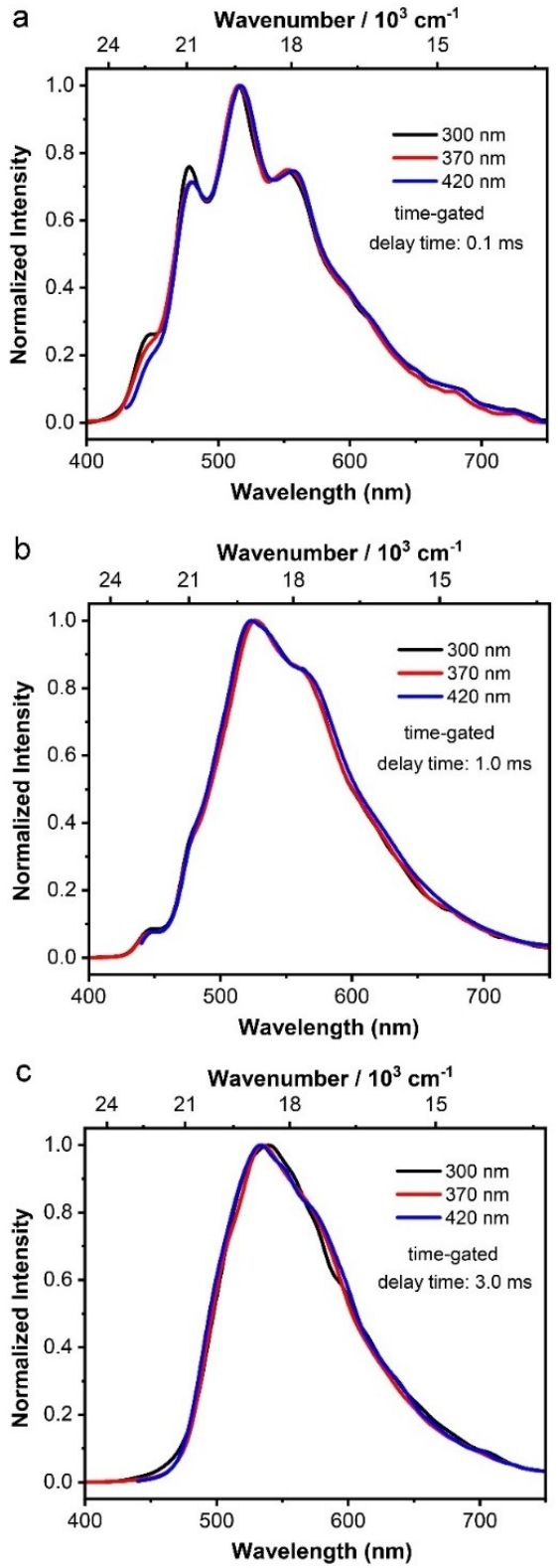

Figure 6. Normalized time-gated phosphorescence spectra of crystalline ***o*-BrTAB** at different excitation wavelengths (λ_{ex} = 300, 370 and 420 nm) and different delay times of (a) 0.1, (b) 1.0, and (c) 3.0 ms.

intermolecular interactions is provided in the crystal structure analysis section (see below).

To explain the experimentally observed dual phosphorescence, we first searched for the most probable pathways from the singlet to the triplet states of the monomer. For the unsubstituted compound phenyl-bis(2,6-dimethylphenyl)borane, we have already shown that the $S_1 \rightarrow T_1$ transition is slower than $S_1 \rightarrow T_2$.[21] This can be rationalized by the stronger change in orbital character when moving from S_1 to T_2 and thus, following El-Sayed's rule,[27] the SOCMEs between S_1 and T_2 are much larger than those for $S_1 \rightarrow T_1$. The bromine substitution increases the SOCMEs in general with respect to those of the unsubstituted compound. As may be expected, the heavy-atom effect is strongest for the *ortho*-substituted compound. Even in this case, the change in excitation character is larger for the $S_1^M \rightarrow T_2^M$ transition. In particular, the p orbital hole at the Br atom changes orientation (see above) as required for an El-Sayed allowed transition.[27] Very close to the T_2^M minimum, however, the T_2^M and T_1^M states of ***o*-BrTAB** undergo a conical intersection without the necessity to surmount a substantial energy barrier. Therefore, the population is not trapped in the T_2^M state but is rapidly transferred to the T_1^M state. The possibility that the dual phosphorescence originates from T_2^M and T_1^M states can be ruled out.

As dual phosphorescence was not observed from isolated molecules in the frozen matrix glass at 77 K but only in the crystalline state and in highly doped PMMA films, we propose that this phenomenon stems from aggregated ***o*-BrTAB** units. To explore this effect, we optimized dimeric systems of the compounds starting from the crystal structures. Spreading the excitation over a dimer is, unfortunately, not sufficient to cause a substantial stabilization of the excitonic state. Their difference densities (Figures S16-S18) reveal that the lowest excited dimer states are composed of excitations similar to those of the monomers. In the ***o*-BrTAB** dimer, the T_1^D state is stabilized by only 0.05 eV with respect to the monomer. Delocalization of the excitation over larger molecular clusters is required to explain the marked redshift of the long lifetime component of the phosphorescence emission in the crystalline state.

To understand the effect of the solid-state structures and the intermolecular packing on the luminescence properties, the structures of ***o*-**, ***m*-** and ***p*-BrTAB** were obtained at low temperature (100 K) and at ambient temperature (290 K for ***o*-BrTAB**, 296 K for ***m*-BrTAB**, and 300 K for ***p*-BrTAB**) using single-crystal X-ray diffraction (Figure 8). Comparison of the molecular geometries of ***o*-**, ***m*-** and ***p*-BrTAB** in their crystal structures shows only a small effect of the Br atom position on the bond lengths and angles. All but one of the B–C bond distances are similar within 3 esd's (1.574(3)–1.585(2) Å at 100 K). Only the B–C bond to the Br-substituted aryl ring in ***p*-BrTAB** is significantly shorter (1.563(2) and 1.561(2) Å for the two non-symmetry equivalent molecules at 100 K, Table S11). The BC_3 moiety is planar in all three compounds with the sum of C–B–C angles being 360° within the standard uncertainties. The individual angles are in the range 118.0(2)–122.9(2)° except for the C1–B–C7 angle in ***o*-BrTAB** which is significantly smaller (116.3(2)° at 100 K, Table S11). This is the angle between the Br-

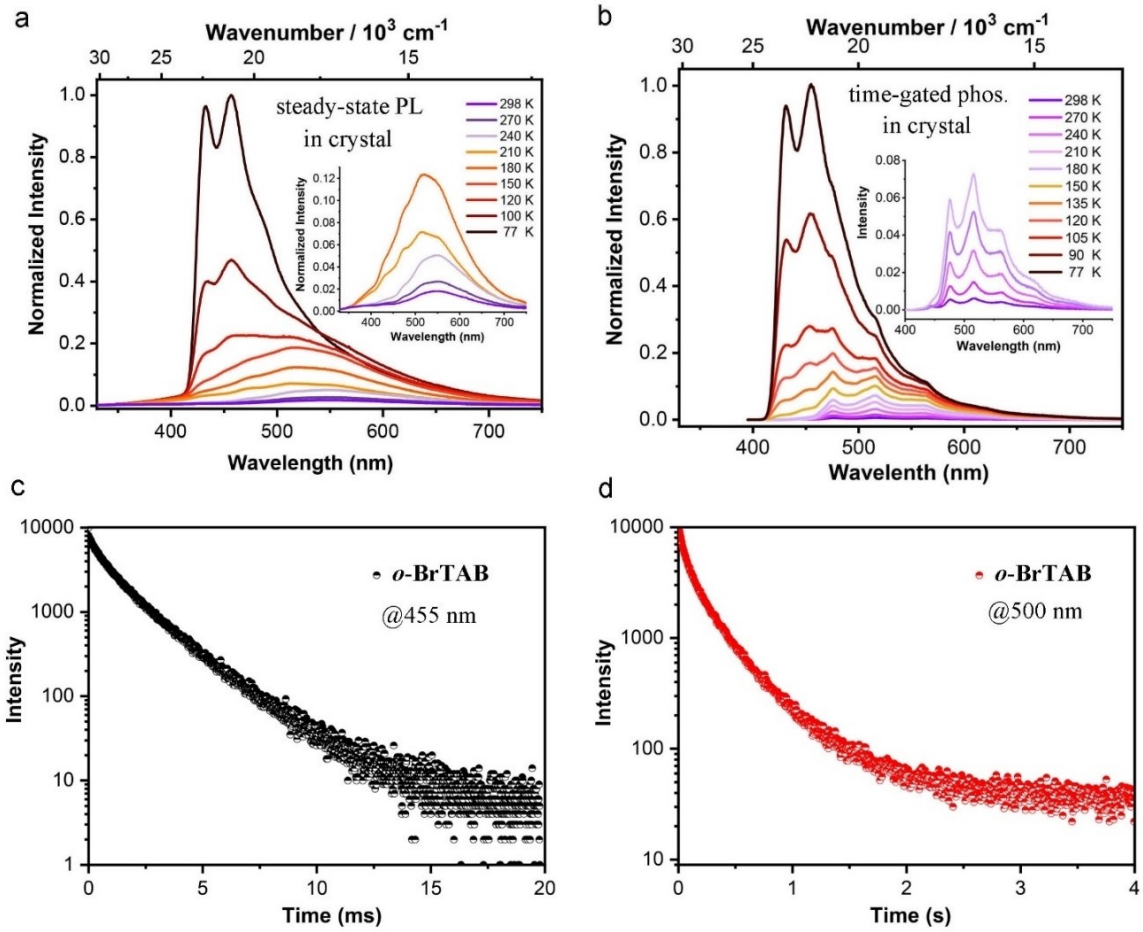

Figure 7. (a) Steady-state photoluminescence and (b) time-gated (delay time 0.01 ms) phosphorescence spectra of crystalline ***o*-BrTAB** at different temperatures (λ_{ex} = 305 nm). Decays of the phosphorescence emission (c) (λ_{em} = 455 nm) and (d) (λ_{em} = 500 nm) of crystalline ***o*-BrTAB** at 77 K.

substituted aryl ring R1 and the m-xylyl group R2 arranged on the opposite side with respect to the Br–C2 bond. Another interesting feature is that the B–C1–C2 angle (127.2(2)°) to the C2 carbon atom to which the Br atom is bonded in ***o*-BrTAB** is significantly larger than all other B–C–C angles in ***o***-, ***m***- and ***p*-BrTAB** which are in the range 117.5(2)–122.9(1)° at 100 K (Table S11), and the B–C1–C6 angle (117.7(2)°) to the other side of the R1 aryl ring is rather small. The larger B–C1–C2 angle in ***o*-BrTAB** is attributed to the bulkiness of the long Br–C bond at the *ortho* position of the R1 ring and the Br atom being close to the central B atom and the C atom of the next-nearest *m*-xylyl group R3 with intramolecular Br···B (3.345(2) Å) and Br···C15 (3.298(2) Å) distances below the sum of van der Waals radii (3.75 Å for Br···B and 3.53 Å for Br···C).[28] The effect of the bulkiness of the substituents and, hence, repulsion between methyl groups and also the Br atom, is further observed in the torsion angles between the aryl groups and the BC_3 planes. While the torsion angles are in a similar range (50.1–68.6°) for the *m*-xylyl groups, a significantly smaller torsion angle (41.9°) is observed for the Br-substituted phenyl rings. Here, the Br *ortho*-substituted phenyl ring shows a larger torsion angle (38.6(1)°) in ***o*-BrTAB** than the Br *meta*- and *para*-substituted phenyl rings (20.1-24.8°) in ***m***- and ***p*-BrTAB** due to repulsion effects (Table S11). The molecular geometries in the solid state of ***o***-, ***m***- and ***p*-BrTAB** at 290 K, 296 K and 300 K, respectively, are very similar to those at 100 K (Table S12).

The molecules are similarly densely packed in the three compounds as is obvious from the crystal packing coefficients (Table S16). The molecular volumes and molecular surface areas are also very similar. However, the volume of the solvent accessible voids in the unit cells, as calculated with the OLEX2 program,[29] is increased in ***p*-BrTAB** (2.7% at 300 K) and in ***m*-BrTAB** (4.4% at 296 K) at ambient temperature, compared to ***o*-BrTAB** (1.7% at 290 K) and to the low-temperature crystal structures at 100 K (0-1.8% in the three compounds). This indicates a looser packing mode in ***p*-BrTAB** and ***m*-BrTAB** than in ***o*-BrTAB** at room temperature.

A Hirshfeld surface analysis based on the crystal structures was performed in order to quantify the nature and type of intermolecular interactions.[30] The Hirshfeld surface is a special

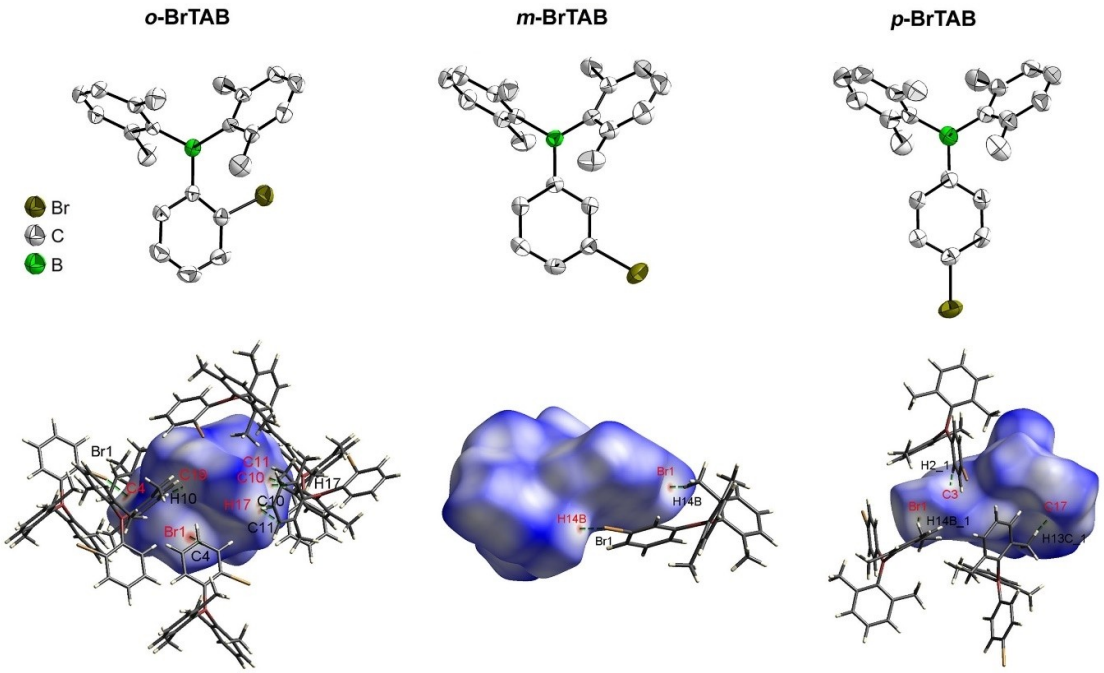

Figure 8. The solid-state molecular structure of ***o*-BrTAB**, ***m*-BrTAB** and ***p*-BrTAB** (top left to right) determined by single-crystal X-ray diffraction at room temperature. Ellipsoids are drawn at the 50% probability level, and H atoms are omitted for clarity. Hirshfeld surfaces of ***o*-BrTAB**, ***m*-BrTAB** and ***p*-BrTAB** (bottom left to right) mapped with d_{norm} over the range −0.12 to 1.50 at room temperature. Neighboring molecules associated with close contacts are shown.

isosurface defined by the weighting function w(**r**) = 0.5 for a particular molecule. This means that the Hirshfeld surface envelops the volume within which the particular molecule contributes more than half of the electron density. Hence, it also includes information on the nearest neighbors and closest contacts to the molecule (Figure 7). The similarity of the amounts and types of interactions in the three compounds is demonstrated in the two-dimensional fingerprint plots and their breakdown to the individual relative contributions (Figures S25 and S26, 100 K).[31] At 100 K, major contributions are from H···H interactions (61–67%), followed by a significant amount from C···H (19–25%) and Br···H (10–15%) interactions. Minor contributions (0.2–1.8%) are Br···C, C···C, and Br···Br interactions with C···C interactions being dominant in ***m*-BrTAB**, Br···Br interactions in one of the symmetry-independent molecules (no. 2) of ***p*-BrTAB**, and Br···C interactions in both ***o*-BrTAB** and ***p*-BrTAB** (Figure S25, Table S16). Relative contributions to intermolecular interactions are very similar for the room temperature structures (Table S16).

At 100 K, the C–H···C interactions are strongest in ***o*-BrTAB**, with C···H distances in the range 2.735(2)-2.812(2) Å, and two nearly linear interactions with C–H···C = 165.82(15)° and 175.45(15)° (Table S13). C–H···C interactions are weaker in ***p*-BrTAB** (C···H = 2.810(2)–2.865(2) Å, C–H···C = 131.16(11)-162.62(11)°) although of similar number as in ***o*-BrTAB** and, significantly, weakest in ***m*-BrTAB** (C···H = 2.836(2)–2.888(3) Å, C–H···C = 143.96(15)–166.26(15)°) as well as being fewer in number. While there are close Br···H contacts (2.9425(12)–3.1001(3) Å) in all three compounds, ***o*-BrTAB** exhibits the closest Br···C contact of 3.354(2) Å. Another close Br···C contact (3.480(2) Å) is found in ***p*-BrTAB**. In addition, ***o*-BrTAB** has a short C···C contact (3.361(3) Å) between an aryl ring and a methyl group, and ***p*-BrTAB** shows two close H···H contacts (2.266 and 2.363 Å) between two aryl rings (Table S16). Interestingly, ***m*-BrTAB** is the only compound in which two weak intermolecular π···π interactions between aryl rings can be found (Table S15). One involves the Br-substituted phenyl rings with an interplanar separation of 3.640(3) Å and an offset shift of 2.261(4) Å. The nearest-neighbor C···C distance is 3.698(5) Å. The other one involves the R3 xylyl rings with a slightly smaller interplanar separation of 3.544(4) Å, but a larger offset shift of 3.457(4) Å, and a nearest-neighbor C···C distance of 3.637(5) Å.

At room temperature (290 K), there are still a significant number of intermolecular C–H···C interactions (C···H = 2.846(4)–2.873(4) Å, C–H···C = 136.4(2)–177.2(3)°) and a close Br···C contact of 3.432(5) Å present in ***o*-BrTAB** (Table S13). However, in ***m*-BrTAB** C···H contacts are long and weak, and the π···π interactions are also insignificant due to large interplanar separations of 3.812(4) Å and 3.645(6) Å with shifts of 2.305(6) Å and 3.437(6) Å, respectively, at 296 K (Table S15). Only a close Br···H interaction (2.9857(8) Å) with a methyl group is still significant. In ***p*-BrTAB**, two intermolecular C–H···C interactions remain (C···H = 2.870(2) Å and 2.887(2) Å, C–H···C = 145.18(15)° and 132.78(13)°) at 300 K, a close H···H interaction with 2.393(1) Å, and close Br···H interaction (2.9648(4) Å) with a methyl group only (Table S15). Thus, only ***o***-

BrTAB exhibits strong intermolecular interactions and, especially, a close Br···C contact at room temperature, which may be the reason that dual phosphorescence is only observed in ***o*-BrTAB** at room temperature.

In summary, the presence of multiple C–H···C and C–H···Br interactions between molecules in the crystals effectively suppresses the nonradiative decay rate k_{nr}, which plays an important role in stabilizing the triplet states and achieving RTP. As the strength of intermolecular interactions is especially distinct between the three compounds at room temperature, and is strongest for ***o*-BrTAB**, this effect may be the reason that we observe DRTP in crystalline ***o*-BrTAB** at room temperature, but only at low temperature for ***m*-BrTAB** and ***p*-BrTAB**.

Conclusions

We reported three bromo-substituted triarylboron isomers which show persistent room temperature phosphorescence (RTP). Among them, (2-bromophenyl)bis(2,6-dimethylphenyl)borane (***o*-BrTAB**) exhibits rare dual room temperature phosphorescence (DRTP) with lifetimes of 0.8 ms (short wavelength component) and 234 ms (long wavelength component), respectively, in the crystalline state. Single-crystal structure analysis shows that multiple molecular C–H···C and C–H···Br contacts in the crystals suppress the nonradiative decay rate k_{nr} and stabilize the triplet states. In addition, the rigid crystalline matrix provides a favorable environment for realizing dual phosphorescence at room temperature.

Crystal structures

Deposition Number(s) 2085814 (for ***o*-BrTAB** at 100 K), 2085815 (for ***m*-BrTAB** at 100 K), 2085816 (for ***p*-BrTAB** at 100 K), 2089473 (for ***o*-BrTAB** at 290 K), 2118234 (for ***m*-BrTAB** at 296 K) and 2118235 (for ***p*-BrTAB** at 300 K) contain(s) the supplementary crystallographic data for this paper. These data are provided free of charge by the joint Cambridge Crystallographic Data Centre and Fachinformationszentrum Karlsruhe Access Structures service.

Acknowledgements

Funding from the Julius-Maximilians-Universität Würzburg and the Deutsche Forschungsgemeinschaft (DFG, German Research Foundation) – GRK2112 and 396890929/GRK 2482 is gratefully acknowledged. We are grateful to the China Scholarship Council for providing a Ph.D. scholarship to Z.W. Open Access funding enabled and organized by Projekt DEAL.

Conflict of Interest

The authors declare no conflict of interest.

Data Availability Statement

The data that support the findings of this study are available in the supplementary material of this article.

Keywords: AIE · luminescence · phosphorescence · triarylborane · triplet

[1] a) S. Hirata, K. Totani, J. Zhang, T. Yamashita, H. Kaji, S. R. Marder, T. Watanabe, C. Adachi, *Adv. Funct. Mater.* **2013**, *23*, 3386–3397; b) L. Dou, J. You, Z. Hong, Z. Xu, G. Li, R. A. Street, Y. Yang, *Adv. Mater.* **2013**, *25*, 6642–6671; c) S. Reineke, F. Lindner, G. Schwartz, N. Seidler, K. Walzer, B. Lussem, K. Leo, *Nature* **2009**, *459*, 234–238; d) S. Hirata, K. Totani, H. Kaji, M. Vacha, T. Watanabe, C. Adachi, *Adv. Opt. Mater.* **2013**, *1*, 438–442.

[2] a) L. Huang, C. Qian, Z. Ma, *Chem. Eur. J.* **2020**, *26*, 11914–11930; b) J. Yang, X. Zhen, B. Wang, X. Gao, Z. Ren, J. Wang, Y. Xie, J. Li, Q. Peng, K. Pu, Z. Li, *Nat. Commun.* **2018**, *9*, 840–849; c) S. Xu, R. Chen, C. Zheng, W. Huang, *Adv. Mater.* **2016**, *28*, 9920–9940; d) J. Zhao, W. Wu, J. Sun, S. Guo, *Chem. Soc. Rev.* **2013**, *42*, 5323–5351; e) H. T. Feng, J. Zeng, P. A. Yin, X. D. Wang, Q. Peng, Z. Zhao, J. W. Y. Lam, B. Z. Tang, *Nat. Commun.* **2020**, *11*, 2617.

[3] a) Z. He, H. Gao, S. Zhang, S. Zheng, Y. Wang, Z. Zhao, D. Ding, B. Yang, Y. Zhang, W. Z. Yuan, *Adv. Mater.* **2019**, *31*, 1807222; b) T. Maldiney, A. Lecointre, B. Viana, A. Bessiere, M. Bessodes, D. Gourier, C. Richard, D. Scherman, *J. Am. Chem. Soc.* **2011**, *133*, 11810–11815; c) X. F. Wang, H. Y. Xiao, P. Z. Chen, Q. Z. Yang, B. Chen, C. H. Tung, Y. Z. Chen, L. Z. Wu, *J. Am. Chem. Soc.* **2019**, *141*, 5045–5050; d) G. Zhang, G. M. Palmer, M. W. Dewhirst, C. L. Fraser, *Nat. Mater.* **2009**, *8*, 747–751; e) K. Y. Zhang, Q. Yu, H. Wei, S. Liu, Q. Zhao, W. Huang, *Chem. Rev.* **2018**, *118*, 1770–1839.

[4] a) P. Long, Y. Feng, C. Cao, Y. Li, J. Han, S. Li, C. Peng, Z. Li, W. Feng, *Adv. Funct. Mater.* **2018**, *28*, 1800791; b) Y. Tao, R. Chen, H. Li, J. Yuan, Y. Wan, H. Jiang, C. Chen, Y. Si, C. Zheng, B. Yang, G. Xing, W. Huang, *Adv. Mater.* **2018**, *30*, 1803856; c) B. Zhou, D. P. Yan, *Adv. Funct. Mater.* **2019**, *29*, 1807599.

[5] a) M. C. Tang, M. Y. Leung, S. L. Lai, M. Ng, M. Y. Chan, V. W. W. Yam, *J. Am. Chem. Soc.* **2018**, *140*, 13115–13124; b) O. S. Wenger, *J. Am. Chem. Soc.* **2018**, *140*, 13522–13533; c) K. Y. Zhang, P. Gao, G. Sun, T. Zhang, X. Li, S. Liu, Q. Zhao, K. K. Lo, W. Huang, *J. Am. Chem. Soc.* **2018**, *140*, 7827–7834; d) W. Liu, J. Wang, Y. Gong, Q. Liao, Q. Dang, Z. Li, Z. Bo, *Angew. Chem. Int. Ed.* **2020**, *59*, 20161–20166; *Angew. Chem.* **2020**, *132*, 20336–20341.

[6] a) C. J. Chen, R. J. Huang, A. S. Batsanov, P. Pander, Y. T. Hsu, Z. G. Chi, F. B. Dias, M. R. Bryce, *Angew. Chem. Int. Ed.* **2018**, *57*, 16407–16411; *Angew. Chem.* **2018**, *130*, 16645–16649; b) L. K. Huang, B. Chen, X. P. Zhang, C. O. Trindle, Y. C. Wang, H. Miao, Y. Luo, G. Q. Zhang, *Angew. Chem. Int. Ed.* **2018**, *57*, 16046–16050; *Angew. Chem.* **2018**, *130*, 16278–16282; c) S. M. A. Fateminia, Z. Mao, S. Xu, Z. Yang, Z. Chi, B. Liu, *Angew. Chem. Int. Ed.* **2017**, *56*, 12160–12164; *Angew. Chem.* **2017**, *129*, 12328–12332; d) K. Jiang, Y. Wang, C. Cai, H. Lin, *Adv. Mater.* **2018**, *30*, 1800783; e) L. Favereau, C. Quinton, C. Poriel, T. Roisnel, D. Jacquemin, J. Crassous, *J. Phys. Chem. Lett.* **2020**, *11*, 6426–6434; f) E. Januszewski, A. Lorbach, R. Grewal, M. Bolte, J. W. Bats, H. W. Lerner, M. Wagner, *Chem. Eur. J.* **2011**, *17*, 12696–12705; g) T. Kushida, C. Camacho, A. Shuto, S. Irle, M. Muramatsu, T. Katayama, S. Ito, Y. Nagasawa, H. Miyasaka, E. Sakuda, N. Kitamura, Z. Zhou, A. Wakamiya, S. Yamaguchi, *Chem. Sci.* **2014**, *5*, 1296–1304.

[7] a) J. Wang, Z. Huang, X. Ma, H. Tian, *Angew. Chem. Int. Ed.* **2020**, *59*, 9928–9933; *Angew. Chem.* **2020**, *132*, 10014–10019; b) L. Bian, H. Shi, X. Wang, K. Ling, H. Ma, M. Li, Z. Cheng, C. Ma, S. Cai, Q. Wu, N. Gan, X. Xu, Z. An, W. Huang, *J. Am. Chem. Soc.* **2018**, *140*, 10734–10739; c) W. Zhao, Z. He, B. Z. Tang, *Nature Res. Mater.* **2020**, *5*, 869–885; d) W. Ratzke, L. Schmitt, H. Matsuoka, C. Bannwarth, M. Retegan, S. Bange, P. Klemm, F. Neese, S. Grimme, O. Schiemann, J. M. Lupton, S. Hoger, *J. Phys. Chem. Lett.* **2016**, *7*, 4802–4808; e) E. Lucenti, A. Forni, C. Botta, L. Carlucci, C. Giannini, D. Marinotto, A. Previtali, S. Righetto, E. Cariati, *J. Phys. Chem. Lett.* **2017**, *8*, 1894–1898; f) W. L. Jia, D. T. Song, S. N. Wang, *J. Org. Chem.* **2003**, *68*, 701–705.

[8] a) M. Louis, H. Thomas, M. Gmelch, A. Haft, F. Fries, S. Reineke, *Adv. Mater.* **2019**, *31*, 1807887; b) H. Shi, Z. An, P. Z. Li, J. Yin, G. Xing, T. He, H. Chen, J. Wang, H. Sun, W. Huang, Y. Zhao, *Cryst. Growth Des.* **2016**, *16*, 808–813; c) H. Tian, X. Ma, C. Xu, J. Wang, *Angew. Chem. Int. Ed.*

2018, *57*, 10854–10858; *Angew. Chem.* **2018**, *130*, 11020–11024; d) J. Wang, C. Wang, Y. Gong, Q. Liao, M. Han, T. Jiang, Q. Dang, Y. Li, Q. Li, Z. Li, *Angew. Chem. Int. Ed.* **2018**, *57*, 16821–16826; *Angew. Chem.* **2018**, *130*, 17063–17068; e) Z. Y. Zhang, Y. Chen, Y. Liu, *Angew. Chem. Int. Ed.* **2019**, *58*, 6028–6032; *Angew. Chem.* **2019**, *131*, 6089–6093; f) J. L. Ma, H. Liu, S. Y. Li, Z. Y. Li, H. Y. Zhang, Y. Wang, C. H. Zhao, *Organometallics* **2020**, *39*, 4153–4158; g) J. Gierschner, J. Q. Shi, B. M. Medina, Sanjuán, S. Varghese, S. Y. Park, *Adv. Opt. Mater.* **2021**, 2002251; h) H. Yuasa, S. Kuno, *Bull. Chem. Soc. Jpn.* **2018**, *91*, 223–229.

[9] a) R. Kabe, C. Adachi, *Nature* **2017**, *550*, 384–387; b) D. Li, F. Lu, J. Wang, W. Hu, X. M. Cao, X. Ma, H. Tian, *J. Am. Chem. Soc.* **2018**, *140*, 1916–1923; c) J. Wei, B. Liang, R. Duan, Z. Cheng, C. Li, T. Zhou, Y. Yi, Y. Wang, *Angew. Chem. Int. Ed.* **2016**, *55*, 15589–15593; *Angew. Chem.* **2016**, *128*, 15818–15822; d) Z. Lin, R. Kabe, K. Wang, C. Adachi, *Nat. Commun.* **2020**, *11*, 191; e) B. Chen, W. Huang, H. Su, H. Miao, X. Zhang, G. Zhang, *Angew. Chem. Int. Ed.* **2020**, *59*, 10023–10026; *Angew. Chem.* **2020**, *132*, 10109–10112; f) O. Bolton, K. Lee, H. J. Kim, K. Y. Lin, J. Kim, *Nat. Chem.* **2011**, *3*, 205–210; g) C. Chen, Z. Chi, K. C. Chong, A. S. Batsanov, Z. Yang, Z. Mao, Z. Yang, B. Liu, *Nat. Mater.* **2020**, *20*, 175–180.

[10] a) Y. Gong, G. Chen, Q. Peng, W. Z. Yuan, Y. Xie, S. Li, Y. Zhang, B. Z. Tang, *Adv. Mater.* **2015**, *27*, 6195–6201; b) Y. Gong, L. Zhao, Q. Peng, D. Fan, W. Z. Yuan, Y. Zhang, B. Z. Tang, *Chem. Sci.* **2015**, *6*, 4438–4444; c) D. C. Green, M. A. Holden, M. A. Levenstein, S. Zhang, B. R. G. Johnson, J. Gala de Pablo, A. Ward, S. W. Botchway, F. C. Meldrum, *Nat. Commun.* **2019**, *10*, 206; d) K. Narushima, Y. Kiyota, T. Mori, S. Hirata, M. Vacha, *Adv. Mater.* **2019**, *31*, 1807268.

[11] a) Q. Li, M. Zhou, M. Yang, Q. Yang, Z. Zhang, J. Shi, *Nat. Commun.* **2018**, *9*, 734; b) H. W. Wu, W. J. Chi, Z. Chen, A. K. Bindra, G. B. Yang, X. G. Liu, Y. L. Zhao, *Adv. Funct. Mater.* **2019**, *29*, 1807243; c) A. D. Nidhankar, ■■ please provide first name ■■ Goudappagouda, D. S. Mohana Kumari, S. K. Chaubey, R. Nayak, R. G. Gonnade, G. V. P. Kumar, R. Krishnan, S. S. Babu, *Angew. Chem. Int. Ed.* **2020**, *59*, 13079–13085; *Angew. Chem.* **2020**, *132*, 13179–13185.

[12] a) Z. Chai, C. Wang, J. Wang, F. Liu, Y. Xie, Y. Z. Zhang, J. R. Li, Q. Li, Z. Li, *Chem. Sci.* **2017**, *8*, 8336–8344; b) X. F. Chen, C. Xu, T. Wang, C. Zhou, X. P. Zhang, J. N. Demas, C. O. Trindle, G. Q. Zhang, *Angew. Chem. Int. Ed.* **2016**, *55*, 9872–9876; *Angew. Chem.* **2016**, *128*, 10026–10030; c) P. K. Samanta, D. Kim, V. Coropceanu, J. L. Bredas, *J. Am. Chem. Soc.* **2017**, *139*, 4042–4051; d) Y. Shoji, Y. Ikabata, Q. Wang, D. Nemoto, A. Sakamoto, N. Tanaka, J. Seino, H. Nakai, T. Fukushima, *J. Am. Chem. Soc.* **2017**, *139*, 2728–2733; e) J. Yang, X. Gao, Z. Xie, Y. Gong, M. Fang, Q. Peng, Z. Chi, Z. Li, *Angew. Chem. Int. Ed.* **2017**, *56*, 15299–15303; *Angew. Chem.* **2017**, *129*, 15501–15505; f) E. Hamzehpoor, D. F. Perepichka, *Angew. Chem. Int. Ed.* **2016**, *59*, 9977–9981; *Angew. Chem.* **2016**, *132*, 10063–10067.

[13] a) S. A. Bagnicha, N. N. Khropika, V. N. Knykshtoa, A. L. Mikhalchuk, *Chem. Phys.* **2001**, *274*, 29–35; b) S. Bhattacharyya, L. R. Sousa, S. Ghosh, *Chem. Phys. Lett.* **1997**, *269*, 314–320; c) T. Itoh, *J. Chem. Phys.* **1987**, *87*, 4361–4367; d) T. Itoh, *J. Lumin.* **2004**, *109*, 221–225; e) T. Nakayama, K. Sakurai, K. Ushida, K. Kawatsura, K. Hamanoue, *Chem. Phys. Lett.* **1989**, *164*, 557–561; f) S. Samanta, M. B. Roy, M. Chatterjee, S. Ghosh, *J. Lumin.* **2007**, *126*, 230–238.

[14] Z. He, W. Zhao, J. W. Y. Lam, Q. Peng, H. Ma, G. Liang, Z. Shuai, B. Z. Tang, *Nat. Commun.* **2017**, *8*, 416.

[15] F. Y. Li, S. Guo, Y. Y. Qin, Y. X. Shi, M. P. Han, Z. F. An, S. J. Liu, Q. Zhao, W. Huang, *Adv. Opt. Mater.* **2019**, *7*, 1900511.

[16] T. Wang, Z. B. Hu, X. C. Nie, L. K. Huang, M. Hui, X. Sun, G. Q. Zhang, *Nat. Commun.* **2021**, *12*, 1364.

[17] Y. Liu, Z. M. Ma, J. W. Liu, M. X. Chen, Z. Y. Ma, X. R. Jia, *Adv. Opt. Mater.* **2021**, *9*, 2001685.

[18] a) S. J. Woo, Y. H. Kim, J. J. Kim, *Chem. Mater.* **2021**, *33*, 5618–5630; b) T. Wang, X. G. Su, X. P. Zhang, X. C. Nie, L. K. Huang, X. Y. Zhang, X. Sun, Y. Luo, G. Q. Zhang, *Adv. Mater.* **2019**, *31*, 1904273; c) C. Zhou, S. Zhang, Y. Gao, H. Liu, T. Shan, X. Liang, B. Yang, Y. Ma, *Adv. Funct. Mater.* **2018**, *28*, 1802407; d) S. K. Behera, S. Y. Park, J. Gierschner, *Angew. Chem. Int. Ed.* **2021**, *60*, 22624–22638; *Angew. Chem.* **2021**, *133*, 22804–22820.

[19] a) A. Fukazawa, S. Yamaguchi, *Chem. Asian J.* **2009**, *4*, 1386–1400; b) X. Wang, S. L. Gong, D. T. Song, Z. H. Lu, S. N. Wang, *Adv. Funct. Mater.* **2014**, *24*, 7257–7271; c) M. Hirai, N. Tanaka, M. Sakai, S. Yamaguchi, *Chem. Rev.* **2019**, *119*, 8291–8331; d) Z. M. Hudson, S. N. Wang, *Acc. Chem. Res.* **2009**, *42*, 1584–1596; e) S. Yamaguchi, A. Wakamiya, *Pure Appl. Chem.* **2006**, *78*, 1413–1424; f) F. Jäkle, *Chem. Rev.* **2010**, *110*, 3985–4022; g) E. Grotthuss, A. John, T. Kaese, M. Wagner, *Asian J. Org. Chem.* **2018**, *7*, 37–53; h) R. J. Kahan, W. Hirunpinyopas, J. Cid, M. J. Ingleson, R. A. W. Dryfe, *Chem. Mater.* **2019**, *31*, 1891–1898; i) S. S. Kothavale, J. Y. Lee, *Adv. Opt. Mater.* **2020**, *8*, 2000922; j) M. Gon, K. Tanaka, Y. Chujo, *Bull. Chem. Soc. Jpn.* **2019**, *92*, 7–18; k) G. Turkoglu, M. E. Cinar, T. Ozturk, *Molecules* **2017**, *22*, 1522; l) H. H. Hackney, D. F. Perepichka, *Aggregate* **2021**, e123; m) H. E. Hackney, D. G. Hall, *ChemPhotoChem* **2022**, e202100219.

[20] a) Z. Yuan, N. J. Taylor, T. B. Marder, I. D. Williams, S. K. Kurtz, L.-T. Cheng, *J. Chem. Soc. Chem. Commun.* **1990**, 1489–1492; b) C. D. Entwistle, T. B. Marder, *Angew. Chem. Int. Ed.* **2002**, *41*, 2927–2931; *Angew. Chem.* **2002**, *114*, 3051–3056; c) C. D. Entwistle, T. B. Marder, *Chem. Mater.* **2004**, *16*, 4574–4585; d) L. Ji, S. Griesbeck, T. B. Marder, *Chem. Sci.* **2017**, *8*, 846–863; e) J. He, F. Rauch, M. Finze, T. B. Marder, *Chem. Sci.* **2021**, *12*, 128–147; f) S. M. Berger, T. B. Marder, *Mater. Horiz.* **2022**, *9*, 112–120; g) Z. Wu, J. C. Roldao, F. Rauch, A. Friedrich, M. Ferger, F. Würthner, J. Gierschner, T. B. Marder, *Angew. Chem. Int. Ed.* **2022**, *61*, e202200599.

[21] a) Z. Wu, J. Nitsch, J. Schuster, A. Friedrich, K. Edkins, M. Loebnitz, F. Dinkelbach, V. Stepanenko, F. Würthner, C. M. Marian, L. Ji, T. B. Marder, *Angew. Chem. Int. Ed.* **2020**, *59*, 17137–17144; *Angew. Chem.* **2020**, *132*, 17285–17292; b) Z. Wu, J. Nitsch, T. B. Marder, *Adv. Opt. Mater.* **2021**, 2100411.

[22] a) Q. Peng, H. Ma, Z. Shuai, *Acc. Chem. Res.* **2021**, *54*, 940–949; b) A. D. Nidhankar, Goudappagouda, V. C. Wakchaure, S. S. Babu, *Chem. Sci.* **2021**, *12*, 4216–4236.

[23] a) V. Stehr, R. F. Fink, B. Engels, J. Pflaum, C. Deibel, *J. Chem. Theory Comput.* **2014**, *10*, 1242–1255; b) M. Tabachnyk, B. Ehrler, S. Bayliss, R. H. Friend, N. C. Greenham, *Appl. Phys. Lett.* **2013**, *103*, 153302.

[24] S. M. Berger, M. Ferger, F. Rauch, T. B. Marder, *Chem. Eur. J.* **2021**, *27*, 9094–9101.

[25] S. Sarkar, H. P. Hendrickson, D. Lee, F. Devine, J. Jung, E. Geva, J. Kim, B. D. Dunietz, *J. Phys. Chem. C* **2017**, *121*, 3771–3777.

[26] C. M. Marian, Spin-Orbit Coupling in Molecules. In Reviews in Computational Chemistry (eds K. B. Lipkowitz, D. B. Boyd), **2001**. https://doi.org/10.1002/0471224413.ch3.

[27] a) ■■ please provide first name ■■ El-Sayed, *M. A. Acc. Chem. Res.* **1968**, *1*, 8–16; b) C. M. Marian, *Annu. Rev. Phys. Chem.* **2021**, *72*, 617–640.

[28] M. Mantina, A. C. Chamberlin, R. Valero, C. J. Cramer, D. G. Truhlar, *J. Phys. Chem. A* **2009**, *113*, 5806–5812.

[29] O. V. Dolomanov, L. J. Bourhis, R. J. Gildea, J. A. K. Howard, H. Puschmann, *J. Appl. Crystallogr.* **2009**, *42*, 339–341.

[30] a) J. J. McKinnon, A. S. Mitchell, M. A. Spackman, *Chem. Eur. J.* **1998**, *4*, 2136–2141; b) J. J. McKinnon, M. A. Spackman, A. S. Mitchell, *Acta Crystallogr. Sect. B* **2004**, *60*, 627–668; c) M. A. Spackman, P. G. Byrom, *Chem. Phys. Lett.* **1997**, *267*, 215–220; d) M. A. Spackman, D. Jayatilaka, *CrystEngComm* **2009**, *11*, 19–32.

[31] a) J. J. McKinnon, D. Jayatilaka, M. A. Spackman, *Chem. Commun.* **2007**, 3814–3816; b) A. Parkin, G. Barr, W. Dong, C. J. Gilmore, D. Jayatilaka, J. J. McKinnon, M. A. Spackman, C. C. Wilson, *CrystEngComm* **2007**, *9*, 648–652; c) M. A. Spackman, J. J. McKinnon, *CrystEngComm* **2002**, *4*, 378–392.

Manuscript received: February 17, 2022
Accepted manuscript online: March 24, 2022
Version of record online: ■■, ■■■

RESEARCH ARTICLE

Bromo-triarylboron *o*-BrTAB exhibits dual phosphorescence at room temperature, a short-lived higher energy emission originates from single molecules (T_1^M) whereas the long-lived component at lower energy results from an aggregate (T_1^A). Under 365 nm UV light irradiation, crystalline ***o*-BrTAB** emits bright pale blue light (fluorescence). After turning off the light, a persistent yellow afterglow remains for 2 s.

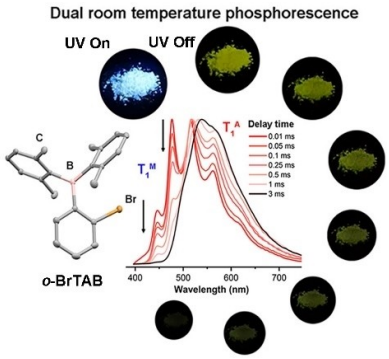

Z. Wu, F. Dinkelbach, Dr. F. Kerner, Dr. A. Friedrich, Prof. Dr. L. Ji, Dr. V. Stepanenko, Prof. Dr. F. Würthner, Prof. Dr. C. M. Marian, Prof. Dr. T. B. Marder**

1 – 12

Aggregation-Induced Dual Phosphorescence from (*o*-Bromophenyl)-Bis(2,6-Dimethylphenyl)Borane at Room Temperature

Aggregation-Induced Dual Phosphorescence from (*o*-Bromophenyl)-Bis(2,6-Dimethylphenyl)Borane at Room Temperature (Marian, Marder et al.) @NPUintl @HHU_de @Uni_WUE

Share your work on social media! *Chemistry - A European Journal* has added Twitter as a means to promote your article. Twitter is an online microblogging service that enables its users to send and read short messages and media, known as tweets. Please check the pre-written tweet in the galley proofs for accuracy. If you, your team, or institution have a Twitter account, please include its handle @username. Please use hashtags only for the most important keywords, such as #catalysis, #nanoparticles, or #proteindesign. The ToC picture and a link to your article will be added automatically, so the **tweet text must not exceed 250 characters**. This tweet will be posted on the journal's Twitter account (follow us @ChemEurJ) upon publication of your article in its final (possibly unpaginated) form. We recommend you to re-tweet it to alert more researchers about your publication, or to point it out to your institution's social media team.

Please check that the ORCID identifiers listed below are correct. We encourage all authors to provide an ORCID identifier for each coauthor. ORCID is a registry that provides researchers with a unique digital identifier. Some funding agencies recommend or even require the inclusion of ORCID IDs in all published articles, and authors should consult their funding agency guidelines for details. Registration is easy and free; for further information, see http://orcid.org/.

Zhu Wu
Prof. Dr. Todd B. Marder http://orcid.org/0000-0002-9990-0169
Dr. Vladimir Stepanenko
Dr. Alexandra Friedrich
Prof. Dr. Lei Ji
Dr. Florian Kerner
Fabian Dinkelbach
Prof. Dr. Christel M. Marian
Prof. Dr. Frank Würthner

Supporting Information

Table of Contents

I. General information.....S2

II. Experimental procedures and characterization.....S5

III. SEM.....S7

IV. Photophysical spectra.....S8

V. Results of the quantum chemical computations.....S14

VI. Single-crystal X-ray diffraction.....S28

VII. ^{1}H, ^{13}C, ^{11}B NMR spectra and GC-MS and HRMS data.....S42

VIII. References.....S50

I. General information

All starting materials were purchased from commercial sources and were used without further purification. The organic solvents for synthetic reactions and for photophysical measurements were HPLC grade, further treated to remove trace water using an Innovative Technology Inc. Pure-Solv Solvent Purification System and deoxygenated using the freeze-pump-thaw method. All synthetic reactions were performed in an Innovative Technology Inc. glovebox or under an argon atmosphere using standard Schlenk techniques. ^{1}H, ^{13}C and ^{11}B NMR spectra were measured on a Bruker Avance 500 MHz (^{1}H, 500 MHz; ^{13}C, 126 MHz; ^{11}B, 160 MHz) NMR spectrometer. Mass spectra were recorded on Agilent 7890A/5975C Inert GC/MSD systems operating in EI mode. High resolution mass spectra were obtained using a Thermo Fisher Scientific Exactive™ Plus Orbitrap MS System with an Atmospheric Solids Analysis Probe (ASAP^{+}). Elemental analyses were performed on a Leco CHNS-932 Elemental Analyser.

General photophysical measurements. All measurements were performed in standard quartz cuvettes (1 cm × 1 cm cross-section). UV-visible absorption spectra were recorded using an Agilent 8453 diode array UV-visible spectrophotometer. The molar extinction coefficients were calculated from three independently prepared samples in hexane solution. The emission spectra were recorded using an Edinburgh Instruments FLSP920 spectrometer equipped with a double monochromator for both excitation and emission, operating in right angle geometry mode, and all spectra were fully corrected for the spectral response of the instrument. All solutions used in photophysical measurements had a concentration lower than 10^{-5} M to minimize inner filter effects during fluorescence measurements.

Quantum yield measurements. The photoluminescent quantum yields were measured using a calibrated integrating sphere (inner diameter: 150 mm) from Edinburgh Instruments combined with the FLSP920 spectrometer described above. For solution-state measurements, the longest-wavelength absorption maximum of the compound in hexane was chosen as the excitation wavelength. For solid-state measurements, the excitation wavelength was 305 nm. The phosphorescence quantum yield of compounds ***o*-**, ***m*-** and ***p*-BrTAB** were obtained using the equation:

$$\boldsymbol{\Phi}_{\mathrm{P}} = \frac{B}{A} \times \boldsymbol{\Phi}_{\mathrm{PL}}$$

where A and B represent the integrated area of the total photoluminescence and phosphorescence spectra, respectively. The phosphorescence component was separated from total photoluminescence (PL) based on the phosphorescence spectrum for phosphorescence quantum yields. Φ_{PL} represents the absolute photoluminescence quantum yields of the compounds in the solid state.

Lifetime measurements. Fluorescence lifetimes were recorded using the time-correlated single-photon counting (TCSPC) method on an Edinburgh Instruments FLSP920 spectrometer equipped with a high-speed photomultiplier tube positioned after a single emission monochromator. Measurements were made in right-angle geometry mode, and the emission was collected through a polarizer set to the magic angle. Solutions were excited with a pulsed diode laser at a wavelength of 316 nm at repetition rates of 5-10 MHz. The instrument response functions (IRF) were *ca.* 230 ps FWHM. The phosphorescence lifetimes were measured using a μF920 pulsed 60 W Xenon microsecond flashlamp, with a repetition rate of 0.2 or 50 Hz at room temperature and 0.1 Hz at 77 K. Decays were recorded to 10000 counts in the peak channel with a record length of at least 2000 channels. Iterative reconvolution of the IRF with a double exponential function and non-linear least-squares analysis were used to analyze the data. The quality of all decay fits was judged to be satisfactory, based on the calculated values of the reduced χ^2 and Durbin-Watson parameters and visual inspection of the weighted residuals. Time-gating was used to measure the emission following a specific delay time the range of 0.01-3 ms.

Powder X-ray diffraction and Phase analysis The compound ***o*-BrTAB** was ground into a powder using an agate mortar until hardly any room-temperature phosphorescence was observed. The powder X-ray diffraction pattern was collected in reflection geometry on a Bruker D8 Discover powder diffractometer with Da Vinci design and linear Lynx-Eye detector. X-ray radiation (Cu-Kα_1; λ = 1.5406 Å) was focused with a Goebel mirror and Cu-Kα_2 radiation was eliminated by a Ni-absorber. Data were collected from $2\theta = 2 – 60°$ in steps of 0.025° at ambient temperature. They were corrected for an offset in 2θ and exported using the Bruker AXS Diffrac-Suite. The diffraction patterns were then converted using CMPR software[1] for further processing with the GSAS program.[2] Cell parameters, background, scaling factor, zero shift and profile parameters were refined using the LeBail method. The data range $2\theta = 2 – 5°$ was excluded from refinement as no reflection was either observed or predicted in this range and due to high background signal at low angles. The starting values for the refinement were taken from the single-crystal structure refinement at 100 K.

Scanning Electron Microscopy SEM images were recorded using a Zeiss Ultra Plus field emission scanning electron microscope equipped with GEMINI e-Beam column operated at 1-3 kV with an aperture size set to 10 or 30 μm to avoid excessive charging and radiation damage of the areas imaged.

Quantum chemical calculations All geometries were obtained using the Turbomole[3] and Gaussian[4] program packages utilizing Kohn–Sham density functional theory (DFT) in combination with the PBE0[5-7] functional. For excited state optimizations, linear response time-dependent DFT (TDDFT) was employed, and, for triplet states, the Tamm–Dancoff approximation (TDDFT-TDA) was additionally used. Vibrational frequency calculations were carried out with the Gaussian program package. In all computations, the def2-SVP[8] basis set was utilized on all atoms except for bromine, for which a cc-pVTZ-PP[9] basis set in combination with the defpp-ecp[9] pseudopotential was employed. Energies and multi reference configuration interaction (MRCI) wavefunctions of the lowest ten excited states of singlet and triplet spin multiplicity, respectively, were optimized with the DFT/MRCI[10-11] method applying the redesigned R2016 Hamiltonian[12] and an initial active space of 12 electrons in 12 frontier orbitals. The orbital basis for the DFT/MRCI calculations is obtained from DFT utilizing the BH-LYP[13-14] functional. Absorption spectra were obtained by broadening the corresponding DFT/MRCI line spectra with Gaussian functions of 1000 cm^{-1} full width at half maximum (FWHM). The SPOCK[15-17] program package was employed to compute spin–orbit coupling matrix elements (SOCMEs) and phosphorescence rate constants from spin–orbit coupled wavefunctions obtained with the MRSOCI procedure. Franck–Condon (FC) emission spectra and intersystem crossing (ISC) rate constants were obtained utilizing a time evolution approach implemented in the VIBES[18-19] program. Here an integration grid of 16384 points over 300 fs time period and a Gaussian damping function of 200 cm^{-1} FWHM was employed for FC spectra. For ISC rate constants, a grid of 1000 points over a 250 fs time period and a Gaussian damping function of 0.3 cm^{-1} FWHM was used. Temperature effects of the population of the vibrational modes were accounted for by a Boltzmann distribution in the initial electronic state.

Crystal structure determinations Crystals suitable for single-crystal X-ray diffraction were selected, coated in perfluoropolyether oil, and mounted on MiTeGen sample holders. Diffraction data were collected on Bruker X8 Apex II 4-circle diffractometers with CCD area detectors using Mo-K_α radiation monochromated by graphite or multi-layer focusing mirrors or on a Bruker D8-Quest diffractometer with a CPA area detector and multi-layer mirror monochromated Mo-K_α radiation. Data were collected at ambient temperature and at 100 K.

The crystals were cooled using an Oxford Cryostream low-temperature device. The images were processed and corrected for Lorentz-polarization effects and absorption as implemented in the Bruker software packages. The structures were solved using the intrinsic phasing method (SHELXT)[20] and Fourier expansion technique. All non-hydrogen atoms were refined in anisotropic approximation, with hydrogen atoms 'riding' in idealized positions, by full-matrix least squares against F^2 of all data, using SHELXL[21] software and the SHELXLE graphical user interface.[22] Diamond[23] software was used for graphical representation. Other structural information was extracted using Mercury[24] and OLEX2[25] software. Hirshfeld surfaces were calculated and analyzed using the Crystal Explorer[26] program. Crystal data and experimental details are listed in Tables S9 and S10; full structural information has been deposited with Cambridge Crystallographic Data Centre. CCDC-2085814 (***o*-BrTAB** at 100 K), CCDC-2085815 (***m*-BrTAB** at 100 K), CCDC-2085816 (***p*-BrTAB** at 100 K), CCDC-2089473 (***o*-BrTAB** at 290 K), CCDC-2118234 (***m*-BrTAB** at 296 K) and CCDC-2118235 (***p*-BrTAB** at 300 K).

II. Experimental procedures and characterization

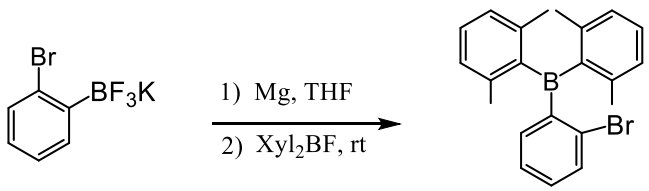

(2-bromophenyl)bis(2,6-dimethylphenyl)borane (*o*-BrTAB)： A 250 mL three-necked round bottom flask, equipped with a dropping funnel and water-cooled condenser, was used. In a typical preparation, an anhydrous THF solution of 2-bromo-1,3-dimethylbenzene (896 mg, 4.5 mmol) was added dropwise to the flask containing magnesium (120 mg, 5.0 mmol) and 100 mL of anhydrous THF. The solution was refluxed during the addition period, which required approximately 3 h, and then allowed to cool to room temperature. To this solution (2-bromophenyl)trifluoroborate potassium salt[27] (789 mg, 3.0 mmol) in anhydrous THF was added and the reaction was stirred overnight. The resulting mixture was subjected to silica gel column chromatography eluting with *n*-hexane to afford ***o*-BrTAB** (722 mg,1.92 mmol) in 64% yield as white a solid: ^{1}H NMR (500 MHz, CD_2Cl_2, rt, ppm): δ 7.58–7.55 (m, 1H), 7.30–7.27 (m, 2H), 7.20–7.16 (m, 3H), 6.95 (d, J = 8 Hz, 4H), δ 2.03 (s, 12H). ^{13}C NMR (126 MHz, CD_2Cl_2, rt, ppm): 149.5 (br), 145.5 (br), 141.0, 136.1, 133.1, 132.3, 130.0, 128.4, 127.8, 127.4, 23.2. ^{11}B NMR (160 MHz, CD_2Cl_2, r.t., ppm): 76 (br). MS (EI^+) m/z: 376

$[M]^+$. HRMS ($ASAP^+$): m/z calcd for 376.0992 $[M]^+$; found: 376.0990 $[M]$ ($|\Delta|$ = 0.53 ppm). Elem. Anal. Calcd (%) for $C_{22}H_{22}BBr$: C, 70.07; H, 5.88; Found: C, 69.91; H, 6.07.

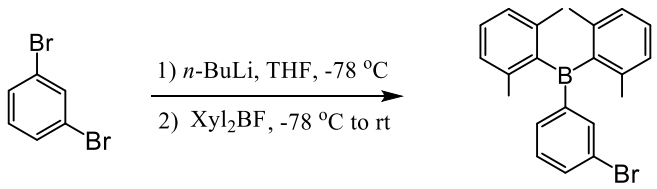

(3-bromophenyl)bis(2,6-dimethylphenyl)borane (*m*-BrTAB)： To a solution of 1,3-dibromobenzene (402 mg, 1.7 mmol) in anhydrous THF (20 mL) was added a hexane solution of *n*-BuLi (1.2 mL, 1.6 M, 1.9 mmol) dropwise by syringe at -78 °C. The mixture was stirred at the same temperature for 1 h. A solution of bis(2,6-dimethylphenyl)fluoroborane[28] (408 mg, 1.7 mmol) in anhydrous THF (5 mL) was added to the reaction mixture via syringe. The reaction mixture was warmed to room temperature and stirred overnight. The reaction was quenched with a saturated solution of NaCl and the aqueous layer was extracted with Et_2O. The combined organic layer was dried over anhydrous Na_2SO_4, filtered, and concentrated under reduced pressure. The resulting mixture was subjected to silica gel column chromatography eluting with *n*-hexane to afford ***m*-BrTAB (**498 mg, 1.3 mmol) in 78% yield as a white solid: ^1H NMR (500 MHz, CD_2Cl_2, rt, ppm): δ 7.68 (ddd, J = 8, 2 and 1 Hz, 1H), 7.65–7.63 (m, 1H), 7.46 (dt, J = 7, 1 Hz, 1H), 7.35–7.28 (m, 1H), 7.25 (t, J = 8 Hz, 2H), 7.08–7.02 (m, 4H), 2.07 (s, 12H). $^{13}C\{^1H\}$ NMR (126 MHz, CD_2Cl_2, rt, ppm): 148.1 (br), 143.9 (br), 140.6, 138.3, 134.8, 134.6, 130.0, 129.4, 127.4, 122.9, 23.3. ^{11}B NMR (160 MHz, CD_2Cl_2, rt, ppm): 75 (br). MS (EI^+) m/z: 376 $[M]^+$. HRMS ($ASAP^+$): m/z calcd for $[M]^+$: 376.0930; found: 376.0937$[M]$ ($|\Delta|$ = 1.86 ppm). Elem. Anal. Calcd (%) for $C_{22}H_{22}BBr$: C, 70.07; H, 5.88; Found: C, 69.98; H, 6.07.

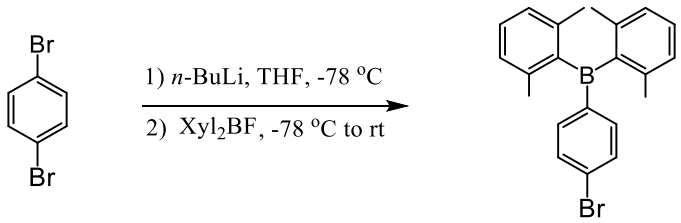

(4-bromophenyl)bis(2,6-dimethylphenyl)borane (*p*-BrTAB)： To a solution of 1,4-dibromobenzene (402 mg, 1.7 mmol) in anhydrous THF (20 mL) was added a hexane solution of *n*-BuLi (1.2 mL, 1.6 M, 1.9 mmol) dropwise by syringe at -78 °C. The mixture was stirred at the same temperature for 1 h. A solution of bis(2,6-dimethylphenyl)fluoroborane[28] (408 mg, 1.7 mmol) in anhydrous THF (5 mL) was added to the reaction mixture via syringe. The reaction mixture was warmed to room temperature and stirred overnight. The reaction

was quenched with a saturated solution of NaCl and the aqueous layer was extracted with Et_2O. The combined organic layer was dried over anhydrous Na_2SO_4, filtered, and concentrated under reduced pressure. The resulting mixture was subjected to silica gel column chromatography eluting with *n*-hexane to afford ***p*-BrTAB (**537 mg, 1.4 mmol) in 84% yield as a white solid: ^{1}H NMR (500 MHz, CD_2Cl_2, rt, ppm): δ 7.55–7.51 (m, 2H), 7.39–7.35 (m, 2H), 7.20 (t, J = 8 Hz, 2H), 7.03–6.98 (m, 4H), 2.03 (s, 12H). $^{13}C\{^1H\}$ NMR (126 MHz, $CDCl_3$, rt, ppm): 144.2 (br), 144.0 (br.), 140.8, 138.1, 131.6, 129.4, 127.9, 127.5, 23.7. ^{11}B NMR (160 MHz, CD_2Cl_2, rt, ppm): 74 (br). MS (EI^+) m/z: 376 $[M]^+$. HRMS ($ASAP^+$): m/z calcd for $[M]^+$: 376.0992; found: 376.0993 $[M]$ (|Δ| = 0.27 ppm). Elem. Anal. Calcd (%) for $C_{22}H_{22}BBr$: C, 70.07; H, 5.88; Found: C, 70.04; H, 6.02.

III. SEM

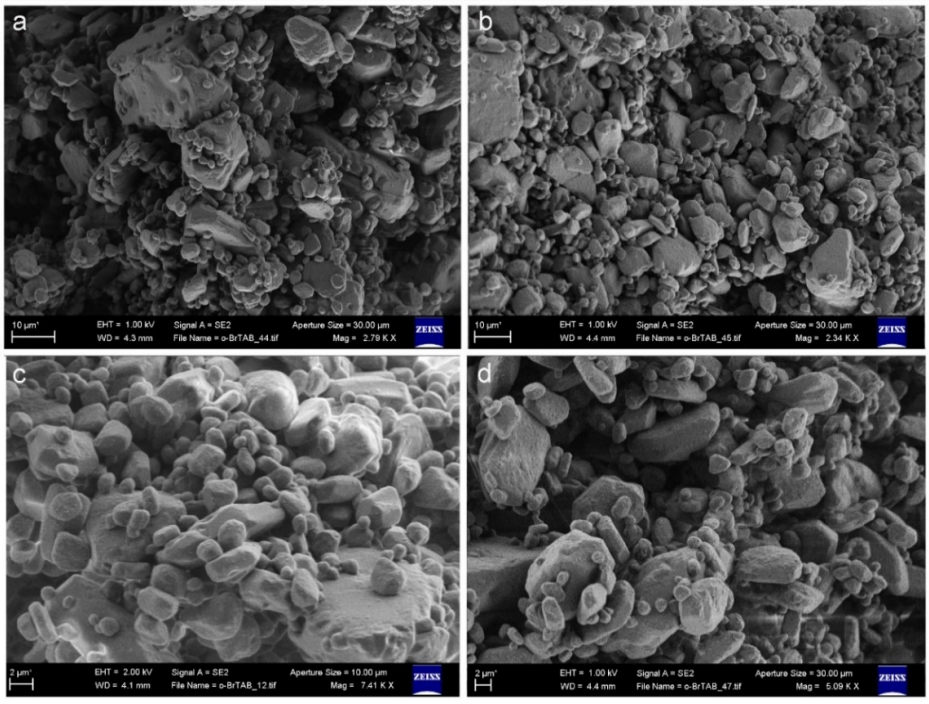

Figure S1. (a)-(d) SEM pictures of ***o*-BrTAB** as a ground powder.

IV. Photophysical spectra

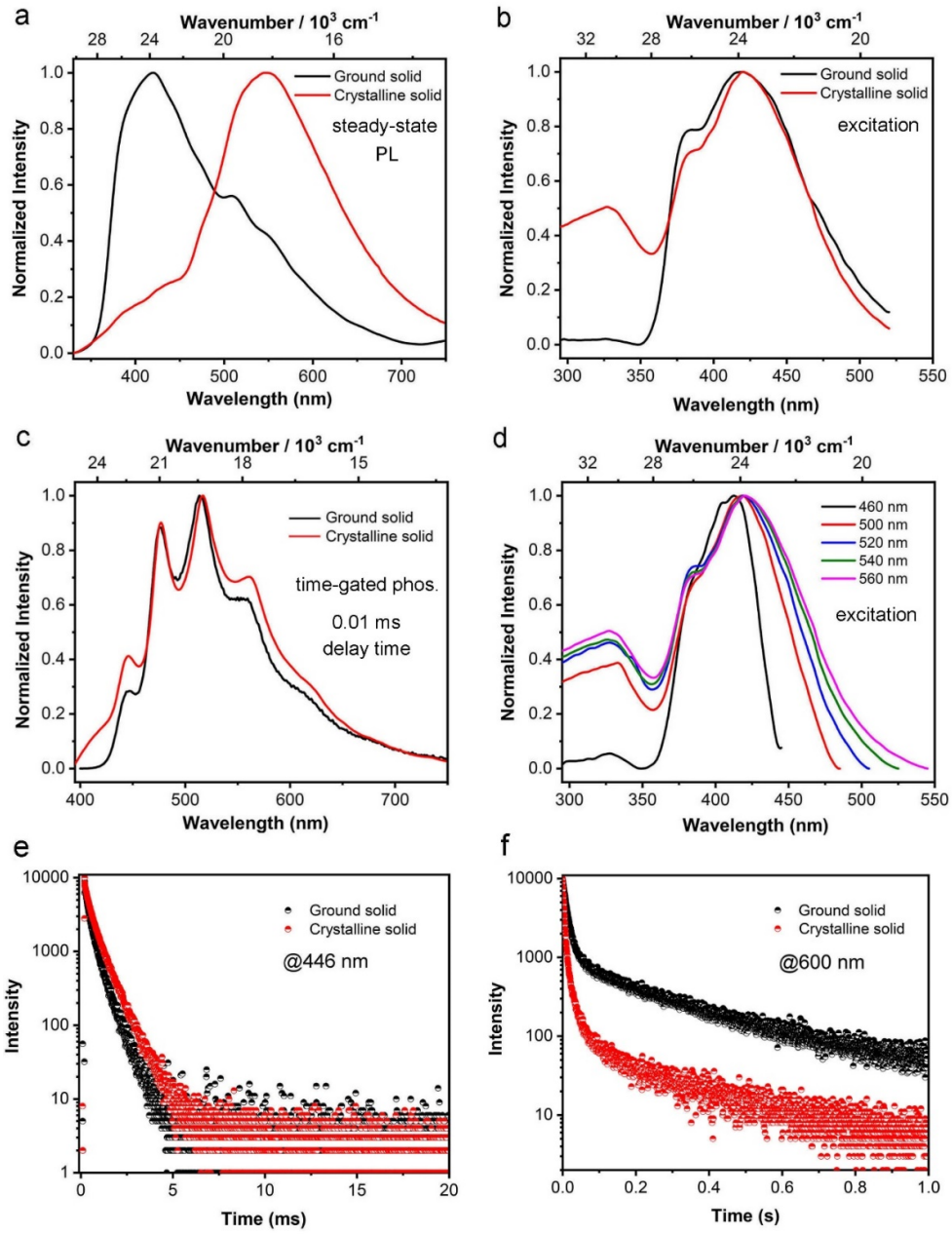

Figure S2. Normalized (a) photoluminescence emission, (b) excitation, and (c) time-gated (delay time 0.01 ms) phosphorescence emission of ***o*-BrTAB** in the crystalline state and ground powder at room temperature in air (λ_{ex} = 305 nm). (d) Normalized wavelength-dependent excitation spectra of ***o*-BrTAB** in the crystalline state from λ_{ex} = 460 to 560 nm. (e) Phosphorescence decay (λ_{em} = 446 nm) of ***o*-BrTAB** in the crystalline state (τ_p= 0.8 ms) and ground powder (τ_p = 0.7 ms) at room temperature in air. (f) Phosphorescence decay (λ_{em} = 600 nm) of ***o*-BrTAB** in the crystalline state (τ_p = 234 ms) and ground powder (τ_p = 191 ms) at room temperature in air.

Table S1. Unit cell parameters of ***o*-BrTAB** obtained from the LeBail refinement of powder X-ray diffraction data at room temperature.

Data	***o*-BrTAB**
λ / Å, radiation	1.5406, Cu-Kα_1
θ range / °	5 – 60
a / Å	8.2022(5)
b / Å	12.1584(5)
c / Å	18.8797(6)
α / °	90.0
β / °	93.312(4)
γ / °	90.0
Volume / Å^3	1879.7(1)
R_p	0.0495
wR_p	0.0798

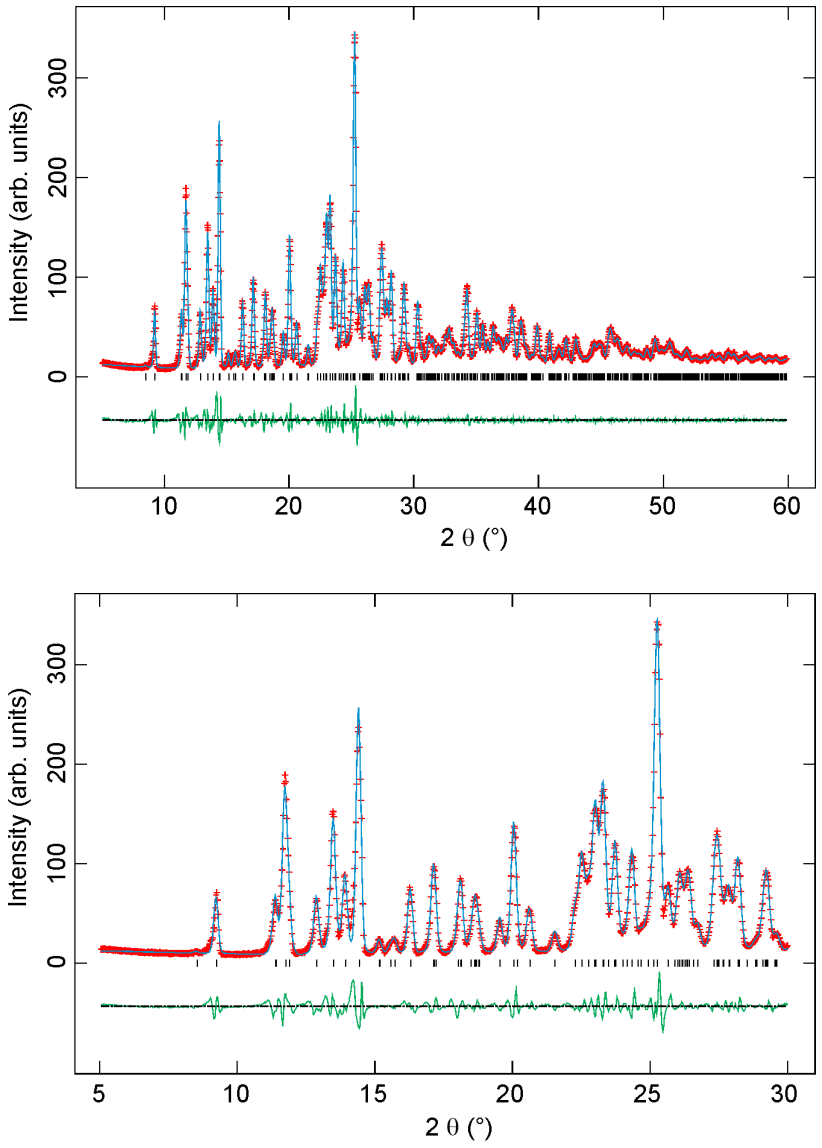

Figure S3. Powder X-ray diffraction patterns of compound ***o*-BrTAB** after grinding crystals in an agate mortar (top) in the full range 5 – 60° and (bottom) in the selected range 2θ = 5 – 30°. Red crosses represent the experimental values. The continuous blue lines show the results of the Le Bail fit to the data. The difference between experimental data and LeBail fit is represented by the green lines at the bottom of the plots. Vertical bars show the positions of the Bragg reflections of ***o*-BrTAB**.

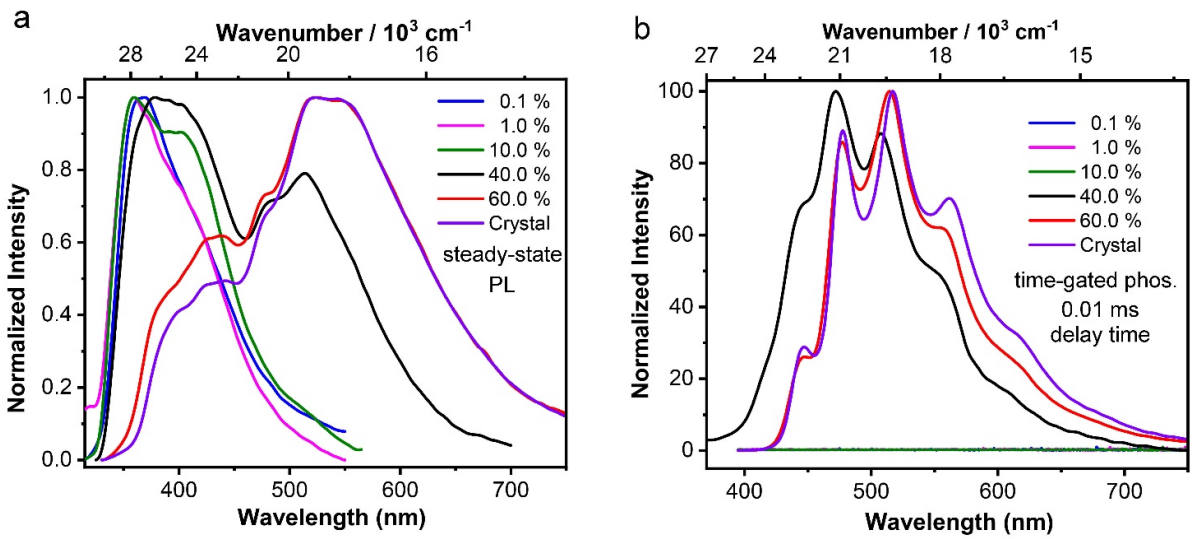

Figure S4. Normalized (a) PL emission and (b) time-gated phosphorescence emission spectra (delay time 0.01 ms) spectra of ***o*-BrTAB** in 0.1, 1.0, 10, 40 and 60 % PMMA film and the crystalline state (λ_{ex} = 305 nm).

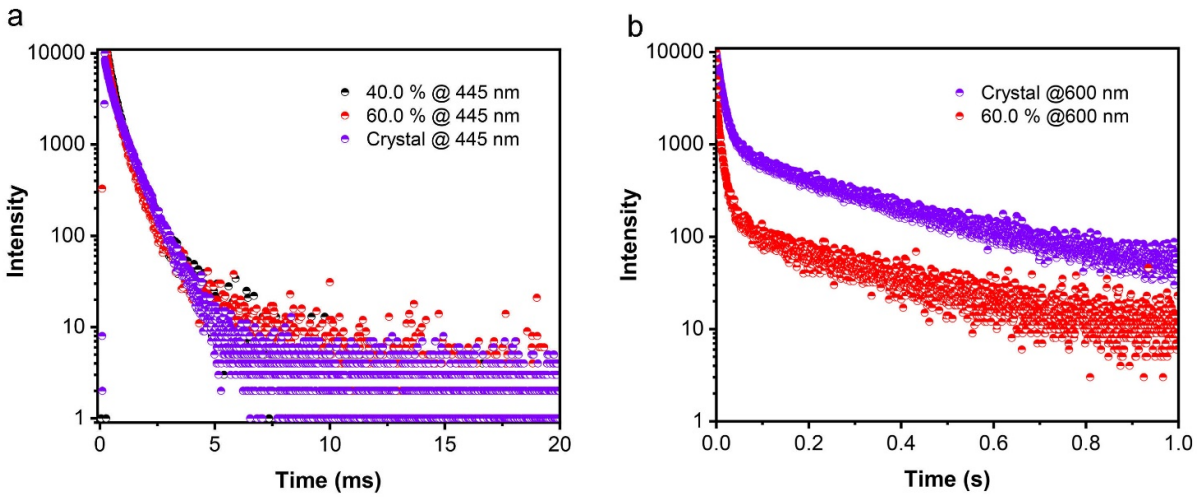

Figure S5. (a) Decays of the phosphorescence emission (λ_{em} = 446 nm, τ_p = 0.8 ms) of ***o*-BrTAB** in 40 % PMMA film, 60 % PMMA film and the crystalline state at room temperature in air. (b) Decays of the phosphorescence emission at 600 nm of ***o*-BrTAB** in 60 % PMMA film (τ_p = 226 ms) and the crystalline state (τ_p = 234 ms) at room temperature in air.

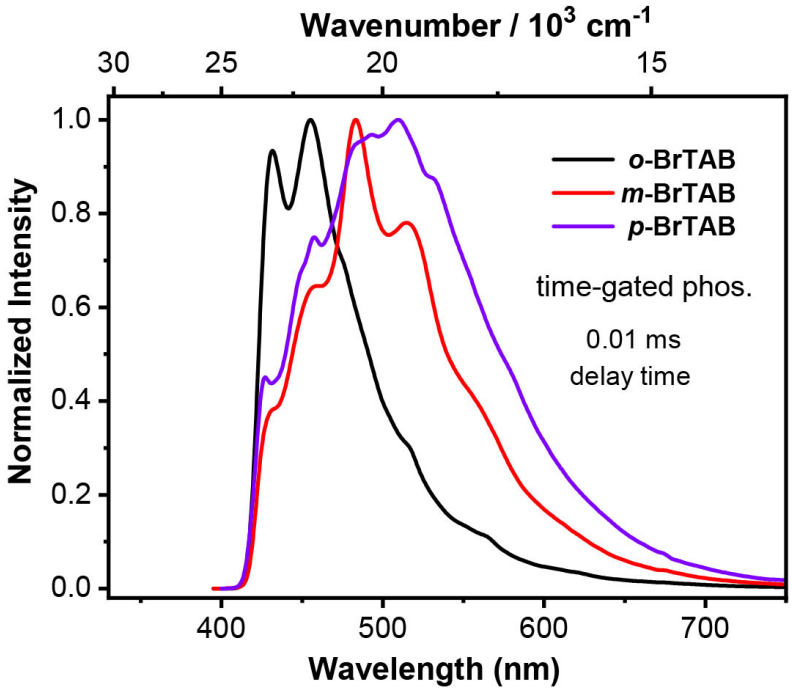

Figure S6. Normalized time-gated (delay time 0.01 ms) phosphorescence emission spectra of crystalline ***o-***, ***m-*** and ***p*-BrTAB** at 77 K (λ_{ex} = 305 nm).

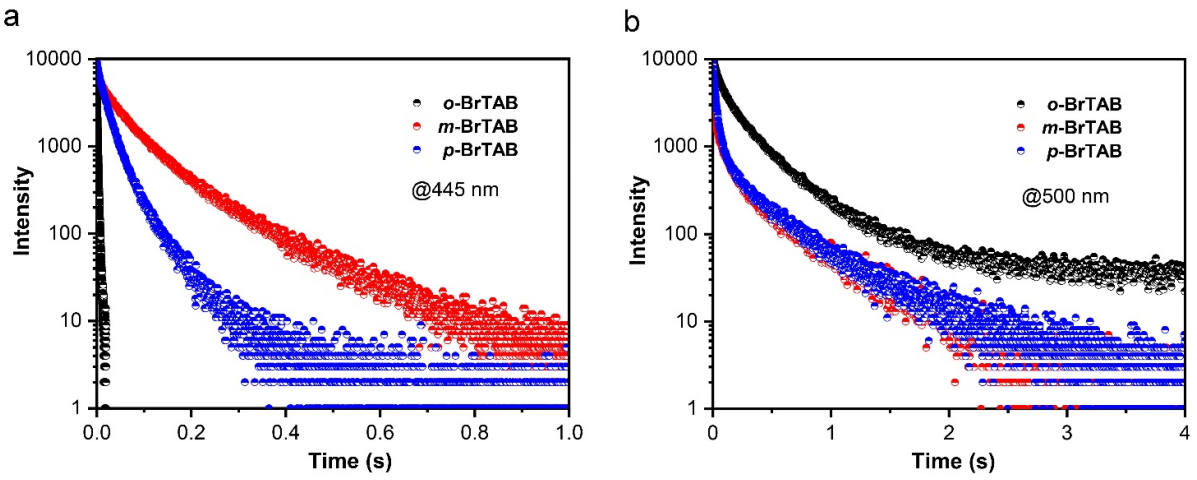

Figure S7. Decays of the phosphorescence emission (a) (λ_{em} = 445 nm) and (b) (λ_{em} = 500 nm) of crystalline ***o-***, ***m-*** and ***p*-BrTAB** at 77 K.

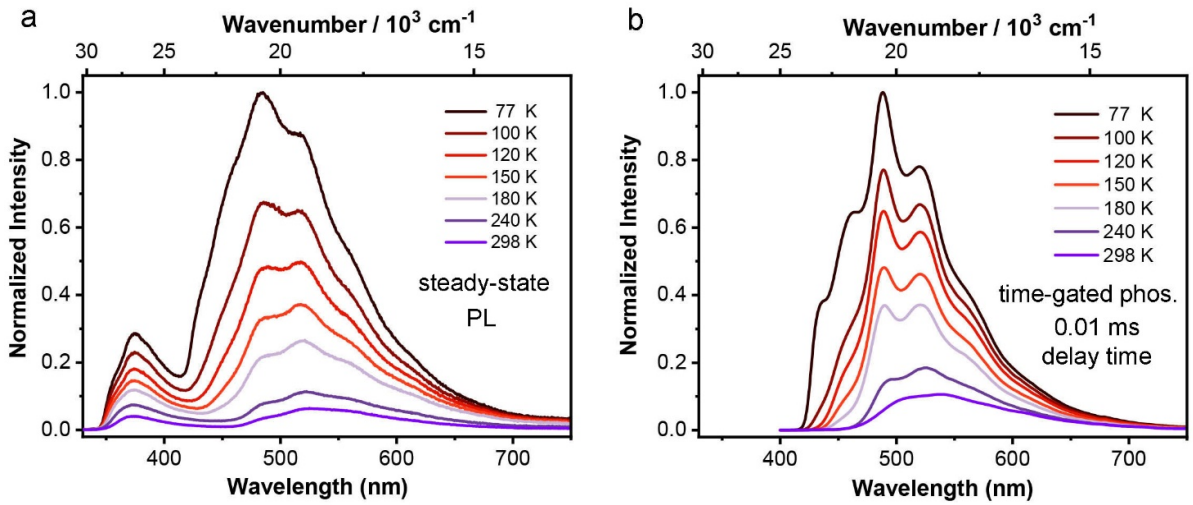

Figure S8. (a) Photoluminescence emission and (b) time-gated (delay time 0.01 ms) phosphorescence emission spectra of crystalline ***m*-BrTAB** at different temperatures (λ_{ex} = 305 nm).

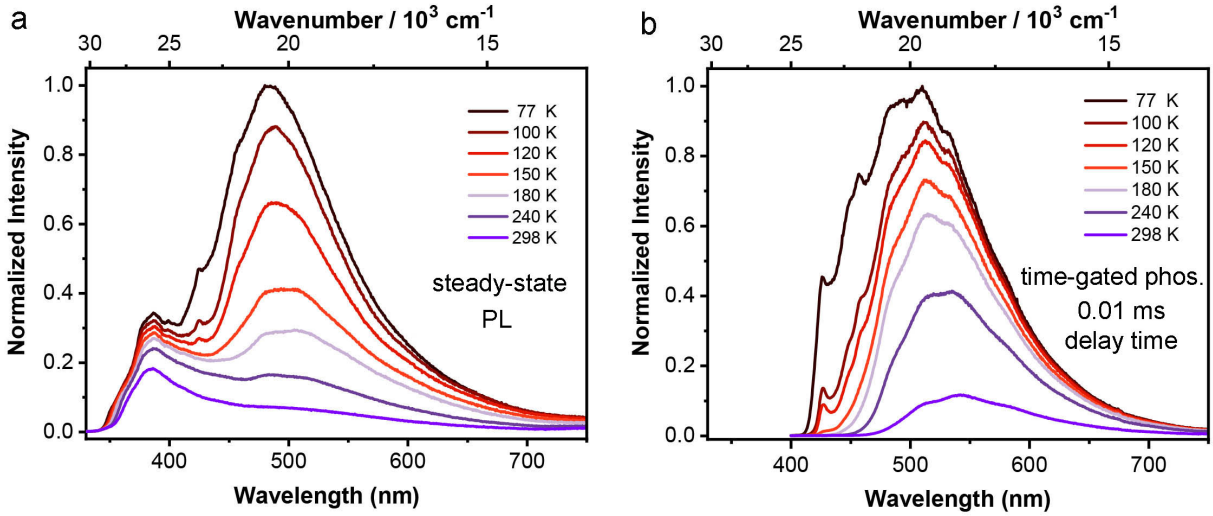

Figure S9. (a) Photoluminescence emission and (b) time-gated (delay time 0.01 ms) phosphorescence emission spectra of crystalline ***p*-BrTAB** at different temperatures (λ_{ex} = 305 nm).

V. Results of the quantum chemical computations

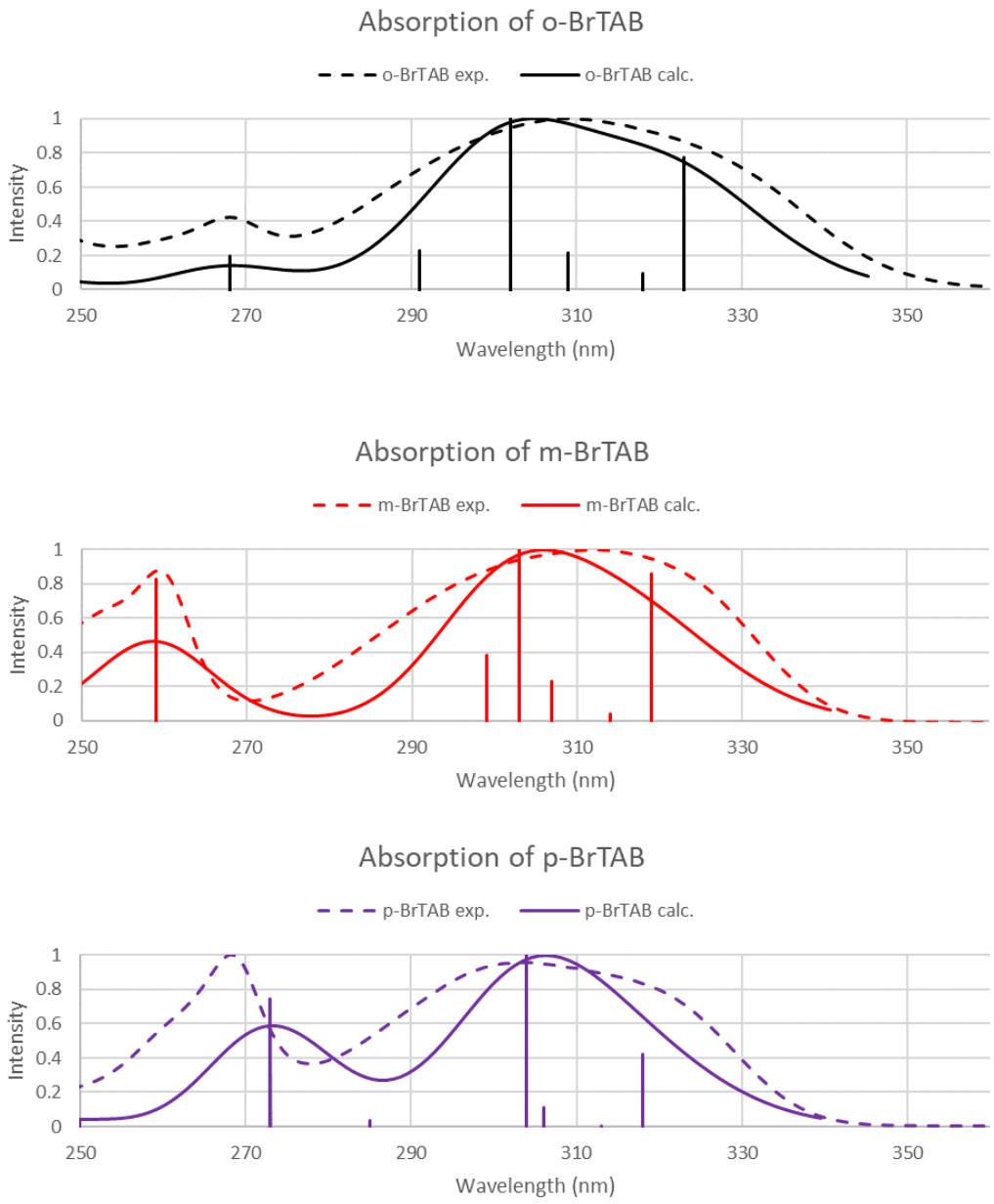

Figure S10. Calculated absorption spectra of ***o*-BrTAB**, ***m*-BrTAB** and ***p*-BrTAB** compared to experimental spectra.

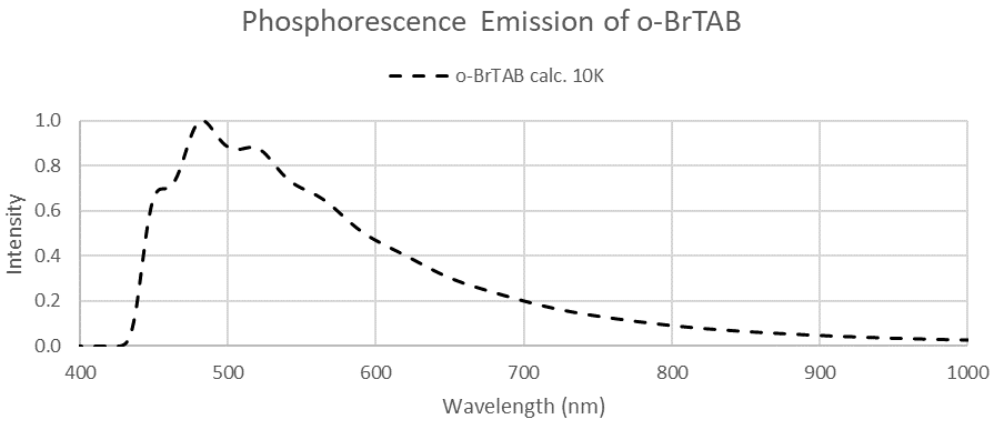

Figure S11. Calculated phosphorescence spectrum of monomeric ***o*-BrTAB** at 10 K.

Table S2: Spin–orbit coupling matrix elements (absolute values, cm^{-1}) of S_1^M, T_1^M, T_2^M and T_3^M states at the respective S_1^M minimum.

SOCME	x	y	z	$(x^2 + y^2 + z^2)$
		***o*-BrTAB**		
$\langle T_1^M \lvert \hat{H}_{SO} \rvert S_1^M \rangle$	4.792	1.299	0.833	25.348
$\langle T_2^M \lvert \hat{H}_{SO} \rvert S_1^M \rangle$	122.773	44.841	39.445	18639.878*
		***m*-BrTAB**		
$\langle T_1^M \lvert \hat{H}_{SO} \rvert S_1^M \rangle$	0.117	0.165	0.106	0.052
$\langle T_2^M \lvert \hat{H}_{SO} \rvert S_1^M \rangle$	7.238	0.901	2.988	62.133
$\langle T_3^M \lvert \hat{H}_{SO} \rvert S_1^M \rangle$	9.894	3.037	3.934	122.585*
		***p*-BrTAB**		
$\langle T_1^M \lvert \hat{H}_{SO} \rvert S_1^M \rangle$	0.263	0.140	2.740	7.594*
$\langle T_2^M \lvert \hat{H}_{SO} \rvert S_1^M \rangle$	0.390	0.055	0.374	0.295
$\langle T_3^M \lvert \hat{H}_{SO} \rvert S_1^M \rangle$	0.353	1.055	1.805	4.497*

* marks the fastest ISC channel of the low lying singlet and triplet states.

Table S3. Photophysical properties of compounds ***o*-BrTAB**, ***m*-BrTAB** and ***p*-BrTAB** *in vacuo* as obtained from quantum chemical calculations.

	λ_{abs} nm [a]	k_{isc} s^{-1} [b]	λ_f nm [c]	k_f s^{-1}	τ_f ns [d]	λ_p nm [c]	k_p s^{-1}	τ_p s [d]
***o*-BrTAB**	305	$\approx 1 \cdot 10^{10}$	500	$1 \cdot 10^7$	81	451, 488, 515, 563	515	0.002
***o*-Dimer**				$1 \cdot 10^7$	96	-	1041	0.001
***m*-BrTAB**	306	$\approx 9 \cdot 10^8$	412	$2 \cdot 10^7$	49	-	0.202	4.94
***p*-BrTAB**	306	$\approx 3 \cdot 10^8$	385	$2 \cdot 10^7$	45	-	1.03	0.97

[a] Absorption maximum of line spectrum broadened by Gaussian function; [b] rate constant for the fastest of the open ISC channels (***o*-BrTAB**: $S_1^M \rightarrow T_2^M$, ***m*-BrTAB**: $S_1^M \rightarrow T_3^M$ and ***p*-BrTAB**: $S_1^M \rightarrow T_1^M/T_3^M$); [c] maximum of 0-0 band, maximum of Franck-Condon spectrum at 10 K; [d] radiative lifetime assuming a quantum yield of 100 %.

Table S4. Calculated phosphorescence lifetimes of the lowest triplet components.

τ_p [s]	T_α	T_β	T_γ	$T_{average}$	$T_{exp,\ short}$ [a]	$T_{exp,\ long}$ [a]
***o*-BrTAB**	0.0007	0.0367	0.0070	0.0019	0.8077	174.2307
***o*-Dimer**	0.0003	0.0200	0.0297	0.0010		
***m*-BrTAB**	2.3030	8.4451	18.3713	4.2161	5.6667	56.8889
***m*-Dimer**	3.6310	0.3058	4.1039	0.7918		
***p*-BrTAB**	1.6762	17.2833	0.4107	0.9712	0.9000	29.0500
***p*-Dimer**	0.2339	3.5239	0.6741	0.4965		

[a] Radiative phosphorescence lifetime (τ_p/Φ_p) obtained from the experimental lifetime (τ_p) measured in the crystal at RT and the phosphorescence quantum yield (Φ_p).

Table S5. Vertical and adiabatic energies of the low-lying excited singlet and triplet states in the monomers. Adiabatic energies are marked in grey.

Energies [eV]	**@S_0^M**	**@S_1^M**	**@T_1^M**	**@T_2^M**	**@T_3^M**
			***o*-BrTAB**		
S_1^M	3.85	3.56	3.64	3.86[a]	
T_1^M	3.26	3.25	2.98	3.17[a]	
T_2^M	3.39	3.80	3.66	3.26[a]	
T_3^M	3.53	3.98	3.79	3.63[a]	
			***m*-BrTAB**		
S_1^M	3.89	3.78	3.96	3.94	3.91
T_1^M	3.32	3.39	3.03	3.83	3.27
T_2^M	3.38	3.52	3.86	3.01	3.38
T_3^M	3.49	3.71	3.95	3.94	3.42
			***p*-BrTAB**		
S_1^M	3.91	3.82	3.99	3.99	3.90
T_1^M	3.32	3.48	2.99	3.93	3.15
T_2^M	3.32	3.41	3.51	3.04	3.29
T_3^M	3.43	4.71	3.61	3.88	3.34

[a] Obtained at the crossing point between T_1 and T_2.

Table S6. Adiabatic energy gaps including vibrational zero-point energies.

Energies [eV]	***o*-BrTAB**	***m*-BrTAB**	***p*-BrTAB**
$S_1^M - S_0^M$	3.48	3.66	3.71
$T_1^M - S_0^M$	2.89	2.91	2.93
$S_1^M - T_1^M$	0.60	0.75	0.83
$S_1^M - T_2^M$		0.76	0.78
$S_1^M - T_3^M$		0.26	0.41

Table S7. Vertical and adiabatic energies of the low-lying excited singlet and triplet states in the dimers. Adiabatic energies are marked in grey.

Energies [eV]	**@S_0^D**	**@S_1^D**	**@T_1^D**
		***o*-BrTAB**	
S_1^D	3.65	3.41	3.51
T_1^D	3.07	3.11	2.93
T_2^D	3.07	3.61	3.52
T_3^D	3.21	3.78	3.54
T_4^D	3.21	3.83	3.71
		***m*-BrTAB**	
S_1^D	3.75	3.64	3.68
T_1^D	3.26	3.33	2.93
T_2^D	3.26	3.54	3.63
T_3^D	3.30	3.80	3.72
T_4^D	3.30	3.81	3.79
		***p*-BrTAB**	
S_1^D	3.79	3.65	3.81
T_1^D	3.20	3.23	3.02
T_2^D	3.24	3.41	3.48
T_3^D	3.25	3.66	3.63
T_4^D	3.37	3.71	3.64

Table S8: Selected bond lengths and angles of the isolated compounds ***o*-BrTAB**, ***m*-BrTAB** and ***p*-BrTAB** as obtained from geometry optimizations of the S_0^M, S_1^M, T_1^M, T_2^M and T_3^M states. R1 = bromo-xylyl, R2 = R3 = xylyl

***o*-BrTAB**	**@S_0^M**	**@S_1^M**	**@T_1^M**		
B-R1	1.581	1.532	1.566		
B-R2	1.578	1.614	1.560		
B-R3	1.582	1.584	1.587		
C-Br	1.896	1.912	1.902		
∠ R1(C)-B-(C-C)R2	49.4	67.2	49.2		
∠ R2(C)-B-(C-C)R3	51.7	47.4	49.7		
∠ R3(C)-B-(C-C)R1	42.4	23.1	31.3		
∠ R2(C)-B-(C-C)R1	44.2	19.3	33.3		
∠ R3(C)-B-(C-C)R2	52.3	58.1	46.3		
∠ R1(C)-B-(C-C)R3	55.3	49.8	51.1		
***m*-BrTAB**	**@S_0^M**	**@S_1^M**	**@T_1^M**	**@T_2^M**	**@T_3^M**
B-R1	1.574	1.531	1.568	1.568	1.553
B-R2	1.581	1.586	1.594	1.560	1.589
B-R3	1.582	1.606	1.559	1.595	1.587
C-Br	1.891	1.900	1.893	1.894	1.873
∠ R1(C)-B-(C-C)R2	54.5	48.4	62.5	36.1	-51.9
∠ R2(C)-B-(C-C)R3	55.0	65.6	42.1	61.7	-55.7
∠ R3(C)-B-(C-C)R1	27.8	13.2	25.6	20.1	-20.1
∠ R2(C)-B-(C-C)R1	27.9	19.6	20.3	25.3	-22.2
∠ R3(C)-B-(C-C)R2	54.6	49.1	61.6	41.9	-51.2
∠ R1(C)-B-(C-C)R3	54.9	69.8	36.4	62.7	-55.7
***p*-BrTAB**	**@S_0^M**	**@S_1^M**	**@T_1^M**	**@T_2^M**	**@T_3^M**
B-R1	1.571	1.530	1.543	1.566	1.561
B-R2	1.583	1.606	1.588	1.559	1.584
B-R3	1.583	1.586	1.588	1.595	1.584
C-Br	1.887	1.890	1.854	1.887	1.872
∠ R1(C)-B-(C-C)R2	55.1	69.5	52.4	35.2	53.4
∠ R2(C)-B-(C-C)R3	55.0	49.1	52.3	63.5	53.1
∠ R3(C)-B-(C-C)R1	27.2	19.8	21.8	19.2	26.4
∠ R2(C)-B-(C-C)R1	27.2	13.2	21.8	24.9	26.4
∠ R3(C)-B-(C-C)R2	55.0	65.5	51.6	41.0	53.1
∠ R1(C)-B-(C-C)R3	55.0	48.4	52.9	63.9	53.4

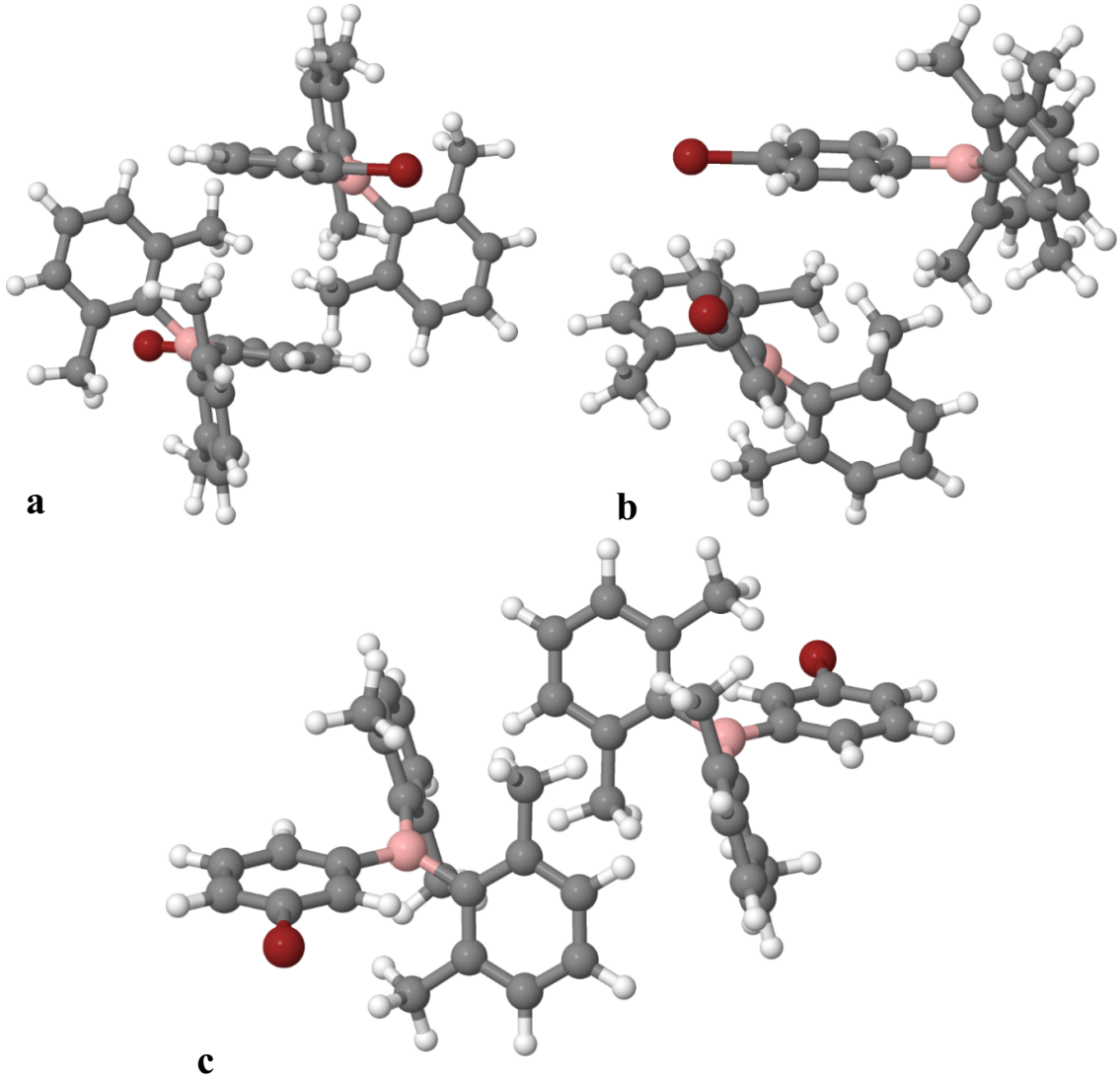

Figure S12. Dimer geometries of ***o*-BrTAB** (a), ***p*-BrTAB** (b) and ***m*-BrTAB** (c).

Difference Densities:

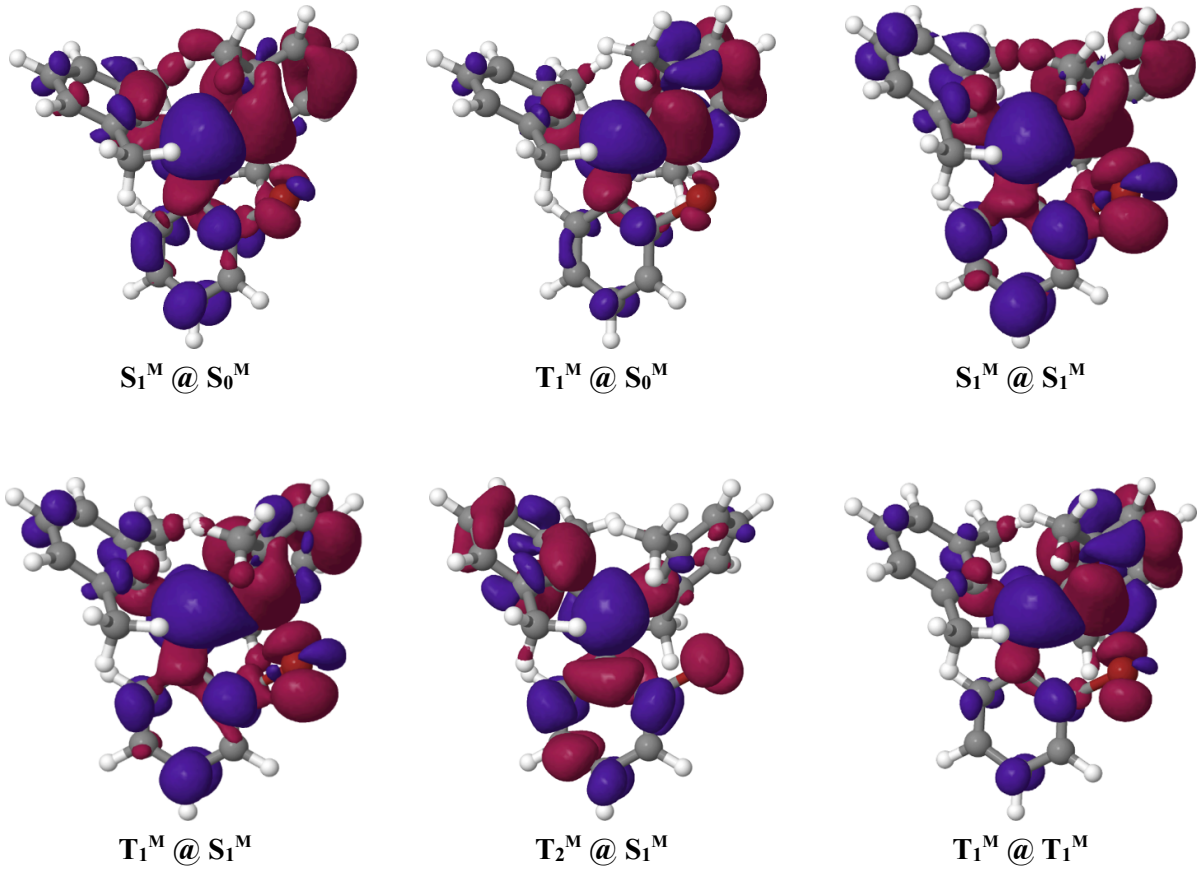

Figure S13. Difference densities of the S_1^M, T_1^M, and T_2^M states of ***o*-BrTAB** at various molecular geometries. Red areas indicate a loss of electron density upon excitation from the electronic ground state, and blue areas a gain.

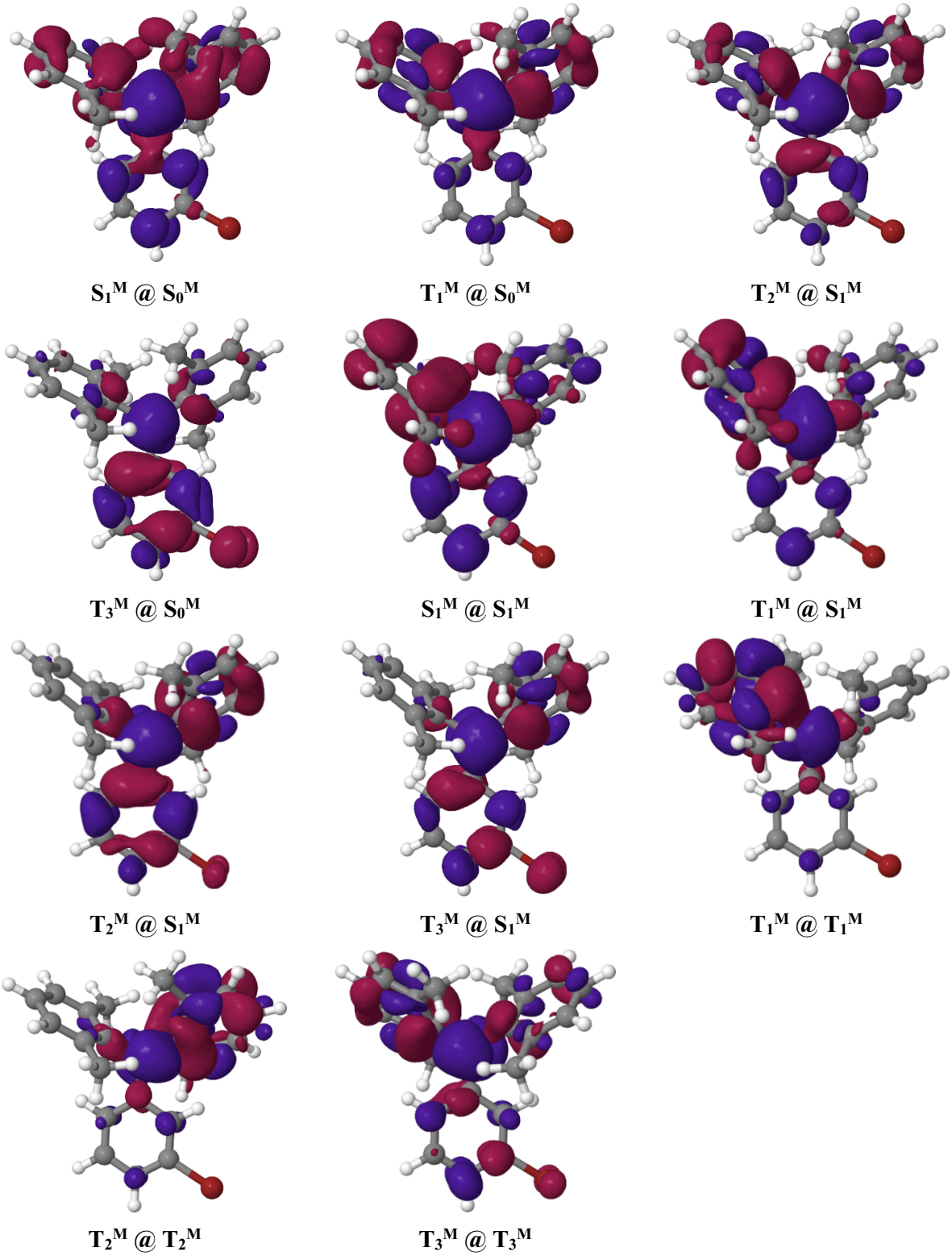

Figure S14. Difference densities of the S_1^M, T_1^M, T_2^M and T_3^M states of ***m*-BrTAB**. For color codes, see above.

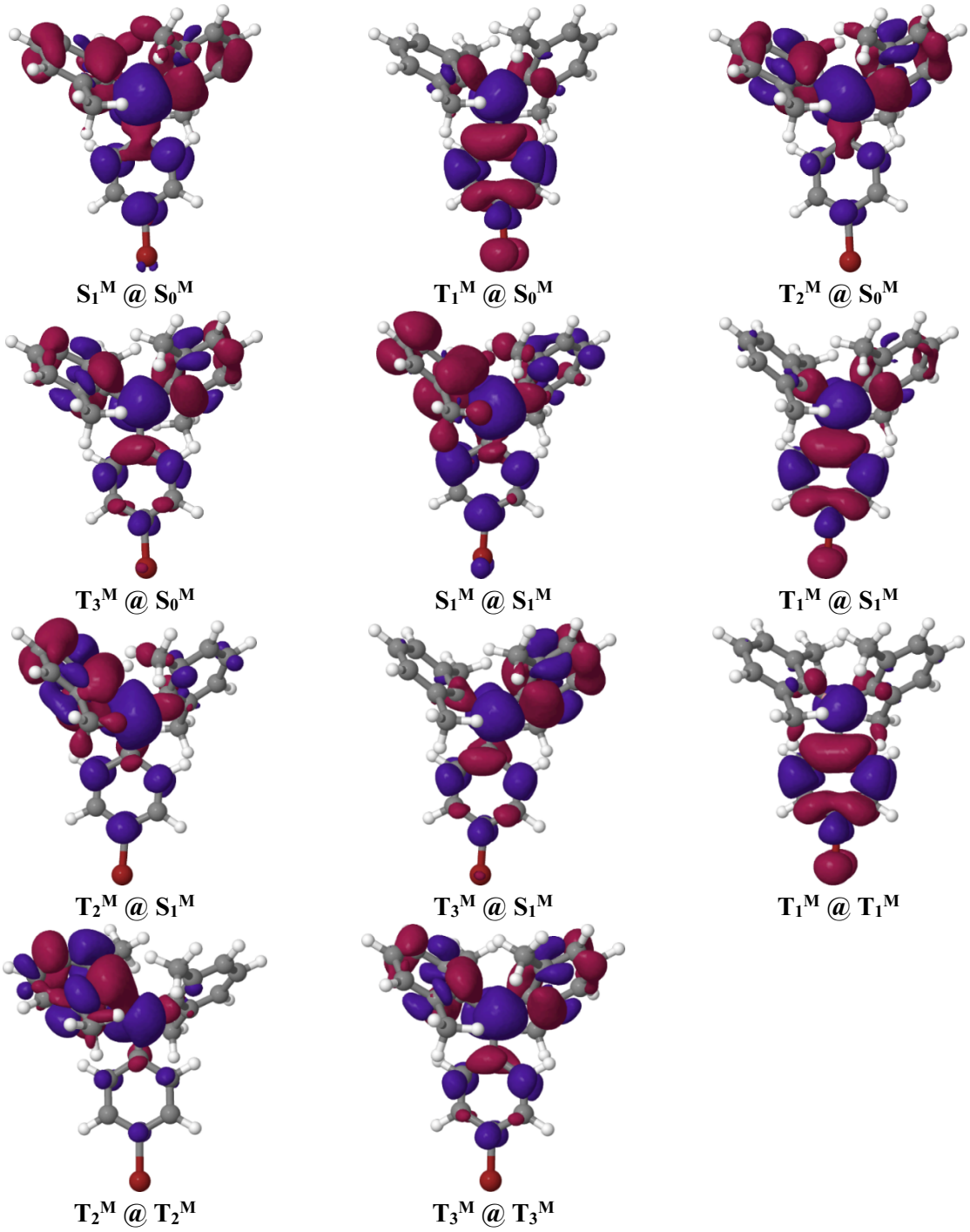

Figure S15. Difference densities of the S_1^M, T_1^M, T_2^M and T_3^M states of ***p*-BrTAB**. For color codes, see above

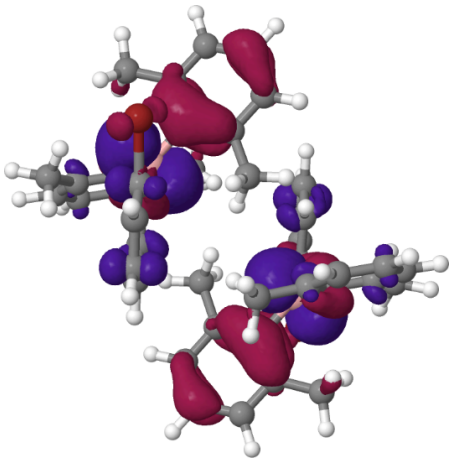

S_1^D @ S_0^D

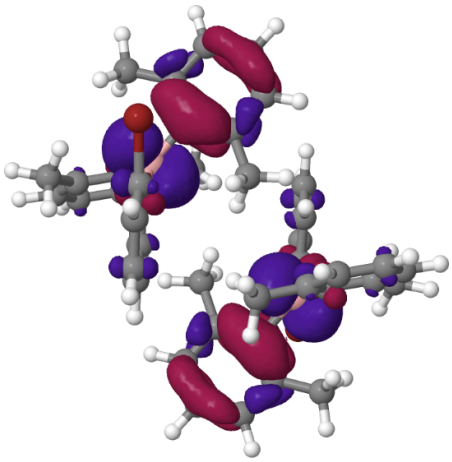

T_1^D @ S_0^D

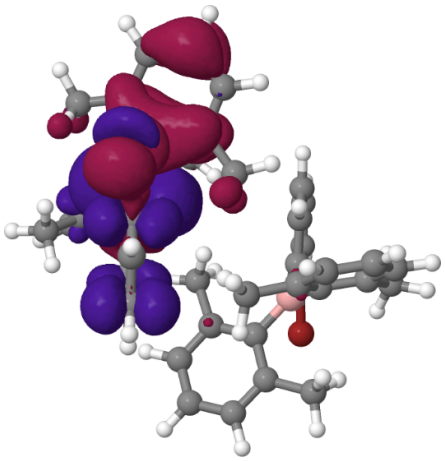

S_1^D @ S_1^D

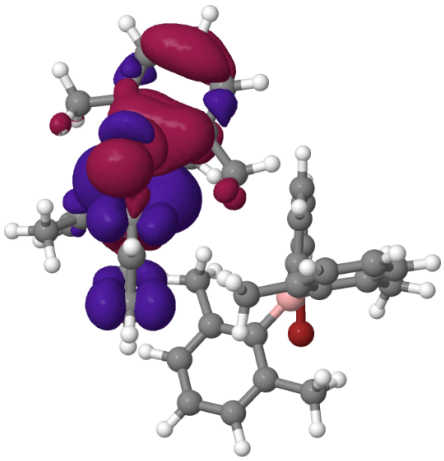

T_1^D @ S_1^D

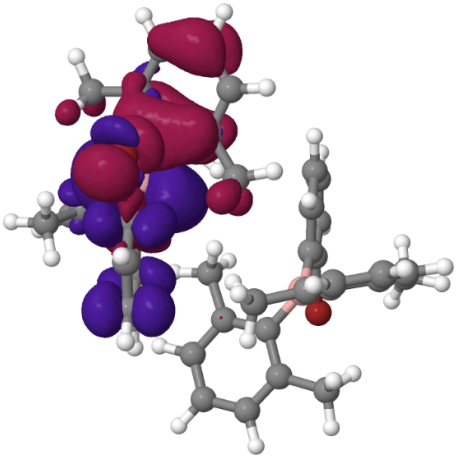

S_1^D @ T_1^D

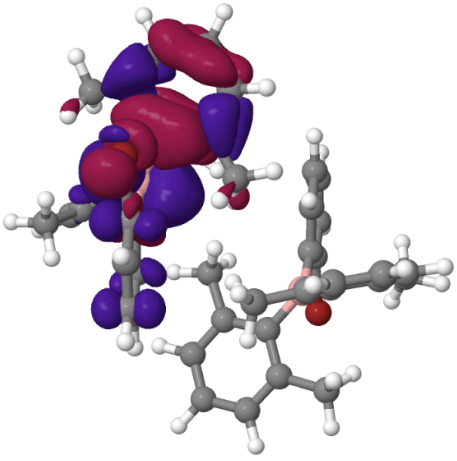

T_1^D @ T_1^D

Figure S16. Difference densities of the S_1^D and T_1^D states of the ***o*-BrTAB** dimer. For color codes, see above.

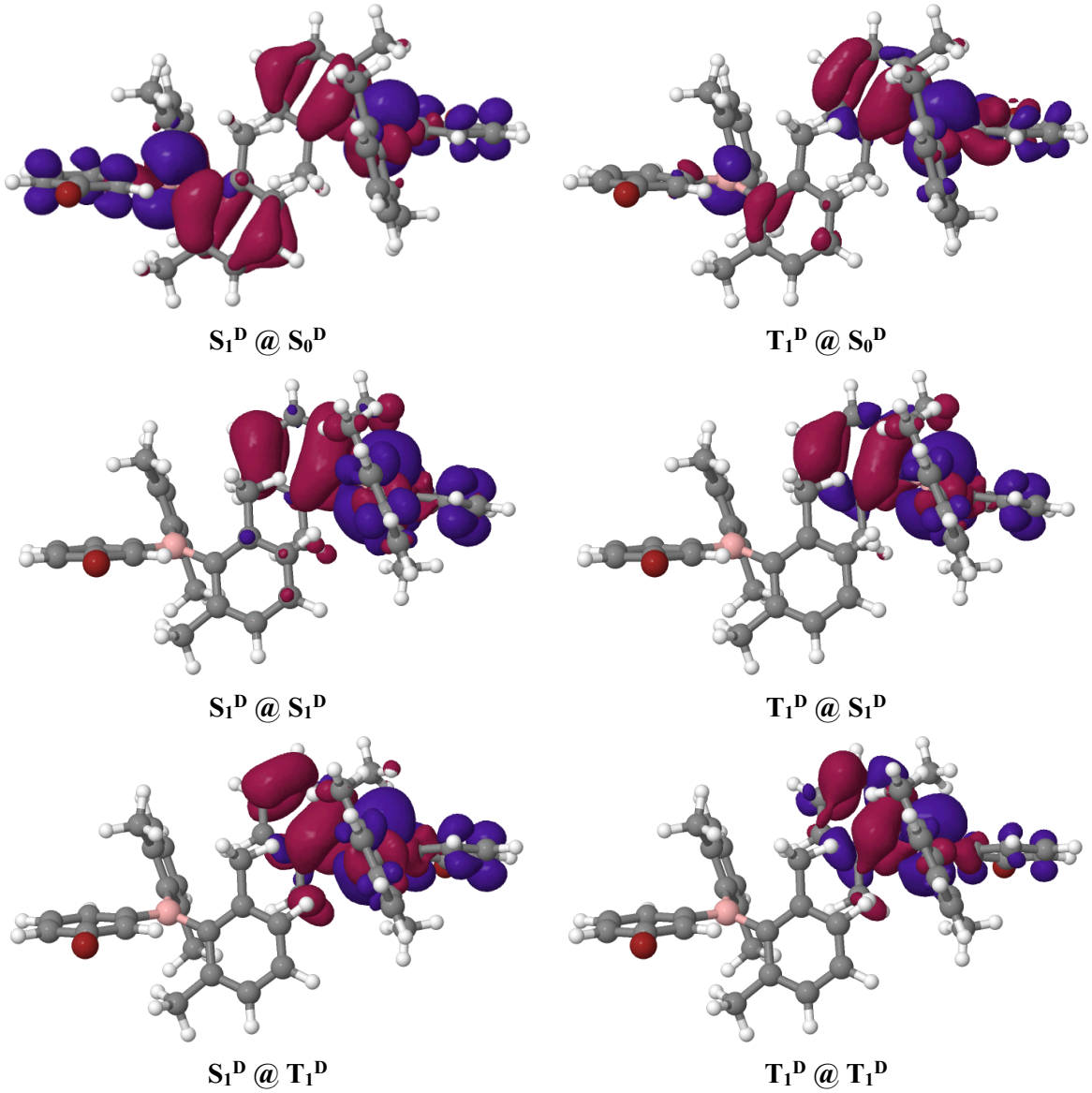

Figure S17. Difference densities of the S_1^D and T_1^D states of the ***m*-BrTAB** dimer. For color codes, see above.

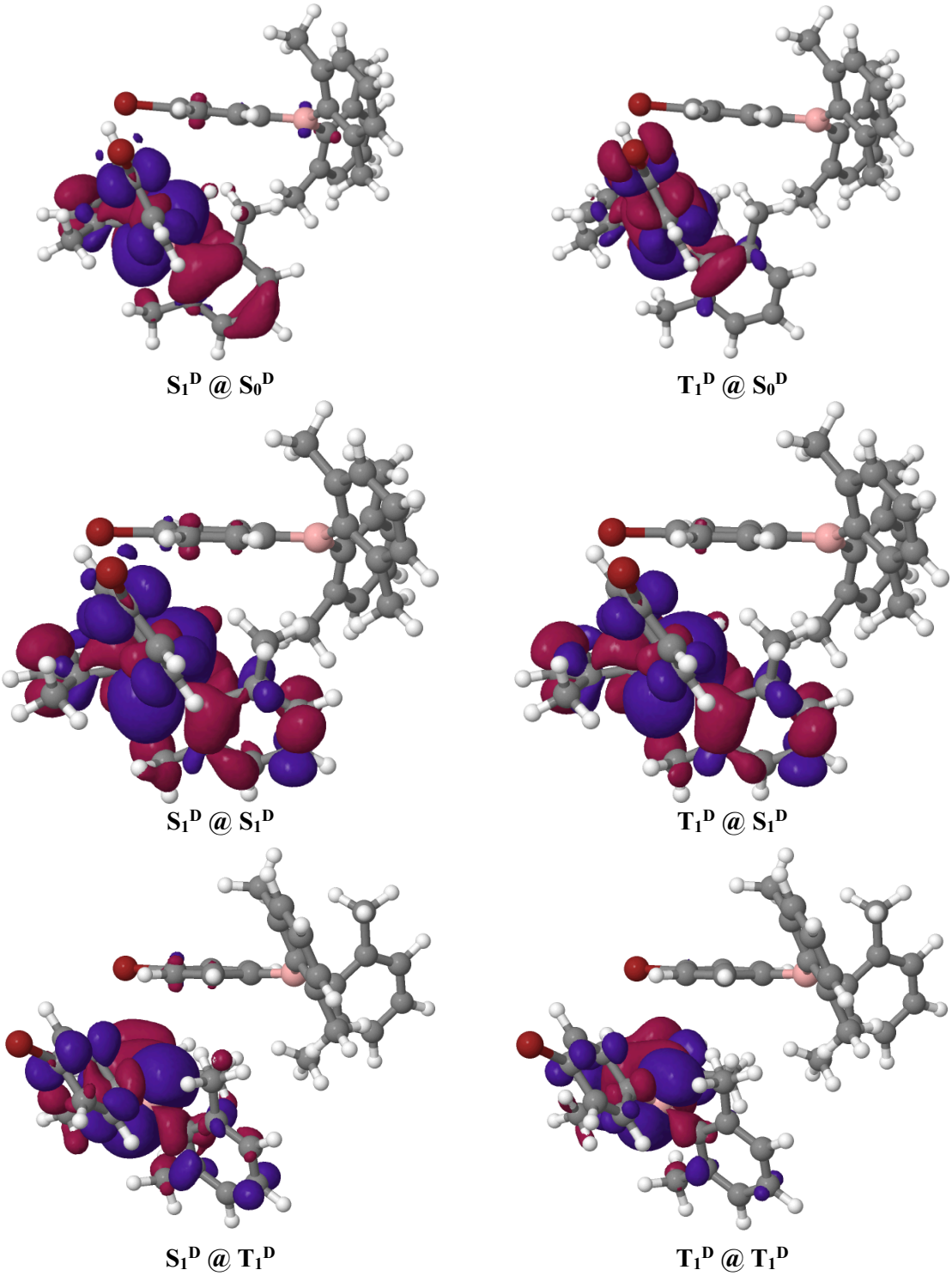

Figure S18. Difference densities of the S_1^D and T_1^D states of the ***p*-BrTAB** dimer. For color codes, see above.

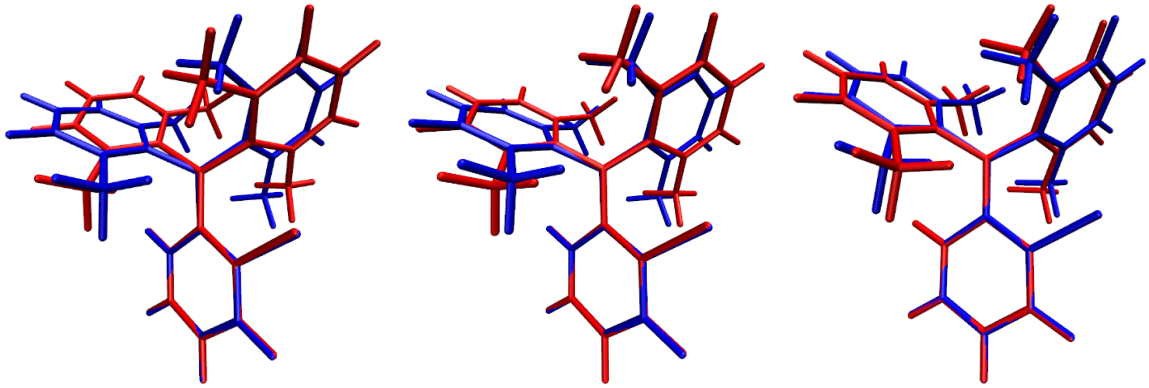

Figure S19. Structure overlays of ***o*-BrTAB**.

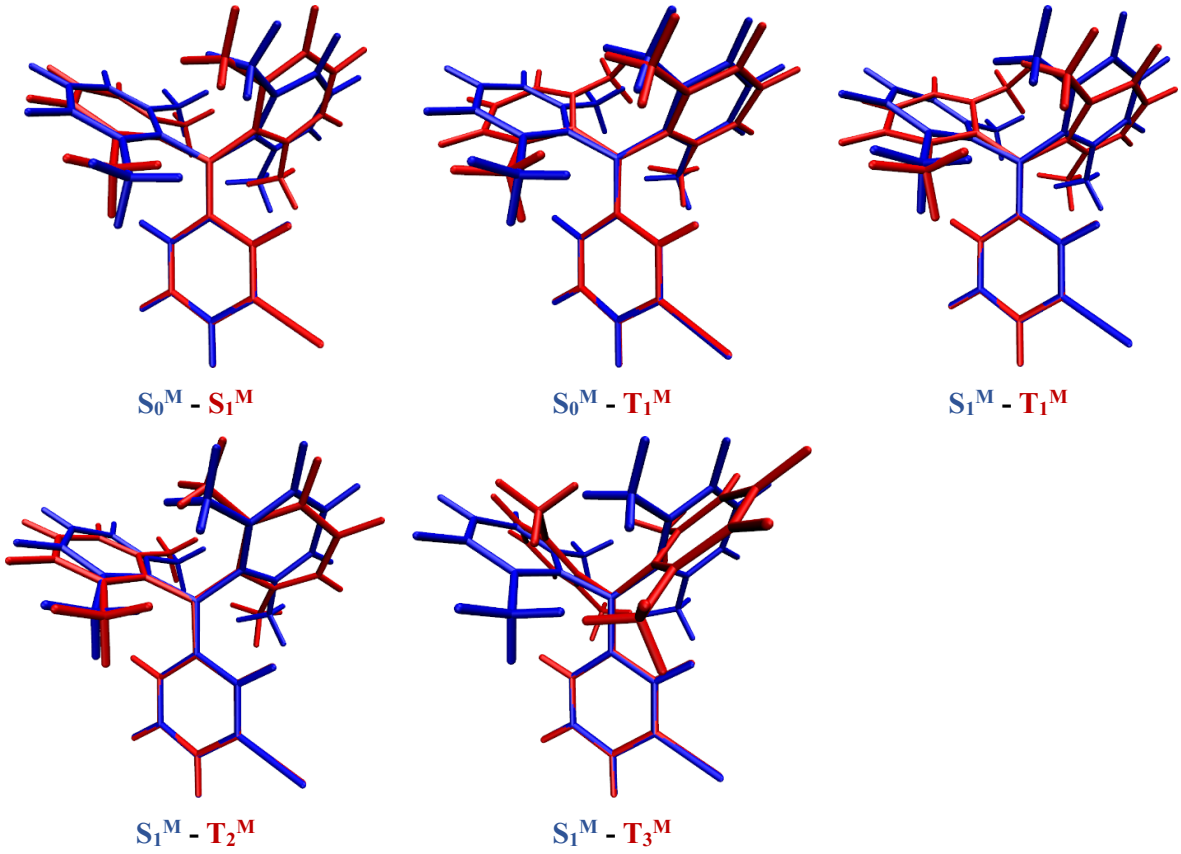

Figure S20. Structure overlays of ***m*-BrTAB**.

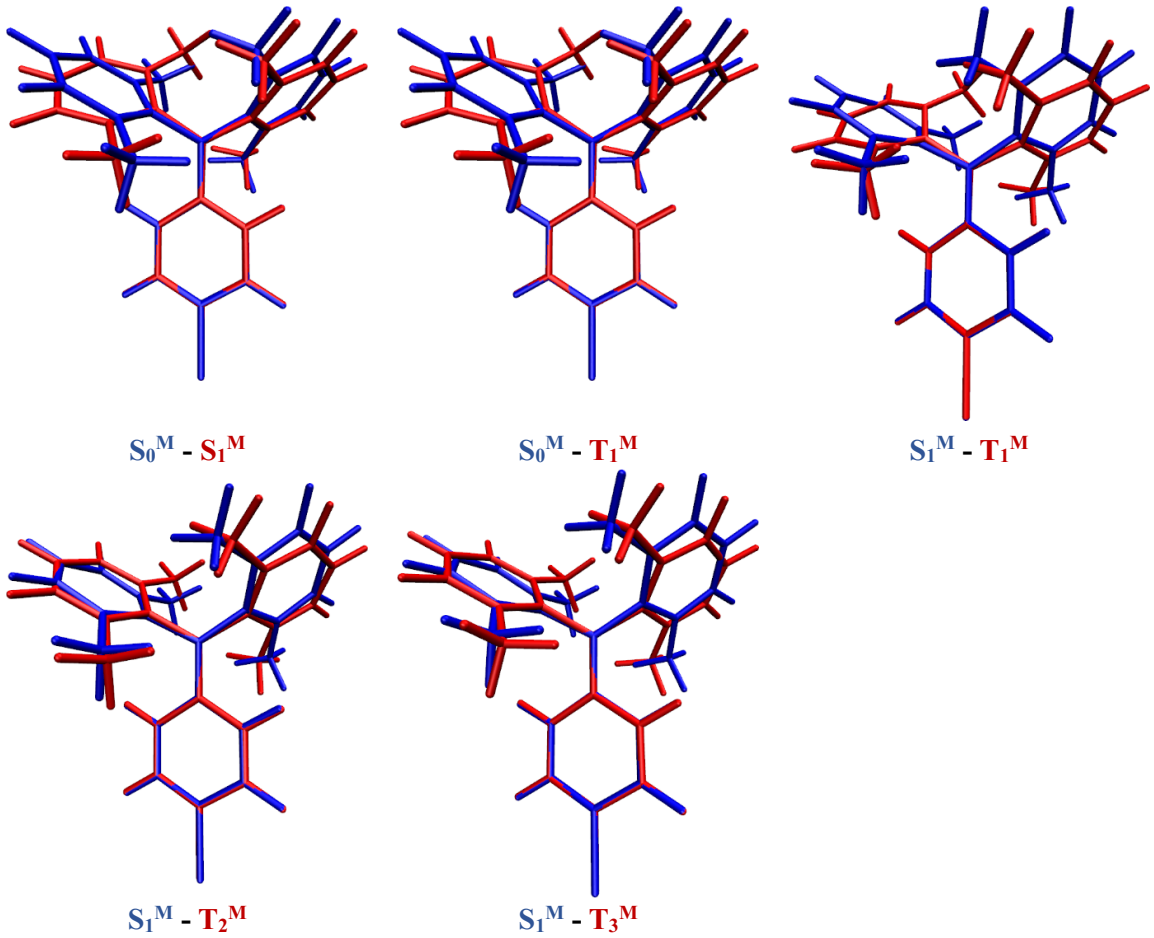

Figure S21. Structure overlays of ***p*-BrTAB**.

VI. Single-crystal X-ray diffraction

Table S9. Single-crystal X-ray diffraction data and structure refinements of ***o*-BrTAB**, ***m*-BrTAB** and ***p*-BrTAB** at 100 K.

Data	***o*-BrTAB**	***m*-BrTAB**	***p*-BrTAB**
CCDC number	2085814	2085815	2085816
Empirical formula	$C_{22}H_{22}BBr$	$C_{22}H_{22}BBr$	$C_{22}H_{22}BBr$
Formula weight / $g \cdot mol^{-1}$	377.11	377.11	377.11
T / K	100(2)	100(2)	100(2)
Radiation, λ / Å	Mo-Kα 0.71073	Mo-Kα 0.71073	Mo-Kα 0.71073
Crystal size / mm^3	0.42×0.29×0.22	0.34×0.21×0.09	0.32×0.30×0.25
Crystal color, habit	colorless block	colorless plate	colorless block
μ / mm^{-1}	2.235	2.230	2.213
Crystal system	Monoclinic	Triclinic	Monoclinic
Space group	$P2_1/n$	$P\ \bar{1}$	$C2/c$
a / Å	8.1374(6)	7.559(3)	21.837(7)
b / Å	12.0614(9)	8.296(3)	18.956(5)
c / Å	18.7609(14)	15.372(6)	17.946(8)
α / °	90	102.84(3)	90
β / °	93.027(2)	94.23(2)	90.31(4)
γ / °	90	99.364(18)	90
Volume / $Å^3$	1838.8(2)	921.3(6)	7429(5)
Z	4	2	16
ρ_{calc} / $g \cdot cm^{-3}$	1.362	1.359	1.349
F(000)	776	388	3104
θ range / °	2.008 - 27.481	2.562 - 29.575	2.149 - 29.574
Reflections collected	36785	25129	95509
Unique reflections	4221	5190	10416
Parameters / restraints	221 / 0	221 / 0	441 / 0
GooF on F^2	1.060	1.059	1.019
R_1 [I>2σ(I)]	0.0350	0.0422	0.0306
wR^2 (all data)	0.0973	0.1117	0.0776
Max. / min. residual electron density / $e \cdot Å^{-3}$	1.278 / –0.548	2.049 / –0.380	0.439 / –0.594

Table S10. Single-crystal X-ray diffraction data and structure refinements of ***o*-BrTAB**, ***m*-BrTAB** and ***p*-BrTAB** at ambient temperature.

Data	***o*-BrTAB**	***m*-BrTAB**	***p*-BrTAB**
CCDC number	2089473	2118234	2118235
Empirical formula	$C_{22}H_{22}BBr$	$C_{22}H_{22}BBr$	$C_{22}H_{22}BBr$
T / K	290(2)	296(2)	300(2)
Radiation, λ / Å	Mo-Kα 0.71073	Mo-Kα 0.71073	Mo-Kα 0.71073
Crystal size / mm³	0.10×0.22×0.31	0.33×0.28×0.07	0.37×0.32×0.20
Crystal color, habit	Colorless block	Colorless plate	Colorless block
μ / mm^{-1}	2.178	2.162	2.213
Crystal system	Monoclinic	Triclinic	Monoclinic
Space group	$P2_1/n$	$P\ \bar{1}$	$C2/c$
a / Å	8.200(6)	7.6560(17)	21.9758(5)
b / Å	12.164(6)	8.3568(9)	19.2403(5)
c / Å	18.944(8)	15.496(3)	18.2089(3)
α / °	90	102.709(10)	90
β / °	93.277(7)	94.76(3)	91.0120(10)
γ / °	90	98.290(19)	90
Volume / $Å^3$	1886.4(17)	950.3(3)	7697.9(3)
Z	4	2	16
ρ_{calc} / $g \cdot cm^{-3}$	1.328	1.318	1.302
F(000)	776	388	3104
θ range / °	1.991 - 26.372	1.357 – 26.370	2.394 – 26.371
Reflections collected	27916	25227	50647
Unique reflections	3859	3891	7870
Parameters / restraints	221 / 0	221 / 0	441 / 0
GooF on F^2	1.120	1.059	1.054
R_1 [I>2σ(I)]	0.0476	0.0489	0.0349
wR^2 (all data)	0.1197	0.1212	0.0990
Max. / min. residual electron density / $e \cdot Å^{-3}$	0.373 / –0.579	0.590 / –0.512	0.412 / –0.716

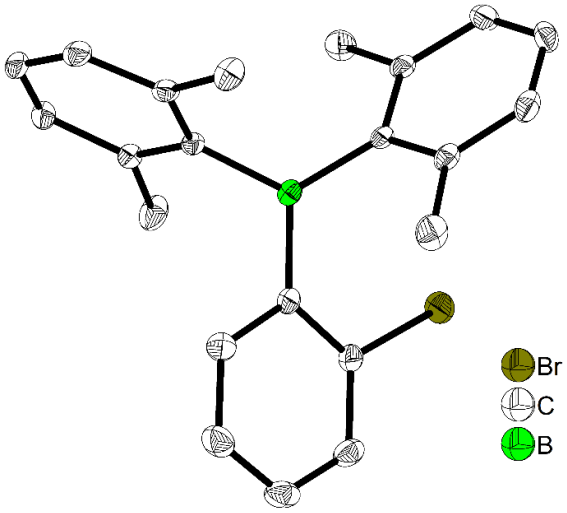

Figure S22. The solid-state molecular structure of ***o*-BrTAB** determined by single-crystal X-ray diffraction at 100 K. Ellipsoids are drawn at the 50% probability level, and H atoms are omitted for clarity.

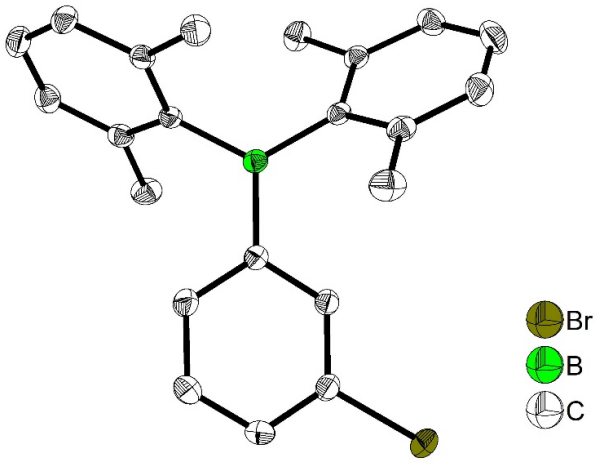

Figure S23. The solid-state molecular structure of ***m*-BrTAB** determined by single-crystal X-ray diffraction at 100 K. Ellipsoids are drawn at the 50% probability level, and H atoms are omitted for clarity.

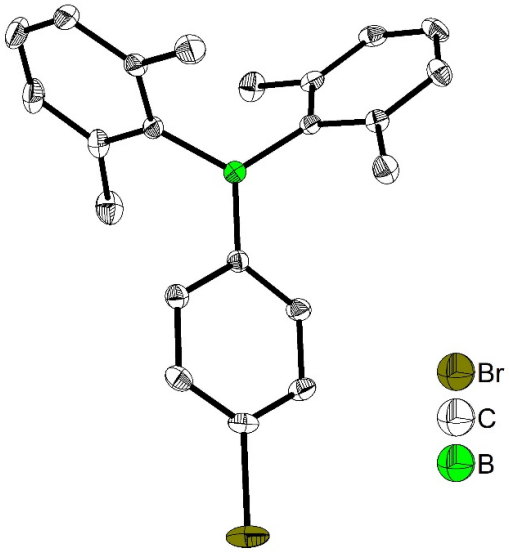

Figure S24. The solid-state molecular structure of ***p*-BrTAB** determined by single-crystal X-ray diffraction at 100 K. Ellipsoids are drawn at the 50% probability level, and H atoms are omitted for clarity. Only one of two non-symmetry-equivalent molecules is shown here.

Table S11. Selected bond lengths (Å), angles (°), and intramolecular contacts (Å) of ***o*-BrTAB**, ***m*-BrTAB** and ***p*-BrTAB** at 100 K. Aryl rings are numbered R1, R2, or R3 according to the C1, C7, or C15 atom being present and bonded to the boron atom, respectively.

	***o*-BrTAB**	***m*-BrTAB**	***p*-BrTAB**	
			Molecule 1	Molecule 2
C–Br	1.906(2)	1.899(2)	1.8982(16)	1.9007(17)
∠ C1–B–C15	121.38(18)	119.06(18)	119.58(14)	119.46(13)
∠ C1–B–C7	**116.28(18)**	118.00(18)	119.16(13)	122.29(13)
∠ C7–B–C15	122.15(19)	122.92(18)	121.26(13)	118.22(13)
Sum ∠ CBC	359.8(2)	360.0(2)	360.0(1)	360.0(1)
B–C1	1.578(3)	1.577(3)	**1.563(2)**	**1.561(2)**
B–C7	1.583(3)	1.579(3)	1.583(2)	1.585(2)
B–C15	1.574(3)	1.575(3)	1.581(2)	1.580(2)
∠ BC3 – aryl R1	38.61(9)	21.33(12)	20.06(8)	24.77(7)
∠ BC3 – aryl R2	61.02(6)	59.69(9)	63.38(7)	53.47(7)
∠ BC3 – aryl R3	55.21(9)	50.09(9)	57.88(7)	68.62(7)
∠ B–C1–C2	**127.2(2)**	121.18(18)	121.27(13)	122.85(14)
∠ B–C1–C6	**117.74(19)**	**117.47(19)**	121.34(14)	119.98(13)
∠ B–C15–C16	120.81(19)	121.33(18)	121.27(14)	120.93(14)
∠ B–C15–C20	120.93(19)	120.69(19)	120.78(14)	120.37(14)
∠ B–C7–C12	121.59(19)	121.47(18)	120.36(13)	120.77(13)
∠ B–C7–C8	119.71(19)	120.22(19)	120.88(14)	121.32(13)
Shortest B–Br contact	3.345(2)			
Shortest C15–Br contact	3.298(2)			

Table S12. Selected bond lengths (Å), angles (°), and intramolecular contacts (Å) of ***o*-BrTAB**, ***m*-BrTAB** and ***p*-BrTAB** at ambient temperature. Aryl rings are numbered R1, R2, or R3 according to the C1, C7, or C15 atom being present and bonded to the boron atom, respectively.

	***o*-BrTAB**	***m*-BrTAB**	***p*-BrTAB**	
T (K)	290(2)	296(2)	300(2)	
			Molecule 1	Molecule 2
C–Br	1.905(4)	1.896(3)	1.896(2)	1.899(2)
∠ C1–B–C15	121.3(4)	119.3(2)	119.35(18)	119.57(17)
∠ C1–B–C7	**116.1(3)**	117.4(3)	118.66(17)	121.78(17)
∠ C7–B–C15	122.4(3)	123.3(3)	121.99(18)	118.63(16)
Sum ∠ CBC	359.8(3)	360.0(3)	360.0(1)	360.0(2)
B–C1	1.578(5)	1.575(4)	**1.561(3)**	**1.560(3)**
B–C7	1.581(5)	1.584(4)	1.581(3)	1.587(3)
B–C15	**1.565(5)**	1.572(4)	1.583(3)	1.579(3)
∠ BC3 – aryl R1	39.27(2)	22.30(12)	22.15(8)	27.05(8)
∠ BC3 – aryl R2	60.38(1)	60.46(12)	63.22(8)	53.57(8)
∠ BC3 – aryl R3	54.78(2)	49.85(12)	57.06(8)	66.37(8)
∠ B–C1–C2	**127.2(3)**	121.5(3)	121.44(17)	122.74(17)
∠ B–C1–C6	**118.0(3)**	**117.4(3)**	121.83(17)	120.54(17)
∠ B–C15–C16	120.8(3)	121.3(3)	121.20(19)	120.93(18)
∠ B–C15–C20	121.6(3)	121.0(3)	120.83(18)	120.17(18)
∠ B–C7–C12	121.4(3)	121.3(3)	120.77(19)	121.04(17)
∠ B–C7–C8	120.2(3)	119.8(3)	120.5(2)	121.03(17)
Shortest B–Br contact	3.350(4)			
Shortest C15–Br contact	3.304(4)			

Table S13. Intermolecular C−H···C/Br, C···C/Br, and H···H interaction distances (Å) and angles (°) in ***o*-BrTAB**, ***m*-BrTAB** and ***p*-BrTAB** at 100 K.

Compound	C−H···C(Br)	H··· C(Br,H)	C···C(Br)	∠(CHC(Br))
***o*-BrTAB**	C4−H4···Br1	**3.1001(3)**	**3.354(2)**	97.16(15)
	C5−H5···C9	2.802(2)	3.618(3)	144.62(15)
	C19−H19···C3	2.802(2)	3.730(3)	165.82(15)
	C10−H10···C19	**2.753(2)**	3.488(3)	134.74(14)
	C17−H17···C10	2.800(2)	3.652(3)	149.78(15)
	C17−H17···C11	2.821(2)	3.768(3)	175.45(15)
	C14···C18 (methyl)		3.361(3)	
***m*-BrTAB**	C22(methyl)−H22B···C18	2.836(2)	3.676(4)	144.13(17)
	C9−H9···C16	2.861(2)	3.790(3)	166.26(15)
	C17−H17···C9	2.888(3)	3.699(4)	143.96(15)
	C14(methyl)−H14B···Br1	**2.9425(12)**	3.898(3)	165.05(14)
	C10−H10···Br1	**3.0346(13)**	3.736(3)	131.85(15)
***p*-BrTAB**	H11_1··· H11_1	2.3628(10)		
	H10_1··· H17_1	2.2659(5)		
	C2−H2_1···C4	2.8390(17)	3.752(2)	161.38(10)
	C3−H3···C9_1	2.821(2)	3.520(3)	131.16(11)
	C3−H3···C10_1	2.820(2)	3.686(3)	152.03(11)
	C9−H9···C16	2.8655(18)	3.783(3)	162.62(11)
	C13(methyl)−H13C_1···C17	2.8102(18)	3.653(3)	144.58(10)
	C3_1···Br1		**3.480(2)**	
	C14(methyl)−H14B_1···Br1	**2.9635(11)**	3.594(2)	123.11(10)

Table S14. Intermolecular C−H···C/Br, C···C/Br, and H···H interaction distances (Å) and angles (°) in ***o*-BrTAB**, ***m*-BrTAB** and ***p*-BrTAB** at ambient temperature. Significant intermolecular contacts as calculated below the sum of van der Waals radii using the Mercury program[24] are shown in black, while longer contacts, which do not play a significant role, are shown in bold for comparison with the close contacts at 100 K given in Table S13.

Compound	C−H···C(Br)	H··· C(Br,H)	C···C(Br)	∠(CHC(Br))
***o*-BrTAB 290(2) K**	C4−H4···Br1	3.1579(9)	**3.432(5)**	99.2(3)
	C5−H5···C9	**2.855(4)**	3.658(5)	145.3(2)
	C19−H19···C3	2.907(5)	3.809(6)	163.8(3)
	C10−H10···C19	**2.846(4)**	3.577(6)	136.4(2)
	C17−H17···C10	**2.873(4)**	3.709(6)	150.4(3)
	C17−H17···C11	**2.873(4)**	3.802(6)	177.2(3)
	C14···C18 (methyl)		3.426(6)	
***m*-BrTAB 296(2) K**	C22(methyl)−H22B···C18	2.981(4)	3.759(6)	139.0(3)
	C9−H9···C16	2.946(3)	3.858(4)	167.2(2)
	C17−H17···C9	2.980(3)	3.779(5)	144.9(2)
	C14(methyl)−H14B···Br1	**2.9857(8)**	3.927(3)	166.77(18)
	C10−H10···Br1	3.1583(6)	3.846(4)	132.3(3)
***p*-BrTAB 300(2) K**	H11_1··· H11_1	2.480(1)		
	H10_1··· H17_1	**2.393(1)**		
	C2−H2_1···C4	2.9083(19)	3.792(3)	159.20(14)
	C3−H3···C9_1	**2.887(2)**	3.585(3)	132.78(13)
	C3−H3···C10_1	2.913(2)	3.763(3)	152.60(13)
	C9−H9···C16	2.982(2)	3.879(4)	162.38(17)
	C9–H9···C17	2.935(2)	3.819(3)	159.24(16)
	C13(methyl)−H13C_1···C17	**2.870(2)**	3.699(3)	145.18(15)
	C3_1···Br1		3.611(3)	
	C14(methyl)−H14B_1···Br1	**2.9648(4)**	3.635(3)	127.98(15)

Table S15. Aryl···aryl (π···π) distances (Å) and angles (°) in crystals of ***m*-BrTAB** at 100 K and 296 K: nearest-neighbour (nn) C···C distances, centroid-centroid distances, interplanar separations, shifts, and slip angles. Aryl rings are numbered R1 or R3 according to the C1 or C15 atom being present and bonding to the boron atom, respectively.

Compound	Aryl···Aryl	nn C···C	Centroid-centroid distance	Interplanar separation	Shift	Slip angle
***m*-BrTAB 100 K**	R1···R1	3.698(5)	4.285(2)	3.640(3)	2.261(4)	31.8
	R3···R3	3.637(5)	4.951(3)	3.544(4)	3.457(4)	44.3
***m*-BrTAB 296 K**	R1···R1	3.871(8)	4.455(3)	3.812(4)	2.305(6)	31.2
	R3···R3	3.750(7)	5.034(3)	3.645(6)	3.473(6)	43.6

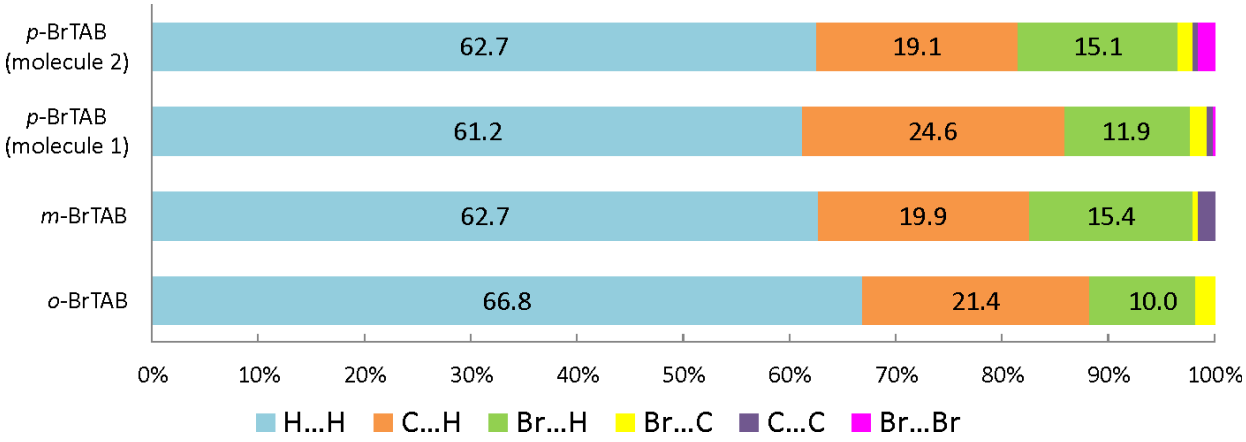

Figure. S25. Percentage contributions to the Hirshfeld surface area for the various close intermolecular contacts in ***o*-BrTAB**, ***m*-BrTAB**, and ***p*-BrTAB** at 100 K. In ***p*-BrTAB**, two symmetrically non-equivalent molecules are distinguished by slightly different contributions.

Table S16. Properties of crystals of ***o*-BrTAB**, ***m*-BrTAB** and ***p*-BrTAB** at ambient temperature and at 100 K: Volume of the molecule within van der Waals (V_m), Hirshfeld (V_H), and of the surface of the crystal voids (V_v), surface area of the molecule within van der Waals (SA_m), Hirshfeld (SA_H), and void surface area (SA_v), crystal packing coefficient (c_k), solvent accessible volume (V_{solv}), and percentage of intermolecular contacts. pfu…per formula unit; van der Waals radii used: C 1.7 Å, H: 1.09 Å, B: 2 Å, Br: 1.85 Å.

	***o*-BrTAB**		***m*-BrTAB**		***p*-BrTAB**			
T (K)	**290**	**100**	**296**	**100**	**Mol. 1 300 K**	**Mol. 2 300 K**	**Mol. 1 100 K**	**Mol. 2 100 K**
V_m / Å³	299.75	302.60	300.52	303.08	300.13	300.93	302.56	303.09
SA_m / Å²	344.28	347.42	345.67	348.27	346.83	346.31	350.12	348.78
V_H / Å³	464.68	452.75	467.53	453.02	472.65	474.25	455.65	457.64
SA_H / Å²	**367.41**	**364.05**	382.95	378.28	382.30	386.48	376.05	380.28
V_v / Å³	263.15	218.07	130.42	104.28	1174.41		912.57	
V_v / Å³ pfu	65.79	54.52	65.21	52.14	**73.40**		57.04	
SA_v / Å²	752.74	644.85	387.91	323.83	3275.62		2820.38	
SA_v / Å² pfu	**188.19**	161.21	193.96	161.92	204.73		176.27	
c_k	0.635	0.658	0.633	0.658	0.624		0.653	
V_{solv} / Å³	**31.9 (1.7%)**	0.0 (0%)	**41.9 (4.4%)**	16.2 (1.8%)	**209.2 (2.7%)**		39.3 (0.5%)	
Br···Br /%	0	0	0	0	0.3	1.8	0.2	1.6
Br···C / %	1.7	1.8	0.4	0.5	1.4	1.4	1.5	1.4
Br···H / %	10.2	10.0	15.6	15.4	12.1	15.5	11.9	15.1
C···C / %	0	0	**1.4**	**1.6**	0.4	0.4	0.6	0.5
C···H / %	20.4	21.4	18.9	19.9	23.5	18.1	24.6	19.1
H···H / %	**67.7**	**66.8**	63.6	62.7	62.4	62.8	61.2	62.3

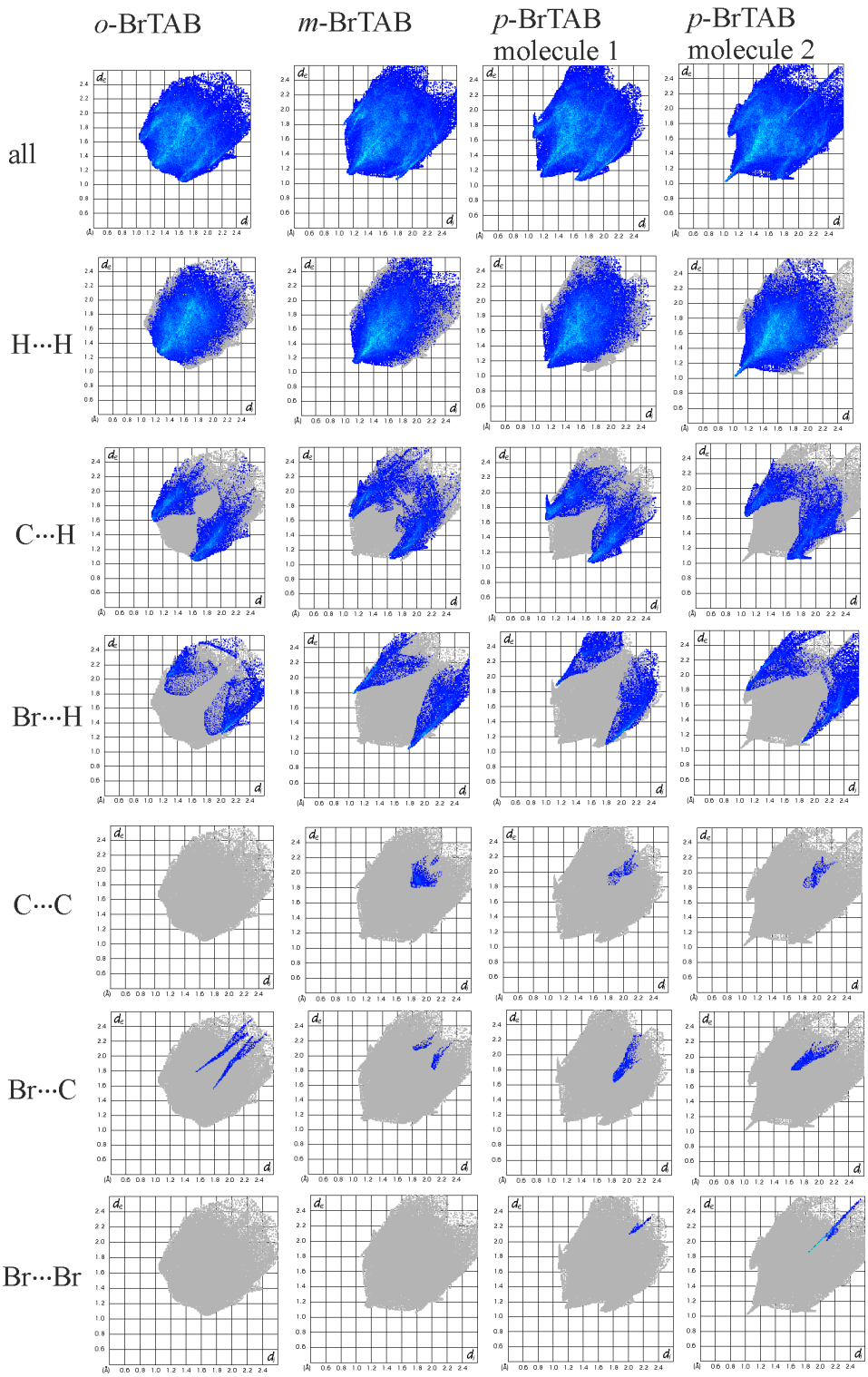

Figure S26. Two-dimensional fingerprint plots of molecules ***o*-BrTAB**, ***m*-BrTAB**, and ***p*-BrTAB** at 100 K calculated from the Hirshfeld surfaces. In ***p*-BrTAB**, two non-equivalent molecules are distinguished. The top row shows the complete fingerprint plots, while the other plots indicate the contributions of the individual intermolecular interactions (H···H, C···H, Br···H, C···C, Br···C, and Br···Br from top to bottom) within the grey area of all contributions.

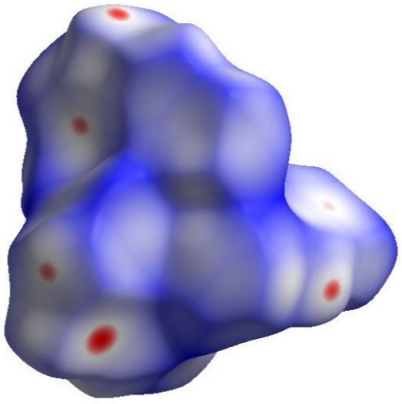

Figure S27. Hirshfeld surface of ***o*-BrTAB** at 100 K mapped with d_{norm} over the range -0.113 to 1.476. Close contacts are shown in red on the surface.

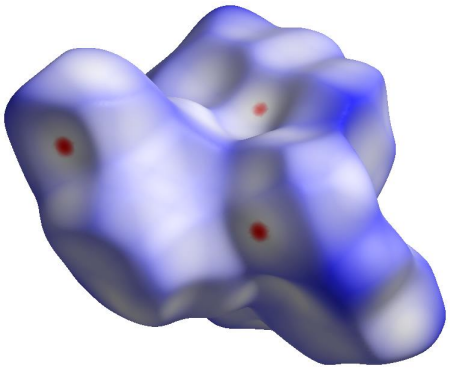

Figure S28. Hirshfeld surface of ***m*-BrTAB** at 100 K mapped with d_{norm} over the range -0.113 to 1.476. Close contacts are shown in red on the surface.

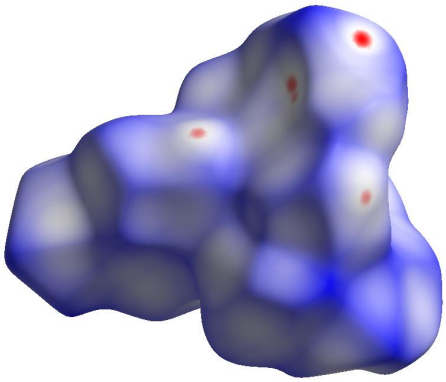

Figure S29. Hirshfeld surface of ***p*-BrTAB** at 100 K mapped with d_{norm} over the range -0.102 to 1.532. Close contacts are shown in red on the surface.

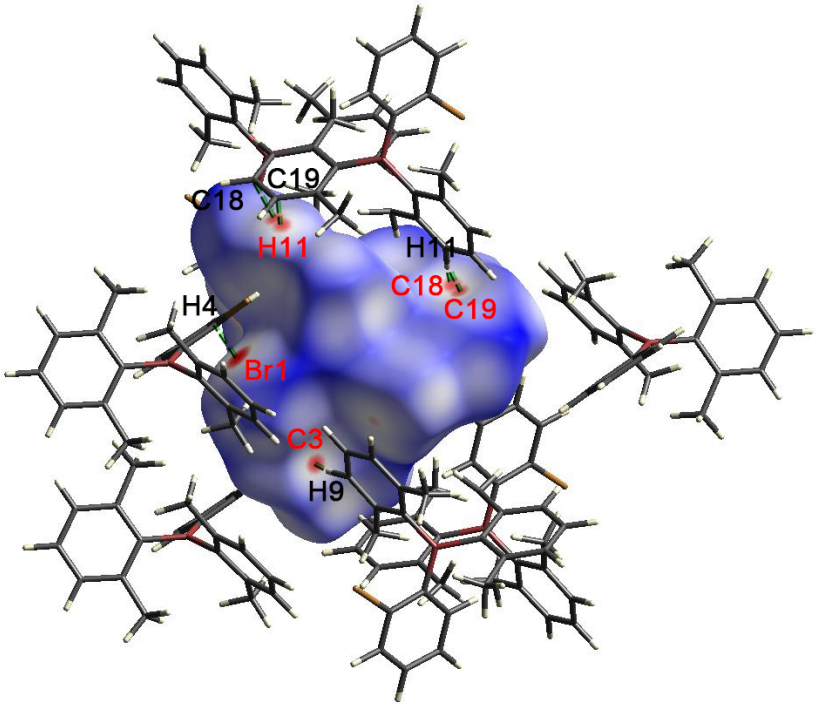

Figure S30. Hirshfeld surface of ***o*-BrTAB** mapped with d_{norm} over the range -0.113 to 1.476 at 100 K. Neighboring molecules associated with close contacts are shown.

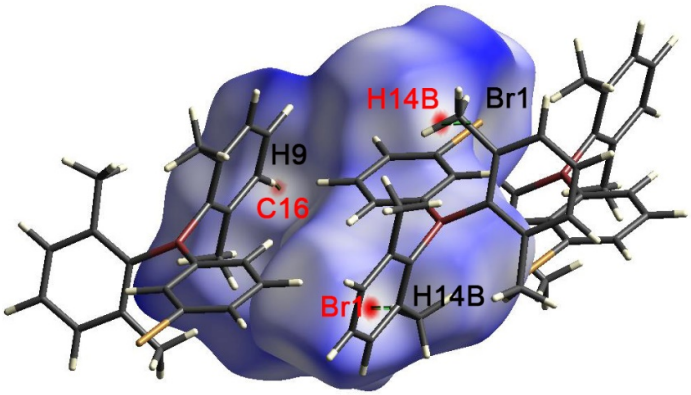

Figure S31. Hirshfeld surface of ***m*-BrTAB** mapped with d_{norm} over the range -0.113 to 1.476 at 100 K. Neighboring molecules associated with close contacts are shown.

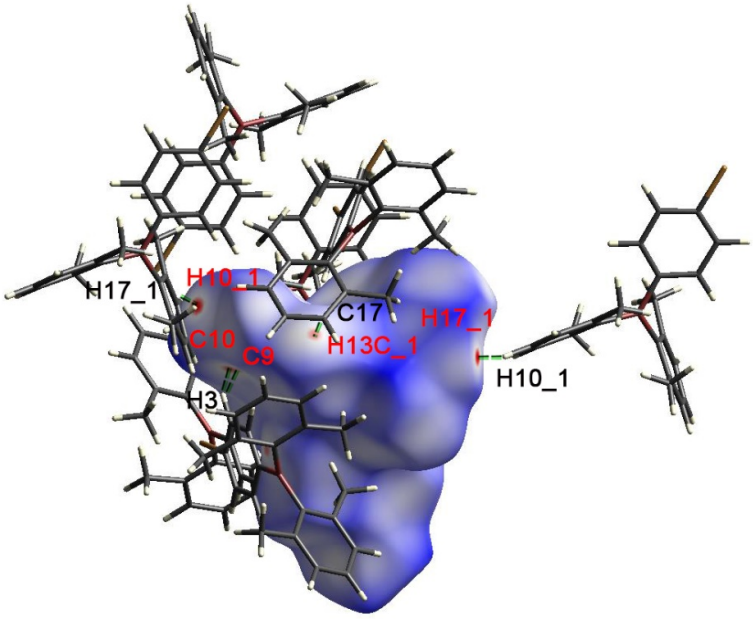

Figure S32. Hirshfeld surface of ***p*-BrTAB** mapped with d_{norm} over the range -0.102 to 1.532 at 100 K. Neighboring molecules associated with close contacts are shown.

VII. ^{1}H, ^{13}C, ^{11}B, GC-MS and HRMS spectra

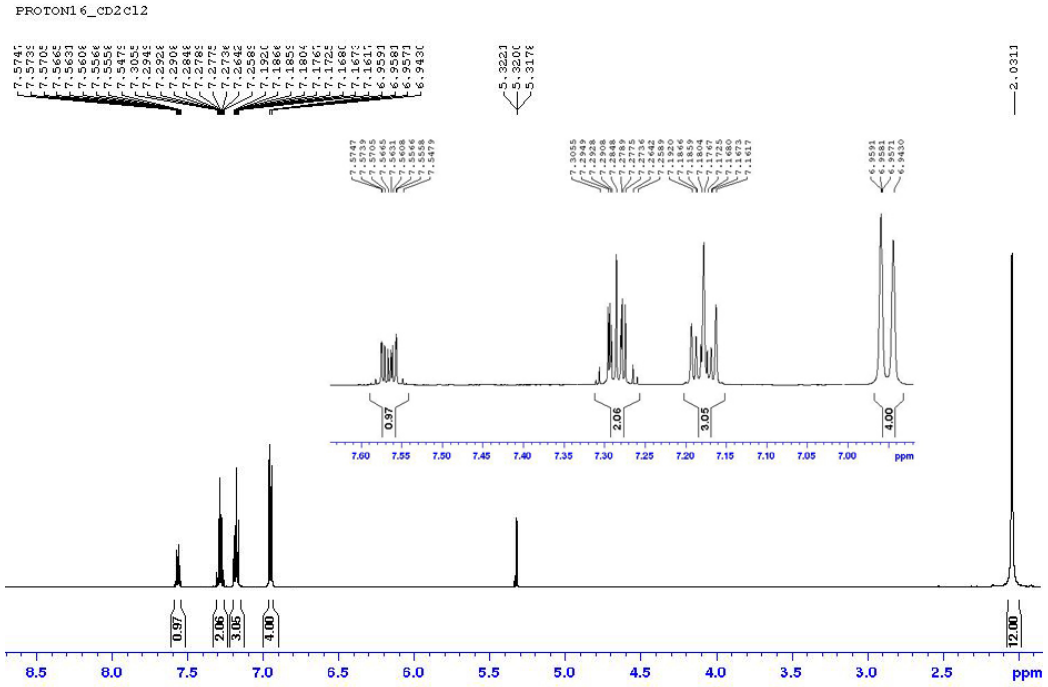

Figure S33. ^{1}H NMR spectrum (500 MHz, CD_2Cl_2) of ***o*-BrTAB**.

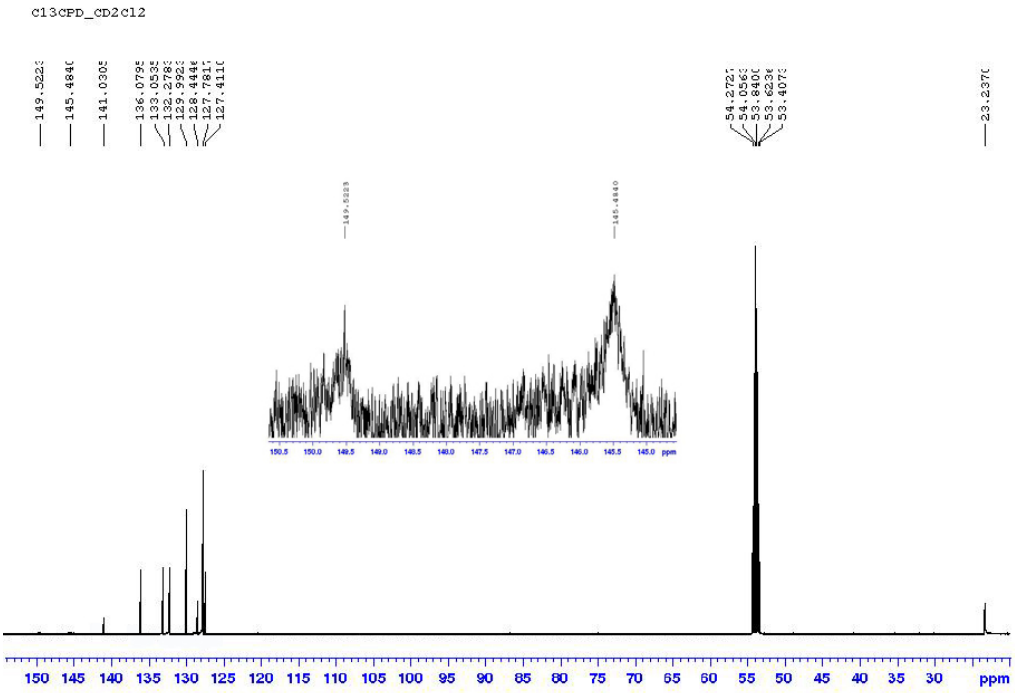

Figure S34. $^{13}C\{^{1}H\}$ NMR spectrum (126 MHz, CD_2Cl_2) of ***o*-BrTAB**.

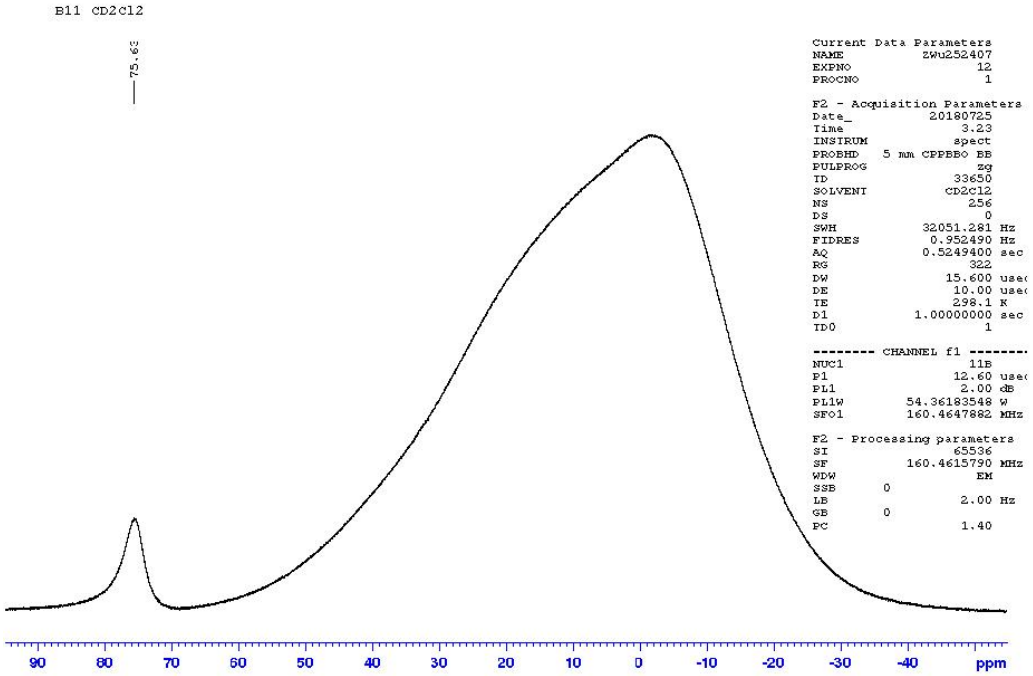

Figure S35. ^{11}B NMR spectrum (160 MHz, CD_2Cl_2) of ***o*-BrTAB**.

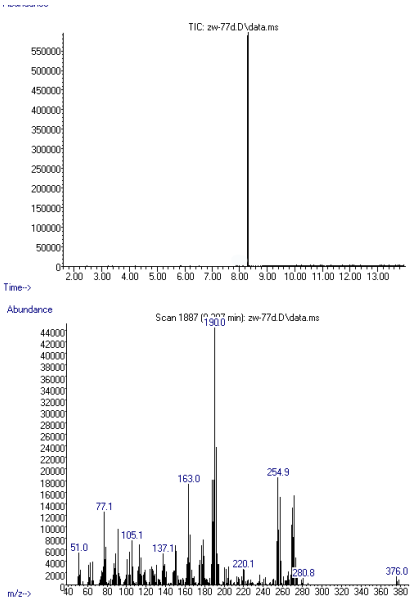

Figure S36. GC-MS total ion chromatogram^{TIC} and MS $(EI)_{m/z}$ of ***o*-BrTAB**.

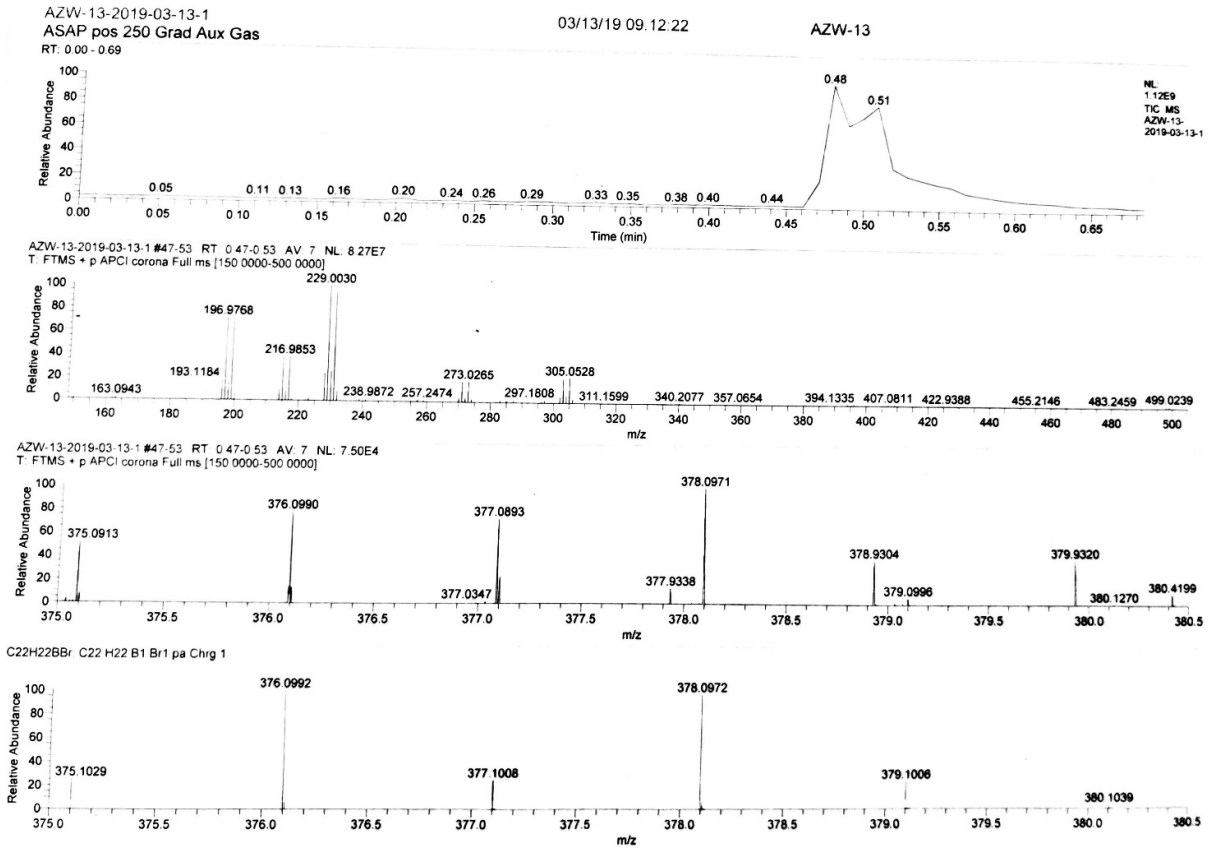

Figure S37. HR-ESI-MS spectrum of ***o*-BrTAB**.

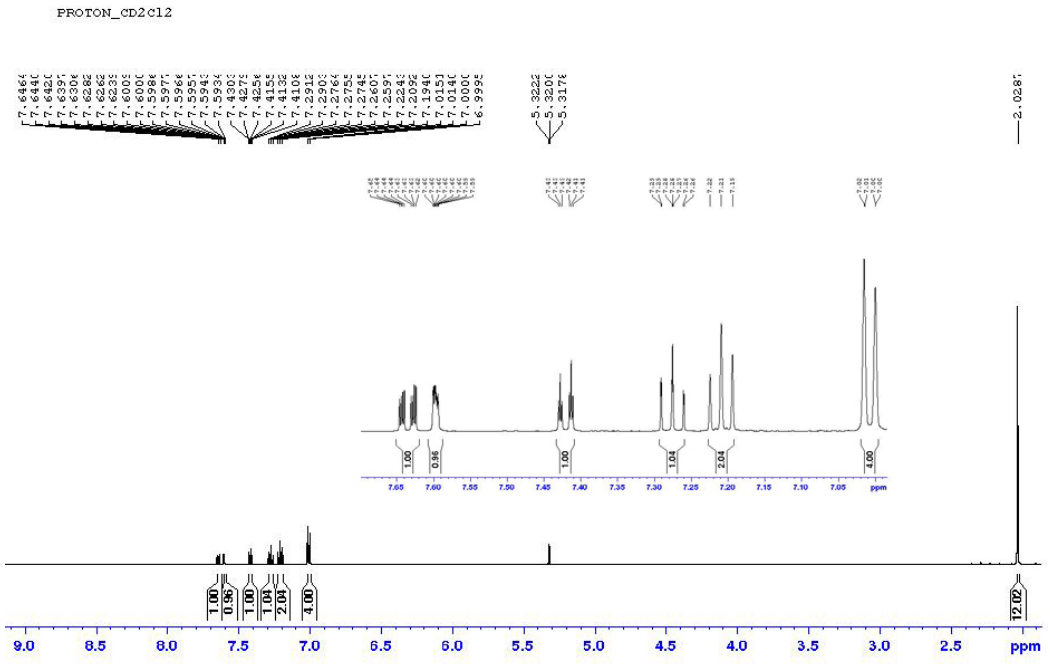

Figure S38. ^{1}H NMR spectrum (500 MHz, CD_2Cl_2) of ***m*-BrTAB**.

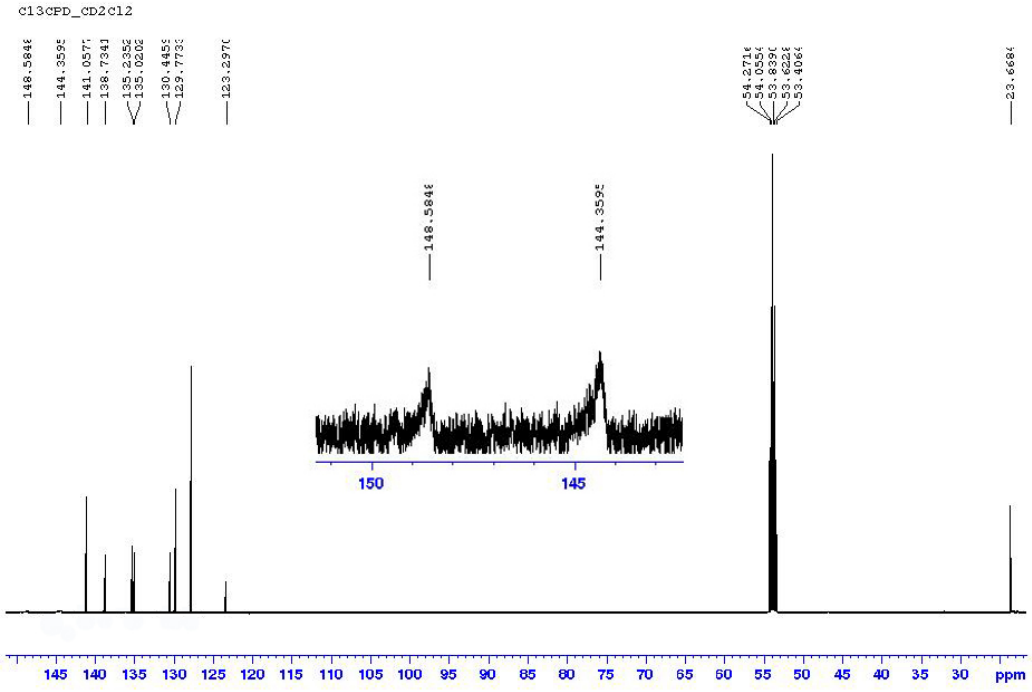

Figure S39. $^{13}C\{^{1}H\}$ NMR spectrum (126 MHz, CD_2Cl_2) of ***m*-BrTAB**.

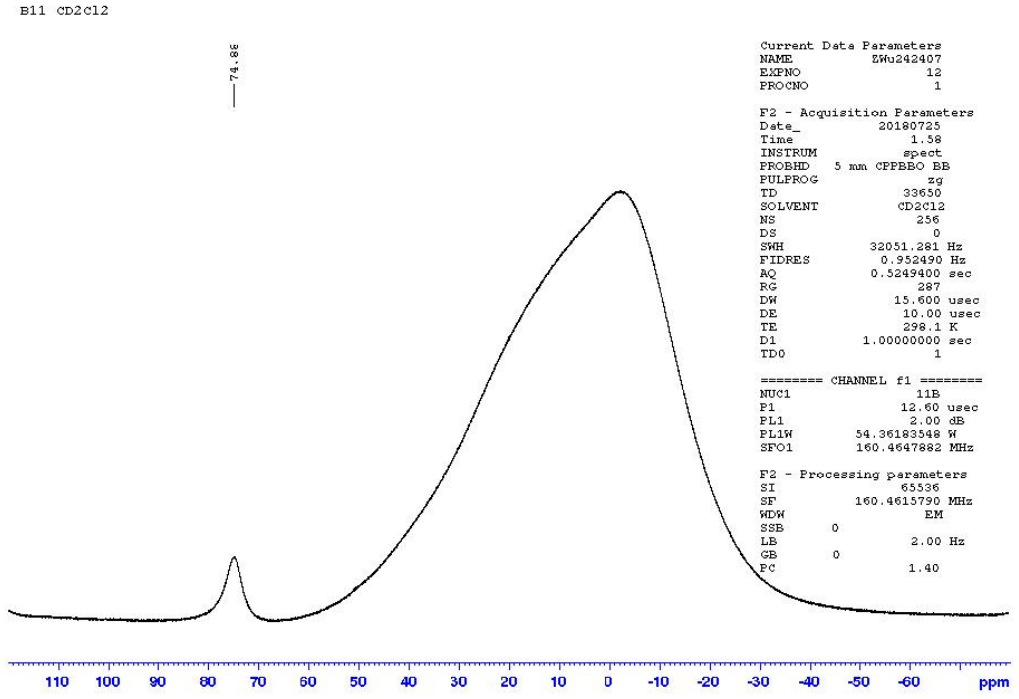

Figure S40. ^{11}B NMR spectrum (160 MHz, CD_2Cl_2) of ***m*-BrTAB**.

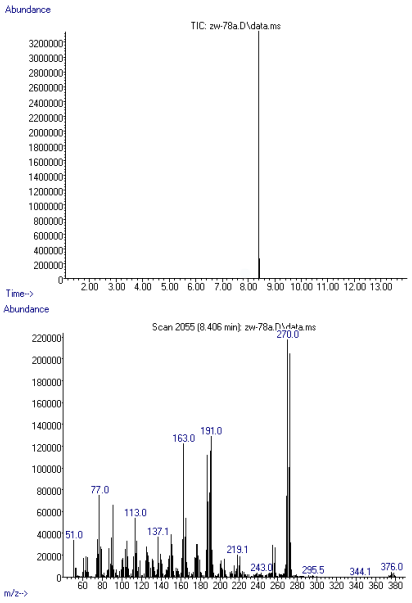

Figure S41. GC-MS total ion chromatogram^{TIC} and MS $(EI)_{m/z}$ of ***m*-BrTAB**.

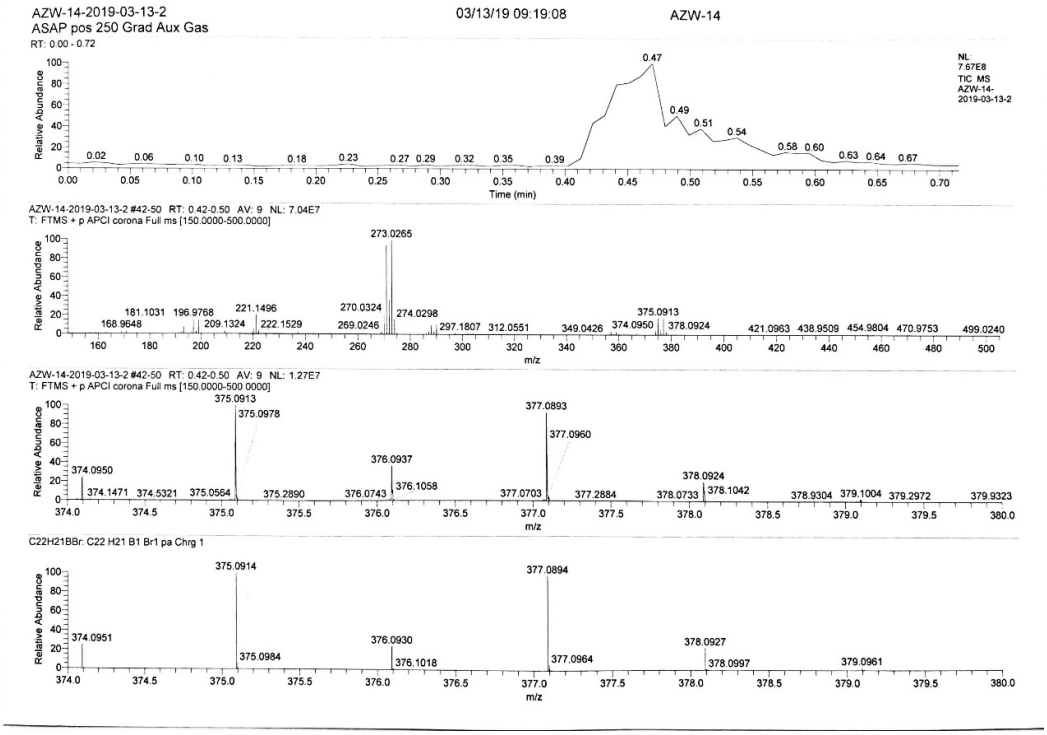

Figure S42. HR-ESI-MS spectrum of ***m*-BrTAB**.

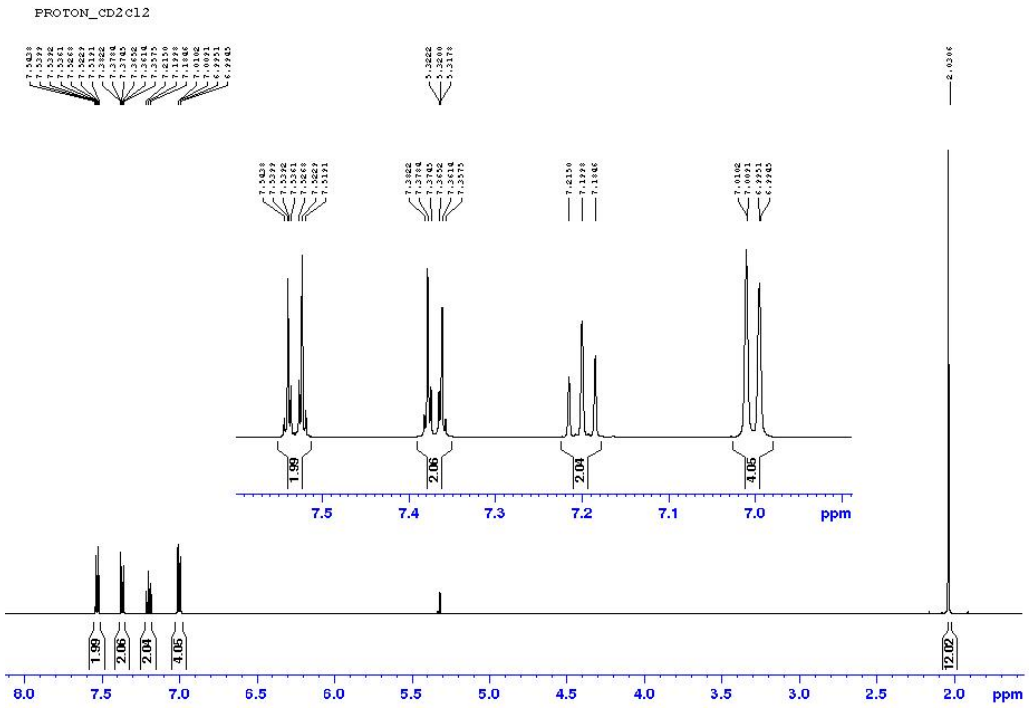

Figure S43. ^{1}H NMR spectrum (500 MHz, CD_2Cl_2) of ***p*-BrTAB**.

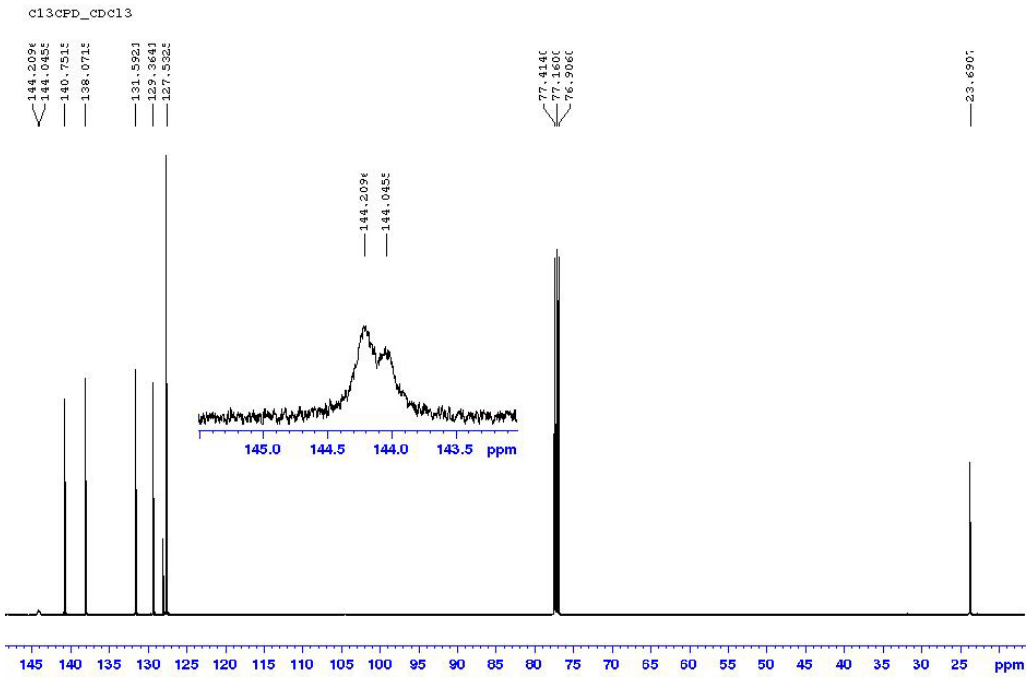

Figure S44. $^{13}C\{^{1}H\}$ NMR spectrum (126 MHz, $CDCl_3$) of ***p*-BrTAB**.

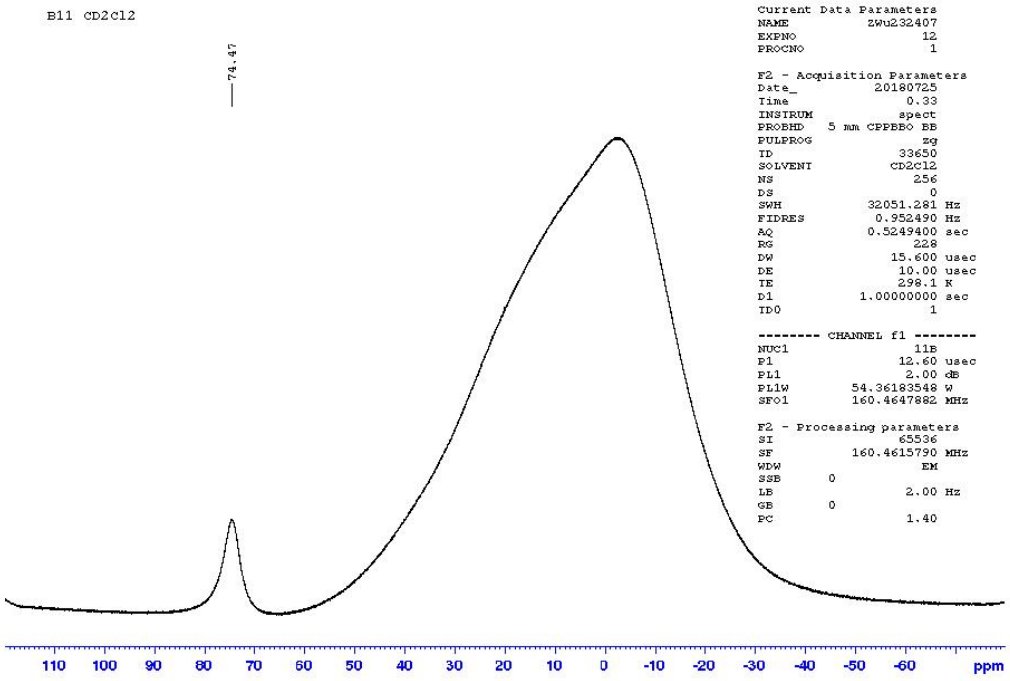

Figure S45. ^{11}B NMR spectrum (160 MHz, CD_2Cl_2) of ***p*-BrTAB**.

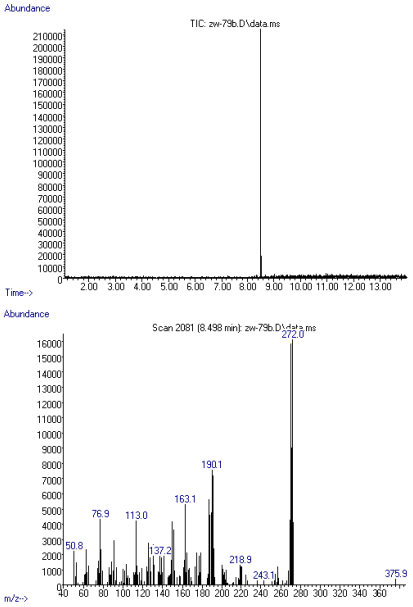

Figure S46. GC-MS total ion chromatogram^{TIC} and MS $(EI)_{m/z}$ of ***p*-BrTAB**.

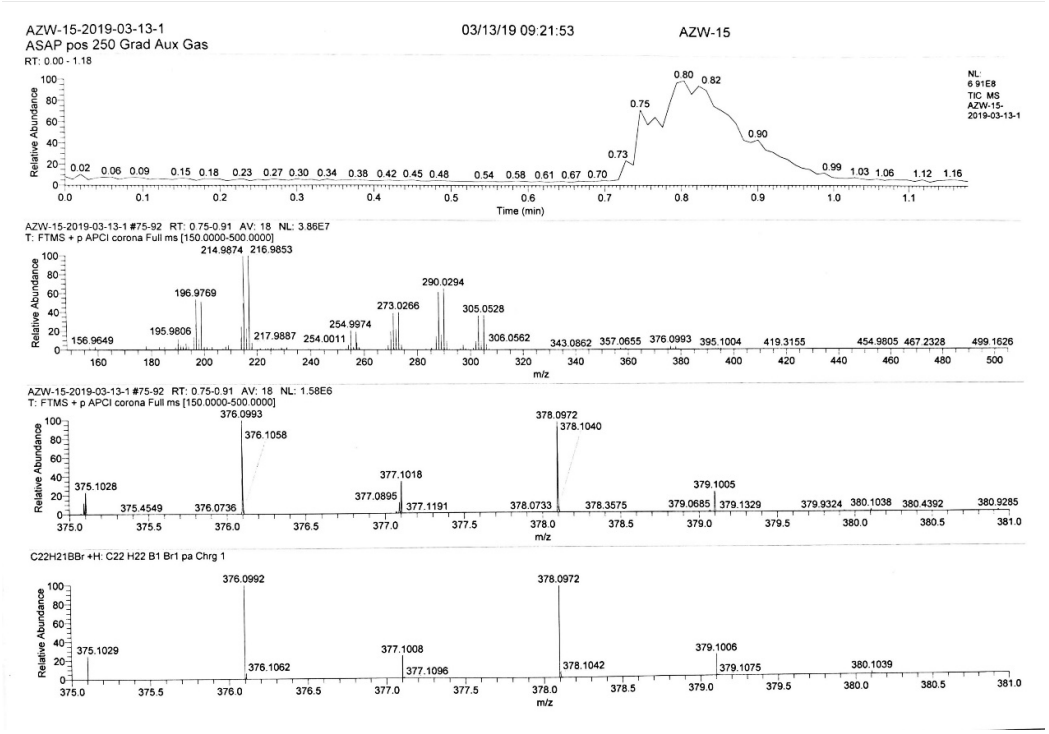

Figure S47. HR-ESI-MS spectrum of ***p*-BrTAB**.

VIII. References

[1] B. H. Toby, *J. Appl. Crystallogr.* **2005**, *38*, 1040-1041.

[2] A. C. Larson, R. B. Von Dreele, Los Alamos National Laboratory Report LAUR, **2004**, pp. 86-748.

[3] TURBOMOLE V7.0 2015, A development of University of Karlsruhe and Forschungszentrum Karlsruhe GmbH, 1989-2007, TURBOMOLE GmbH, since 2007, available from http://www.turbomole.com.

[4] Gaussian 98 g09, Revision E.01, M. J. Frisch, G. W. Trucks, H. B. Schlegel, G. E. Scuseria, M. A. Robb, J. R. Cheeseman, G. Scalmani, V. Barone, B. Mennucci, G. A. Petersson, H. Nakatsuji, M. Caricato, X. Li, H. P. Hratchian, A. F. Izmaylov, J. Bloino, G. Zheng, J. L. Sonnenberg, M. Hada, M. Ehara, K. Toyota, R. Fukuda, J. Hasegawa, M. Ishida, T. Nakajima, Y. Honda, O. Kitao, H. Nakai, T. Vreven, J. A. Montgomery, Jr., J. E. Peralta, F. Ogliaro, M. Bearpark, J. J. Heyd, E. Brothers, K. N. Kudin, V. N. Staroverov, T. Keith, R. Kobayashi, J. Normand, K. Raghavachari, A. Rendell, J. C. Burant, S. S. Iyengar, J. Tomasi, M. Cossi, N. Rega, J. M. Millam, M. Klene, J. E. Knox, J. B. Cross, V. Bakken, C. Adamo, J. Jaramillo, R. Gomperts, R. E. Stratmann, O. Yazyev, A. J. Austin, R. Cammi, C. Pomelli, J. W. Ochterski, R. L. Martin, K. Morokuma, V. G. Zakrzewski, G. A. Voth, P. Salvador, J. J. Dannenberg, S. Dapprich, A. D. Daniels, O. Farkas, J. B. Foresman, J. V. Ortiz, J. Cioslowski, and D. J. Fox, Gaussian, Inc., Wallingford CT, 2013.

[5] J. P. Perdew, M. Ernzerhof and K. Burke, *J. Chem. Phys*. **1996**, *105*, 9982–9985.

[6] J. P. Perdew, K. Burke and M. Ernzerhof, *Phys. Rev. Lett*. **1996**, *77*, 3865–3868.

[7] C. Adamo and V. Barone, *J. Chem. Phys*. **1999**, *110*, 6158–6170.

[8] K. Eichkorn, F. Weigend, O. Treutler, R. Ahlrichs, *Theor. Chem. Acc.,* **1997**, 97, 119.

[9] K.A. Peterson, D. Figgen, E. Goll, H. Stoll and M. Dolg, *J. Chem. Phys.*, **2003**, 119, 11113.

[10] S. Grimme, Mirko Waletzke, J. Chem. Phys. **1999**, 111, 5645-5655.

[11] C. M. Marian, A. Heil and M. Kleinschmidt, *WIREs Comput. Mol. Sci*. **2019**, 9, e1394.

[12] I. Lyskov*,* M. Kleinschmidt*,* C. M. Marian, *J. Chem., Phys.*, **2016**, 144, 034104

[13] A. D. Becke, *J. Chem. Phys.*, **1993**, 98, 1372.

[14] C. Lee, W. Yang, and R. G. Parr, *Phys. Rev. B* **1988**, 37, 785.

[15] M. Kleinscmidt, J. Tatchen and C. M. Marian, *J. Chem. Phys*. **2006**, *124*, 124101.

[16] M. Kleinschmidt and C. M. Marian, *Chem. Phys*. **2005**, *311*, 71-79.

[17] M. Kleinschmidt, J. Tatchen and C. M. Marian, *J. Comput. Chem*. **2002**, *23*, 824-833.

[18] M. Etinski, J. Tatchen and C. M. Marian, *J. Chem. Phys*. **2011**, *134*, 154105.

[19] M. Etinski, J. Tatchen and C. M. Marian, *Phys. Chem. Chem. Phys*. **2014**, *16*, 4740-4751.

[20] G. M. Sheldrick, *Acta Crystallogr. A Found Adv.* **2015**, *71*, 3-8.

[21] G. M. Sheldrick, *Acta Crystallogr. A* **2008**, *64*, 112-122.

[22] C. B. Hübschle, G. M. Sheldrick, B. Dittrich, *J. Appl. Crystallogr.* **2011**, *44*, 1281-1284.

[23] K. D. Brandenburg, Crystal and Molecular Structure Visualization, Crystal Impact, H. Putz & K. Brandenburg GbR, Bonn (Germany), 2017.

[24] C. F. Macrae, I. J. Bruno, J. A. Chisholm, P. R. Edgington, P. McCabe, E. Pidcock, L. Rodriguez-Monge, R. Taylor, J. van de Streek, P. A. Wood, *J. Appl. Crystallogr.* **2008**, *41*, 466-470.

[25] O. V. Dolomanov, L. J. Bourhis, R. J. Gildea, J. A. K. Howard, H. Puschmann, *J. Appl. Crystallogr.* **2009**, *42*, 339-341.

[26] P. R. Spackman, M. J. Turner, J. J. McKinnon, S. K. Wolff, D. J. Grimwood, D. Jayatilaka, M. A. Spackman, CrystalExplorer21 (2021), University of Western Australia, http://crystalexplorer.net.

[27] Y. A. Cho, D. S. Kim, H. R. Ahn, B. Canturk, G. A. Molander, J. Ham, *Org. Lett*. **2009**, *11*, 4330-4333.

[28] a) M. Ferger, S. M. Berger, F. Rauch, M. Schonitz, J. Ruhe, J. Krebs, A. Friedrich, T. B. Marder, *Chem. Eur. J*. **2021**,

27, 9094-9101; b) Z. Wu, J. Nitsch, J. Schuster, A. Friedrich, K. Edkins, M. Loebnitz, F. Dinkelbach, V. Stepanenko, F. Würthner, C. M. Marian, L. Ji, T. B. Marder, *Angew. Chem. Int. Ed*. **2020**, *59*, 17137-17144.

Journal of the Serbian Chemical Society
JSCS-info@shd.org.rs • www.shd.org.rs/JSCS
J. Serb. Chem. Soc. *84* (8) 819–836 (2019)
JSCS–5227
UDC 547.861+533.6.013.7:532.14+547.556.31
Original scientific paper

Vibronic and spin–orbit coupling effects in the absorption spectra of pyrazine: A quantum chemical approach

FABIAN DINKELBACH and CHRISTEL M. MARIAN*

Institute of Theoretical and Computational Chemistry, Heinrich-Heine-University Düsseldorf, Universitätsstraße 1, 40225 Düsseldorf, Germany

(Received 10 May, accepted 20 May 2019)

Abstract: Derivatives of dipole transition moments between spin–orbit coupled (SOC) multireference configuration interaction wave functions have been used in conjunction with vibrational frequencies from density functional theories to compute vibronic $S_1 \leftarrow S_0$ ($1^1B_{3u} \leftarrow 1^1A_g$) and $T_1 \leftarrow S_0$ ($1^3B_{3u} \leftarrow 1^1A_g$) absorption spectra in Herzberg–Teller approximation. The experimentally known spectra are well reproduced. The calculations reveal unexpectedly small spin–orbit couplings between the 1^3B_{3u} ($^3n\pi^*$) state and nearby optically bright $^1B_{2u}$ ($^1\pi\pi^*$) states, thus explaining the absence of the $1b_{1g}{}^1_0$ ($\nu_{10a}{}^1_0$) fundamental in the vibrational fine-structure of the $T_1 \leftarrow S_0$ transition. Adiabatically, two triplet states are found below the S_1 state. The out-of-plane distorted T_2 minimum results from a pseudo Jahn–Teller interaction between two $^3\pi\pi^*$ states of B_{1u} and B_{2u} symmetry. At the D_{2h}-symmetric S_0 and S_1 minimum geometries, the latter states are located well above S_1. The S_1 and T_2 potentials intersect at geometries far away from the Franck–Condon region. This explains the apparently contradictory results that the linewidth in the higher energy regime above the $T_1 \leftarrow S_0$ origin suddenly broadens while no trace of a second triplet state, located energetically below the S_1 origin, could be identified in phosphorescence excitation spectra of the ultracold isolated pyrazine molecule.

Keywords: density functional theory; multireference configuration interaction; Herzberg–Teller coupling; singlet–triplet transitions; azabenzenes.

INTRODUCTION

Pyrazine (1,4-diazabenzene) is a prominent example where it has been proven necessary to go beyond the Franck–Condon approximation for understanding the intensity distribution in the $S_1 \leftarrow S_0$ absorption spectrum. Its first excited singlet state is of $n\pi^*$ type and known to borrow the intensity from higher-lying optically bright $\pi\pi^*$ states by vibronic coupling *via* the ν_{10a} (b_{1g}) and ν_5 (b_{2g}) vibrational modes. A comprehensive review of the experimental and theoretical knowledge on its vibronic spectra as of 1988 has been presented by Innes *et al.*[1]

* Corresponding author. E-mail: Christel.Marian@hhu.de
https://doi.org/10.2298/JSC190510048D

For the corresponding singlet–triplet absorption, similar vibronic activity might be expected as the vibrational frequencies in the first excited triplet state closely resemble those of S_1.[2] In contrast to the $S_1 \leftarrow S_0$ absorption, the $T_1 \leftarrow S_0$ phosphorescence excitation spectrum in a supersonic jet shows no evidence of strong vibronic coupling. Tomer *et al.*[3] report that the fundamental ν_{10a}^1 and ν_{50}^1 transitions are absent in the $T_1 \leftarrow S_0$ spectrum. Instead, the overtones of ν_{10a} are seen in phosphorescence excitation spectra of neat crystals.[1] Another intriguing experimental result concerns the question whether one or two triplet states are located below S_1. Hochstrasser and Marzzacco[4] observed a sudden increase of bandwidth from 1 to 15 cm^{-1} in the singlet–triplet absorption spectrum of pyrazine crystals at 4.2 K, about 1600 cm^{-1} above the origin transition. Methylation of pyrazine in 2- and 6-positions lowers this threshold to about 50 cm^{-1} while tetramethylpyrazine shows only a diffuse spectrum. These results were interpreted as a manifestation of a perturbation on the $^3n\pi^*$ state by a $^3\pi\pi^*$ state that is located below the first excited singlet state and has some negligible electric dipole oscillator strength.[4] Resonance-enhanced multi-photon ionization experiments in supersonic jets point in the same direction. Villa *et al.*[5] were unable to induce one-colour photoionization of 2-methylpyrazine when the excitation energy was tuned to higher-lying vibronic levels of T_1. These authors consider displacements along a vibronically active out-of-plane coordinate, due to strong pseudo-Jahn–Teller distortion as a possible cause for the poor Franck––Condon factors aggravating the one-colour photoionization. However, no trace of a second triplet state, located energetically below the S_1 origin, could be found in phosphorescence excitation spectra of the ultracold isolated pyrazine molecule.[3] The signals appearing in the $T_1 \leftarrow S_0$ absorption spectra in this energy regime at higher temperatures were interpreted as hot bands of the $S_1 \leftarrow S_0$ absorption.[2,3,6]

So far, the quantum chemical simulations of the vibronic spectra of pyrazine focussed on the singlet absorption and fluorescence. Woywod *et al.*[7] employed a vibronic-coupling model Hamiltonian based on the Taylor expansion of diabatic potentials to model the absorption spectrum of the interacting S_1–S_2 manifold. Besides the S_1–S_2 coupling mode ν_{10a}, they took three totally symmetric tuning modes (ν_1, ν_{6a}, ν_{9a}) into consideration. Berger *et al.*[8] used a Herzberg–Teller expansion in all vibrational coordinates to model the S_0–S_1 absorption and fluorescence spectra at 0 and 300 K. Herein, the strongly anharmonic ν_{10a} coupling mode was expanded in terms of harmonic oscillators. Weber and Reimers[9] presented an extensive quantum chemical study on the vibrational frequencies in the T_1 state but did not address any spin-forbidden T_1–S_0 transitions. Siebrand and Zgierski[10] as well as Fischer[2] modelled the interaction between vibronic and spin–orbit coupling in pyrazine, but they had to estimate the magnitudes of the coupling matrix elements or treated them as fitting parameters.

The main focus of the present paper is on the apparent contradictions relating to the interpretation of the measured $T_1 \leftarrow S_0$ and $S_1 \leftarrow S_0$ spectra of pyrazine. In particular, we want to understand why the $T_1 \leftarrow S_0$ spectrum shows significantly less vibronic activity than the $S_1 \leftarrow S_0$ spectrum. Further, we will try to clarify the energetic position of the T_2 state and its possible role in the spectral broadening of the higher-lying $T_1 \leftarrow S_0$ bands. To this end, we will carry out the extensive quantum chemical calculations on the ground and electronically excited states of pyrazine including both vibronic and spin–orbit coupling effects.

THEORY AND COMPUTATIONAL METHODS

In the framework of the Franck–Condon (FC) approximation,[11,12] the transition moment, in an intensity calculation of molecular absorption or emission spectra, can be written as a simple product of an electronic term and FC factors depending solely on the vibrational degrees of freedom. For strong electronic transitions of polyatomic molecules, *e.g.*, spin-allowed ππ* transitions, this approximation is usually sufficient to describe the intensity distribution of the vibrational fine-structure of a band. The picture changes when it comes to the electronic transitions with small oscillator strengths, *e.g.*, nπ* excitations of heteroaromatic molecules, or if highly resolved spectra are to be interpreted. In this case, the transition moment cannot be considered independent of the nuclear motion and the coupling between the vibrational and electronic degrees of freedom, *i.e.*, vibronic coupling has to be taken into account in the modelling. For small triatomic and tetraatomic molecules, the sophisticated Hamiltonians have been worked out by Perić and co-workers[13-15] which include these couplings and are applicable to vibronic transitions involving even large-amplitude motions. In the more general case of polyatomic molecules, the formulation of such model Hamiltonians is too complicated and simpler strategies have to be pursued. One way to proceed is to follow the approach of Herzberg and Teller who formulated a coupling model in which the electric dipole transition moment is expanded about a reference point (typically the equilibrium geometry Q_0) as a function of the normal mode displacements, Q_k:[16]

$$\mu_{ij} = \mu_{ij}(Q_0) + \sum_{k}^{N} \left(\frac{\partial \mu_{ij}}{\partial Q_k} \right)_0 Q_k + \ldots \tag{1}$$

If the normal mode composition differs strongly between the initial and final states of the transition, it is wise to include Duschinsky effects[17] in the Herzberg–Teller (HT) treatment of the vibronic coupling.[18] A further complication arises if the initial and final states exhibit different spin multiplicities which is the case, *e.g.*, in singlet–triplet transitions. In these cases, an additional coupling term between the spin and spatial electronic angular momenta is required in the Hamiltonian to make the radiative transition allowed.[19] Perturbation theories addressing spin–forbidden radiative transitions by sum-over-states expressions are known to be slowly convergent with respect to the number of states included.[20] Here, we propose a conceptually simple, though resource-intensive way to include spin–orbit coupling and Herzberg–Teller coupling simultaneously. To this end, the spin–orbit-coupled correlated wave functions Ψ_i and Ψ_j and the corresponding electric dipole transition moments are generated by a variational multireference spin–orbit configuration interaction (MRSOCI)[21] procedure and the first derivative of the transition matrix element with respect to the dimensionless normal coordinate Q_k is calculated by finite differences:

$$\frac{\partial\left\langle\psi_i\left|\hat{\mu}\right|\psi_j\right\rangle\big|_{Q_0}}{\partial Q_k} \approx \frac{\left\langle\psi_i\left|\hat{\mu}\right|\psi_j\right\rangle\big|_{Q_0+\varepsilon\epsilon_k} - \left\langle\psi_i\left|\hat{\mu}\right|\psi_j\right\rangle\big|_{Q_0-\varepsilon\epsilon_k}}{2\varepsilon} \tag{2}$$

where ϵ_k denotes the unit vector in the direction of the normal mode Q_k and ε is the step length.

The electronic ground-state geometry of pyrazine was optimized at the level of density functional theory (DFT). For the optimization of the excited singlet states, the full linear response time-dependent density functional theory (TDDFT) was used, while the Tamm–Dancoff approximation (TDA) was employed for the triplet calculations.[22] Herein, the PBE0 density functional[23,24] in combination with a valence triple zeta basis set with polarization functions (TZVP)[25] was utilized. All structures were optimized starting with D_{2h}-symmetry constraints, while lowering the point-group symmetry if the stationary point turned out to be a saddle point. For an easier comparison with the experimental literature, the D_{2h}-symmetric molecule was chosen to lie in the *yz* plane, with the *z* axis running through the nitrogen centres. The geometry optimizations and the computation of two-electron integrals in a resolution-of-the-identity (RI) approximation were performed with the Turbomole 7.1 program package[26]. In the RI step, the auxiliary basis sets[27] optimized for Møller–Plesset calculations were engaged. The minima were verified by the numerical harmonic frequency analysis utilizing the SNF program.[28] The numerical frequencies were scaled by 0.9944 to account for systematic errors of the PBE0 functional.[29]

To calculate the vertical excitation energies, the dipole transition moments and the oscillator strengths at DFT or TDDFT optimized geometries, the DFT/MRCI method was used employing the original Hamiltonian developed by Grimme and Waletzke.[30,31] Herein, Kohn–Sham molecular orbitals (MOs) in conjunction with the BH-LYP density functional[32,33] serve as the one-particle basis. Secular equations for the electronic ground state and 40 excited singlet and triplet states, distributed equally over all irreducible representations, were solved. The DFT/MRCI wave functions were used to calculate spin–orbit coupling matrix elements (SOCMEs) utilizing the spin–orbit coupling kit (SPOCK)[34,35] developed in our laboratory. In SPOCK, an effective one-electron spin–orbit mean-field (SOMF) Hamiltonian[36] is used, which treats the two-electron interactions in a Hartree–Fock-like manner. Additionally, the one-centre atomic mean-field integral (AMFI)[37] approach is used to reduce the computational cost. The spin–orbit coupled wave functions for the lowest 20 states and their electric dipole transition moments, μ, in length form were determined using the DFT/MRSOCI method[21] implemented in SPOCK.

The first-order derivatives of the dipole transition moments, μ, at the ground state geometry were computed numerically. To this end, the minimum structure was distorted by ±0.1 units along the dimensionless normal modes. At each distorted geometry, DFT/MRCI and concomitant DFT/MRSOCI single-point calculations were carried out, followed by a computation of the dipole transition moment and its first derivative according to Eq. (2). A complication arises due to the fact that the phases of the matrix elements are arbitrary. They are determined by the phases of the wave functions Ψ_i and Ψ_j and of the MOs from which the determinants are constructed. These phases can change from point to point. Tatchen *et al.*[38] used the reference matrix elements involving a third, strongly coupling state to fix the phases of the matrix elements relative to the undistorted geometry. In the pyrazine case, the dipole transition matrix elements between the ground state (A_g) and the first excited singlet or triplet state (B_{3u}) are needed. For this combination of *gerade* and *ungerade* states, a reference state with two non-vanishing couplings could not be found. Therefore, we employed a more rigorous

approach to fix the phases. At each displaced geometry, the MO phases were set to match the ones of the equilibrium geometry. To accomplish this, we calculated the overlap matrix between both structures. The off-diagonal blocks of the overlap matrix easily show whether MOs changed their phases or switched their ordering. The phases of the DFT/MRCI wave functions were adjusted in such a way that the largest coefficient of each wave function is positive.

Franck–Condon and Herzberg–Teller absorption spectra were obtained by a Fourier transform approach implemented in the VIBES program.[39,40] In the calculation of the integrals over the vibrational wave functions of the initial and final states, a Duschinsky transformation[17] was applied. Temperature effects were included assuming a Boltzmann population of the vibrational levels in the initial state. Before the integration (time interval 5.5 ps, 2×10^5 grid points), the time correlation function was damped with a Gaussian of 5 cm^{-1} full width at half maximum.

RESULTS AND DISCUSSION

Electronic ground and excited states

Vertical and adiabatic DFT/MRCI excitation energies, computed at DFT/ /TDDFT converged geometries in D_{2h}-symmetry, are listed in Table I. The excited states of *gerade* symmetries have been omitted from this list because their electric dipole transitions from the ground state are forbidden in FC approximation and because they do not lie among the lowest singlet or triplet states. The T_1 (1^3B_{3u}) and S_1 (1^1B_{3u}) states correspond to nπ* excitations from the highest occupied molecular orbital (HOMO), an in-plane orbital of n/σ type, to the lowest unoccupied molecular orbital (LUMO) of π* type (Fig. 1). Their adiabatic energies are close to the experimental band origins.[1] This is also true for the optically bright ^{1}ππ* states, 1^1B_{2u} and 1^1B_{1u}, and the second *ungerade* ^{3}nπ* state, 1^3A_u. Note, however, that the D_{2h}-symmetric stationary points of the latter states

TABLE I. DFT/MRCI excitation energies compared with experimental results taken from Fischer[2]. Vertical excitation energies and oscillator strengths (in parentheses) are given at the ground state minimum

State	Character	$\Delta E_{DFT/MRCI}$ / eV			ΔE_{exp} / eV
		Vertical	Relaxed (D_{2h})	Adiabatic	
1^1A_g			0.00		0.00
1^3B_{3u}	n → π*	3.56	3.46	3.46	3.33
1^1B_{3u}	n → π*	4.03 (0.01102)	3.92	3.92	3.83
1^3B_{1u}	π → π*	4.39	3.93[a]	3.72 (C_1)	4.0
1^3B_{2u}	π → π*	4.34	4.17[a]		4.4
1^3A_u	n → π*	4.89	4.18[a]		4.2
1^1A_u	n → π*	4.97 (0.0)	4.29[a]	3.99 (C_{2h})	5.0
1^1B_{2u}	π→ π*	5.09 (0.10819)	4.82[a]		4.7
1^1B_{1u}	π→ π*	6.78 (0.09446)	6.46[a]	5.34 (C_1)	6.31
2^1B_{2u}	π→ π*	7.90 (0.57811)			
2^1B_{1u}	π→ π*	7.96 (0.62602)			
4^1B_{2u}	n→ σ*/Ry	8.62 (0.26377)			

[a]Saddle point

represent only the transition states. While the D_{2h}-constrained adiabatic excitation energies of all other states are within ≈ 0.2 eV of the experimental data, we notice an untypical deviation by ≈ 0.7 eV for the corresponding 1^1A_u (HOMO→ →LUMO+1) state. Because the $1^1A_u \leftarrow 1^1A_g$ transition is optically forbidden, the assignment of a broad band at approximately 5.0 eV in a near-threshold electron-energy loss spectrum was based on older MRCI calculations.[41]

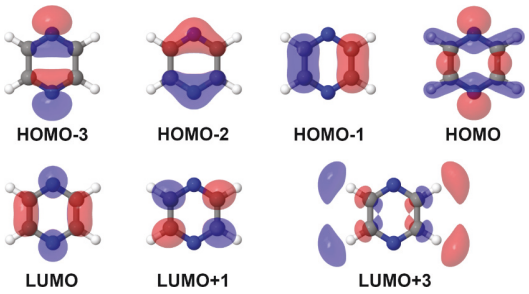

Fig. 1. Molecular orbitals at the ground state minimum relevant for spin–orbit coupling.

This energy regime corresponds roughly to the vertical excitation energy of this transition in our calculations. We also list vertical excitation energies of a few higher-lying bright singlet states which play a key role in the singlet-triplet absorption spectrum with regard to the intensity borrowing. The lowest $^1\pi\pi^*$ states have multiconfigurational character: 1^1B_{2u} and 2^1B_{2u} (HOMO-1→LUMO with admixtures of HOMO-2→LUMO+1 and *vice versa*), 1^1B_{1u} and 2^1B_{2u} (HOMO-1→LUMO+1 with admixtures of HOMO-2→LUMO and *vice versa*). 4^1B_{2u} represents a high-lying optically bright mixed $n\sigma^*$ and Rydberg state (HOMO→LUMO+3) which lends the intensity to the triplet absorption.

Using the D_{2h}-symmetry constraints, only the ^1A_g and $^3B_{3u}$ optimizations could be verified as minima. For the first excited singlet state, 1^1B_{3u}, one imaginary frequency was obtained for a b_{3g} mode. A scan of the energy profile along this mode revealed that the potential energy surface exhibits a shallow double well at the TDDFT level whereas a true minimum is found at the DFT/MRCI level. To obtain an estimate of the force constant of this mode, we used the curvature of the outer branches of the TDDFT scan to fit the harmonic frequency. Herein, the data with a distance of at least 3.5 units and at most 4.5 units away from the undistorted geometry were used. This fit yields a harmonic frequency of 1025 cm^{-1} for the $3b_{3g}$ mode which matches nicely the frequency of 1075 cm^{-1} in the related 1^3B_{3u} potential. The geometrical parameters of these minima may be found in Table II.

Further optimizations led to minimum structures for 1^3B_{1u}, 1^1A_u and 1^1B_{1u}. The molecule retains planarity in the 1^1A_u state, but in-plane movement of both nitrogen atoms in opposite directions lowers the symmetry towards C_{2h}. In the case of 1^3B_{1u} and 1^1B_{1u}, the symmetry is completely broken. In addition to an

asymmetric stretch of the C–N bonds, we observed a twist of the C–C bonds by about 30° on each side (Fig. 2, left). Its electronic structure points toward a pseudo Jahn–Teller rotation with the B_{2u} state (Fig. 2, right). Despite the out-of--plane distortion of the nuclear arrangement, the ππ* electronic character of the state is widely preserved.

TABLE II. Geometrical parameters of ground and first excited singlet and triplet state obtained with TDDFT (TZVP/PBE0)

State	CC / Å	CN / Å	CH / Å	∠ NCC / °	∠ CNC / °	∠ NCH / °
^1A_g	1.389	1.328	1.086	122.0	115.9	117.1
$^3B_{3u}$	1.389	1.335	1.084	120.0	115.9	117.1
$^1B_{3u}$	1.385	1.339	1.083	120.4	119.1	120.0
^1A_u (C_{2h})	1.413	1.289/1.362	1.089	122.0/116.2	121.8	120.2/122.0
$^3B_{1u}$ (C_1)	1.465	1.283/1.396	1.089/1.082	120.4/117.6	112.7	118.8/118.0
$^1B_{1u}$ (C_1)	1.452	1.301/1.372	1.089/1.085	117.4/116.2	112.8	119.3/117.9
Experiment[25]	1.403	1.339	1.115	122.2	115.6	113.9

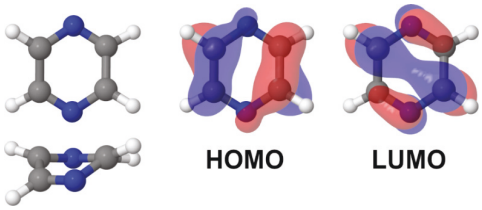

Fig. 2. Top and side view of the T_2 minimum structure (left) and molecular orbitals involved in the excitation at the T_2 minimum geometry (right).

The question, whether a second triplet state is located below or above the S_1 state, has been heavily debated in the literature.[2,3,4,5] Our DFT/MRCI calculations place the 1^3B_{1u} state (^{3}ππ*) state vertically ≈ 0.36 eV above the S_1 state in the FC region and ≈ 0.63 eV above the S_1 state at the S_1 minimum geometry. The geometry optimization in the T_2 potential leads to the highly distorted minimum (Fig. 2, left) with an adiabatic excitation energy ≈0.20 eV below the S_1 and ≈0.24 eV above the T_1 minimum. The latter value agrees well with the estimated T_2-T_1 splitting of 1600 cm^{-1} (≈0.20 eV), deduced by Hochstrasser and Marzzacco,[4] from the onset of the spectral broadening in their experiments. The presence of an intersection between the S_1 and T_2 potentials, far away from the FC region and the S_1 minimum geometry, provides a rationale for the conflicting experimental findings that (1) sharp absorption bands can be observed in a narrow energy regime above the origin of the 1^1B_{3u}←1^1A_g transition and that (2) there is significant line broadening in the region between the S_1 and T_1 origins even at cryogenic temperatures[3,4] which precludes their assignment as hot bands of the 1^1B_{3u}←1^1A_g absorption.

Vibrational frequencies

The calculated vibrational frequencies of the 1^1A_g ground state as well as the 1^3B_{3u} and 1^1B_{3u} excited states are generally in good agreement with the experi-

mentally obtained ones (Table III). An exception, relevant for the discussion of the vibronic spectra in the next section, is the $1b_{1g}$ (ν_{10a}) frequency in the 1^1B_{3u} state which is overestimated by 89 cm^{-1} relative to its experimentally deduced value of 383 cm^{-1}.

TABLE III. Vibrational frequencies of ground state and first excited singlet and triplet states compared to experimental values from Tomer *et al.*[4]; at the TDDFT level of theory, a saddle point and a shallow double minimum is obtained for this mode whereas DFT/MRCI shows a true minimum. Therefore, the frequency was fitted using the data from the outer branches of a TDDFT scan along the normal mode

Mode		^1A_g / cm^{-1}		$^1B_{3u}$ / cm^{-1}		$^3B_{3u}$ / cm^{-1}	
		Calc.	Exp.	Calc.	Exp.	Calc.	Exp.
$1a_u$	16a	340	342	419	400	440	400?
$1b_{3u}$	16b	430	416	228	237	261	237
$1a_g$	6a	607	597	618	585	619	620
$1b_{3g}$	6b	720	662	693	624	629	
$1b_{2g}$	4	773	705	502	552	405	557
$2b_{3u}$	11	801	791	726	577	729	563
$1b_{1g}$	10a	941	918	472	383	285	440
$2a_u$	17a	969	974	802	743	842	
$2b_{2g}$	5	974	757	805	518	823	522
$1b_{1u}$		1033		617		619	
$2a_g$	1	1052	1016	1040	970	1040	980
$1b_{2u}$		1096		1083		1087	
$2b_{1u}$		1173		1027		1026	
$2b_{2u}$		1246		1299		1318	
$3a_g$	9a	1257	1232	1197	1104	1201	1146
$2b_{3g}$		1371		1289		1304	
$3b_{2u}$		1446		1370		1364	
$3b_{1u}$		1520		1393		1399	
$3b_{3g}$		1605		1025*		1075	
$4a_g$	8a	1634	1579	1561	1377	1579	1230
$4b_{3g}$		3159		3164		3187	
$4b_{1u}$		3160		3174		3188	
$4b_{2u}$		3174		3196		3211	
$5a_g$		3180		3200		3214	

Berger *et al.*[8] have shown that it is necessary to go beyond the harmonic oscillator approximation to describe this vibration appropriately. Most frequencies vary only slightly among the three states. They can nevertheless appear prominently in the FC spectrum if their origins are markedly displaced. In a molecular transition in which the initial and final electronic states retain D_{2h} symmetry, this requirement can only be fulfilled by the totally symmetric (a_g) tuning modes. The modes $1b_{3u}$ (ν_{16b}), $1b_{2g}$ (ν_4), $1b_{1g}$ (ν_{10a}) and $3b_{3g}$ experience large frequency changes going from the ground state to the excited states. Their overtones are expected to be seen in the FC spectra, too. Moreover, the $1b_{1g}$ (ν_{10a})

and to a lesser extent also the $1b_{2g}$ (ν_4) and $2b_{2g}$ (ν_5) modes are made responsible for the strong vibronic coupling in the singlet moiety.[2,42] Since the frequency changes are similar in the 1^3B_{3u} potential, the question arises why their fundamentals are absent or at least very weak in the singlet-triplet absorption.[3,4]

S_1←S_0 absorption spectra

The FC and HT S_1←S_0 absorption spectra, calculated for 0 and 293 K, respectively, are shown in Fig. 3 and 4. The dipole transition moment of the 1^1B_{3u}←1^1A_g absorption has a value of $-0.33395ea_0$ in a FC approximation which is indicative of a moderately strong electronic transition. As expected for transitions between two D_{2h}-symmetric states, only totally symmetric modes, here $1a_g$ (ν_{6a}) and $3a_g$ (ν_9), generate high-intensity peaks in the FC spectrum. In addition, the overtones of $1b_{3u}$ (ν_{16b}), $1b_{1g}$ (ν_{10a}), and $1b_{2g}$ (ν_4) modes are visible. When HT coupling is switched on, additional transitions become symmetry-allowed. The derivatives of μ with respect to the vibronically most active modes are displayed in Table IV.

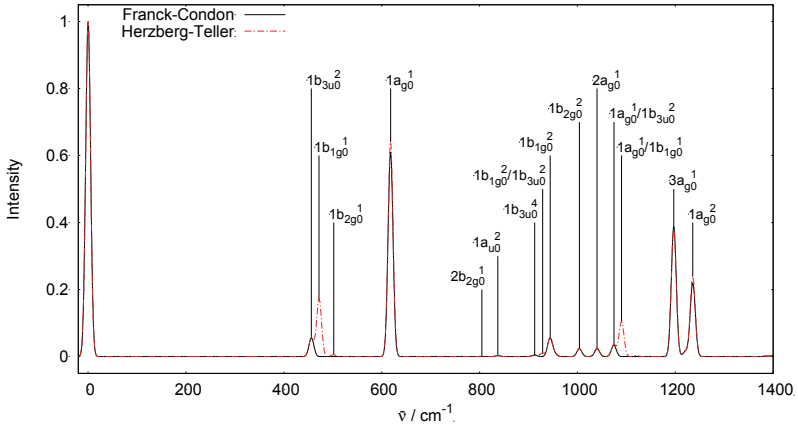

Fig. 3. Franck–Condon and Herzberg–Teller S_1←S_0 absorption spectra at 0 K.

The distortions along the $1b_{1g}$ (ν_{10a}) normal modes generate the by far largest gradients, explaining the intensity borrowing from the optically bright 1^1B_{2u}←1^1A_g and 2^1B_{2u}←1^1A_g excitations. The $1b_{1g0}^1$ (ν_{10a0}^1) fundamental and a $1a_{1g0}^1\ 1b_{1g0}^1$ ($\nu_{6a0}^1\ \nu_{10a0}^1$) combination transition are clearly visible in Fig. 3. Vibronic coupling to $^1B_{1u}$←1^1A_g transitions via the $1b_{2g}$ (ν_4) and $2b_{2g}$ (ν_5) modes leads to the minor peaks in the HT spectrum. The a_g modes are HT active to a lesser extent. Their contributions cause small intensity changes of the FC allowed transitions only. Apart from the slight spectral shifts of the bands engaging the $1b_{1g}$ (ν_{10a}) mode, the agreement between the simulated 0 K spectrum (Fig. 3) and the supersonic jet spectrum of Tomer *et al.*[3] is very good, thus lending support to

our theoretical approach. When heating up to 293 K, hot bands appear near the 0-0 signal in the simulated spectrum (Fig. 4). These hot bands are also present in the vapour spectrum measured by Nakamura[6] at 300 K.

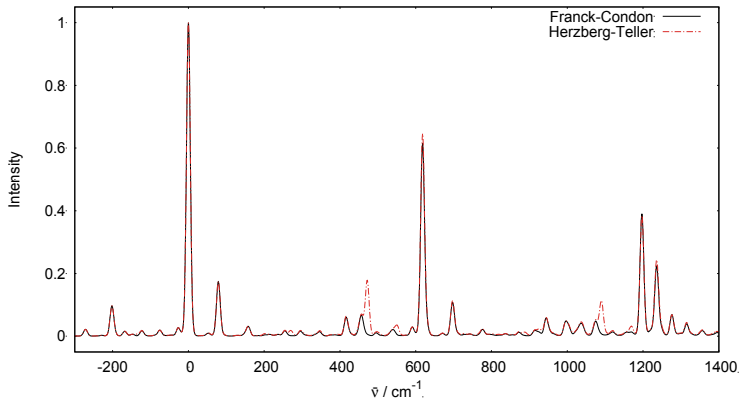

Figure 4. Franck-Condon and Herzberg-Teller $S_1 \leftarrow S_0$ absorption spectra at 293 K.

TABLE IV. Dipole transition moment derivatives (ea_0) for the $S_1 \leftarrow S_0$ transition at the ground state geometry

Mode k	Derivative		
	$\partial\langle^1B_{3u}\|\mu_x\|^1A_g\rangle/\partial Q_k$	$\partial\langle^1B_{3u}\|\mu_y\|^1A_g\rangle/\partial Q_k$	$\partial\langle^1B_{3u}\|\mu_z\|^1A_g\rangle/\partial Q_k$
$1a_g$	0.01009	0.0	0.0
$1b_{2g}$	0.0	0.0	0.04610
$1b_{1g}$	0.0	0.24924	0.0
$2b_{2g}$	0.0	0.0	0.01295
$2a_g$	0.00504	0.0	0.0
$3a_g$	0.00372	0.0	0.0
$4a_g$	0.02028	0.0	0.0
$5a_g$	0.00869	0.0	0.0

$T_1 \leftarrow S_0$ absorption spectra

When simulating the vibrational fine-structure of spin-forbidden radiative transitions, one must simultaneously account for spin–orbit, electric dipole and vibronic couplings.[10,19,43] To this end, we calculated the electric dipole transition moments of the multiplicity-mixed DFT/MRSOCI wave functions engaged in the $T_1 \leftarrow S_0$ absorption and their derivatives with respect to all normal modes. These data are sufficient for computing the vibronic singlet–triplet spectra, but they do not provide much qualitative insight. A detailed analysis of the direct and indirect contributions to the intensities will be presented after the discussion of the spectrum. The gradients of the dipole transition moments are all close to zero, indicating that vibronic coupling plays a minor role in the lower part of the

$T_1 \leftarrow S_0$ absorption spectrum. Accordingly, the FC and HT absorption spectra, displayed in Fig. 5, look basically the same. This finding is in agreement with the notion that all relatively intensive bands in the first 1250 cm^{-1} of the $T_1 \leftarrow S_0$ phosphorescence excitation spectrum, recorded by Tomer *et al*. in a supersonic jet, have been assigned to totally symmetric fundamentals, overtones and combinations.[3] We find only one noteworthy fundamental transition from a weakly active HT mode in the low energy regime of the spectrum around 400 cm^{-1} which we assign to $1b_{2g0}^{1}$ (ν_{40}^{1}). The overtone of that transition gives rise to a more intensive signal around 800 cm^{-1} for which the assignment by Tomer *et al*.[3] was uncertain. The peak at 880 cm^{-1} in the experimental spectrum is attributed to an overtone of the $1a_u$ (ν_{16a}) mode.

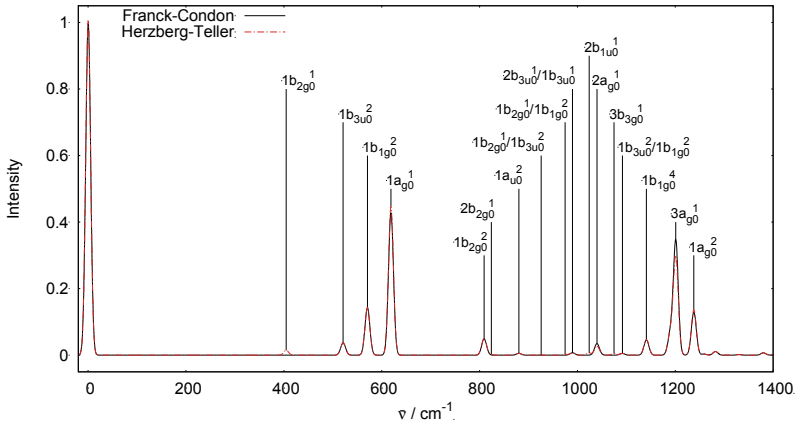

Fig. 5. Franck–Condon and Herzberg–Teller $T_1 \leftarrow S_0$ SOCI absorption spectrum at 0 K.

Consequently, the weak signal at 1114 cm^{-1} must have a different origin than the assignment (ν_{40}^{2}) proposed by Tomer *et al*. We found a combination band $1b_{3u0}^{2}\,1b_{1g0}^{2}$ ($\nu_{16b0}^{2}\,\nu_{10a0}^{2}$) in this energy regime. Most details of the measured phosphorescence excitation spectrum are well reproduced by our simulation, except for a signal at 570 cm^{-1} which arises from the $1b_{1g0}^{2}$ (ν_{10a0}^{2}) overtone and which is not observed in that experiment. At the same time, the intensity is missing in the $1a_{g0}^{1}$ (ν_{6a0}^{1}) signal at 620 cm^{-1}. While the frequency of the $1b_{1g}$ (ν_{10a}) mode was overestimated in the 1^1B_{3u} state, it appears to be underestimated in the 1^3B_{3u} potential by our calculations. If placed at slightly higher energy, its first overtone would overlay with the $1a_{g0}^{1}$ transition and recover the missing intensity of that signal. In addition, the second overtone $1b_{1g0}^{4}$ (ν_{10a0}^{4}) would be shifted to about 1200 cm^{-1} and add to the signal strength of the $3a_{g0}^{1}$ (ν_{9a0}^{1}) fundamental.

The leading terms of the DFT/MRSOCI wave functions and their projections onto the unperturbed DFT/MRCI states are shown in Table V. Under the influence of spin–orbit coupling, the 1^3B_{3u} state splits into three sublevels with an energy separation of less than 0.1 cm^{-1}. Their individual radiative singlet–triplet transitions are therefore spectrally not resolved.

TABLE V. Spin–orbit coupled states calculated by DFT/MRSOCI at the S_0 minimum geometry

State	Projection onto DFT/MRCI states	
	Largest triplet contributions	Largest singlet contributions
1	$1^3B_{1g}((m_s = 1) - (m_s = -1))$ $(8.0\times10^{-4}i)$	1^1A_g **0.99999**)
2	$1^3B_{3u}(m_s = 0)$ **(–0.99999*i*)**	2^1A_u (-5.7×10^{-4})
3	$1^3B_{3u}((m_s = 1) + (m_s = -1))$ **(–0.69301 + 0.14049*i*)**	1^1B_{2u} $(1.3\times10^{-4} - 0.3\times10^{-4}i)$ 4^1B_{2u} $(-1.3\times10^{-4} + 0.3\times10^{-4}i)$
4	$1^3B_{3u}((m_s = 1) - (m_s = -1))$ **(0.00384 + 0.70710*i*)**	1^1B_{1u} (2.7×10^{-4}) 2^1B_{1u} (-4.0×10^{-4})
5	$1^3B_{1u}((m_s = 1) - (m_s = -1))$ $(2.9\times10^{-3}i)$ $2^3B_{1u}((m_s = 1) - (m_s = -1))$ $(1.4\times10^{-3}i)$ $1^3B_{2u}((m_s = 1) + (m_s = -1))$ (-7.8×10^{-4})	1^1B_{3u} **(-0.99999**)

Setting aside the triplet-triplet transitions, there are two symmetry-allowed pathways which do not involve vibronic activity. They are characterized by intensity borrowing from intermediate B_{1u} and B_{2u} singlet states. The third pathway *via* ^1A_u states is electric dipole forbidden in D_{2h} symmetry. We will therefore have a closer look at matrix elements of the type $\langle 1^3B_{3u}|H_{SO}|^1B_{1u}\rangle \langle ^1B_{1u}|er|1^1A_g\rangle$ and $\langle 1^3B_{3u}|H_{SO}|^1B_{2u}\rangle \langle ^1B_{2u}|er|1^1A_g\rangle$.

The lowest excited SOCI state consists mostly of the $m_s = 0$ component of the 1^3B_{3u} state. It exhibits A_u combined spatial and spin symmetry and is therefore not visible in the FC spectrum. The second excited SOCI state is dominated by the positive linear combination of the $m_s = 1$ and $m_s = -1$ spin components of the 1^3B_{3u} state. With the present choice of coordinate axes, this transition is *y*-polarized and borrows its intensity mainly from $^1B_{2u}$ states. Although the interacting states have different orbital characters and the coupling is allowed according to the El-Sayed rules,[44] the SOCMEs between the $^3n\pi$ state and the two lowest $^1\pi\pi^*$ states of B_{2u} symmetry are surprisingly small ($\langle 1^3B_{3u}|H_{SO}|1^1B_{2u}\rangle$ = = –1.63 cm^{-1}, $\langle 1^3B_{3u}|H_{SO}|2^1B_{2u}\rangle$ = 0.36 cm^{-1}). To rationalize this result, one must remember that the spin–orbit Hamiltonian is short-ranged and dominated by effective one-electron terms. The leading configurations of the 1^3B_{3u} and 1^1B_{2u} wave functions differ by a HOMO-1→HOMO single excitation and could hence be connected by a one-electron operator. Closer inspection of the involved orbitals (Fig. 1) reveals, however, that the HOMO-1 has a nodal plane running through the nitrogen atoms where the HOMO exhibits the largest amplitudes. The main configuration of the second singlet state in B_{2u} symmetry is doubly excited with respect to the dominant 1^3B_{3u} configuration. Their coupling would

require two-electron terms of the spin–orbit Hamiltonian which are much smaller than the effective one-electron terms. A medium-sized SOCME is found for the higher-lying 4^1B_{2u} state of $^1n\sigma^*$ type ($\langle 1^3B_{3u} | H_{SO} | 4^1B_{2u}\rangle$ = 5.28 cm^{-1}) which is connected to the 1^3B_{3u} state by a LUMO→LUMO+3 excitation in the orbital picture. The coupling is caused mostly by one-centre integrals between basis functions at carbon atoms, which are smaller than the corresponding integrals at nitrogen atoms, due to the reduced nuclear charge. The moderate spin–orbit interaction between the 1^3B_{3u} state and the $^1B_{2u}$ states is not the only reason why the transition to this triplet substate is very weak. The relative phases of the 1^1B_{2u} and 4^1B_{2u} coefficients in the second excited SOCI wave function are such that their dipole transition moments (Table VI) nearly cancel each other. The $T_1 \leftarrow S_0$ absorption and the corresponding phosphorescence derive their intensities nearly exclusively from *z*-polarized transitions to the third triplet sublevel. Its SOCI wave function is dominated by the negative linear combination of the $m_s = 1$ and $m_s = -1$ spin components of the $^3B_{3u}$ state. This substate mainly borrows intensity from the bright 1^1B_{1u} and 2^1B_{1u} states. Their spin–orbit interactions with the 1^3B_{3u} state are stronger than for the B_{2u}-symmetric $\pi\pi^*$ states ($\langle 1^3B_{3u} | H_{SO} | 1^1B_{1u}\rangle$ = = 6.89 cm^{-1}, $\langle 1^3B_{3u} | H_{SO} | 2^1B_{1u}\rangle$ = –13.97 cm^{-1}). The different magnitudes of the SOCMEs can be rationalized by investigating the MOs involved in the couplings. The two lowest $^1B_{1u}$ states are multiconfigurational states with major contributions from HOMO-1→LUMO+1 and HOMO-2→LUMO excitations. While the former represents a double excitation with respect to the leading HOMO→ →LUMO term of the 1^3B_{3u} state and does not couple *via* an effective one-electron operator, the latter is connected to 1^3B_{3u}, by a single excitation from HOMO-2 to HOMO. Their spin–orbit integral is quite large, as both MOs exhibit substantial amplitudes at the nitrogen atoms. The intensity contributions from the 1^1B_{1u} and 2^1B_{1u} states partially cancel each other as well, but the remainder is larger, owing to the larger weighting coefficient in the SOCI expansion and the substantial dipole transition moment of the $2^1B_{1u} \leftarrow 1^1A_g$ transition.

TABLE VI. DFT/MRCI dipole transition moments with respect to the electronic ground state

State	Dipole transition moment, ea_0
1^1B_{2u}	0.9316 (*y*)
4^1B_{2u}	1.1174 (*y*)
1^1B_{1u}	0.7543 (*z*)
2^1B_{1u}	1.7919 (*z*)

The intensity of the $1b_{1g}$ (ν_{10a}) fundamental in the $T_1 \leftarrow S_0$ spectrum is governed by matrix elements of the form[2,3,10] $\langle 1^3B_{3u} | H_{SO} | 1^1B_{2u}\rangle \langle 1^1B_{2u} | H_{vib}(b_{1g}) | 1^1B_{3u}\rangle \langle 1^1B_{3u} | er | 1^1A_g\rangle$ and $\langle 1^3B_{3u} | H_{vib}(b_{1g}) | 1^3B_{2u}\rangle \langle 1^3B_{2u} | H_{SO} | 1^1B_{3u}\rangle \langle 1^1B_{3u} | er | 1^1A_g\rangle$. The first spin–vibronic pathway via the $1b_{1g}$ (ν_{10a}) mode would engage the same small SOCME as the one involved in the direct SOC mech-

anism of the second triplet substate. The second spin–vibronic pathway involves the S_1 (1^1B_{3u}) state and the B_{2u} symmetric triplet state. The contributions of the 1^3B_{2u} substates to the SOCI wave function of the S_1 state are somewhat larger than those of the 1^1B_{2u} state in the T_1 wave function (Table V). Siebrand and Zgierski argued that the vibronic intensities induced via the two pathways might cancel out due to the interference.[10] We could not exclude this possibility, but we considered the electronic structures of the involved states and their weak SOC the main reason for the missing vibronic activity of the $1b_{1g}$ (ν_{10a}) mode in the $T_1 \leftarrow \leftarrow S_0$ spectrum. In accordance with that, we expected the much larger matrix elements of the form $\langle 1^3B_{3u} | H_{SO} | 1^1B_{1u} \rangle \langle 1^1B_{1u} | H_{vib}\ (b_{2g}) | 1^1B_{3u} \rangle \langle 1^1B_{3u} | \mathrm{er} | 1^1A_g \rangle$ and $\langle 1^3B_{3u} | H_{vib}\ (b_{2g}) | 1^3B_{1u} \rangle \langle 1^3B_{1u} | H_{SO} | 1^1B_{3u} \rangle \langle 1^1B_{3u} | \mathrm{er} | 1^1A_g \rangle$ to govern the intensity of the vibronic coupling *via* the $1b_{2g}$ (ν_4) and $2b_{2g}$ (ν_5) modes. We expected the vibronic coupling terms $\langle 1^1B_{1u} | H_{vib}\ (b_{2g}) | 1^1B_{3u} \rangle$ to be the limiting factors in these pathways because the frequency shifts of the b_{2g} modes were not very pronounced. Indeed, the traces of HT activity of the $1b_{2g}$ (ν_4) mode in the singlet-triplet absorption spectrum can be seen (Fig. 5) around 400 cm^{-1}.

We did not investigate the vibronic fine structure in the higher energy regime of the $T_1 \leftarrow S_0$ absorption. Our results suggest, however, that the nonadiabatic coupling between T_1 and the highly distorted T_2 (1^3B_{1u}) state, whose minima are located energetically below the S_1 minimum, will lead to the substantial broadening of the signals. Tomer *et al.*[3] did not find any evidence for a 1^3B_{1u} state in the phosphorescence excitation spectrum of the isolated pyrazine molecule. We explain this fact by the double-well shape of the T_2 potential with a saddle point at D_{2h}-symmetric structures and nearly vanishing 0-0 vibrational overlap between the 1^3B_{1u} and 1^1A_g states. This interpretation is also compatible with the lack of intensity in the one-colour photoionization spectrum of 2-methylpyrazine which was ascribed to be due to the poor Franck–Condon factors caused by pseudo-Jahn–Teller out-of-plane distortions.[5]

CONCLUSION

In the present work, we have studied the spectral properties of pyrazine by means of the high-level quantum chemical methods. In addition to the D_{2h}-symmetric T_1 and S_1 (B_{3u}, $n\pi^*$) minima, we find an out-of-plane distorted T_2 ($\pi\pi^*$) minimum with twisted C–C bonds and an unequal C–N bond lengths which is located adiabatically below the S_1 minimum. Its electronic structure is reminiscent of a mixture between two $^3\pi\pi^*$ wave functions of B_{1u} and B_{2u} symmetry. At the D_{2h}-symmetric S_0 and S_1 minimum geometries, the 1^3B_{1u} and 1^3B_{2u} states are located well above the S_1 state. The $^3\pi\pi^*$ states can interact vibronically with T_1 and *via* spin–orbit coupling with S_1. Among the spin–orbit interactions, the couplings between the B_{3u} and B_{1u} states prevail while the couplings between the B_{3u} and B_{2u} states are surprisingly small in comparison to their respective $n\pi^*$ and $\pi\pi^*$ orbital characters. The geometry relaxation in the T_2 potential leads to an

intersection with the S_1 potential energy surface at geometries far away from the Franck-Condon region. We have not quantitatively determined the energetic location of the conical intersection, but the presence of an energy barrier for the intersystem crossing from S_1 to T_2 qualitatively explains the following, apparently contradictory experimental observations that: a) sharp lines can be seen in the $S_1 \leftarrow S_0$ absorption spectrum close to the origin and no trace of a second triplet state could be identified in the phosphorescence excitation spectra of the ultracold isolated pyrazine molecule[3] whereas b) the linewidth of the $S_1 \leftarrow S_0$ absorption spectrum in the higher energy regime above the $T_1 \leftarrow S_0$ origin suddenly broadens.[4]

The dipole transition moments between the spin–orbit coupled multireference configuration interaction wave functions and their derivatives, with respect to all normal coordinates, have been used in conjunction with the vibrational frequencies from density functional theories to model the vibronic $S_1 \leftarrow S_0$ and $T_1 \leftarrow S_0$ absorption spectra in Franck–Condon and Herzberg–Teller approximation. The results of our study confirm that the vibronic coupling plays an important role in the $S_1 \leftarrow S_0$ absorption spectrum where the most prominent coupling modes are $1b_{1g}$ (ν_{10a}) and $1b_{2g}$ (ν_4). The low Herzberg–Teller activity of the $1b_{1g}$ (ν_{10a}) mode in the $T_1 \leftarrow S_0$ absorption and phosphorescence excitation spectra was traced back to the unexpectedly small $\langle 1^3B_{3u} \left| H_{SO} \right| 1^1B_{2u} \rangle$ and $\langle 1^3B_{3u} \left| H_{SO} \right| 1^1B_{2u} \rangle$ matrix elements. The $T_1 \leftarrow S_0$ absorption and the corresponding phosphorescence derive their intensities nearly exclusively from *z*-polarized transitions to the third triplet sublevel mainly represented by the negative linear combination of the $m_s = 1$ and $m_s = -1$ spin components of the $^3B_{3u}$ state. The intensity of the spin-forbidden transition is borrowed from the optically bright 1^1B_{1u} and 2^1B_{1u} states by a direct spin–orbit mechanism, without the necessity to invoke spin–vibronic coupling. The good agreement between our simulated spectra and the experimentally observed ones establishes confidence in the applied quantum methods and the procedures for computing vibronic spectra under the influence of spin–orbit coupling.

Acknowledgements. It is a pleasure to dedicate this article to Prof. em. Miljenko Perić (University of Belgrade) on the occasion of his 70th birthday. C.M.M. would like to thank him for his longstanding friendship and fruitful scientific collaborations.

ИЗВОД

ЕФЕКТИ ВИБРОНСКОГ И СПИН–ОРБИТНОГ СПРЕЗАЊА У АПСОРПЦИОНОМ СПЕКТРУ ПИРАЗИНА: КВАНТНО-ХЕМИЈСКИ ПРИСТУП

FABIAN DINKELBACH и CHRISTEL M. MARIAN

Institute of Theoretical and Computational Chemistry, Heinrich-Heine-University Düsseldorf, Universitätsstraße 1, 40225 Düsseldorf, Germany

Изводи диполних момената прелаза између таласних функција добијених помоћу спин–орбитно спрегнуте вишереферентне интеракције конфигурација коришћени су,

заједно са вибрационим фреквенцијама добијеним из теорије фунционала густине, да би се израчунао вибронски апсорпциони спектар $S_1 \leftarrow S_0$ ($1^1B_{3u} \leftarrow 1^1A_g$) и $T_1 \leftarrow S_0$ ($1^3B_{3u} \leftarrow 1^1A_g$) у Херцберг–Телер апроксимацији. Спектар добијен експерименталним путем је добро репродукован. Израчунавања откривају неочекивано мало спин-орбитно спрезање између 1^3B_{3u} ($^3n\pi^*$) стања и суседног оптички активног $^1B_{2u}$ ($^1\pi\pi^*$) стања, објашњавајући на тај начин одсуство $1b_{1g}^1 0_0^1$ ($\nu_{10a}^1 0_0^1$) фундаменталне вибрације у вибрационој финој структури $T_1 \leftarrow S_0$ прелаза. Адијабатски гледано, два триплетна стања се налазе испод S_1 стања. Налажење T_2 минимума ван равни је последица псеудо Јан–Телерове интеракције између два $^3\pi\pi^*$ стања B_{1u} и B_{2u} симетрије. При D_{2h}-симетричним S_0 и S_1 геометријама минимума, наведена стања се налазе знатно изнад S_1. S_1 и T_2 потенцијали се секу на геометријама које су знатно удаљене од Франк–Кондоновог региона. То објашњава наизглед контрадикторни резултат да се ширина линија у вишој енергетској области изнад $T_1 \leftarrow S_0$ почетка одједном увећава, док се друго триплетно стање, лоцирано енергетски испод S_1 почетка не може идентификовати у фосфоресцентном ексцитационом спектру ултрахладног изолованог молекула пиразина.

(Примљено 10. маја, прихваћено 20. маја 2019)

REFERENCES

1. K. K. Innes, I. G. Ross, W. R. Moomaw, *J. Mol. Spectrosc.* **132** (1988) 492 (https://dx.doi.org/10.1016/0022-2852(88)90343-8)
2. G. Fischer, *Can. J. Chem.* **71** (1993) 1537 (https://dx.doi.org/10.1139/v93-193)
3. J. L. Tomer, K. W. Holtzclaw, D. W. Pratt, L. H. Spangler, *J. Chem. Phys.* **88** (1988) 1528 (https://dx.doi.org/10.1063/1.454132)
4. R. M. Hochstrasser, C. Marzzacco, *J. Chem. Phys.* **49** (1968) 971 (https://dx.doi.org/10.1063/1.1670262)
5. E. Villa, M. Terazima, E. C. Lim, *Chem. Phys. Lett.* **129** (1986) 336 (https://dx.doi.org/10.1016/0009-2614(86)80354-2)
6. K. Nakamura, *J. Am. Chem. Soc.* **93** (1971) 3138. (https://dx.doi.org/10.1063/1.466618)
7. C. Woywod, W. Domcke, A. L. Sobolewski, H. J. Werner, *J. Chem. Phys.* **100** (1994) 1400 (https://dx.doi.org/10.1063/1.466618)
8. R. Berger, C. Fischer, M. Klessinger, *J. Phys. Chem., A* **102** (1998) 7157 (https://dx.doi.org/10.1021/JP981597W)
9. P. Weber, J. R. Reimers, *J. Phys. Chem., A* **103** (1999) 9830 (https://dx.doi.org/10.1021/JP991404K)
10. W. Siebrand, M. Z. Zgierski, *Chem. Phys. Lett.* **67** (1979) 13 (https://dx.doi.org/10.1016/0009-2614(79)87096-7)
11. J. Franck, *Trans. Faraday Soc*. **21** (1926) 536 (http://dx.doi.org/10.1039/tf9262100536)
12. E. U. Condon, *Phys. Rev*. **28** (1926) 1182 (https://dx.doi.org/10.1103/PhysRev.28.1182)
13. M. Perić, S. D. Peyerimhoff, R. J. Buenker, *Z. Phys., D* **24** (1992) 177 (https://dx.doi.org/10.1007/bf01426704)
14. M. Perić, F. Grein, M. R. J. Hachey, *J. Chem. Phys.* **113** (2000) 9011 (https://dx.doi.org/10.1063/1.1319645)
15. M. Perić, S. Jerosimić, M. Mitić, M. Milovanović, R. Ranković, *J. Chem. Phys.* **142** (2015) 174306 (https://dx.doi.org/10.1063/1.4919285)
16. G. Herzberg, E. Teller, *Z. Phys. Chem. Abt. B* **21** (1933) 410 (https://dx.doi.org/10.1515/zpch-1933-2136)
17. F. Duschinsky, *Acta Physicochim.* **7** (1937) 551
18. G. J. Small, *J. Chem. Phys.* **54** (1971) 3300 (https://dx.doi.org/10.1063/1.1675343)

19. C. M. Marian, in *Reviews in Computational Chemistry,* Vol. 17, K. B. Lipkowitz, D. B. Boyd, Eds., Wiley-VCH, New York, 1999, p. 99
20. S. R. Langhoff, E. R. Davidson, *J. Chem. Phys.* **64** (1976) 4699 (https://dx.doi.org/10.1063/1.432056)
21. M. Kleinschmidt, J. Tatchen, C. M. Marian, *J. Chem. Phys.* **124** (2006) 124101 (https://dx.doi.org/10.1063/1.2173246)
22. S. Hirata, M. Head-Gordon, *Chem. Phys. Lett.* **314** (1999) 291 (https://dx.doi.org/10.1016/S0009-2614(99)01149-5)
23. J. P. Perdew, K. Burke, M. Ernzerhof, *Phys. Rev. Lett.* **77** (1996) 3865 (https://dx.doi.org/10.1103/PhysRevLett.77.3865)
24. C. Adamo, V. Barone, *J. Chem. Phys*. **110** (1999) 6158 (https://dx.doi.org/10.1063/1.478522)
25. A. Schäfer, C. Huber, R. Ahlrichs, *J. Chem. Phys.* **100** (1994) 5829 (https://dx.doi.org/10.1063/1.467146)
26. *TURBOMOLE V7.1*, a development of University of Karlsruhe and Forschungszentrum Karlsruhe GmbH, 1989–2007, TURBOMOLE GmbH, since 2007; available from http://www.turbomole.com, 2017.
27. F. Weigend, M. Häser, H. Patzelt, R. Ahlrichs, *Chem. Phys. Lett.* **294** (1998) 143 (https://dx.doi.org/10.1016/S0009-2614(98)00862-8)
28. J. Neugebauer, M. Reiher, C. Kind, B. A. Hess, *J. Comput. Chem.* **23** (2002) 895 (https://dx.doi.org/10.1002/jcc.10089)
29. M. K. Kesharwani, B. Brauer, J. M. L. Martin, *J. Phys. Chem., A* **119** (2015) 1701 (https://dx.doi.org/10.1021/jp508422u)
30. S. Grimme, M. Waletzke, *J. Chem. Phys.* **111** (1999) 5645 (https://dx.doi.org/10.1063/1.479866)
31. C. M. Marian, A. Heil, M. Kleinschmidt, *WIREs Mol. Sci.* **9** (2019) e1394 (https://dx.doi.org/10.1002/wcms.1394)
32. A. D. Becke, *J. Chem. Phys.* **98** (1993) 1372 (https://dx.doi.org/10.1063/1.464304)
33. C. Lee, W. Yang, R. G. Parr, *Phys. Rev., B* **37** (1988) 785 (https://dx.doi.org/10.1103/PhysRevB.37.785)
34. M. Kleinschmidt, J. Tatchen, C. M. Marian, *J. Comput. Chem.* **23** (2002) 824 (https://dx.doi.org/10.1002/jcc.10064)
35. M. Kleinschmidt, C. M. Marian, *Chem. Phys.* **311** (2005) 71 (https://dx.doi.org/10.1016/J.CHEMPHYS.2004.10.025)
36. B. A. Heß, C. M. Marian, U. Wahlgren, O. Gropen, *Chem. Phys. Lett.* **251** (1996) 365 (https://dx.doi.org/10.1016/0009-2614(96)00119-4)
37. B. Schimmelpfennig, *AMFI is an atomic spin-orbit integral program,* University of Stockholm, 1996
38. J. Tatchen, N. Gilka, C. M. Marian, *Phys. Chem. Chem. Phys.* **9** (2007) 5209 (https://dx.doi.org/10.1039/b706410a)
39. M. Etinski, J. Tatchen, C. M. Marian, *J. Chem. Phys.* **134** (2011) 154105 (https://dx.doi.org/10.1063/1.3575582)
40. M. Etinski, V. Rai-Constapel, C. M. Marian, *J. Chem. Phys.* **140** (2014) 114104 (https://dx.doi.org/10.1063/1.4868484)
41. I. C. Walker, M. H. Palmer, *Chem. Phys.* **153** (1991) 169 (https://dx.doi.org/10.1016/0301-0104(91)90017-N)
42. M. de Groot, W. J. Buma, *J. Chem. Phys.* **127** (2007) 104301 (https://dx.doi.org/10.1063/1.2764075)

43. T. J. Penfold, E. Gindensperger, C. Daniel, C. M. Marian, *Chem. Rev.* **118** (2018) 6975 (https://dx.doi.org/10.1021/acs.chemrev.7b00617)
M. A. El-Sayed, *J. Chem. Phys.* **38** (1963) 2834 (https://dx.doi.org/10.1063/1.1733610).

PCCP

PAPER

View Article Online
View Journal | View Issue

Cite this: *Phys. Chem. Chem. Phys.*, 2021, **23**, 3668

Intersystem crossing processes in the 2CzPN emitter: a DFT/MRCI study including vibrational spin–orbit interactions†

Angela Rodriguez-Serrano, Fabian Dinkelbach and Christel M. Marian *

Multireference quantum chemical calculations were performed in order to investigate the (reverse) intersystem crossing ((R)ISC) mechanisms of 4,5-di(9*H*-carbazol-9-yl)-phthalonitrile (**2CzPN**). A combination of density funcional theory (DFT) and multireference configuration interaction methods (MRCI) was used. The excellent agreement of the computed absorption spectrum with available experimental absorption spectra lends confidence to the chosen computational protocol. Vertically, two triplet excited states (T_1 and T_2) are found below the S_1 state. At the excited state minima, the calculated adiabatic energies locate only the T_1 state below the S_1 state. The enhanced charge transfer (CT) character of the geometrically relaxed excited states causes their mutual (direct) spin–orbit coupling (SOC) interaction to be low. Contributions of vibronic SOC to the (R)ISC probability, evaluated by a Herzberg–Teller-like procedure for a temperature of 300 K, are small but not negligible. For ISC, the $S_1 \rightarrow T_1$ channel is the fastest (8×10^6 s^{-1}), while the $S_1 \rightarrow T_2$ channel is found to be thermally activated (9×10^4 s^{-1}) and less efficient when proceeding from the adiabatic S_1 state. Our calculations also reveal, however, a barrierless $S_1 \rightarrow T_2$ ISC pathway near the Franck–Condon region. RISC is found to essentially proceed *via* the $T_1 \rightarrow S_1$ channel, with a rate constant of (3×10^4 s^{-1}) if our adiabatic singlet–triplet energy gap in vacuum (ΔE_{ST} = 0.12 eV) is employed. Shifting the potentials to match two experimentally reported singlet–triplet energy gaps in toluene (ΔE_{ST} = 0.21 and 0.31 eV, respectively) leads to a drastic reduction of the computed rate constant by up to 4 orders of magnitude. The T_2 state is not expected to play a major role in mediating triplet–singlet transitions in **2CzPN** unless it is directly populated by hot excitons. No indication for a strong vibronic coupling of the T_2 and T_1 potentials is found, which could help overcome the negative exponential dependence of the RISC rate constant on the magnitude of the energy gap.

Received 19th November 2020,
Accepted 12th January 2021

DOI: 10.1039/d0cp06011a

rsc.li/pccp

1. Introduction

The carbazolyl dicyanobenzene (CDCB) family of compounds has been widely investigated as thermally-activated delayed fluorescence (TADF) emitters in organic light emitting diodes (OLEDs).[1] The devices, built using these prototype compounds have shown high luminescence efficiencies and excellent operational stability.[2–8]

As first proposed by Uoyama *et al.*,[9] CDCB emitters were constituted by carbazole (**Cz**) units as donors (D) and the dicyanobenzene (DCB) moiety acting as an acceptor (A). These systems showed strong intramolecular charge-transfer (ICT) emission with the luminescence colour varying (from sky blue to orange) with the number and relative position of the **Cz** and cyano groups in the DCB unit. Of this series, the sky blue emitter **2CzPN** (4,5-di(9*H*-carbazol-9-yl)-phthalonitrile, Fig. 1) had the smallest external quantum efficiency (EQE) of 8.0% in toluene and 2,8-bis(diphenylphosphoryl)-dibenzo[*b*,*d*]thiophene (PPT)

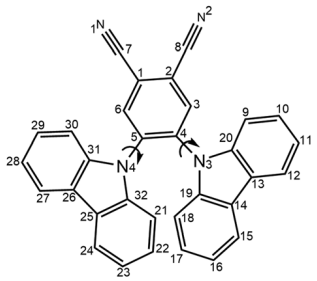

Fig. 1 Chemical structure of 4,5-di(9*H*-carbazol-9-yl)-phthalonitrile (**2CzPN**).

Institut für Theoretische Chemie und Computerchemie, Heinrich-Heine-Universität Düsseldorf, Universitätsstraße 1, D-40225 Düsseldorf, Germany.
E-mail: Christel.Marian@hhu.de; Tel: +49 211 8113209

† Electronic supplementary information (ESI) available: Characterization of the optimized electronic states in terms of geometries, MOs, vertical excitation energies, fragmentation analyses and Cartesian coordinates, derivatives of the SOMEs and vibrational coupling modes. See DOI: 10.1039/d0cp06011a

film, while the green emitter **4CzIPN** showed the highest external quantum efficiency (EQE) in toluene and 4,4′-*N*,*N*′-dicarbazole-biphenyl (CBP) film (19.3%).[9] The lower efficiency of **2CzPN** has been attributed to a large roll-off with current increase, which is dominated by strong contributions of singlet–triplet annihilation (STA) and triplet–triplet annihilation (TTA) as shown by Masui *et al.* by using an exciton-quenching model.[10] Later, its efficiency was further improved by including a mixed co-host system, which included electron/hole transporting materials in the device.[11] This architecture improved its efficiency to an EQE of 21.8% that is stated to be one of the highest for blue TADF OLEDs.

In TADF, the chromophore exhibits delayed fluorescence (DF) from the lowest-lying (S_1) singlet state, which is thermally populated from an energetically close-by triplet excited state (T_n) by reverse intersystem crossing (RISC). Therefore, with RISC being the rate limiting process in TADF, a small singlet–triplet energy gap (ΔE_{ST}) in the range of the thermal energy in conjunction with an effective spin–orbit coupling (SOC) between target states is crucial for facilitating the up-conversion of the triplet population into emissive singlets.[12] This is particularly critical for **2CzPN** and its derivatives,[5,6] where the reported ΔE_{ST} values are large compared to those of other TADF emitters.[1] For **2CzPN**, ΔE_{ST} values between 0.21 eV[13] and 0.31 eV[7] have been determined in toluene solution yielding RISC rate constants (k_{RISC}) of 6×10^3 s^{-1} and 1.7×10^5 s^{-1}, respectively. The latter value is remarkably high in view of the sizable singlet–triplet splitting. An exceptionally small ΔE_{ST} value of 0.09 eV was determined in a 1,3-bis(*N*-carbazolyl)benzene (mCP) OLED, yielding a k_{RISC} value of 5.6×10^3 s^{-1}.[10] These observations bring to light interesting optical properties of these emitters that are influencing their k_{RISC} and, consequently, the TADF efficiencies.

The optical and electronic properties of the sky blue **2CzPN** emitter have been extensively studied in solution[5,11,13] and in a variety of OLED ensembles.[8,10,11,14–17] In toluene, hexane and dichloromethane (DCM) solutions, **2CzPN** shows similar ultraviolet absorption spectra, which are constituted by three bands: two bands (a maximum and a shoulder) in the range of 300 and 350 nm that were assigned to LE on the **Cz** moiety and a wide CT band peaking at *ca.* 375 nm.[11,13,16] The absorption spectrum in tetrahydrofuran (THF) solution is found to be blue-shifted by a few nanometers.[5] The emission of **2CzPN** shows up at *ca.* 475 nm in toluene and is blue-shifted to 447 nm in hexane,[16] while this peak is red-shifted to 501 nm in diluted THF solution.[13] Bathochromic shifts of the emission maxima with increasing solvent polarity are typical for CT transitions in liquid solution. For all solvents, the reported rate constant for the radiative decay is similar ($\sim 10^7$ s^{-1}).

Experimental works supported by theoretical calculations have played a significant role in rationalizing mechanistic details about the (R)ISC of TADF emitters. A D–A type of architecture in multi-chromophoric systems leads to a large spatial separation between the frontier molecular orbitals (HOMO and LUMO) and thus promoting a small ΔE_{ST}. Consequently, their lowest-lying excited states are typically of charge transfer (CT) character. According to the empirical El-Sayed's rules for SOC, the coupling between singlet and triplet states of the same character is forbidden, *e.g.* between (ππ*) CT states. Therefore, vibrationally induced SOC becomes of great importance in mediating efficient (R)ISC for TADF emitters, which in fact has been elegantly demonstrated in experiments and *via* theoretical calculations.[18–24] Vibronic coupling can boost the coupling between two (ππ*) CT states by borrowing its intensity from a close-lying state with a local excitation (LE) character. This state can typically bridge the energy gap between the lowest singlet and triplet states as shown by Gibson *et al.*[20] and Etherington *et al.*[22] for D–A and D–A–D TADF active compounds between phenothiazine as a D and dibenzo thiophene-*S*-*S*-dioxide as an A. The influence of multiple excited states and vibrational effects in SOC and their role in TADF has been recently discussed by Marian and Penfold *et al.*[25,26]

For **2CzPN**, previous studies have demonstrated that conformational freedom modulates the degree of admixture of the LE character in the S_1 and T_1 (CT ππ*) states. These include experimental transient absorption spectroscopy (TAS)[13] and transient electron-spin resonance[27] as well as several theoretical TDDFT-based approaches[28–33]. Such studies focus on substitution effects on the electronic and excited state properties of several CDCBs performed mainly on ground state geometries. Other computational works calculate first-order SOC values in order to obtain (R)ISC rate constants *via* semiclassical Marcus theory using the adiabatic T_1 state[34,35] or involving the singlet–triplet crossing seam[36].

In this study, we aim at understanding the underlying excited state decay mechanisms that drive the (R)ISC process in **2CzPN**. To this end, we carried out extensive hybrid density functional theory/multireference interaction (DFT/MRCI) calculations. The DFT/MRCI method[37,38] has been largely used in our laboratory for getting mechanistic insights into (R)ISC of organic[39] and inorganic[40,41] compounds. Furthermore, we give a detailed overview on the (R)ISC efficiencies and their implications for TADF emission.

2. Computational details

As it is well known, substantial errors are obtained when calculating excitation energies of CT states with time-dependent density functional theory (TDDFT) and standard exchange–correlation (xc) functionals. Several computational studies have evaluated the performance of TDDFT for a wide range of TADF emitters (including **2CzPN**) correlating (vertical) singlet and triplet transition energies with experimental absorption energies. This, with the purpose of finding an optimal percentage of Hartree–Fock (HF) exchange contribution to the xc functional that allows the evaluation of transition energies for CT states and singlet–triplet energy gaps in a more precise manner.[42–44] This empirical calibration seems to work very well for states with strong CT character but has limited applicability for mixed CT–LE states and in cases where the LE contributions to a desired state vary with geometry distortions. A more promising ansatz toward a balanced

description of CT and LE states in donor–acceptor compounds in TDDFT calculations is optimal tuning where the ω parameter of a range-separated functional is adjusted such that the negative HOMO energy equals the molecular vertical ionisation.[45,46]

In this context, we performed an evaluation of the performance of different density functionals such as B3LYP, PBE0, CAM-B3LYP and BHLYP and of *ab initio* methods such as RI-CC2 and ADC2 on the ground and excited state geometries (Tables S1 and S3 and Fig. S2 of the ESI†).[47] For all the DFT calculations, Grimme's dispersion corrections (D3) together with Becke and Johnson (BJ) damping were accounted for.[48,49]

We found the best agreement with the experimental absorption spectra in toluene and DCM[11,13] for a combination of PBE0[50,51]-D3/def-SV(P)[52] geometries and DFT/MRCI excitation energies and oscillator strengths. Therefore, all further calculations were performed following this computational protocol. The conductor-like screening model (COSMO) was used to mimic the solvent environment (ε = 2.380 for toluene and ε = 8.930 for DCM).[53,54] The geometries of the electronic ground and excited states of **2CzPN** were all optimized without symmetry constraints. The optimized minima of the low-lying singlet excited states were obtained by using TDDFT.[55] For the triplet excited states, the Tamm–Dancoff approximation (TDA)[56] to TDDFT was employed. The TURBOMOLE program was used for all the geometry optimizations.[57] The harmonic vibrational frequency calculations were performed employing the AOFORCE module[58,59] of TURBOMOLE for the ground state, and the SNF program[60] for the excited states.

Vertical and adiabatic excitation energies and optical electronic properties were computed using the DFT/MRCI method.[37] The tight parametrization of the Hamiltonian, reported in ref. 38, was employed (DFT/MRCI-R2016), which has been specially designed for multichromophoric systems. Up to 10 roots were calculated for each singlet and triplet manifold. For a better understanding of the relaxation of the system, linearly interpolated potential energy profiles (LIPs) between target singlet and triplet state minima were computed.

A wavefunction analysis of the singlet and triplet states was performed by using a Löwdin orthogonalization[61] of the one-electron transition density matrix (1TDM) as implemented in the TheoDORE program of F. Plasser.[62] This ansatz was used to characterize the nature of the electronically excited states in the singlet and triplet manifold. In this context, the triplet wavefunction analysis requires singlet–triplet transition density matrices. These densities were not available from the current DFT/MRCI code. Therefore, we extended the DFT/MRCI program to supply singlet–triplet transition density matrices and TheoDORE was modified to read these new density matrices enabling the triplet wavefunction analysis. Here, the system was decomposed into three fragments for calculating the charge transfer numbers (Ω_{AB}), charge transfer character (ωCT), and natural transition orbitals (NTOs) of the Ω matrices for the individual states.[63,64] The **Cz** rings of **2CzPN** constituted each one fragment (separately) and the phthalonitrile (**PN**) moiety the third fragment.

The spin–orbit matrix elements (SOMEs) coupling target singlet and triplet states were calculated with the spin–orbit coupling kit (SPOCK) developed in our group.[65–67] Herein, the spin–orbit coupling (SOC) is described by the Breit–Pauli Hamiltonian and the spin–orbit-mean-field-approximation (SOMF) is employed.[68,69] Rate constants for ISC and RISC between singlet and triplet states were determined in the framework of the Fermi golden-rule approximation and a time-dependent approach to ISC mediated by SOC within the Condon and Herzberg–Teller approximations as implemented in the VIBES program.[70,71] The derivatives of the SOMEs (∂SOMEs) with respect to mass-weighted normal coordinates were obtained as the average of two-point finite differences using a displacement of ±0.1 along the dimensionless coordinates.[72] For fixing the phases of the DFT/MRCI wave functions, the MO phases at each displaced geometry were set to match the ones of the equilibrium geometry. The overlap matrix between them was calculated, where the off-diagonal elements give an indication of a change of phase or ordering of the MOs. Then, the phases of the wave functions were adjusted in such a way that the largest coefficient of each wave function is positive.[73] Temperature effects on the rate constants were accounted for by assuming a Boltzmann distribution of the harmonic vibrational state populations in the initial electronic state.[74] Zero-point vibrational energy (ZPVE) corrections are automatically included in the VIBES calculations. For further details on the theory and the methods used for calculating ISC rate constants check the previously published review article.[25]

3. Results and discussion

In the following we present the results obtained by our quantum chemical calculations. First, the ground state geometrical and optical properties are discussed considering also other experimental and theoretical reports. The energetics is analysed in terms of the DFT/MRCI vertical and adiabatic transition energies and interpolated pathways between target states. The characters of the low-lying excited states are analysed and the kinetics of different (R)ISC decay pathways are discussed considering direct and vibronic SOC. The Cartesian coordinates of all the computed minima, the frontier molecular orbitals (MOs) (Fig. S1 and S4–S9, ESI†) and electronic spectra (Tables S5–S8, ESI†) calculated at each of these geometries together with additional electronic structural information are provided in the ESI.†

3.1. Geometries and electronic structure at the S_0 state

The optimized ground state minima of **2CzPN** at the PBE0/def-SV(P) level of theory are displayed in Fig. 2a and b. Two conformers were found (S_0 and S_0'), where the difference between them is the relative orientation of the **Cz** groups w.r.t. the **PN** moiety. As expected by steric effects, a rather distorted orientation of the two bulky **Cz** groups is found, thus preventing the possibility of finding stable minima of higher symmetry in this emitter. The two optimized minima of **2CzPN** are not the optical reflection of one another. For the S_0', the opening angle of the **Cz** rings is wider. In fact, their ground

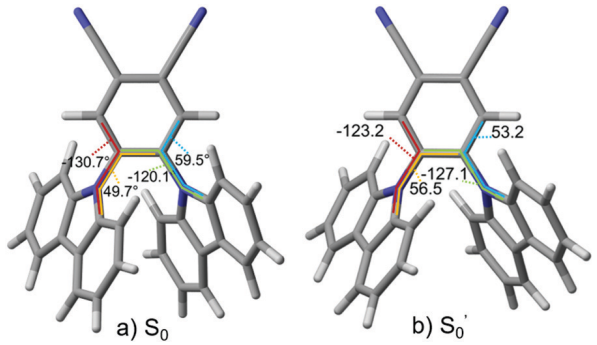

Fig. 2 Selected geometrical parameters (dihedral angles) of the ground state minima of **2CzPN** optimized at the PBE0-D3(BJ)/def-SV(P) level of theory.

state energies differ by 0.074 eV (1.7 kcal mol^{-1}), with the S_0 geometry in Fig. 2a being more stable.

The calculated geometries agree well with the experimental X-ray structures reported by M. Wong *et al.*[75] A comparison between these geometries and other S_0 minima obtained at other theoretical levels can be found in the ESI† (Table S1). We also expect enantiomers for S_0 and S_0' to exist.

The calculated DFT/MRCI-R2016 absorption spectra of both conformers of the isolated **2CzPN** are presented in Fig. 3a. The first absorption band is composed of two CT transitions. While the wavelengths of the intensive S_2 absorptions and hence the positions of the peak maxima are nearly identical in both cases, the widths of the first absorption band varies. Due to its red-shifted S_1 absorption, interaction of the S_0 conformer (Fig. 2a) with visible light yields a broader first absorption band. Also the relative intensities and energetic positions of the second absorption bands of the two conformers differ. For comparison with experimental results, the calculations were repeated in toluene and DCM environments. The DFT/MRCI-R2016 solution spectra of the S_0 conformer are shown in Fig. 3b

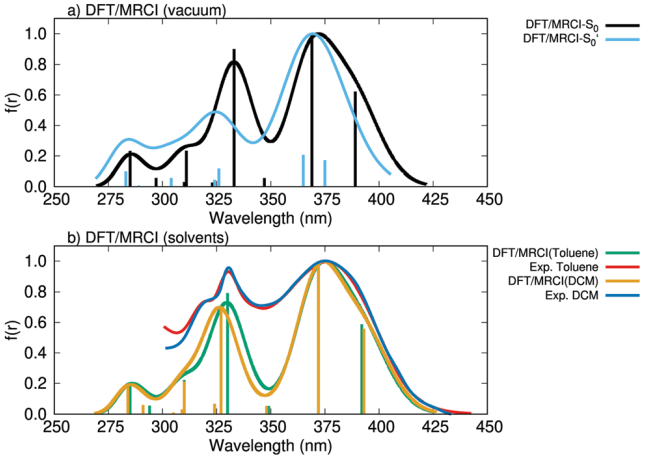

Fig. 3 DFT/MRCI-R2016 absorption spectra of **2CzPN** calculated at the S_0 minimum optimized at the PBE0-D3(BJ)/def-SV(P) level of theory: (a) in vacuum and (b) in toluene and dichloromethane (DCM) using the COSMO model. The experimental absorption spectra in toluene[13] and DCM[11] are also presented.

without any empirical tuning, together with two experimental absorption spectra measured in toluene[13] and DCM.[11] Solvent effects on the absorption spectra appear to be very small. Excellent agreement between the computed DFT/MRCI-R2016 spectra of the most stable S_0 conformer in Fig. 2a and the experimental data is observed. In the following, we therefore focus the analysis on this conformer.

The DFT/MRCI-R2016 vertical energies of the low-lying singlet and triplet states calculated at the S_0 state geometry of **2CzPN** are listed in Table 1. These are compared to other theoretical and experimental reports which are also displayed in this table. Experimental excitation energies and oscillator strengths (in toluene and DCM) agree well with the calculated values of the **2CzPN** in vacuum. All these excited states can be associated with $\pi\pi^*$ electronic transitions, and the corresponding frontier MOs relevant to these states are presented in Fig. 4a. From this figure, it can be observed that the H and H−2 MOs are mostly localized on the **Cz** units but present also some amplitudes on the **PN** unit. While the H−2 is mostly located on the **Cz** units, the H−6 contains strong localization on the **PN** unit and lower density in the **Cz** units. Regarding the MOs unoccupied in the electronic ground state, the L and L+1 MOs present amplitudes on the **PN** unit and at the nitrogen atom of the **Cz** units, while the L+2 and L+3 are mostly localized on the **Cz** units.

The fragmentation analysis is presented in Fig. 5b for the low-lying singlet and triplet states. This procedure will allow us to characterize the nature of the calculated DFT/MRCI-R2016 excited states of **2CzPN** in a simple manner. The lowest excited states present a considerably large CT character from the **Cz** substituents to the **PN** unit (in blue region of the bars) combined with some (lower) contributions of local excitations within the **PN** (in orange) unit and the **Cz** units (in green).

Among the low-lying singlets, there are three states with considerable oscillator strength (Table 1), namely S_1, S_2 and S_4. The wavefunction of the S_1 CT state of **2CzPN** is strongly dominated by an H → L electronic transition and shows up at 3.19 eV (in the gas phase), which is expected to be slightly red-shifted due to solvent–solute interactions. This value agrees well with the experiment (3.19 eV) in toluene. Here it is interesting to note that functionals like CAM-B3LYP and ωB97X-D yield excitation energies above 3.6 eV for this state.[34,42] At 0.17 eV above, the S_2 state is found arising from a H−2 → L transition. Like S_1, the S_2 excitation has predominantly CT character, mixed with LE on the **PN** unit. Together, they form the first absorption band with maximum around 375 nm. At variance with the interpretation of Hosokai *et al.*[13] who assigned the band with maximum at approx. 325 nm to originate from $\pi\pi^*$ electronic transitions within the **Cz** units, our fragmentation analysis reveals the S_4 state to have mainly CT character. It is a multiconfigurational state with a leading term corresponding to a H → L+1 excitation. The S_3 state, with much lower oscillator strength, corresponds to a H−1 → L transition and shows up 0.38 eV above the S_1 state.

The electronic structure of the low-lying triplet states is more mixed in the Franck–Condon (FC) region, *i.e.*, the weight

Table 1 DFT/MRCI-R2016 vertical excitation energies (ΔE_v, eV) of low-lying singlet and triplet states of the isolated **2CzPN** calculated at the S_0 minimum optimized at the PBE0-D3(BJ)/def-SV(P) level of theory

State	ΔE_v	Transition	% weight	f(L)	Theory[a]	Exp.[b]
S_0	0.00					
S_1	3.19	H → L	78.0	0.126	2.98,[c] 3.27,[d] 3.22,[f] 3.13,[g] 3.68,[h] 3.15[i]	3.19,[e] 3.30,[j] 3.32[k]
S_2	3.36	H−2 → L	80.3	0.202	3.17,[c] 3.55[d]	
S_3	3.57	H−1 → L	79.0	0.011		
S_4	3.72	H → L+1	69.4	0.182		
S_5	3.83	H−3 → L	81.7	0.006		
T_1	2.79	H → L	59.1		2.68,[c] 3.02,[d] 2.70,[g] 2.81,[l] 2.50[m]	
		H−6 → L	15.1			
		H−1 → L	11.7			
T_2	3.13	H−2 → L	72.4		3.04[f]	
T_3	3.24	H−1 → L+3	25.9			
		H−3 → L+2	24.7			
		H−1 → L	14.3			
T_4	3.27	H−1 → L+2	31.5			
		H−3 → L+3	28.2			
		H → L + 2	12.5			
T_5	3.50	H → L+1	28.8			
		H → L+2	21.2			
		H−2 → L+3	16.8			

[a] Other theoretical reports. [b] Experimental reports. [c] TD-PBE0(D3)/SV(P). [d] TD-ADC(2)/SV(P). [e] Ref. 42, in cyclohexane. [f] Ref. 35, TD-LC-w*PBE/6-31+G* in toluene (PCM). [g] Ref. 42, TD-MPW1B95/6-31G*. [h] Ref. 42, TD-CAMB3LYP/6-31G*. [i] Ref. 45, TDA-B2(GP)-PLYP/def2-TZVP//PBE0-D3(BJ)/def2-TZVP in toluene (COSMO). [j] Ref. 13, toluene solution. [k] Ref. 16, hexane solution. [l] Ref. 46, TDA-LC-w*PBE/6-31+G* in toluene (PCM). [m] Ref. 42, TD-B3LYP/6-31G*.

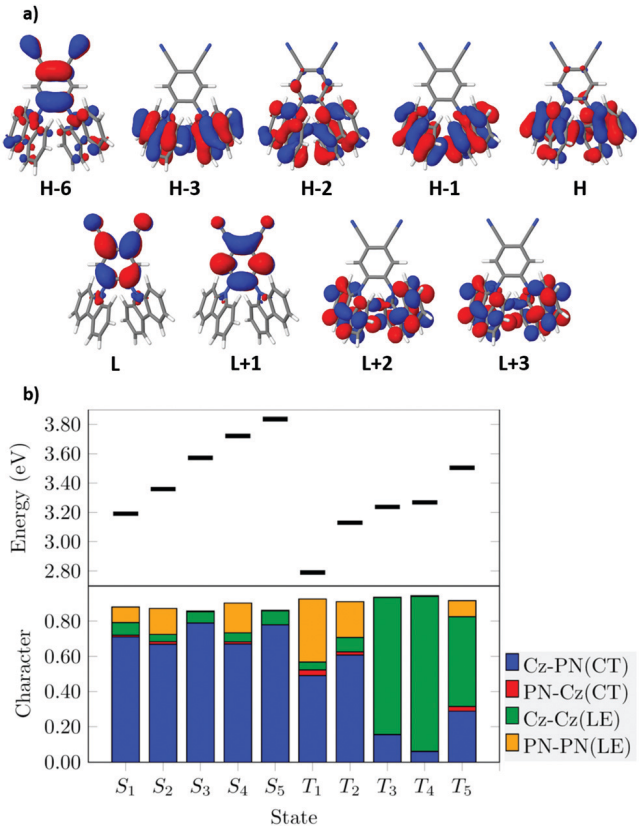

Fig. 4 (a) BH-LYP frontier molecular orbitals of **2CzPN** calculated at the S_0 geometry optimized at the PBE0-D3(BJ)/def-SV(P) level of theory. (b) Fragment-based analysis for the vertical singlet and triplet state DFT/MRCI-R2016 wavefunctions.

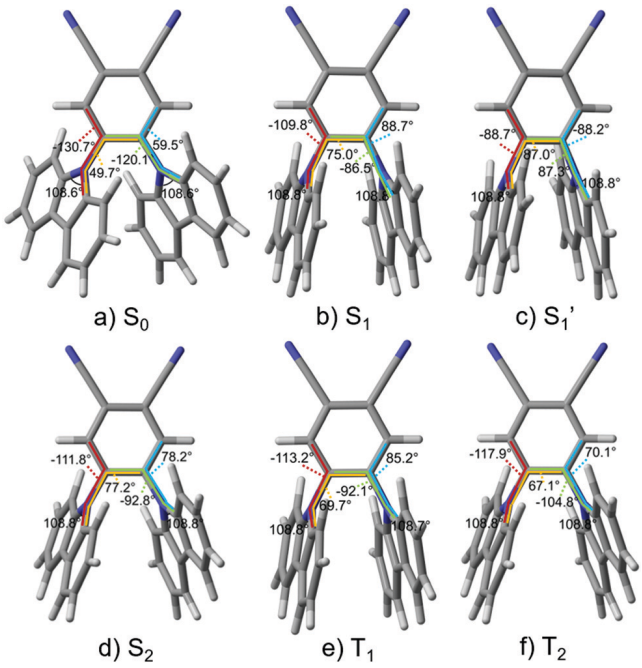

Fig. 5 Selected geometrical parameters (dihedral angles) of the ground and excited state minima of **2CzPN** optimized at the PBE0-D3(BJ)/def-SV(P) level of theory. TDDFT was used for the optimization of the excited singlet states, while TDA was used for the optimization of the triplet states.

percentage of their dominant contributions is lower than in the corresponding singlet states and have a more combined CT – LE character as shown by the fragmentation analysis of the transition densities (see Fig. 4b). Vertically, two triplet states below the S_1 state can be found. The T_1 state shows up at 2.79 eV (ΔE_{ST} = 0.40 eV) and arises from a linear combination of three excitations: H → L (59%), H−6 → L (15%) and H−1 → L (12%). Here, the H−6 → L transition is largely occurring between MOs localized at the **PN** moiety. As such, this state

has a higher LE character compared to its singlet counterpart (S_1 state) in this geometry. Other theoretical reports have also assigned the T_1 state of **2CzPN** with a strongly mixed CT-LE character, *e.g.* by using optimally tuned long-range corrected functionals and PCM[54] and uncorrected TDA-PBE0[28] and TD-B3LYP[34] functionals. In addition, Huang *et al.*[42] have shown how the LE contribution of this state increases with the increase of the HF exchange in conventional functionals.

Only 0.06 eV below the S_1 state is the T_2 state, characterized by a large contribution from a H−2 → L (72%) CT excitation. This energy separation is smaller than when using an empirically corrected TD-LC-w*PBE functional and the 6-31+G* basis set (*ca.* 0.1 eV).[35] The following (T_3–T_5) states present a substantial LE character emerging from transitions between the **Cz** units as shown in Fig. 4.

3.2. Minima of the low-lying excited states

The energy distribution and nature of the adiabatic minima of the low-lying singlet and triplet excited states of **2CzPN** may drive the plausible energy relaxation channels, for instance, ISC and RISC. The DFT/MRCI-R2016 adiabatic excitation energies of the optimized low-lying singlet and triplet states are listed in Table 2. The corresponding geometries are presented in Fig. 5.

Minima for the S_1, S_2, T_1 and T_2 states were found. Two enantiomeric minima for each excited state related to the opposite orientation of the **Cz** groups in space are obtained. We have considered the two geometries for the S_1 state (S_1 and S_1') for the present analysis. In this manner, we are able to cover relaxation pathways arising from both directions of coordinate space. The minimum geometries of the S_2', T_1' and T_2' states are given in Fig. S3 of the ESI.†

A common feature of these optimized excited state minima is the altered orientation of the **Cz** rings. They arrange in a more parallel fashion with respect to one another and in a more perpendicular fashion with regard to the **PN** ring. This trend is the largest for the $S_1(S_1')$ minima, followed by the T_1 and T_2 geometries (Fig. 5). Concomitantly, the CT character of these states increases upon geometry relaxation (compare Fig. 4, 6 and Fig. S10, ESI†). The change in electronic structure is especially pronounced for the T_1 state, which exhibits a considerable CT-LE mixing in the FC region but adiabatically it is

Table 2 DFT/MRCI-R2016 adiabatic excitation energies (ΔE^{ad}, eV) of low-lying singlet and triplet states of **2CzPN** calculated at their corresponding equilibrium geometry in vacuum

State	ΔE (eV)	Transition	% weight	ZPVE	Exp.	Theory[b]
S_1	2.91	H → L	89.3	−0.09	2.94,[a] 2.96[e]	2.84,[c] 2.99[d]
S_1'	2.92	H → L	89.4	−0.10		
S_2	3.13	H−2 → L	83.1	−0.01		
T_1	2.79	H → L	84.7	−0.10	2.75,[a] 2.65[e]	2.50,[c] 2.53,[d]
T_2	3.01	H−2 → L	83.4	−0.07		2.71[c]

[a] Ref. 13, onset of the fluorescence and phosphorescence (77 K) spectra in toluene. [b] Other theoretical reports. [c] Ref. 42, TD-B3LYP/6-31G*, UDFT for the triplet states. [d] Ref. 42, TD-PBE0/6-31G*, UDFT for the triplet states. [e] Ref. 7, calculated from the highest peak of the emission spectrum in toluene at 77 K.

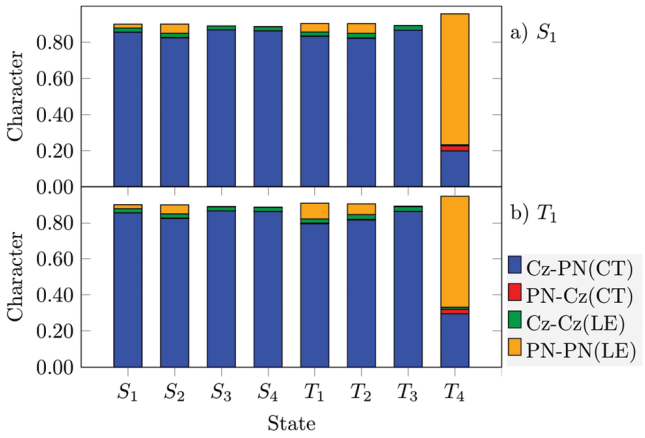

Fig. 6 Fragment-based analysis of the DFT/MRCI-R2016 wavefunctions performed at the (a) S_1 and (b) T_1 state minima.

mainly a CT state. This result is at variance with conclusions drawn by other authors who predict a much higher LE character for the adiabatic T_1 state of **2CzPN** (near 50%, LC-ω*PBE/6-31G*) on the basis of CT indices obtained by orbital composition analysis[42] and natural transition orbital analysis[35].

In line with the large geometry change, the geometry relaxation effect leads to an energy stabilization of the S_1 state by *ca.* 0.28 eV w.r.t. the FC region. The onsets of the experimental emission spectra in toluene[7,13] (2.94–2.96 eV) match the DFT/MRCI-R2016 adiabatic energy for the S_1 state of 2.91 eV very closely (Table 2). A similar stabilizing effect is found for the S_2 state (by 0.23 eV). In contrast, the geometry relaxation effect on the T_1 state energy is significantly lower than in the S_1 state, with the consequence that the ΔE_{ST} between the S_1 and T_1 adiabatic states is substantially smaller than that in the FC region. Experimental estimates of ΔE_{ST} vary between 0.09 eV and 0.35 eV, depending on the molecular environment and on the underlying model.[5,7,10,13,76] Our adiabatic ΔE_{ST} gap of 0.12 eV (0.13 eV after inclusion of ZPVE corrections) agrees well with the experimental value in an mCP OLED (0.09 eV), estimated from peak emission fluorescence (300 K) and phosphorescence (5 K) wavelengths.[10] By considering the threshold energies of the experimental fluorescence and phosphorescence bands (77 K) in toluene solution as a reference, a ΔE_{ST} gap of 0.21 eV is derived.[13] An even larger ΔE_{ST} value of 0.31 eV is obtained if the T_1^{0-0} transition energy is taken to coincide with the first phosphorescence band maximum (77 K), while S_1^{0-0} is derived from the crossing point of the absorption and fluorescence bands at 300 K.[7,42] Other TDDFT and TDA reports best agreeing with this (latter) value were ΔE_{ST} values of *e.g.* 0.49, 0.34 and 0.46 eV, which can be obtained when using TD-ωB97X/6-31G*,[30] TD-B3LYP and TD-PBE0[34] with the same basis set.

The T_2 CT state is influenced by a small percentage of LE character (Fig. S10, ESI†). Its minimum shows up 0.10 eV above the adiabatic S_1 state. This situation is different from the FC region where this state is located below the S_1 state. In contrast, TD-B3LYP calculations predict this state to be located adiabatically below the S_1 state (by 0.17 eV) being the only study reporting about the participation of this state in the (R)ISC

decay processes on **2CzPN**.[34] Preliminary DFT/MRCI calculations locate two adiabatic triplet states (T_1 and T_2) below the S_1 state in the **4CzIPN** TADF emitter,[12] with the T_2 state being halfway from the T_1 and S_1 states. This strongly suggests marked differences between the TADF mechanisms of both emitters: for **4CzIPN**, the presence of the intermediate T_2 state helps to accelerate the (R)ISC processes, while for **2CzPN,** pathways involving the adiabatic T_2 state are thermally activated.

3.3. Relaxation channels

To shed light on possible energy dissipation mechanisms arising upon photoexcitation, we constructed LIPs connecting the optimized electronic states as displayed in Fig. 7. These LIPs offer a qualitative view of the overall photophysics of the excited molecule. The LIPs were calculated using the respective adiabatic minimum internal coordinates.

Fig. 7a shows the LIP between the minima of the S_0 and the S_1 states. Photoexcitation at the FC point eventually results in the population of the adiabatic S_1 state due to Kasha's rule. Along this relaxation path that includes marked changes in the **Cz** torsional angles, we found a crossing between the S_1 and T_2 PESs in the vicinity of the FC region. A value of 0.18 cm^{-1} for their mutual SOC at this crossing point indicates that ISC is possible, in principle. However, while these two states are separated by only −0.06 eV in the FC region, their energy gap rises to 0.44 eV at the S_1 minimum. A crossing of the S_1 and T_2 PESs also occurs along a pathway connecting their adiabatic minima (Fig. 7c), in this case with a small energy barrier (∼0.1 eV). In contrast, the T_1 and T_2 PESs do not intersect (Fig. 7f), suggesting that their vibronic coupling is small. The interconversion of the S_1 and S_1' enantiomers proceeds without a substantial barrier (Fig. 7b). As the **Cz** units are nearly perpendicular to the **PN** ring, the interconversion coordinate is mainly a sheering distortion. The S_1 and T_1 PESs show parallel tracks during this interconversion. Note the close energetic proximity of the S_1 and T_1 PESs at these geometries, a consequence of the similar nuclear arrangements at the S_1 and T_1 minima and the drastically reduced LE character of the adiabatic T_1 state in comparison to those of the FC region.

From the S_1 minimum, only the T_1 state is accessible in a downhill process, whereas the T_2 state is lying 0.10 eV above the adiabatic S_1 state. Therefore, ISC channels in **2CzPN** may arise from $S_1 \rightarrow T_1$ and $S_1 \rightarrow T_2$ decay, where the latter is thermally activated. In electroluminescent devices, RISC is expected to proceed mainly through a $T_1 \rightarrow S_1$ channel as this is the only state lying energetically close by (see Fig. 7d). However, contributions involving the T_2 state cannot be excluded *per se*. Several factors are decisive for efficient (R)ISC between target states such as the size of SOC, their adiabatic energy difference and their mutual vibrational overlap, which in turn also displays temperature dependence. In the following, the properties driving the mentioned (R)ISC channels are discussed in detail.

The component-averaged SOMEs between these target singlet and triplet states calculated at each minimum are displayed in Table 3. As expected from El-Sayed's rule, the magnitude of these SOMEs is in general small as also commonly found for transitions between ππ* CT states of organic molecules. The

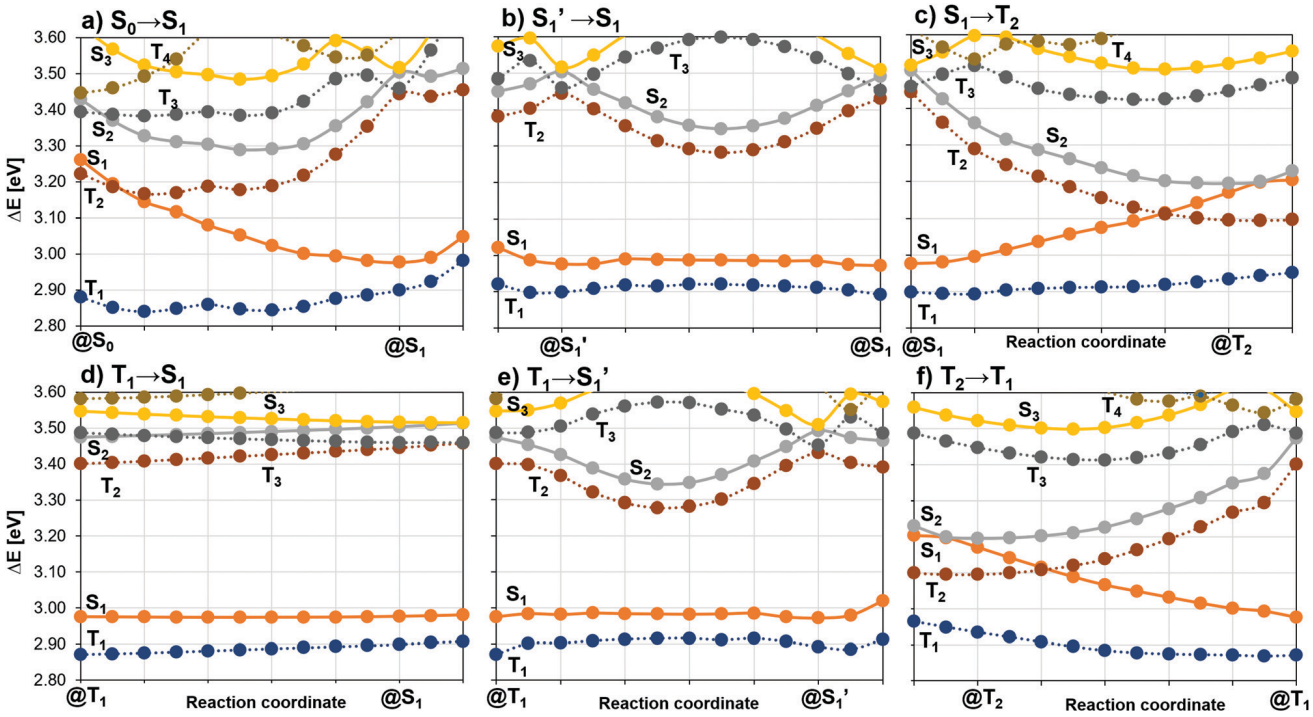

Fig. 7 DFT/MRCI-R2016 energies calculated at linear interpolated pathways (LIPs) between target electronic state minima of **2CzPN**. Dashed lines correspond to triplet state PESs, while continuous lines correspond to singlet states. Excitation energies calculated relative to the S_0 state at its corresponding minimum.

Table 3 Component-averaged spin–orbit matrix elements (SOMEs, cm^{-1}) between low-lying singlet and triplet states of **2CzPN** calculated at the optimized minima

SOMEs	@S_0	@S_1	@S_1'	@T_1	@T_2
$\langle T_1\|\hat{H}_{SO}\|S_1\rangle$	0.479	0.211	0.217	0.292	0.499
$\langle T_2\|\hat{H}_{SO}\|S_1\rangle$	0.183	0.223	0.249	0.240	0.228
$\langle T_3\|\hat{H}_{SO}\|S_1\rangle$	0.033	0.085	0.086	—	

coupling between the S_1 and T_1 CT states ($\sim$0.2 cm^{-1} at their corresponding minima) arises mainly from the minor LE contributions to the triplet wavefunction (Fig. 6). The larger $\langle T_1|\hat{H}_{SO}|S_1\rangle$ value at the S_0 geometry correlates with the higher percentage of LE **PN** configurations and the increased ΔE_{ST} gap in the FC region. Other computational studies report higher SOC values at the excited-state minima as well, *e.g.*, $SOME_{S1\rightarrow T1}$ = 0.737 cm^{-1}@T_1 minimum.[34] The authors mention, however, that the underlying B3LYP-TDA/6-31G* calculations significantly overestimate the S_1 and T_1 excitation energies.

The effect of vibronic SOC in **2CzPN** has been analysed in the literature by combining molecular dynamics (MD) and TDDFT-TDA calculations.[27,28] Torsional motions modulating the CT–LE mixture were found to facilitate the SOC-driven ISC in **2CzPN**. The polarization of experimentally observed ESR signals also supported a spin–vibronic ISC mechanism in this emitter.[27] In contrast, a study applying time-resolved infrared vibrational spectroscopy in conjunction with (TD)DFT calculations comes to the conclusion that the suppression of structural changes upon S_1–T_1 conversion assists the TADF process in Cz benzonitrile derivatives.[15]

As an alternative to non-adiabatic MD, static approaches based on Herzberg–Teller (HT)-like expansions can be used to determine spin–vibronic interactions.[26] To this end, derivatives of the SOMEs (∂SOMEs) with respect to distortions along the dimensionless normal mode (ν_i) displacements have to be computed. The resulting ∂SOME values (Table S10, ESI†) are very small. For the S_1–T_1 coupling, the maximum variation of the ∂SOMEs is found in the second decimal place, using either the S_1 or T_1 minimum nuclear arrangements as the expansion origin, while for the S_1–T_2 coupling a few values between 0.2 and 0.4 cm^{-1} can be found. As a consequence, vibronic contributions to the S_1–T_1 (R)ISC rate constants are expected to be weak.

The (R)ISC rate constants (k_{ISC}/k_{RISC}) calculated in the framework of the FC and HT approximations at 300 K for **2CzPN** are collected in Table 4. In this table, the rate constants involving the $S_1 \rightarrow T_1$ and $T_1 \rightarrow S_1$ channels were also calculated considering the reported experimental ΔE_{ST} gaps of 0.21 eV[13] and 0.31 eV[7] in toluene solution. Pathways connecting different enantiomers (*e.g.* $S_1' \rightarrow T_{1,2}$ or $T_1 \rightarrow S_1'$) result in very low values for the associated (R)ISC rate constants. They are therefore not displayed in Table 4. Due to the large geometrical (spatial) difference between the initial and final states, their vibrational overlaps are very small. Instead, interconversion of the enantiomers can easily proceed on the S_1 or T_1 PESs, as shown in Fig. 7b and e.

Table 4 Computed (R)ISC rate constants $k_{(R)ISC}$ (s^{-1}) for **2CzPN** (300 K) in the Condon ($k^{C}_{(R)ISC}$) and Herzberg–Teller approximations ($k^{HT}_{(R)ISC}$) in comparison to experimental results at room temperature

ISC	ΔE_{ST} (eV)	k^{C}_{ISC} (300 K)	k^{HT}_{ISC} (300 K)	k_{ISC} (exp.)
S_1–T_1	+0.12	3.2×10^6	7.6×10^6	
	+0.09[a]			3.1×10^7 [a]
	+0.21[b]	8.9×10^5	3.7×10^6	2.1×10^7 [b]
	+0.29[c]	—	—	2.9×10^7 [c]
	+0.31[d]	5.8×10^5	1.6×10^6	3.5×10^7 [d]
	+0.35[e]	—	—	3.0×10^7 [e]
S_1–T_2	−0.10	1.1×10^4	9.3×10^4	
RISC	ΔE_{ST} (eV)	k^{C}_{RISC} (300 K)	k^{HT}_{RISC} (300 K)	k_{RISC} (exp.)
T_1–S_1	−0.12	1.9×10^4	2.7×10^4	
	−0.09[a]			5.6×10^3 [a]
	−0.21[b]	1.5×10^2	4.3×10^2	6.0×10^3 [b]
	−0.29[c]	—	—	5.4×10^3 [c]
	−0.31[d]	2.1	2.9	1.7×10^5 [d]
	−0.35[e]	—	—	7.9×10^4 [e]
	NR[f]	—	—	3.5×10^6 [f]
T_2–S_1	+0.10	9.1×10^5	—	—

[a] Ref. 10, in mCP OLED. [b] Ref. 13, toluene (10^{-4} M) solution. [c] Ref. 76, co-deposited films (mCBP host matrix). [d] Ref. 7, toluene (10^{-5} M) solution. [e] Ref. 5, THF solutions. [f] Ref. 77, toluene (NR: not reported).

Vibronic SOC enhances the (R)ISC rate constants roughly by a factor of 2 at 300 K, as may be seen when comparing the $k^{HT}_{(R)ISC}$ values with the direct k^{C}_{ISC} values in Table 4. While an exponential decrease of the nonradiative transition rate constant may be expected from the energy gap law for weak coupling cases,[26] no correlation between the experimentally derived k_{ISC} and ΔE_{ST} values of **2CzPN** can be made out. All experimental studies agree that k_{ISC} ($S_1 \rightarrow T_1$) is in the range of 2.1–3.5 $\times$ 10^7 s^{-1}. In contrast, k_{RISC} ($T_1 \rightarrow S_1$) depends substantially (varying by *ca.* three orders of magnitude) on the experimental conditions and the model for determining the kinetic constants from the measurements. The Adachi group reports k_{RISC} ($T_1 \rightarrow S_1$) values varying slightly in the range of 5.4–6.0 $\times$ 10^3 s^{-1}, despite appreciable ΔE_{ST} shifts (0.09–0.29 eV).[10,13,76] Much higher RISC rate constants (7.9 $\times$ 10^4–1.7 $\times$ 10^5 s^{-1}) were published by two Chinese work groups although their experimentally deduced ΔE_{ST} values (0.31–0.35 eV) are even larger.[5,7] Our computed $S_1 \rightarrow T_1$ ISC rate constant (7.6 $\times$ 10^6 s^{-1} at 300 K for an energy gap of ΔE_{ST} = 0.12 eV) is smaller than the experimentally determined ones by a factor of about 3 (Table 4). Unlike the experimental values, the computed ISC rate constants decrease to 1.6 $\times$ 10^6 s^{-1}, if the PESs are vertically shifted to match ΔE_{ST} = 0.31 eV. The impact of the energy gap on the RISC rate constant is even more pronounced, as may be expected for TADF from the Boltzmann relation. Our computed k_{RISC} ($T_1 \rightarrow S_1$) value of 2.7 $\times$ 10^4 s^{-1} (300 K) is approximately in the right ballpark given the high sensitivity of the results with respect to the singlet–triplet energy gap. With the increase of ΔE_{ST} from 0.12 to 0.31 eV, we observe a substantial reduction of the computed RISC rate constant by 4 orders of magnitude.

So far, we have not discussed the involvement of the T_2 state in the ISC and RISC processes. According to our calculations, T_2 is located adiabatically 0.22 eV above the T_1 state and 0.10 eV

above S_1. Population of the T_2 state thus requires thermal activation. With a computed HT rate constant of approximately 9.3×10^4 s^{-1}, the $S_1 \rightarrow T_2$ transition cannot compete with the much faster $S_1 \rightarrow T_1$ process. The reverse $T_2 \rightarrow S_1$ transition is a downhill process, but requires the population of the T_2 levels either by ISC from the S_1 state or by activated internal conversion from T_1. Assuming a Boltzmann relation for the latter spin-allowed process yields a prefactor of about 10^{-4}, showing that the $T_2 \rightarrow S_1$ RISC does not essentially contribute to the TADF process unless hot excitons are available.

By using semiclassical Marcus theory to compute the Franck–Condon-weighted density of states and TDDFT-TDA potentials, Xu *et al.*[34] computed much higher rate constants. They obtained values of 1.3–21.1 $\times 10^7$ s^{-1} for the $S_1 \rightarrow T_1$ ISC and of 0.2–2.8 $\times 10^6$ s^{-1} for the $T_1 \rightarrow S_1$ RISC processes, respectively, depending on the choice of reorganization energy. The very fast $S_1 \rightarrow T_2$ transition ($k_{ISC} = 2.9 \times 10^7$ s^{-1}) reported by these authors is caused by the fact that the T_2 state is placed adiabatically below the S_1 state in their calculations at the B3LYP-TDA/6-31G* level of theory. Interestingly, Aizawa *et al.*[36] have recently calculated the RISC constants for a variety of TADF emitters using a method involving the singlet–triplet crossing seam-optimized geometry (TDA-LC-BLYP/6-31+G*) and Marcus non-adiabatic theory. In agreement with our findings, the authors state that there is no crossing between the S_1 and T_1 states of **2CzPN** but that the optimized intersection corresponds to a crossing with the T_2 state. A RISC rate constant in the order of 10^3 s^{-1} together with an activation energy of *ca.* 0.25 eV has been reported for isolated **2CzPN** using their methodology.

4. Conclusions

By means of combined PBE0/SV(P) and DFT/MRCI-R2016 quantum chemical computations, we have studied in detail excited-state decay pathways and (R)ISC mechanisms of the blue TADF emitter **2CzPN**. To this end, vertical and adiabatic electronic excitation energies, vibrational frequencies and wave functions as well as (R)ISC rate constants including direct and vibronic SOC were determined.

Two minima differing by 0.074 eV (1.7 kcal mol^{-1}) in energy were located in the electronic ground state of **2CzPN**. Their nuclear arrangements differ mainly in the orientation and the opening angle of the **Cz** molecular planes. Based on energetic considerations and on their spectral properties, we decided to focus on the more stable conformer in the following. Enantiomers of both structures exist that are separated from their respective mirror images by high barriers in the electronic ground state.

In the FC region, two triplet excited states are located below the S_1 state with energy separations of $\Delta E(S_1–T_1)$ = 0.40 eV and $\Delta E(S_1–T_2)$ = 0.06 eV according to the DFT/MRCI-R2016 calculations. The excited-state transition densities, studied through fragmentation analysis of the natural transition density, revealed the nature of these states to have a strong CT component. The admixture with LE character is substantial in the triplet manifold (*e.g.* for the T_1 state) and less pronounced in the low-lying excited singlet states. The excellent agreement of the computed absorption spectrum in vacuum with available experimental absorption spectra in toluene, THF and DCM solutions and the negligible solvent effect on the spectral properties lends confidence to the chosen computational protocol.

The calculated adiabatic DFT/MRCI-R2016 excitation energies in vacuum locate only the T_1 state below the S_1 state (by 0.12 eV), while the T_2 state lies 0.10 eV above. The intersection of the S_1 and T_2 PESs occurs close to the FC point. Considering the small magnitude of the electronic SOC (component averaged $\langle T_2|\hat{H}_{SO}|S_1\rangle = 0.18$ cm^{-1}) renders the dynamic ISC $S_1 \rightarrow T_2$ along the S_1 geometry relaxation path not very likely. At the optimized equilibrium structures of the S_1 and T_1 states, the **Cz** rings are markedly more perpendicular to the **PN** plane than in the ground state. The electronic decoupling of their π-systems facilitates the charge separation in these donor–acceptor systems, thus enhancing their CT character. Moreover, it enables a nearly barrierless interconversion of the enantiomers in the first excited singlet and triplet states by a sheering motion of the **Cz** units. Because of the small overlaps of the vibrational wavefunctions of the two enantiomeric potential energy wells, we nevertheless have indications that cross-couplings, such as $S_1' \rightarrow T_1$ ISC, do not play an important role among the excited-state decay processes.

The mutual (direct) SOCs between the S_1 and T_1 states at their respective minimum geometries are reduced in comparison to the FC point, a direct consequence of the varying LE contributions to the wave functions. Furthermore, the calculated derivatives of the S_1–T_1 SOMEs with respect to dimensionless normal mode displacements are small, but not negligible indicating that the contributions of Herzberg–Teller vibronic SOC to the $k_{(R)ISC}$ constants are moderate. Spin–vibronic interactions are found to speed up the S_1–T_1 ISC and T_1–S_1 RISC processes by a factor of about 2. The triplet state formation is predicted to proceed predominantly *via* the $S_1 \rightarrow T_1$ channel with a rate constant of 8×10^6 s^{-1} at room temperature, somewhat smaller than the experimentally derived values of 2–3 $\times 10^7$ s^{-1},[5,7,10,13,76] but in the right ballpark. In addition, a thermally activated $S_1 \rightarrow T_2$ channel is available, but predicted to be less efficient ($k_{ISC} = 9 \times 10^4$ s^{-1}).

Our calculated RISC rate constant associated with the back population of the S_1 state of **2CzPN** in vacuum through the T_1–S_1 channel ($k_{RISC} = 3 \times 10^4$ s^{-1}) certainly is one order of magnitude larger than the smallest constants (5–6 $\times 10^3$ s^{-1}) reported in solution and in OLEDs,[10,13,76] but significantly smaller than the highest value (3.5×10^6 s^{-1})[77] determined by kinetic modelling of transient triplet absorption spectra in toluene solution. Astonishingly, the experimentally derived RISC rate constants and ΔE_{ST} values do not appear to be correlated. On one hand, nearly constant k_{RISC} values have been reported, despite appreciably different ΔE_{ST} gaps (0.09–0.29 eV).[10,13,76] On the other hand, a variation of experimentally derived rate constants by *ca.* 2 orders of magnitude can be made out when comparing different measurements of

2CzPN RISC in toluene solutions with similar singlet–triplet energy gaps of 0.31 and 0.29 eV, respectively.[7,13] Following this consideration, we repeated the (R)ISC rate constant calculations using ΔE_{ST} values of two of these experimental reports, *i.e.* 0.21[13] and 0.31 eV[7,42] in addition to our computed value of 0.12 eV to test the impact of singlet–triplet separation on the transition probabilities. As expected for a thermally activated process in the weak coupling limit, the RISC rate constant decreases exponentially (by *ca.* 4 orders of magnitude) when increasing ΔE_{ST} from 0.12 eV to 0.31 eV, while keeping the electronic coupling terms constant. The downhill $S_1 \rightarrow T_1$ ISC process is less affected (less than one order of magnitude) by this variation of the energy gap.

Although the T_2 state lies adiabatically close to S_1, it is not expected to play a major role in mediating the spin-flips in **2CzPN** unless the T_2 state is directly populated by hot excitons from the embedded OLED layer. Starting from the equilibrated S_1 state, the $S_1 \rightarrow T_2$ ISC is an activated process that cannot compete with the much faster $S_1 \rightarrow T_1$ ISC. Moreover, we found no indication for a strong vibronic coupling of the T_2 and T_1 potentials that could help overcome the negative exponential dependence of the RISC rate constant on the magnitude of the energy gap.

In comparison, DFT/MRCI calculations on the very efficient **4CzIPN** TADF emitter[12] show a significant CT-LE mixing in the low-lying triplet states and minor effects in the S_1 state. This complements with a T_2 state energetically located halfway from the S_1 and T_1 state, acting as an intermediate between these states, thereby accelerating the (R)ISC processes.

Our calculations show that the (R)ISC probability in **2CzPN** depends mainly on the interplay between the S_1 and T_1 states with spin–vibronic interactions accelerating the nonradiative transitions only marginally. One possible explanation for the strange findings with regard to the RISC rate constants in relation to the S_1–T_1 energy gap in **2CzPN** is that the models employed for deriving ΔE_{ST} values from spectroscopic data are not adequate. Could, alternatively, a larger singlet–triplet splitting, caused by higher LE contributions to the excited-state wave functions, be compensated by an increase of the electronic SOC strength? In principle, this is possible but difficult to imagine in this particular case. At the S_0 geometry, where the $\Delta E(S_1–T_1)$ is relatively large (0.40 eV), the magnitude of $\langle T_1|\hat{H}_{SO}|S_1\rangle$ differs by a factor of *ca.* 2 from the values at the relaxed excited-state geometries. The increased electronic coupling would lead to an acceleration of the ISC probability by a factor of about 4 in FC approximation, as opposed to a deceleration by 4 orders of magnitude caused by the reduced vibrational overlaps of the shifted potentials. The most plausible explanation for the high RISC rates, reported in some experimental studies,[5,7,77] is the participation of other processes such as triplet–triplet annihilation or hot exciton transfer in the delayed fluorescence.

Conflicts of interest

There are no conflicts to declare.

Acknowledgements

Financial support from the Deutsche Forschungsgemeinschaft (DFG) through projects MA 1051/17-1 and 396890929/GRK 2482 is gratefully acknowledged.

References

1 B. Wex and B. R. Kaafarani, *J. Mater. Chem. C*, 2017, **5**, 8622–8653.
2 D. R. Lee, S.-H. Hwang, S. K. Jeon, C. W. Lee and J. Y. Lee, *Chem. Commun.*, 2015, **51**, 8105–8107.
3 R. Wang, Y.-L. Wang, N. Lin, R. Zhang, L. Duan and J. Qiao, *Chem. Mater.*, 2018, **30**, 8771–8781.
4 Y. J. Cho, K. S. Yook and J. Y. Lee, *Sci. Rep.*, 2015, **5**, 7859.
5 S. Gan, S. Hu, X.-L. Li, J. Zeng, D. Zhang, T. Huang, W. Luo, Z. Zhao, L. Duan, S.-J. Su and B. Z. Tang, *ACS Appl. Mater. Interfaces*, 2018, **10**, 17327–17334.
6 G. H. Kim, R. Lampande, J. B. Im, J. M. Lee, J. Y. Lee and J. H. Kwon, *Mater. Horiz.*, 2017, **4**, 619–624.
7 Y. Zhang, D. Zhang, T. Tsuboi, Y. Qiu and L. Duan, *Sci. China: Chem.*, 2019, **62**, 393–402.
8 Y. J. Cho, B. D. Chin, S. K. Jeon and J. Y. Lee, *Adv. Funct. Mater.*, 2015, **25**, 6786–6792.
9 H. Uoyama, K. Goushi, K. Shizu, H. Nomura and C. Adachi, *Nature*, 2012, **492**, 234–238.
10 K. Masui, H. Nakanotani and C. Adachi, *Org. Electron.*, 2013, **14**, 2721–2726.
11 J. W. Sun, K.-H. Kim, C.-K. Moon, J.-H. Lee and J.-J. Kim, *ACS Appl. Mater. Interfaces*, 2016, **8**, 9806–9810.
12 H. Yersin, *Highly efficient OLEDs: materials based on thermally activated delayed fluorescence*, Wiley-VCH Verlag GmbH & Co. KGaA, Germany, 2019.
13 T. Hosokai, H. Matsuzaki, H. Nakanotani, K. Tokumaru, T. Tsutsui, A. Furube, K. Nasu, H. Nomura, M. Yahiro and C. Adachi, *Sci. Adv.*, 2017, **3**, e1603282.
14 S. Haseyama, A. Niwa, T. Kobayashi, T. Nagase, K. Goushi, C. Adachi and H. Naito, *Nanoscale Res. Lett.*, 2017, **12**, 268.
15 M. Saigo, K. Miyata, S. Tanaka, H. Nakanotani, C. Adachi and K. Onda, *J. Phys. Chem. Lett.*, 2019, **10**(10), 2475–2480.
16 R. Ishimatsu, S. Matsunami, T. Kasahara, J. Mizuno, T. Edura, C. Adachi, K. Nakano and T. Imato, *Angew. Chem., Int. Ed.*, 2014, **53**, 6993–6996.
17 M. Inoue, T. Serevičius, H. Nakanotani, K. Yoshida, T. Matsushima, S. Juršėnas and C. Adachi, *Chem. Phys. Lett.*, 2016, **644**, 62–67.
18 D. de Sa Pereira, C. Menelaou, A. Danos, C. Marian and A. P. Monkman, *J. Phys. Chem. Lett.*, 2019, **10**(12), 3205–3211.
19 J. Gibson and T. J. Penfold, *Phys. Chem. Chem. Phys.*, 2017, **19**, 8428–8434.
20 F. B. Dias, J. Santos, D. R. Graves, P. Data, R. S. Nobuyasu, M. A. Fox, A. S. Batsanov, T. Palmeira, M. N. Berberan-Santos, M. R. Bryce and A. P. Monkman, *Adv. Sci.*, 2016, **3**, 1600080.
21 J. Gibson, A. P. Monkman and T. J. Penfold, *ChemPhysChem*, 2016, **17**, 2956–2961.
22 M. K. Etherington, J. Gibson, H. F. Higginbotham, T. J. Penfold and A. P. Monkman, *Nat. Commun.*, 2016, **7**, 13680.

23 I. Lyskov and C. M. Marian, *J. Phys. Chem. C*, 2017, **121**, 21145–21153.
24 C. M. Marian, *J. Phys. Chem. C*, 2016, **120**(7), 3715–3721.
25 C. M. Marian, *Wiley Interdiscip. Rev.: Comput. Mol. Sci.*, 2012, **2**, 187–203.
26 T. J. Penfold, E. Gindensperger, C. Daniel and C. M. Marian, *Chem. Rev.*, 2018, **118**, 6975–7025.
27 E. W. Evans, Y. Olivier, Y. Puttisong, W. K. Myers, T. J. H. Hele, S. M. Menke, T. H. Thomas, D. Credgington, D. Beljonne, R. H. Friend and N. C. Greenham, *J. Phys. Chem. Lett.*, 2018, **9**, 4053–4058.
28 Y. Olivier, B. Yurash, L. Muccioli, G. D'Avino, O. Mikhnenko, J. C. Sancho-García, C. Adachi, T.-Q. Nguyen and D. Beljonne, *Phys. Rev. Mater.*, 2017, **1**, 075602.
29 D. Kim, *Bull. Korean Chem. Soc.*, 2017, **38**, 899–903.
30 K. Lee and D. Kim, *J. Phys. Chem. C*, 2016, **120**, 28330–28336.
31 Y. Olivier, J.-C. Sancho-Garcia, L. Muccioli, G. D'Avino and D. Beljonne, *J. Phys. Chem. Lett.*, 2018, **9**, 6149–6163.
32 T. J. Penfold, *J. Phys. Chem. C*, 2015, **119**, 13535–13544.
33 Y. Olivier, M. Moral, L. Muccioli and J.-C. Sancho-Garcia, *J. Mater. Chem. C*, 2017, **5**, 5718–5729.
34 S. Xu, Q. Yang, Y. Wan, R. Chen, S. Wang, Y. Si, B. Yang, D. Liu, C. Zheng and W. Huang, *J. Mater. Chem. C*, 2019, **7**, 9523–9530.
35 P. K. Samanta, D. Kim, V. Coropceanu and J.-L. Brédas, *J. Am. Chem. Soc.*, 2017, **139**, 4042–4051.
36 N. Aizawa, Y. Harabuchi, S. Maeda and Y.-J. Pu, *Nat. Commun.*, 2020, **11**, 3909.
37 S. Grimme and M. Waletzke, *J. Chem. Phys.*, 1999, **111**, 5645–5655.
38 I. Lyskov, M. Kleinschmidt and C. M. Marian, *J. Chem. Phys.*, 2016, **144**, 034104.
39 C. M. Marian, A. Heil and M. Kleinschmidt, *Wiley Interdiscip. Rev.: Comput. Mol. Sci.*, 2019, **9**, e1394.
40 J. Föller and C. M. Marian, *J. Phys. Chem. Lett.*, 2017, **8**, 5643–5647.
41 N. Lüdtke, J. Föller and C. M. Marian, *Phys. Chem. Chem. Phys.*, 2020, **22**, 23530–23544.
42 S. Huang, Q. Zhang, Y. Shiota, T. Nakagawa, K. Kuwabara, K. Yoshizawa and C. Adachi, *J. Chem. Theory Comput.*, 2013, **9**, 3872–3877.
43 X. Tian, H. Sun, Q. Zhang and C. Adachi, *Chin. Chem. Lett.*, 2016, **27**, 1445–1452.
44 M. Alipour and N. Karimi, *J. Chem. Phys.*, 2017, **146**, 234304.
45 R. Baer, E. Livshits and U. Salzner, *Annu. Rev. Phys. Chem.*, 2010, **61**, 85–109.
46 H. Sun, C. Zhong and J.-L. Brédas, *J. Chem. Theory Comput.*, 2015, **11**, 3851–3858.
47 M. Loebnitz, *Einfluss des Torsionswinkels zwischen Donor- und Akzeptor-Einheiten von Isomeren des bis(Carbazolyl)-Dicyanobenzols auf die spektroskopischen Eigenschaften*, Bachelor's thesis, Heinrich-Heine Düsseldorf Universität, 2016.
48 S. Grimme, J. Antony, S. Ehrlich and H. Krieg, *J. Chem. Phys.*, 2010, **132**, 154104.
49 S. Grimme, S. Ehrlich and L. Goerigk, *J. Comput. Chem.*, 2011, **32**, 1456–1465.
50 J. P. Perdew, K. Burke and M. Ernzerhof, *Phys. Rev. Lett.*, 1996, **77**, 3865–3868.
51 C. Adamo and V. Barone, *J. Chem. Phys.*, 1999, **110**, 6158–6170.
52 A. Schäfer, H. Horn and R. Ahlrichs, *J. Chem. Phys.*, 1992, **97**, 2571–2577.
53 A. Klamt and G. Schüürmann, *J. Chem. Soc., Perkin Trans. 2*, 1993, 799–805.
54 A. Schäfer, A. Klamt, D. Sattel, J. Lohrenz and F. Eckert, *Phys. Chem. Chem. Phys.*, 2000, **2**, 2187–2193.
55 F. Furche and R. Ahlrichs, *J. Chem. Phys.*, 2002, **117**, 7433–7447.
56 S. Hirata and M. Head-Gordon, *Chem. Phys. Lett.*, 1999, **314**, 291–299.
57 TURBOMOLE V7.0 2015, A development of University of Karlsruhe and Forschungszentrum Karlsruhe GmbH, 1989–2007, TURBOMOLE GmbH, since 2007, available from http://www.turbomole.com.
58 P. Deglmann, F. Furche and R. Ahlrichs, *Chem. Phys. Lett.*, 2002, **362**, 511–518.
59 P. Deglmann and F. Furche, *J. Chem. Phys.*, 2002, **117**, 9535–9538.
60 J. Neugebauer, M. Reiher, C. Kind and B. A. Hess, *J. Comput. Chem.*, 2002, **23**, 895–910.
61 F. Plasser and H. Lischka, *J. Chem. Theory Comput.*, 2012, **8**, 2777–2789.
62 F. Plasser, TheoDORE 1.7.2: A Package for Theoretical Density, Orbital Relaxation, and Exciton Analysis, n.d.
63 A. A. Voityuk, *J. Chem. Phys.*, 2014, **140**, 244117.
64 S. Mai, F. Plasser, J. Dorn, M. Fumanal, C. Daniel and L. González, *Coord. Chem. Rev.*, 2018, **361**, 74–97.
65 M. Kleinschmidt, J. Tatchen and C. M. Marian, *J. Comput. Chem.*, 2002, **23**, 824–833.
66 M. Kleinschmidt and C. M. Marian, *Chem. Phys.*, 2005, **311**, 71–79.
67 M. Kleinschmidt, J. Tatchen and C. M. Marian, *J. Chem. Phys.*, 2006, **124**, 124101.
68 B. A. Heß, C. M. Marian, U. Wahlgren and O. Gropen, *Chem. Phys. Lett.*, 1996, **251**, 365–371.
69 B. Schimmelpfennig, *AMFI, an atomic mean-field spin–orbit integral program*, Stockholm University, 1996.
70 M. Etinski, J. Tatchen and C. M. Marian, *J. Chem. Phys.*, 2011, **134**, 154105.
71 M. Etinski, V. Rai-Constapel and C. M. Marian, *J. Chem. Phys.*, 2014, **140**, 114104.
72 J. Tatchen, N. Gilka and C. M. Marian, *Phys. Chem. Chem. Phys.*, 2007, **9**, 5209–5221.
73 F. Dinkelbach and C. M. Marian, *J. Serb. Chem. Soc.*, 2019, **84**, 819–836.
74 M. Etinski, J. Tatchen and C. M. Marian, *Phys. Chem. Chem. Phys.*, 2014, **16**, 4740–4751.
75 M. Y. Wong, S. Krotkus, G. Copley, W. Li, C. Murawski, D. Hall, G. J. Hedley, M. Jaricot, D. B. Cordes, A. M. Z. Slawin, Y. Olivier, D. Beljonne, L. Muccioli, M. Moral, J.-C. Sancho-Garcia, M. C. Gather, I. D. W. Samuel and E. Zysman-Colman, *ACS Appl. Mater. Interfaces*, 2018, **10**, 33360–33372.
76 T. Furukawa, H. Nakanotani, M. Inoue and C. Adachi, *Sci. Rep.*, 2015, **5**, 8429.
77 R. J. Vázquez, J. H. Yun, A. K. Muthike, M. Howell, H. Kim, I. K. Madu, T. Kim, P. Zimmerman, J. Y. Lee and T. Goodson, *J. Am. Chem. Soc.*, 2020, **142**, 8074–8079.

Electronic Supplementary Material (ESI) for Physical Chemistry Chemical Physics.

ELECTRONIC SUPPORTING INFORMATION (ESI)

Intersystem crossing processes in the 2CzPN emitter: A DFT/MRCI study including vibrational spin–orbit interactions.

Angela Rodriguez-Serrano, Fabian Dinkelbach, Christel M. Marian*

*Institut für Theoretische Chemie und Computerchemie, Heinrich-Heine-Universität Düsseldorf, Universitätsstraße 1, D-40225 Düsseldorf, Germany

Table S1. Selected geometrical parameters (dihedrals, in degrees) of the ground state S_0 minimum of **2CzPN** optimized at the indicated level of theory.

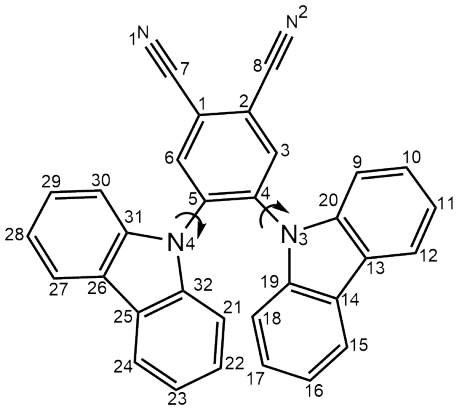

Dihedral	Crystal* structure	Crystal* structure 2	PBE0/ def2-TZVP*	PBE0-D3(BJ)/ def2-TZVP	PBE0-D3(BJ)/ def-SV(P)
C3-C4-N3-C20	114.9	-123.8	129.8	-128.6	-130.7
C3-C4-N3-C19	-55.7	42.6	-57.1	55.6	59.5
C5-C4-N3-C20	-63.8	56.1	-20.3	51.5	49.7
C5-C4-N3-C19	125.6	-137.5	122.7	-124.3	-120.1
C4-C5-N4-C31	125.5	-131.3	122.7	-124.3	-120.0
C4-C5-N4-C32	-56.4	57.1	-50.3	51.3	49.7
C6-C5-N4-C31	-54.6	49.9	-57.1	55.6	59.5
C6-C5-N4-C32	123.5	-121.7	129.8	-128.8	-130.8
C4-N3-C20-C19	171.9	168.3	-174.1	-176.3	-171.1
C5-N4-C32-C31	178.4	172.8	-174.1	-176.2	-171.1
	B3LYP/ 6-31G*	**B3LYP-D3(BJ)/ def2-TZVP**	**BHLYP-D3(BJ)/ def2-TZVP**	**RI-ADC(2)/ def-SV(P)**	**RI-CC2/ defSV(P)**
C3-C4-N3-C20	-51.9	-129.3	-124.2	-137.7	-138.2
C3-C4-N3-C19	120.0	57.2	56.6	63.2	62.6
C5-C4-N3-C20	128.2	50.8	53.2	44.0	43.3
C5-C4-N3-C19	-59.9	-122.7	-123.1	-115.1	-115.8
C4-C5-N4-C31	128.2	-122.6	-123.0	-115.1	-115.8
C4-C5-N4-C32	-59.8	50.6	53.0	44.0	43.3
C6-C5-N4-C31	-51.9	57.1	56.6	63.2	62.6
C6-C5-N4-C32	120.1	-129.7	-127.4	-137.6	-138.2
C4-N3-C20-C19	173.2	-174.4	-176.8	-161.9	-162.0
C5-N4-C32-C31	173.2	-174.1	-176.6	-161.9	-162.0

*M. Y. Wong, S. Krotkus, G. Copley, W. Li, C. Murawski, David Hall, G. J. Hedley, M. Jaricot, D. B. Cordes, A. M. Z. Slawin, Y. Olivier, D. Beljonne, L. Muccioli, M. Moral, J.-C. Sancho-Garcia, M. C. Gather, I. D. W. Samuel, E. Zysman-Colman, Deep-blue oxadiazole-containing thermally activated delayed fluorescence emitters for organic light-emitting diodes, ACS Appl. Mater. Interfaces, 2018, 10, 33360−33372.

Table S2. Vertical excitation energies (ΔE_v, eV) of low-lying singlet (TD-DFT) and triplet states (TDA) of **2CzPN** calculated at the S_0 geometry optimized at the PBE0-D3(BJ)/def-SV(P) level of theory.

State	ΔE_v	Transition	%weight	f(*L*)	State	ΔE_v	Transition	%weight
S_0	0.00							
S_1	2.98	H→L	98.9%	0.061	T_1	2.68	H→L	84.5%
S_2	3.17	H-1→L	94.7%	0.102	T_2	2.92	H-1→L	94.8%
S_3	3.24	H-2→L	99.5%	0.013	T_3	3.15	H-2→L	81.2%
S_4	3.50	H-3→L	94.6%	0.000	T_4	3.32	H→L+1	82.2%
S_5	3.55	H→L+1	90.0%	0.125	T_5	3.35	H-3→L	31.0%
S_6	3.67	H-1→L+1	98.5%	0.003			H-2→L+2	23.6%
S_7	3.83	H-2→L+1	98.8%	0.011			H-3→L+3	17.1%
S_8	4.09	H-3→L+1	98.9%	0.000	T_6	3.42	H-1→L+1	78.1%
S_9	4.22	H→L+2	81.2%	0.039	T_7	3.45	H-2→L+3	34.6%
S_{10}	4.25	H→L+3	69.4%	0.006			H-3→L+2	28.5%
		H-1→L+1	19.5%		T_8	3.53	H-3→L	61.1%
							H-2→L+2	14.9%

Fig. S1 Kohn-Sham frontier molecular orbitals of **2CzPN** calculated at the S_0 geometry optimized at the PBE0-D3(BJ)/def-SV(P) level of theory.

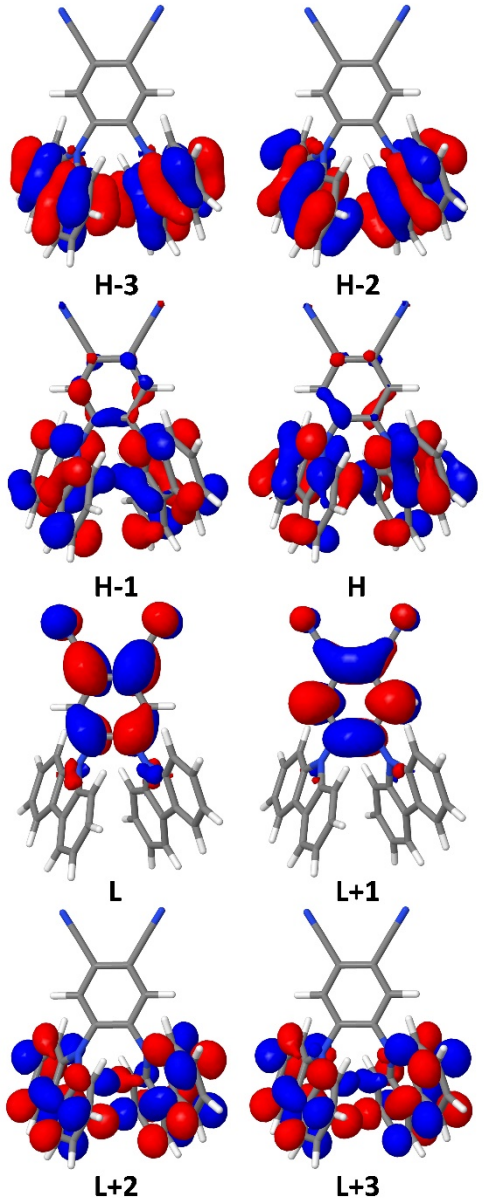

Table S3. Vertical excitation energies (ΔE_v, eV) of low-lying singlet and triplet states of **2CzPN** calculated at the S_0 geometry optimized at the indicated level of theory.

State	ΔE_v	Transition	%Weight	ΔE_v	Transition	%Weight
	RI-ADC2/def-SV(P)			**RI-CC2/def-SV(P)**		
S_1	3.27	H-1 → L	50.4%	3.30	H-1 → L	47.1%
		H → L	38.5%		H → L	41.9%
S_2	3.55	H-2 → L	63.3%	3.61	H-2 → L	61.0%
		H-3 → L	21.1%		H-3 → L	18.4%
S_3	3.78	H → L	55.6%	3.78	H → L	51.3%
		H-1 → L	39.2%		H-1 → L	43.1%
T_1	3.02	H-1 → L	52.8%	3.05	H-1 → L	51.5%
		H → L	22.1%		H → L	23.4%
		H-6 → L	15.2%		H-6 → L	15.1%
T_2	3.44	H-2 → L	60.2%	3.48	H-2 → L	60.7%
		H-3 → L	18.6%		H-3 → L	16.2%
T_3	3.54	H → L	28.3%	3.52	H → L	28.7%
		H → L+3	27.9%		H → L+2	27.3%
					H-1 → L	10.1%
	BHLYP-D3(BJ)/def2-TZVP			**B3LYP-D3(BJ)/def2-TZVP**		
S_1	3.81	H → L	91.1%	2.87	H → L	99.0%
S_2	3.98	H-1 → L	91.5%	3.02	H-1 → L	93.5%
S_3	4.28	H-2 → L	93.3%	3.11	H-2 → L	99.6%
T_1	2.58	H-6 → L	31.4%	2.53	H → L	83.6%
		H → L	27.3%			
		H-8 → L+1	16.3%			
T_2	2.77	H-2 → L+3	25.9%	2.78	H-1 → L	95.7%
		H-3 → L+2	24.9%			
T_3	2.78	H-2 → L+3	27.6%	3.00	H-2 → L	70.3%
		H-3 → L+3	24.2%			
T_4	3.43	H-1 → L	28.8%	3.11	H-2 → L+2	29.0%
					H-3 → L	26.4%
					H-3 → L+3	20.1%
T_5	3.51	H-1 → L+2	16.9%	3.14	H → L+1	89.6%
		H → L+3	16.4%			
T_6	3.67	H-1 → L	41.8%	3.21	H-1 → L+1	73.3%
		H → L+2	16.2%			
		H-1 → L+3	11.7%			
		H-8 → L	10.7%			
	PBE0-D3(BJ)/def2-TZVP			**PBE0-D3(BJ)/def-SV(P)**		
S_1	3.05	H → L	98.7%	2.98	H → L	98.9%
S_2	3.19	H-1 → L	93.8%	3.17	H-1 → L	94.7%
S_3	3.33	H-2 → L	99.5%	3.24	H-2 → L	99.5%
T_1	2.58	H → L	72.2%	2.68	H → L	84.5%
		H-6 → L	13.6%			
T_2	2.90	H-1 → L	92.1%	2.92	H-1 → L	94.8%
T_3	3.03	H-2 → L+3	26.5%	3.15	H-2 → L	81.2%
		H-3 → L+2	24.6%			
		H-2 → L	20.2%			
T_4	3.06	H-2 → L+2	34.1%	3.32	H → L+1	82.2%
		H-3→ L+3	26.2%			
T_5	3.27	H → L+1	86.4%	3.35	H-3 → L	31.0%
					H-2 → L+2	23.6%
					H-3 → L+3	17.1%
T_6	3.28	H-1 → L+1	52.0%	3.42	H-1 → L+1	78.1%
		H → L	16.6%			
		H-9 → L+1	13.0%			

Fig. S2 a) PBE0-D3(BJ)/def-SV(P) and DFT/MRCI-R2016 absorption spectra calculated at the corresponding S_0 minimum. b) RI-ADC2/def-SV(P) and RI-CC2/def-SV(P) absorption spectra calculated at their corresponding S_0 minimum. The experimental absorption spectra of **2CzPN** in toluene* and DCM** is also presented.

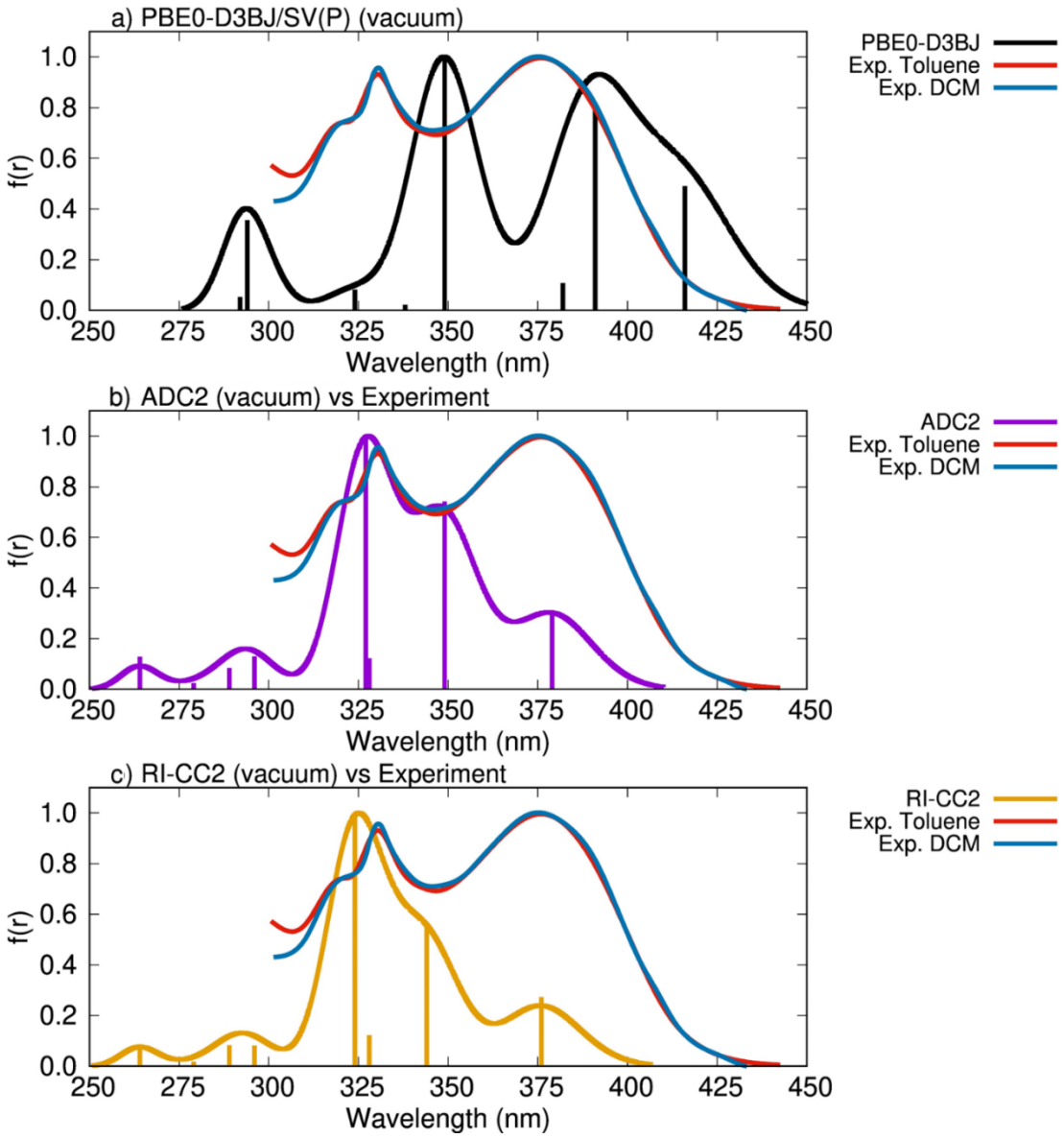

*T. Hosokai, H. Matsuzaki, H. Nakanotani, K. Tokumaru, T. Tsutsui, A. Furube, K. Nasu, H. Nomura, M. Yahiro, C. Adachi, Evidence and mechanism of efficient thermally activated delayed fluorescence promoted by delocalized excited states, Sci. Adv. 2017, 3, e1603282(1-9).

**J. W. Sun, K.-H. Kim, C.-K. Moon, J.-H. Lee, J.-J. Kim, Highly efficient sky-blue fluorescent organic light emitting diode based on mixed cohost system for thermally activated delayed fluorescence emitter (2CzPN), ACS Appl. Mater. Interfaces, 2016, 8, 9806−9810.

Fig. S3 Selected geometrical parameters (dihedral angles) of the S_2', T_1' and T_2' excited state minima of **2CzPN** optimized at the PBE0-D3(BJ)/def-SV(P) level of theory. TDDFT was used for the optimization of the excited singlet states, while TDA approximation was used for the optimization of the triplet states.

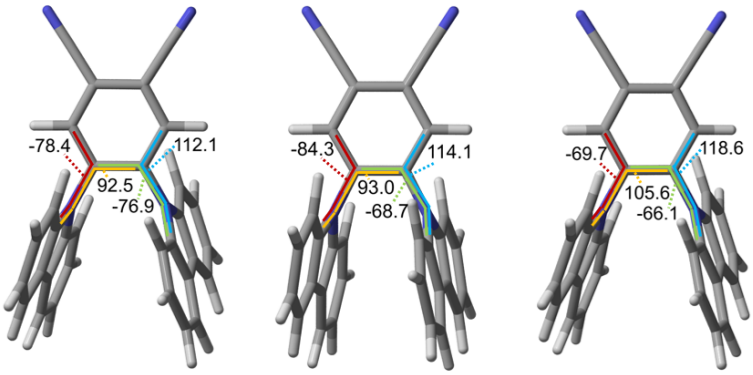

a) S_2' b) T_1' c) T_2'

Table S4. Adiabatic excitation energies (ΔE^{ad}, eV) of low-lying singlet and triplet states of **2CzPN** calculated at its corresponding equilibrium geometry. Optimizations were performed at the PBE0-D3(BJ)/def-SV(P) level of theory: For the singlet states by using TDDFT and for the triplet states using TDA approximation.

State	ΔE(eV)	Transition	%DC	f(L)	ZPVE
S_1	2.43	H→L	99.4%	0.001	-0.09
S_1'	2.43	H→L	99.4%	0.001	-0.10
S_2	2.71	H-1→L	98.6%	0.010	-0.01
T_1	2.40	H→L	98.2%		-0.10
T_2	2.64	H-1→L	97.8%		-0.07

The ZPE values were scaled by 0.9944 to account for systematic errors of the PBE0 functional according to (M. K. Kesharwani, B. Brauer, J. M. L. Martin, J. Phys. Chem., A 119 (2015) 1701)

Fig. S4 Frontier molecular orbitals of **2CzPN** calculated at the corresponding excited state geometry optimized at the PBE0-D3(BJ)/def-SV(P) level of theory.

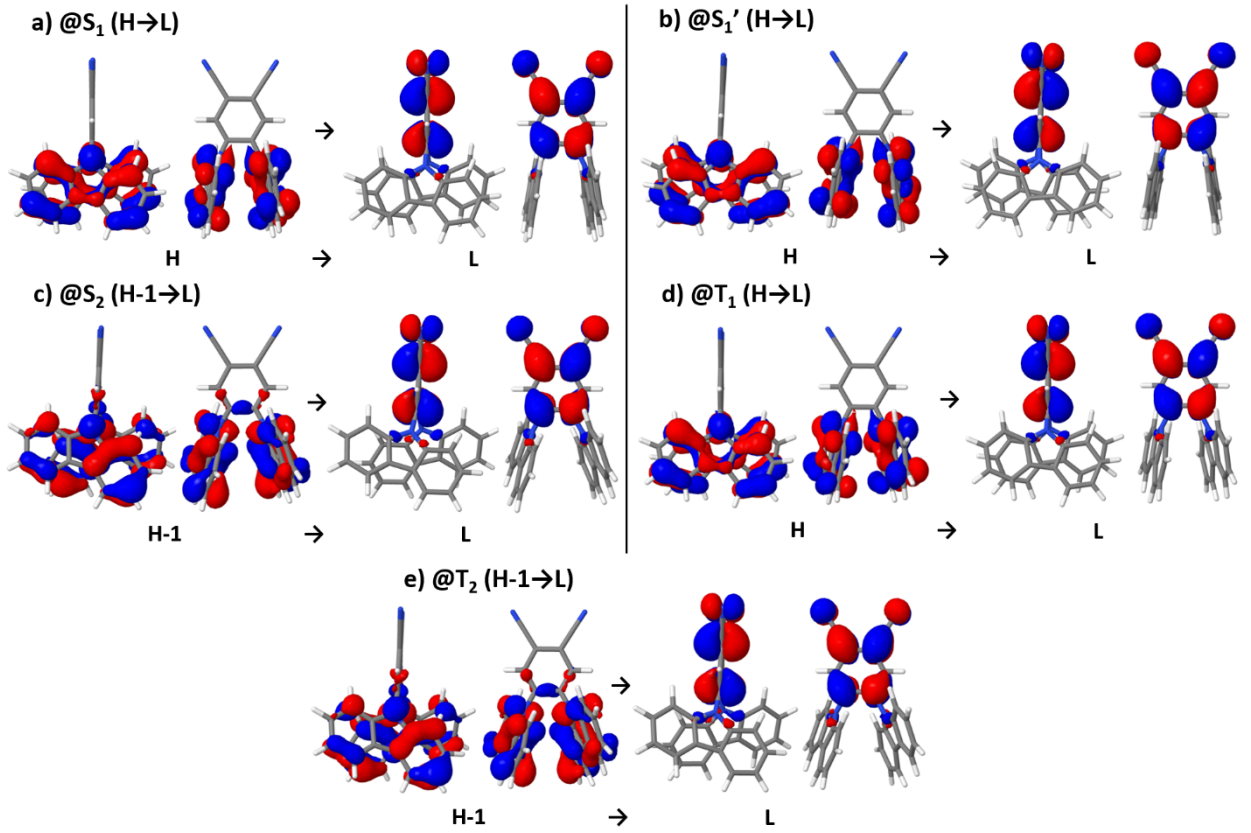

Fig. S5 BHLYP Frontier molecular orbitals of **2CzPN** calculated at the indicated excited state geometry.

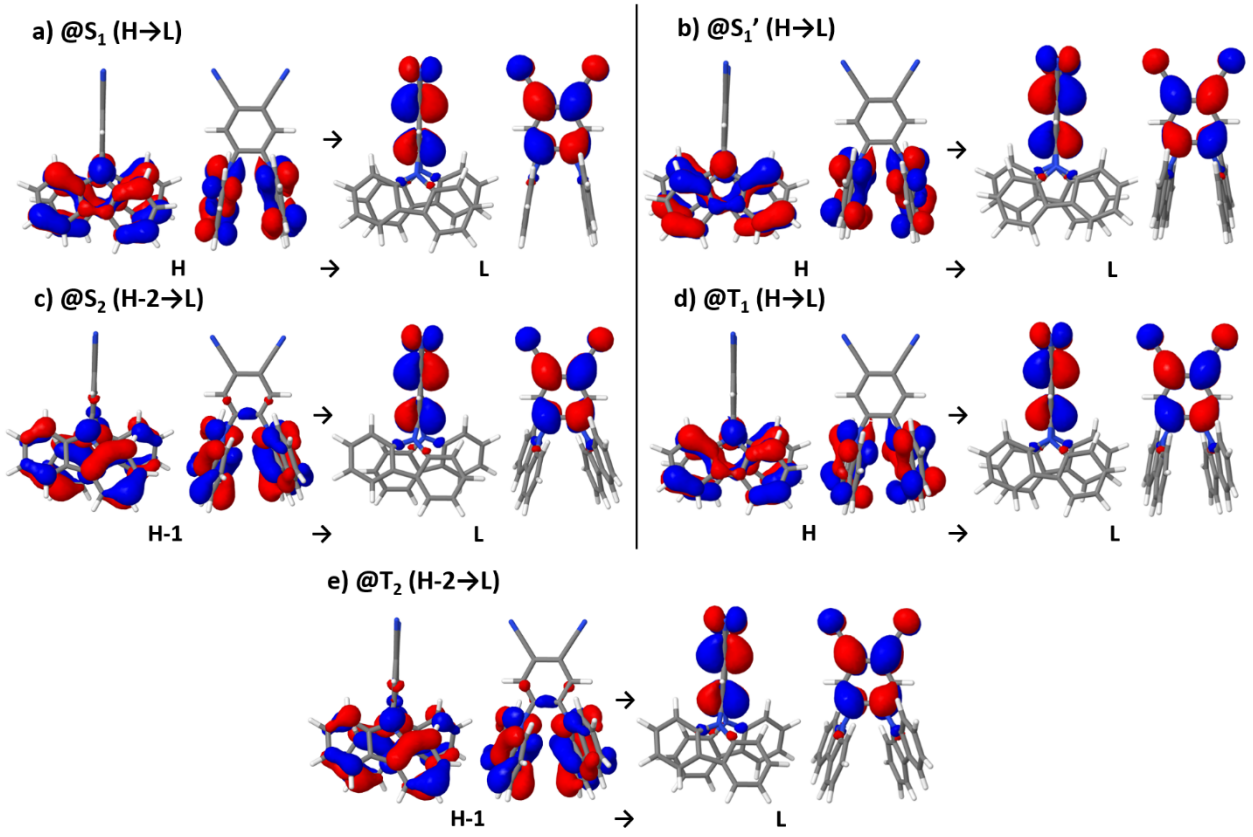

Table S5. DFT/MRCI excitation energies (ΔE, eV) of low-lying singlet and triplet states of **2CzPN** calculated at the S_1 minimum.

State	ΔE(eV)	Transition	%DC
S_0	0.48		
S_1	2.91	H → L	89.3%
S_2	3.42	H-3 → L	85.1%
S_3	3.45	H-1 → L	88.0%
S_4	3.72	H-2 → L	87.1%
T_1	2.83	H → L	87.5%
T_2	3.35	H-3 → L	84.4%
T_3	3.38	H-1 → L	87.3%
T_4	3.51	H-7 → L	60.3%
		H-2 → L	14.5%

Fig. S6 BH-LYP frontier molecular orbitals of **2CzPN** calculated at the S_1 minimum.

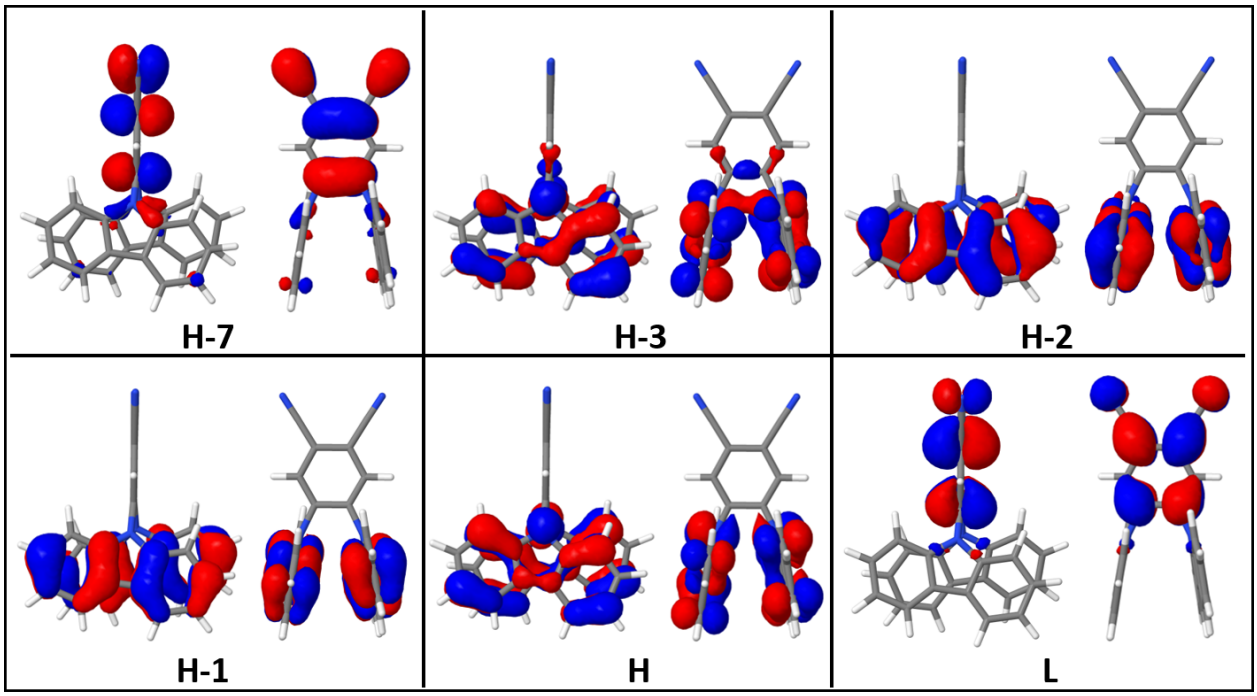

Table S6. DFT/MRCI excitation energies (ΔE, eV) of low-lying singlet and triplet states of **2CzPN** calculated at the S_1' minimum.

State	ΔE(eV)	Transition	%DC
S_0	0.48		
S_1	2.92	H → L	89.4%
S_2	3.41	H-2 → L	47.3%
		H-3→ L	39.3%
S_3	3.45	H-1 → L	87.7%
S_4	3.75	H-3→ L	48.5%
		H-2 → L	48.2%
T_1	2.83	H → L	87.4%
T_2	3.34	H-2 → L	47.0%
		H-3→ L	39.0%
T_3	3.39	H-1 → L	87.0%
T_4	3.52	H-7 → L	62.4%
		H-5→ L	8.1%

Fig. S7 BH-LYP frontier molecular orbitals of **2CzPN** calculated at the S_1' minimum.

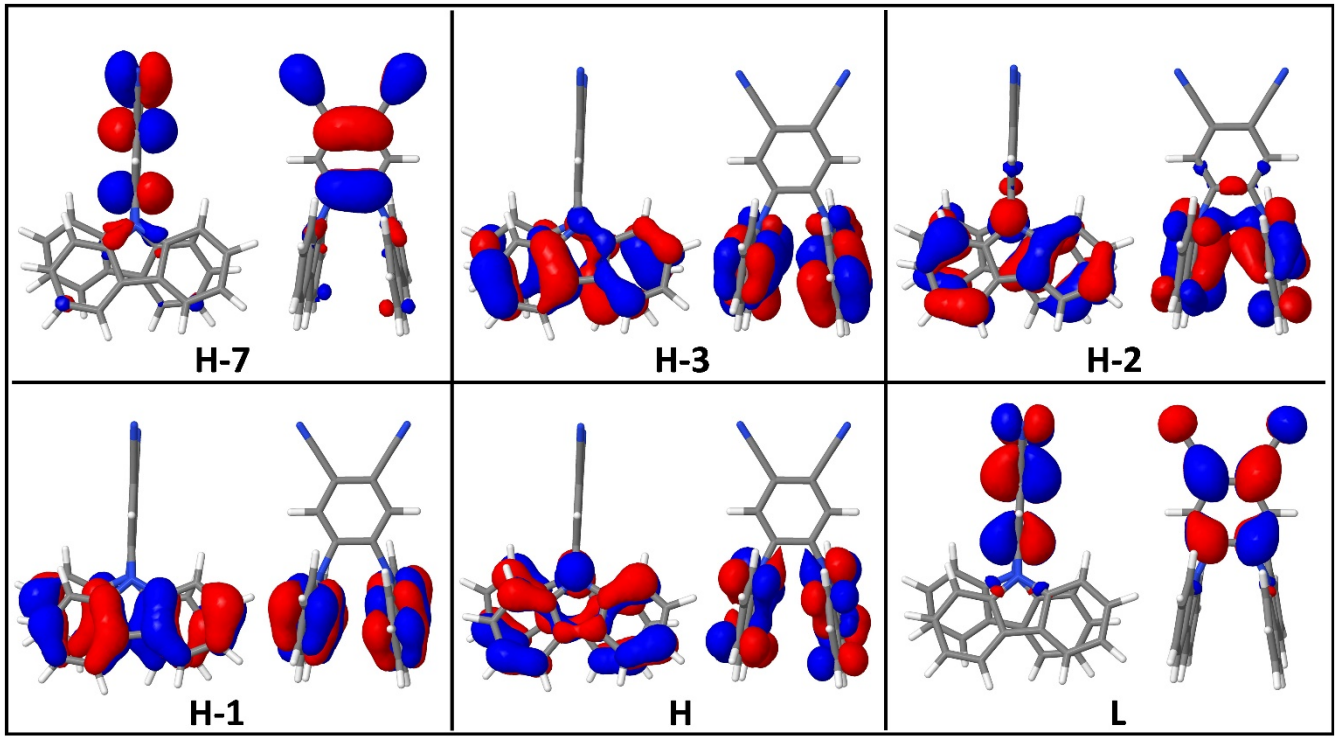

Table S7. DFT/MRCI excitation energies (ΔE, eV) of low-lying singlet and triplet states of **2CzPN** calculated at the T_1 minimum.

State	ΔE(eV)	Transition	%DC
S_0	0.43		
S_1	2.91	H → L	89.1%
S_2	3.39	H-3 → L	81.0%
S_3	3.48	H-1 → L	82.1%
S_4	3.66	H-2 → L	88.6%
T_1	2.79	H → L	84.7%
T_2	3.30	H-3 → L	80.6%
T_3	3.41	H-1 → L	81.9%
T_4	3.47	H-7 → L	50.2%
		H-2 → L	22.0%

Fig. S8 BH-LYP frontier molecular orbitals of **2CzPN** calculated at the T_1 minimum.

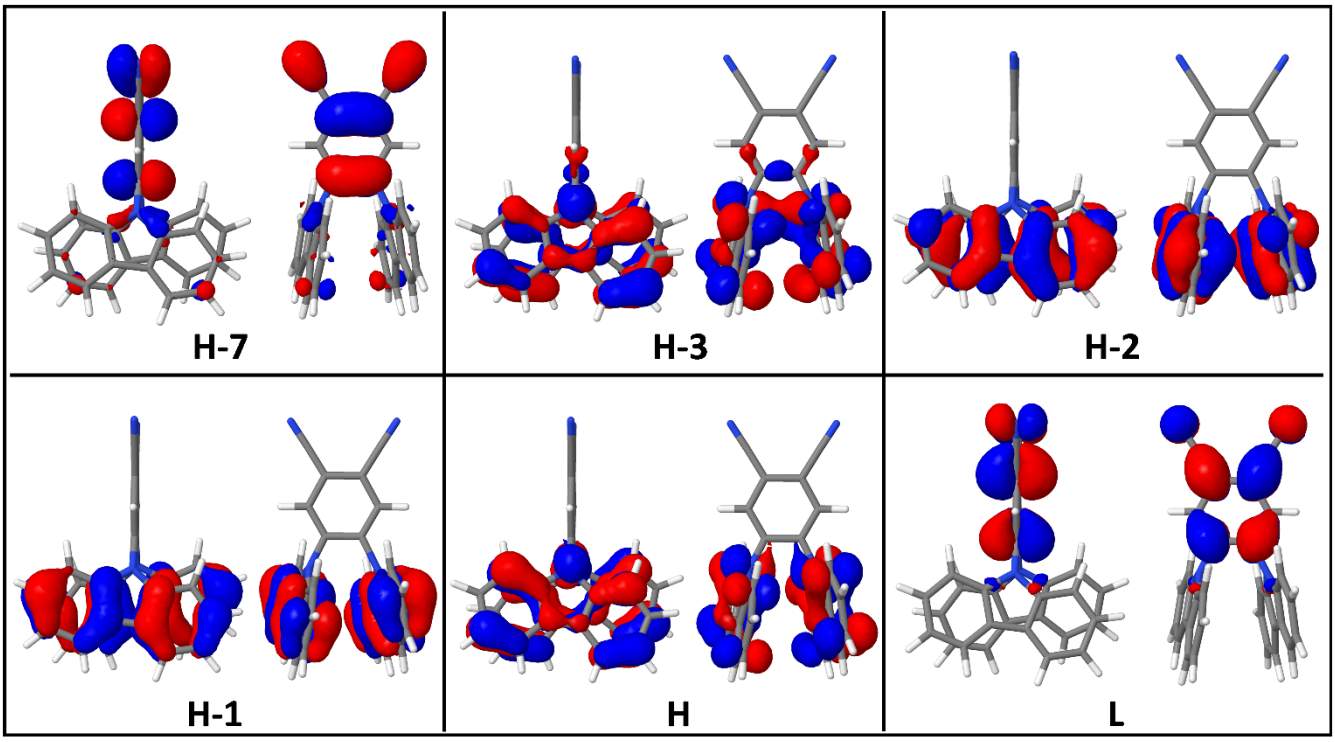

Table S8. DFT/MRCI excitation energies (ΔE, eV) of low-lying singlet and triplet states of **2CzPN** calculated at the T_2 minimum.

State	ΔE(eV)	Transition	%DC
S_0	0.32		
S_1	3.10	H → L	86.7%
S_2	3.12	H-1 → L	84.8%
S_3	3.45	H-2 → L	87.1%
S_4	3.71	H-3 → L	84.4%
T_1	2.84	H → L	69.4%
		H-6 → L	15.8%
T_2	3.01	H-1 → L	83.4%
T_3	3.36	H-2 → L	78.4%
T_4	3.59	H-3 → L	54.9%
		H-2→ L+3	13.7%

Fig. S9 BH-LYP frontier molecular orbitals of **2CzPN** calculated at the T_2 minimum.

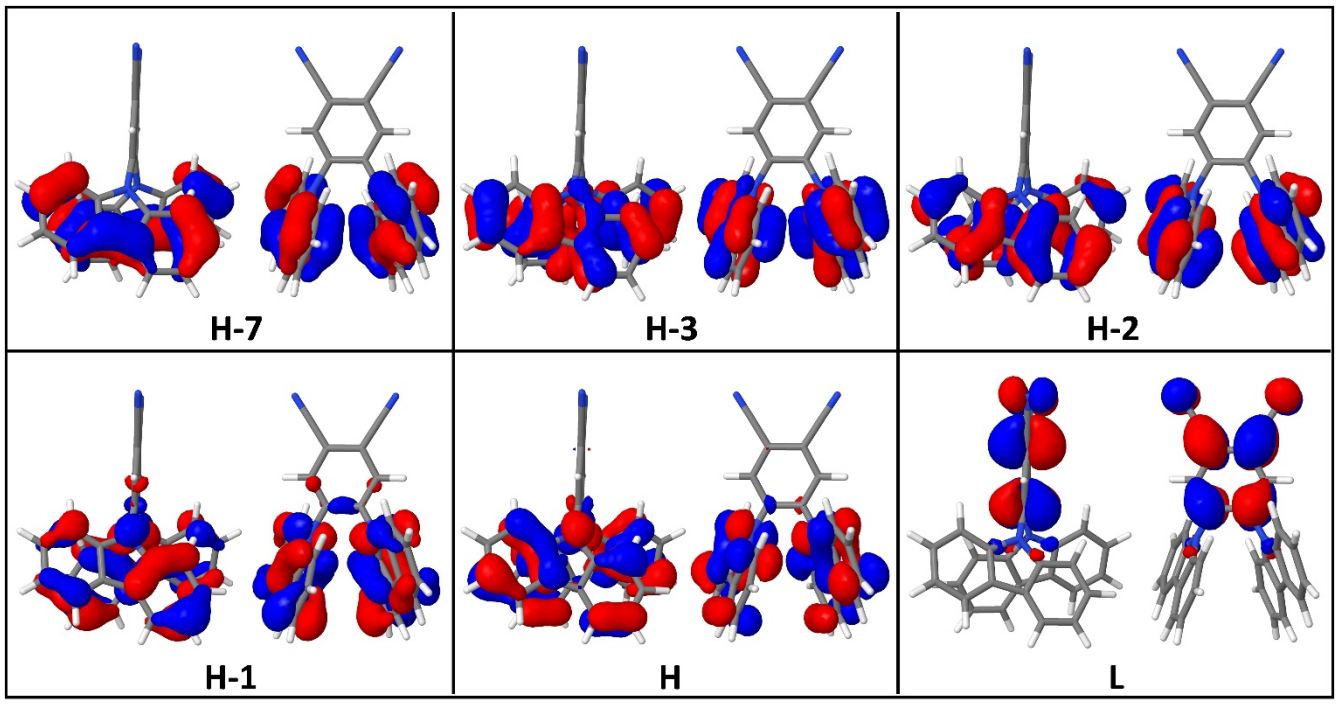

Table S9. Dihedral angles (in degrees) of the ground and excited state minima of **2CzPN** optimized at PBE0-D3(BJ)/def-SV(P) level of theory: For the singlet states by using TDDFT and for the triplet states using TDA approximation.

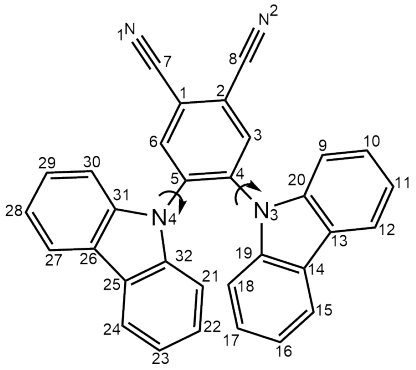

Dihedral	S_0	S_1	S_1'	S_2	T_1	T_2
C3-C4-N3-C20	-130.7	-109.9	-88.2	-111.8	-113.3	-117.8
C3-C4-N3-C19	59.5	88.7	110.0	78.2	85.2	70.1
C5-C4-N3-C20	49.7	74.9	87.3	77.1	69.5	67.3
C5-C4-N3-C19	-120.1	-86.5	-74.5	-92.8	-92.1	-104.8
C4-C5-N4-C31	-120.0	-86.6	-74.3	-92.9	-92.3	-104.7
C4-C5-N4-C32	49.7	75.0	87.0	77.2	69.7	67.1
C6-C5-N4-C31	59.5	88.7	110.0	78.1	84.8	70.3
C6-C5-N4-C32	-130.8	-109.8	-88.7	-111.8	-113.2	-117.9
C4-N3-C20-C19	-171.1	-163.8	-164.3	-171.3	-164.0	-173.2
C5-N4-C32-C31	-171.1	-163.9	-163.9	-171.4	-164.4	-172.9

Table S10. Harmonic frequencies (ν_i, cm^{-1}) and component-averaged ∂SOMEs (cm^{-1}) with respect to the corresponding (dimensionless) normal coordinates calculated at the S_1, S_1' and T_1 state minima of **2CzPN**.

Mode	ν_i@S_1	S_1-T_1	S_1-T_2	ν_i@S1'	S_1'-T_1	S_1'-T_2	ν_i@T_1	T_1-S_1
1	33.7	0.009	0.051	31.9	0.002	0.100	29.0	0.043
2	37.5	0.020	0.096	35.7	0.006	0.061	33.1	0.036
3	39.7	0.031	0.060	37.8	0.031	0.118	34.6	0.007
4	51.0	0.007	0.034	50.8	0.004	0.112	47.9	0.003
5	67.0	0.006	0.125	63.3	0.005	0.033	61.1	0.012
6	73.8	0.007	0.086	73.5	0.006	0.043	70.7	0.006
7	82.0	0.044	0.052	81.5	0.042	0.122	75.8	0.046
8	115.5	0.003	0.010	113.7	0.002	0.061	110.9	0.004
9	118.8	0.002	0.060	116.3	0.002	0.045	116.5	0.003
10	119.8	0.002	0.060	118.9	0.001	0.104	119.5	0.003
11	141.8	0.012	0.018	140.1	0.012	0.071	137.8	0.015
12	152.0	0.005	0.096	150.1	0.006	0.117	147.2	0.007
13	159.0	0.029	0.023	157.4	0.024	0.099	153.3	0.031
14	180.5	0.003	0.036	178.4	0.002	0.020	176.5	0.005
15	187.0	0.003	0.149	185.9	0.003	0.098	182.9	0.006
16	196.2	0.001	0.061	195.7	0.001	0.082	195.5	0.005
17	208.0	0.014	0.033	206.6	0.016	0.105	202.4	0.022
18	216.2	0.024	0.068	215.3	0.022	0.134	211.9	0.028
19	270.1	0.002	0.093	269.4	0.002	0.079	269.6	0.004
20	298.3	0.006	0.040	296.6	0.007	0.009	295.2	0.031
21	299.1	0.029	0.030	297.7	0.029	0.102	295.4	0.009
22	313.0	0.002	0.110	311.7	0.004	0.128	308.5	0.005
23	321.1	0.021	0.007	321.2	0.016	0.036	320.9	0.033
24	340.6	0.011	0.299	339.8	0.014	0.165	340.0	0.020
25	406.1	0.009	0.023	405.1	0.011	0.039	399.8	0.007
26	419.9	0.020	0.027	418.7	0.020	0.040	416.9	0.029
27	420.8	0.004	0.064	420.2	0.004	0.052	419.4	0.005
28	432.6	0.003	0.229	430.9	0.002	0.117	429.1	0.002
29	437.7	0.005	0.437	435.1	0.005	0.242	432.2	0.010
30	442.3	0.002	0.118	442.5	0.004	0.030	442.2	0.003
31	442.9	0.001	0.013	442.8	0.002	0.110	442.7	0.003
32	447.4	0.001	0.028	446.2	0.003	0.115	445.2	0.009
33	461.7	0.040	0.035	459.7	0.039	0.071	456.1	0.043
34	480.1	0.005	0.266	478.3	0.003	0.276	469.0	0.001
35	511.3	0.015	0.113	510.7	0.017	0.039	512.7	0.008
36	515.4	0.009	0.029	515.3	0.022	0.121	513.1	0.018
37	518.2	0.005	0.103	517.6	0.005	0.037	518.9	0.018
38	531.8	0.005	0.094	532.0	0.001	0.127	531.8	0.003
39	545.4	0.003	0.127	544.4	0.002	0.095	542.3	0.007
40	575.7	0.006	0.051	575.3	0.006	0.071	574.5	0.006
41	583.8	0.000	0.022	582.6	0.001	0.080	582.4	0.002
42	586.2	0.001	0.009	585.0	0.002	0.006	584.7	0.003
43	608.7	0.001	0.014	607.5	0.001	0.031	606.6	0.006

Mode	ν_i@S_1	S_1-T_1	S_1-T_2	ν_i@S1'	S_1'-T_1	S_1'-T_2	ν_i@T_1	T_1-S_1
44	613.6	0.008	0.170	613.0	0.007	0.128	612.3	0.015
45	617.3	0.009	0.099	617.3	0.007	0.015	617.9	0.012
46	619.7	0.005	0.043	619.7	0.006	0.118	620.0	0.005
47	636.8	0.002	0.051	636.7	0.005	0.079	635.5	0.004
48	642.0	0.002	0.015	641.5	0.003	0.126	641.4	0.004
49	665.7	0.007	0.029	664.8	0.004	0.052	663.6	0.008
50	685.8	0.007	0.040	685.2	0.007	0.004	685.2	0.013
51	703.7	0.002	0.078	703.4	0.003	0.042	703.3	0.004
52	722.1	0.026	0.038	721.7	0.029	0.116	720.7	0.038
53	729.6	0.002	0.029	727.7	0.006	0.035	725.1	0.009
54	742.6	0.024	0.009	742.2	0.025	0.047	741.8	0.028
55	750.1	0.003	0.053	748.6	0.003	0.028	747.6	0.005
56	757.2	0.000	0.011	755.5	0.000	0.021	754.4	0.002
57	768.1	0.001	0.083	768.0	0.002	0.049	767.3	0.008
58	770.7	0.009	0.021	768.9	0.012	0.046	767.9	0.003
59	774.9	0.001	0.059	772.9	0.003	0.105	771.7	0.002
60	778.6	0.010	0.040	778.8	0.012	0.073	778.6	0.006
61	801.1	0.007	0.024	799.7	0.007	0.010	797.8	0.011
62	804.3	0.004	0.007	802.9	0.008	0.010	801.3	0.013
63	806.0	0.016	0.015	804.5	0.015	0.071	803.8	0.019
64	810.0	0.002	0.178	808.9	0.003	0.142	807.5	0.003
65	873.7	0.001	0.014	873.4	0.001	0.017	873.9	0.002
66	889.8	0.009	0.033	888.8	0.009	0.005	888.0	0.012
67	894.2	0.010	0.022	893.2	0.007	0.023	892.7	0.015
68	905.6	0.009	0.015	904.7	0.010	0.078	903.3	0.010
69	907.9	0.003	0.050	906.6	0.005	0.094	905.6	0.005
70	923.1	0.008	0.001	921.7	0.009	0.030	922.8	0.012
71	925.8	0.004	0.018	924.3	0.006	0.097	923.7	0.003
72	958.5	0.003	0.293	956.8	0.001	0.134	957.5	0.004
73	960.9	0.013	0.055	959.5	0.019	0.118	959.3	0.011
74	968.5	0.003	0.050	967.2	0.001	0.124	966.3	0.001
75	970.0	0.002	0.082	969.4	0.003	0.065	968.5	0.005
76	972.4	0.002	0.029	971.5	0.005	0.116	970.5	0.007
77	974.7	0.002	0.124	973.9	0.003	0.020	973.6	0.004
78	975.5	0.002	0.057	974.4	0.002	0.102	974.1	0.003
79	1004.5	0.008	0.101	1003.5	0.010	0.009	1004.1	0.010
80	1009.2	0.002	0.022	1008.7	0.002	0.102	1007.8	0.006
81	1011.7	0.004	0.131	1011.2	0.006	0.027	1011.1	0.007
82	1013.0	0.006	0.046	1012.2	0.003	0.083	1011.9	0.008
83	1017.3	0.008	0.139	1016.9	0.010	0.037	1018.9	0.016
84	1025.9	0.006	0.057	1026.0	0.007	0.077	1026.3	0.006
85	1049.8	0.001	0.002	1049.3	0.002	0.016	1049.4	0.001
86	1052.3	0.014	0.030	1051.8	0.012	0.042	1052.0	0.020
87	1053.0	0.003	0.128	1052.3	0.003	0.004	1052.6	0.003
88	1053.1	0.003	0.029	1052.4	0.001	0.060	1053.1	0.004
89	1094.0	0.007	0.084	1093.6	0.007	0.052	1094.9	0.008
90	1102.5	0.012	0.095	1101.8	0.015	0.030	1107.2	0.020

Mode	ν_i@S_1	S_1-T_1	S_1-T_2	ν_i@S1'	S_1'-T_1	S_1'-T_2	ν_i@T_1	T_1-S_1
91	1123.6	0.009	0.045	1123.1	0.006	0.062	1122.0	0.015
92	1124.9	0.002	0.115	1124.4	0.004	0.119	1125.3	0.008
93	1143.5	0.002	0.073	1143.4	0.003	0.065	1144.6	0.003
94	1164.9	0.001	0.080	1164.4	0.002	0.003	1165.2	0.005
95	1168.6	0.001	0.073	1168.4	0.005	0.147	1168.0	0.001
96	1170.5	0.001	0.104	1170.0	0.001	0.012	1169.5	0.003
97	1170.8	0.002	0.036	1170.2	0.001	0.103	1169.6	0.001
98	1181.2	0.002	0.066	1180.2	0.007	0.108	1180.6	0.011
99	1181.6	0.004	0.133	1181.1	0.004	0.076	1181.5	0.008
100	1211.2	0.007	0.010	1210.0	0.007	0.014	1204.4	0.010
101	1244.3	0.017	0.133	1243.5	0.019	0.065	1246.5	0.032
102	1247.3	0.029	0.037	1246.7	0.026	0.114	1246.8	0.027
103	1259.8	0.001	0.087	1259.4	0.001	0.054	1260.1	0.004
104	1274.6	0.007	0.108	1274.3	0.009	0.085	1273.2	0.006
105	1302.3	0.001	0.027	1302.1	0.004	0.102	1302.0	0.007
106	1312.8	0.008	0.100	1312.1	0.009	0.027	1314.5	0.014
107	1340.3	0.013	0.067	1340.3	0.010	0.117	1339.5	0.016
108	1340.5	0.005	0.073	1340.4	0.002	0.007	1340.6	0.002
109	1345.7	0.012	0.169	1345.5	0.014	0.137	1343.2	0.010
110	1365.8	0.004	0.251	1365.6	0.004	0.207	1368.9	0.006
111	1390.2	0.003	0.081	1388.0	0.005	0.036	1392.9	0.007
112	1400.9	0.029	0.091	1398.6	0.034	0.125	1397.7	0.044
113	1407.0	0.006	0.167	1406.0	0.006	0.159	1403.5	0.002
114	1412.8	0.009	0.078	1412.2	0.009	0.092	1407.5	0.012
115	1423.1	0.038	0.021	1422.9	0.039	0.053	1422.3	0.055
116	1431.3	0.004	0.187	1429.8	0.003	0.089	1428.2	0.006
117	1457.6	0.012	0.050	1455.9	0.016	0.073	1454.1	0.026
118	1471.2	0.009	0.155	1469.9	0.011	0.026	1472.0	0.015
119	1478.5	0.009	0.075	1477.8	0.010	0.094	1478.2	0.014
120	1501.4	0.017	0.059	1500.9	0.020	0.077	1500.4	0.023
121	1509.0	0.001	0.115	1509.0	0.002	0.053	1506.9	0.003
122	1516.9	0.004	0.106	1516.6	0.004	0.078	1515.5	0.007
123	1525.3	0.010	0.049	1525.2	0.009	0.056	1523.6	0.056
124	1527.7	0.006	0.096	1528.4	0.005	0.135	1524.2	0.009
125	1531.3	0.048	0.124	1530.8	0.044	0.127	1525.4	0.076
126	1555.9	0.003	0.051	1555.3	0.003	0.077	1554.5	0.004
127	1567.2	0.063	0.146	1566.6	0.060	0.194	1559.4	0.079
128	1596.7	0.006	0.030	1596.1	0.009	0.033	1590.0	0.005
129	1639.6	0.007	0.108	1639.3	0.008	0.074	1641.1	0.012
130	1642.9	0.003	0.083	1642.2	0.003	0.008	1644.9	0.008
131	1649.5	0.003	0.061	1649.2	0.003	0.127	1650.3	0.014
132	1658.2	0.024	0.084	1657.9	0.019	0.096	1657.5	0.018
133	1659.7	0.004	0.103	1659.3	0.007	0.114	1659.9	0.012
134	1660.4	0.002	0.130	1660.3	0.003	0.050	1660.3	0.003
135	1678.9	0.002	0.054	1679.0	0.001	0.036	1677.8	0.001
136	1711.4	0.040	0.016	1711.1	0.048	0.059	1707.7	0.061
137	2295.4	0.003	0.038	2291.8	0.003	0.037	2294.2	0.003

Mode	ν_i@S_1	S_1-T_1	S_1-T_2	ν_i@S1'	S_1'-T_1	S_1'-T_2	ν_i@T_1	T_1-S_1
138	2325.5	0.054	0.024	2322.3	0.048	0.005	2324.4	0.043
139	3205.3	0.002	0.007	3205.9	0.001	0.005	3205.3	0.002
140	3205.6	0.002	0.006	3206.0	0.001	0.006	3205.5	0.002
141	3206.3	0.001	0.008	3206.6	0.001	0.001	3205.9	0.001
142	3206.8	0.001	0.004	3206.8	0.002	0.006	3206.5	0.001
143	3216.2	0.001	0.005	3216.4	0.001	0.017	3215.7	0.002
144	3216.6	0.001	0.009	3216.7	0.001	0.009	3216.3	0.002
145	3217.0	0.001	0.006	3217.4	0.001	0.016	3216.8	0.001
146	3217.7	0.004	0.011	3217.8	0.002	0.061	3217.4	0.002
147	3219.8	0.001	0.004	3221.9	0.001	0.003	3219.2	0.001
148	3221.9	0.005	0.004	3223.8	0.005	0.008	3221.2	0.006
149	3226.6	0.005	0.002	3226.6	0.001	0.003	3226.1	0.001
150	3227.4	0.002	0.002	3226.7	0.002	0.012	3226.5	0.001
151	3227.7	0.003	0.008	3227.5	0.001	0.003	3227.6	0.003
152	3228.5	0.001	0.012	3227.8	0.006	0.018	3227.9	0.003
153	3237.1	0.002	0.036	3237.9	0.001	0.024	3235.5	0.004
154	3238.2	0.004	0.008	3238.8	0.005	0.022	3236.7	0.010
155	3244.4	0.002	0.010	3244.1	0.001	0.015	3241.4	0.003
156	3245.3	0.001	0.008	3245.8	0.001	0.050	3242.5	0.006

Fig. S10 Fragment-based analysis for the low-lying singlet and triplet state DFT/MRCI-R2016 wavefunctions calculated at the S_1' and T_2 minima of **2CzPN**.

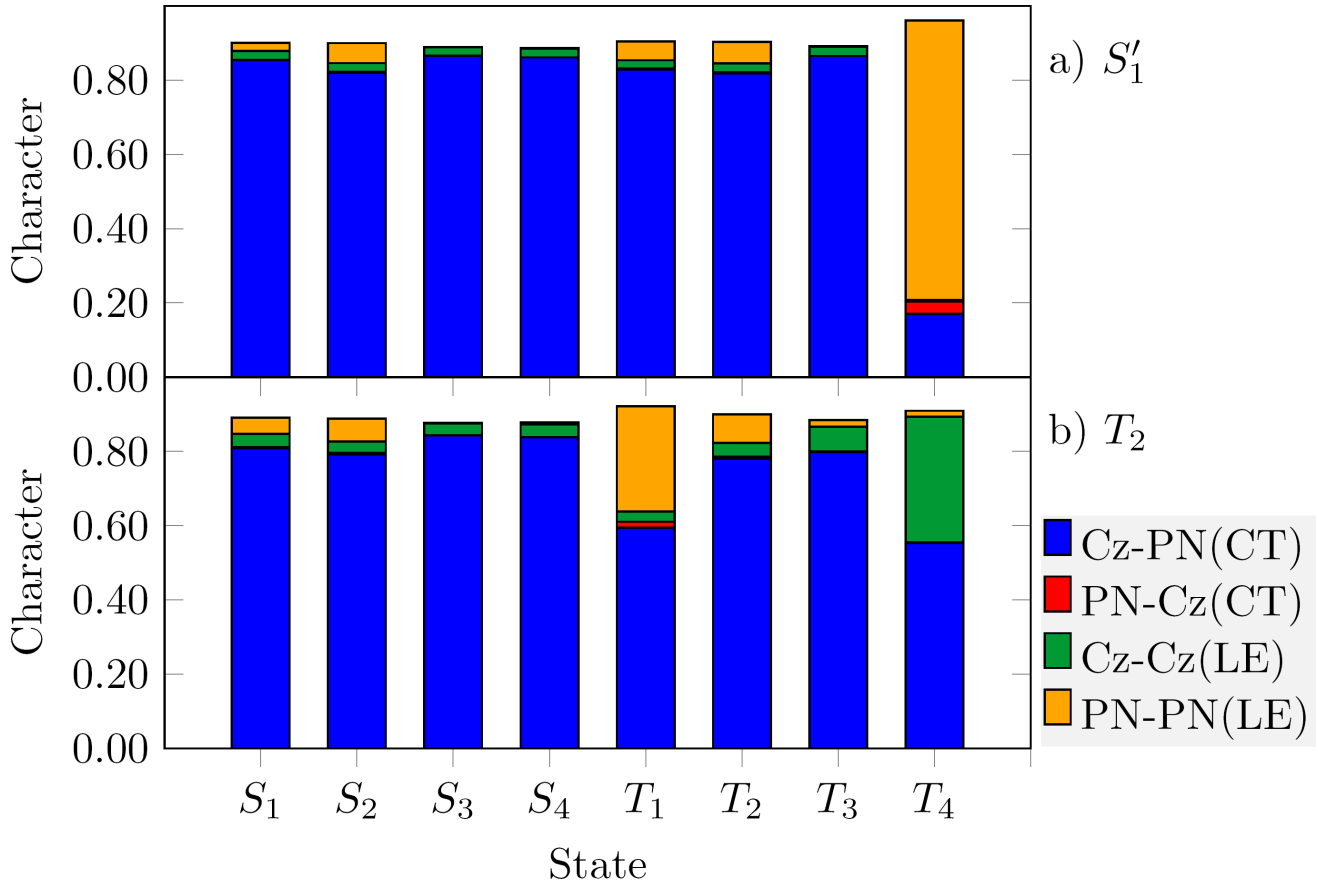

Fig. S11 DFT/MRCI-R2016 energies calculated at linear interpolated pathways (LIPs) between target electronic state minima of **2CzPN**. Dashed lines correspond to triplet state PESs while continuum lines correspond to singlet states. Excitation energies calculated relative to the S_0 state at its corresponding minimum.

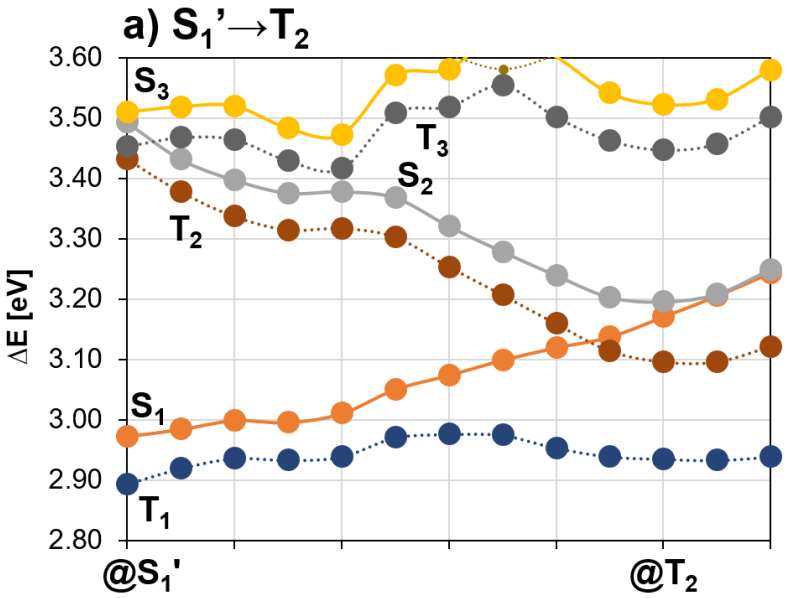

Cartesian coordinates for the optimized structures

S_0

H	-1.2257387	0.1246830	-0.0481976
C	-0.4032055	0.0336602	0.6633205
C	1.7260656	-0.1213609	2.4405020
C	0.6542922	-0.8335650	0.3871090
C	-0.4166625	0.8296167	1.8113968
C	0.6617764	0.7367841	2.7280028
C	1.7431403	-0.9037309	1.2853726
H	2.5428169	-0.2039069	3.1597109
C	0.6308074	-1.6191586	-0.8075789
N	0.5913717	-2.2471982	-1.7806981
C	2.8475989	-1.7783555	1.0400550
N	3.7524441	-2.4796641	0.8602139
N	0.6924641	1.4862300	3.9063718
N	-1.4961556	1.6888287	2.0299134
C	-0.3414348	1.5902477	4.8404237
C	-2.0959952	2.1815983	6.8965180
C	-0.0212479	2.6099766	5.7643485
C	-1.5020497	0.8291131	4.9588971
C	-2.3799431	1.1486920	5.9904438
C	-0.9126617	2.9064817	6.7986217
H	-1.7245872	0.0093737	4.2739010
H	-3.3072166	0.5778926	6.0921521
H	-0.6810850	3.6953504	7.5198412
H	-2.8070377	2.4075351	7.6959940
C	1.6871641	2.4125430	4.2376809
C	3.2843075	4.4417452	5.2427558
C	1.2727982	3.1329535	5.3815794
C	2.8811921	2.7054118	3.5796686
C	3.6731308	3.7268538	4.1004965
C	2.0843038	4.1521694	5.8850237
H	3.1898445	2.1667732	2.6804785
H	4.6168196	3.9728154	3.6050942
H	1.7737006	4.7190638	6.7671478
H	3.9297922	5.2360450	5.6274353
C	-2.8290768	1.2811228	2.1495966
C	-5.5393909	0.9588229	2.6278782
C	-3.6020954	2.3812952	2.5870037
C	-3.3901239	0.0179578	1.9654304
C	-4.7549230	-0.1252520	2.2078593
C	-4.9683893	2.2128268	2.8227290
H	-2.7885745	-0.8389559	1.6527443
H	-5.2199123	-1.1051214	2.0663319
H	-5.5769486	3.0548580	3.1642678
H	-6.6081745	0.8135281	2.8071956
C	-1.4135307	3.0433858	2.3624095
C	-1.7663833	5.6833232	3.1118558
C	-0.3120978	3.8952165	2.3218941
C	-2.6991247	3.5038981	2.7245928
C	-2.8706365	4.8372046	3.1056372
C	-0.5043047	5.2164502	2.7147045
H	0.6700323	3.5500011	1.9948086
H	-3.8585619	5.2081076	3.3925982
H	0.3496088	5.8997280	2.7095891
H	-1.8836062	6.7274300	3.4149136

S_0'

H	-0.01688060	0.54647780	3.39174190
C	-0.48870760	1.00742570	2.52187820
C	-1.61469890	2.21869600	0.29699210
C	-1.30549550	2.12413960	2.69702860
C	-0.21801680	0.48036690	1.25380610
C	-0.80604330	1.09044490	0.11763960
C	-1.87147740	2.74812350	1.56139790
H	-2.08163230	2.67245170	-0.57927350
C	-1.53883540	2.62884850	4.01542290
N	-1.71574380	3.01819720	5.09261290
C	-2.71593960	3.89616480	1.68857380
N	-3.40056240	4.82799830	1.76732460
N	-0.61294940	0.60199560	-1.17942830
N	0.62998770	-0.62830140	1.15461160
C	-0.16790110	1.36374520	-2.26389450
C	0.71087240	2.40693100	-4.67936690
C	-0.13465970	0.54429030	-3.41490050
C	0.24958200	2.69558650	-2.30290120
C	0.68438910	3.20374000	-3.52525730
C	0.30722130	1.07646550	-4.62948990
H	0.24452960	3.32717240	-1.41079810
H	1.01157390	4.24618910	-3.58106870
H	0.33784330	0.45219480	-5.52722720
H	1.05597120	2.83649350	-5.62401100
C	-0.89239730	-0.69152640	-1.63128700
C	-1.32784080	-3.05478150	-3.01489390
C	-0.60018840	-0.76451190	-3.01216640
C	-1.43193720	-1.77667670	-0.94116210
C	-1.63767850	-2.95721070	-1.65001800
C	-0.81702860	-1.95998970	-3.70361030
H	-1.69515730	-1.71515500	0.11642170
H	-2.05208690	-3.82370140	-1.12643470
H	-0.59436190	-2.02872550	-4.77238860
H	-1.50038980	-3.99755120	-3.54165810
C	1.80707400	-0.71094960	0.40428470
C	4.20269160	-1.35188830	-0.83622920
C	2.39098460	-1.98123290	0.61163620
C	2.42443210	0.25527030	-0.38955670
C	3.62314330	-0.08610500	-1.01009630
C	3.59633090	-2.30075000	-0.02027610
H	1.99803040	1.25120120	-0.52318630
H	4.12033260	0.65371000	-1.64422660
H	4.05765190	-3.28075700	0.13232890
H	5.14471590	-1.58805310	-1.33912630
C	0.46861050	-1.82498090	1.85918840
C	0.56756470	-4.36693460	2.96548740
C	-0.55996870	-2.21966280	2.71701120
C	1.53600980	-2.69308700	1.53593880
C	1.58123150	-3.97195670	2.09825900
C	-0.49207710	-3.49842040	3.26623140
H	-1.39774510	-1.55887160	2.95399760
H	2.40198200	-4.65310840	1.85545490
H	-1.28429090	-3.82780500	3.94502980
H	0.59250650	-5.36373770	3.41464510

S_1

H	-0.4367595	-1.1876881	-3.3905492
C	0.2530677	-1.4511440	-2.5864127
C	2.0514475	-2.0895804	-0.5085810
C	1.2269214	-2.4456267	-2.8145028
C	0.1709539	-0.8022118	-1.3793565
C	1.0876281	-1.1309800	-0.3167529
C	2.1676151	-2.7702027	-1.7384257
H	2.7332155	-2.3421878	0.3057614
C	1.2741276	-3.0926863	-4.0654117
N	1.2974511	-3.6138488	-5.1094978
C	3.1737038	-3.7442069	-1.8961950
N	4.0121544	-4.5490666	-2.0034144
N	0.8643743	-0.4791853	0.9402775
N	-0.7358187	0.2781785	-1.1245471
C	0.0194135	-0.9621761	1.9163149
C	-1.6875776	-1.4688584	4.0245699
C	-0.2973949	0.0813026	2.8264468
C	-0.5004696	-2.2533110	2.0529780
C	-1.3522741	-2.4910298	3.1300848
C	-1.1667692	-0.1752747	3.8779620
H	-0.2307292	-3.0372237	1.3440598
H	-1.7664011	-3.4909358	3.2745792
H	-1.4396037	0.6118007	4.5842248
H	-2.3625589	-1.6826710	4.8558546
C	1.1511953	0.8417079	1.2144822
C	1.3345477	3.4575849	2.0775686
C	0.4268717	1.2525543	2.3650374
C	1.9915892	1.7133479	0.5149643
C	2.0677114	3.0285650	0.9650347
C	0.5182821	2.5715359	2.7923880
H	2.5747537	1.3585758	-0.3345962
H	2.7075355	3.7373713	0.4362627
H	-0.0392555	2.9161785	3.6660015
H	1.4123139	4.4970468	2.4026720
C	-1.8403218	0.2119015	-0.2997803
C	-3.9615031	0.5645558	1.4315538
C	-2.2368953	1.5259151	0.0638748
C	-2.5123960	-0.9225153	0.1645559
C	-3.5779324	-0.7227910	1.0381939
C	-3.3020676	1.6981036	0.9398998
H	-2.2177381	-1.9171956	-0.1695385
H	-4.1199614	-1.5875837	1.4251351
H	-3.6188439	2.6976970	1.2451424
H	-4.7991083	0.6871333	2.1211862
C	-0.4370108	1.6024538	-1.3601692
C	-0.1764482	4.3465795	-1.4949292
C	0.5779310	2.1339205	-2.1630695
C	-1.3340049	2.4274127	-0.6298288
C	-1.1897676	3.8069478	-0.6900427
C	0.6858009	3.5216759	-2.2258188
H	1.2437791	1.4755680	-2.7226342
H	-1.8539601	4.4648472	-0.1254878
H	1.4590314	3.9709913	-2.8522098
H	-0.0624161	5.4308404	-1.5563266

S_1'

H	-0.7583505	0.5843402	-0.4201523
C	-0.1081312	0.2789935	0.4030996
C	1.5318661	-0.5262716	2.5516938
C	0.8355783	-0.7470661	0.1875351
C	-0.2320179	0.8839248	1.6296235
C	0.6092158	0.4756968	2.7263485
C	1.6784764	-1.1744856	1.3074393
H	2.1756016	-0.8215004	3.3836395
C	0.9363631	-1.3348295	-1.0892261
N	1.0000037	-1.8080280	-2.1542543
C	2.6312096	-2.2041647	1.1736693
N	3.4283077	-3.0522335	1.0862081
N	0.4893419	1.2359308	3.9356083
N	-1.2403772	1.8570011	1.9308413
C	-0.5585561	1.1546834	4.8292408
C	-2.5566694	1.4743492	6.7087995
C	-0.5731094	2.3164141	5.6459879
C	-1.5096043	0.1386612	4.9656326
C	-2.5095525	0.3196237	5.9179209
C	-1.5842678	2.4757333	6.5862504
H	-1.4464781	-0.7658592	4.3593391
H	-3.2707902	-0.4540047	6.0471139
H	-1.6256960	3.3674317	7.2178294
H	-3.3566974	1.5885395	7.4451642
C	1.1971472	2.3916509	4.1860168
C	2.2558490	4.8089177	4.9960925
C	0.5703173	3.1128831	5.2368212
C	2.3477554	2.8606938	3.5434370
C	2.8726334	4.0781154	3.9740206
C	1.0996232	4.3341803	5.6324285
H	2.8138837	2.2790789	2.7455450
H	3.7786692	4.4682002	3.5027446
H	0.6299411	4.9178282	6.4288439
H	2.6855249	5.7646038	5.3084340
C	-2.4933313	1.5379680	2.4081308
C	-5.0056307	1.3515831	3.5370169
C	-3.0869900	2.6905640	2.9880103
C	-3.1430353	0.2994973	2.3801071
C	-4.4149921	0.2286441	2.9460975
C	-4.3457147	2.5889237	3.5654360
H	-2.6661380	-0.5670931	1.9178290
H	-4.9570816	-0.7205969	2.9298017
H	-4.8208651	3.4563858	4.0314332
H	-6.0015428	1.2649869	3.9798442
C	-1.0157210	3.2022447	2.1376896
C	-0.9623432	5.8681729	2.8567446
C	0.1012460	3.9636359	1.7796307
C	-2.1250636	3.7658903	2.8222694
C	-2.0909073	5.1064185	3.1876259
C	0.1093998	5.3053040	2.1527671
H	0.9176854	3.5176637	1.2102421
H	-2.9262926	5.5608542	3.7274274
H	0.9693095	5.9273641	1.8916037
H	-0.9243937	6.9238537	3.1385423

S_2

H	-0.7931883	0.6667337	-0.3434750
C	-0.1383779	0.3690719	0.4794047
C	1.4599632	-0.4559566	2.6275915
C	0.8033725	-0.6540941	0.2607800
C	-0.2976850	0.9697604	1.7075240
C	0.5608146	0.5697364	2.8115416
C	1.6095985	-1.1099692	1.3900147
H	2.1089934	-0.7451915	3.4580104
C	0.9204780	-1.2244533	-1.0237448
N	0.9972656	-1.6843525	-2.0930864
C	2.5452069	-2.1583397	1.2693354
N	3.3277783	-3.0199797	1.1913866
N	0.5853987	1.3653384	3.9893895
N	-1.4004791	1.8284606	1.9668870
C	-0.3707992	1.3797454	4.9657356
C	-2.1047716	1.8472114	7.0606633
C	-0.1144617	2.4573657	5.8661949
C	-1.4757612	0.5278829	5.1163805
C	-2.3374307	0.7799806	6.1716556
C	-0.9944543	2.6861867	6.9173533
H	-1.6438099	-0.2932407	4.4185043
H	-3.2141075	0.1426617	6.3134798
H	-0.8290201	3.5089815	7.6180137
H	-2.8069120	2.0218813	7.8804742
C	1.4912815	2.3980068	4.2319517
C	2.9851427	4.5547094	5.0925209
C	1.0927765	3.1037846	5.3903840
C	2.6314059	2.7358761	3.5088857
C	3.3711484	3.8321653	3.9567773
C	1.8473895	4.1933990	5.8207123
H	2.9261602	2.1634578	2.6265104
H	4.2719393	4.1265581	3.4110833
H	1.5588986	4.7559290	6.7130527
H	3.5878276	5.4060238	5.4201316
C	-2.6972953	1.3950229	2.2426770
C	-5.3478044	1.0106457	2.9142077
C	-3.4790981	2.4989153	2.6539361
C	-3.2192304	0.1088191	2.1413776
C	-4.5600143	-0.0664914	2.4895630
C	-4.8158053	2.3012796	2.9946299
H	-2.5974587	-0.7239556	1.8052313
H	-5.0023399	-1.0643833	2.4229607
H	-5.4407005	3.1390892	3.3164581
H	-6.3958287	0.8415407	3.1756929
C	-1.3335155	3.1778238	2.1742603
C	-1.6455868	5.8469128	2.8012858
C	-0.2282362	4.0292174	2.0241051
C	-2.6031571	3.6535456	2.6207497
C	-2.7502876	4.9991697	2.9360046
C	-0.4025590	5.3653257	2.3471314
H	0.7286542	3.6412235	1.6730435
H	-3.7081848	5.3907403	3.2885483
H	0.4398465	6.0553815	2.2518651
H	-1.7483838	6.9061712	3.0522832

T_1

H	-0.5081960	-1.2917378	-3.3462221
C	0.2246134	-1.5083175	-2.5652706
C	2.1009413	-2.0593690	-0.5335232
C	1.2191541	-2.4770133	-2.8074954
C	0.1616633	-0.8352636	-1.3688399
C	1.1192465	-1.1201124	-0.3275467
C	2.1925078	-2.7667970	-1.7491984
H	2.8258485	-2.2658284	0.2573706
C	1.2517531	-3.1360673	-4.0526104
N	1.2566500	-3.6697933	-5.0904621
C	3.2089123	-3.7289992	-1.9133921
N	4.0601016	-4.5193645	-2.0269131
N	1.0171666	-0.3427331	0.8685264
N	-0.8610491	0.1151990	-1.0597963
C	-0.0117350	-0.4392814	1.7855123
C	-1.9680637	-0.1577703	3.7141287
C	-0.0381278	0.7288870	2.5900785
C	-0.9263178	-1.4819768	1.9590857
C	-1.9069529	-1.3196104	2.9355469
C	-1.0284204	0.8692133	3.5556826
H	-0.8498989	-2.3930650	1.3638583
H	-2.6404341	-2.1145169	3.0931934
H	-1.0767469	1.7647166	4.1812322
H	-2.7515841	-0.0574338	4.4699256
C	1.7025054	0.8316880	1.0942459
C	2.6991204	3.2943501	1.8460416
C	1.0761732	1.5487923	2.1488438
C	2.8218497	1.3291454	0.4184707
C	3.3153838	2.5688695	0.8187460
C	1.5744781	2.7923252	2.5151800
H	3.2871176	0.7541791	-0.3847696
H	4.1953215	2.9825941	0.3189542
H	1.1012252	3.3730437	3.3115709
H	3.1045725	4.2682090	2.1337339
C	-2.0999960	-0.2127356	-0.5524062
C	-4.5756321	-0.4142051	0.6535310
C	-2.6992054	0.9437228	0.0147416
C	-2.7265707	-1.4630545	-0.5280052
C	-3.9791459	-1.5422283	0.0769384
C	-3.9394375	0.8346582	0.6299609
H	-2.2454825	-2.3345404	-0.9765192
H	-4.5013624	-2.5022634	0.1047117
H	-4.4154781	1.7052709	1.0889691
H	-5.5565780	-0.5082994	1.1272565
C	-0.6547118	1.4698251	-0.8861952
C	-0.6407573	4.1564731	-0.2470669
C	0.4371227	2.2423079	-1.2926883
C	-1.7596381	2.0307058	-0.1950904
C	-1.7460752	3.3823197	0.1294152
C	0.4265487	3.5947126	-0.9579648
H	1.2483855	1.7971226	-1.8704152
H	-2.5813232	3.8363090	0.6696717
H	1.2676480	4.2254224	-1.2568260
H	-0.6194062	5.2205146	0.0031982

T_2

H	-0.5470791	-1.2278405	-3.2780222
C	0.1879853	-1.4364253	-2.4966040
C	2.0401660	-1.9823610	-0.4749429
C	1.1833104	-2.4005668	-2.7450537
C	0.0913388	-0.7629102	-1.2996869
C	1.0729926	-1.0268698	-0.2573875
C	2.1410784	-2.6966977	-1.6838283
H	2.7694271	-2.1811314	0.3144404
C	1.2159773	-3.0571026	-3.9923040
N	1.2222609	-3.5916729	-5.0293151
C	3.1639045	-3.6546065	-1.8392289
N	4.0205329	-4.4391460	-1.9484242
N	1.0895690	-0.2300662	0.9167007
N	-1.0053149	0.0981003	-1.0356233
C	0.1113719	-0.2083368	1.8740382
C	-1.6605011	0.2693535	3.9331143
C	0.3745136	0.8457381	2.7972869
C	-1.0103538	-1.0414545	1.9910146
C	-1.8939538	-0.7816931	3.0280201
C	-0.5246923	1.0814048	3.8297413
H	-1.1743199	-1.8590173	1.2881743
H	-2.7849200	-1.4046167	3.1424534
H	-0.3542472	1.8870982	4.5488469
H	-2.3773781	0.4506551	4.7385968
C	2.0224261	0.7657181	1.2037925
C	3.5514319	2.8660042	2.1405188
C	1.6151077	1.4612886	2.3661948
C	3.1839801	1.0930751	0.5092200
C	3.9419497	2.1591833	0.9965767
C	2.3875423	2.5212907	2.8348775
H	3.4817210	0.5373583	-0.3826745
H	4.8600123	2.4428592	0.4747173
H	2.0912492	3.0761953	3.7293994
H	4.1688565	3.6939739	2.4989164
C	-2.3193724	-0.3120893	-0.8130049
C	-4.9951159	-0.6504694	-0.2182153
C	-3.0889963	0.8010964	-0.4014395
C	-2.8646339	-1.5866291	-0.9431192
C	-4.2180409	-1.7380137	-0.6355922
C	-4.4376698	0.6266905	-0.1003202
H	-2.2518927	-2.4302011	-1.2686542
H	-4.6782299	-2.7257212	-0.7271064
H	-5.0521630	1.4715012	0.2232328
H	-6.0533361	-0.8011807	0.0116824
C	-0.9171764	1.4439579	-0.8024490
C	-1.1873272	4.1045796	-0.1266843
C	0.2054182	2.2758766	-0.9201653
C	-2.1866878	1.9364043	-0.3794455
C	-2.3131443	3.2770879	-0.0377722
C	0.0525621	3.6088435	-0.5690761
H	1.1583634	1.8806513	-1.2736162
H	-3.2713673	3.6820080	0.2983589
H	0.9099226	4.2834663	-0.6379608
H	-1.2748576	5.1598597	0.1460012

THE JOURNAL OF PHYSICAL CHEMISTRY A
A JOURNAL OF THE AMERICAN CHEMICAL SOCIETY

pubs.acs.org/JPCA Article

Large Inverted Singlet−Triplet Energy Gaps Are Not Always Favorable for Triplet Harvesting: Vibronic Coupling Drives the (Reverse) Intersystem Crossing in Heptazine Derivatives

Fabian Dinkelbach, Mario Bracker, Martin Kleinschmidt, and Christel M. Marian*

Cite This: J. Phys. Chem. A 2021, 125, 10044−10051 Read Online

ACCESS | Metrics & More | Article Recommendations | Supporting Information

ABSTRACT: Heptazine derivatives are promising dopants for electroluminescent devices. Recent studies raised the question whether heptazines exhibit a small regular or an inverted singlet−triplet (IST) gap. It was argued that the $S_1 \leftarrow T_1$ reverse intersystem crossing (RISC) is a downhill process in IST emitters and therefore does not require thermal activation, thus enabling efficient harvesting of triplet excitons. Rate constants were not determined in these studies. Modeling the excited-state properties of heptazine proves challenging because fluorescence and intersystem crossing (ISC) are symmetry-forbidden in first order. In this work, we present a comprehensive theoretical study of the photophysics of heptazine and its derivative HAP-3MF. The calculations of electronic excitation energies and vibronic coupling matrix elements have been conducted at the density functional theory/multireference configuration interaction (DFT/MRCI) level of theory. We have employed a finite difference approach to determine nonadiabatic couplings and derivatives of spin−orbit coupling and electric dipole transition matrix elements with respect to normal coordinate displacements. Kinetic constants for fluorescence, phosphorescence, internal conversion (IC), ISC, and RISC have been computed in the framework of a static approach. Radiative $S_1 \leftrightarrow S_0$ transitions borrow intensity mainly from optically bright E′ $\pi \rightarrow \pi^*$ states, while $S_1 \leftrightarrow T_1$ (R)ISC is mediated by E″ states of n $\rightarrow \pi^*$ character. Test calculations show that IST gaps as large as those reported in the literature are counterproductive and slow down the $S_1 \leftarrow T_1$ RISC process. Using the adiabatic DFT/MRCI singlet−triplet splitting of −0.02 eV, we find vibronically enhanced ISC and RISC to be fast in the heptazine core compound. Nevertheless, its photo- and electroluminescence quantum yields are predicted to be very low because $S_1 \rightarrow S_0$ IC efficiently quenches the luminescence. In contrast, fluorescence, IC, ISC, and RISC proceed at similar time scales in HAP-3MF.

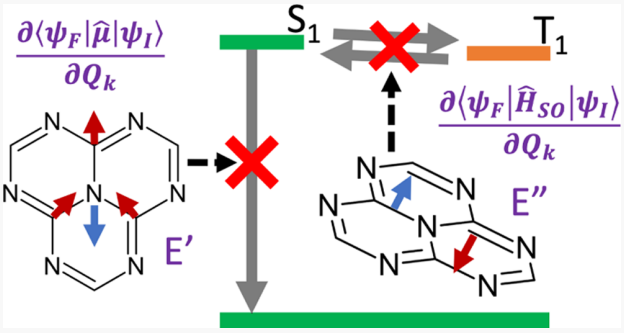

INTRODUCTION

Organic light-emitting diodes (OLEDs), which are based on thermally activated delayed fluorescence (TADF), require the singlet−triplet splitting ΔE_{ST} to be not too large versus thermal energy. If the spin−orbit coupling (SOC) strength is sufficient, $S_1 \leftarrow T_1$ reverse intersystem crossing (RISC) may compete against nonradiative deactivation of the triplet state at room temperature and triplet excitons can be harvested in addition to the singlet excitons.[1]

The energy difference ΔE_{ST} between a singlet and triplet-coupled open-shell configuration depends on the exchange interaction of the unpaired electrons. This interaction is small when the density distributions of the orbitals involved in the excitation do not overlap substantially. Typically, this requirement is fulfilled by charge-transfer (CT) states of donor−acceptor compounds whose unpaired electrons are spatially far apart. Very small singlet−triplet splittings can also be achieved in molecular systems where the electron density distributions in the half-occupied orbitals peak at different atoms and hence are disjunct. Such a situation occurs, for example, in electronically excited nonalternant conjugated hydrocarbons, with pentalene and azulene as well-known representatives.[2−4] One might therefore suppose that, in addition to donor−acceptor compounds, organic molecules with disjunct π-electron distributions in the highest occupied molecular orbital (HOMO) and the lowest unoccupied molecular orbital (LUMO) are well-suited dopants for TADF-based OLEDs. Unfortunately, the spatial overlap of the electron density distributions in the initial and final states plays a decisive role for the magnitudes of the electronic SOC and the electric dipole transition moment as well. The electronic couplings are

Received: October 21, 2021
Published: November 10, 2021

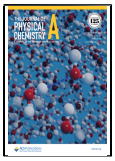

https://doi.org/10.1021/acs.jpca.1c09150
J. Phys. Chem. A 2021, 125, 10044−10051

typically very small in CT compounds, but vibronic interactions with nearby locally excited states can enhance (R)ISC and fluorescence rate constants appreciably.[5,6]

Very recently, triangle-shaped compounds with inverted singlet−triplet (IST) gap such as cycl[3.3.3]azine or heptazine (1,3,4,6,7,9,9*b*-heptaazaphenalene) and derivatives thereof were proposed as promising molecular OLED emitters for efficient triplet harvesting.[7−9] It was argued that the $S_1 \leftarrow T_1$ RISC is a downhill process in IST emitters due to the inversion of the energy gap and therefore does not require thermal activation. Indeed, heptazine-based π-conjugated materials such as HAP-3MF (2,5,8-tris(4-fluoro-3-methylphenyl)-1,3,4,6,7,9,9*b*-heptaazaphenalene) have been used as OLED emitters with high triplet harvesting capabilities.[10−15] Unfortunately, an experimental value for its ΔE_{ST} was not reported. One peculiarity of HAP-3MF is the spatial orientation of the peripheral substituents in relation to the heptazine core. In contrast to most organic CT emitters, their π-systems are not perpendicular or twisted but co-planar.

The frontier molecular orbitals of heptazine and HAP-3MF are π orbitals with spatially disjunct electron density distributions (Figure 1). Therefore, one might expect ΔE_{ST} in the HOMO → LUMO excited S_1 and T_1 states to be small, but not negative. The inversion of the regular order of open-shell singlet and triplet states with equal orbital occupation can be brought about by spin polarization.[2,16] In spin-restricted calculations, the effect only shows up in wavefunction-based excited-state correlation methods such as ADC(2), CC2, EOM-CCSD, or CASPT2, which explicitly include doubly excited configurations or if double-hybrid functionals are employed in time-dependent density functional theory (TDDFT).[7,8,17,18] The combined density functional theory (DFT) and multireference configuration interaction (MRCI) method,[19,20] utilized in this work, has this capability as well. In contrast, conventional TDDFT using a frequency-independent kernel yields a regular singlet−triplet energy splitting.[18]

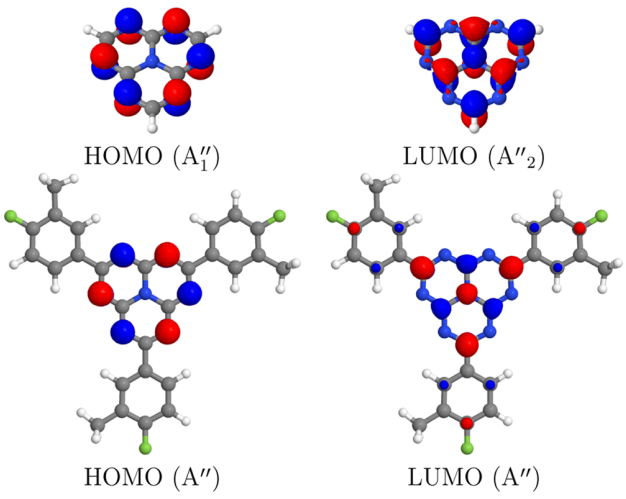

Figure 1. Frontier molecular orbitals of heptazine (top) and HAP-3MF (bottom).

Irrespective of the question whether the triangle-shaped π-chromophores are TADF or IST systems, a problem arises in the highly symmetric cyclazine, heptazine, and HAP-3MF systems because their S_1−T_1 spin−orbit and S_1−S_0 electric dipole couplings vanish due to point-group symmetry selection rules in Franck−Condon (FC) approximation. One way to lift the restrictions on the electric dipole coupling is the asymmetric substitution of the azaphenalene core, which was shown to result in small but non-negligible oscillator strengths for the $S_1 \rightarrow S_0$ emissions.[8] Still, the S_1−T_1 SOC and hence the (R)ISC processes remain forbidden in first order, even in those compounds. For ISC and RISC between a singlet and triplet state with equal orbital occupation to occur, the inclusion of spin−vibronic interactions is mandatory.[6] In the present work, we therefore move past the FC approximation and investigate the details of the radiative and nonradiative transitions by explicitly including vibronic interactions in our model, employing Herzberg−Teller (HT) expansions of the electric dipole couplings for absorption and emission, HT expansions of the spin−orbit coupling matrix elements (SOCMEs) for ISC and RISC, and nonadiabatic coupling matrix elements of the S_1 and S_0 potentials to get an estimate of the internal conversion (IC) rate constants.

COMPUTATIONAL METHODS

Ground- and excited-state geometries were optimized using the DFT and TDDFT methods, respectively, implemented in TURBOMOLE.[21] For triplets, the Tamm−Dancoff approximation (TDDFT-TDA)[22] was employed in addition. Throughout, the PBE0 density functional[23,24] was used in combination with a valence triple zeta basis set with polarization functions (TZVP).[25] Stationary points were verified to be minima by frequency analyses performed with GAUSSIAN.[26] To account for systematic errors, the harmonic frequencies were scaled by 0.9944.[27]

Note that TDDFT methods were employed solely for the optimization of the nuclear coordinates and the vibrational frequencies of the potentials. In these calculations, the full point-group symmetry, namely, D_{3h} (heptazine) and C_{3h} (HAP-3MF), was applied. The electronic excitation energies of 20 singlet and triplet states as well as all coupling matrix elements were based on MRCI wavefunctions utilizing the DFT/MRCI method[19,20] in conjunction with the R2016 Hamiltonian.[28] For heptazine, we used the standard parameter set with a selection threshold of 1.0 E_h and an initial active space of double excitations of 12 electrons in 10 orbitals. The short parameter set paired with a selection threshold of 0.8 E_h and an initial active space of single excitations of 20 electrons in 20 orbitals was used for HAP-3MF. Due to technical reasons, the DFT/MRCI calculations were performed in the Abelian subgroups C_{2v} and C_s.

The DFT/MRCI wavefunctions were employed to compute SOCMEs with the spin−orbit coupling kit (SPOCK).[29,30] SPOCK uses an effective one-electron spin−orbit mean-field Hamiltonian[31] in conjunction with the atomic mean-field integral (AMFI)[32] approximation. Phosphorescence rate constants were computed at the level of quasi-degenerate perturbation theory.

Vibronic contributions to the ISC ($\hat{O} = \hat{H}_{SO}$) and electric dipole transitions ($\hat{O} = \hat{\mu}$) between an initial molecular state Ψ_{Ia} and a set of final molecular states Ψ_{Fb} were treated within the HT approximation,[33] where the coupling matrix element is expanded about a reference point (Q_0) as a function of the normal mode coordinates Q_k.

https://doi.org/10.1021/acs.jpca.1c09150
J. Phys. Chem. A 2021, 125, 10044−10051

$$\sum_b \langle \Psi_{Fb}|\hat{O}|\Psi_{Ia}\rangle = \langle \psi_F|\hat{O}|\psi_I\rangle\Big|_{Q_0} \sum_b \langle v_{Fb}|v_{Ia}\rangle + \sum_k^N \frac{\partial\langle \psi_F|\hat{O}|\psi_I\rangle}{\partial Q_k}\Big|_{Q_0} \sum_b \langle v_{Fb}|Q_k|v_{Ia}\rangle + ... \quad (1)$$

Herein, ψ_I and ψ_F denote the electronic parts and v_{Ia} and v_{Fb} denote the vibrational parts of the molecular wavefunctions. For IC, only the linear coupling terms of the nonadiabatic corrections

$$\sum_k^N \langle \Psi_{Fb}|\frac{\partial^2}{\partial Q_k^2}|\Psi_{Ia}\rangle = \sum_k^N \langle \psi_F|\frac{\partial}{\partial Q_k}|\psi_I\rangle|_{Q_0}\langle v_{Fb}|\frac{\partial}{\partial Q_k}|v_{Ia}\rangle + ... \quad (2)$$

were taken into account. The gradients of the matrix elements and the derivative couplings were obtained by distorting the nuclear framework along dimensionless normal modes using a step size of 0.5 units, utilizing averaged two-point finite difference techniques.[34,35] The phases of these gradients are arbitrary and need to be aligned properly by relating the phases of the molecular orbitals and of the DFT/MRCI wavefunctions to a reference calculation as performed in earlier work.[36] Evaluation of nonradiative rate constants in the energy domain according to

$$k_{nr} = \frac{2\pi}{\hbar}\sum_b |\langle \Psi_{Fb}|\hat{O}|\Psi_{Ia}\rangle|^2 \delta(E_{Fb} - E_{Ia}) \quad (3)$$

is not practicable for molecules as large as those investigated here because the density of vibrational states is too high. A way to avoid the explicit summation over all final vibrational states b is to transform Fermi's golden rule into the Heisenberg picture. To this end, the Dirac δ function is expressed as the Fourier integral

$$\delta(E_{Fb} - E_{Ia}) = \frac{1}{2\pi}\int_{-\infty}^{+\infty} e^{i(E_{Fb}-E_{Ia})/\hbar} dt \quad (4)$$

In the harmonic oscillator approximation, analytical expressions for the generating functions of ISC and IC rate transitions including a Duschinsky transformation of the respective normal coordinates can be derived.[35,37−42] In the VIBES program, correlation functions were implemented, which use the normal coordinates of the initial state as a common basis for evaluating the FC factors and the nuclear coupling terms.[35,40−42] ISC, RISC, and IC rate constants are then obtained by numerically integrating the resulting correlation functions in the time domain. A further advantage of the Fourier transform approach is that it is easily extended to include temperature effects by assuming a Boltzmann population of the vibrational levels in the initial electronic state.[35,41,42] To speed up the numerical integration, a Gaussian damping function is introduced. The width of the damping function, the integration interval, and the number of grid points are technical parameters that have to be chosen with great care. For ISC and RISC rate constants, we used an integration time of 25 ps, a grid of 2^{16} points, and a damping of 1 cm^{-1} full width at half-maximum (FWHM). Because of the higher fluctuation of the correlation function of the $S_1 \rightarrow S_0$ IC, the number of grid points was increased to 2^{18} (heptazine) and 2^{19} (HAP-3MF) in the evaluation of IC rate constants. To make sure that the calculated rate constants are converged, the width of the damping function was varied between 0.1 and 10 cm^{-1}. For the weaker damping functions, the integration parameters had to be adapted. Technical details of these calculations are given in the Supporting Information, where also the shapes of the correlation functions are displayed. Vibrationally resolved spectra were obtained with the VIBES[40,41] program at 300 K with an integration time of 300 fs, a grid of 2^{14} points, and a Gaussian damping function of 50 cm^{-1} FWHM. Additional calculations were performed for stronger damping functions with 100 and 200 cm^{-1} FWHM. HT fluorescence rate constants were computed by integrating the HT spectrum $I^{HT}(\omega)$.[43,44] Since the spectral density $S(\omega)$ is not properly normalized in the VIBES program, it has to be renormalized making use of the closure relation for the FC spectral density $S^{FC}(\omega)$.

$$k_F^{HT} = \int I^{HT}(\omega)d\omega = \frac{4}{3\hbar c_0^3}\frac{\int \omega^3 S^{HT}(\omega)d\omega}{\int S^{FC}(\omega)d\omega} \quad (5)$$

RESULTS AND DISCUSSION

We find heptazine and HAP-3MF to be D_{3h} and C_{3h} symmetric, respectively, in their electronic ground states. TDDFT lowers the symmetry in the first excited singlet and triplet states. At this level of theory, the D_{3h} and C_{3h} structures represent first-order transition states where the minima are reached by lifting the central nitrogen atom out of the heptazine core plane, thus breaking the horizontal mirror plane in the process. In contrast, scans along the imaginary frequency mode at the DFT/MRCI level show minima at the higher-symmetry points. Therefore, we will concentrate on the D_{3h}- and C_{3h}-symmetric structures in our analysis. The frequency of the imaginary mode was approximated by its harmonic force constant fitted to the curvature of the outer branches of a TDDFT scan along the normal mode. The fits yield frequencies of 131 cm^{-1} for the S_1 state and 178 cm^{-1} for the T_1 state in heptazine. For HAP-3MF, we obtained 232 and 253 cm^{-1}, respectively.

Electronic excitation energies of heptazine and HAP-3MF and the oscillator strengths of the electric dipole-allowed transitions at the ground-state and first excited-state geometries are given in Tables S1−S6, respectively. Difference densities illustrating the characters of the most important excited states are displayed in Figures 2 and S1−S6. They reveal that the S_1 and T_1 states originate from $\pi \rightarrow \pi^*$ excitations shifting electron density from the nitrogen atoms on the rim of the heptazine ring to the carbon atoms and the central nitrogen atom. In HAP-3MF, additionally, small CT contributions are visible, moving electron density from the heptazine core to π orbitals on the phenyl rings. This is remarkable because heptazine is typically considered an electron acceptor, not a donor. Substantial CT from the peripheral substituents to the heptazine core is observed in the optically very bright E′-symmetric S_2 state, which lies about 0.9 eV above the S_1 state in HAP-3MF and has the proper symmetry to lend intensity to the electric dipole-forbidden S_1-S_0 transitions via vibronic coupling.

In our DFT/MRCI calculations, the S_1 and T_1 states (A_2') of heptazine are located vertically at 2.59 and 2.60 eV, respectively, at the D_{3h}-symmetric ground-state geometry, corroborating the inversion of the typical singlet−triplet order reported by Sobolewski, Domcke, and co-workers[9,17] in

https://doi.org/10.1021/acs.jpca.1c09150
J. Phys. Chem. A 2021, 125, 10044−10051

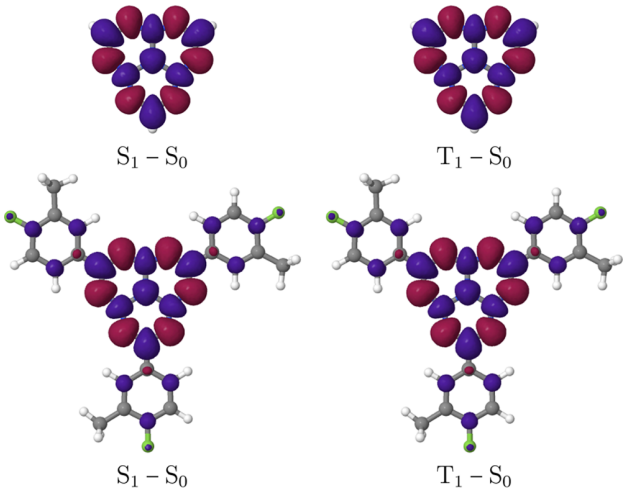

Figure 2. Differences of the electron density distributions in the S_1 and T_1 states of heptazine (top) and HAP-3MF (bottom) with regard to the density distribution in the respective S_0 states. Areas losing electron density upon excitation from the electronic ground state are shown in dark red, and areas gaining electron density are shown in violet.

principle. The highest-intensity peaks in the absorption spectrum of heptazine (Figure 3) correspond to E′-symmetric $\pi \rightarrow \pi^*$ transitions to the S_4 state at 4.32 eV (287 nm) and to the S_{10} state at 5.73 eV (216 nm). Besides the bright $\pi \rightarrow \pi^*$ states, we find dark n $\rightarrow \pi^*$ states, which are of particular interest for vibronically enhanced ISC. In heptazine, the lowest n $\rightarrow \pi^*$ states are the A_1''-symmetric T_3 and S_2 states, located at 3.76 and 3.86 eV, respectively. Their leading configuration is the HOMO-1 → LUMO excitation. The HOMO-2 → LUMO and HOMO-3 → LUMO excitations together form the lowest E″-symmetric triplet (T_4) and singlet (S_3) states, which are essential promotors of the symmetry-forbidden $S_1 \leftrightarrow T_1$ ISC and RISC as will become apparent below. Interactions of the n orbitals with the peripheral ligands lead to a blue shift of the corresponding n $\rightarrow \pi^*$ states by about 0.20 eV in HAP-3MF in comparison to heptazine. Comparing the difference densities of the bright states in heptazine and HAP-3MF reveals that the S_4 state in heptazine corresponds to the S_8 state in HAP-3MF, which is slightly red-shifted due to the extension of the π system. Additional $\pi \rightarrow \pi^*$ CT states appear in the low-energy region of the HAP-3MF spectrum, of which the $S_2 \leftarrow S_0$ transition is the brightest. Compared to the experimental UV–vis spectrum with maximum at 331 nm in toluene solution,[13] the calculations underestimate the excitation energy of the first intense CT band by about 0.15 eV, whereas the position of the first very weak absorption band matches its experimental counterpart perfectly (Figure 3). Due to its low oscillator strength, Li et al. assigned an n $\rightarrow \pi^*$ excitation to this $S_1 \leftarrow S_0$ transition, at variance with our results. We find the S_1 and T_1 states (A′) to have $\pi \rightarrow \pi^*$ character, in accordance with the results of the ADC(2) calculations by Sobolewski and Domcke.[9] Symmetry selection rules forbid absorption into the S_1 state in FC approximation, but vibrations of E′ ($A_2' \otimes E'_{vib} = E'[x, y]$) and A_1'' ($A_2' \otimes A''_{1,vib} = A_2''[z]$) can break the symmetry constraints and render the vibronic transition weakly allowed. The gradients of the dipole transition moments (Table S16) show that mainly E′ normal modes in the wavenumber range between approximately 1400 and 1700 cm^{-1} drive the absorption by borrowing intensity from the bright E′ states. The vibrational progression in the HT absorption spectrum is in good agreement with the experimentally resolved vibrational fine structure of the $S_1 \leftarrow S_0$ transition, thus lending support to our computational model.

Geometry relaxation in the excited states of heptazine and HAP-3MF entails only small changes in the vertical excitation energies, due to the strong geometric constraints imposed by the annelated rings. We find the S_1 and T_1 states adiabatically at 2.50 and 2.52 eV, respectively, in heptazine and at 2.66 and 2.65 eV, respectively, in HAP-3MF. Thus, the small energy gap and the singlet–triplet order found at the ground-state nuclear arrangement are maintained upon geometry relaxation. Zero-point vibrational energy (ZPVE) corrections change the picture and restore the typical singlet–triplet order of the S_1 and T_1 states. In our computational setup, the first vibrational level of the S_1 state of heptazine is located 0.06 eV above the vibrational ground state of the T_1 state in the D_{3h} symmetry. A similar energy separation of the zero vibrational levels (0.07 eV) of the S_1 and T_1 potentials is obtained for HAP-3MF in the C_{3h} symmetry. As we will see below, the question whether heptazines are IST or TADF systems plays a minor role for the interconversion of their singlet and triplet populations.

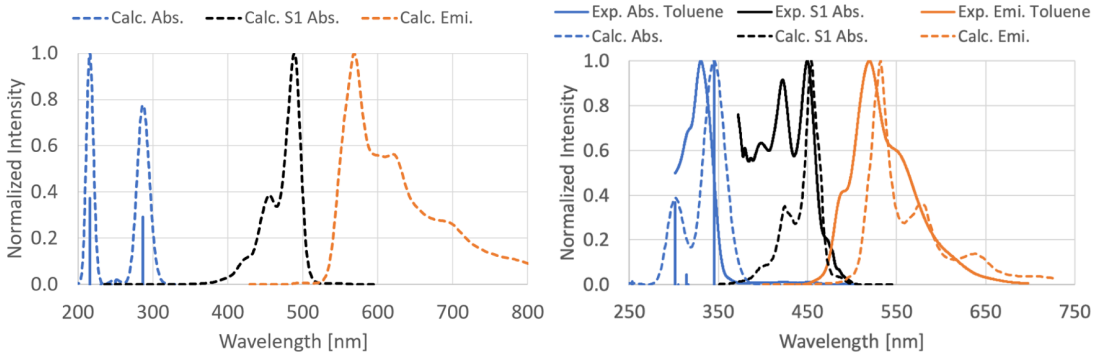

Figure 3. Absorption and emission spectra of heptazine (left) and HAP-3MF (right). Vibronic spectra were computed only for the S_1 absorption (black) and emission (orange) transitions. Their HT spectra are not drawn to scale but were normalized separately. The spectral lines of the electric dipole-allowed electronic transitions in the shorter-wavelength regime (blue) were broadened with Gaussian functions of 1000 cm^{-1} FWHM. Digitized experimental spectra were read from Figure 2 of an article by Li et al.,[13] where the S_1 absorption intensity was magnified by a factor of 100. The measurements were conducted in toluene by these authors, while our computational results are obtained in vacuum.

https://doi.org/10.1021/acs.jpca.1c09150
J. Phys. Chem. A 2021, 125, 10044–10051

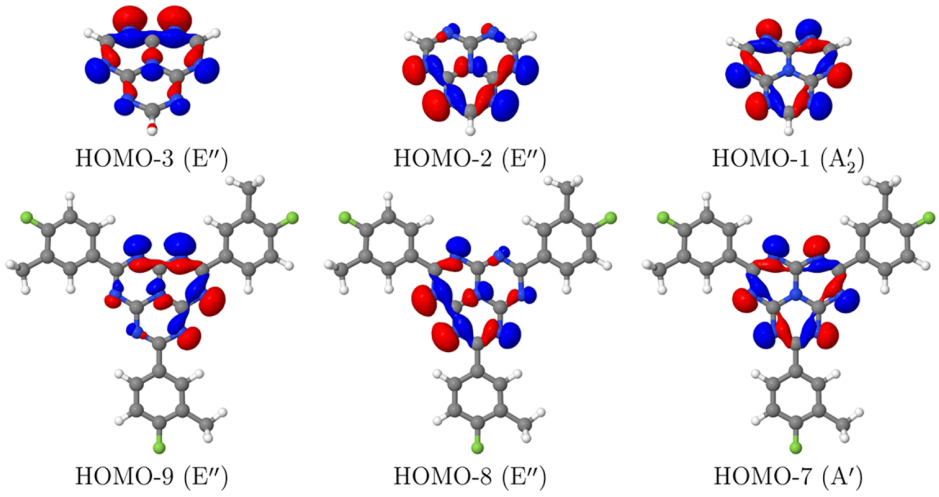

Figure 4. Nonbonding lone-pair molecular orbitals of heptazine (top) and HAP-3MF (bottom).

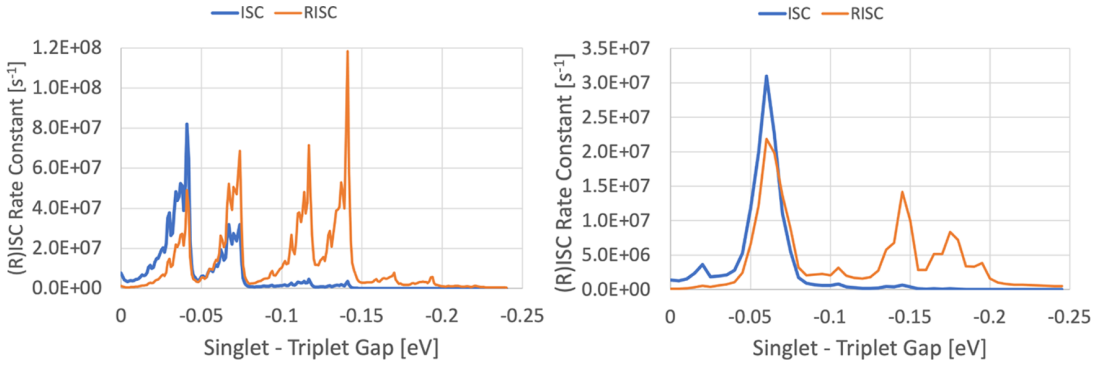

Figure 5. Rate constants for $S_1 \leftrightarrow T_1$ (R)ISC in heptazine (left) and HAP-3MF (right) computed in HT approximation for various singlet−triplet energy gaps ΔE_{ST}. The scan of the energy splitting was performed with a resolution of 0.001 eV for heptazine and of 0.005 eV for HAP-3MF. A negative ΔE_{ST} value indicates that the triplet state is located adiabatically above the singlet state. For 0−0 energies, ZPVE energy corrections (+0.08 eV for heptazine, +0.06 eV for HAP-3MF) have to be added.

Application of heptazine and its derivatives in OLEDs requires an efficient luminescence of the emitter in conjunction with fast (R)ISC to harvest all possible singlet and triplet excitons. However, direct ISC and RISC are forbidden by symmetry selection rules. S_1 and T_1 exhibit A_2' spatial symmetry in heptazine, and there is no component of the angular momentum operator coupling these states, as $\hat{\mathcal{L}}_z$ is A_2' symmetric and $\hat{\mathcal{L}}_x$ and $\hat{\mathcal{L}}_y$ transform according to the E″ irreducible representation. For ISC to be fast, El-Sayed's rules[6,45] need to be satisfied, which requires states to be singly excited with respect to each other and to involve a change of orbital type. Both requirements appear to be fulfilled for states of $n \rightarrow \pi^*$ type. HOMO, HOMO-1, HOMO-2, and HOMO-3 are MOs with large contributions from 2p atomic orbitals on the outer ring of N atoms. While HOMO is a linear combination of $2p_z$ orbitals perpendicular to the molecular plane (Figure 1), HOMO-1, HOMO-2, and HOMO-3 are linear combinations of in-plane $2p_x$ and $2p_y$ orbitals on the same centers (Figure 4). In the local one-particle picture underlying El-Sayed's rule, $2p_z$ and $2p_x$ or $2p_y$ can strongly interact via the angular momentum operators contained in $\hat{\mathcal{H}}_{SO}$. A closer look at the character table of D_{3h} reveals, however, that the local contributions to the orbital angular momentum coupling matrix element of HOMO-1 and HOMO cancel each other because HOMO is of A_1'' symmetry, HOMO-1 transforms according to A_2' and their direct product representation $A_1'' \otimes A_2' = A_2''$ does neither contain A_2' nor E″, which are the proper irreducible representations for $\hat{\mathcal{L}}$. In contrast, the orbital angular momentum coupling between HOMO and HOMO-2 or HOMO-3 is symmetry-allowed, and so are $\langle T_4|\hat{\mathcal{H}}_{SO}|S_1\rangle$, $\langle T_4|\hat{\mathcal{H}}_{SO}|T_1\rangle$, and $\langle S_3|\hat{\mathcal{H}}_{SO}|T_1\rangle$.

Vibrational SOC is therefore solely promoted by E″-symmetric modes in heptazine (Tables S9 and S10). For HAP-3MF, the mutual SOC between S_1 and T_1 is symmetry-allowed in principle but vanishes at the minima. Irrespective of the molecular point-group symmetry, SOCMEs between orbitally nondegenerate singlet and triplet states with equal orbital occupations are zero because the angular momentum operator has purely imaginary cartesian components.[46] Non-vanishing SOC between them can only be brought about by multiconfiguration effects or by spin−vibronic interactions. In HAP-3MF, the HOMO-7 → LUMO excitation gives rise to the A″-symmetric S_3 and T_7 states, which do not interact with S_1 and T_1 via SOC, whereas the E″-symmetric S_6 and T_8 states, dominated by the HOMO-8 → LUMO and HOMO-9 → LUMO excitations, have the appropriate spatial symmetry. It is therefore not surprising that the largest SOCME gradients arise along E″-symmetric distortions of the nuclear framework

https://doi.org/10.1021/acs.jpca.1c09150
J. Phys. Chem. A 2021, 125, 10044−10051

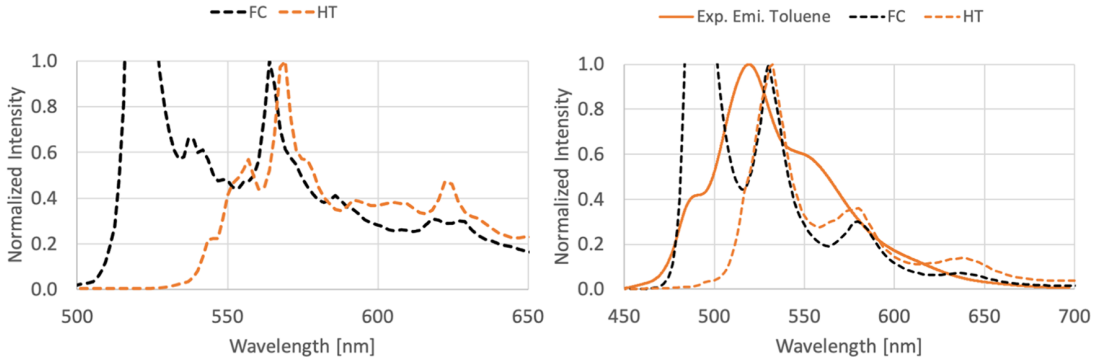

Figure 6. Overlay of the computed HT emission spectra of heptazine (left) and HAP-3MF (right) with the corresponding FC spectral density. Note that the emission is forbidden in FC approximation in full point-group symmetry, i.e., D_{3h} (heptazine) and C_{3h} (HAP-3MF). For HAP-3MF, the experimental emission spectrum, recorded by Li et al.[13] in toluene solution, is depicted as well.

(Tables S18 and S19). We obtain ISC and RISC rate constants of $k_{ISC} = 1 \times 10^7$ s^{-1} and $k_{RISC} = 3 \times 10^6$ s^{-1} for heptazine at 300 K. Somewhat smaller but still sizeable rate constants of $k_{ISC} = 7 \times 10^6$ s^{-1} and $k_{RISC} = 3 \times 10^5$ s^{-1} are determined for HAP-3MF at 300 K if our computed S_1−T_1 energy separation is employed.

The ISC and RISC rate constants do hardly change if the technical parameters for their evaluation are varied (Tables S21 and S22), but they are sensitive with respect to the energy separation between the initial and final states. Because the magnitude of our adiabatic DFT/MRCI singlet−triplet gap (−0.02 eV) differs markedly from values reported in various other theoretical works,[8,9,17,18] we recomputed the HT R(ISC) rate constants for ΔE_{ST} values ranging from 0 to −0.24 eV. The results of these scans are displayed in Figure 5. The ISC and RISC transition probabilities peak at several maxima indicating energies, where the S_1 and T_1 vibrational wavefunctions optimally overlap. The scans also show that a large negative singlet−triplet energy gap is not necessarily favorable for a spin population transfer between the T_1 and S_1 states of heptazine: The constants decrease to $k_{ISC} = 3 \times 10^2$ s^{-1} and $k_{RISC} = 5 \times 10^5$ s^{-1} if the ADC(2) value (−0.24 eV), reported by Sobolewski and Domcke,[9] is employed. In HAP-3MF, the optimum for the interconversion of singlet and triplet population lies at $\Delta E_{ST} = -0.06$ eV.

Emission from the S_1 state follows the same selection rules as the absorption and is therefore enhanced vibronically by the same normal modes. The 0−0 transition is absent in the computed HT spectra of heptazine and HAP-3MF (Figure 6) as it should be the case for molecules with a first-order symmetry-forbidden dipole transition in harmonic oscillator approximation. Obviously, HAP-3MF does not fully comply with the restrictions of the harmonic oscillator model in reality so that a 0−0 transition becomes weakly allowed and is visible as a shoulder in the experimental spectra. Moreover, the experimental peaks are broader than the computed ones and the peak positions are slightly shifted, but otherwise, the vibrational progressions are very similar. They can be assigned to totally symmetric C−N bond stretching modes of the heptazine core.

With a rate constant of $k_F = 3 \times 10^5$ s^{-1}, fluorescence is 1 to 2 orders of magnitudes slower in heptazine than ISC and RISC and 3 orders of magnitude slower than IC to the ground state (Table 1). We therefore expect the photo- and electroluminescence quantum yields to be very low for the heptazine core compound. IC is mainly driven by the A_2'-symmetric

Table 1. Rate Constants of Radiative and Nonradiative Transitions in Heptazine and Hap-3MF Calculated Including Vibronic Interactions at 300 K

rate constant [s^{-1}]	process	heptazine	HAP-3MF
k_F	$S_1 \rightarrow S_0$	3×10^5	9×10^5
k_P	$T_1 \rightarrow S_0$	2×10^0	
k_{IC}	$S_1 \rightarrow S_0$	3×10^8	9×10^5
k_{ISC}	$S_1 \rightarrow T_1$	1×10^7	7×10^6
k_{RISC}	$S_1 \leftarrow T_1$	3×10^6	3×10^5

coupling mode 39 (Figure S9), which entails torsional motions about the central C_3 axis. The $S_1 \rightarrow S_0$ IC rate constant, listed in Table 1, should be considered only a rough estimate: Due to the large energy splitting of the S_1 and S_0 states, the harmonic oscillator model underlying the calculations is far from being ideal. Vibronic interactions also enhance the T_1 phosphorescence probability. However, with a rate constant of about $k_P = 2$ s^{-1} in HT approximation, the process is too slow to compete against other triplet deactivation channels such as RISC or triplet−triplet annihilation.

The ratios of the radiative and nonradiative decay constants are more favorable in the case of HAP-3MF. Replacement of the heptazine hydrogen atoms by fluorinated toluene substituents appears to slow down the nonradiative deactivation of the first excited singlet state to the electronic ground state. IC is promoted by A′-symmetric torsion modes in HAP-3MF, the most dominant coupling mode being mode 135 with a vibrational frequency of 1598 cm^{-1} (Figure S14). According to our calculations, IC and fluorescence proceed approximately at the same time scale at 300 K (Table 1). The rate-determining process for the prompt fluorescence decay following photoexcitation appears to be the ISC to the T_1 state. Our computed fluorescence rate constant of $k_F = 9 \times 10^5$ s^{-1} is in good agreement with the findings by Li et al.,[13] who estimated an emissive rate constant of 1×10^6 s^{-1} for this compound based on a measured fluorescence lifetime of 252 ns and a photoluminescence quantum yield of 0.26 in toluene at room temperature. RISC is somewhat slower than ISC and fluorescence ($k_{RISC} = 10^5$ s^{-1}), suggesting both prompt and delayed fluorescence to take place, as seen by Li et al.[13] who observed a delayed component in addition to the prompt fluorescence in oxygen-free toluene and in solid films of HAP-3MF. The computed rate constants cannot explain the experimentally determined ratios of delayed vs prompt and luminescence components following photoexcitation (4%) and

https://doi.org/10.1021/acs.jpca.1c09150
J. Phys. Chem. A 2021, 125, 10044−10051

electric excitation (71%) in 6 wt %-doped DPEPO film, however.

CONCLUSIONS

Summarizing the discussion of the excited-state processes (Figure 7), we find that ISC and RISC allow efficient singlet−triplet interconversion in heptazine and HAP-3MF. These processes are solely enabled by vibronic coupling, where E″-symmetric modes enhance ISC and RISC transitions between the S_1 and T_1 states while vibrations of the E′ symmetry boost the radiative transitions. However, fluorescence cannot compete against nonradiative deactivation of the S_1 state by IC in the parent heptazine compound. We therefore expect its electroluminescence quantum yield to be very small, despite the fact that heptazine appears to be an IST system with slightly negative ΔE_{ST}. ZPVE corrections are found to restore the regular singlet−triplet energetic order in this compound. A regular singlet−triplet energy separation does not impair the potential of heptazine derivatives as OLED emitters. On the contrary, test calculations show that IST gaps as large as the ones reported in recent quantum chemical works[8,9,17,18] substantially reduce the rate constant of a $T_1 \rightarrow S_1$ spin−vibronic transition in heptazine.

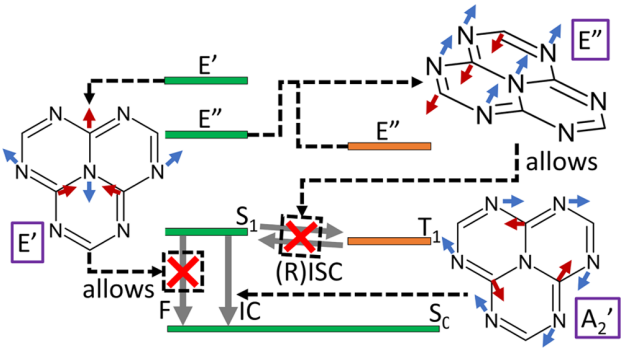

Figure 7. Schematic of the fluorescence, IC, and (R)ISC processes in heptazine. Modes of E′ symmetry enable intensity borrowing from bright E′ states and mediate fluorescence, while E″-symmetric modes mix E″ states of n → π* character into the S_1 and T_1 wavefunctions. IC is promoted by A_2' normal modes.

Due to the heavier peripheral substituents, the IC process is slowed down in HAP-3MF in comparison to the parent heptazine molecule so that light emission occurs with a higher probability and singlet as well as triplet excitons can be harvested efficiently in electroluminescent devices. For HAP-3MF, the DFT/MRCI picture of a TADF emitter with nearly degenerate S_1 and T_1 states and vibronically enhanced ISC, RISC, and electric dipole transitions is in good agreement with the experimental observations,[13] where delayed fluorescence on the microsecond time scale is seen in oxygen-free toluene solutions and in solid HAP-3MF films.

ASSOCIATED CONTENT

Supporting Information

The Supporting Information is available free of charge at https://pubs.acs.org/doi/10.1021/acs.jpca.1c09150.

Vertical and adiabatic excitation energies of heptazine and HAP-3MF utilizing the DFT/MRCI method; difference densities of the most important electronic states; pictures of most relevant vibrational coupling modes; gradients and derivative couplings along normal mode displacements for vibronic absorption, fluorescence, IC, ISC, and RISC; correlation functions and rate constants for varying technical parameters of the VIBES calculations; FC and HT spectra for different damping functions (PDF)

AUTHOR INFORMATION

Corresponding Author

Christel M. Marian − *Institute of Theoretical and Computational Chemistry, Heinrich-Heine-University Düsseldorf, 40225 Düsseldorf, Germany;* orcid.org/0000-0001-7148-0900; Phone: +49 (0)211 8113210; Email: christel.marian@hhu.de

Authors

Fabian Dinkelbach − *Institute of Theoretical and Computational Chemistry, Heinrich-Heine-University Düsseldorf, 40225 Düsseldorf, Germany*

Mario Bracker − *Institute of Theoretical and Computational Chemistry, Heinrich-Heine-University Düsseldorf, 40225 Düsseldorf, Germany*

Martin Kleinschmidt − *Institute of Theoretical and Computational Chemistry, Heinrich-Heine-University Düsseldorf, 40225 Düsseldorf, Germany*

Complete contact information is available at: https://pubs.acs.org/10.1021/acs.jpca.1c09150

Notes

The authors declare no competing financial interest.

ACKNOWLEDGMENTS

This research was funded by the Deutsche Forschungsgemeinschaft (DFG, German Research Foundation)—396890929/GRK 2482. The authors thank Prof. Wolfgang Domcke for bringing the heptazine singlet−triplet inversion to their attention.

REFERENCES

(1) Yersin, H. *Highly Efficient OLEDs, Materials Based on Thermally Activated Delayed Fluorescence*; Wiley-VCH, 2018.

(2) Koseki, S.; Nakajima, T.; Toyota, A. Violation of Hund's multiplicity rule in the electronically excited states of conjugated hydrocarbons. *Can. J. Chem.* **1985**, *63*, 1572−1579.

(3) Klan, P.; Wirz, J. *Photochemistry of Organic Compounds: From Concepts to Practice*, John Wiley & Sons, Weinheim, 2009; p 151.

(4) Vosskötter, S.; Konieczny, P.; Marian, C. M.; Weinkauf, R. Towards an understanding of the singlet−triplet splittings in conjugated hydrocarbons: azulene investigated by anion photoelectron spectroscopy and theoretical calculations. *Phys. Chem. Chem. Phys.* **2015**, *17*, 23573−23581.

(5) Penfold, T. J.; Gindensperger, E.; Daniel, C.; Marian, C. M. Spin-Vibronic Mechanism for Intersystem Crossing. *Chem. Rev.* **2018**, *118*, 6975−7025.

(6) Marian, C. M. Understanding and Controlling Intersystem Crossing in Molecules. *Annu. Rev. Phys. Chem.* **2021**, *72*, 616−640.

(7) Sanz-Rodrigo, J.; Ricci, G.; Olivier, Y.; Sancho-García, J. C. Negative Singlet−Triplet Excitation Energy Gap in Triangle-Shaped Molecular Emitters for Efficient Triplet Harvesting. *J. Phys. Chem. A* **2021**, *125*, 513−522.

(8) Pollice, R.; Friederich, P.; Lavigne, C.; dos Passos Gomes, G.; Aspuru-Guzik, A. Organic molecules with inverted gaps between first excited singlet and triplet states and appreciable fluorescence rates. *Matter* **2021**, *4*, 1654−1682.

(9) Sobolewski, A. L.; Domcke, W. Are Heptazine-Based Organic Light-Emitting Diode Chromophores Thermally Activated Delayed Fluorescence or Inverted Singlet−Triplet Systems? *J. Phys. Chem. Lett.* **2021**, *12*, 6852−6860.
(10) Li, J.; Tao, L.; Wang, Y.; Yao, Y.; Guo, Q. Heptazine-Based π-Conjugated Materials for Light-Emitting. *Front. Chem.* **2021**, *9*, No. 717569.
(11) Kim, J. H.; Han, S. H.; Lee, J. Y. Concentration quenching resistant donor-acceptor molecular structure for high efficiency and long lifetime thermally activated delayed fluorescent organic light-emitting diodes via suppressed non-radiative channel. *Chem. Eng. J.* **2020**, *395*, No. 125159.
(12) Li, J.; Nomura, H.; Miyazaki, H.; Adachi, C. Highly efficient exciplex organic light-emitting diodes incorporating a heptazine derivative as an electron acceptor. *Chem. Commun.* **2014**, *50*, 6174−6176.
(13) Li, J.; Zhang, Q.; Nomura, H.; Miyazaki, H.; Adachi, C. Thermally activated delayed fluorescence from $^3n\pi^*$ to $^3n\pi^*$ up-conversion and its application to organic light-emitting diodes. *Appl. Phys. Lett.* **2014**, *105*, No. 013301.
(14) Li, J.; Nakagawa, T.; MacDonald, J.; Zhang, Q.; Nomura, H.; Miyazaki, H.; Adachi, C. Highly Efficient Organic Light-Emitting Diode Based on a Hidden Thermally Activated Delayed Fluorescence Channel in a Heptazine Derivative. *Adv. Mater.* **2013**, *25*, 3319−3323.
(15) Bala, I.; Gupta, S. P.; Kumar, S.; Singh, H.; De, J.; Sharma, N.; Kailasam, K.; Pal, S. K. Hydrogen-bond mediated columnar liquid crystalline assemblies of C3-symmetric heptazine derivatives at ambient temperature. *Soft Matter* **2018**, *14*, 6342−6352.
(16) Kollmar, H.; Staemmler, V. Violation of Hundas rule by spin polarization in molecules. *Theor. Chim. Acta* **1978**, *48*, 223−239.
(17) Ehrmaier, J.; Rabe, E. J.; Pristash, S. R.; Corp, K. L.; Schlenker, C. W.; Sobolewski, A. L.; Domcke, W. Singlet-triplet inversion in heptazine and in polymeric carbon nitrides. *J. Phys. Chem. A* **2019**, *123*, 8099−8108.
(18) de Silva, P. Inverted Singlet-Triplet Gaps and Their Relevance to Thermally Activated Delayed Fluorescence. *J. Phys. Chem. Lett.* **2019**, *10*, 5674−5679.
(19) Grimme, S.; Waletzke, M. A combination of Kohn-Sham density functional theory and multi-reference configuration interaction methods. *J. Chem. Phys.* **1999**, *111*, 5645−5655.
(20) Marian, C. M.; Heil, A.; Kleinschmidt, M. The DFT/MRCI method. *WIREs Comput. Mol. Sci.* **2019**, *9*, No. e1394.
(21) TURBOMOLE V7.5, a development of University of Karlsruhe and Forschungszentrum Karlsruhe GmbH, 1989-2007, TURBOMOLE GmbH, since 2007. 2020, https://www.turbomole.org.
(22) Hirata, S.; Head-Gordon, M. Time-dependent density functional theory within the Tamm−Dancoff approximation. *Chem. Phys. Lett.* **1999**, *314*, 291−299.
(23) Perdew, J. P.; Burke, K.; Ernzerhof, M. Generalized Gradient Approximation Made Simple. *Phys. Rev. Lett.* **1996**, *77*, 3865−3868.
(24) Adamo, C.; Barone, V. Toward reliable density functional methods without adjustable parameters: The PBE0 model. *J. Chem. Phys.* **1999**, *110*, 6158−6170.
(25) Schäfer, A.; Huber, C.; Ahlrichs, R. Fully optimized contracted Gaussian basis sets of triple zeta valence quality for atoms Li to Kr. *J. Chem. Phys.* **1994**, *100*, 5829−5835.
(26) Frisch, M. J.; Trucks, G. W.; Schlegel, H. B.; Scuseria, G. E.; Robb, M. A.; Cheeseman, J. R.; Scalmani, G.; Barone, V.; Petersson, G. A.; Nakatsuji, H. et al.*Gaussian 16*. revision C.01, Gaussian Inc., Wallingford CT 2016.
(27) Kesharwani, M. K.; Brauer, B.; Martin, J. M. L. Frequency and Zero-Point Vibrational Energy Scale Factors for Double-Hybrid Density Functionals (and Other Selected Methods): Can Anharmonic Force Fields Be Avoided? *J. Phys. Chem. A* **2015**, *119*, 1701−1714.
(28) Lyskov, I.; Kleinschmidt, M.; Marian, C. M. Redesign of the DFT/MRCI Hamiltonian. *J. Chem. Phys.* **2016**, *144*, No. 034104.
(29) Kleinschmidt, M.; Tatchen, J.; Marian, C. M. Spin-orbit coupling of DFT/MRCI wavefunctions: Method, test calculations, and application to thiophene. *J. Comput. Chem.* **2002**, *23*, 824−833.
(30) Kleinschmidt, M.; Marian, C. M. Efficient generation of matrix elements for one-electron spin−orbit operators. *Chem. Phys.* **2005**, *311*, 71−79.
(31) Heß, B. A.; Marian, C. M.; Wahlgren, U.; Gropen, O. A mean-field spin-orbit method applicable to correlated wavefunctions. *Chem. Phys. Lett.* **1996**, *251*, 365−371.
(32) Schimmelpfennig, B. *AMFI is an Atomic Spin-Orbit Integral Program*, University of Stockholm, 1996.
(33) Herzberg, G.; Teller, E. Schwingungsstruktur der Elektronenübergänge bei mehratomigen Molekülen. *Z. Phys. Chem.* **1933**, *21B*, 410−446.
(34) Tatchen, J.; Gilka, N.; Marian, C. M. Intersystem crossing driven by vibronic spin−orbit coupling: a case study on psoralen. *Phys. Chem. Chem. Phys.* **2007**, *9*, 5209−5221.
(35) Bracker, M.; Marian, C. M.; Kleinschmidt, M. Internal conversion of singlet and triplet states employing numerical DFT/MRCI derivative couplings: Implementation, tests, and application to xanthone. *J. Chem. Phys.* **2021**, *155*, No. 014102.
(36) Dinkelbach, F.; Marian, C. M. Vibronic and spin−orbit coupling effects in the absorption spectra of pyrazine: A quantum chemical approach. *J. Serb. Chem. Soc.* **2019**, *84*, 819−836.
(37) Islampour, R.; Miralinaghi, M. Dynamics of Radiationless Transitions: Effects of Displacement-Distortion-Rotation of Potential Energy Surfaces on Internal Conversion Decay Rate Constants. *J. Phys. Chem. A* **2007**, *111*, 9454−9462.
(38) Peng, Q.; Yi, Y.; Shui, Z.; Shao, J. Excited State Radiationless Decay Process with Duschinsky Rotation Effect: Formalism and Implemantation. *J. Chem. Phys.* **2007**, *126*, No. 114302.
(39) Niu, Y.; Peng, Q.; Deng, C.; Gao, X.; Shuai, Z. Theory of excited state decays and optical spectra: Application to polyatomic molecules. *J. Phys. Chem. A* **2010**, *114*, 7817−7831.
(40) Etinski, M.; Tatchen, J.; Marian, C. M. Time-dependent approaches for the calculation of intersystem crossing rates. *J. Chem. Phys.* **2011**, *134*, No. 154105.
(41) Etinski, M.; Rai-Constapel, V.; Marian, C. M. Time-dependent approach to spin-vibronic coupling: Implementation and assessment. *J. Chem. Phys.* **2014**, *140*, No. 114104.
(42) Etinski, M.; Tatchen, J.; Marian, C. M. Thermal and solvent effects on the triplet formation in cinnoline. *Phys. Chem. Chem. Phys.* **2014**, *16*, 4740−4751.
(43) Banerjee, S.; Baiardi, A.; Bloino, J.; Barone, V. Temperature Dependence of Radiative and Nonradiative Rates from Time-Dependent Correlation Function Methods. *J. Chem. Theory Comput.* **2016**, *12*, 774−786.
(44) Lyskov, I.; Etinski, M.; Marian, C. M.; Russo, S. P. Exciton energy transfer in organic light emitting diodes with thermally activated delayed fluorescence dopants. *J. Mater. Chem. C* **2018**, *6*, 6860−6868.
(45) El-Sayed, M. A. Triplet state. Its radiative and nonradiative properties. *Acc. Chem. Res.* **1968**, *1*, 8−16.
(46) Marian, C. *Reviews in Computational Chemistry*;Lipkowitz, K.; Boyd, D., Eds.; Wiley-VCH, Weinheim, 2001; Vol. *17*, pp 99−204.

https://doi.org/10.1021/acs.jpca.1c09150
J. Phys. Chem. A 2021, 125, 10044−10051

Supporting Information for: Large Inverted Singlet–Triplet Energy Gaps Are Not Always Favorable for Triplet Harvesting: Vibronic Coupling Drives the (Reverse) Intersystem Crossing in Heptazine Derivatives

Fabian Dinkelbach, Mario Bracker, Martin Kleinschmidt, and Christel M. Marian*

Institute of Theoretical and Computational Chemistry, Heinrich-Heine-University Düsseldorf, Düsseldorf, Germany

E-mail: christel.marian@hhu.de

Phone: +49 (0)211 8113210

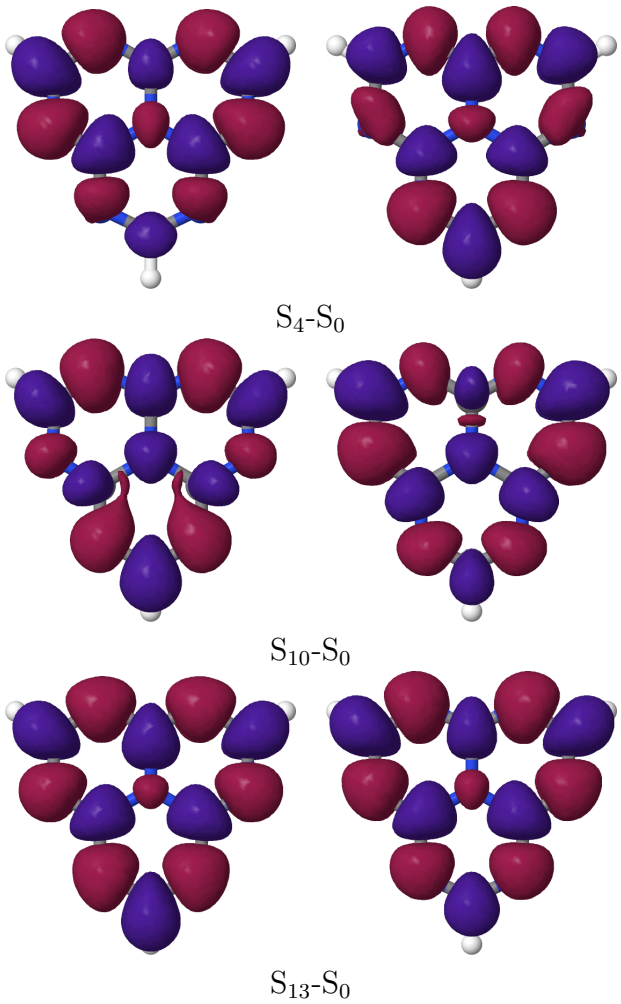

Figure S1: Difference densities of E′ symmetric singlet states contributing to vibronic fluorescence in heptazine. Areas losing electron density in comparison to the electronic ground state are shown in red, areas gaining electron density in blue.

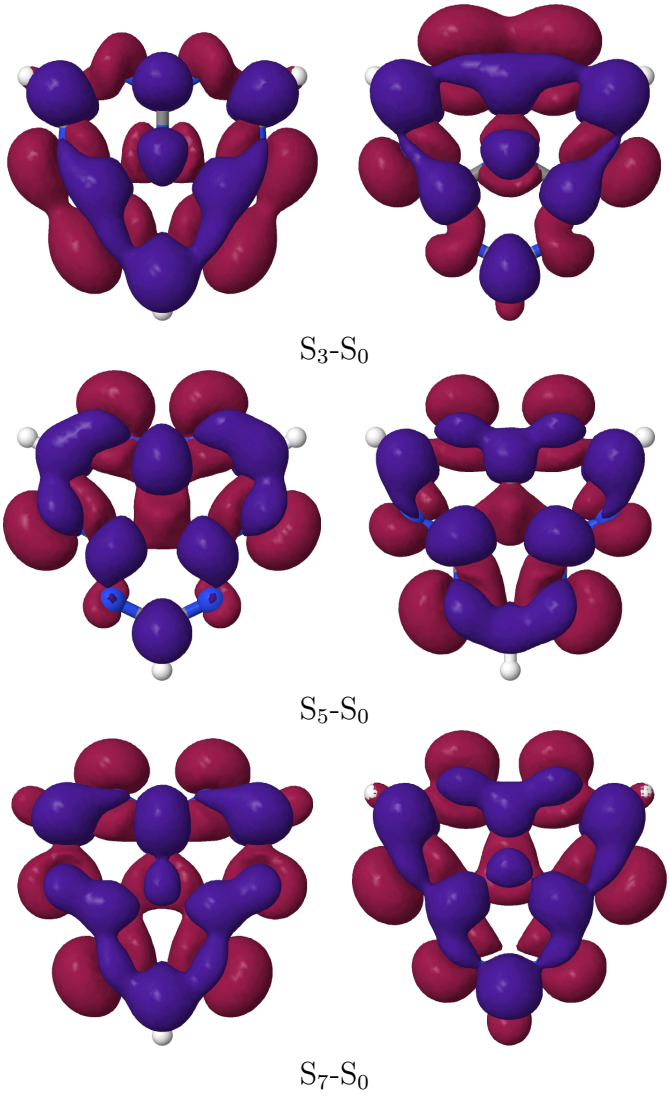

Figure S2: Difference densities of E″ symmetric singlet states contributing to vibronic SOC in heptazine. For color codes, see Figure S1.

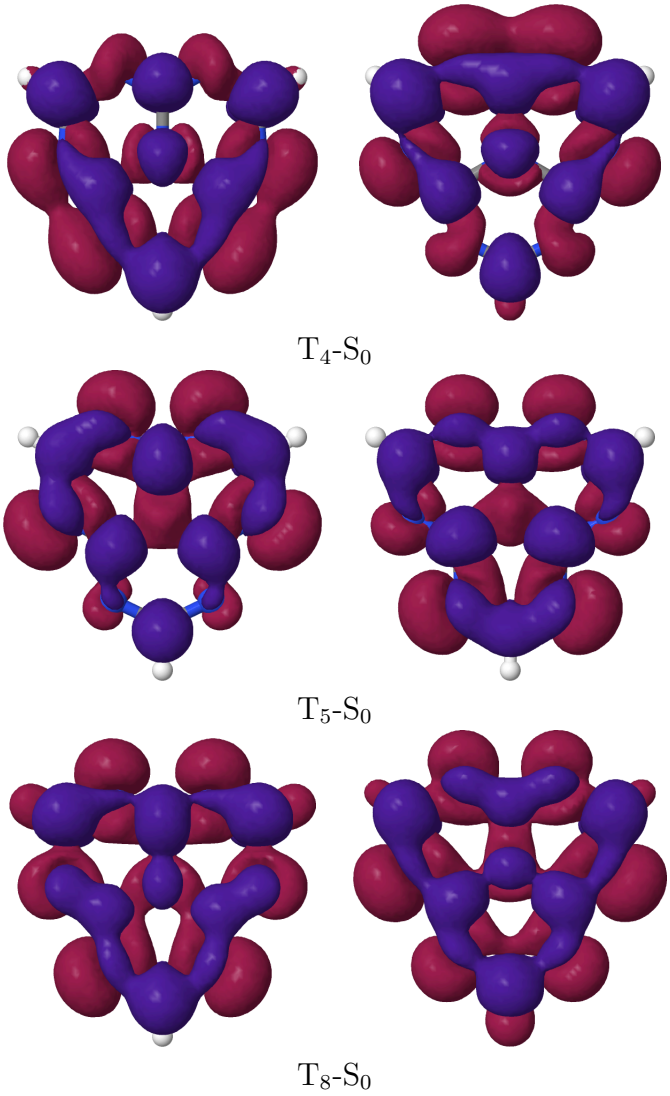

Figure S3: Difference densities of E″ symmetric triplet states contributing to vibronic SOC in heptazine. For color codes, see Figure S1.

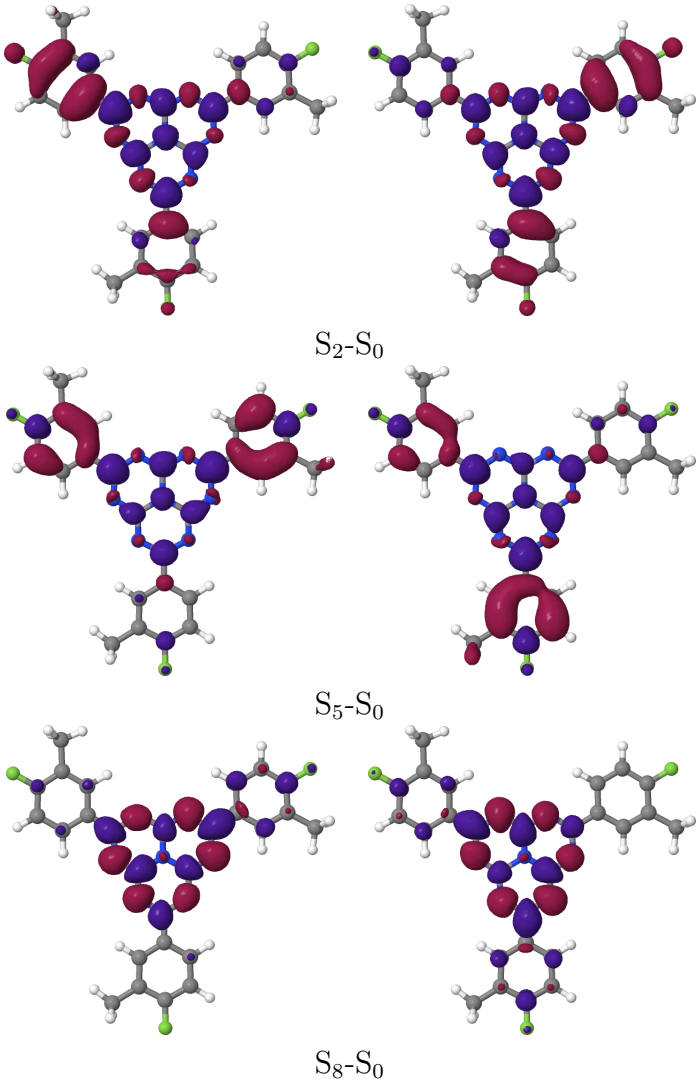

Figure S4: Difference densities of E′ symmetry singlet states contributing to vibronic fluorescence in HAP-3MF. For color codes, see Figure S1.

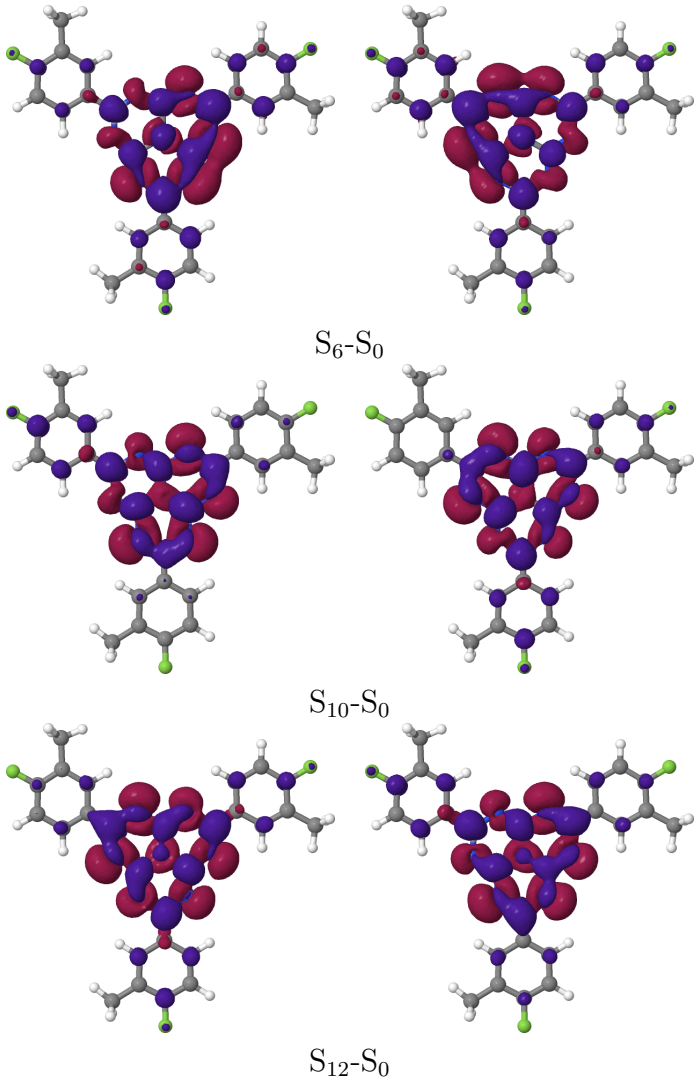

Figure S5: Difference densities of E″ symmetric singlet states contributing to vibronic SOC in HAP-3MF. For color codes, see Figure S1.

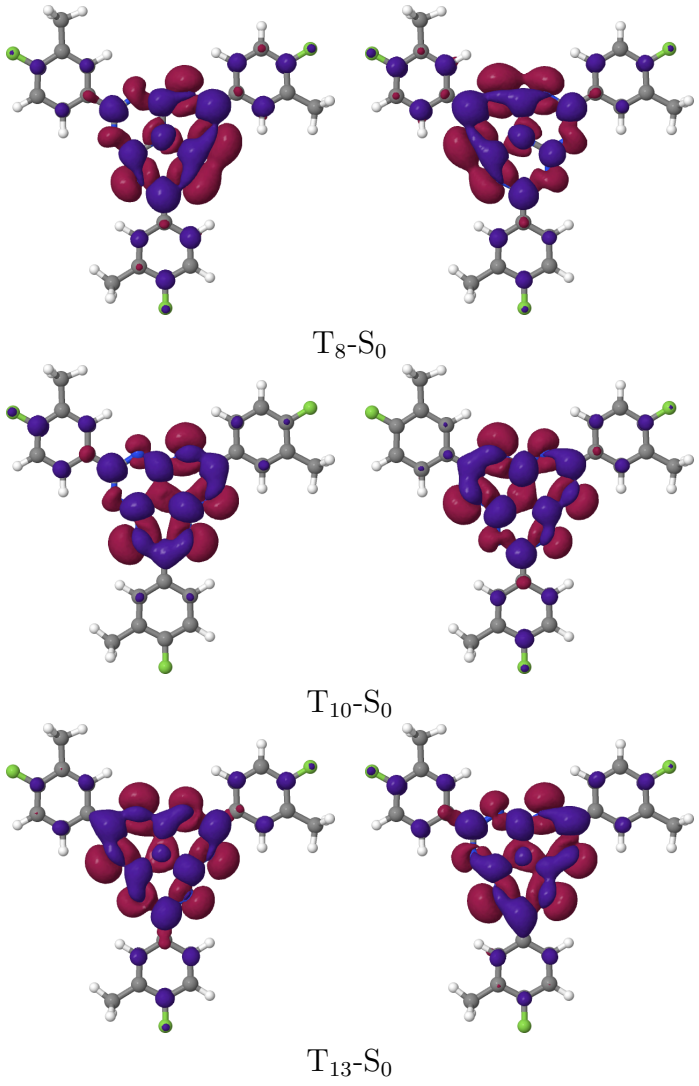

Figure S6: Difference densities of E″ symmetric triplet states contributing to vibronic SOC in HAP-3MF. For color codes, see Figure S1.

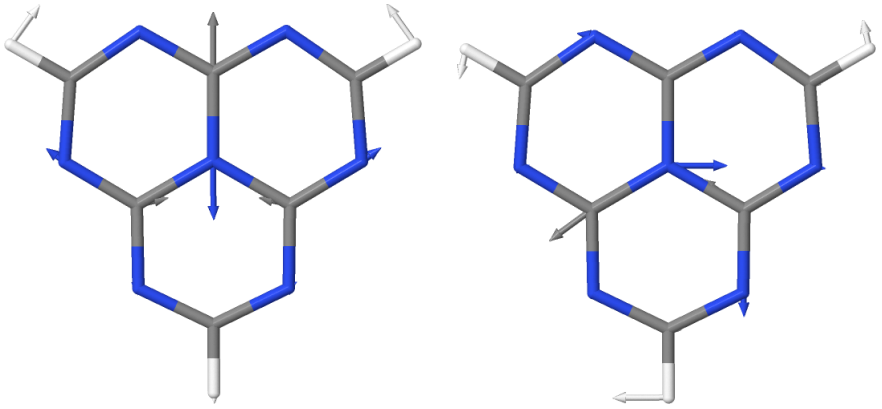

Mode 26 | E′ | 1193.47 cm^{-1} Mode 27 | E′ | 1193.58 cm^{-1}

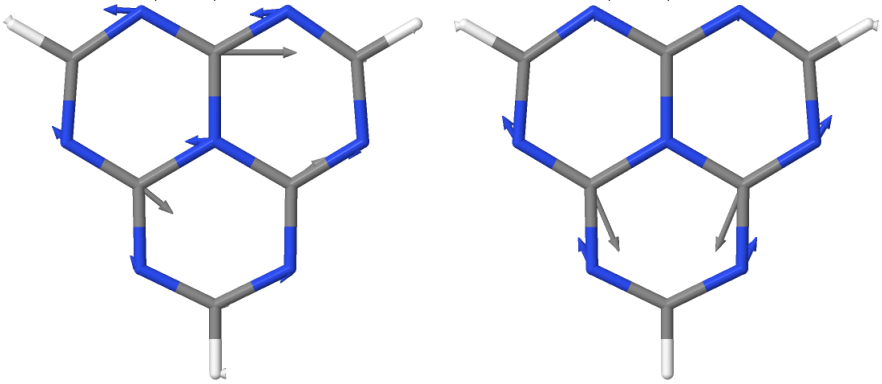

Mode 38 | E′ | 1676.75 cm^{-1} Mode 39 | E′ | 1676.80 cm^{-1}

Figure S7: Vibrational modes at the S_0 minimum contributing to vibronic absorption in heptazine.

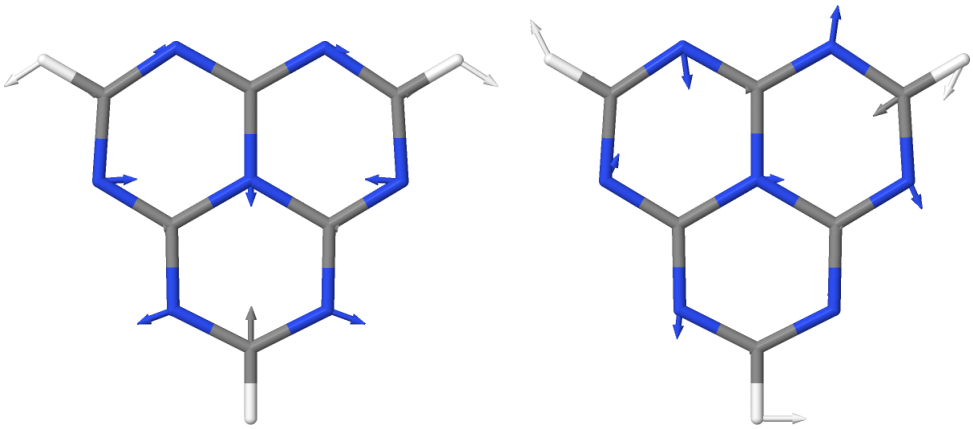

Mode 18 | E′ | 849.06 cm^{-1} Mode 19 | E′ | 849.10 cm^{-1}

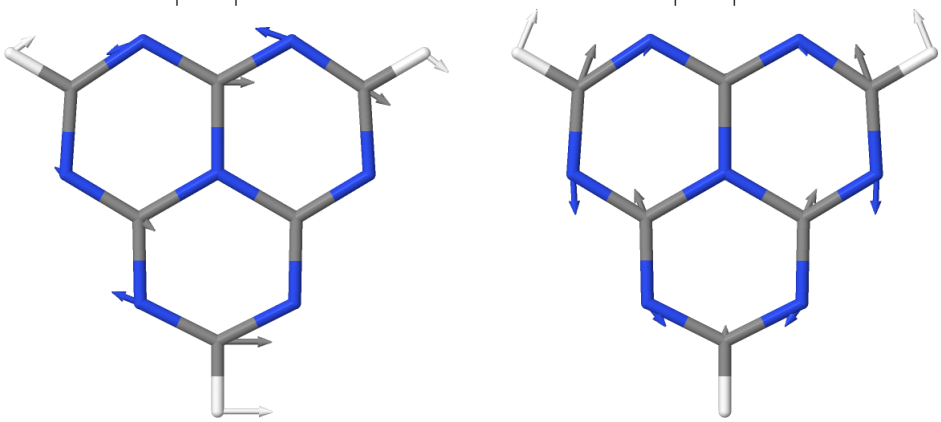

Mode 23 | E′ | 1035.57 cm^{-1} Mode 24 | E′ | 1035.62 cm^{-1}

Figure S8: Vibrational modes at the S_1 minimum contributing to vibronic fluorescence in heptazine.

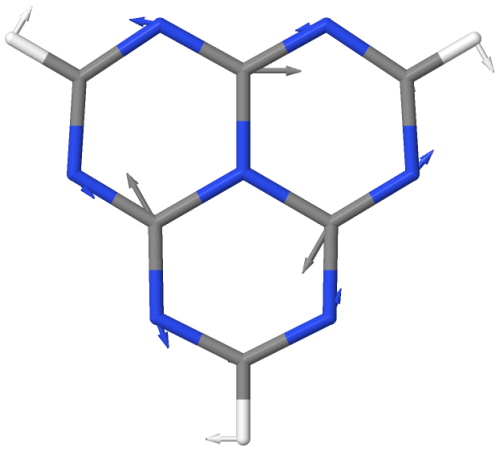

Mode 39 | A_2' | 1652.45 cm^{-1}

Figure S9: Vibrational modes at the S_1 minimum contributing to IC in heptazine.

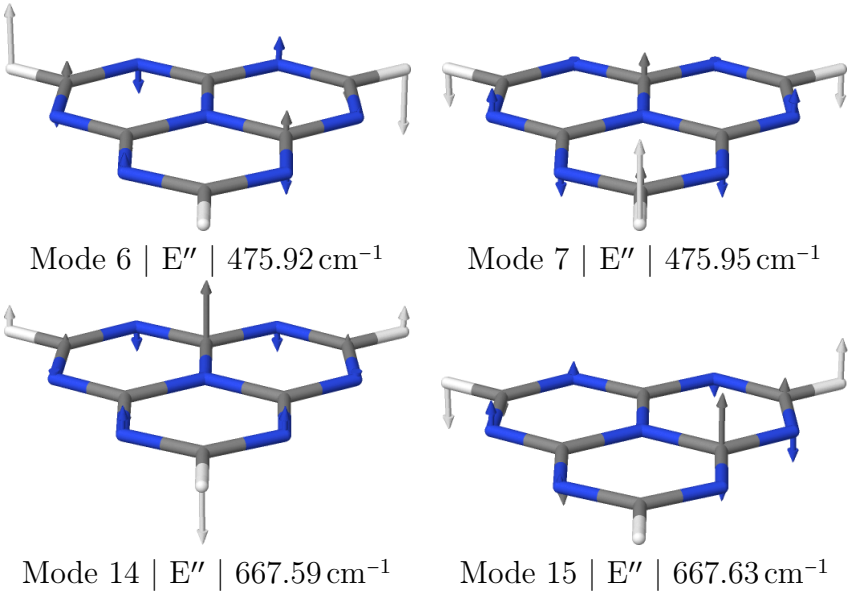

Figure S10: Vibrational modes at the S_1 minimum contributing to vibronic SOC in heptazine.

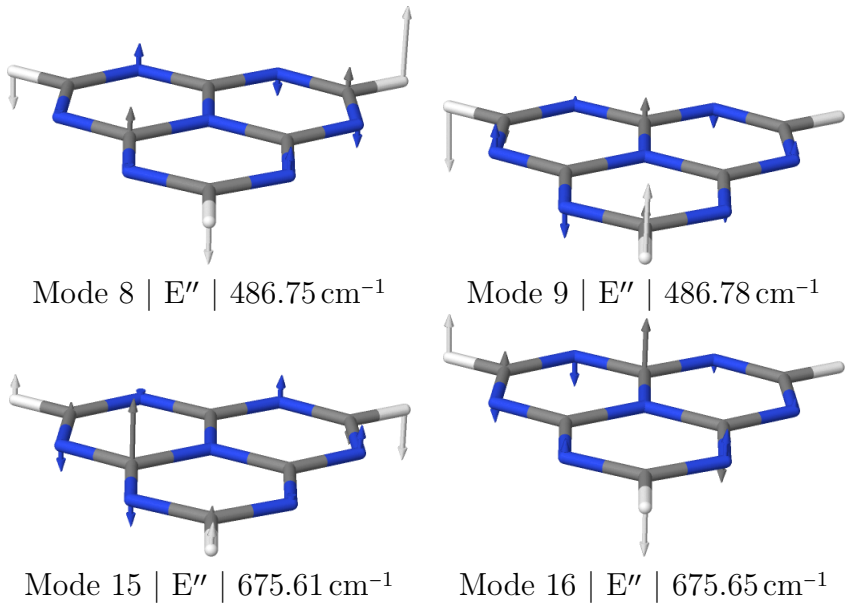

Figure S11: Vibrational modes at the T_1 minimum contributing to vibronic SOC in heptazine.

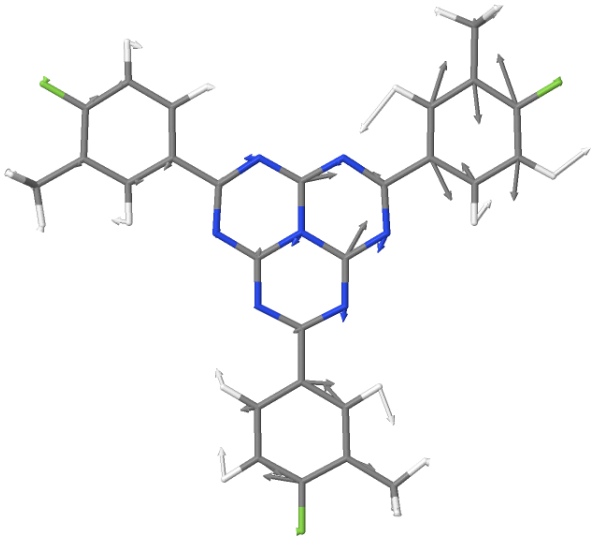

Mode 137 | E′ | 1660.40 cm^{-1}

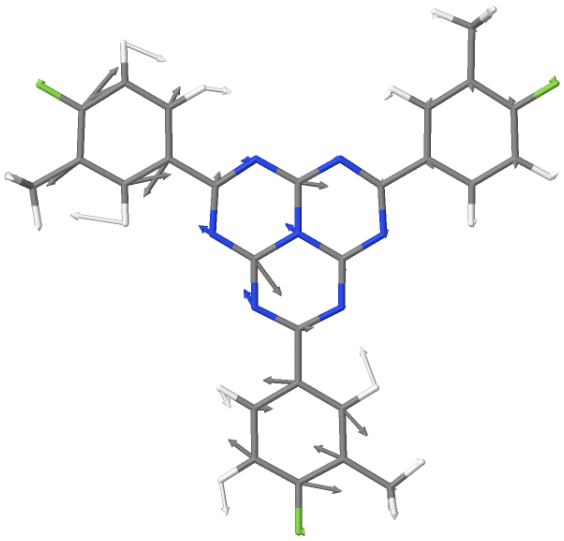

Mode 138 | E′ | 1660.42 cm^{-1}

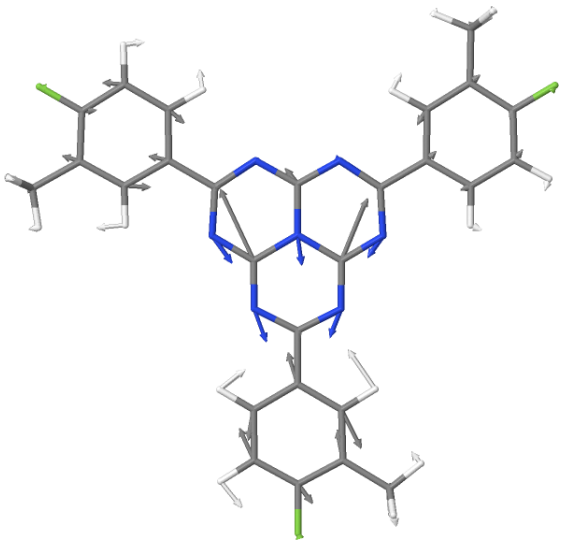

Mode 140 | E′ | 1682.87 cm^{-1}

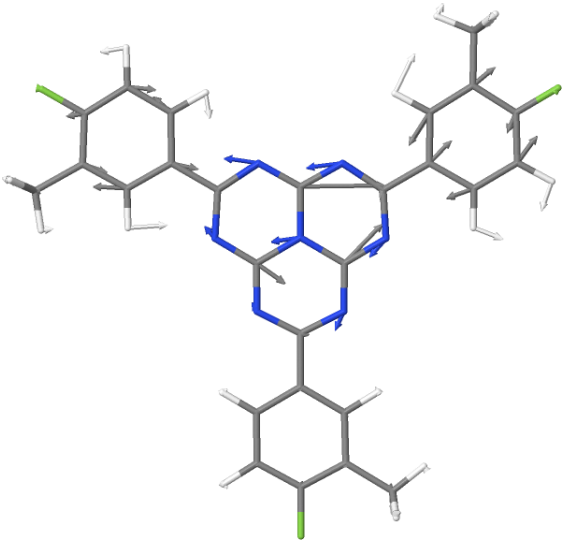

Mode 141 | E′ | 1682.92 cm^{-1}

Figure S12: Vibrational modes at the S_0 minimum contributing to vibronic absorption in HAP-3MF.

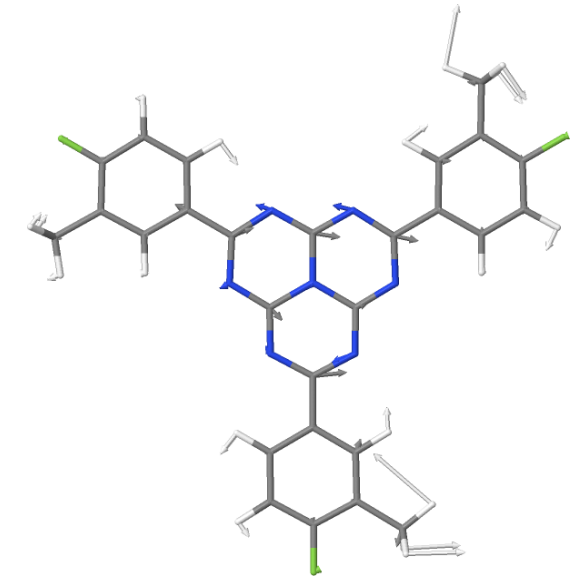

Mode 85 | E′ | 1020.43 cm^{-1}

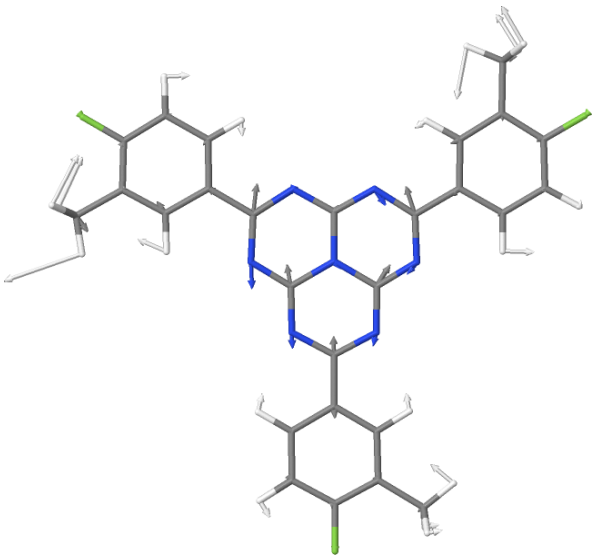

Mode 86 | E′ | 1020.52 cm^{-1}

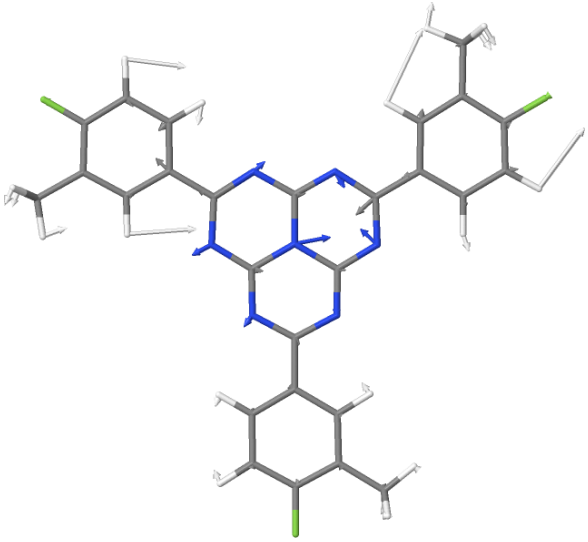

Mode 91 | E′ | 1084.36 cm^{-1}

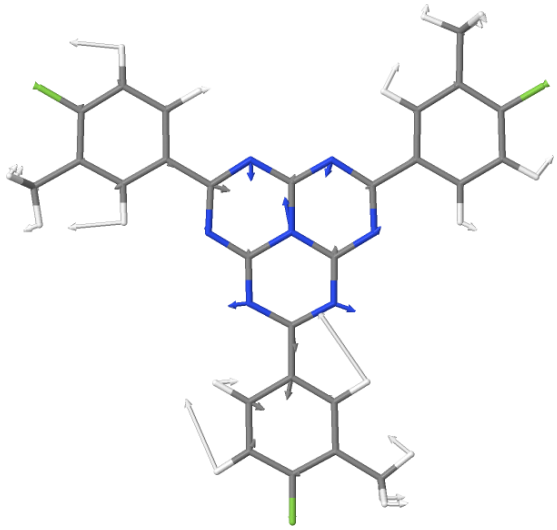

Mode 92 | E′ | 1084.38 cm^{-1}

Figure S13: Vibrational modes at the S_1 minimum contributing to vibronic fluorescence in HAP-3MF.

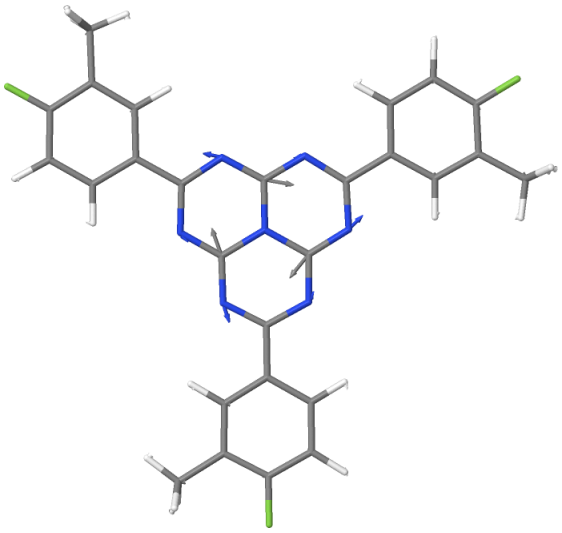

Mode 135 | A′ | 1598.29 cm^{-1}

Figure S14: Vibrational modes at the S_1 minimum contributing to IC in HAP-3MF.

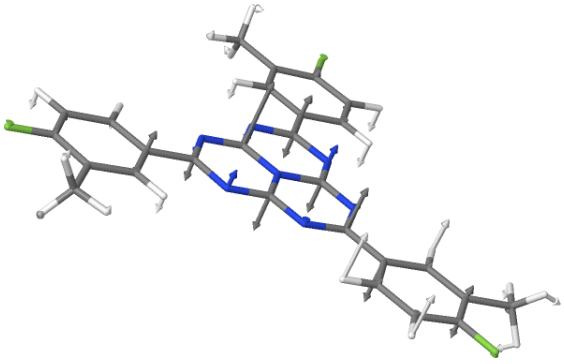

Mode 50 | E″ | 583.84 cm^{-1}

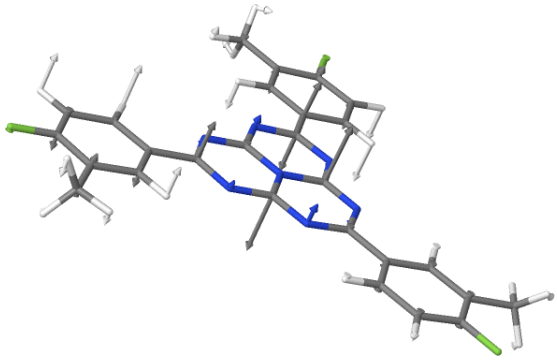

Mode 51 | E″ | 583.87 cm^{-1}

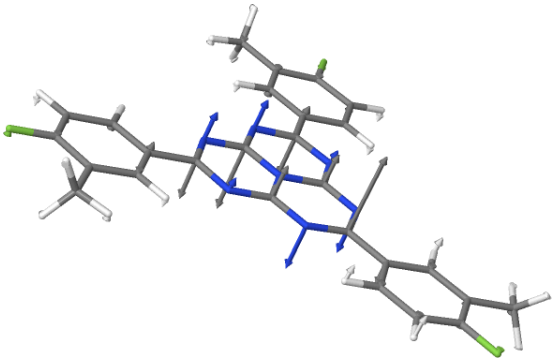

Mode 60 | E″ | 676.72 cm^{-1}

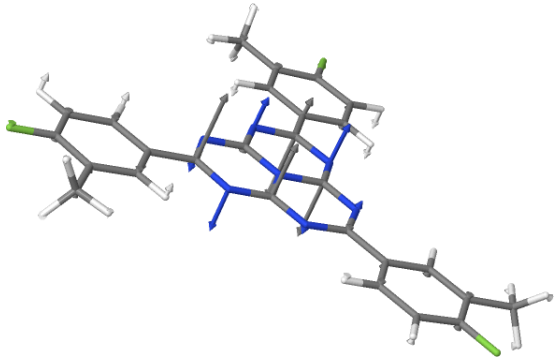

Mode 61 | E″ | 676.75 cm^{-1}

Figure S15: Vibrational modes at the S_1 minimum contributing to vibronic SOC in HAP-3MF.

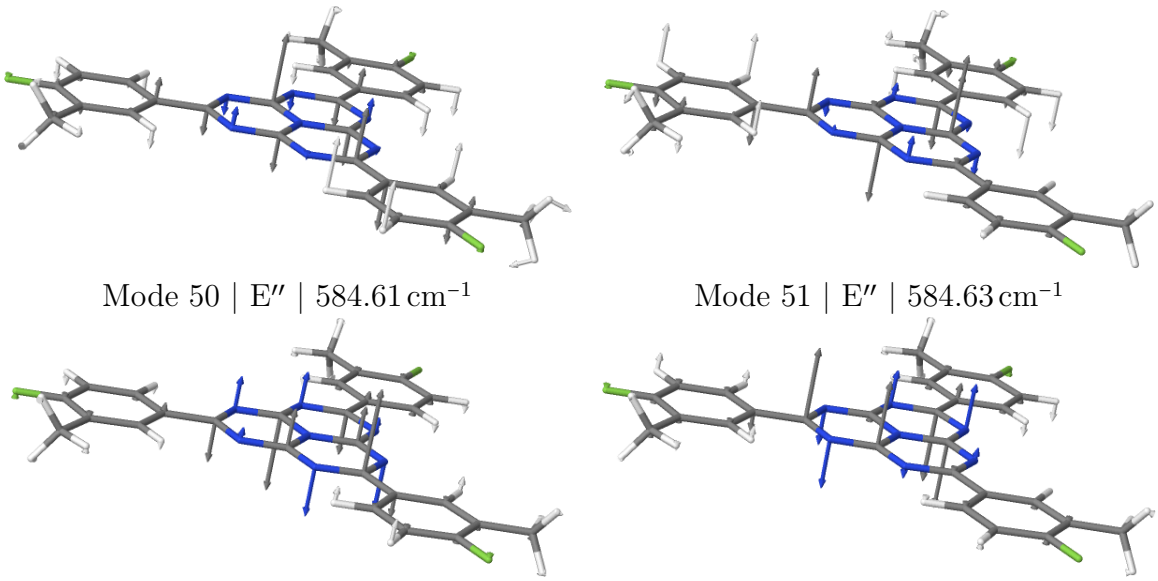

Mode 50 | E″ | 584.61 cm^{-1} Mode 51 | E″ | 584.63 cm^{-1}

Mode 62 | E″ | 677.04 cm^{-1} Mode 63 | E″ | 677.07 cm^{-1}

Figure S16: Vibrational modes at the T_1 minimum contributing to vibronic SOC in HAP-3MF.

Table S1: Vertical DFT/MRCI excitation energies of heptazine at the S_0 minimum.

State	D_{3h}	C_{2v}	ΔE [eV]	Osc. Strength f(L)
S_0	A_1'	A_1	0.00	
S_1	A_2'	B_1	2.59	0.00000
T_1	A_2'	B_1	2.60	
T_2	E′	A_1	3.35	
	E′	B_1	3.35	
T_3	A_1''	A_2	3.76	
T_4	E″	A_2	3.81	
	E″	B_2	3.81	
S_2	A_1''	A_2	3.86	0.00000
S_3	E″	A_2	3.92	0.00000
	E″	B_2	3.92	0.00000
S_4	E′	A_1	4.32	0.29062
	E′	B_1	4.32	0.28927
T_5	E″	A_2	4.63	
	E″	B_2	4.64	
T_6	A_2''	B_2	4.77	
T_7	E′	B_1	4.82	
	E′	A_1	4.82	
S_5	E″	A_2	4.87	0.00000
	E″	B_2	4.88	0.00001
T_8	E″	A_2	4.95	
	E″	B_2	4.96	
S_6	A_2''	B_2	4.97	0.01530
T_9	A_1''	A_2	4.98	
S_7	E″	A_2	5.04	0.00000
	E″	B_2	5.05	0.00002
S_8	A_1''	A_2	5.10	0.00000
T_{10}	A_1'	A_1	5.21	
T_{11}	A_2''	B_2	5.22	
S_9	A_2''	B_2	5.36	0.00006
T_{12}	E′	A_1	5.69	
	E′	B_1	5.70	
S_{10}	E′	B_1	5.73	0.37346
	E′	A_1	5.73	0.37348
T_{13}	A_1'	A_1	5.89	
S_{11}	A_1'	A_1	6.05	0.00000
T_{14}	A_2'	B_1	6.15	
S_{12}	A_2'	B_1	6.26	0.00000
S_{13}	E′	B_1	6.51	0.03363
	E′	A_1	6.52	0.02905
S_{14}	E′	A_1	6.53	0.00339

Table S2: Vertical DFT/MRCI excitation energies of heptazine at the S_1 minimum relative to S_0 minimum.

State	D_{3h}	C_{2v}	ΔE [eV]	Osc. Strength f(L)
S_0	A_1'	A_1	0.08	
S_1	A_2'	B_1	2.50	0.00000
T_1	A_2'	B_1	2.53	
T_2	E′	A_1	3.39	
	E′	B_1	3.39	
T_3	A_1''	A_2	3.63	
T_4	E″	A_2	3.70	
	E″	B_2	3.70	
S_2	A_1''	A_2	3.74	0.00000
S_3	E″	A_2	3.81	0.00000
	E″	B_2	3.81	0.00000
S_4	E′	A_1	4.35	0.27737
	E′	B_1	4.35	0.27652
T_5	E″	A_2	4.65	
	E″	B_2	4.66	
T_6	E′	B_1	4.73	
	E′	A_1	4.73	
T_7	A_2''	B_2	4.81	
S_5	E″	A_2	4.88	0.00000
	E″	B_2	4.89	0.00000
T_8	E″	A_2	4.91	
	E″	B_2	4.91	
T_9	A_1''	A_2	4.95	
S_6	A_2''	B_2	5.00	0.01334
S_7	E″	A_2	5.00	0.00000
	E″	B_2	5.02	0.00025
T_{10}	A_1'	A_1	5.06	
S_8	A_1''	A_2	5.08	0.00000
T_{11}	A_2''	B_2	5.19	
S_9	A_2''	B_2	5.31	0.00000
S_{10}	E′	B_1	5.64	0.37613
	E′	A_1	5.65	0.37707
T_{12}	E′	A_1	5.67	
	E′	B_1	5.68	
S_{11}	A_1'	A_1	5.86	0.00000
T_{13}	A_1'	A_1	5.87	
T_{14}	A_2'	B_1	6.17	
S_{12}	A_2'	B_1	6.25	0.00000
S_{13}	E′	B_1	6.47	0.02152
	E′	A_1	6.49	0.01898
S_{14}	E′	A_1	6.48	0.00183

Table S3: Vertical DFT/MRCI excitation energies of heptazine at the T_1 minimum relative S_0 minimum.

State	D_{3h}	C_{2v}	ΔE [eV]	Osc. Strength f(L)
S_0	A_1'	A_1	0.08	
S_1	A_2'	B_1	2.50	0.00000
T_1	A_2'	B_1	2.52	
T_2	E′	A_1	3.39	
	E′	B_1	3.39	
T_3	A_1''	A_2	3.62	
T_4	E″	A_2	3.70	
	E″	B_2	3.70	
S_2	A_1''	A_2	3.73	0.00000
S_3	E″	A_2	3.81	0.00000
	E″	B_2	3.81	0.00000
S_4	E′	A_1	4.35	0.27714
	E′	B_1	4.35	0.27628
T_5	E″	A_2	4.65	
	E″	B_2	4.65	
T_6	E′	B_1	4.72	
	E′	A_1	4.72	
T_7	A_2''	B_2	4.81	
S_5	E″	A_2	4.88	0.00000
	E″	B_2	4.89	0.00000
T_8	E″	A_2	4.90	
	E″	B_2	4.91	
T_9	A_1''	A_2	4.95	
S_6	A_2''	B_2	5.00	0.01316
S_7	E″	A_2	5.00	0.00000
	E″	B_2	5.01	0.00030
T_{10}	A_1'	A_1	5.07	
S_8	A_1''	A_2	5.08	0.00000
T_{11}	A_2''	B_2	5.19	
S_9	A_2''	B_2	5.30	0.00002
S_{10}	E′	B_1	5.64	0.37729
	E′	A_1	5.65	0.37753
T_{12}	E′	A_1	5.67	
	E′	B_1	5.67	
S_{11}	A_1'	A_1	5.85	0.00000
T_{13}	A_1'	A_1	5.88	
T_{14}	A_2'	B_1	6.17	
S_{12}	A_2'	B_1	6.25	0.00000
S_{13}	E′	B_1	6.47	0.02205
	E′	A_1	6.48	0.01330
S_{14}	E′	A_1	6.48	0.00803

Table S4: Vertical DFT/MRCI excitation energies of HAP-3MF at the S_0 minimum.

State	C_{3h}	C_s	ΔE [eV]	Osc. Strength f(L)
S_0	A′	A′	0.00	
T_1	A′	A′	2.70	
S_1	A′	A′	2.72	0.00000
T_2	E′	A′	3.00	
	E′	A′	3.01	
T_3	A′	A′	3.05	
T_4	E′	A′	3.32	
	E′	A′	3.32	
T_5	E′	A′	3.59	
	E′	A′	3.59	
S_2	E′	A′	3.60	1.00453
	E′	A′	3.60	1.00442
T_6	A′	A′	3.61	
T_7	A″	A″	3.82	
T_8	E″	A″	3.90	
	E″	A″	3.90	
S_3	A″	A″	3.92	0.00000
S_4	A′	A′	3.92	0.00160
S_5	E′	A′	3.95	0.04609
	E′	A′	3.95	0.04604
S_6	E″	A″	4.00	0.00000
	E″	A″	4.00	0.00000
T_9	A′	A′	4.04	
S_7	A′	A′	4.06	0.00038
S_8	E′	A′	4.12	0.36871
	E′	A′	4.12	0.36922
S_9	A′	A′	4.56	0.00065
T_{10}	E″	A″	4.60	
	E″	A″	4.60	
T_{11}	A″	A″	4.72	
S_{10}	E″	A″	4.80	0.00000
	E″	A″	4.80	0.00000
T_{12}	A″	A″	4.87	
T_{13}	E″	A″	4.88	
	E″	A″	4.88	
S_{11}	A″	A″	4.90	0.01353
S_{12}	E″	A″	4.95	0.00000
	E″	A″	4.95	0.00000
S_{13}	A″	A″	4.99	0.00001
T_{14}	E″	A″	5.43	
S_{14}	E″	A″	5.52	0.00000

Table S5: Vertical DFT/MRCI excitation energies of HAP-3MF at the S_1 minimum relative to S_0 minimum.

State	C_{3h}	C_s	ΔE [eV]	Osc. Strength f(L)
S_0	A′	A′	0.09	
T_1	A′	A′	2.65	
S_1	A′	A′	2.66	0.00000
T_2	E′	A′	3.02	
	E′	A′	3.02	
T_3	A′	A′	3.07	
T_4	E′	A′	3.32	
	E′	A′	3.32	
S_2	E′	A′	3.61	1.04103
	E′	A′	3.62	1.04104
T_5	E′	A′	3.62	
	E′	A′	3.62	
T_6	A′	A′	3.64	
T_7	A″	A″	3.70	
S_3	A″	A″	3.80	0.00000
T_8	E″	A″	3.80	
	E″	A″	3.81	
S_4	E″	A″	3.91	0.00000
	E″	A″	3.91	0.00000
S_5	A′	A′	3.95	0.00115
S_6	E′	A′	3.98	0.02872
	E′	A′	3.98	0.02890
S_7	A′	A′	4.10	0.12909
S_8	E′	A′	4.10	0.34830
	E′	A′	4.10	0.24979
T_9	A′	A′	4.10	
T_{10}	E″	A″	4.58	
	E″	A″	4.59	
S_9	A′	A′	4.59	0.00052
T_{11}	A″	A″	4.74	
S_{10}	E″	A″	4.76	0.00000
	E″	A″	4.77	0.00000
T_{12}	E″	A″	4.78	
	E″	A″	4.79	
T_{13}	A″	A″	4.81	
S_{11}	E″	A″	4.88	0.00000
	E″	A″	4.89	0.00001
S_{12}	E″	A″	4.90	0.00771
	E″	A″	4.92	0.00420
T_{14}	A″	A″	5.38	
S_{13}	A″	A″	5.47	0.00000

Table S6: Vertical DFT/MRCI excitation energies of HAP-3MF at the T_1 minimum relative S_0 minimum.

State	C_{3h}	C_s	ΔE [eV]	Osc. Strength f(L)
S_0	A′	A′	0.09	
T_1	A′	A′	2.65	
S_1	A′	A′	2.66	0.00000
T_2	E′	A′	3.02	
	E′	A′	3.03	
T_3	A′	A′	3.07	
T_4	E′	A′	3.32	
	E′	A′	3.32	
T_5	E′	A′	3.62	
	E′	A′	3.62	
S_2	E′	A′	3.62	1.04111
	E′	A′	3.62	1.04105
T_6	A′	A′	3.64	
T_7	A″	A″	3.69	
S_3	A″	A″	3.80	0.00000
T_8	E″	A″	3.80	
	E″	A″	3.80	
S_4	E″	A″	3.91	0.00000
	E″	A″	3.91	0.00000
S_5	A′	A′	3.95	0.00118
S_6	E′	A′	3.98	0.02893
	E′	A′	3.98	0.02915
S_7	E′	A′	4.10	0.32906
	E′	A′	4.10	0.36092
T_9	A′	A′	4.10	
S_8	A′	A′	4.10	0.03749
T_{10}	E″	A″	4.58	
	E″	A″	4.58	
S_9	A′	A′	4.59	0.00002
T_{11}	A″	A″	4.74	
S_{10}	E″	A″	4.76	0.00000
	E″	A″	4.76	0.00000
T_{12}	E″	A″	4.78	
	E″	A″	4.79	
T_{13}	A″	A″	4.80	
S_{11}	E″	A″	4.87	0.00000
	E″	A″	4.89	0.00001
S_{12}	E″	A″	4.90	0.00799
	E″	A″	4.91	0.00398
T_{14}	A″	A″	5.38	
S_{13}	A″	A″	5.47	0.00000

Table S7: Transition dipole moment gradients above 0.01 ea_0 per displacement along dimensionless normal mode for the $S_0 \rightarrow S_1$ transition in heptazine at the S_0 minimum.

Mode	Symmetry D_{3h}	Frequency [cm^{-1}]	x	y	z
10	E′	529.41	0.011887	-0.000001	0.000001
11	E′	529.47	0.000000	0.012795	-0.000000
18	E′	880.06	0.056349	0.000000	-0.000011
19	E′	880.10	0.000000	0.056545	0.000001
23	E′	1089.89	0.000000	-0.070317	-0.000002
24	E′	1089.89	0.070596	0.000005	0.000002
26	E′	1193.47	-0.000001	-0.081889	-0.000002
27	E′	1193.58	0.082462	-0.000000	-0.000009
29	E′	1312.15	-0.075081	-0.000003	0.000000
30	E′	1312.15	-0.000010	0.074846	-0.000004
32	E′	1437.77	0.011774	0.000000	-0.000003
33	E′	1437.79	-0.000004	-0.011792	0.000013
36	E′	1601.53	-0.026703	-0.000003	-0.000002
37	E′	1601.54	-0.000015	0.026817	0.000003
38	E′	1676.75	-0.115710	0.000002	-0.000010
39	E′	1676.80	-0.000000	0.114856	-0.000000
40	E′	3177.84	0.027071	0.000001	-0.000008
41	E′	3177.84	-0.000000	-0.027109	-0.000005

Table S8: Transition dipole moment gradients above 0.01 ea_0 per displacement along dimensionless normal mode for the $S_1 \rightarrow S_0$ transition in heptazine at the S_1 minimum.

Mode	Symmetry D_{3h}	Frequency [cm^{-1}]	x	y	z
10	E′	515.92	0.014603	0.000001	0.000000
11	E′	515.98	-0.000001	0.016257	-0.000000
18	E′	849.06	-0.084349	-0.000000	-0.000001
19	E′	849.10	-0.000001	0.082111	0.000000
23	E′	1035.57	-0.106727	-0.000005	0.000002
24	E′	1035.62	0.000010	0.108133	-0.000000
25	E′	1075.34	0.000002	-0.079176	0.000001
26	E′	1075.35	0.081727	0.000003	-0.000000
28	E′	1255.07	0.000001	-0.061916	0.000000
29	E′	1255.17	0.063576	0.000002	0.000001
31	E′	1310.83	0.030800	0.000002	0.000002
32	E′	1310.87	0.000005	0.033557	0.000000
33	E′	1450.88	0.000128	-0.052916	0.000000
34	E′	1450.88	0.053776	0.000137	0.000003
36	E′	1508.25	-0.047447	-0.000007	-0.000001
37	E′	1508.29	-0.000002	0.047263	-0.000000
40	E′	3210.66	-0.000005	-0.026335	0.000000
41	E′	3210.67	0.025920	0.000002	-0.000000

Table S9: SOCME gradients above 0.01 cm^{-1} per displacement along dimensionless normal mode for the $S_1 \rightarrow T_1$ transition in heptazine at the S_1 minimum.

Mode	Symmetry D_{3h}	Frequency [cm^{-1}]	x	y	z
2	E″	127.02	0.059280	-0.000070	0.000000
3	E″	127.03	0.000300	0.055460	0.000000
6	E″	475.92	0.000090	-0.054300	0.000000
7	E″	475.95	0.070810	-0.000010	0.000000
14	E″	667.59	-0.000300	0.074200	0.000000
15	E″	667.63	0.082460	0.000340	0.000000
21	E″	886.02	-0.000030	0.005460	0.000000
22	E″	886.14	-0.012210	0.000020	0.000000

Table S10: SOCME gradients above 0.01 cm^{-1} per displacement along dimensionless normal mode for the $T_1 \rightarrow S_1$ transition in heptazine at the T_1 minimum.

Mode	Symmetry D_{3h}	Frequency [cm^{-1}]	x	y	z
2	E″	130.56	0.053180	0.000110	0.000000
3	E″	130.58	0.000380	0.052140	0.000000
8	E″	486.75	-0.000170	-0.055650	0.000010
9	E″	486.78	-0.084070	0.000130	0.000000
15	E″	675.61	0.000030	0.076770	0.000000
16	E″	675.65	0.082210	0.000240	0.000000

Table S11: NACMEs above 0.01 a_0^{-1} per displacement along dimensionless normal mode for the $S_1 \rightarrow S_0$ transition in heptazine at the S_1 minimum.

Mode	Symmetry D_{3h}	Frequency [cm^{-1}]	NACME
30	A_2'	1301.79	0.030724
35	A_2'	1459.45	-0.044209
39	A_2'	1652.45	-0.125802

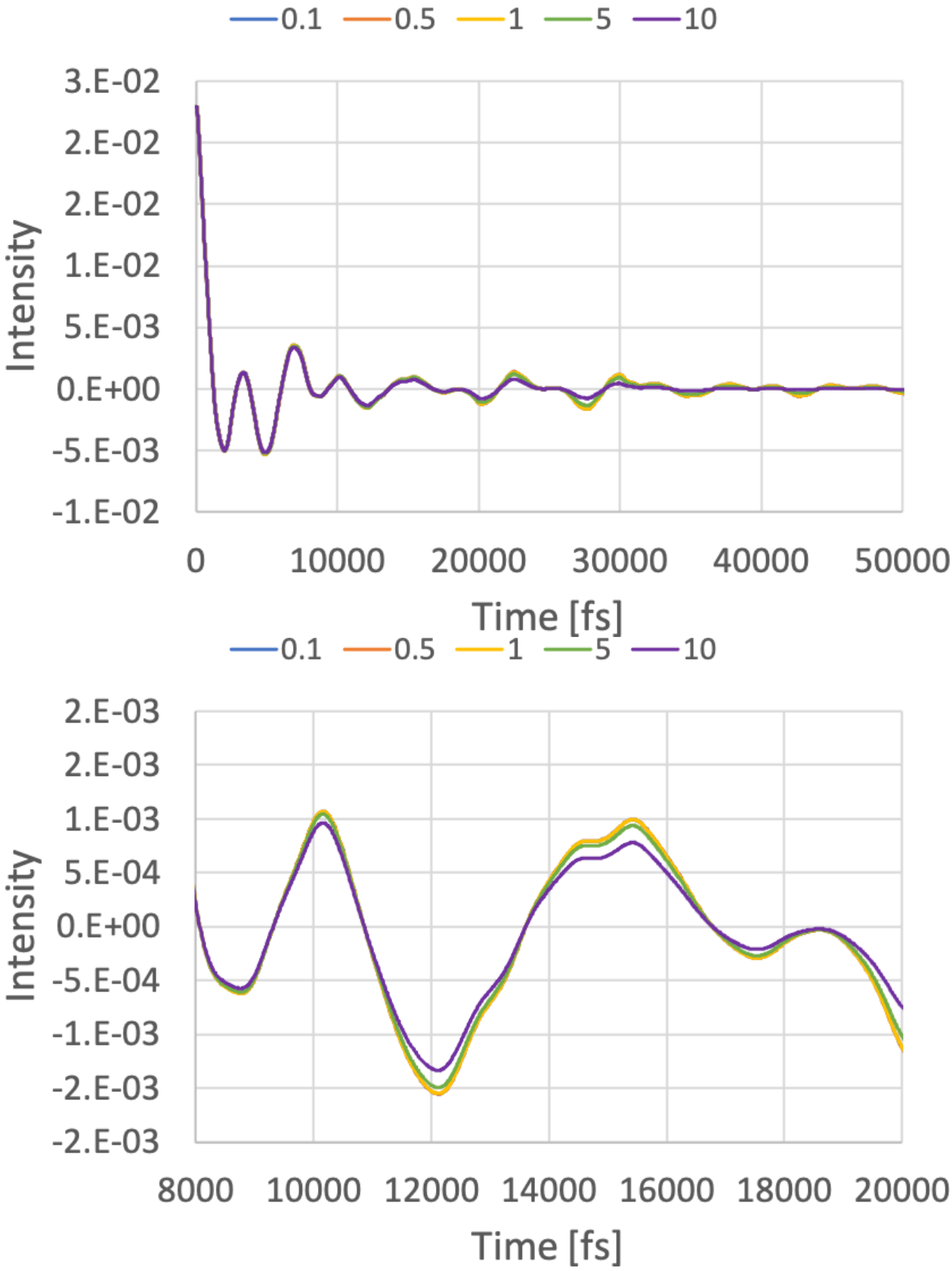

Figure S17: Correlation function of the $S_1 \rightsquigarrow T_1$ ISC transition of heptazine computed with different correlation function dampings in the time interval 0-50 ps (upper panel) and 8-20 ps (lower panel).

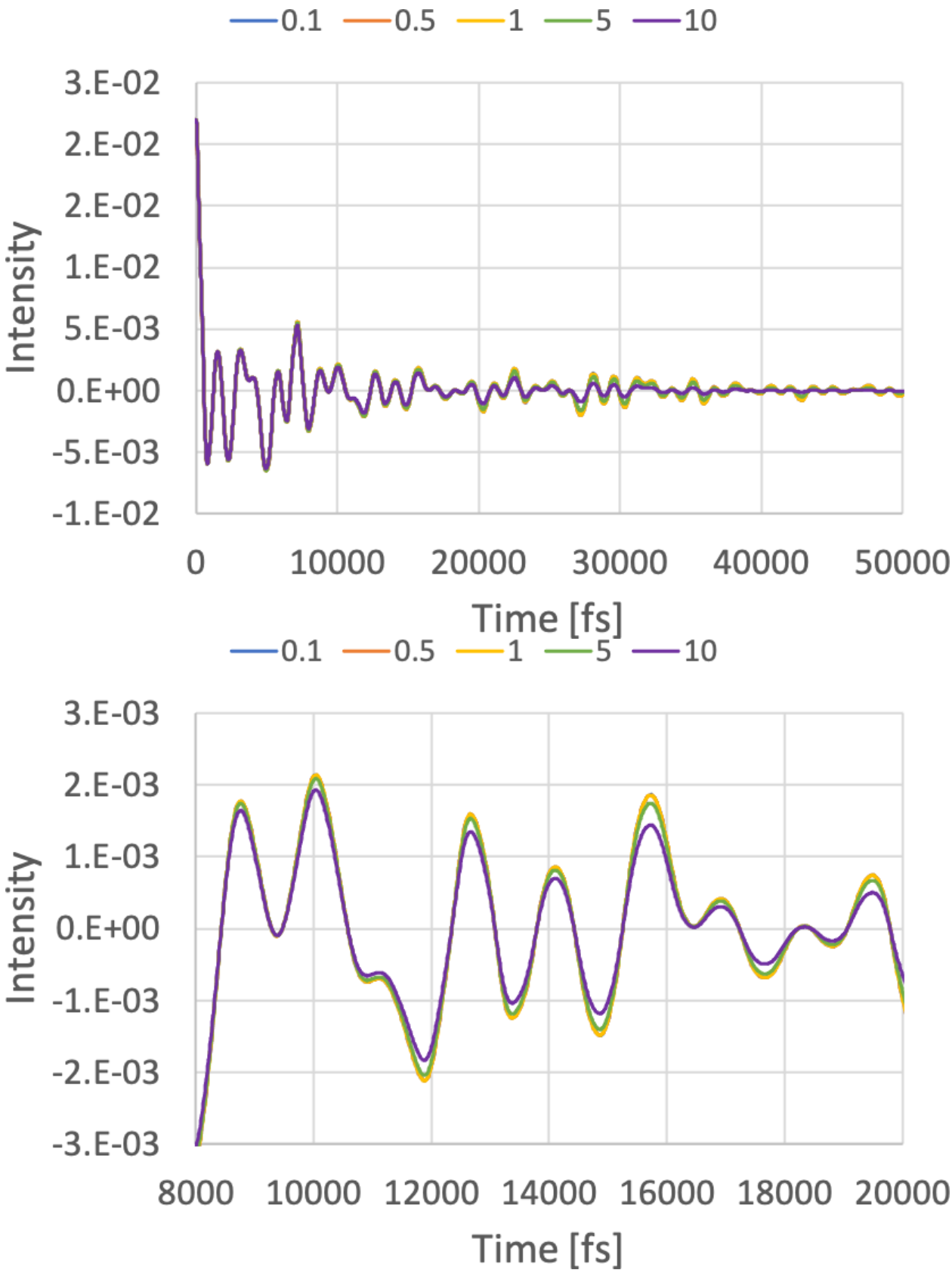

Figure S18: Correlation function of the $S_1 \backsim T_1$ RISC transition of heptazine computed with different correlation function dampings in the time interval 0-50 ps (upper panel) and 8-20 ps (lower panel).

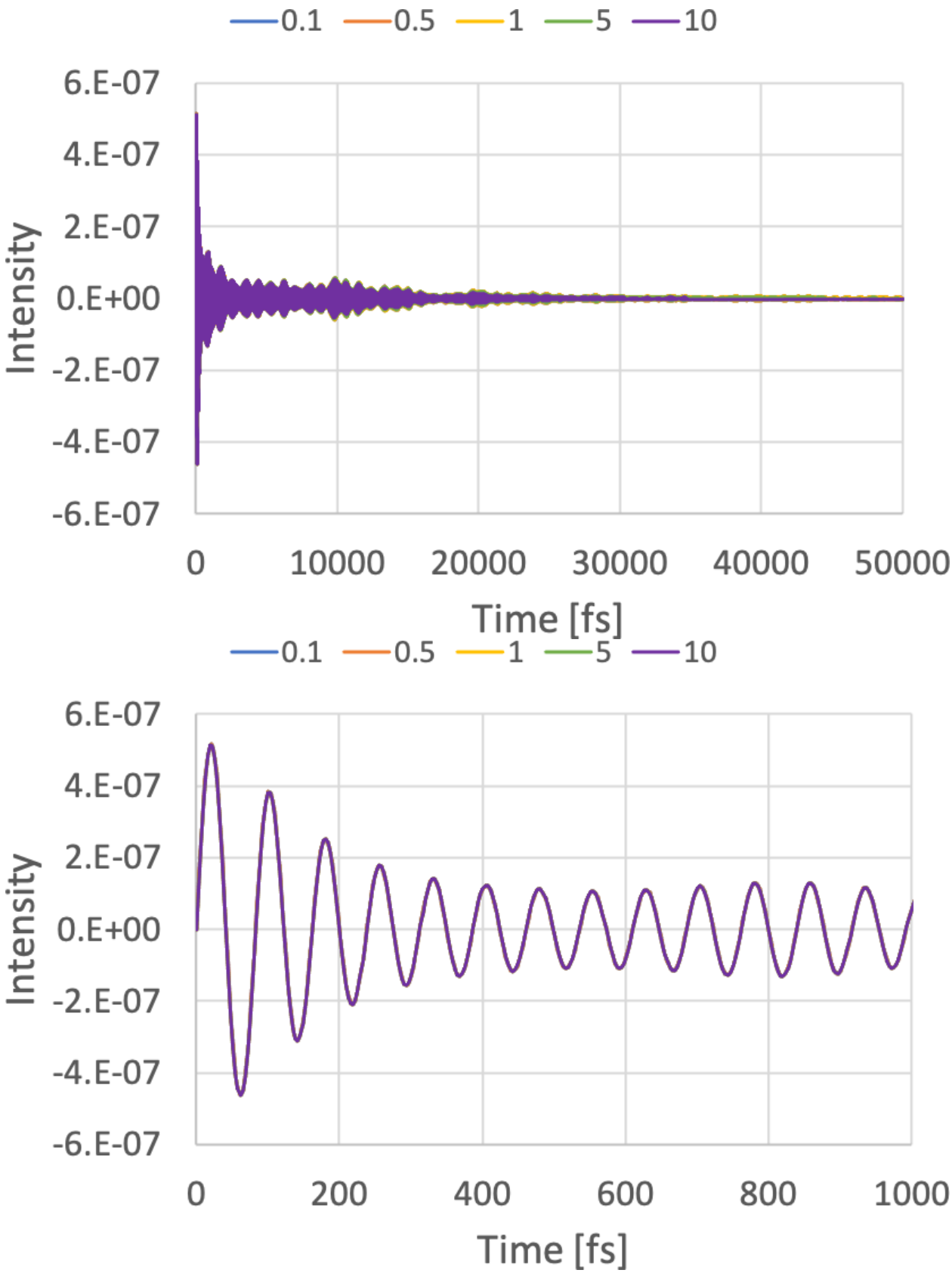

Figure S19: Correlation function of the $S_1 \rightsquigarrow S_0$ IC transition of heptazine computed with different correlation function dampings in the time interval 0-50 ps (upper panel) and 0-1 ps (lower panel).

Table S12: ISC rate constants of heptazine computed with different correlation function dampings.

Damping [cm^{-1}]	Rate Constant [s^{-1}]	Points	Time [fs]
10	1.10×10^7	65536	25000
5	1.07×10^7	65536	25000
1	1.05×10^7	65536	25000
0.5	1.05×10^7	262144	250000
0.1	1.58×10^7	262144	250000

Table S13: RISC rate constants of heptazine computed with different correlation function dampings.

Damping [cm^{-1}]	Rate Constant [s^{-1}]	Points	Time [fs]
10	2.93×10^6	65536	25000
5	2.85×10^6	65536	25000
1	2.77×10^6	65536	25000
0.5	2.76×10^6	262144	250000
0.1	4.11×10^6	262144	250000

Table S14: IC rate constants of heptazine computed with different correlation function dampings.

Damping [cm^{-1}]	Rate Constant [s^{-1}]	Points	Time [fs]
10	3.29×10^8	262144	25000
5	3.29×10^8	262144	25000
1	3.29×10^8	262144	25000
0.5	3.29×10^8	2097152	250000
0.1	3.33×10^8	2097152	250000

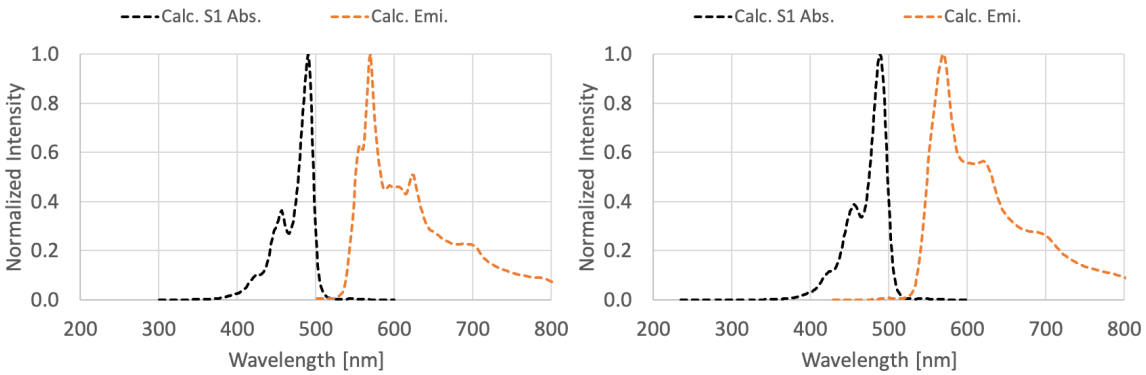

Figure S20: Herzberg–Teller $S_1 \leftarrow S_0$ absorption (black) and $S_1 \rightarrow S_0$ emission spectra (orange) of heptazine computed with damping functions of 100 cm^{-1} (left) and 200 cm^{-1} (right) FWHM.

Table S15: Fluorescence rate constants of heptazine computed with different correlation function dampings utilizing a grid of 16384 points and a integration time of 300 fs.

Damping [cm^{-1}]	Rate Constant [s^{-1}]
200	3.38×10^5
100	3.38×10^5
50	3.37×10^5

Table S16: Transition dipole moment gradients above 0.03 ea_0 per displacement along dimensionless normal mode for the $S_0 \rightarrow S_1$ transition in HAP-3MF at the S_0 minimum.

Mode	Symmetry C_{3h}	Frequency [cm^{-1}]	x	y	z
47	E′	576.42	0.019965	-0.004847	0.000000
48	E′	576.44	-0.003987	-0.020305	0.000000
72	E′	886.86	0.005433	0.036192	0.000000
73	E′	886.88	-0.035720	0.005195	0.000000
89	E′	1095.94	0.044478	-0.046685	0.000000
90	E′	1095.96	0.047719	0.043983	-0.000000
91	E′	1133.59	-0.034098	0.002810	-0.000000
92	E′	1133.61	0.003384	0.034064	0.000000
95	E′	1168.12	0.042855	-0.052048	0.000000
96	E′	1168.14	-0.049546	-0.045109	0.000000
98	E′	1216.24	-0.030173	0.004750	-0.000000
99	E′	1216.26	-0.005066	-0.029560	0.000000
101	E′	1258.07	-0.019202	0.050103	0.000000
102	E′	1258.12	0.050579	0.017673	0.000000
107	E′	1295.54	-0.046228	-0.021871	-0.000000
108	E′	1295.55	0.022149	-0.045843	-0.000000
116	E′	1414.99	-0.095684	0.075514	0.000000
117	E′	1415.01	0.078282	0.093569	0.000000
119	E′	1454.68	-0.094077	0.034328	-0.000000
120	E′	1454.70	0.033754	0.093096	0.000000
129	E′	1543.01	0.020205	-0.083653	0.000000
130	E′	1543.04	0.081213	0.018791	-0.000000
131	E′	1568.29	-0.053025	0.019623	0.000000
132	E′	1568.30	0.025369	0.051186	0.000000
134	E′	1635.64	0.073614	0.076834	-0.000000
135	E′	1635.67	-0.078274	0.072094	0.000000
137	E′	1660.40	-0.136477	0.062325	-0.000000
138	E′	1660.42	-0.063430	-0.131732	0.000000
140	E′	1682.87	-0.008610	0.160439	0.000000
141	E′	1682.92	-0.153660	-0.006416	0.000000

Table S17: Transition dipole moment gradients above 0.03 ea_0 per displacement along dimensionless normal mode for the $S_1 \rightarrow S_0$ transition in HAP-3MF at the S_1 minimum.

Mode	Symmetry C_{3h}	Frequency [cm^{-1}]	x	y	z
62	E′	682.38	-0.005935	0.030365	0.000000
63	E′	682.38	-0.031854	-0.005643	0.000001
72	E′	875.87	0.025089	0.066125	0.000000
73	E′	875.89	0.066319	-0.024701	0.000000
80	E′	953.51	0.020998	0.042101	0.000000
81	E′	953.52	0.043011	-0.020569	-0.000001
83	E′	1001.19	0.034578	0.085011	-0.000000
84	E′	1001.29	-0.093650	0.036575	-0.000000
85	E′	1020.43	0.059134	0.095785	-0.000000
86	E′	1020.52	-0.103727	0.064975	-0.000000
91	E′	1084.36	0.039720	-0.109463	-0.000002
92	E′	1084.38	0.108221	0.039233	-0.000000
97	E′	1167.77	-0.046567	0.077512	0.000001
98	E′	1167.80	0.078278	0.046128	-0.000000
100	E′	1217.64	-0.034896	0.005579	-0.000000
101	E′	1217.65	-0.005969	-0.034952	-0.000000
118	E′	1423.43	0.061657	-0.032615	-0.000000
119	E′	1423.47	0.032420	0.061856	0.000000
120	E′	1443.26	-0.065747	0.024752	0.000000
121	E′	1443.29	0.025576	0.064032	0.000001
129	E′	1499.37	0.002231	0.045185	0.000000
130	E′	1499.41	-0.045225	0.001456	-0.000000
136	E′	1636.58	0.007133	-0.034717	0.000002
137	E′	1636.59	0.033706	0.010540	0.000001

Table S18: SOCME gradients above 0.02 cm^{-1} per displacement along dimensionless normal mode for the $S_1 \rightarrow T_1$ transition in HAP-3MF at the S_1 minimum.

Mode	Symmetry C_{3h}	Frequency [cm^{-1}]	x	y	z
3	E″	22.21	0.010060	0.009240	0.000000
4	E″	22.36	-0.008640	0.009840	0.000000
10	A″	94.23	0.002460	0.006500	0.000000
11	E″	94.54	0.007540	-0.010680	0.000000
12	E″	95.72	-0.007980	-0.005280	0.000000
32	E″	344.14	0.006460	0.011150	0.000000
33	E″	344.17	-0.012830	0.006260	0.000000
50	E″	583.84	-0.018440	-0.002480	0.000000
51	E″	583.87	-0.002100	0.019560	0.000000
60	E″	676.72	-0.040940	0.007660	0.000000
61	E″	676.75	0.005340	0.035510	0.000000
69	E″	823.19	-0.010920	-0.012900	0.000000
70	E″	823.24	0.013600	-0.008500	0.000000
74	A″	897.15	-0.009000	0.012740	0.000000
75	E″	897.30	-0.007340	-0.014830	0.000000
76	E″	897.34	0.017820	0.001140	0.000000
78	E″	942.86	-0.016080	0.009220	0.000000
79	E″	942.93	-0.007240	-0.015600	0.000000
88	E″	1050.48	-0.015660	-0.002440	0.000000
89	E″	1050.49	-0.000700	-0.013390	0.000000

Gradients along mode 10 and 74 arise due to mixing with close lying E″ modes.

Table S19: SOCME gradients above 0.01 cm^{-1} per displacement along dimensionless normal mode for the $T_1 \rightarrow S_1$ transition in HAP-3MF at the T_1 minimum.

Mode	Symmetry C_{3h}	Frequency [cm^{-1}]	x	y	z
11	E″	94.00	0.008320	-0.010740	0.000000
12	E″	95.23	-0.007820	-0.007300	0.000000
32	E″	344.74	0.006200	0.009270	0.000000
33	E″	344.77	-0.010280	0.005800	0.000000
50	E″	584.61	-0.019140	0.000780	0.000000
51	E″	584.63	0.000770	0.019270	0.000000
62	E″	677.04	-0.035120	0.006500	0.000000
63	E″	677.07	0.006140	0.034360	0.000000
71	E″	823.15	-0.007640	-0.011040	0.000000
72	E″	823.20	0.012620	-0.010800	0.000000
76	A″	896.30	-0.008700	0.013080	0.000000
77	E″	896.44	-0.004090	-0.016620	0.000000
78	E″	896.48	0.018480	0.003740	0.000000
80	E″	942.23	-0.016640	0.010970	0.000000
81	E″	942.30	-0.010100	-0.014780	0.000010
88	E″	1050.29	-0.015540	-0.003170	0.000000
89	E″	1050.30	0.001710	-0.013480	0.000000

Gradients along mode 76 arise due to mixing with close lying E″ modes.

Table S20: NACMEs above 0.01 a_0^{-1} per displacement along dimensionless normal mode for the $S_1 \rightarrow S_0$ transition in HAP-3MF at the S_1 minimum.

Mode	Symmetry C_{3h}	Frequency [cm^{-1}]	NACME
13	A′	107.57	-0.016199
34	A′	373.94	0.016374
41	A′	500.39	0.011468
47	A′	568.81	0.010195
59	A′	651.91	-0.011899
110	A′	1324.66	-0.041613
114	A′	1375.71	-0.029828
122	A′	1450.45	0.012254
134	A′	1592.89	0.026079
135	A′	1598.29	-0.104239
138	A′	1636.67	-0.023678
139	A′	1659.98	0.013319

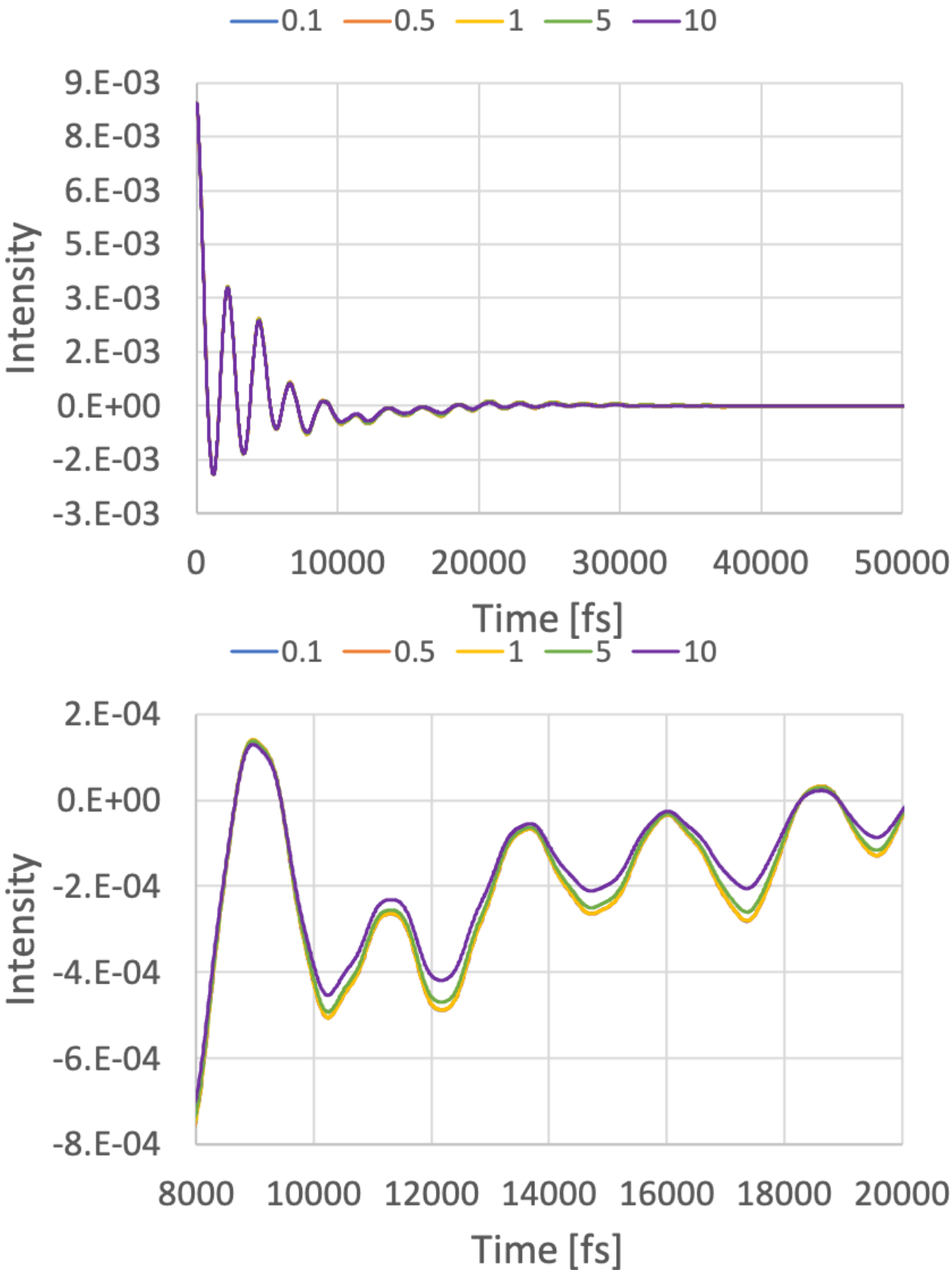

Figure S21: Correlation function of the $S_1 \rightsquigarrow T_1$ ISC transition of HAP-3MF computed with different correlation function dampings in the time interval 0-50 ps (upper panel) and 8-20 ps (lower panel).

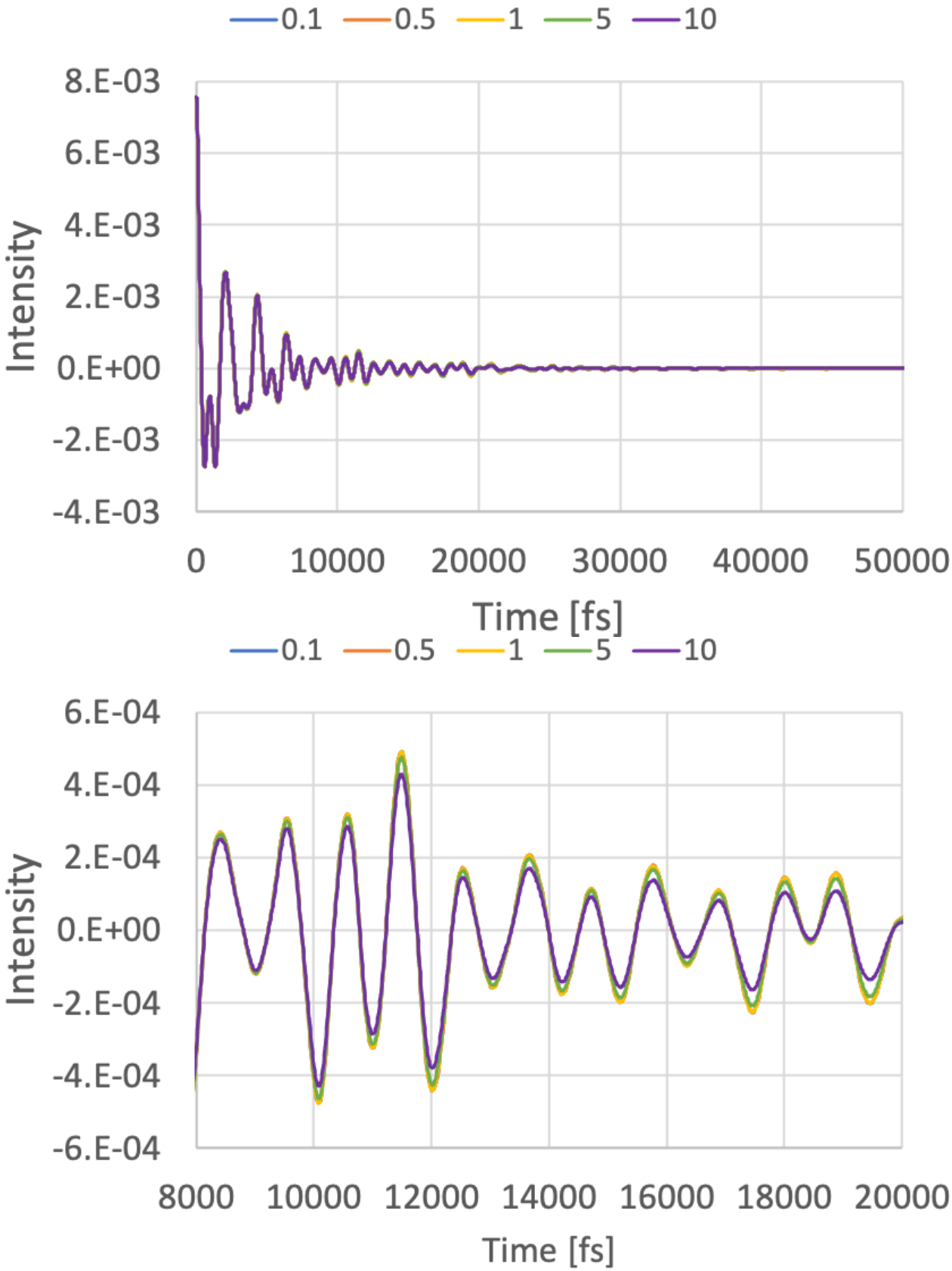

Figure S22: Correlation function of the $S_1 \backsim T_1$ RISC transition of HAP-3MF computed with different correlation function dampings in the time interval 0-50 ps (upper panel) and 8-20 ps (lower panel).

Table S21: ISC rate constants of HAP-3MF computed with different correlation function dampings.

Damping [cm^{-1}]	Rate Constant [s^{-1}]	Points	Time [fs]
10	7.68×10^6	65536	25000
5	7.42×10^6	65536	25000
1	7.33×10^6	65536	25000
0.5	7.33×10^6	262144	250000
0.1	7.33×10^6	262144	250000

Table S22: RISC rate constants of HAP-3MF computed with different correlation function dampings.

Damping [cm^{-1}]	Rate Constant [s^{-1}]	Points	Time [fs]
10	3.25×10^5	65536	25000
5	3.16×10^5	65536	25000
1	3.13×10^5	65536	25000
0.5	3.13×10^5	262144	250000
0.1	3.13×10^5	262144	250000

Table S23: IC rate constants of HAP-3MF computed with different correlation function dampings.

Damping [cm^{-1}]	Rate Constant [s^{-1}]	Points	Time [fs]
10	8.61×10^5	524288	25000
5	8.61×10^5	524288	25000
1	8.61×10^5	524288	25000
0.5	8.61×10^5	524288	25000
0.1	8.61×10^5	524288	25000

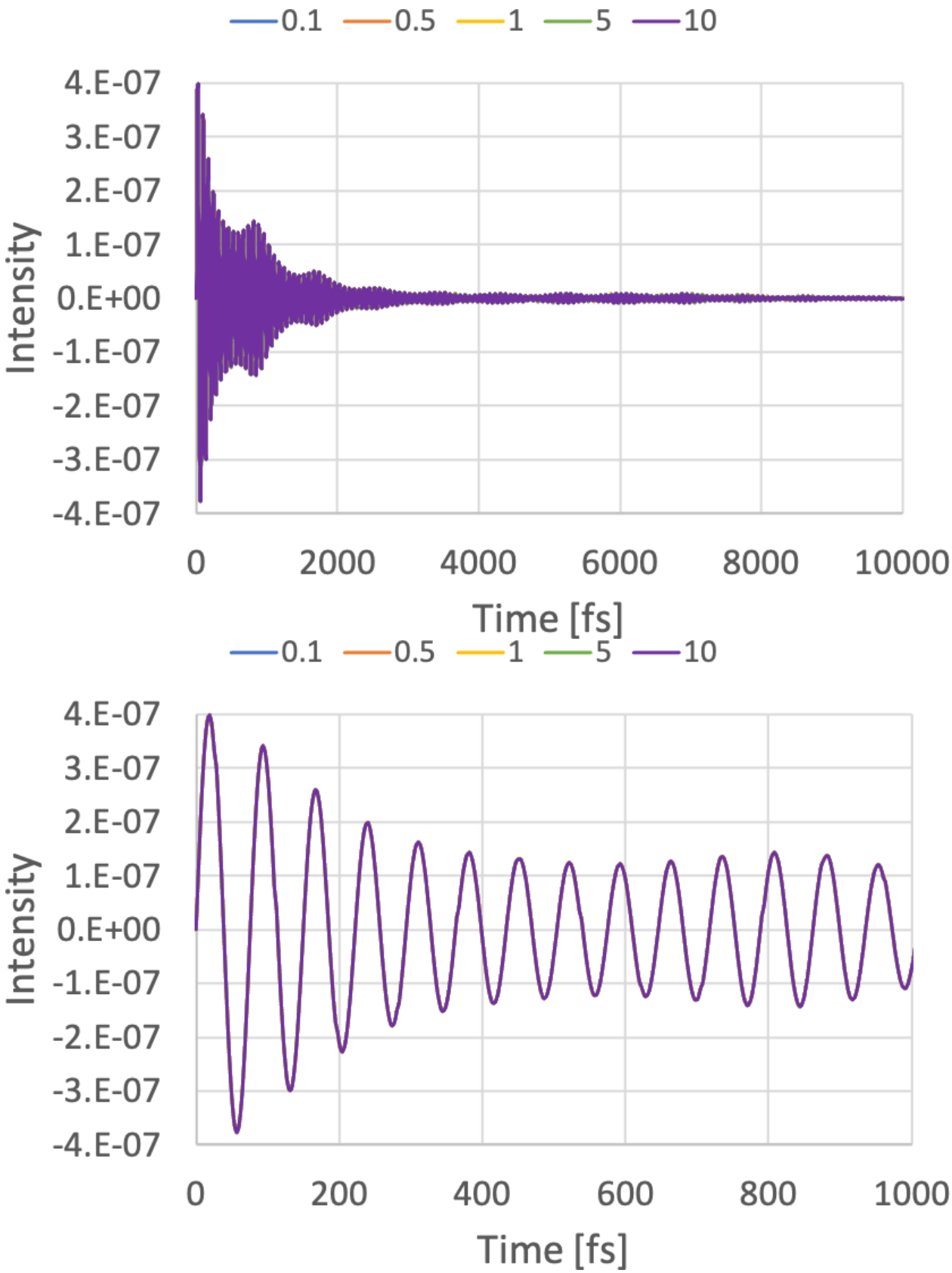

Figure S23: Correlation function of the $S_1 \rightsquigarrow S_0$ IC transition of HAP-3MF computed with different correlation function dampings in the time interval 0-10 ps (upper panel) and 0-1 ps (lower panel).

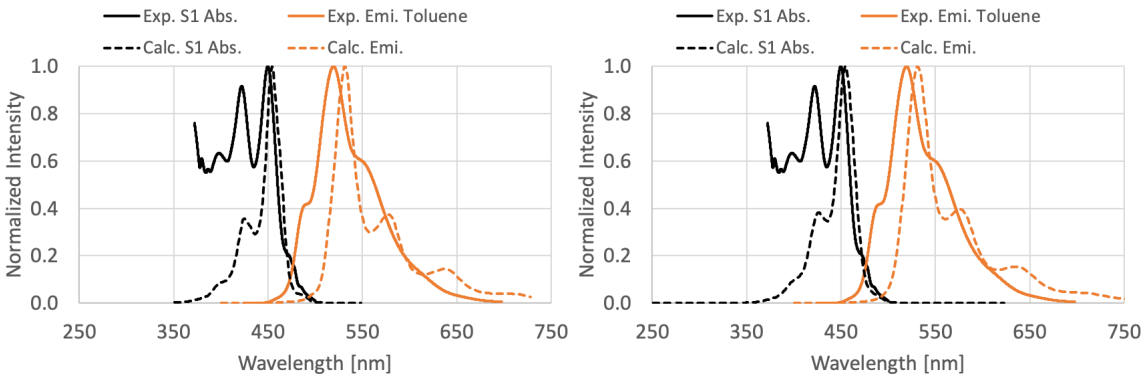

Figure S24: Herzberg–Teller $S_1 \leftarrow S_0$ absorption (black) and $S_1 \rightarrow S_0$ emission spectra (orange) of HAP-3MF computed with damping functions of 100 cm^{-1} (left) and 200 cm^{-1} (right) FWHM.

Table S24: Fluorescence rate constants of HAP-3MF computed with different correlation function dampings utilizing a grid of 16384 points and a integration time of 300 fs.

Damping [cm^{-1}]	Rate Constant [s^{-1}]
200	9.11×10^5
100	9.11×10^5
50	9.11×10^5